

Editors

W. Schröder/Aachen
B.J. Boersma/Delft
K. Fujii/Kanagawa
W. Haase/München
M.A. Leschziner/London
J. Periaux/Paris
S. Pirozzoli/Rome
A. Rizzi/Stockholm
B. Roux/Marseille
Y. Shokin/Novosibirsk

Nature-Inspired Fluid Mechanics

Results of the DFG Priority Programme 1207
“Nature-inspired Fluid Mechanics” 2006–2012

Cameron Tropea and Horst Bleckmann (Eds.)



Springer

Editors

Prof. Cameron Tropea
Technische Universität Darmstadt
FB 16 Maschinenbau
FG Strömungslehre und Aerodynamik
Darmstadt
Germany

Prof. Dr. Horst Bleckmann
University of Bonn
Poppelsdorfer Schloß
Germany

ISSN 1612-2909
ISBN 978-3-642-28301-7
DOI 10.1007/978-3-642-28302-4
Springer Heidelberg New York Dordrecht London

e-ISSN 1860-0824
e-ISBN 978-3-642-28302-4

Library of Congress Control Number: 2012931924

© Springer-Verlag Berlin Heidelberg 2012

This work is subject to copyright. All rights are reserved by the Publisher, whether the whole or part of the material is concerned, specifically the rights of translation, reprinting, reuse of illustrations, recitation, broadcasting, reproduction on microfilms or in any other physical way, and transmission or information storage and retrieval, electronic adaptation, computer software, or by similar or dissimilar methodology now known or hereafter developed. Exempted from this legal reservation are brief excerpts in connection with reviews or scholarly analysis or material supplied specifically for the purpose of being entered and executed on a computer system, for exclusive use by the purchaser of the work. Duplication of this publication or parts thereof is permitted only under the provisions of the Copyright Law of the Publisher's location, in its current version, and permission for use must always be obtained from Springer. Permissions for use may be obtained through RightsLink at the Copyright Clearance Center. Violations are liable to prosecution under the respective Copyright Law.

The use of general descriptive names, registered names, trademarks, service marks, etc. in this publication does not imply, even in the absence of a specific statement, that such names are exempt from the relevant protective laws and regulations and therefore free for general use.

While the advice and information in this book are believed to be true and accurate at the date of publication, neither the authors nor the editors nor the publisher can accept any legal responsibility for any errors or omissions that may be made. The publisher makes no warranty, express or implied, with respect to the material contained herein.

Printed on acid-free paper

Springer is part of Springer Science+Business Media (www.springer.com)

NNFM Editor Addresses

Prof. Dr. Wolfgang Schröder
(General Editor)
RWTH Aachen
Lehrstuhl für Strömungslehre und
Aerodynamisches Institut
Wüllnerstr. 5a
52062 Aachen
Germany
E-mail: office@aia.rwth-aachen.de

Prof. Dr. Kozo Fujii
Space Transportation Research Division
The Institute of Space
and Astronautical Science
3-1-1, Yoshinodai, Sagamihara
Kanagawa, 229-8510
Japan
E-mail: fujii@flab.eng.isas.jaxa.jp

Dr. Werner Haase
Hohenkirchener Str. 19d
D-85662 Hohenbrunn
Germany
E-mail: office@haa.se

Prof. Dr. Ernst Heinrich Hirschel
(Former General Editor)
Herzog-Heinrich-Weg 6
D-85604 Zorneding
Germany
E-mail: e.h.hirschel@t-online.de

Prof. Dr. Ir. Bendiks Jan Boersma
Chair of Energytechnology
Delft University of Technology
Leeghwaterstraat 44
2628 CA Delft
The Netherlands
E-mail: b.j.boersma@tudelft.nl

Prof. Dr. Michael A. Leschziner
Imperial College of Science
Technology and Medicine
Aeronautics Department
Prince Consort Road
London SW7 2BY
U.K.
E-mail: mike.leschziner@ic.ac.uk

Prof. Dr. Sergio Pirozzoli
Università di Roma “La Sapienza”
Dipartimento di Meccanica e Aeronautica
Via Eudossiana 18
00184, Roma, Italy
E-mail: sergio.pirozzoli@uniroma1.it

Prof. Dr. Jacques Periaux
38, Boulevard de Reuilly
F-75012 Paris
France
E-mail: jperiaux@free.fr

Prof. Dr. Arthur Rizzi
Department of Aeronautics
KTH Royal Institute of Technology
Teknikringen 8
S-10044 Stockholm
Sweden
E-mail: rizzi@aero.kth.se

Dr. Bernard Roux
L3M – IMT La Jetée
Technopole de Chateau-Gombert
F-13451 Marseille Cedex 20
France
E-mail: broux@l3m.univ-mrs.fr

Prof. Dr. Yurii I. Shokin
Siberian Branch of the
Russian Academy of Sciences
Institute of Computational
Technologies
Ac. Lavrentyeva Ave. 6
630090 Novosibirsk
Russia
E-mail: shokin@ict.nsc.ru

Preface

This book is the closing report of the national priority program *Nature-Inspired Fluid Mechanics* (Schwerpunktprogramm SPP 1207: Strömungsbeeinflussung in der Natur und Technik). The priority programs of the German Science Foundation (DFG) support broad research topics over a period of up to six years, involving numerous research groups throughout Germany and with a focus on topics which are amenable to strong collaboration between participating groups. Furthermore, topical areas which promise interdisciplinary collaboration are particularly welcome and the present topic – *Nature-inspired Fluid Mechanics* - has indeed been able to meet these expectations. In particular, the funded projects involved colleagues from mechanical engineering, zoology, cell biology, mathematics, physics, motion science, aircraft design and design of lightweight structures, experimental aerodynamics and micro-system technology. As such the program offered a unique and outstanding opportunity for scientific exchange between these disciplines.

Nature-inspired fluid mechanics is one subset of biomimetics, a discipline which has received increased attention over the last decade, with numerous faculties and degree courses devoted solely to exploring ‘nature as a model’ for engineering applications. For instance, rheophilic fish, but also marine mammals, birds and insects are often exposed to unstable air or water currents. To save locomotion energy, evolution has optimized the design of these animals such that friction loss is minimized. In addition to many morphological adaptations, animals that are often exposed to water or air currents have developed special behaviors that allow them to use the energy contained in air or water fluctuations for energy savings. Such flow manipulation and control is not only important for many animals, but also for many engineering applications. Since living beings have been optimized by several million years of evolution it is very likely that many engineering disciplines can profit from the study of systems found in nature. Curiously, there has been little serious cross-disciplinary work and information exchange on the topic of fluid dynamics and flow control and this was the initial motivation to establish this national priority program.

Overall more than 35 principal investigators from approx. 20 German universities were involved in the program from 2006 until 2012, covering a wide range of research topics from fish locomotion to seal vibrissae, flapping and gliding bird flight, human swimming, cell motility, noise reduction, etc. The contributions to this volume summarize the scientific accomplishments of the individual projects, including both past and more recent results. The projects have been grouped into four categories: Locomotion in Liquids, Locomotion in Air, Influencing Drag, and Acoustics.

Complementing the scientific program were a number of measures to promote the interdisciplinary nature of the work and to initiate new projects outside of the national priority program. These included annual colloquia, numerous workshops, and a regular appearance of international guests as keynote lecturers. Furthermore, a forum was established by which researchers, and especially doctoral students, could stay abreast of the most recent developments in the area of experimental fluid mechanics. This was supported by the procurement of advanced imaging and velocimetry equipment for capturing time-resolved and volumetric velocity fields and kinematics of moving surfaces, made available to all participants on a rotational basis according to a booking schedule. Hence, beyond the scientific achievements of the program, a network has been established among researchers throughout Germany which facilitates future cooperation on this topic.

We would like to thank the German Science Foundation for generously supporting this initiative over the past six years and the referees, who were charged with evaluating new and renewal proposals several times over the duration of the program. We also thank Springer Verlag, Heidelberg for the constructive and pleasant collaboration in preparing this volume.

Prof. Dr.-Ing. Cameron Tropea, Technische Universität Darmstadt
Prof. Dr. Horst Blechmann, Universität Bonn

Contents

Part I: Flow Control in Single Cell Organisms

Theoretical and Experimental Investigations of Amoeboid Movement and First Steps of Technical Realisation	3
<i>Wolfgang Alt, Valter Böhm, Tobias Kaufhold, Elka Lobutova, Christian Resagk, Danja Voges, Klaus Zimmermann</i>	
Swimming at Low Reynolds Number: From Sheets to the African Trypanosome	25
<i>Sujin B. Babu, Christian Schmeltzer, Holger Stark</i>	
African Trypanosomes as Model System for Functional Analyses of Microbial Motility	43
<i>Markus Engstler, Niko Heddergott, Tim Krüger, Eric Stellamanns, Sravanti Uppaluri, Thomas Pfohl</i>	

Part II: Flow Control in Insects and Birds

Wake Structure and Vortex Development in Flight of Fruit Flies Using High-Speed Particle Image Velocimetry	65
<i>Fritz-Olaf Lehmann</i>	
Experimental Quantification and Numerical Simulation of Unsteady Flow Conditions during Free Flight Maneuvers of Insects	81
<i>Andrei Shishkin, Peter Schützner, Claus Wagner, Fritz-Olaf Lehmann</i>	
Barn Owl Flight	101
<i>Thomas Bachmann, S. Blazek, T. Erlinghagen, W. Baumgartner, H. Wagner</i>	
Flow Field Analysis and Contour Detection of a Natural Owl Wing Using PIV Measurements	119
<i>Andrea Winzen, Stephan Klän, Michael Klaas, Wolfgang Schröder</i>	

Shape and Deformation Measurement of Free Flying Birds in Flapping Flight	135
<i>Wolf Thomas, Konrath Robert, Erlinghagen Thomas, Wagner Hermann</i>	

A Discussion on Vortex Growth and Saturation in Dragonfly-Inspired Flight	149
<i>David E. Rival, Alex Widmann, Cameron Tropea</i>	

Part III: Flow Control in Fish, Dolphins and Seals

Station Holding of Trout: Behavior, Physiology and Hydrodynamics	161
<i>Horst Bleckmann, A. Przybilla, A. Klein, A. Schmitz, S. Kunze, Christoph Brücker</i>	

Learning from Dolphin Skin – Active Transition Delay by Distributed Surface Actuation	179
<i>Andreas Pätzold, Inken Peltzer, Wolfgang Nitsche</i>	

Development and Fabrication of Active Microstructures for Wave Control on Airfoils	193
<i>Daniel Haller, Sebastian Neiss, Michael Kroener, Peter Woias</i>	

Learning from Dolphin Skin – Drag Reduction by Active Delay of Transition: Flow Control by Distributed Wall Actuation	207
<i>Nikolas Goldin, Rudibert King</i>	

Linear-Stability Investigations for Flow-Control Experiments Related to Flow over Compliant Walls	223
<i>Marcus Zengl, Ulrich Rist</i>	

Analysis of the Relation between Skin Morphology and Local Flow Conditions for a Fast-Swimming Dolphin	239
<i>Vadim Pavlov, Donald Riedeberger, Ulrich Rist, Ursula Siebert</i>	

Hydrodynamic Perception in Pinnipeds	255
<i>Wolf Hanke, Sven Wieskotten, Benedikt Niesterok, Lars Miersch, Matthias Witte, Martin Brede, Alfred Leder, Guido Dehnhardt</i>	

On the Wake Flow Dynamics Behind Harbor Seal Vibrissae – A Fluid Mechanical Explanation for an Extraordinary Capability	271
<i>Matthias Witte, Wolf Hanke, Sven Wieskotten, Lars Miersch, Martin Brede, Guido Dehnhardt, Alfred Leder</i>	

Part IV: Flow Control in Human Swimmers

Experimental and Numerical Investigation of the Unsteady Flow around a Human Underwater Undulating Swimmer	293
<i>Stefan Hochstein, Steffen Pacholak, Christoph Brücker, Reinhard Blickhan</i>	

**Part V: Flow Control with Aid of Compliant Walls,
Airfoils, Wave-Like Riblets**

Influence of Wave-Like Riblets on Turbulent Friction Drag	311
<i>René Grüneberger, Felix Kramer, Erik Wassen, Wolfram Hage, Robert Meyer, Frank Thiele</i>	
Aerodynamics and Structural Mechanics of Flapping Flight with Elastic and Stiff Wings	331
<i>Stephan Bansmer, Nadine Buchmann, Rolf Radespiel, Ralf Unger, Matthias Haupt, Peter Horst, Ralf Heinrich</i>	
Nature-Inspired Porous Airfoils for Sound Reduction	355
<i>Thomas Geyer, Ennes Sarradj, Christoph Fritzsche</i>	
Author Index	371

Part I

**Flow Control in Single Cell
Organisms**

Theoretical and Experimental Investigations of Amoeboid Movement and First Steps of Technical Realisation

Wolfgang Alt, Valter Böhm, Tobias Kaufhold, Elka Lobutova, Christian Resagk, Danja Voges, and Klaus Zimmermann

Abstract. We report about the investigation of the amoeboid locomotion at *Amoeba proteus*. Based on the detailed experimental study of the internal cytoplasm flow and the variation of the contour of the amoeba with optical flow measurement techniques like particle image velocimetry (PIV) we found characteristic velocity fields and motions of the center of mass. Furthermore a peripheral cell model is developed, in which a contractile backward flow of actin-myosin in the cortex stabilizes cell polarity and locomotion by inducing more protrusions in the front and stronger retraction in the rear. The results from the experimental and theoretical study were used to realise prototypes of locomotion systems, composed of silicon elastomer body with controlled elasticity and driven by a magnetic system, based on amoeboid motion principles.

1 Introduction

Amoeba proteus is the classic specimen to study amoeboid movement. The genus Amoeba (aquatic or parasitic) is a representative unicellular organism with a cell membrane, a thick cortical gel layer (ectoplasm), an endoplasm (sol) and many endogenous particles like lipid bodies or food vacuoles.

Amoeboid movement is ubiquitary in the animal kingdom (protozoa, slime molds, leukocytes...). It is the most common type of movement characterised by

Valter Böhm · Tobias Kaufhold · Elka Lobutova · Christian Resagk · Danja Voges

Klaus Zimmermann

Faculty of Mechanical Engineering, Ilmenau University of Technology, P.O. Box 100565,
98684 Ilmenau, Germany

e-mail: klaus.zimmermann@tu-ilmenau.de

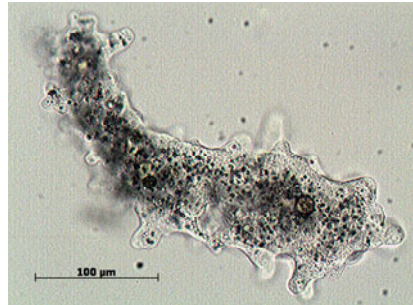
Wolfgang Alt

Theoretical Biology, IZMB, University of Bonn, Kirschallee 1, 53115 Bonn, Germany

e-mail: wolf.alt@uni-bonn.de

cytoplasmic streaming and continuous changing the body shape, let's call it *shape variability*. Three main phases of amoeboid locomotion can be defined: a) protrusion (extension of pseudopodia), b) attachment (connection to substratum), and c) traction (forward movement of body) [1, 2, 3]. Pseudopodia (number not fixed) can build at any region of the body (Fig. 1). This is a continuous process which can in general be described by *local changes in the mechanical compliance of the cell cortex*.

Fig. 1 Amoeba proteus



Since more than 200 years scientists explore the phenomenon of cytoplasmic streaming, its reasons and physical mechanism. Obviously involved is an interaction of the actin-myosin-complex, calcium-ions, actin-binding proteins, osmotic pressure and the sol-gel transformation during crawling of amoeba [4, 5, 6].

Less described in detail in the literature are the properties of the cytoplasmic streaming. In this work we will take a look at the amoeba from the fluid mechanical point of view in order to find new motion parameters and fluid properties for the modelling of the amoeboid locomotion and for the development of prototypes for robotic applications. To realise technical locomotion systems based on amoeboid movement a systematic modelling of the biological object is meaningful and help to find important system properties. In particular, we have explored the viscous-reactive-contractive two-phase cytoplasmic flow model with moving cell boundary and adhesion kinetics [7, 8] in a simplified geometry of a circular cell with peripheral protrusions and cortical flow.

Terrestrial locomotion systems are dominated by systems with legs and wheels, but they have a limited field of application. Future robots with high mobility require the use of new, non-conventional locomotion principles, which can be satisfactorily applied to specific tasks (e.g. inspection). Biologically inspired technical locomotion systems are developed due to the paradigms worms and snakes [9], [10]. Because of deficits of motion in difficult terrains the investigation of amoeboid locomotion is of special interest and importance in developing mobile robots. For an engineer this principle of locomotion offers a fascinating characteristic: the possibility to combine the function of locomotion and manipulation for systems operating in difficult terrains [11].

2 Investigation of the Amoeboid Movement Using Micro Particle Image Velocimetry (μ PIV)

2.1 Materials, Methods and Experimental Setup

A. proteus was ordered from science Supply Company¹ and carried in a laboratory in mineral water with pH 7.0 and 2% soil water medium. Amoeba is fed on *Chilomonas*. Individuals were transferred to a micro-slide together with some drops of the original culture medium. The IBIDI² μ -slide was then placed on the stage of the microscope ready for the experiment and left for about 10 min before the beginning of the observations. This allowed the amoeba to adapt to the new conditions.

Common micro particle image velocimetry (μ PIV) is used to measure the cytoplasmic streaming and the movement of the amoeba. With this optical flow measurement technique a thin plane of the fluid with tracer particles is illuminated and the images of the tracer particles are recorded by a digital camera through an optical imaging system. From the cross-correlation function of image pairs with known temporal displacement the velocity of the tracer particles can be reconstructed resulting in a 2D vector plot of the fluid velocity field [12].

In our case we used an inverted microscope in the phase-contrast mode as the imaging system and the microscope's own halogen lamp for the illumination. Dependent on the depth of field of the microscope lens the measurement volume had a height of less than 10 microns. The granules of the cytoplasm are best suited as natural tracer particles. Their size is about 5 μm . Videos were taken by a 1.4 Mpix monochrome microscope camera at a rate of 12 frames per second.

The experimental setup of the μ PIV measurement is shown in Fig. 2. It consists of a MOTIC AE31 inverted microscope in the phase contrast mode, an IBIDI μ -slide with 50x50x0.4 mm³ size and a MOTICAMP PRO 1.4 Mpix CCD camera. A desktop computer with ILA VidPIV software was used for image processing and PIV analysis. A dc power supply provides the voltage to two platinum electrodes at both ends of the water-filled μ -slide and a current meter is used to control the electrical field in the slide.

2.2 Results

2.2.1 Movement of *A. Proteus* in an External Electric Field

A. proteus is moving using pseudopodia. Normally there is more than one pseudopodium at the same time. The movement is not intense and has no preferred direction. In order to stimulate the movement of the amoeba in a certain direction, it was exposed to dc electric field during the measurements. A comparison between free moving amoeba and amoeba in electric field is shown in Fig. 3.

¹ Lebendkulturen – Schulbedarf, 83209 Prien, Germany

² www.ibidi.com

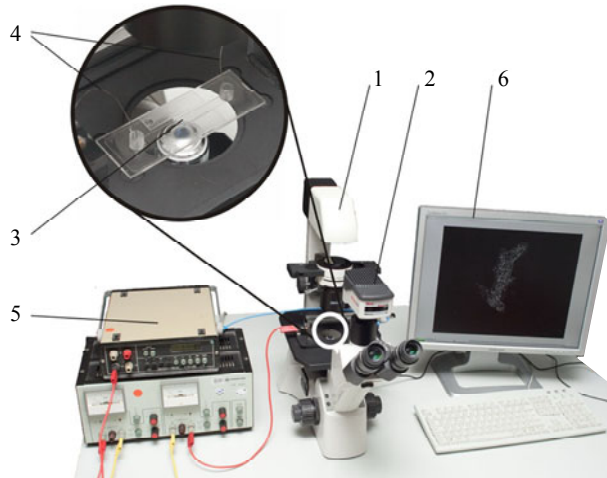


Fig. 2 Experimental setup for the μ PIV measurements in a micro-channel applying a dc electric field. 1 – MOTIC AE31 phase contrast inverted microscope, 2 – MOTICAM PRO 385C 1.4 Mpix ccd camera, 3 - IBIDI μ -slide 50x5x0.4 mm³, 4 – Platinum electrodes for applying a dc electric field, 5 – dc source, 6 – data processing.

Exposed to dc electric field amoeba typically migrate towards the cathode [13, 14]. The strength of the electric field was estimated with a method commonly used in research involving cell electrophoresis in cylindrical or rectangular chambers [15, 16]. The field strength $E = I / \sigma A$, where I is the current in Amperes [A], σ is the electrical conductivity of the medium in Siemens per centimetre [$S\text{cm}^{-1}$] and A is the cross-section area of the chamber in cm^2 . The current intensity used in our experiments was in the range of 0.026 mA – 0.029 mA. And the resulting field strength $6.5 \text{ Vcm}^{-1} – 7.25 \text{ Vcm}^{-1}$.

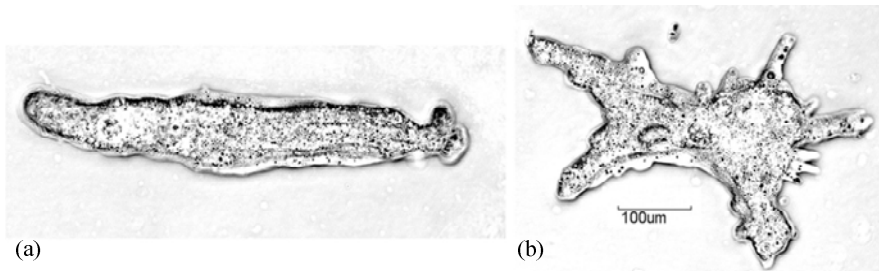


Fig. 3 Comparison between microscope image of *Amoeba proteus* with horizontal electric field (a) and without electric field (b).

However we observed that there is no change in the velocity field in the cytoplasm at different strengths of the electric field until the damage threshold leading to a galvanic disruption of the amoeba. The presence of electric field influenced only the direction of the internal cytoplasm flow. Fig. 4 and Fig. 5 show the magnitude of flow velocity in amoeba without and with an applied electric field. The strength of the field is 6.5 Vcm^{-1} and will be used as a boundary condition for all further discussion in this contribution.

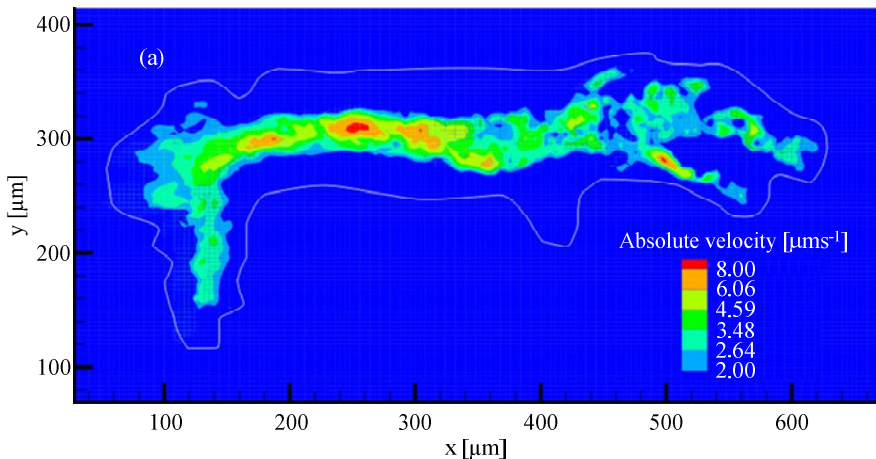


Fig. 4 Magnitude of the cytoplasm velocity in the amoeba without electric field, in the x-y-plane. The velocity field is averaged over 98 single frames.

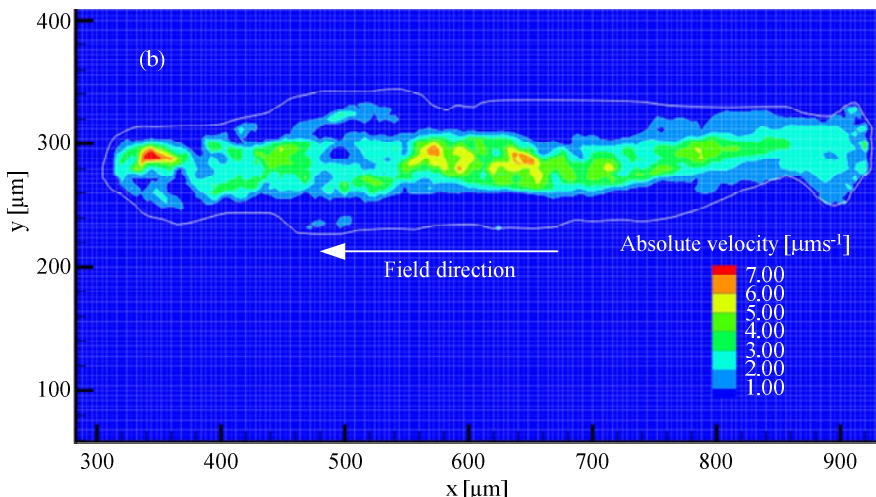


Fig. 5 Magnitude of the cytoplasm velocity in the amoeba with electric field, in the x-y-plane. The strength of the field is 6.5 Vcm^{-1} . The velocity field is averaged over 98 single frames.

2.2.2 Internal Cytoplasm Flow

Using μ PIV we successfully measured the whole velocity field within a crawling amoeba, see Fig. 6. The spatial resolution of the measurement is 4 μm and the temporal resolution is 83 ms.

The velocity profiles from different cross-sections show the intersection of the inner liquid part of the cytoplasm (endoplasm) and the outer viscoelastic layer of the cytoplasm (ectoplasm), Fig. 7 c and d. In contrast to the velocity profiles in the front part the profiles in the rear part of the amoeba are more flat, and there is no clear boundary line between liquid and viscous layers, Fig. 7 a, b, e and f.

If we compare the velocity magnitude of the cytoplasm flow in the front and in the rear part of the amoeba (Fig. 4 – Fig. 7) we observe a much lower velocity in the rear part. With $3 \mu\text{ms}^{-1}$ it is only half as large the cytoplasm flow in the front section. The higher cytoplasm velocity in front of the moving amoeba can be explained with the development of a pseudopod. Therefore the amoeba needs to pump cytoplasm from the rear part to the front part using a kind of hydrostatic pump. This pumping mechanism is thought to be based on a sol-gel transformation in the cytoplasm, inducing the formation of a viscoelastic contractile actin cortex “gel” at the lateral and rearward boundaries and a simultaneous forward flow of the bulk “sol” fluid.

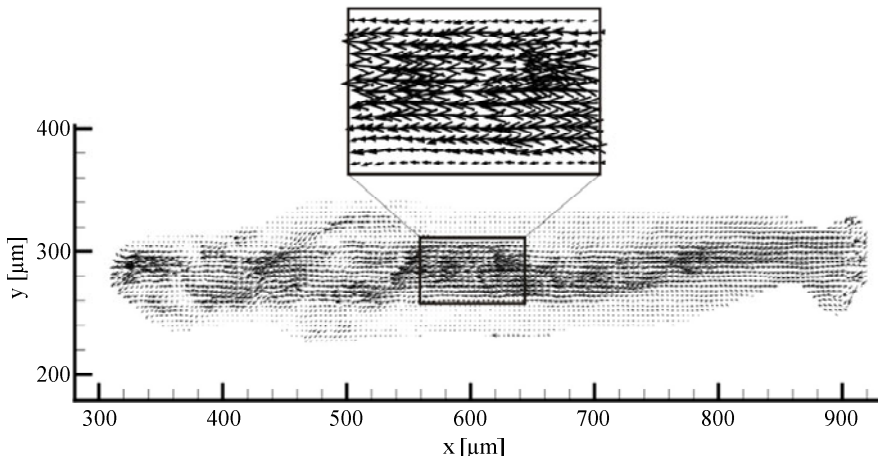


Fig. 6 Vector field of the cytoplasm flow of an amoeba. It is averaged over 98 single frames.

The velocity profile averaged over 400 single frames at the central part of the amoeba shows, in agreement with the findings from Rogers et al. [1], a parabolic profile in the inner part of the cross section and constant velocity in the outer part (Fig. 8a). The latter we can explain a slow forward movement of the viscoelastic ectoplasm (cortex).

We measured not only the internal flow of the cytoplasm but also studied the movement of the amoeba body using image processing methods. In Fig. 8b the

movement of the center of mass of the amoeba exposed to the electric field is plotted over the time. As result we see a strongly linear movement with a velocity of $3 \mu\text{ms}^{-1}$. This velocity is half as large as the maximum internal instantaneous velocities and 66% of the averaged cytoplasm velocity at the center of the amoeba.

In Fig. 9 time series of the maximum cytoplasm velocity at different positions of the center line are plotted. We find velocity fluctuations up to $10 \mu\text{ms}^{-1}$,

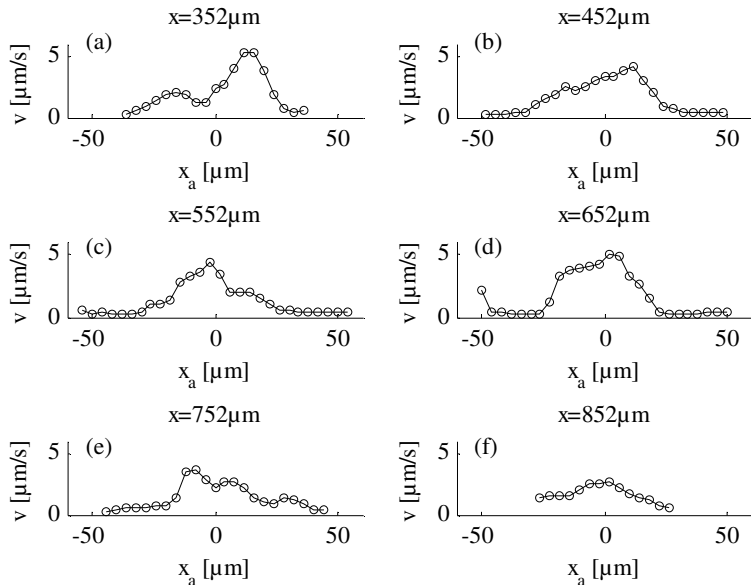


Fig. 7 Velocity profiles at different cross-sections of an amoeba. The profiles are extracted from the 2d vector plot in Fig. 6.

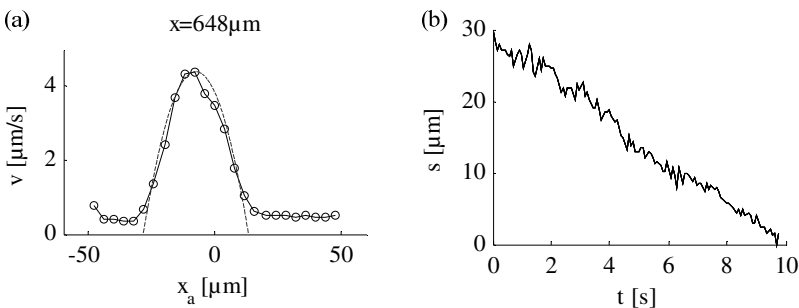


Fig. 8 Velocity profile from the central part of the amoeba averaged over 400 single frames (a). Path of the center of mass of the amoeba (b).

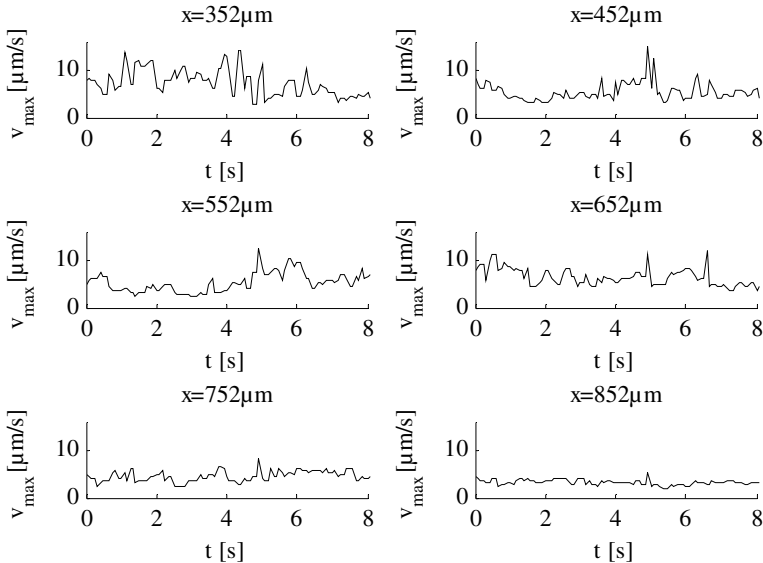


Fig. 9 Time series of the maximum cytoplasm velocity at different positions, revealing less fluctuations in the rear.

especially in the front part of the amoeba where a pseudopod is developing. Less fluctuations in the rear part are indicating a higher hydrostatic pressure during the pumping process.

3 Cellular Motion and Cytoplasmic Flow

3.1 Principles of Amoeboid Cell Locomotion

With the challenge to construct artificial locomotive devices that resemble biological cell motion and are able to translocate in viscous media or on adhesive substrates, the question is repeatedly posed, whether various types of unicellular motion occurring in different species or at different places in multicellular organisms are based on a joint general principle or not. For example, the “amoeboid”-type cell motion of slime mold cells (*Dictyostelium*) or blood cells (leukocytes) often is distinguished from the “mesenchymal”-type motion of tissue cells (fibroblasts or keratinocytes) [17].

In the former case, thicker pseudopodia-like protrusions extend, particularly into 3-d media, resembling the lobopodia of true amoeba cells and often revealing a visible outward flow of cytoplasm and organelles (see the experimental flow results in section 2.2 above, and the sketch Fig. 10 left).

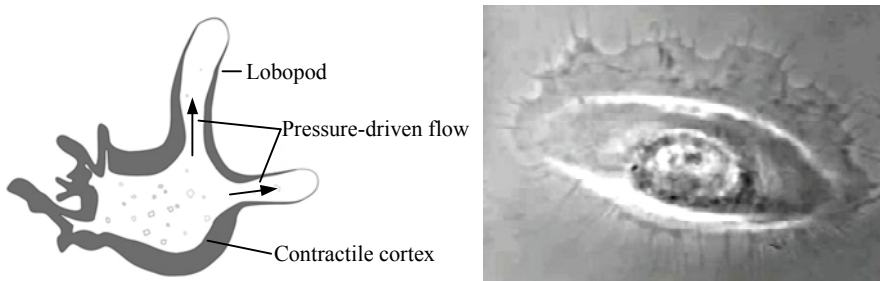


Fig. 10 left: Locomotion mechanism of amoeba, after [1]; **right:** Human epidermal keratinocyte [18].

In the other case, 1-d filopodia protrude along the contacting substrate and are followed by broader flat (almost 2-d sheets of) lamellipodia, often revealing ruffles at their upper surface, which eventually are pulled backwards to the cell center together with an observable centripetal actin filament flow (Fig. 10 right: “forward front” at the top), whereas at the rear attaching fibers are retracted (Fig. 10 right: at the bottom).

However, this seemingly contrasting observation of “forward” versus “backward” flow is more due to the different scales and structural morphologies of these cells, rather than to principle differences in the underlying physical mechanism. Fore, independently of the kind of resistance in the surrounding medium caused by motion and forces at the cell boundary (3-d viscous medium flow around a rigid cell border, or gliding cytoplasmic flow along a rigid cell-substrate adhesion layer), there appears the basic common feature of viscous (or viscoelastic) two-phase flow of the intracellular cytoplasm: namely by spatial/structural differentiation into more rigid “ectoplasm” (“cytogel”, contractile cortex) and more fluidlike “endoplasm” (“cytosol”, containing solutes and smaller filaments or organelles), as detailed profiles of Fig. 7; or, in the case of tissue and blood cells, by a mixed two-phase system of a highly viscous “filament network phase” (“actin cytoskeleton”) embedded into an “aqueous phase” (“cytosol” containing only solutes and monomers). In both cases, the protrusion of a pseudo- or lamellipod usually involves a counter-flow of cytosol forward/outward and of cytogel/network backward/inward.

3.2 Two-Dimensional Model of Cell Locomotion

In this project we restricted the investigation of such basal mechanisms to the simpler case of cell translocation in a two-dimensional situation, when cells or artificial devices migrate along a flat substratum, to which they adhere in a more or less strong manner, e.g. by weak attraction forces or via diffusible trans-membrane proteins as integrin, which can bind to both substratum and cytoskeleton, thereby serving as force transducing anchoring spots.

Interestingly, even cell “fragments”, that have been disrupted from broad cell lamellae, are likewise able to perform a directionally persistent migration on the substratum, once they have attained a polarised shape, for instance after pushing them at one side [19]. This again proves that the phenomenon of (at least transient) cell polarization and translocation must rely on relatively simple physical-chemical principles, not dependent on “central” control via gene expression. Clearly, a whole series of regulating proteins as Rho or Rac could be responsible to establish and maintain chemical gradients across the cell, which control cell polarity and, thus, also the actual direction of cell migration. Indeed, corresponding mathematical models have been proposed and analyzed in order to explain the observed cell shapes and locomotion paths of single cell random motion and chemotaxis, see e.g. [20] and [21].

However, earlier simulation results for the reactive two-phase flow model developed by M. Dembo and W. Alt [7], have proven that spontaneous or induced cell polarity and subsequent cell migration can be reproduced without assuming any additional regulating proteins, just by considering the spatial-temporal kinetics of adhesion and force application to the substratum. For a two-dimensional simulation result see [8], for a one-dimensional [18]: both simulation models have been developed within a VW-project “Coupling of cytoplasm dynamics and adhesion kinetics”. In the 1-d model (Fig. 11) the force distribution within a polarised cell shows a high maximum near the rear and a low plateau at the front (red curve in Fig. 11).

This modelling and simulation result is consistent with a long-standing observation by Jürgen Bereiter-Hahn, that cells migrating on adhesive substrates are “softer” in their front parts compared to their rear parts [23]. In a case study we have tried to prove, whether such a principle can be used as the general basis for simulating spontaneous cell polarization and translocation in a simplified biomimetic “model cell”. In its most elementary version, the model cell consists of an elastically deformable membrane, filled with a viscous internal fluid and embedded into an external medium that could also be a viscous fluid. When a membrane surface element is freely moving, it experiences a viscous (or frictional) drag and equilibrates in shape due to relatively low (“soft”) surface tension; however, as soon as it touches the substrate surface (anteriorly), then adhesion starts to alter its tensile properties to a higher (“hard”) value. The important assumption to be made is that both processes “softening” and “hardening” have certain time constants: thus, when an attached elastic surface element happens to become located near to the (posterior) edge of the contact zone, due to stronger surface tension the probability of disruption from the substrate increases. Once this asymmetric “hardness” distribution beneath the cell is created (e.g. by randomly induced translocations) then translocation towards the “softer” front is enhanced which, in a positive feedback, stabilises the driving “hardness” gradient, thus cell polarization and migration is established.

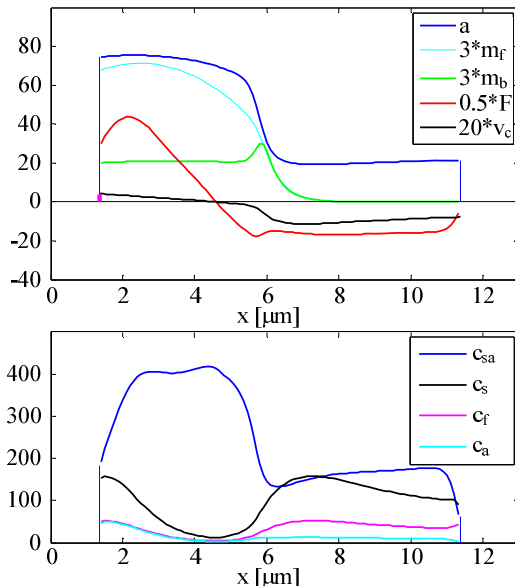


Fig. 11 Cell polarization (tip to the right) showing distributions of F-actin (a), free and bound myosin (m_f and m_b), substrate force (F), retrograde flow (v_c) and, in the lower picture, the four states of integrin, particularly the substrate-and-actin bound focal adhesions (c_{sa}), from [22]

In a 2-dimensional section model the “model cell” is just given by an elastic chain, so that a suitable choice of model parameters gives rise to an autonomous forward motion (Fig. 12). Note that the only energy needed to drive this adhesive cell motion is the active “hardening” of the elastic chain points during attachment to the surface, the reverse process of “softening” on top of the moving cell can be purely passive. The effect of the local energy input at the contact area induces a global deformation of the chain and a corresponding flow of the internal fluid from the more stretched posterior side into the more protruded anterior side of the “model cell” (Diploma thesis by Jörg Bandura [24]; further treatment and generalization of this model is currently performed within the DFG-Graduiertenkolleg “Bionik – Interaktionen an Grenzflächen zur Außenwelt” at the University of Bonn).

Since this principle of spontaneous motility by adhesion-induced spatial-temporal gradients had been established in a simplified cross-sectional 2-d model, but without explicitly considering the fluid flow inside or around the “model cell”, within this project we elaborated a complementary modelling framework in generalization of an earlier model [25], namely a two-layer cytoplasm model (Fig. 13)

for moving cells on a substratum, so that in a top-view the dynamics of 2-d cytoplasm flow becomes restricted to the lamellipodial seam around the circular cell body (Fig. 14). This can be realistically applied to cell types mentioned above, in particular to human epidermal keratinocytes, which have been experimentally and theoretically investigated in our group.

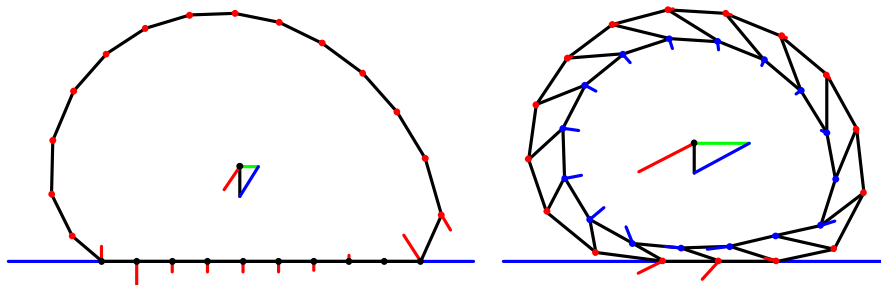


Fig. 12 left: Single-chain “model cell” with 24 elastic nodes connected by bending springs, which “harden” when attached and “soften” when moving free. (red lines: force vectors, green bar: forward velocity); **right:** Double-chain “model cell” with 32 elastic nodes connected by lateral and segmental springs; the latter “harden” when the outer segment is attached and “soften” when it moves freely (blue lines: free force vectors, red lines: attached forced vectors, green bar: forward velocity, from [24]).

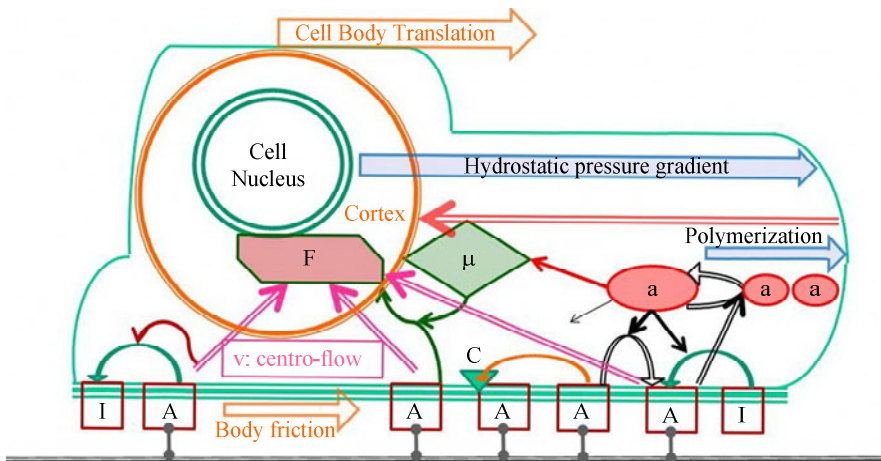


Fig. 13 Sketch (vertical slice) of a cell adhering to a substrate (via adhesion proteins, A, that are activated integrin molecules, I), migrating to the right hand side due to asymmetric force distribution within a cytoplasmic ‘centro-flow’ (strong at the rear and soft in the advancing lamella). Driving forces (in the upper cytoplasmic cell layer) for cell protrusion is the sum of a hydrostatic pressure gradient and additional pressure at the tip, induced by polymerizing actin filaments (a). Transduction of forces (F) to the cell body is mediated by the contractile action of myosin (μ).

3.3 Lamella Polarization and Cell Migration

The developed “peripheral cell model” with variable radial lamella extension around the circular cell body and reaction-transport-diffusion equations for all relevant protein concentrations (F-actin, integrin/cadherin bound to the moving tip, myosin attached to actin filaments) gives rise to spontaneous polarization of the lamella shape and persistent forward motion of the cell body.

Focal adhesions (bright pixels in Fig. 14), complexes of substrate bound integrins together with an associated actin filament layers (viscously coupled to the retrograde cytoplasmic flow) dynamically change their strength, but stay fixed to the substrate. Thus, relative to the migrating polarised cell, this adhesion layer includes a “backward flow” around the cell body (Fig. 14 left).

Moreover, additional modelling of the contractile actin-myosin network in the cell body periphery induces a related cortical “backward flow” towards the rear of the cell, where the network attains its highest concentration (in Fig. 14 right). Both these flows around the cell body are energy driven (by active adhesion and contraction, respectively) and thereby maintain the established cell polarity.

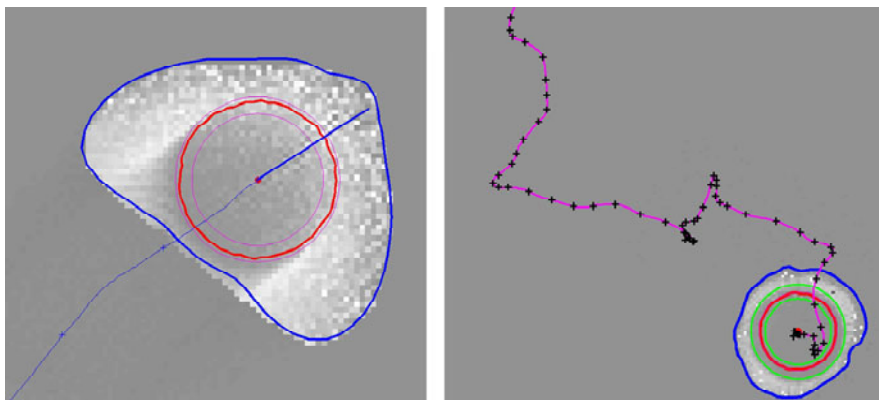


Fig. 14 Simulation runs of the “peripheral cell model” with circular cell body (magenta) and moving lamellar tip (blue). **Left:** Cell polarization and persistent cell translocation due to non-symmetric lamella shape and adhesion site distribution; **right:** Longer run revealing a transiently persistent random walk with interrupting phases of cell stagnation and reorientation.

Due to thermic fluctuations in lamellipodial protrusion and/or substrate binding, the polarised cell migration state is only transiently stable, so that after randomly distributed times of directionally persistent (“almost straight”) forward motion, cell polarization breaks down, translocation and backward flows slow down. Then, after a randomly distributed “stopping time”, spontaneous repolarization and migration starts into a new direction, randomly distributed around the former (see Fig. 14 right). Statistical correlation analysis of the induced directionally persistent random walk can be performed according to an established model

framework. The related simulations and statistical evaluations are contained in the currently finished Bachelor thesis of the student coworker of our project, Benjamin Schneid [26].

4 Selected Aspects of Technical Realisation

From the technical point of view the most relevant advantage of amoeboid locomotion is due to the large shape variability (I), the primary target of known developments is the adaptation of this property. In the biological model shape variability is based on an intrinsic mechanical compliance (II). The implementation of this property in technical systems is also advantageous, because it allows their simple construction. Further important features are that the locomotion is induced by a single drive mechanism (III), and that the direction of locomotion is defined by local change of the mechanical compliance (IV).

In current robotic research, however, trials to adapt amoeboid locomotion is dominated by systems consisting of a large numbers of elementary locomotor units (systems of type A) representing amoeboid behaviour only as a swarm [27, 28]. To avoid the disadvantages of these systems, such as multiple complex construction and distributed control effort, recently first studies of amoeboid locomotion systems as single locomotor units (systems of type B) have been presented. The locomotion of these systems is based on their deformability. The first group of these systems consists of a conventional cascaded planar set of elements, which are able to change their length and/or their mechanical compliance [29], [30]. In the latter case a global drive provides the change of the element lengths. Shape variability of systems in the second group is based on their intrinsic mechanical compliance as in the biological model [31, 32, 33]. Possible realization strategies for these systems are (sorted with increasing abstraction):

- internal fluid flow (pressure gradient) in the whole body without/with locally variable mechanical compliance, which induces the deformation of the body (type B/I);
- uniform pressure in the whole body with locally variable mechanical compliance, whereby the local change of compliance causes deformation of the body (type B/II), compare the cell robot model in section 3.2;
- locally differing deformation of a compliant body without/with change the mechanical compliance (type B/III).

Realization of systems of type B/I would need very strong efforts, so that hitherto known systems are those of type B/II or B/III. These systems primarily use electro-active polymers (EAP), shape memory alloys (SMA) or ionic polymer-metal composites (IPMC) as actuators or pneumatic/hydraulic drives. They all require large numbers of actuators with partly large time constants. Alternatively, the implementation of magnetic-based actuators in combination with elastomeric materials offers new actuation possibilites for robotic applications [34, 35] as well as amoeboid locomotion systems. This combination allows higher actuation forces as

well as an increased deformation range while the response time is being reduced. These robots are actuated by shifting elastomeric structure parts, with integrated NdFeB magnets, due to a magnetic force. The magnetic force is generated by external or integrated solenoids. Also several advantageous properties offer the application of magneto-sensitive elastomeric materials: magneto rheological elastomers (MRE) and elastomer–ferromagnetic composites (EFC) [36, 37]. These materials are composites consisting of small magnetic particles dispersed in a highly elastic polymeric matrix. In contrast to other compliant materials a complex deformation of these materials can easily be achieved with inhomogeneous magnetic fields.

In the following, two planar miniaturized locomotion systems are considered based on magnetic actuation offering type B/III. Both variants are characterized by a marked flexibility, a simple construction and an integrated actuation mechanism. As a first example we investigate an amoeboid locomotion system on the basis of a magneto-sensitive elastomer without change the mechanical compliance. As a second one a locomotion system with variable mechanical compliance is introduced, showing principal similarities with the previously described rotating cell robot model (Fig. 12).

4.1 Prototype 1

The prototype 1 only consists of two components: a symmetric magneto-sensitive elastomeric body and six embedded solenoids: the combination of micro-coils and MSE-structures allows a simple system design (Fig. 15) [11]. The locomotion of the system is based on a periodic deformation of a compliant magneto-sensitive elastomeric body, generated by integrated micro-coils. A periodically alternating magnetic field causes an oscillation of the compliant body. The friction forces between the substratum and the system changes periodically, locally repeating and simultaneously in several segments. The coils, in combination with the mechanical compliance of the MSE-structure, generate complex vibration modes and the performed locomotion is highly depending on the driving frequency. To analyse this specific behaviour, geometric nonlinear transient structural finite element analyses were carried out with the software package ANSYS v12.1, according to the high vibration amplitudes of the MSE-structure. For testing locomotion of the system an elementary load case was analysed by actuating two micro-coils simultaneous. The numerical simulations indicate that the system moves along the symmetry axis of the excited micro-coils. The obtained results, focusing on the velocity of the centre of mass in dependence of the driving frequency, are shown in Fig. 15. By activating the micro-coils at different positions the system is able to move in the plane because of its symmetric design. Furthermore, locomotion along a curved path is made possible by an asymmetric excitation of selected micro-coils.

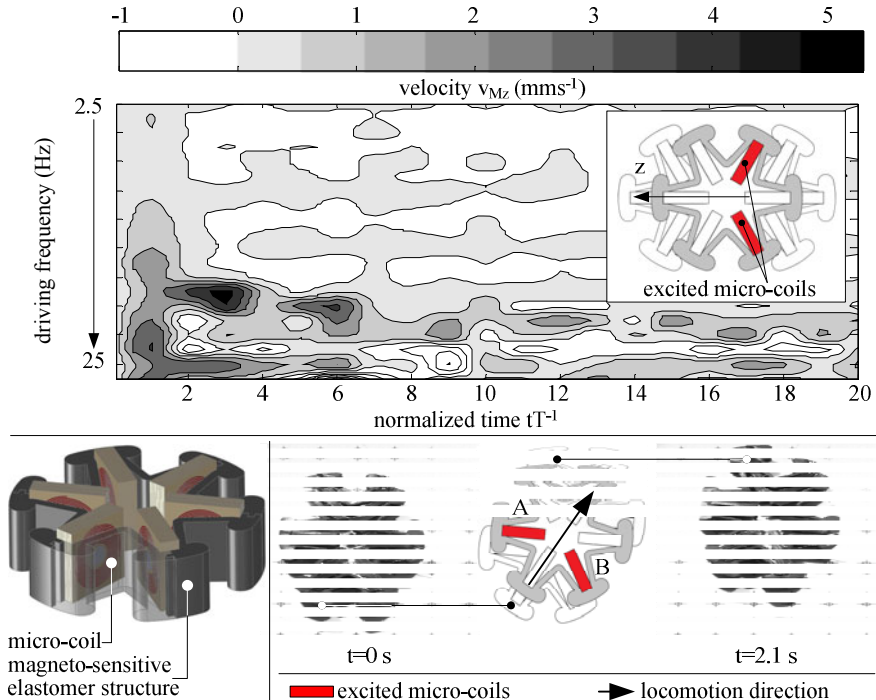


Fig. 15 top: Velocity of the simulated robot in dependence of the driving frequency (actuation: square wave signal with duty cycle 25%); **bottom left:** basic configuration of the prototype (dimensions: 40 mm x 40 mm x 12 mm, mass: 14.4 g); **bottom right:** snapshots of the motion at the driving frequency $f=20 \text{ Hz}$

Fig. 15 shows the assembled prototype. The MSE-structure was created by adding carbonyl iron particles (particle size 6 μm) to liquid silicone elastomer with a weight ratio of 75%. As mentioned before, high performance micro-coils (manufactured by Wuerth Elektronik GmbH & Co. KG with Falt-Flex-technology, layer count: 34, turns: 195, conductor cross-section: 0.014 mm^2 , resistor: 12.5 Ω) were integrated into the prototypes to generate the electromagnetic forces on the MSE-structure. Because of the large permitted current density of more than 50 A mm^{-2} at short time rating the micro-coils (dimension: 11.5 mm x 11.7 mm x 3.1 mm), combined with iron cores, are able to achieve magnetic fields of more than 100 mT. The coils were triggered by periodic square wave signals with 50% duty cycle (input voltage $U=24 \text{ V}$) to achieve locomotion of the prototypes. The maximum average speed of the system is 5 mm s^{-1} attained at a driving frequency $f=20 \text{ Hz}$.

Based on the experimental results, it is possible to realise a more advanced planar locomotion system, in which only three symmetrically arranged coils are used as actuators, because the acting force of only one coil is sufficient to achieve forward movement of the system [38]. With modification of the geometry of the

MSE-structure, it would even be possible to realise planar locomotion systems with only one actuator.

4.2 Prototype 2

By the design of the second prototype three advantageous properties of the biological locomotion principle were taken into consideration. Similar as the prototype 1, this system is based on the periodic asymmetric deformation of a compliant body. The periodic deformation is magnetically induced only by one central rotary drive. The direction of movement is defined by changing the mechanical compliance on selected areas of the body using the so-called jamming effect, by which a transition between a liquid-like and a solid-like state of granular materials is used [39]. The implementation of this effect is a recently discussed topic in robotic applications with variable mechanical compliance [32].

The developed system (Fig. 16, diameter: 67.5 mm, height: 21.5 mm, total mass: 18.4 g) is driven by a single brushless DC-Gearmotor (mass: 2.8 g, diameter: 12.5 mm, height: 10.8 mm) with a torque of 5 Nmm (continuous operation) at an output speed of 111 rpm. Six permanent magnets (material: NdFeB, dimensions: 5 x 5 x 2 mm, B_{rem} : 1.35 T) are attached to the shaft of the motor in pairs of two.

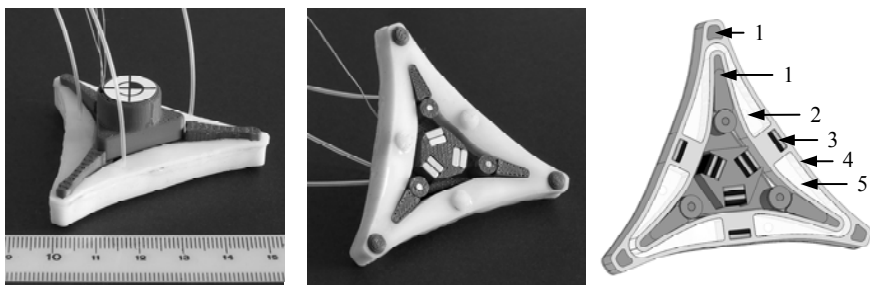


Fig. 16 Prototype and CAD-model (bottom view, silicone elastomer body cut open), 1: plastic skeleton, 2: hose connection, 3: permanent magnet, 4: silicone elastomer body, 5: chamber filled with glass balls.

The compliant body (mass: 4.4 g) is made of condensation curing silicone elastomer (shore hardness: A8) and is divided into three chambers which are filled with glass balls (diameter: 75 – 150 μm). Each chamber has a hose connection by which the compliance of the body can be locally changed when evacuating the air. Moreover a permanent magnet is installed in the middle of each side (Fig. 16). The motor is enclosed by, and the silicone elastomer body is attached to, a plastic material skeleton (ABS-Copolymer, density: 1.04 g cm^{-3}) manufactured with rapid prototyping.

The geometry of the system is based on an equilateral triangle. Due to the 3 axes of symmetry the system is possible to form large symmetrical systems (combination of 3, 6, 10... systems by connection of selected corner points). These

systems enable advanced manipulation tasks, such as the enclosing and a subsequent transport of objects.

The amplitude of the velocity of the system depends on the magnitude of the under pressure load, on the number of pressurised chambers and on the speed of the motor. The direction of the locomotion is controlled by a uniform or varying pressure in selected chambers.

The experiments have shown that locomotion in the plain is possible with this prototype. Selected results for actuation parameters: 167 rpm output speed of the motor (direction: clockwise) and 97% vacuum connected to the chambers, are shown in Fig. 17. In this case an average speed of 2.65 mms^{-1} in both displayed locomotion directions was determined. Deviation in the paths of the center point of the system for the two locomotion directions is due to manufacturing tolerances.

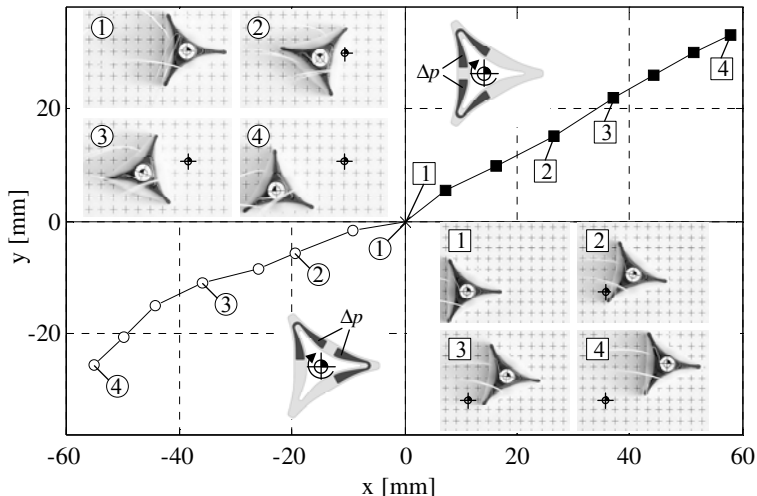


Fig. 17 Experimental results of the second prototype. Locomotion in the plane in different directions by changing the mechanical compliance at different areas of the system.

5 Summary

We studied the internal flow of the cytoplasm inside *Amoeba proteus* using micro PIV. The one-dimensional movement of the amoeba was controlled by a weak external electric field applied through platinum wires in the water-filled μ -slide. We observed that the magnitude of the internal flow velocity field is not dependent on the external field but with field the generation of pseudopods occurs only in the direction of the field and the amoeba's body is aligned parallel to the streamlines. From the PIV measurements we calculated time-dependent velocity plots, time-averaged velocity profiles and velocity time series. In agreement with the findings of Rogers et al. [1] the flow in the cytoplasm is similar to a viscose pipe flow of a

Newtonian fluid with a parabolic profile at a Reynolds number of $Re = 10^4$. The maximum velocity in the center of the amoeba varies between 0.3 and $10 \mu\text{ms}^{-1}$. The specific flow rate (per height) of the cytoplasm in the $40 \mu\text{m}$ wide cytoplasm channel is in the order of $Q/h = 80 \mu\text{m}^2\text{s}^{-1}$. Furthermore, we quantified the linear movement of *Amoeba proteus* in an external electric field. In further investigations we want to systematically study the cytoplasm flow under different boundary conditions like external surface and volume forces. To get more knowledge about the variations in cytoplasmic viscosity, the local concentration of Calcium ions or other stained regulatory proteins could be measured by fluorescence microscopy.

In comparison, the adhesive locomotion of tissue cells, e.g. human epidermal keratinocytes, on planar substrates have been studied in extent by experimental measurements. In adequate mathematical models, considering the cytoplasm as a two-phase flow system, we could show that this type of cell migration is based on very similar principles as in amoeboid locomotion: cell polarity and forward translocation is induced and maintained by a front-to-rear gradient in contractility of the actin-myosin cytoskeleton, together with a corresponding gradient of viscous drag forces onto the dynamically regulated adhesion contacts. In the simplified situation of a circular cell, with peripheral lamella protrusions forming the varying cell shape, we explored the degree of cell polarity, speed of cell migration and the statistic properties of resulting migration paths.

Based on the experimental measurements of single amoebae cells and supported by the above mentioned mathematical simulation models for cell migration, we could use the relevant advantages of amoeboid movement for implementation in technical locomotion systems. In accordance with the explored biological principles and mechanisms, constructive features and basic characteristics of two miniaturized prototypes have been developed. Both magnetically actuated prototypes enable locomotion in the plane. The locomotion is based on intrinsic mechanical compliance. The direction of locomotion is defined by asymmetric periodic deformation of the compliant segments, without/with active changes in their compliance. For the developed systems optimal control strategies, based on the results of the measurements on the biological object and under consideration of the modelling aspects, will be determined. Furthermore, future work is addressed to increase shape variability and to investigate the behaviour in liquid media.

Acknowledgements. The work was financially supported by the Deutsche Forschungsgemeinschaft under grant no. AL 162/5-1, Re 1066/10-1, ZI 540/14-1. We thank L. Ling and B. Schneid for fruitful discussions and technical help.

References

1. Rogers, S.S., Waigh, T.A., Lu, J.R.: Intracellular microrheology of motile *Amoeba proteus*. *Biophys. J.* 94, 3313–3322 (2008)
2. Stossel, T.P.: On the crawling of animal cells. *Science* 260, 1086–1094 (1993)
3. Condeelis, J.: Life at the leading edge: formation of cell protrusion. *Annu. Rev. Cell. Biol.* 9, 414–440 (1993)

4. Mitchison, T.J., Cramer, L.P.: Actin-based cell motility and cell locomotion. *Cell* 84, 371–379 (1996)
5. Pomorski, P., Krzeminski, A., Wasik, A., Wierzbicka, K., Baranska, J., Klopocka, W.: Actin dynamics in Amoeba proteus motility. *Protoplasma* 231, 31–41 (2007)
6. Patrick, Y.J., Peter, A.P., Scott, A.W., Elliot, L.E.: A mechanical function of myosin II in cell motility. *J. of Cell Sci.* 108, 387–393 (1995)
7. Alt, W., Dembo, M.: Cytoplasm dynamics and cell motion: two-phase flow models. *Math. Biosciences* 156, 207–228 (1999)
8. Kuusela, E., Alt, W.: Continuum model of cell adhesion and migration. *J. Math. Biol.* 58, 135–161 (2009)
9. Zimmermann, K., Zeidis, I., Behn, C.: Mechanics of Terrestrial Locomotion – With a Focus on Non-pedal Motion Systems. Springer, Berlin (2009)
10. Zimmermann, K., Naletova, V.A., Zeidis, I., Böhm, V., Kolev, E.: Modelling of locomotion systems using deformable magnetizable media. *J. Physics: Condens. Matter* 18, 2973–2983 (2006)
11. Zimmermann, K., Böhm, V.: A contribution to the amoeboid locomotion of mobile robots. In: Proc. of the 41st Int. Symp. on Robotics, München, pp. 1152–1157 (2010)
12. Raffel, M., Willert, C.E., Kompenhans, J.: Particle Image Velocimetry: A Practical Guide. Springer, Heidelberg (1997)
13. Korohoda, W., Mycielska, M., Janda, E., Madeja, Z.: Immediate and long-term galvanotactic responses of amoeba proteus to electric fields. *Cell Motil. Cytoskeleton* 45, 10–26 (2000)
14. Teixeira-Pinto, A.A., Nejelski Jr., L.L., Cutler, J.L., Heller, J.H.: The behavior of unicellular organisms in an electromagnetic field. *Exp. Cell Res.* 20, 548–564 (1960)
15. Abramson, H.A., Moyer, L.S., Gorin, M.H.: Electrophoresis of proteins and the chemistry of cell surfaces. Reinhold, New York (1942)
16. Seaman, G.V.F.: Electrophoresis using a cylindrical chamber. In: Ambrose, E.J. (ed.) *Cell Electrophoresis*, pp. 4–21. J&A. Churchill Ltd., London (1965)
17. Friedl, P.: Prespecification and plasticity; shifting mechanisms of cell migration. *Curr. Opin. Cell Biol.* 16, 14–23 (2004)
18. Möhl, C.: Modellierung von Adhäsions- und Cytoskelett-Dynamik in Lamellipodien migratorischer Zellen. Diploma thesis. University Bonn (2005)
19. Verkhovsky, A.B., Svitkina, T.M., Borisy, G.G.: Self-polarization and directional motility of cytoplasm. *Curr. Biol.* 9, 11–20 (1999)
20. Wolgemuth, C.W., Stajic, J., Mogilner, A.: Redundant mechanisms for stable cell locomotion revealed by minimal models. *Biophys. J.* 101, 545–553 (2011)
21. Jilkine, A., Edelstein-Keshet, L.: A comparison of mathematical models for polarization of single eukaryotic cells in response to guided cues. *PLoS Comput. Biol.* 7(4) (2011)
22. Alt, W., Bock, M., Möhl, C.: Coupling of cytoplasm and adhesion dynamics determines cell polarization and locomotion. In: Chauviere, A., Preziosi, L., Verdier, C. (eds.) *Cell Mechanics: From Single Cell-Based Models to Multiscale Modeling*, pp. 89–131. Taylor & Francis (2010)
23. Bereiter-Hahn, J., Lüers, H.: Subcellular tension fields and mechanical resistance of the lamella front related to the direction of locomotion. *Cell Biochem. Biophys.* 29, 243–262 (1998)
24. Bandura, J.: Simulation eines mechanischen Roboter-Modells zur Zellmigration. Diploma thesis. University Bonn (2008)

25. Alt, W., Tranquillo, R.T.: Protrusion-retraction dynamics of an annular lamellipodial seam. In: Alt, W., Dunn, G., Deutsch, A. (eds.) *Dynamics of Cell and Tissue Motion*, pp. 73–81. Birkhäuser, Basel (1997)
26. Schneid, B.: Simulation der Migration von Keratinozyten mit Fokus auf die Zytoskelettdynamik. Bachelor thesis. University Bonn (to appear, 2012)
27. Østergaard, E.H., Christensen, D.J., Eggenberger, P., Taylor, T., Ottery, P., Hautop Lund, H.: HYDRA: From Cellular Biology to Shape-Changing Artefacts. In: Duch, W., Kacprzyk, J., Oja, E., Zadrożny, S. (eds.) *ICANN 2005. LNCS*, vol. 3696, pp. 275–281. Springer, Heidelberg (2005)
28. Murata, S., Kurokawa, H.: Self-Reconfigurable Robots. *IEEE Robotics & Automation Magazine*, 71–78 (March 2007)
29. Ishiguro, A., Umedachi, T., Kitamura, T., Nakagaki, T., Kobayashi, R.: A Fully Decentralized Morphology Control of an Amoeboid Robot by Exploiting the Law of Conservation of Protoplasmic Mass. *Distributed Autonomous Robotic Systems* 8, 193–202 (2009)
30. Umedachi, T., Takeda, K., Nakagaki, T., Kobayashi, R., Ishiguro, A.: Fully decentralized control of a soft-bodied robot inspired by true slime mold. *Biol. Cybern.* 102, 261–269 (2010)
31. Hong, D.W., Ingram, M., Lahr, D.: Whole Skin Locomotion Inspired by Amoeboid Motility Mechanisms. *ASME J. of Mechanisms and Robotics* 1/011015, 1–7 (2009)
32. Steltz, E., Mozeika, A., Rodenberg, N., Brown, E., Jaeger, H.M.: JSEL - Jamming Skin Enabled Locomotion. In: Proc. of the IEEE/RSJ Int. Conf. on Int. Robots and Systems, St. Louis, pp. 5672–5677 (2009)
33. Hou, J., Luo, M., Mei, T.: The design and control of amoeba-like robot. In: Proc. of the IEEE Int. Conf. on Computer Application and System Modeling (ICCASM 2010), Taiyuan, pp. V188–V191 (2010)
34. Tortora, G., Caccavaro, S., Valdastri, P., Menciassi, A., Dario, P.: Design of an autonomous swimming miniature robot based on a novel concept of magnetic actuation. In: Proc. of the IEEE Int. Conf. on Robotics and Automation, Anchorage, pp. 1592–1597 (2010)
35. Kim, S.H., Hashi, S., Ishiyama, K.: Methodology of Dynamic Actuation for Flexible Magnetic Actuator and Biomimetic Robotics Application. *IEEE Transactions on Magnetics* 46, 1366–1369 (2010)
36. Zhou, G.Y., Jiang, Z.Y.: Deformation in magnetorheological elastomer and elastomer–ferromagnet composite driven by a magnetic field. *J. Smart Mater. Struct.* 13, 309–316 (2004)
37. Varga, Z., Filipcsei, G., Zrinyi, M.: Magnetic field sensitive functional elastomers with tuneable elastic modulus. *Polymer* 47, 227–233 (2006)
38. Zimmermann, K., Böhm, V., Zeidis, I.: Vibration-driven mobile robots based on magneto-sensitive elastomers. In: Proc. of the IEEE/ASME Int. Conf. on Intelligent Advanced Mechatronics, Budapest, pp. 730–735 (2011)
39. Liu, A., Nagel, S.: Jamming is not just cool any more. *Nature* 396, 21 (1998)

Swimming at Low Reynolds Number: From Sheets to the African Trypanosome

Sujin B. Babu, Christian Schmeltzer, and Holger Stark

Abstract. The African trypanosome is a protozoan which causes sleeping sickness in mammals. To study the dynamics of this microorganism at low Reynolds number, we implement and investigate three swimmer models, the Taylor sheet, a constant-torque swimmer, and a model for the African trypanosome. The first two swimmers are based on a semi-flexible sheet and the third is a full three-dimensional model. We simulate the viscous fluid environment of the swimmers using a technique called multi-particle collision dynamics. We verify our technique by implementing the Taylor sheet which is activated by a bending wave traveling along the sheet. Its ballistic motion turns into diffusive motion when the sheet becomes passive. For the constant-torque swimmer we apply a torque to the semi-flexible sheet which assumes a cork-screw shape and then generates the thrust force for propelling the swimmer forward. Whereas the angular velocity scales linearly with the torque, the swimming velocity displays a non-linear dependence. Finally, our trypanosome model swims with the help of a beating flagellum attached to the cell body. Since it wraps around the body, the model trypanosome displays a helical swimming trajectory. The swimming velocity displays a non-linear increase with the beating frequency of the flagellum.

1 Introduction

The locomotion of microorganisms in viscous environment at low Reynolds number has recently received increasing attention. One reason is the development of new experimental techniques that allow to explicitly study cell motility by using fluorescent staining of bacterial flagella [29], by measuring forces on the single cell level [6],

Sujin B. Babu · Christian Schmeltzer · Holger Stark

Institut für Theoretische Physik, Technische Universität Berlin, Hardenbergstraße 36, D-10623 Berlin, Germany

e-mail: sujin@itp.physik.tu-berlin.de, christian.schmeltzer@gmx.de,
holger.stark@tu-berlin.de

and by monitoring the kinematics of a cell using optical traps or video microscopy [6]. The physics governing swimming in the microscopic world is completely different from the macroscopic world. On a micron scale inertia is negligible and microorganisms have to resort to a propulsion mechanism where they are constantly in motion in order to translate forward [19, 26]. These propulsion mechanisms are numerous and include the flagellar breast stroke of *Chlamydomonas reinhardtii* [9] and the planar flagellar beating of sperm cells [5, 28]. In the latter case a wave runs along the flagellum which pushes the sperm cell forward. The propulsion mechanisms are adapted to the environment in which they have to survive.

The goal of the present study is to model the locomotion of the African trypanosome, the microorganism which causes the sleeping sickness, a deadly disease in humans [27]. Trypanosomes are passed into the blood stream of a mammal after a bite from the carrier tsetse fly through its saliva. Their life cycle mainly consists of two stages. First, they reproduce in the carrier's mid gut. Second, they travel through their host's blood vessels and after passing through the blood-brain barrier they cause the deadly disease. The elongated cell body of trypanosomes has the shape of a spindle [see Fig. 1(c)] and the cytoskeleton is made up from microtubules, a very stiff biopolymer with a persistence length of order 1mm [34].

The microtubules start from the thick posterior end and extend along the long axis of the cell body towards the thin anterior end. However, not all microtubules reach the anterior end [27]. In addition, they are linked to each other by proteins. This gives the whole cell body of the African trypanosomes a bending stiffness.

Furthermore, the trypanosome has a single flagellum attached to the cytoskeleton of the cell body. So, as the flagellum beats, the cell body of the trypanosome also bends and twists with the flagellum [11, 29]. The flagellum has the classical 9+2 microtubule axonem as in most eukaryotic cells [4]. The African trypanosome is about $25\mu m$ in length and travels at a speed of $20\mu m/s$ in the highly crowded, viscoelastic blood environment [11]. Experiments have shown that the trypanosome survives in the blood stream since it is able to evade attack from human antibodies by using its motility [11]. So, to prevent this survival strategy, it is very important to fully understand the motility of the trypanosome including the way the flagellum is attached to the cell body and also the flagellar beating pattern. This may help to identify an effective cure for sleeping sickness as the motility of the organism comes only from the flagellum [4].

To study various propulsion mechanism, simplified models have been introduced such as the Taylor sheet [32], the Purcell swimmer [26], and the squirming sphere [8, 20]. They capture the basic physics of the different propulsion mechanisms. In the following, we aim at understanding the locomotion of trypanosomes by first introducing and studying simplified swimmers before we address the complex swimming mode of the African trypanosome. All natural swimmers use drag anisotropy (as explained in Sect. 2.3) to propel themselves through the fluid [19]. In the first artificial swimmer proposed by Taylor in 1951 a sine wave passes along a planar sheet and pushes it forward [32]. We will model it as a semiflexible sheet, which resists

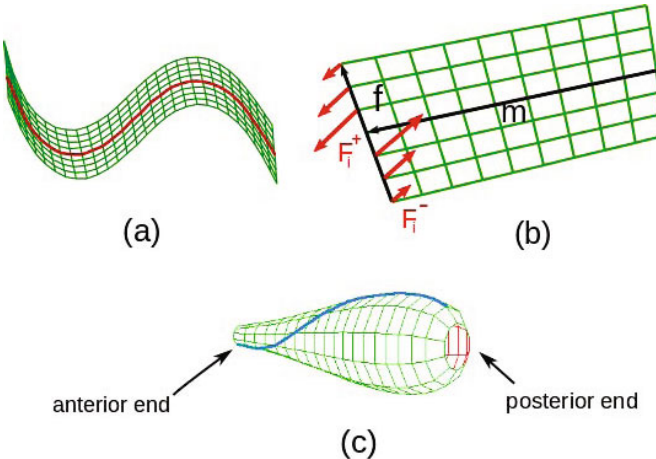


Fig. 1 Illustration of the three swimmers: (a) Undulating Taylor sheet, (b) constant torque swimmer with forces acting along one edge and (c) African trypanosome with the attached flagellum.

bending, and call it the Taylor sheet [see Fig. 1(a)]. In the following, we will explain how we model the sheet, how we actuate it by a sine-wave deformation, and how we couple it to a viscous environment. The moving Taylor sheet initiates flow fields in the fluid, which we simulate with a method called multi-particle collision dynamics (MPCD) [14]. MPCD solves the Navier-Stokes equations using fictitious or coarse grained fluid particles that obey artificial dynamics which locally conserve momentum. Thermal fluctuations are inherent within the technique. MPCD has been widely used to study a variety of problems such as the dynamic properties of semiflexible polymers or sheets [2, 7], single and collective behavior of micro swimmers at low Reynolds number [8, 36], and sedimentation of colloids [24].

In Sect. 2 we explain in detail how we model the swimming Taylor sheet, introduce a second artificial swimmer, which we name constant-torque swimmer, and introduce our model for the African trypanosome based on the semiflexible sheet. Details about our simulation method including a description of MPCD follow. Finally, we finish Sect. 2 with some comments on swimming at low Reynolds number. In Sect. 3 we present our results for the different types of swimmers. In Sect. 3.1 we will show that our modeled Taylor sheet reproduces the swimming behavior as predicted in [32]. In Sect. 3.2 we discuss how angular and linear velocity of the torque swimmer scale with the acting torque. Finally, in Sect. 3.3 we will demonstrate that our model for the African trypanosome captures the essential features seen in experiments. More details of this investigation will be presented in Ref. [3]. We close with conclusions in Sect. 4.

2 Modeling Three Swimmers

In modeling all three swimmers (see Fig. 1) reported in this work, we use a network of vertices connected by springs and with additional bending rigidity to form semiflexible surfaces. Fig. 1(a) illustrates the Taylor sheet [32], where a sine wave propagates along a semiflexible plane surface. It pushes the sheet forward similar to the flagellar beat of a sperm cell. In the constant-torque swimmer of Fig. 1(b) a torque is applied to one edge of a semiflexible sheet. It deforms to a screw-like object which creates a thrust force that propels the swimmer. Finally, Fig. 1(c) shows the complete three-dimensional model of the African trypanosome where the blue line represents the flagellum attached to the cell body. When a wave passes along the flagellum, the whole cell body distorts. Now, we introduce the modeling of each swimmer in the following subsections.

2.1 Taylor Sheet

In Ref. [2] we have explained in detail how we model a semiflexible sheet in three dimensions, when we studied its thermal motion in a viscous fluid. Here we just mention the key features. The vertices of the sheet are distributed on a square lattice. Adjacent vertices with equilibrium distance l_0 are connected by Hookean springs with the potential energy

$$U_s = \frac{1}{2} \kappa_s (l - l_0)^2, \quad (1)$$

where l is the actual distance. In order to prevent the sheet from shearing, next-nearest neighbor vertices along the diagonal of the square unit cell are also connected by springs. In order to prevent the sheet from crumpling, we also apply a bending potential along the two main directions of the sheet,

$$U_b = \kappa_b (1 - \cos \theta). \quad (2)$$

Here κ_b is the bending stiffness and θ is the angle between two bond vectors that point from one vertex to its two nearest neighbors [13].

To propel the sheet, we apply a bending wave along the center line of the sheet using the potential

$$U_w = \kappa_w (1 - \cos[\mathbf{t}_{i+1} \cdot \mathbf{R}(\alpha_w) \mathbf{t}_i]) \quad \text{with} \quad \alpha_w = A \sin(kd_i - \omega_w t). \quad (3)$$

Here κ_w is again some bending stiffness with respect to a bent reference state. To introduce this state, we rotate one tangent or bond vector of the sheet, \mathbf{t}_i , against the neighboring bond vector \mathbf{t}_{i+1} using the rotation matrix $\mathbf{R}(\alpha_w)$, where $|\mathbf{t}_i| = |\mathbf{t}_{i+1}| = 1$. The matrix $\mathbf{R}(\alpha_w)$ rotates \mathbf{t}_i by an angle α_w about the direction perpendicular to the center line and tangential to the sheet. Now, the rotation angle α_w varies like a

propagating sine wave along the center line with amplitude A , which is always one in all our simulations. Further characteristics of the wave are the wave number $k = \frac{2\pi}{\lambda}$, where λ is the wavelength, and the angular frequency ω_w . Time t is measured in the time unit of the MPCD method and d_i is the distance from one end of the sheet to the vertex i on the centerline of the sheet.

2.2 Constant-Torque Swimmer

The second swimmer reported here is a semiflexible sheet which we set in rotation with the help of an external torque. In practice, we apply forces on the vertices along one edge of the sheet as illustrated in Fig. 1 (b). The total torque \mathbf{M} becomes

$$\mathbf{M} = \kappa_t \sum_i \mathbf{r}_i \times \mathbf{F}_i. \quad (4)$$

Here \mathbf{r}_i points from the centerline to one vertex. We introduce a unit vector \mathbf{t} as tangent to the centerline and define the vector $\mathbf{F}_i = \mathbf{r}_i \times \mathbf{t}/r_i^2$ such that each vertex contributes the same torque κ_t . Thereby we keep the edge of the sheet straight. The forces from both sides of the centerline cancel each other so that the total force on the sheet is zero. Since the sheet is semiflexible, it assumes the shape of a corkscrew when it rotates. Thereby a thrust force is generated which pushes the swimmer forward.

2.3 African Trypanosome

In Fig. 1(c) we show our model surface for the African trypanosome which we used in the simulations. The diameters for the different cross sections of the cell body vary according to

$$S(i) = (i + 0.15)^{1/4} \exp[-0.006(i + 0.15)^2], \quad 0 \leq i < 20. \quad (5)$$

The diameters are given in units of l_0 and i is the index of the cross section starting with 0 at the thicker posterior end. The function $S(i)$ was constructed such that it reproduces the characteristic shape of the trypanosome. On each circle with diameter $S(i)$ 10 vertices are equally distributed so that they define a dodecagon. All vertices shown in Fig. 1(c) are connected by Hookean springs using the spring potential of Eq. (1). In addition, internal springs connect opposite vertices of the cross-sectional dodecagon. This helps to keep the shape and thereby the volume of the cell body. We chose relatively high values for the spring constant ($\kappa_s = 10^7$) which means very stiff springs.

To mimic the microtubules which run along the long axis of the cell body, we apply a bending potential along each line of vertices from the posterior to the anterior end:

$$U_b = \frac{1}{2} \kappa_b (\cos \theta_0 - \cos \theta)^2. \quad (6)$$

Here θ is the angle between two adjacent bond vectors and θ_0 is the equilibrium angle according to the equilibrium shape of the cell body given by Eq. (5). The bending stiffness κ_b allows for deformations of the cell body. In real African trypanosomes not all microtubules reach the anterior end, so this end is more flexible than the posterior end. To simulate this effect, we progressively reduce the bending stiffness by a factor of 0.95 starting from the center of the cell body so that the bending stiffness at the anterior end is given by $(0.95)^{10} \kappa_b = 0.60 \kappa_b$. Reducing this factor further destabilizes the model cell body. In the simulations both the anterior and posterior end are closed by hemispheres. They are not visible in Fig. 1(c). The length-to-thickness ratio of the African trypanosome is around 8, in our modeling we always keep this value at approximately 7.5 thereby being as close as possible to the real cell body.

We define the flagellum using the vertices of the cell body. So the model flagellum is by definition firmly attached to the cell body and thereby mimics the real trypanosome. There is a current debate how the flagellum runs along the cell body: Is it straight or does it wrap about the cell body [29]. Following observations from our experimental colleagues [10], the flagellum is straight starting from the thick posterior end till the center of the cell body and then wraps in a half turn around the cell body as shown by the blue line in Fig. 1(c). Along this flagellum, we pass a planar bending wave with the help of the potential given in Eq. (3). The only difference is that the matrix $\mathbf{R}(\alpha_w)$ refers to a rotation about the local normal of the cell body. Experiments have demonstrated that the end-to-end distance of the cell body of a swimming trypanosome amounts to ca. 60% of its cell body length [33]. We have adjusted the values of the parameters κ_s , κ_b and κ_w such that in the simulations the end-to-end distance is around 76%. A further reduction destabilizes the cell body.

2.4 Dynamics of the Swimmers

Vertices that define the surfaces of our swimmers experience forces through the spring and bending potentials. We assign to each vertex a mass $m = 1$ (in MPCD units introduced below) and move it by a typical molecular dynamics step. Positions and velocities are updated using the velocity Verlet algorithm [1] where δt_{MD} is the integration time step:

$$\mathbf{r}_i(t + \delta t_{MD}) = \mathbf{r}_i(t) + \delta t_{MD} \mathbf{v}_i(t) + \frac{1}{2} \delta t_{MD}^2 \frac{\mathbf{F}_i(t)}{m} \quad (7)$$

$$\mathbf{v}_i(t + \delta t_{MD}) = \mathbf{v}_i(t) + \frac{1}{2} \delta t_{MD} \left[\frac{\mathbf{F}_i(t)}{m} + \frac{\mathbf{F}_i(t + \delta t_{MD})}{m} \right]. \quad (8)$$

Here \mathbf{r}_i and \mathbf{v}_i are the respective position and velocity of the i th vertex of the cell body and $\mathbf{F}_i = -\nabla_i(U_s + U_b + U_w)$ is the force acting on this vertex. To perform the gradient ∇_i of the spring, bending, and bending wave potentials $U_s + U_b + U_w$ with respect to \mathbf{r}_i , the energies are discretized in the position variables \mathbf{r}_i . To keep the cell body stable, we always chose $\delta t_{MD} \ll 1$ in all the simulations reported here. While

both the total force and torque acting on the Taylor sheet and the model trypanosome are zero, only the total force on the constant-torque swimmer vanishes.

The swimmers also experience frictional forces from their viscous environment. We now describe how we model the fluid flow created by the swimmers when they move around.

2.5 Modeling the Newtonian Fluid

We determine the flow field around the swimmers with a method called multi-particle collision dynamics (MPCD). This method introduces coarse-grained or fictitious fluid particles that obey an artificial dynamics through a succession of ballistic and collision steps. The important point is that during the collision step momentum is conserved. So, on sufficiently long time and length scales, the MPCD method is equivalent to solving the Navier-Stokes equations [21, 22]. For the MPCD algorithm one can also derive analytic expressions for the fluid viscosity and thereby control it easily. At low Reynolds number, where one has to solve Stokes equations, MPCD is a quick simulation technique and relatively easy to implement [14]. In addition, MPCD includes thermal fluctuations. After some equilibration, the velocities of the fluid particles are Gaussian distributed with a variance of $3k_B T/m$ around a mean value as expected for a fluid in local thermal equilibrium.

We start the simulations by placing point particles in a simulation box with linear dimension L_{box} . To reduce the equilibration time, we already assign to each of the fluid particles a velocity from a Gaussian distribution with variance $3k_B T/m$, where k_B is the Boltzmann constant, T is temperature, and m is the mass of the fluid particle. In MPCD units, we set thermal energy $k_B T = 1$ and $m = 1$. Now, MPCD launches a two-step dynamics consisting of the streaming and collision step. In the streaming step the fluid particles move ballistically during a small time interval δt :

$$\mathbf{r}_i(t + \delta t) = \mathbf{r}_i(t) + \delta t \mathbf{v}_i(t) . \quad (9)$$

Here $\mathbf{r}_i(t)$ and $\mathbf{r}_i(t + \delta t)$ are the respective positions of the particle i before and after the streaming step and $\mathbf{v}_i(t)$ is its velocity. In the collision step we divide our simulation box into cells with linear dimension $a = 1$. The density of the fluid particles ρ_0 is kept at 10, which means, on average, 10 particles per cell. We now follow a procedure known from the Anderson thermostat in a conventional molecular dynamics simulation [14]. We calculate the center of mass velocity of each cell, $\mathbf{V}(t)$, and then assign to each particle in the cell a random relative velocity $\mathbf{v}_{i,ran}$ from a Gaussian distribution with variance $3k_B T/m$:

$$\begin{aligned} \mathbf{v}_i^{\text{new}}(t) &= \mathbf{V}(t) + \mathbf{v}_{i,ran} - \sum_{\text{cell}} \mathbf{v}_{i,ran} / N_c \\ &+ m \Pi^{-1} \sum_{j \in \text{cell}} [\mathbf{r}_{j,c} \times (\mathbf{v}_j - \mathbf{v}_j^{ran})] \times \mathbf{r}_{i,c}. \end{aligned} \quad (10)$$

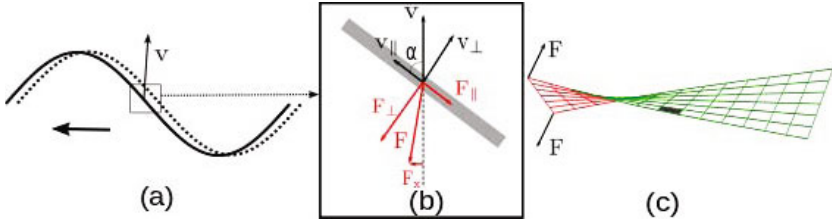


Fig. 2 (a) A bending wave propagates along a filament to the right which pushes the filament to the left indicated by thick black arrow. (b) Blow up of a local segment of the filament. Anisotropic friction produces a thrust force to the left. (c) Rotating segment of the constant torque swimmer also produce a thrust force.

The third term on the right-hand side is added to conserve the center of mass velocity or momentum during collision in the cell. The last term in Eq. (10) implements angular momentum conservation. For example, in our system where the trypanosome also rotates in space, it is important to avoid unphysical behavior. The advantage of using the idea of the Anderson thermostat for the collision step is also that temperature is, by definition, kept constant. Finally, we shift the simulation grid randomly before each collision step, in order to avoid unphysical correlations between the particle velocities and thereby restore Galilean invariance [16, 17].

To couple our swimmers to the MPCD fluid, we include their vertices in the collision step. In addition, for the model trypanosome the fluid particles are not allowed to go through the cell body by applying a stochastic bounce back rule [23, 25], which implements the no-slip boundary condition at the surface. However, for our sheet swimmers, we let the fluid particles move through the sheet during the streaming step. In Ref. [2] we showed that this procedure does not change the dynamics of the sheets but saves considerable simulation time. The reason is the following. Both, collision and streaming steps contribute to the viscosity of the MPCD fluid [14]. However, in particular at low Reynolds number the collision step mainly determines viscosity and the transfer of momentum between the fluid particle and the vertices mainly comes from the collision step. So details of the streaming step are not important.

2.6 Swimming at Low Reynolds Number

The African trypanosome has a typical length of $L \approx 25\mu m$ and swims in water with a velocity of about $v \approx 5\mu m$. This results in a Reynolds number $Re = Lv\rho/\eta \approx 10^{-4}$ where η is the viscosity of water and ρ its density. So inertia does not play any role and fluid flow is governed by the Stokes equations, which result from the Navier-Stokes equations by setting the inertial term to zero. Microorganisms swimming in this world of low Reynolds number cannot drift by inertia [31]. When they stop with their actuation mechanism they almost immediately stop moving forward. In other words, the momentum of the swimmer is dissipated into the fluid instantaneously

which is called overdamped limit. A passive body only moves when an external force is applied and its velocity is proportional to this force. This is the signature of Aristotelian mechanics.

The Stokes equations, $\mathbf{0} = -\nabla p + \eta \nabla^2 \mathbf{u}$, where p is pressure and \mathbf{u} is the velocity field, allow for time-reversed solutions, when also pressure forces and external forces are reversed. This kinematic reversibility has important consequences. A potential swimmer cannot move forward with a reciprocal actuation cycle, meaning a cycle which looks the same under time reversal. This is the content of Purcell's famous scallop theorem [26]. Swimming at low Reynolds number needs a non-reciprocal actuation cycle.

Figure 2(a) shows a wave traveling along a filament at two instances of time. Obviously, the motion is non-reciprocal. The local segment has to move upwards to realize the filament at a later time. A thrust force that pushes the filament forward [see Fig. 2(b)] can only exist since the friction coefficients for moving the segment parallel (ξ_{\parallel}) or perpendicular (ξ_{\perp}) to its axis differ. In fact, $\xi_{\parallel} = F_{\parallel}/v_{\parallel} < \xi_{\perp} = F_{\perp}/v_{\perp}$, which explains the thrust force F_x in Fig. 2(b). Calculating F_x results in

$$F_x = (\xi_{\parallel} - \xi_{\perp}) v \sin \alpha \cos \alpha. \quad (11)$$

In principle, all three swimmers use anisotropic friction coefficients to generate their thrust force. The Taylor sheet is just the waving filament extended into the second dimension. Rotating the constant-torque swimmer [see Fig. 2(c)], one locally has the situation as in Fig. 2(b), in principle. Finally, the whole body of the African trypanosomes performs a wave-like motion initiated by the attached flagellum.

3 Results

We now present our simulation results for the three swimmers introduced in the previous section.

3.1 Taylor Sheet

As explained in Sect. 2.1, we apply a sine bending wave along the centerline of the semiflexible sheet. In Fig. 3 we plot a snapshot of the sheet and the trajectory of one of its vertices. The whole sheet takes over the bending wave of the centerline and travels in opposite direction to the wave propagation as explained in Sect. 2.6. [32]. Since our sheet is essentially inextensible, each vertex moves along a figure 8 instead of just oscillating up and down as suggested in Fig. 2(b).

The mean-square displacement (MSD) for the center of mass of the sheet is defined as

$$\langle R^2 \rangle = \langle [\mathbf{r}_{cm}(t) - \mathbf{r}_{cm}(0)]^2 \rangle, \quad (12)$$

where \mathbf{r}_{cm} denotes the position of the center of mass. As long as the sheet is propelled by the bending wave, it moves ballistically as indicated in Fig. 4, where

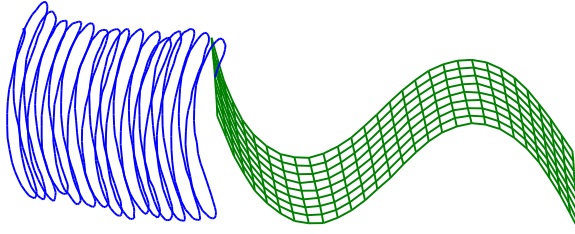


Fig. 3 Snapshot of the Taylor sheet moving to the right while the bending wave propagates to the left. The trajectory of one vertex is plotted.

$\langle R^2 \rangle \propto t^2$. When we stop the actuation of the sheet, the sheet behaves as a passive object or Brownian particle with the typical diffusive behavior, $\langle R^2 \rangle \propto t$, as demonstrated in Fig. 4 and in agreement with our earlier work [2].

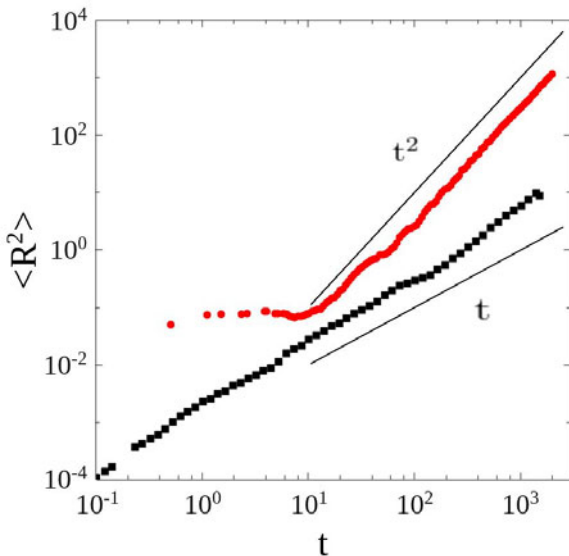


Fig. 4 MSD of the center of mass for the Taylor sheet swimmer (red) and a passive semiflexible sheet (black). The ballistic and diffusive motion are indicated, respectively, by the power laws $\propto t^2$ and $\propto t$.

3.2 Constant-Torque Swimmer

As explained in Sect. 2.2, we apply a torque to a semiflexible sheet parallel to its long axis and very similar to the flexible polymer swimmer of Ref. [12] where the

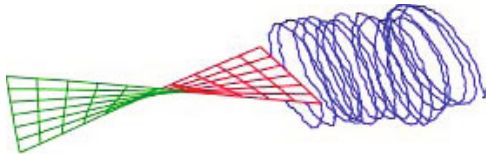


Fig. 5 The constant-torque swimmer assumes the shape of a cork screw when it rotates due to an applied torque. The rotation generates a thrust force and moves parallel to the applied torque as indicated by the trajectory of one vertex.

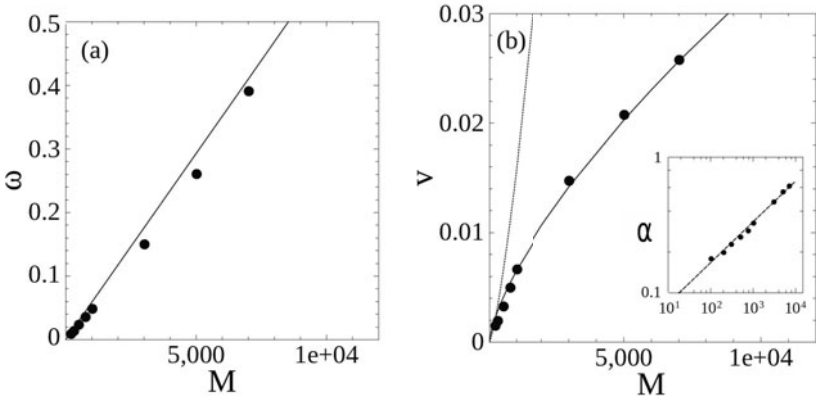


Fig. 6 (a) Angular velocity ω versus driving torque M in MPCD units. Dots indicate results from the MPCD simulations and the solid line is $\omega = M/\xi_r$. (b) Translational velocity versus driving torque M in MPCD units. Dotted line: Scaling law $v \propto M^{1.3}$ valid for small torques. Full line: Scaling law $v \propto M^{0.7}$ valid for large torques. Inset: Pitch angle α versus torque M . The dashed line is a fit to $\alpha \propto M^{0.3}$.

torque is realized by a rotating magnetic field. Depending on the magnitude of the bending stiffness and the torque, the sheet assumes the shape of a cork screw, as illustrated in Fig. 5 for a sheet of length $L_l = 13$ and width $L_b = 6$. In Sect. 2.6 we just described how the rotation then generates the thrust forces which pushes the screw forward. As a result, the constant-torque swimmer moves parallel to the torque axis. The screw-like motion is indicated by the trajectory of one vertex.

In Fig. 6(a) we plot the angular velocity ω as a function of the applied torque. It increases nearly linearly with the torque. Deviations result from the screw deformation which becomes more pronounced for larger torques. The rotational friction coefficient for a square sheet is isotropic, similar to that of a disc [15], and we determined it with MPCD simulations as $\xi_r = 20\eta L^3$ [30]. As an estimate for our elongated sheet, we use the same formula but replace L by $L = \sqrt[3]{L_l L_b^2}$. Note that $\pi(L_b/2)^2 L_l$ is the cylindrical volume covered by the sheet during a 2π rotation. The

solid line in Fig. 6(a) is just the linear relation $\omega = M/\xi_r$ and good fit to the results from our simulations.

In Fig. 6(b) we plot the translational velocity v versus the applied torque. The dependence is clearly non-linear due to the fact that the sheet deforms into a helical structure with pitch angle α which is defined in Fig. 2(c). The deformation of the sheet into the cork screw structure increases with M which we demonstrate by the inset of Fig. 6(b) for the torque dependence of the pitch angle α . We find that $\alpha \propto M^{0.3}$. For a helical structure translation and rotation are coupled and the following linear relations for force F and torque M acting on the helical structure exist: $F = Av + B\omega$ and $M = Bv + C\omega$. In particular, the non-zero coupling coefficient B produces linear motion from an applied torque. In our case, the applied force F is zero. Eliminating ω with both equations results in the velocity-torque dependence

$$v = \frac{B}{B^2 + AC}M \quad (13)$$

For a helical filament, $B \propto \alpha$ for small pitch angle α [19, 35] and we expect the same to be valid for a twisted sheet. With $\alpha \propto M^{0.3}$ we therefore obtain $B \propto M^{0.3}$. For sufficiently small M or $B^2 \ll AC$ in Eq. (13), we arrive at $v \propto M^{1.3}$ which we fitted with an appropriate prefactor in Fig. 6(b) by the dotted line. Clearly, the scaling law is only valid for the smallest values of M . In our simulations it is difficult to access the regime as it needs a lot of simulation time. On the other hand, for large torques such that $B^2 \gg AC$, one arrives at $v \propto M/B \propto M^{0.7}$ which results in a good fit as the solid line in Fig. 6(b) shows.

3.3 Swimming of the Model African Trypanosome

With the results from the sheet swimmers in mind, we have established a three-dimensional model for the African trypanosome. As explained in Sect. 2.3, a planar sine bending wave passes along the flagellum and tangential to the cell body of the model trypanosome [Fig. 1(c)]. Figure 7(a) shows a snapshot of the swimming trypanosome model. The sine wave propagates from the thin anterior end to the

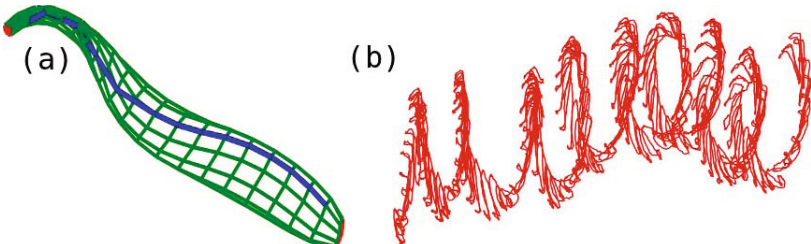


Fig. 7 Snapshot of the African trypanosome during swimming in the MPCD fluid. (b) Helical trajectory of the posterior end of the African trypanosome model simulated for a long time such that helical motion becomes visible.

thick posterior end and pushes the African trypanosome in the opposite direction as explained in Sect. 2.6. In Fig. 7(b) we show the trajectory of one of the vertices at the posterior end. As the bending wave passes through the flagellum, the posterior end moves back and forth on the time scale of the period of the bending wave. For long times the trypanosome moves on a helical trajectory since the flagellum wraps around the cell body. We have followed here new experimental results [10]. In these experiments, the trypanosome needs eight beating cycles of its flagellum to perform a full 2π rotation. In contrast, our model needs 23 beating cycles.

The real swimming trypanosome has an average end-to-end distance $\bar{\varepsilon}$ of about 60% of its cell length [33]. In Fig. 8(a) we plot the time dependence of ε for our model trypanosome during swimming which is similar to experiments [33]. However, $\varepsilon(t)$ varies between 0.7 and 0.85 with an average of about 0.76 which is above the experimental value. Our attempts to reduce this value failed since the model trypanosome became unstable. We also performed relaxation experiments reported elsewhere where we let the model trypanosome relax under a steady bending wave [3]. Typically, the relaxation time is smaller than the period of the beating flagellum in a swimming trypanosome. The model trypanosome thus goes through quasi-equilibrium states such that its shape is always fully relaxed. We have indications that the real trypanosome swims in the same regime [3].

Figure 8(b) plots the velocity as a function of the angular frequency on a double logarithmic scale for 2 different viscosities in MPCD units. The velocity increases with frequency following the scaling law $v \propto \omega_w^{1/2}$ as indicated by the line. In contrast, for the Taylor sheet or the beating flagellum one expects a linear relationship [32]. The main reason is that the beating flagellum of the trypanosome has to move a large cell body with a large friction coefficient. Using an idea of Lauga [18] we are able to deduce the $\omega_w^{1/2}$ scaling law [3]. Deviations from it are visible in

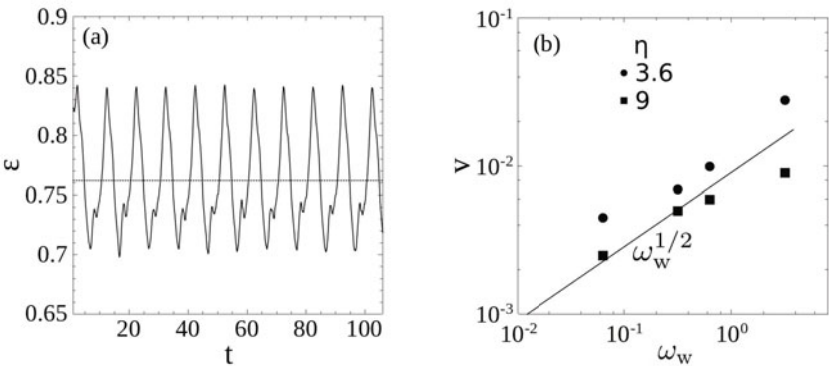


Fig. 8 (a) End-to-end distance ε of the swimming model trypanosome (in units of the body length) as a function of time. The dashed line is $\bar{\varepsilon} = 0.76$. (b) Swimming velocity v versus beating frequency ω_w of the flagellum for two different viscosities η in MPCD units.

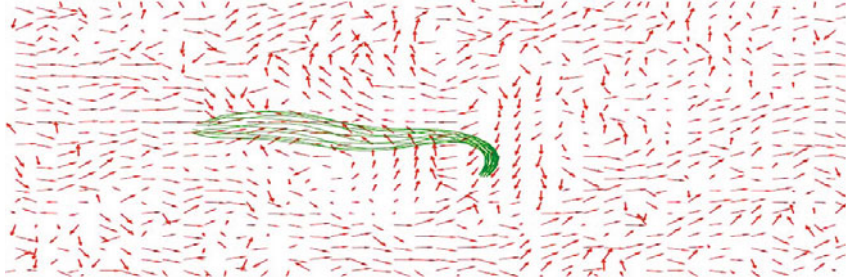


Fig. 9 The average flow field as obtained from simulations. The cell body is shown as guide to the eye.

Fig. 8(b) at the larger viscosity and for large ω . Larger viscosity means that the relaxation time under a static bending wave increases. So beyond $\omega_w = 1$, our model trypanosome does not pass anymore through quasi-equilibrium states. Clearly, increasing viscosity results in a decrease of the swimming speed since the drag force on the cell body increases. Ultimately, for very long time the model trypanosome will change its direction due to rotational diffusion of the cell body and will perform a random walk similar to the real trypanosome [37]. However, in our simulations rotational diffusion would be only of thermal origin whereas in the real trypanosome intrinsic noise enhances the rotational diffusion constant [37].

From MPCD simulations we also obtain the flow field of the fluid around the moving trypanosome. In Fig. 3.3 we plot the flow field in the plane which contains the trypanosome. The plot is an average over the calculated flow fields for several 2π rotations of the trypanosome. For clarity, all velocities have the same strength and we show one snapshot of the model trypanosome. We observe that close to the cell body there is flow from the thin anterior end towards the thick posterior end and also flow from the posterior end towards the swimming direction. A small particle close to the anterior end is propelled by the flow field towards the posterior end where the flagellum pocket is situated. Experiments showed that antibodies from the host are dragged along the surface of the cell body towards the flagellum pocket where they are internalized into the cell body [11]. The trypanosome uses such a strategy to defend itself against antibodies. The flow field from our simulations, at least, qualitatively confirms the strategy. It also gives us confidence that our simulations with the model trypanosome generate a swimming behavior very close to the real organism.

4 Conclusion

In this article we introduced and investigated three swimmer models with the help of the particle based MPCD method which allows to calculate flow fields in arbitrary geometries. The Taylor sheet is a semi-flexible sheet propelled by a bending wave along its center line. Whereas the active sheet moves ballistically, the passive sheet

displays conventional diffusive behavior in agreement with our earlier work [2]. The constant-torque swimmer is set into rotation by forces along one of its edges. It deforms into a cork screw through the friction with the surrounding fluid and thereby creates a thrust force that pushes the swimmer forward. The angular velocity is nearly linear in the applied torque M . The translational velocity displays a non-linear dependence on M due to the changing pitch angle of the cork screw. The frictional coupling coefficient directly depends on this pitch angle. After having implemented semi-flexible sheet structures, we were able to introduce a three-dimensional model for the African trypanosome and to couple it to the MPCD fluid. The bending wave passing along the attached flagellum from the thin anterior to the thick posterior end propels the trypanosome towards the anterior end while the trypanosome rotates due to the helical attachment of the flagellum. We obtain oscillations in the end-to-end distance of the cell body as observed in experiments. The translational velocity scales as $\omega_w^{1/2}$, where ω_w is the angular frequency of the bending wave. In Ref. [3] we have developed an understanding for this scaling.

With such a realistic model for the African trypanosome at hand, we are able to study its swimming in microchannels which mimic blood vessels. We will also introduce simple red-blood cells into the MPCD fluid to obtain a more realistic model for blood and investigate why these obstacles under certain conditions improve the swimming of the African trypanosome. So our modeling helps to explore the swimming of the African trypanosome in realistic environments and thereby contributes to its understanding.

Acknowledgements. We like to thank Engstler M, Pfohl T, Kruger T, Uppaluri S and Steliamanns E for helpful discussions. This work has been supported by DFG under grants STA 352/7-2 and STA 352/9-1.

References

1. Allen, M.P., Tildesley, D.J.: Computer Simulation of Liquids. Clarendon, Oxford (1991)
2. Babu, S.B., Stark, H.: Dynamics of semi-flexible tethered sheet. *Eur. Phys. J. E* 34, 136–142 (2011), doi:10.1140/epje/i2011-11136-2
3. Babu, S.B., Stark, H.: (in preparation, 2012)
4. Broadhead, R., Dawe, H.R., Farr, H., et al.: Flagellar motility is required for the viability of the bloodstream trypanosome. *Nature* 440, 224–227 (2006), doi:<http://dx.doi.org/10.1038/nature04541>
5. Camalet, S., Julicher, F.: Generic aspects of axonemal beating. *New J. Phys.* 2, 24.1–24.23 (2000), doi:10.1088/1367-2630/2/1/3240
6. Chattopadhyay, S., Moldovan, R., Yeung, C., et al.: Swimming efficiency of bacterium Escherichiacoli. *Proc. Nat. Acad. Sci.* 103, 13712–13717 (2006), doi:10.1073/pnas.0602043103
7. Chelakkot, R., Winkler, R.G., Gompper, G.: Semiflexible polymer conformation, distribution and migration in microcapillary flows. *J. Phys. Condens. Matter* 23, 184117(1-13) (2011), doi:10.1088/0953-8984/23/18/184117

8. Downton, M.T., Stark, H.: Simulation of a model microswimmer. *J. Phys. Condens. Matter* 21, 204101(1-6) (2009), doi:10.1088/0953-8984/21/20/204101
9. Drescher, K., Goldstein, R.E., Michel, N., et al.: Direct Measurement of the Flow Field around Swimming Microorganisms. *Phys. Rev. Lett.* 105, 168101(1-4) (2010), doi:10.1103/PhysRevLett.105.168101
10. Engstler, M., Heddergott, N., Kruger, et al.: African trypanosome as model system for functional analyses of microbial motility. *NNFM* 119, 43–61 (2012)
11. Engstler, M., Pfohl, T., Herminghaus, S., et al.: Hydrodynamic Flow-Mediated Protein Sorting on the Cell Surface of Trypanosomes. *Cell* 131, 505–515 (2007), doi:10.1016/j.cell.2007.08.046
12. Garstecki, P., Tierno, P., Weibel, D.B., et al.: Propulsion of flexible polymer structures in a rotating magnetic field. *J. Phys. Condens. Matter* 21, 204110(1-8) (2009), doi:10.1088/0953-8984/21/20/204110
13. Gauger, E.M., Stark, H.: Numerical study of a microscopic artificial swimmer. *Phys. Rev. E* 74, 021907(1-10) (2006), doi:10.1103/PhysRevE.74.021907
14. Gompper, G., Ihle, T., Kroll, D.M., et al.: Multi-Particle Collision Dynamics: A Particle-Based Mesoscale Simulation Approach to the Hydrodynamics of Complex Fluids. *Adv. Polym. Sci.* 221, 1–87 (2009), doi:10.1007/978-3-540-87706-6_1
15. Happel, J., Brenner, H.: Low Reynolds number hydrodynamics: with special application to particulate media. Kluwer, Hauge (1983)
16. Ihle, T., Kroll, D.M.: Stochastic rotation dynamics: A Galilean-invariant mesoscopic model for fluid flow. *Phys. Rev. E* 63, 020201(1-4) (2001), doi:10.1103/PhysRevE.63.020201
17. Ihle, T., Kroll, D.M.: Stochastic rotation dynamics. I. Formalism, Galilean invariance, and Green-Kubo relations. *Phys. Rev. E* 67, 066705(1-11) (2003), doi:10.1103/PhysRevE.67.066705
18. Lauga, E.: Floppy swimming: Viscous locomotion of actuated elastica. *Phys. Rev. E* 75, 041916(1-16) (2007), doi:10.1103/PhysRevE.75.041916
19. Lauga, E., Powers, T.R.: The hydrodynamics of swimming microorganisms. *Rep. Prog. Phys.* 72, 096601(1-36) (2009), doi:10.1088/0034-4885/72/9/096601
20. Lighthill, M.J.: On the squirming motion of nearly spherical deformable bodies through liquids at very small reynolds numbers. *Commun. Pure Appl. Math.* 5, 109–118 (1952), doi:10.1002/cpa.3160050201
21. Malevanets, A., Kapral, R.: Mesoscopic model for solvent dynamics. *J. Chem. Phys.* 110, 8605–8613 (1999), doi:10.1063/1.478857
22. Malevanets, A., Kapral, R.: Solute molecular dynamics in a mesoscale solvent. *J. Chem. Phys.* 112, 7260–7269 (2000), doi:10.1063/1.481289
23. Padding, J.T., Louis, A.A.: Hydrodynamic interactions and Brownian forces in colloidal suspensions: Coarse-graining over time and length scales. *Phys. Rev. E* 74, 031402(1-29) (2006), doi:10.1103/PhysRevE.74.031402
24. Padding, J.T., Louis, A.A.: Interplay between hydrodynamic and Brownian fluctuations in sedimenting colloidal suspensions. *Phys. Rev. E* 77, 011402(1-11) (2008), doi:10.1103/PhysRevE.77.011402
25. Padding, J.T., Wysocki, A., Lowen, H., et al.: Stick boundary conditions and rotational velocity auto-correlation functions for colloidal particles in a coarse-grained representation of the solvent. *J. Phys. Condens. Matter* 17, S3393–S3399 (2005), doi:10.1088/0953-8984/17/45/027
26. Purcell, E.M.: Life at low Reynolds number. *Am. J. Phys.* 45, 3–11 (1977), doi:10.1119/1.10903

27. Ralston, K.S., Kabututu, Z.P., Melehani, J.H., et al.: The Trypanosoma brucei Flagellum: Moving Parasites in New Directions. *Ann. Rev. Microbiol.* 63, 335–362 (2009), doi:10.1146/annurev.micro.091208.073353
28. Riedel Kruse, I.H., Hilfinger, A., Howard, J., et al.: How molecular motors shape the flagellar beat. *HFSP J.* 1, 192–208 (2007), doi:10.2976/1.2773861
29. Rodriguez, J.A., Lopez, M.A., Thayer, C.M., et al.: Propulsion of African trypanosomes is driven by bihelical waves with alternating chirality separated by kinks. *Proc. Nat. Acad. Sci.* 106, 19322–19327 (2009), doi:10.1073/pnas.0907001106
30. Schmeltzer, C.: unpublished work
31. Strak, H.: Immer in Bewegung Bleiben. *Physik. Journal* 6(11), 31–37 (2007)
32. Taylor, G.: Analysis of the Swimming of Microscopic Organisms. *Proc. R Soc. A* 209, 447–461 (1951), doi:10.1098/rspa.1951.0218
33. Uppaluri, S., Nagler, J., Stellamanns, E., et al.: Impact of Microscopic Motility on the Swimming Behavior of Parasites: Straighter Trypanosomes are More Directional. *PLoS Comput. Biol.* 7, e1002058(1-8) (2011), doi:10.1371/journal.pcbi.1002058
34. Van den Heuvel, M.G.L., de Graaff, M.P., Dekker, C.: Microtubule curvatures under perpendicular electric forces reveal a low persistence length. *Proc. Nat. Acad. Sci.* 105, 7941–7946 (2008), doi:10.1073/pnas.0704169105
35. Vogel, R., Stark, H.: Submitted to *Eur. Phys. J. E* (2012)
36. Yang, Y., Elgeti, J., Gompper, G.: Cooperation of sperm in two dimensions: Synchronization, attraction, and aggregation through hydrodynamic interactions. *Phys. Rev. E* 78, 061903(1-9) (2008), doi:10.1103/PhysRevE.78.061903
37. Zaburdaev, V., Uppaluri, S., Pfohl, T., et al.: Langevin Dynamics Deciphers the Motility Pattern of Swimming Parasites. *Phys. Rev. Lett.* 106, 208103(1-4) (2011), doi:10.1103/PhysRevLett.106.208103

African Trypanosomes as Model System for Functional Analyses of Microbial Motility

Markus Engstler, Niko Heddergott, Tim Krüger, Eric Stellamanns,
Sravanti Uppaluri, and Thomas Pfohl

The locomotion of microorganisms in a microscopic world, where cells move through a fluid environment without using inertial forces, is a fascinating phenomenon in life science. Nature offers clever and inspiring strategies for self-propelling in an environment of no inertia. The flagellate African trypanosome, which causes African sleeping sickness, moves with help of a flagellum, which is firmly attached to its cell body. The beating flagellum leads to a strong distortion of the cell body and therefore to a swimming agitation of trypanosomes. We have found that trypanosomes use a hydrodynamic mechanism to defend against host's immune attacks. Owing to continuous and directional swimming, host-derived antibodies attached to surface glycoproteins of the cell are dragged to the posterior cell pole, where they are rapidly internalized and destroyed. In the following we present new methodology and techniques to quantify the movements of proteins and the motility of cells. Moreover trypanosome motility schemes and their influence on cellular lifestyle and survival strategies are characterized.

Flagella are essential - not only for motility

In biology nothing is static. Most cells have the ability to move. Frequently, the driving force behind cellular locomotion comes from the beating of one or more flagella. Countless bacteria like Helicobacter or Vibrio and numerous eukaryotic protozoa like Chlamydomonas or Paramecium reveal flagellar motion. Also many cell types of multicellular organisms contain flagella. In the human body billions

Markus Engstler · Niko Heddergott · Tim Krüger
Biozentrum, Department for Cell and Developmental Biology, University of Würzburg,
Würzburg, Germany

Eric Stellamanns · Sravanti Uppaluri · Thomas Pfohl
Max-Planck-Institute for Dynamics and Self-Organization, Göttingen, Germany

Thomas Pfohl
Department of Chemistry, University of Basel, Basel, Switzerland

of flagella and cilia beat, not only driving sperm motility, but also transport of cargo in many organs such as lung, brain, kidney or oviduct. The biological functions of flagella are manifold and not just restricted to locomotion. Primary cilia exist on virtually all vertebrate cells, at least transiently during development [1]. They do not beat but rather fulfill sensory functions. Prominent examples are the photoreceptors of the eye, the olfactory receptors in the nose epithelia or the stereocilia that measure the flow of body fluids [2]. During embryogenesis cilia act as essential sensors for environmental cues. In a nutshell: without cilia no higher eukaryote would exist.

There is no basic difference between flagellum and cilium. Flagella are generally longer and - in contrast to cilia - can exist as single copies, while most ciliated cells contain numerous cilia. The molecular architecture of both organelles is basically identical. However, there are fundamental differences between bacterial and eukaryotic flagella. Unfortunately, the term "flagellum" is used for two totally different structures. Since our work is focused on biophysical aspects of trypanosome locomotion, we will not deal with the prokaryotic flagellum.

The architecture of the eukaryotic flagellum

The central functional structure of all eukaryotic flagella and cilia is the axoneme, which consists of 9 radial and 2 central microtubule doublets. The force driving the flagellar beat is exerted through relative displacement of neighboring microtubules by dyneins, motor proteins that are distributed along the entire length of the axoneme. Each microtubule doublet features inner and outer dyneins, as has been documented by electron microscopy. In virtually all species the distance between dynein molecules along the longitudinal axis is 24 nm and the radius of the axoneme is 200 nm. Nexins cross-link the neighboring radial microtubules, which are in addition connected to the central pair by radial spoke proteins. Nexin is thought to act as elastic spring that counteracts microtubule displacement. Recent work suggests that nexin could be the elusive dynein regulatory complex [3].

The axoneme originates in the basal body, which anchors the flagellum within the cell through the cytoskeleton. The basal body must counterbalance the mechanical force exerted by the beating flagellum. It consists of 9 radial microtubule triplets. How this complex structure is duplicated during mitosis is just one enigma of flagellum biology.

Obviously, axoneme and basal body are not the only components of the eukaryotic flagellum. In fact, a cohort of some 650 proteins makes the flagellum an amazingly complex organelle [4]. Even basic questions regarding flagellum biogenesis and maintenance remain unanswered. For example, new flagella and cilia are not formed at the base but from the tip. This means that in growing flagella all material has to be transported along the length of the organelle by a complex intraflagellar transport system, which is not only active during cell division, but has maintenance functions throughout the cell cycle [5].

What makes a flagellum beat?

About 750 dynein motors are lined up within a single micrometer of axoneme. Would all those motor proteins be active in parallel, the flagellum would be paralyzed. This means that dynein activity has to be tightly controlled in space and time. How this is achieved is still a matter of debate - with rather contrasting models. A biochemical regulation of the flagellar beat through calcium gradients was suggested as early as 1971 [6]. Clearly, the Ca^{2+} and K^+ ion concentrations influence flagellar beat direction and frequency in Chlamydomonas and Paramecium, but the general relevance of this mechanism has not been proven. An alternative and straightforward possibility suggests that activation of dyneins occurs progressively through the propagating flagellar wave itself, being sensed as transient axonemal bending [7]. Another model proposes that the central pair of axonemal microtubules is involved in dynein activation, especially since it rotates in some species and it is absent from non-motile primary cilia [8]. However, in trypanosomes and many metazoa the central microtubules do not rotate, which at least points against a generally applicable mechanism [9]. A more recent model explains the flagellar activity purely based on biomechanical considerations: a flagellar beat is thought to be produced by interactions of simple entities such as springs, stiff elements and nano-motors that produce stable oscillations that can be described mathematically [10]. On one hand, it is remarkable that a fundamental biological question such as the control of flagellar beating remains enigmatic – even after 40 years of intensive research. On the other hand, one could ask why this phenomenon continues to generate significant amount of interest. The answer may lie - as quite often in today's biology - in its medical relevance. Numerous diseases are caused by dysfunctional cilia or flagella [11]. Important hereditary disorders such as polycystic kidney disease (PKD) or Usher syndrome are in fact ciliopathies. In patients suffering from Kartagener syndrome (situs inversus) the entire body architecture is mirrored as the result of malfunctioning of cilia during embryonic development. Thus, understanding the biomechanical mode of operation of cilia will unequivocally be of direct clinical relevance. We postulate that new model systems are required that are more stringent and more easily manipulable. African trypanosomes appear to be prime candidates.

African trypanosomes are killers and model cells

The African parasite *Trypanosoma brucei* was first described by David Bruce (1894) as the causative agent of Nagana disease in cattle. The flagellate protozoan parasite has a digenetic lifestyle that alternates between the insect vector, the infamous tsetse fly, and the bloodstream of the mammalian host. Three morphologically identical subspecies have a vast medical and economic impact in sub-Saharan Africa. *Trypanosoma b. gambiense* and *Trypanosoma b. rhodesiense* cause African sleeping sickness in humans, if untreated ultimately resulting in death. Thus, this parasite is a constant threat in 36 sub-Saharan countries where 300.000-500.000 people are infected annually [12]. In addition to the tremendous

human health burden posed by these deadly pathogens, their rampant infection of wild and domestic livestock by *Trypanosoma b. brucei* makes it nearly impossible to sustain a healthy economy in endemic regions [13] [14].

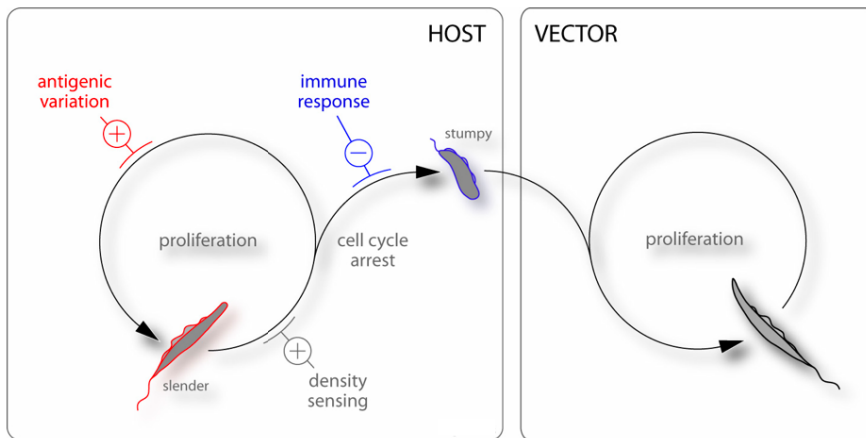


Fig. 1 The life cycle of *Trypanosoma brucei*

The life cycle of *T. brucei* alternates between proliferating and cell cycle arrested stages [15,16]. When an infected tsetse fly feeds on a mammalian host, metacyclic trypanosomes enter the dermal connective tissue through the saliva of the fly, resulting in a local skin infection. This infecting population rapidly undergoes cell cycle re-entry and distinct morphological changes occur. After two to 4 weeks the parasite migrates via the lymphatic system into the bloodstream. Once established in the mammalian host, the bloodstream parasite population is heterogeneous, comprising of proliferative slender cells during the ascending phase of parasitaemia and non-proliferative stumpy cells at the peak of parasitaemia. The slender trypanosomes continuously replicate by binary division, requiring a significant amount of energy that is taken up in the form of glucose from the blood of the mammal. As extracellular parasites, these cells are continuously exposed to the host's immune system. By exchanging the dominant cell surface protein, the variant surface glycoprotein (VSG), long slender forms are able to escape the immune response. This process is called antigenic variation [17]. The trypanosome genome includes several hundred different VSG genes. However, only one VSG is expressed and located at the cell surface at any given time. During an increase in parasitaemia, the host produces antibodies against this specific glycoprotein. By chance, a few cells switch their expression to another, immunologically distinct VSG. From these newly switched cells another population of trypanosomes is able to grow until the antibody attack directed against their surface protein eliminates also those cells and a switch to yet another VSG occurs. The mechanisms of regulation for the activity of expression sites are

not fully understood, but recent evidence confirms that epigenetic processes are involved [18].

The trypanosome surface coat

The biochemical basis of antigenic variation is the trypanosome cell surface coat that is completely covered by VSGs, homodimeric glycoproteins that adopt similar shapes [19,20]. Each VSG monomer has a molecular mass of 45–55 kDa. VSGs are the prototypic GPI-anchored proteins (GPI-APs): a lipid moiety anchors the protein to the outer leaflet of the plasma membrane. In contrast to the large diversity of membrane-spanning peptide domains, GPI-anchors provide a relatively constant and comparable mode of membrane attachment [21]. Therefore, the effect of the ectodomain should be more pronounced for these GPI-anchored proteins than for membrane proteins embedded in the membrane through bulky peptide chains. All GPI anchors contain a conserved core glycan that is linked to the C-terminal residue of a protein via a peptide bond and attached to the membrane through two fatty acid chains.

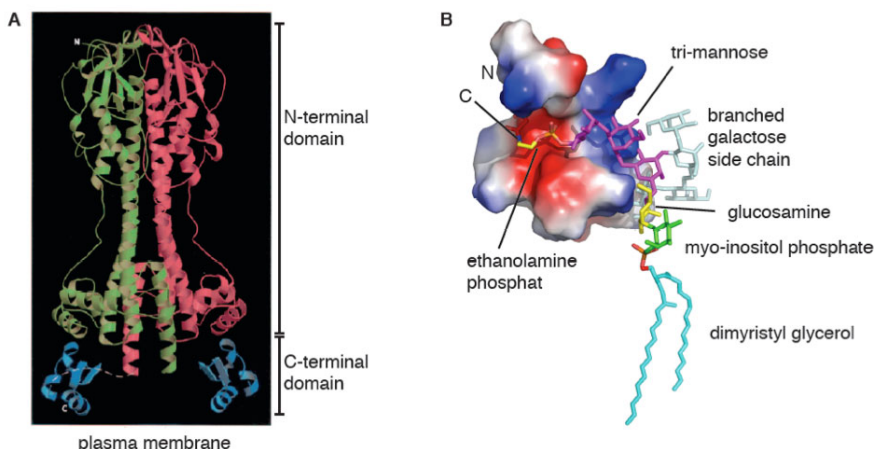


Fig. 2 The molecular structure of the trypanosome variant surface glycoprotein (VSG). **A.** Model of the complete VSG MITat 1.2 based on the N-terminal domain crystal structure and the C-terminal domain NMR structure. **B.** Model of the lipid bilayer proximal C2 domain of ILTat 1.24 with its GPI-anchor (stick model).

The VSG coat is unique in nature. There is no other cell surface that is dominated by just one type of protein. Thus, trypanosomes are ideally suited for studies on the behavior of membrane proteins. Despite diffusion in a three dimensional fluid being well understood many questions remain regarding the mobility of cell surface proteins. Why is it difficult to predict the movement of membrane proteins? For a protein attached to a cell membrane, which can be

described as a 2-dimensional liquid, there is no direct solution for the Stokes equation, which is known as the Stokes paradox. Saffman and Delbrück solved this problem by taking into account that the two dimensional membrane is embedded in a 3-dimensional fluid [22]. In their hydrodynamic model, which is still the most accepted theoretical model for diffusion of membrane proteins, the lipid bilayer is defined as an infinite plane sheet of viscous fluid embedded in an infinite bulk fluid of much lower viscosity. The protein is assumed to span the entire membrane thickness. The ingenious theoretical considerations of the Saffmann-Delbrück approximation infer that the membrane-spanning domain is the major determinant of diffusion and that the radius of this domain shows only a weak logarithmic relation to the diffusion coefficient. Experimental studies of diffusion constants have shown that some membrane systems are adequately described by this theory, whereas others are not. The Singer-Nicolson description of protein organization on a biological membrane assumes a relatively low density of protein on the cell surface. The protein is thought to be randomly distributed and to show free diffusion [23]. It has since however become clear that proteins can be densely packed on the cell membrane and that the cell membrane and surface architecture is more complex. The mobility of a membrane protein may be governed not only by the properties of the protein itself, but also by its environment. Research on trypanosomes has provided compelling evidence that this is the case [24].

Antibody removal exploits hydrodynamic drag

Since lateral spacing between VSG dimers is just 3 nm, host immune effector molecules such as antibodies cannot recognize invariant proteins hidden beneath the VSG coat. Therefore, host antibodies always bind to the exposed, highly variable N-terminal parts of the VSG. Strikingly, once bound to VSG, these antibodies are removed from the cell surface of bloodstream trypanosomes. We found that this process is surprisingly fast. Within 20-40 s VSG-bound IgGs (VSG-IgG) accumulate at the flagellar pocket region. This small invagination of the plasma membrane is the sole place for endocytosis and membrane recycling in *T. brucei*. VSGs are rapidly internalized via clathrin-mediated endocytosis. 3D-fluorescence microscopy and quantitative colocalization analyses with organelle-specific marker proteins confirm that a significant amount of antibody is routed via late endosomes to the lysosome, while VSG is recycled to the cell surface. The internalization of antibody-bound VSG from the trypanosome cell surface comprises three consecutive steps each displaying distinct temperature sensitivity. Initially, VSG-IgG accumulate at the posterior pole of the cell. The kinetics of this process is comparatively independent of temperature; even at 12°C rapid antibody accumulation is observed. In contrast, the rate of entry of VSG-IgG into the flagellar pocket is significantly decelerated at 24°C, and at 12°C the process almost halts. Once arrived in the flagellar pocket, VSG-IgG is internalized by bulk membrane uptake. The endocytosis of IgG-bound VSG exhibits similar

temperature sensitivity as the entry into the flagellar pocket. When compared to yeast or mammalian cells, endocytosis in *T. brucei* is less temperature-dependent; significant plasma membrane recycling proceeds even at temperatures below 12°C. Hence, we assume that the observed temperature-sensitivity of VSG-IgG internalization is due to slow traffic through the flagellar pocket, which is filled with a dense, gel-like, carbohydrate-rich matrix. Our experiments suggest a three-step process with posterior accumulation of antibodies as immediate event and passage through the flagellar pocket as rate-limiting step. To our surprise, we found that the first step of antibody clearance, the posterior accumulation of VSG-IgG, is not due to VSG-shedding and is independent of endocytosis. Down-regulation by RNA-interference (RNAi) of clathrin heavy chain causes a block of all endocytic traffic. Although in clathrin-depleted cells endocytosis is stalled, VSG-IgG accumulates at the flagellar pocket in a similar manner as in control cells. To determine whether the posterior accumulation of VSG-IgG requires energy, cells were incubated with anti-VSG antibodies in the presence of sub-lethal amounts of the glycolytic inhibitor 2-deoxyglucose. With increasing concentrations of the drug the number of cells revealing a posterior accumulation of VSG-IgG decreased. When cellular motility stalled due to ATP-depletion, no antibody-accumulation was observed, but all trypanosomes remained uniformly coated with immunoglobulins. In those cells the plasma membrane, the VSG coat and the cellular morphology remained unaffected. This suggested a correlation of cellular motility and antibody clearance. Bloodstream stage *T. brucei* swim with an average speed of about $20 \mu\text{m s}^{-1}$. The directional motion is mediated by a single flagellum, which emerges from the flagellar pocket, attaches to the cell body and extends beyond the anterior pole of the cell. The FlaI protein is essential for the connection of the flagellum to the cell body. Down-regulation by RNAi of FlaI results in detachment of the flagellum and loss of directional motility. FlaI-depleted trypanosomes retain their VSG coat and VSG-bound antibodies are internalized from the flagellar pocket with similar kinetics as in control cells. Strikingly, however, the obstruction of directional swimming coincides with the loss of accumulation of antibody-bound VSG at the posterior cell surface. Conversely, a marked reduction of antibody staining is observed in the flagellar pocket area, which is explained by continuing membrane recycling in the absence of antibody accumulation. These results indicated a direct involvement of cell motility and endocytosis in antibody clearance. To determine the specificity of the process, trypanosomes were treated with immunoglobulins of different classes, as well as with antibody fragments and other surface-binding proteins. Specific polyclonal and monoclonal IgG were removed from the cell surface of live trypanosomes with virtually identical kinetics, while the corresponding F(ab')2 and Fab were internalized with markedly reduced kinetics. Since IgG and F(ab')2 bind VSG with equal valency and avidity, the difference in the uptake rates must be a function of the Fc part of the IgG. IgG molecules attached to VSG would protrude about 15 nm above the surface coat, while Fab fragments or streptavidin

are much smaller. Thus, the size, but not necessarily the nature of the protein bound to VSG was critical for the accelerated removal from the cell surface. Due to its pentameric nature IgM is much larger than IgG. Therefore, we compared the rate of removal from the cell surface of VSG-specific IgG and IgM. Both immunoglobulins were internalized from the VSG coat in a concentration-dependent manner; however, the overall kinetics of IgM-uptake was significantly faster. But, what is the actual driving force behind the motion of VSG-Ig? A motor activity acting from inside the cell and the specific recognition of antibody-bound VSGs by e.g. adapter proteins appear unlikely, since VSGs are anchored via a lipid moiety only into the outer leaflet of the plasma membrane. We have shown that VSG-Ig movement strictly depends on cell motility and the size of the bound molecule. Therefore, we assume that hydrodynamic flow acting on the directionally swimming trypanosome specifically drags antibody-bound VSGs towards the flagellar pocket, from where they are rapidly endocytosed. Though this scenario suits all experimental results, one may ask whether hydrodynamic forces would actually suffice to drag molecules on cell surfaces? According to Boltzmann's law, the probability of finding a particle at this characteristic distance h_0 is 37% ($1/e$) that of finding it at zero distance. Since h_0 is in the order of magnitude of the trypanosome length L , the potential due to the drag force is in fact strong enough to generate the gradient in the distribution of VSG-antibody complexes on the trypanosome surface, which has been found in the experiments. Furthermore, blood vessels with diameters in the order of magnitude of the size of a trypanosome, such as capillaries (diameter $d \approx 8 \mu\text{m}$) and venules ($d \approx 20 \mu\text{m}$), influence local flow fields in the vicinity of trypanosome surfaces and therefore the timescale of the removal of VSG-antibody complexes. The influence of these confining geometries on velocity fields is modeled by using numerical finite element method simulations. The incompressible Navier-Stokes-equation is solved in two dimensions with an axial symmetry (symmetry axis at $x = 0$) using about 30,000 elements to obtain a stationary solution. The trypanosome is modeled by an axial symmetric body and the flow is simulated by applying a constant velocity profile of $v_t = 20 \mu\text{m/s}$ at $z = 0$ and a vanishing velocity at the trypanosome surface, $v_s = 0$. A decrease of the capillary diameter leads to a strong increase of the velocity in the vicinity of the trypanosome surface. Owing to the increased local velocity, a higher drag force is acting on the VSG-antibody complexes leading to faster removal of the antibodies. Thus, depending on the current habitation within the mammalian bloodstream the motion of VSG-Ig on the trypanosome cell surface may vary. Besides antigenic variation *T. brucei* has evolved a subtle defense strategy, in which directional cell motility and plasma membrane recycling function cooperatively in the removal of host antibodies from the cell surface. Our work has established that hydrodynamics influences the behavior of proteins on cells. Since many cells are capable of swimming (faster than trypanosomes), flow-induced movement of proteins may well be a general, organizing theme in biology [24].

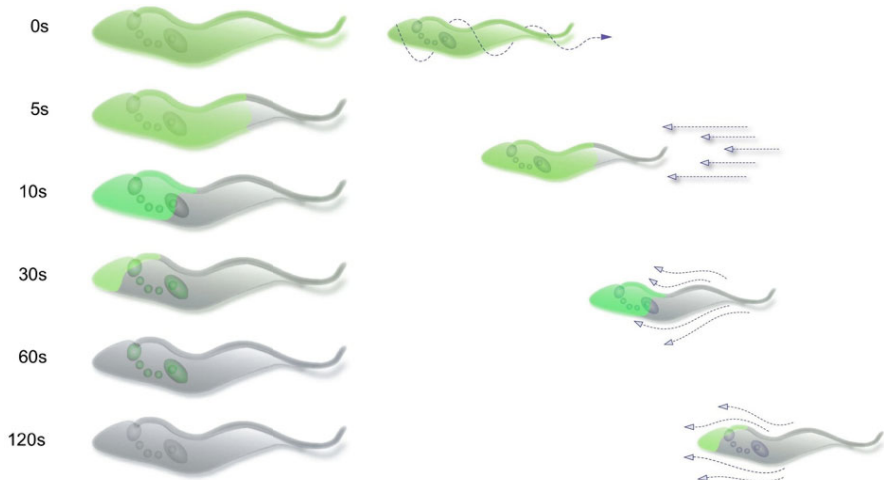


Fig. 3 African trypanosomes continuously swim and thereby generate directional flow fields on their cell surface. These flow forces become functional when the surface coat, which is dominated by variant surface glycoproteins (VSG), is attacked by host immunoglobulins. Antibody-VSG complexes are caught by hydrodynamic forces and dragged towards the rear of the cell, where they are endocytosed. This means that pure physical forces can sort proteins in the plane of the plasma membrane. The schematic drawing depicts rapid redistribution and endocytosis of antibody (green) bound to VSG (grey).

Trypanosomes reveal a complex mode of motility

The unicellular green algae Chlamydomonas is an accepted model system for studies on flagellate motility [25] [26]. Chlamydomonas features two flagella, which work cooperatively. The cell can control swimming direction in response to light signals. Most facts we know about formation and maintenance of eukaryotic flagella come from research on Chlamydomonas. Based on their unique cell architecture and the VSG coat, as well as their incessant motion, African trypanosomes must be regarded a new prime model for functional analyses on microbial motility. All state-of-the-art molecular techniques, such as reverse and forward genetics, in vitro-cultivation and manipulation are established [27]. The genomes of several trypanosome species have been sequenced. Transcriptome and proteome data are available. In view of all these achievements it appears almost awkward that the exact mode of trypanosome motility still appears to be controversial. However, if one takes a closer look at the trypanosome flagellum, our lack of understanding becomes less surprising.

Trypanosome motion is amazingly complex. Unlike Chlamydomonas and other flagellate protozoa trypanosome feature an attached flagellum. Only a minor portion extends beyond the anterior cell pole. The flagellum originates at the flagellar pocket, which is located close to the posterior end of the parasite. Live trypanosomes move too quickly for the human eye and also for conventional

microscope cameras. Our understanding of trypanosome motion mainly comes from the morphological interpretation of dead cells and microscopic observation with insufficient temporal resolution. It became common knowledge that an undulating membrane links the flagellum to the cell body and that the cells move in a corkscrew-like fashion due to the flagellum being wrapped around the cell body. However, how the flagellum is oriented and how many turns it makes around the trypanosome cell and in which orientation was unknown. We performed a systematic analysis and obtained 3-dimensional high-resolution images of hundreds of cells using deconvolution fluorescence microscopy. In addition scanning electron microscopy was performed on carefully fixed samples. The experiments clearly show that (1) an undulating membrane does not exist and (2) the flagellum just makes a left-handed half-turn around the cell. Thus, the trypanosomes reveal a rather uniform cellular asymmetry that must influence their mode of motility. To analyze the trypanosome swimming at sufficient spatial and temporal resolution we adopted high-speed imaging. Besides bright field illumination, for the first time sCMOS-technology was applied allowing observation of trypanosomes fluorescently stained on the cell surface, including flagellar pocket and flagellum. The amount of image data generated by both techniques is substantial. Each second of imaging produces about 4 gigabytes of data. Thus, the analysis and interpretation of such large image sequences is elaborate and requires profound understanding of trypanosome cell architecture. Therefore, we have developed semi-automated analysis tools for unambiguous tracking of cell axis and flagellar tip. To facilitate the extraction of true 3-dimensional information from 2-dimensional image series we have applied time-dependent tomography: *xyt*-image series of directionally swimming trypanosomes were acquired at frame rates of 500-1000 Hz. Successive flagellar beats were analyzed and one image depicting the beginning of each beat was selected. The two-dimensional view of these images was compared and identical periodically repeating phases were identified. The images selected from this period of movement were used for the tomography, using the 3ds Max software (Autodesk Inc., San Rafael, CA). The cell contours were traced in each image and extruded to a three-dimensional object. These 3D-representations of successive beats were then aligned to an anterior-posterior axis. The 3D-models were rotated around this axis by a constant angle per beat and the intersecting regions of the rotated models were calculated and extracted to produce a tomographic 3D-model of the original object. A correct three-dimensional model of a trypanosome cell body was only produced when the rotational angle per beat was in the range of $50^\circ \pm 10^\circ$ and the rotation was unidirectional. The data obtained using time-dependent tomography were confirmed by *z*-axis-oscillation high-speed microscopy. This novel technique makes use of extremely fast piezo-driven *z*-focus oscillations. The periodic repositioning of the microscope objective yields 3-dimensional information from high-speed movies.

By combining those novel techniques with our morphometric data we were able to draw an unequivocal picture of the trypanosome mode of motility:

The trypanosome flagellum produces waves that move unidirectional from the flagellar tip to the base with a constant frequency of about 18 Hz. At any given

time 2-3 waves propagate along the flagellum, the youngest one at the flagellar tip. While the amplitude is damped by the cell body, a change in the frequency of the flagellar beat was not observed. Locomotion occurs step-wise with each flagellar beat. Due to the virtual absence of inertia at low Reynolds numbers, cell propulsion stops transiently for several milliseconds. This demonstrates that the major propelling force of trypanosome movement is likely to be produced by the beat of the free anterior part of the flagellum. This follows from the observation that the damped waves, continuing along the asymmetrical cell body, caused the cell to rotate, but not with sufficient angular velocity to propel the body to the observed swimming speed. Besides, the rotation speed was not found to be dependent on propagation speed. Again, we did not find any support for the existence of an undulating membrane, the flexible, fin-like extension between cell body and the attached flagellum, which was thought to contribute to trypanosome motion. In summary, our work details the mode of trypanosome swimming and clearly contradicts an alternative model in which the cells are driven by the progression of kinks along the cell body axis [28] [29].

The swimming trypanosome: identifying three motility classes

In order to analyze the motility patterns of the trypanosomes, we examined trajectories under non-flow conditions in a two-dimensional environment. Recent studies of trypanosome motility have focused exclusively on cells swimming directionally [28] [30]. However, it is known that more than half of a trypanosome population is dividing under normal culture conditions underscoring the importance of carrying out population-wide analysis for quantitative characterization. Cell swimming was observed between two microscope slides in HMI-9 complete medium in a 2-dimensional setting between a microscope slide and a coverslip [31]. The cells are in a homogeneous environment with no chemical gradients, therefore specific chemo-attraction may be ruled out as the basis for cell locomotion in this study. The swimming cells are recorded for several minutes with a camera frame rate of about 7 Hz. As seen in the trajectories (fig. 4a), trypanosomes from the same population taken from the same cell culture, which are exposed to identical environmental conditions evidently, do not follow a single motility mode. A combined data analysis of all individual trajectories reveals two characteristic times in the motion of the trypanosome that differ by an order of magnitude. The locomotion of the trypanosome can be described by a superposition of a persistent motion with a large relaxation time of about 10 s and a highly fluctuating component resulting from strong and fast deformations of the trypanosome's body with a typical time < 1s [32] [33].

In a more detailed analysis of the cell trajectories within a trypanosome population, we can identify three different motility classes: the first motility mode is one in which trypanosomes “tumble” with no persistent motion, trypanosomes of the second motility class show a strong persistent motion, whereas the third motility class is a combination of both classes: cells swim directionally with constant cell orientation but occasionally stop, tumble and reorient themselves and then move directionally again. Characteristic trajectories, mean square

displacement (MSD) given by $\langle x(\tau)^2 \rangle = \langle (r(t) - r(t-\tau))^2 \rangle$, where $\langle x^2 \rangle$ is the MSD, r is position, and τ the ‘profile’ time, and velocity distributions of the different motility classes are shown in fig. 4.

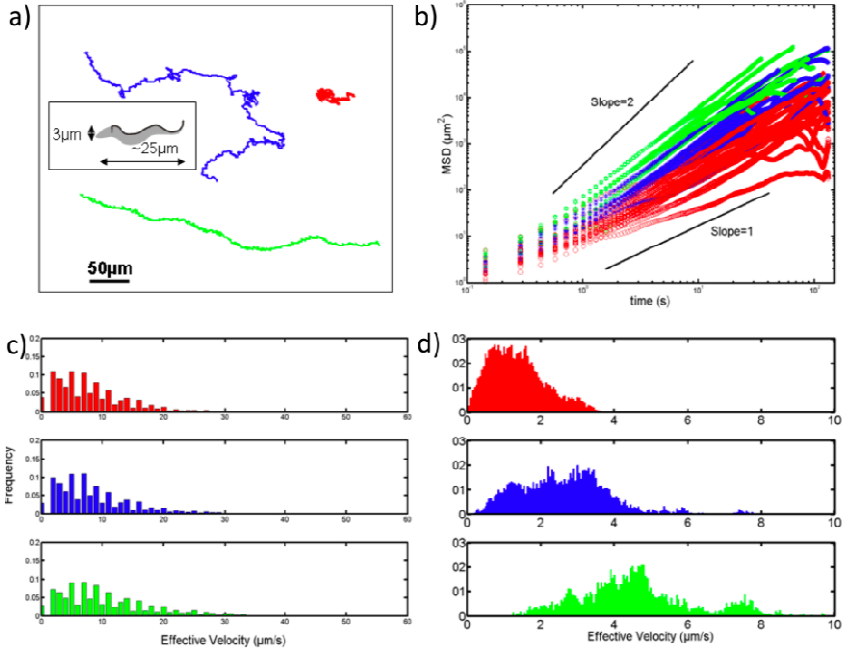


Fig. 4 Characterization of trypanosome trajectories: a) diversity in trypanosome trajectories, reveals three motility modes; b) mean squared displacement of population shows that scaling is different for each mode; c), d) population wide velocity distributions are identical, motility modes are revealed when profiling time increases.

In order to investigate the microscopic origin of the observed macroscopic motility behavior, we examine trypanosomes at higher magnifications with bright field illumination and higher temporal resolution using camera frame rates of 1000 Hz for a minimum of 7 s [33]. Since the cell body of the trypanosome is not amenable to an easy analysis, we chose a straightforward approach and examine the variations in the distance between the posterior end and the anterior end of the cell (“end-to-end distance”) over time. Trypanosomes are tracked for a period of time in order to ascertain their motility class followed by high-speed recordings of their movement. Recorded images are processed as in fig. 5a). A skeleton line through the center of the cell body is obtained and the end-to-end distance is found for each frame. Thus a time series normalized to the contour length is obtained as shown in fig 5b).

Histograms of the end-to-end distances show clear differences between the swimming behaviors (fig. 5c) and indicate that directional persistence could be the result of an elongated cell shape. Cells with a directional persistence have on average a more stretched body shape with much less flexibility than cells with a random walk/tumbling motion. The mean normalized end-to-end distance of persistent cells is 0.6 - about 1.5 times that of random walkers for which it is about 0.4. Describing the shape of the trypanosome as a worm-like chain [34] [35], the mean squared end-to-end distance can be attributed either to a difference of cell energy consumption or of flexural rigidity of the cell body. Taking into account almost equal energy utilization for trypanosomes of the different motility classes, we find a 3 times higher flexural rigidity for the persistent cells in comparison to tumbling cells [33]. The directional cells may be stiffer due to reorganization of motor proteins and cross-linking within the microtubules found both in the cell body and the flagellum. It is of course not unlikely that these observations are due to an interplay of differences in flexural rigidity and also energy utilization for cell motion.

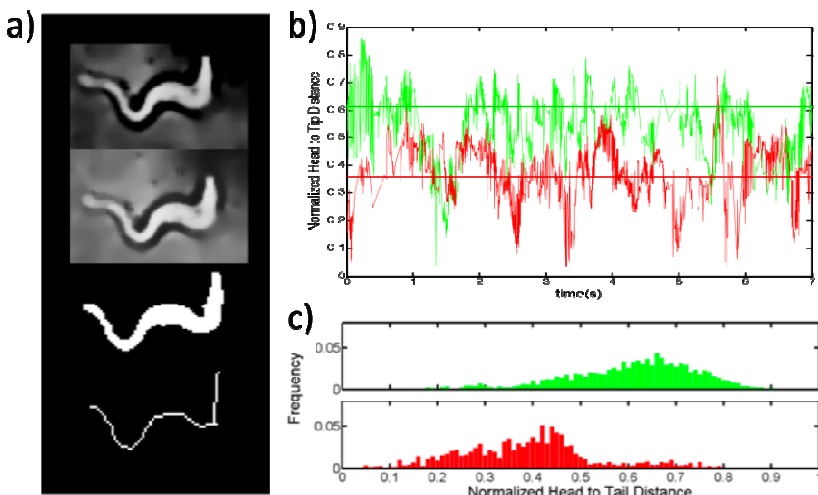


Fig. 5 Analysis of trypanosome motility on the millisecond time scale: a) image processing method of reconstruction “head to tail distance” (posterior to anterior end) to obtain a skeleton line; b) end to end distance of trypanosomes of different classes versus time; c) distribution of end to end distance in trypanosomes of different classes.

Trypanosomes in geometric confinement

During both their life and cell division cycles trypanosomes have to migrate through various kinds of tissues into the lymphatic system, the blood stream and into tissue again. All these environments are very different in their spatial structure and trypanosome motility has to be well adapted to these conditions.

Using microfluidic devices we constructed microchannels of varying sizes in order to examine trypanosome motility within geometric confinements that mimic dimensions of both the blood capillary and the interstitial (spaces between cells and lymph) habitat [36].

The devices are fabricated by soft lithography and the trypanosomes are imaged by brightfield microscopy. In order to analyze trypanosome motility in confinement, it is necessary to create strict stop flow conditions. Therefore, we developed a microfluidic stop flow device with channels orientated perpendicular to the pressure gradient existing between inlet and outlet. Trypanosome motility is analyzed in channels of different widths. We found that trypanosomes can penetrate through channels, which are narrower than the diameter of the parasites (fig. 6).

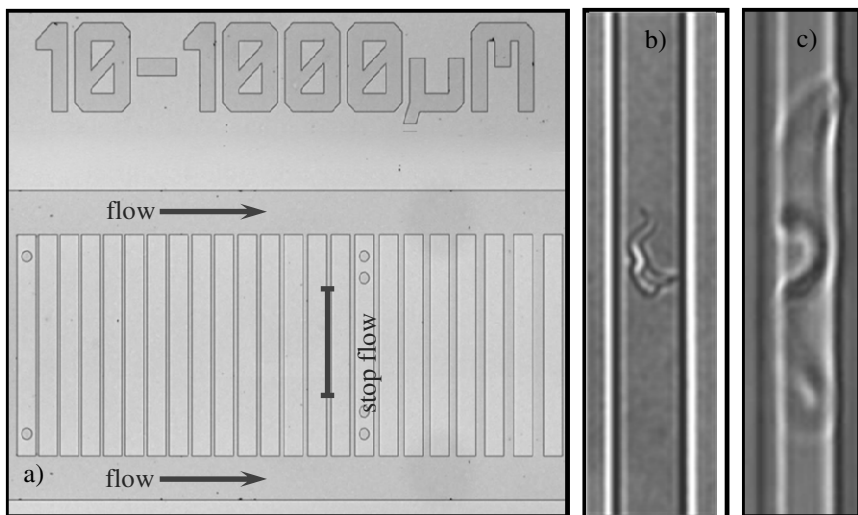


Fig. 6 a) Image of a microfluidic stop flow device. Trypanosomes in b) 10 μm and c) 2 μm microfluidic stop flow channel [36].

Two different velocities can be characterized. The mean velocity \bar{v}_{xy} is given by the center of mass displacement and the mean x -directional (parallel to the channel orientation) velocity \bar{v}_x is given by the x -axis displacement (fig. 7). In the largest channels (width = 20 μm), $\bar{v}_{xy} = 20 \mu\text{m}\cdot\text{s}^{-1}$ is higher than $\bar{v}_x = 15 \mu\text{m}\cdot\text{s}^{-1}$, indicating that there is almost no impact of confinement on the cell motility (where $\bar{v}_x/\bar{v}_{xy} = 1/\sqrt{2} \approx 0.707$ for free motility $\bar{v}_x = \bar{v}_y$). With decreasing channel width the geometric constraints increase and the ratio of \bar{v}_x/\bar{v}_{xy} approaches 1 (almost no \bar{v}_x -component) with a mean velocity of

$\bar{v}_{\min} = 6.5 \mu\text{m}\cdot\text{s}^{-1}$ in channels of 2 μm . Whereas directional persistent cells are decelerated by the increased friction with the walls of smaller channels, a different behavior is observed for tumbling cells: confinement induces a weak but yet directional motion.

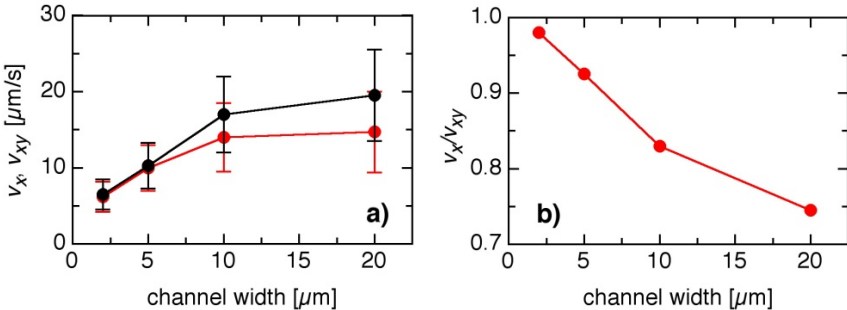


Fig. 7 a) \bar{v}_x and \bar{v}_{xy} for different channel widths; b) \bar{v}_x / \bar{v}_{xy} for different channel widths

Turn angle distributions depending on channel widths are analyzed as well. We characterize the turn angle distributions by the full width at half maximum, σ . The impact of the channel width on σ is shown in fig. 8. In the widest channels (20 μm), where the channel width almost equals the length of the cells, σ shows a small effect of confinement, however the cell motion is only weakly restricted. Decreasing the channel width from 20 to 10 μm the orientation increases weakly (σ decreases), whereas decreasing the channel width further a strong increase of orientation can be found with a minimal $\sigma \approx 10^\circ$ for a channel width of 2 μm . At channels width $\leq 10 \mu\text{m}$ the amount of wall contacts increases and therefore the friction between the trypanosomes and the walls as well. Due to the increased friction σ is dramatically reduced and the freedom of turn angle displacement is strongly restricted.

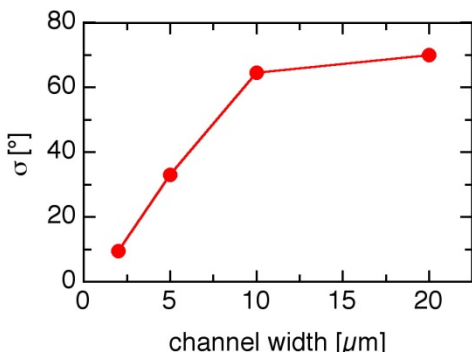


Fig. 8 σ for different channel widths

Trypanosomes in optical confinement

Optical micromanipulation of biological matter and living cells is a remarkable and interesting biophysical tool [37]. Although the shape and dimensions of trypanosomes strongly differ from commonly manipulated and caught biomaterials and cells, we are able to optically trap and micromanipulate trypanosomes in microfluidic environment. We are using an optical tweezers setup with infrared laser diodes (≈ 800 nm) to optically trap living trypanosomes. Therefore, we are able to repeatedly and for extended periods (over 10 min) trap trypanosomes in flow cells without harming the parasite or interfering with the flagellar beat. Caught self-propelling trypanosomes rotate with a frequency of 2 – 3 Hz within the optical trap. Trypanosomes can be trapped at more or less any position along the cell body; however, the most probable position is close to the flagellar pocket. Living trypanosomes are successfully trapped within a microfluidic flow chamber at different laser powers. A linear flow ramp is repeatedly applied and the cells are recorded until they get dragged out of the trap. The positioning and trapping of trypanosomes within hydrodynamic flow controlled microdevices is shown in fig. 9.

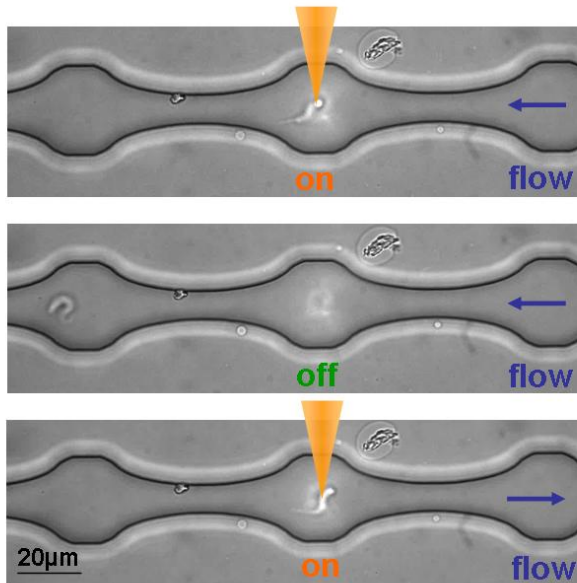


Fig. 9 Control of positioning of trypanosomes in microfluidic channels owing to the combination of hydrodynamic flow and optical tweezers [36].

Owing to the self-propelling of trypanosomes and the beating of the flagellum, a force is acting on the surrounding fluid molecules. At the same time the cell body is deformed and forces act on the intracellular environment as well. In order to distinguish fluid drag from trypanosome's propulsion forces, which have

contributions to stall forces in tweezers experiments, the experiments have to be repeated with immobilized cells. Cell immobilization with 2-deoxy-D-glucose as glucose substitute is reversible for incubation times smaller than 45 min whilst the overall cell structure remains unchanged [38]. Taking the cell morphology and friction coefficients into account, we can determine from the optical stall forces of living and immobilized trypanosomes the generated self-propelling force. The obtained propulsion force is in the order of magnitude of 1 – 2 pN and leads to lower escape flow velocities in case of motile trypanosomes.

Trypanosomes not only need the measured force generation in the order of magnitude of a few pN for self-propulsion but also to penetrate through tissue meshes and the blood-brain barrier.

We have presented new methodology and techniques to quantify the movements of proteins and the motility of cells in order to analyze and characterize motility schemes and their influence on cellular lifestyle and survival strategies. Extending the present experiments to include flow for further investigations into the biological relevance of motility schemes may thus help identify the importance of cell swimming in various infective stages.

Acknowledgments. We thank Vasily Zaburdaev, Holger Stark, Jan Nagler, Sujin Babu, Axel Hochstetter, and Stephan Herminghaus for helpful discussions.

References

1. Salisbury, J.L.: Primary cilia: putting sensors together. *Current Biology*: CB 14(18), R765–R767 (2004), doi:10.1016/j.cub.2004.09.016
2. Egorova, A.D., van der Heiden, K., Poelmann, R.E., Hierck, B.P.: Primary cilia as biomechanical sensors in regulating endothelial function. *Differentiation; Research in Biological Diversity* (2011), doi:10.1016/j.diff.2011.11.007
3. Heuser, T., Raytchev, M., Krell, J., Porter, M.E., Nicastro, D.: The dynein regulatory complex is the nexin link and a major regulatory node in cilia and flagella. *The Journal of Cell Biology* 187(6), 921–933 (2009), doi:10.1083/jcb.200908067
4. Fliegauf, M., Omran, H.: Novel tools to unravel molecular mechanisms in cilia-related disorders. *Trends in Genetics*: TIG 22(5), 241–245 (2006), doi:10.1016/j.tig.2006.03.002
5. Baldari, C.T., Rosenbaum, J.: Intraflagellar transport: it's not just for cilia anymore. *Current Opinion in Cell Biology* 22(1), 75–80 (2010), doi:10.1016/j.ceb.2009.10.010
6. Miles, C.A., Holwill, M.E.: A mechanochemical model of flagellar activity. *Biophysical Journal* 11(11), 851–859 (1971), doi:10.1016/S0006-3495(71)86259-8
7. Brokaw, C.J.: Introduction: generation of the bending cycle in cilia and flagella. *Progress in Clinical and Biological Research* 80, 137–141 (1982)
8. Yagi, T., Kamiya, R.: Novel mode of hyper-oscillation in the paralyzed axoneme of a Chlamydomonas mutant lacking the central-pair microtubules. *Cell Motility and the Cytoskeleton* 31(3), 207–214 (1995), doi:10.1002/cm.970310304
9. Lindemann, C.B., Lesich, K.A.: Flagellar and ciliary beating: the proven and the possible. *Journal of Cell Science* 123(Pt 4), 519–528 (2010), doi:10.1242/jcs.051326
10. Mitchison, T.J., Mitchison, H.M.: Cell biology: How cilia beat. *Nature* 463(7279), 308–309 (2010), doi:10.1038/463308a

11. Afzelius, B.A.: Asymmetry of cilia and of mice and men. *The International Journal of Developmental Biology* 43(4), 283–286 (1999)
12. Paliwal, S.K., Verma, A.N., Paliwal, S.: Neglected disease - african sleeping sickness: recent synthetic and modeling advances. *Scientia Pharmaceutica* 79(3), 389–428 (2011), doi:10.3797/scipharm.1012-08
13. Davis, S., Aksoy, S., Galvani, A.: A global sensitivity analysis for African sleeping sickness. *Parasitology* 138(4), 516–526 (2011), doi:10.1017/S0031182010001496
14. Malvy, D., Chappuis, F.: Sleeping sickness. *Clinical microbiology and infection. The Official Publication of the European Society of Clinical Microbiology and Infectious Diseases* 17(7), 986–995 (2011), doi:10.1111/j.1469-0691.2011.03536.x
15. Engstler, M., Boshart, M.: Cold shock and regulation of surface protein trafficking convey sensitization to inducers of stage differentiation in *Trypanosoma brucei*. *Genes & Development* 18(22), 2798–2811 (2004), doi:10.1101/gad.323404
16. Fenn, K., Matthews, K.R.: The cell biology of *Trypanosoma brucei* differentiation. *Current Opinion in Microbiology* 10(6), 539–546 (2007), doi:10.1016/j.mib.2007.09.014
17. Field, M.C., Lumb, J.H., Adung'a, V.O., Jones, N.G., Engstler, M.: Macromolecular trafficking and immune evasion in african trypanosomes. *International Review of Cell and Molecular Biology* 278, 1–67 (2009), doi:10.1016/S1937-6448(09)78001-3
18. Horn, D., McCulloch, R.: Molecular mechanisms underlying the control of antigenic variation in African trypanosomes. *Current Opinion in Microbiology* 13(6), 700–705 (2010), doi:10.1016/j.mib.2010.08.009
19. Carrington, M., Boothroyd, J.: Implications of conserved structural motifs in disparate trypanosome surface proteins. *Molecular and Biochemical Parasitology* 81(2), 119–126 (1996)
20. Overath, P., Haag, J., Lischke, A., O'Huigin, C.: The surface structure of trypanosomes in relation to their molecular phylogeny. *International Journal for Parasitology* 31(5-6), 468–471 (2001)
21. Thomas, J.R., Dwek, R.A., Rademacher, T.W.: Structure, biosynthesis, and function of glycosylphosphatidylinositols. *Biochemistry* 29(23), 5413–5422 (1990)
22. Saffman, P.G., Delbrück, M.: Brownian motion in biological membranes. *Proceedings of the National Academy of Sciences of the United States of America* 72(8), 3111–3113 (1975)
23. Singer, S.J., Nicolson, G.L.: The structure and chemistry of mammalian cell membranes. *The American Journal of Pathology* 65(2), 427–437 (1971)
24. Engstler, M., Pfohl, T., Herminghaus, S., Boshart, M., Wiegertjes, G., Heddergott, N., Overath, P.: Hydrodynamic flow-mediated protein sorting on the cell surface of trypanosomes. *Cell* 131(3), 505–515 (2007), doi:10.1016/j.cell.2007.08.046
25. Stahl, N., Mayer, A.M.: Experimental Differentiation between Phototaxis and Motility in *Chlamydomonas snowiae*. *Science* 141(3587), 1282–1284 (1963), doi:10.1126/science.141.3587.1282
26. Bloodgood, R.A., Leffler, E.M., Bojczuk, A.T.: Reversible inhibition of *Chlamydomonas* flagellar surface motility. *The Journal of Cell Biology* 82(3), 664–674 (1979)
27. Field, M.C., Allen, C.L., Dhir, V., Goulding, D., Hall, B.S., Morgan, G.W., Veazey, P., Engstler, M.: New approaches to the microscopic imaging of *Trypanosoma brucei*. *Microscopy and microanalysis. The Official Journal of Microscopy Society of America, Microbeam Analysis Society, Microscopical Society of Canada* 10(5), 621–636 (2004), doi:10.1017/S1431927604040942

28. Rodriguez, J.A., Lopez, M.A., Thayer, M.C., Zhao, Y., Oberholzer, M., Chang, D.D., Kisalu, N.K., Penichet, M.L., Helguera, G., Bruinsma, R., Hill, K.L., Miao, J.: Propulsion of African trypanosomes is driven by bihelical waves with alternating chirality separated by kinks. *Proceedings of the National Academy of Sciences of the United States of America* 106(46), 19322–19327 (2009), doi:10.1073/pnas.0907001106
29. Heddergott, M.: Zellbiologische Aspekte der Motilität von *Trypanosoma brucei* unter Berücksichtigung der Interaktion mit der Mikroumwelt. PhD-Thesis. University of Wuerzburg (2011)
30. Ralston, K.S., Kabututu, Z., Melehani, J.H., Oberholzer, M., Hill, K.L.: The *Trypanosoma brucei* flagellum: moving parasites in new directions. *Annual Review of Microbiology* 63, 335–362 (2009), doi:10.1146/annurev.micro.091208.073353
31. Uppaluri, S.: Unicellular parasite motility: a quantitative perspective. PhD-thesis. University of Göttingen (2011)
32. Zaburdaev, V., Uppaluri, S., Pfohl, T., Engstler, M., Friedrich, R., Stark, H.: Langevin dynamics deciphers the motility pattern of swimming parasites. *Phys. Rev. Lett.* 106, 208103 (2011), doi:10.1103/PhysRevLett.106.208103
33. Uppaluri, S., Nagler, J., Stellamanns, E., Heddergott, N., Herminghaus, S., Engstler, M., Pfohl, T.: Impact of microscopic motility on the swimming behavior of parasites: straighter trypanosomes are more directional. *PLoS Comput. Biol.* 7, e1002058 (2011), doi:10.1371/journal.pcbi.1002058
34. Köster, S., Pfohl, T.: An in vitro model system for cytoskeletal confinement. *Cell Motil Cytoskeleton* 66, 771–776 (2009), doi:10.1002/cm.20336
35. Howard, J.: Mechanics of Motor Proteins and the Cytoskeleton. Sinauer Associates, Inc., Sunderland (2001)
36. Stellamanns, E.: Cell motility in microfluidic environments. PhD-Thesis. University of Göttingen (2011)
37. Ashkin, A., Dziedzic, J.M.: Optical trapping and manipulation of viruses and bacteria. *Science* 235, 1517–1520 (1987), doi:10.1126/science.3547653
38. Parsons, M., Nielsen, B.: Active transport of 2-deoxy-D-glucose in *Trypanosoma brucei* procyclic forms. *Mol. Biochem. Parasitol.* 42, 197–203 (1990), doi:10.1016/0166-6851(90)90162-F

Part II

Flow Control in Insects and Birds

Wake Structure and Vortex Development in Flight of Fruit Flies Using High-Speed Particle Image Velocimetry

Fritz-Olaf Lehmann

Abstract. Understanding the dynamics of force and energy control in flying insects requires the exploration of how oscillating wings interact with the surrounding fluid. In two-winged insects, such as flies, the fluid acceleration fields produced by each wing strongly interact during wing stroke reversals, when the wings reverse their flapping direction. The main finding of this study is that this wing-wake interaction potentially budgets the elevated energy expenditures required for wing flapping by actively lowering the kinetic energy in the wake. This is demonstrated by quantitative flow measurements in flying fruit flies using high-speed particle image velocimetry and measurements in robotic, model wings. Vorticity estimates suggest that, compared to rigid robotic wings, elastic fly wings recycle energy from detached leading edge vortices by a novel mechanism termed vortex trapping. This finding is of great interest in the field of biomimetic aircraft design because it may help to improve the endurance of the next generation of man-made wing-flapping aerial devices such as micro air vehicles.

1 Introduction

The extraordinary evolutionary success of flying insects is due in large part to their ability to precisely control locomotor behavior in response to sensory stimuli. In the past, numerous studies emphasized the complexity of the feedback cascade that allows insects to convert sensory information, coming from the compound eyes, the gyroscopic halteres or the wing's campaniform sensilla, into locomotor activity (Dickinson and Palka 1987, Egelhaaf and Borst 1993, Kern et al. 2006, Nalbach 1994, Sherman and Dickinson 2004, Taylor 2001). Behavioral performance may be limited at each step of this cascade including the fluid dynamic

Fritz-Olaf Lehmann
BioFuture Research Group, Institute of Neurobiology, University of Ulm,
Albert-Einstein-Allee 11, 89081 Ulm, Germany
e-mail: fritz.lehmann@uni-ulm.de

processes with which flapping insect wings produce aerodynamic lift and drag. Force production and flight control in insects become most complex when fluid acceleration fields interfere with the flapping wings (Birch and Dickinson 2003). Consequently, in a freely flying animal, the production of vorticity and shedding of vortical structures in each stroke cycle depends on several factors such as (1) the instantaneous wake structure produced by the wing's own motion, (2) wake components produced in a preceding half stroke or preceding stroke cycles, (3) flow components resulting from force generation of wings flapping in close distance, (4) changes in fluid velocity at the wings due to the animal's body motion, and finally, (5) external disturbances in the surrounding air. Altogether, these components determine the instantaneous flow regime around a flapping insect wing and thus lift and drag production. To answer the question of how the neuromuscular system of flying insects copes with changing fluid environments is intriguing and requires a deeper understanding of the fluid dynamic processes occurring in flapping insect wings (Lehmann 2008, Sane 2003).

In the past, the majority of studies on insect flight aerodynamics focused on the performance of single flapping wings and widely ignored the significance of wake patterns (wake history) produced by previous stroke cycles (Ellington 1984). Fluid dynamic effects due to wake history, however, may be quite distinct which was demonstrated in a robotic fruit fly wing mimicking hovering conditions (Birch and Dickinson 2001). In their study, the authors showed that the first stroke in a fruit fly model wing produces approximately 9% more lift than the subsequent strokes. The initial acceleration of the induced flow is responsible for this effect, because under the given experimental conditions induced flow may attenuate the wing's effective angle of attack by more than 10° (approximately 40° during first stroke cycle, 28–32° in subsequent cycles).

The same kinematic pattern may also produce different amounts of lift due to the interaction of wakes produced by two flapping wings. The clap-and-fling mechanism that produces wake interferences between an ipsi- and contralateral wing and kinematic phase lag effects manipulating the flow regime between ipsilateral fore- and hindwings, are presumably the most prominent examples of wake-wing interactions in flapping flight (Maybury and Lehmann 2004, Saharon and Luttges 1989).

The dorsal clap-and-fling mechanism in two- and four-winged insects had first been described by Weis-Fogh (1973) and subsequently was found in many insects in a vast variety of flight modes. It was subject of several detailed experimental evaluations. Quite recently, new approaches in experimental design have provided several new insights, and numerical modeling (computational fluid dynamics, CFD) has much contributed to our understanding of this particular kinematic maneuver. The clap-and-fling is a close apposition of the ipsi- and contralateral wing at dorsal stroke reversal preceding pronation. During the clap, the insect brings the leading edges of the two wings together, then pronates them until the 'v-shaped' gap vanishes and the wings are parallel in close apposition. During the fling, the wings pronate about their trailing edges, creating a growing gap as the leading edge pulls apart. In Weis-Fog's classical reconstruction, the axis of wing rotation changes from rotation around the leading edge (upstroke) to a rotation around the

trailing wing edge (down stroke) during pronation. This clap-and-fling kinematic pattern has been used for several experimental and numerical approaches. Recent reconstructions of wing motion in tethered flight, however, have shown that during fling phase, the fruit fly apparently rotates its wings around the leading rather than the trailing wing edge. In rigid wings the latter maneuver would require that the wings be quickly pulled apart during rotation whereas in the elastic wing of the fruit fly, chordwise flexion permits the wings to rotate large angles of attack even at low gap angles.

The latter kinematic pattern has previously been described as the ‘peel’ motion and found in several insects such as flies (Götz 1987), butterflies (Brodsky 1991), bush cricket (Brackenbury 1990), and locust (Cooter and Baker 1977). 2D-DPIV data on the wake structure of flying fruit flies during fling motion imply some fundamental fluid dynamic differences between rigid and elastic wings, particularly when considering the sign of circulation around the wings during pronation.

Even within a single stroke cycle, a single wing may benefit from wake-wing interaction namely at the beginning of each half stroke. This phenomenon is termed wake capture and describes a mechanism by which the animal extracts kinetic energy from the fluid (Dickinson et al. 1999, Srygley and Thomas 2002). Wake capture at the beginning of the half stroke benefits from an inter-vortex stream produced by the leading- and trailing edge vortex system that accelerates the fluid during wing rotation at the end of each half stroke (Birch and Dickinson 2003). However, this interpretation of wake capture force generation has been questioned by computational fluid dynamics modeling of flapping insect wings, suggesting that the rotational-independent lift peak is due to a reaction of accelerating an added mass of fluid and does not rely on a momentum transfer of the fluid (Sun and Tang 2002). In the past the effect of inertial reaction forces during the stroke reversals was well recognized and discussed as a cause for wing rotation, twisting and bending (Daniel and Combes 2002, Ennos 1988). For example, in two species of flies, the blow fly *Calliphora vicina* and the hover fly *Eristalis tenax*, the high stroke frequency ranging from 100 to 200 Hz produces inertial forces sufficiently high to elicit passive wing pitch (angle of attack) changes when the wing reverses its direction of motion. Besides this controversial view on the wake capture mechanism, it remains unclear how wake capture exactly contributes to forces in flapping insect wings rather than in robotic wings and during maneuvering flight of an insect when the wings experience additional fluid components produced by the animal’s own body motion.

This book chapter focuses on research funded by the National-Priority-Program SPP1207 of the German Science Foundation, presenting novel quantitative flow measurements and approaches towards the flow regime during physical wing-wing interaction at the dorsal stroke reversal of tethered flying fruit flies *Drosophila virilis* and robotic models.

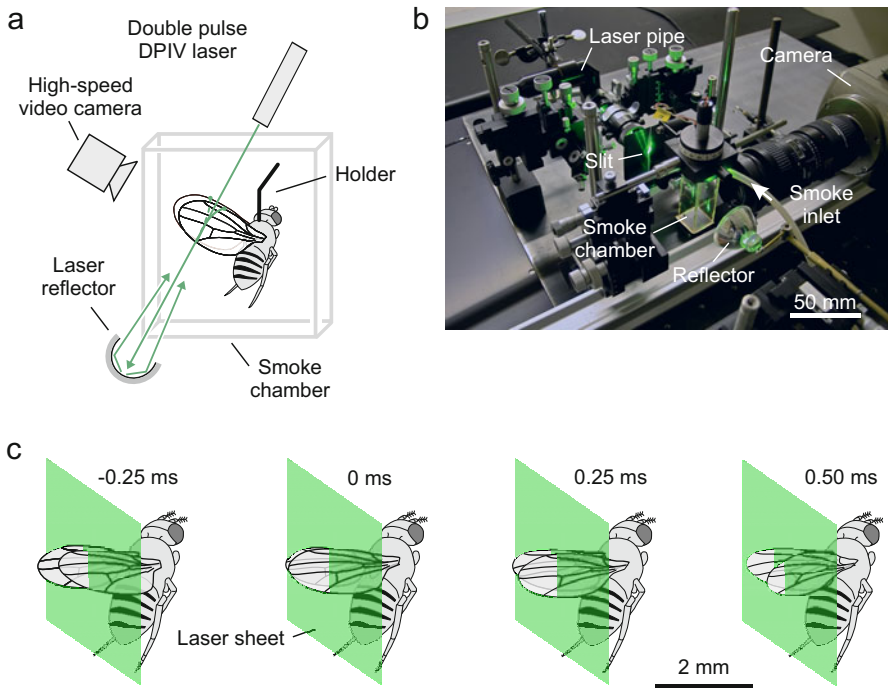


Fig. 1 Experimental setup for high-speed particle-image-velocimetry in flying fruit flies during dorsal wing-wing interaction (clap-and-fling). **a,b** The fruit fly *Drosophila virilis* is tethered to a tungsten wire and flown inside a flight chamber filled with smoke. The double pulse laser system runs through a 100 μm lens system and is narrowed by a mechanical slit with 0.5 mm width. A laser reflector enhances laser illumination of the smoke. The laser sheet is orientated normal to the wings' longitudinal axes during dorsal stroke reversal and slices the wings at approximately 0.5 wing length. A high-speed video camera takes images at a sample rate of 10 kHz. **c** The clap-and-fling of wing motion occurs within approximately 0.5 ms at the dorsal stroke reversal. During the clap, the insect brings the leading edges of the two wings together, while pronating them until the 'v-shaped' gap vanishes and the wings are parallel in close apposition. During the fling, the wings pronate about their trailing edge, creating a growing gap as the leading edges pull part. Drawing in **a** is not to scale.

2 Experimental Approaches

Two methods are commonly employed to quantify fluid velocity fields, wakes and vortical structures produced by flapping wings of insects in greater detail: High-speed digital particle-image velocimetry (DPIV) on tethered animals flying in a smoke chamber and DPIV on mechanical wings that are flapped by a mechanical apparatus and controlled by a computer. Mechanical wings often suffer from their tight limits to mimic natural flight conditions. Thus, a comparison between both

approaches is a necessary bridge in the attempt to link the various fluid mechanics mechanisms in physical model wings with their natural antetype. The comparison further fuels research on more specific aspects of wing flapping and structural requirements in insects such as the significance of wing elasticity for the production of aerodynamic forces and moments. The following section thus describes the two methods we employed to derive DPIV velocity and vorticity fields in flies and mechanical fly wings.

2.1 High-Speed Flow Measurements in Flying Insects

For tethered flight experiments, we used 3-day old females *Drosophila virilis* with a mean body mass of 1.94 mg and approximately 3.0 mm wing length from an inbred laboratory stock. The flies were tethered to a tungsten holder using a light-curing adhesive and flown in an approximately 20 cm³ smoke chamber (Fig. 1). The chamber was seeded with submicrometre-sized particles of burned plant-olive debris pellets. Seeding concentration was kept relatively low, since fruit flies cease flying at elevated smoke density.

For DPIV measurements, we generated a 0.5 mm thin planar laser sheet by a dual head double-pulsed DPIV laser (Litron LDY303) with approximately 2.0 mJ flash energy. A charge-coupled device camera (Phantom V12.1) captured image pairs with 512 x 536 pixel resolution and separated by 25 µs. Frame rate of laser and camera amounted to 10 KHz. Velocity and vorticity fields were calculated using a commercial software package (Dantec DynamicStudio) and a final 32x32 pixel interrogation area with 50% overlap. The measurement uncertainty was approximately ±1%, employing a high sub-pixel accuracy algorithm and selecting an average particle displacement of 0.25 interrogation size (8 pixel).

To track the illuminated wing profiles in the video images, we employed a self-written tracking tool developed under Matlab. Camber deformation was defined as the ratio between rise and span of the wing profile, a value of zero thus characterizes a flat wing. To determine the flow conditions within the boundary of the wings (no-slip boundary condition), we post-processed the raw correlation data, replacing the DPIV vectors of the wing profiles from cross-correlation by vectors of the local wing velocity determined from bending measurements. These vectors were interpolated and resampled from 10 equally spaced wing velocity vectors, in order to achieve a data structure similar to that of DPIV velocity processing.

2.2 Robotic Approaches Using Insect Model Wings

To compare the development of wake and vortical structures between elastic fruit fly wings and rigid model wings, we employed a dynamically scaled mechanical fruit fly model, flapping its wing in a tank filled with high viscous mineral oil.

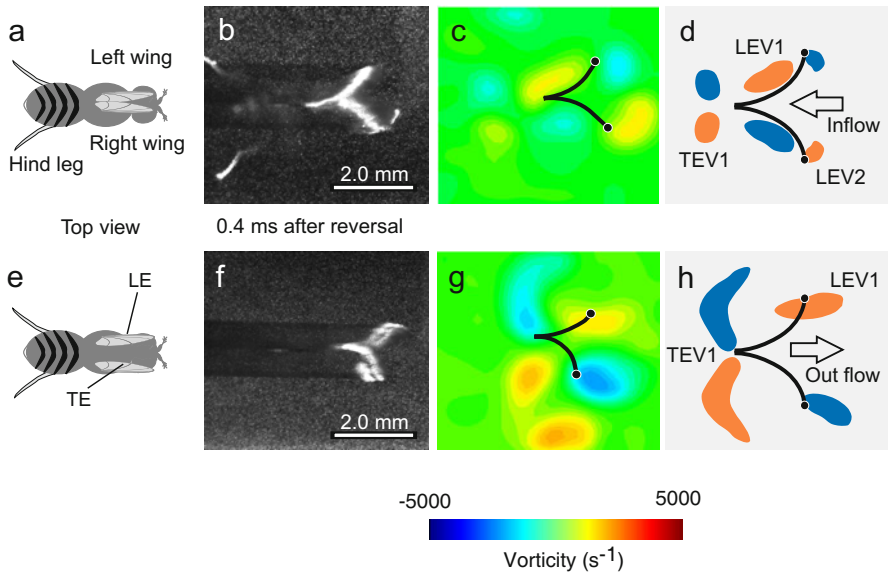


Fig. 2 Two types of leading edge vortex development during full-clap condition in **a-d** and near-clap condition in **e-h**. **a** Wing-wing contact (full-clap condition) occurs when the fruit fly maximizes aerodynamic force production and thus stroke amplitude. **e** A slight reduction of dorsal wing excursion of approximately 3° lead to near-clap condition, in which the wings do not physically clap together but still may interact during the fling period. **b,f** Raw DPLV images during fling motion yield similar kinematics and chordwise wing bending after full- and near-clap conditions. **c,g** Vorticity fields of vortical structures produced by wing motions shown on the left. Despite similar kinematics during fling, vortex spin and vortex shedding distinctly vary between both conditions due to the changes in wake structure during wing flap. **d,h** Schematic reconstruction of vortices suggests changes in flow direction between the wings leading edges. For abbreviations see Figs 4 and 5.

Wing size, velocity of wing motion and viscosity of the oil matched the Reynolds number of wing flapping in the fruit fly (~ 124) to that of the robotic apparatus. The wings flapped with 160° stroke amplitude and had a mean geometric angle of attack at mid half stroke of 45° . Wing rotation was symmetric about the stroke reversal with 4% of the wing rotation occurring before and 4% after stroke reversal. The Plexiglas wings (wing length= 25 cm) were immersed in a 2 m^3 (1 m x 1 m x 2 m) tank of mineral oil (density= $0.88 \times 10^3 \text{ Kg m}^{-3}$; kinematic viscosity= 115 cSt). To visualize wake structure, the oil was seeded with bubbles by pumping air through a ceramic water-purifier filter. The seeding consisted of evenly sized small air bubbles with low upward velocity ($< 0.5 \text{ mm s}^{-1}$) and high concentration. For the robotic experiments, we used a TSI dual mini-Nd:YAG laser to create two identically positioned light sheets through the wing at 60% wing length similar to the location we employed in the flying animal. DPLV analysis on the velocity fields, including calculation of vorticity, was performed using TSI Insight v5.1 and Matlab.

3 Fluid Regimes and Vortex Recycling

The following paragraphs describe results from analyses on wing kinematics during wing-wing interaction, wing bending and cambering, vortex development and shedding, numerical modeling of vortices and on how an insect wing may recycle energy from vortical structures.

3.1 Wing Kinematics during Dorsal Stroke Reversal

From DPIV images we estimated translational and rotational velocities during dorsal wing-wing interaction in the 200 Hz stroke cycle of *Drosophila*. The data show that translational velocity is approximately 2.0 ms^{-1} prior to the clap and the wing decelerates by approximately 4.0 ms^{-2} when the wing reverses its flapping direction. After the reversal, the wing accelerates to its final translation speed of 2.0 ms^{-1} within 1.5 ms in the subsequent downstroke. Rotational wing motion in fruit flies is extraordinary fast and may reach angular velocities of up to $86,000 \text{ deg s}^{-1}$. The wings achieve this value within approximately 0.5 ms during the dorsal reversal. Rapid wing rotation produces pronounced peaks in lift due to rotational circulation and also facilitates vortex shedding at the end of each half stroke. In flapping flight, vortex shedding is required because the wing may not produce a lift-enhancing leading edge vortex (LEV) with the appropriate sign before shedding the LEV from the preceding half stroke. Despite their high stiffness, fruit fly wings bend chordwise during wing rotation and spanwise when translational velocity reverses. In general, wing deformation in flies is due to aerodynamic, inertial and mechanical loads and their dependencies have been investigated in a side project of this SPP1207 investigation (Lehmann et al. 2011).

3.2 Wing Bending during Dorsal Stroke Reversal

In an initial approach, we focused on chordwise bending of the two wings during their physical contact at the stroke reversal. In this analysis, we reconstructed the wing chord from video images in which the laser highlighted the wing chord at 20, 40, 60, and 80% wing length without using seeding particles, and subsequently determined camber deformation in 95 stroke cycles of 6 tethered flies. Our data show that maximum camber peaks at approximately 15% and occurs when the leading edges of both wings separate while the trailing wing edges are still connected (equals 0.5 ms after the stroke reversal at which the wing chords are parallel). Due to the small distance between both wing hinges of approximately 1.0mm, chordwise bending occurs in all tested wing blades. In some blades, the wing even sharply bends at the contact point of left and right wing surface, producing up to 45° kinks (Figs 2b, 3g). Wing camber vanishes, once the trailing edges of the two wings detach and the wings begin their downstroke. We observed chordwise bending only during physical wing-wing interaction and not in stroke cycles, in which the wings did not touch.

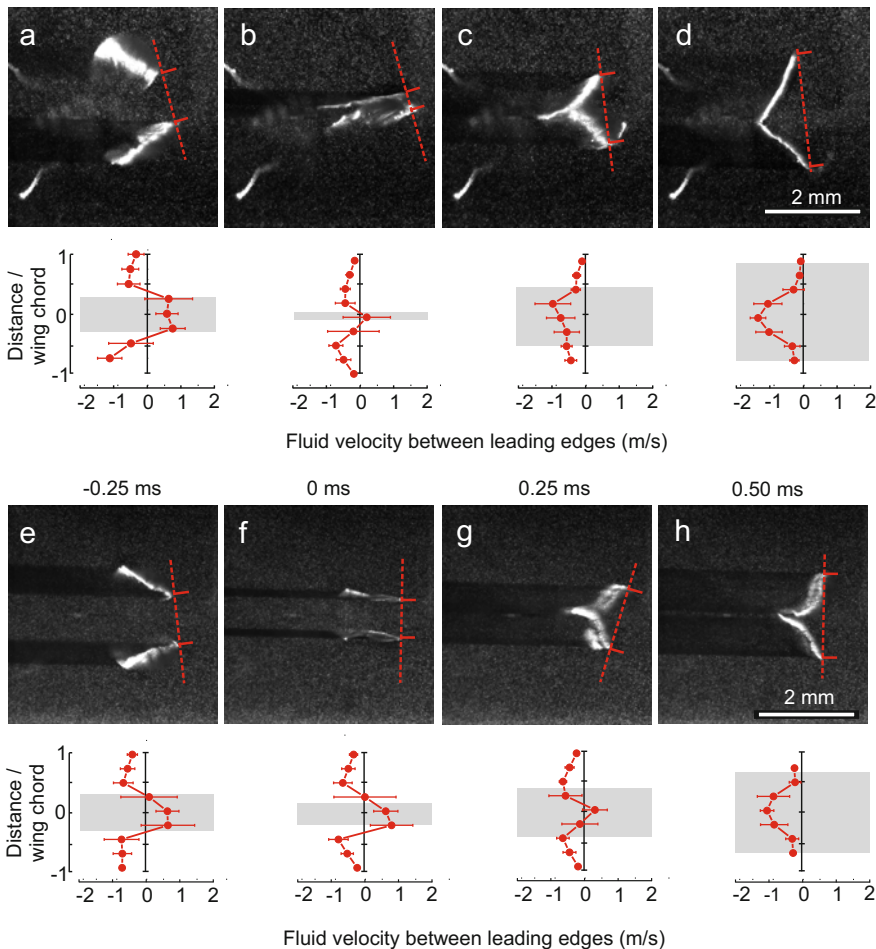


Fig. 3 DPIV raw images of a tethered flying fruit fly recorded during dorsal stroke reversal. The graph shows four characteristic phases with 0.25 ms equidistant time steps. The dotted line is normally orientated to the mean angular position of both wings and the two solid lines indicate the wings' leading edges. Data show measurements of fluid velocity between both leading edges, where positive and negative values indicate outflow and inflow into the cleft, respectively. Grey area indicates the distance between the wings' left and right leading edges. **a-d** Wing position and flow measurements during full clap condition as shown in **b**. **e-h** Near-clap wing motion, in which the wings do not physically touch at the reversal as shown in **f**. Note the differences in flow direction in **c** and **g**. Means \pm S.D., N=72 stroke cycles from 6 flies. See figure 2 for orientation of the animal.

3.3 Reversed Fluid Regime at Wing Stroke Reversal

Previous studies pointed out that in many insects the wings reverse their flapping direction at the dorsal position without physically clapping together. Several insect

species such as dragonflies or hover flies never clap their wings together while damselflies, butterflies and fruit flies regularly show wing clapping. We reconstructed the exact three-dimensional clap-and-fling kinematics in freely flying fruit flies in a second SPP1207 project and also scored body kinematics during this particular type of wing motion (see second book chapter on insect flight). In contrast to previous findings on freely flying fruit flies (Fry et al. 2003), we found that cruising fruit flies experience physical wing contact with their trailing edges (near-clap condition) in approximately 11.2% of 1939 reconstructed stroke cycles. Physical wing tip contact (full-clap condition) was scored in 2% of all cycles. In tethered flies, however, wing clapping occurs more often because under this flight condition fruit flies maximize aerodynamic lift due to the lack of appropriate feedback from their sensory organs.

Alterations in wing kinematics of the tethered animals allowed us to investigate the difference in the fluid regime between full-clap and near-clap conditions. In the latter case, the wings are held parallel during the dorsal stroke reversal but with a small distance of 0.6 mm at 50% wing length (Figs 2 and 3). This corresponds to an angular change in stroke amplitude of approximately 3° of the 164° stroke amplitude required for hovering flight force production. Since maximum steering angles in fruit flies are scattered around 5°, the kinematic difference between full- and near-clap condition likely corresponds to an approximately 60% change in force production required for maneuvering control.

Despite the small difference between both kinematic patterns, our DPIV measurements suggest pronounced changes in vorticity due to wing clapping. In particular during the early fling phase, 0.4 ms after stroke reversal, the sign of the vortex system following a full wing clap is reversed with respect to near-clap condition (Fig. 2c,g). In other words: at full-clap condition the wings generate a leading edge vortex with the appropriate sign for the downstroke, while at near-clap conditions the wings' upstroke LEVs is still attached to the wings' leading edges at the comparable moment. We assume that at this brief moment, the wings generate negative lift due to opposite signs of velocity and vortex spin, in turn lowering aerodynamic efficiency and increasing the power requirements for flapping flight. This unexpected finding raises the question why LEVs from the upstroke are maintained throughout rotational wing motion under near-clap conditions.

To tackle this question, we quantified speed and direction of the flow between the leading edges of the left and right wing throughout the dorsal stroke reversal. This analysis is summarized in figure 3. The positive velocities of up to 1.0 ms^{-1} in figure 3a,b,e,f indicate that fluid is pressed out of the closing gap through both leading wing edges. Under near-clap condition, this flow direction persists during the reversal (0 ms) and also at the early fling phase (0.25 ms), while full-clap wing motion produces a pronounced under pressure region inside the opening cleft. In contrast to the overpressure during near-clap kinematics, this under pressure pulls air into the gap and reinforces the induction of a new leading edge vortex at the beginning of the downstroke.

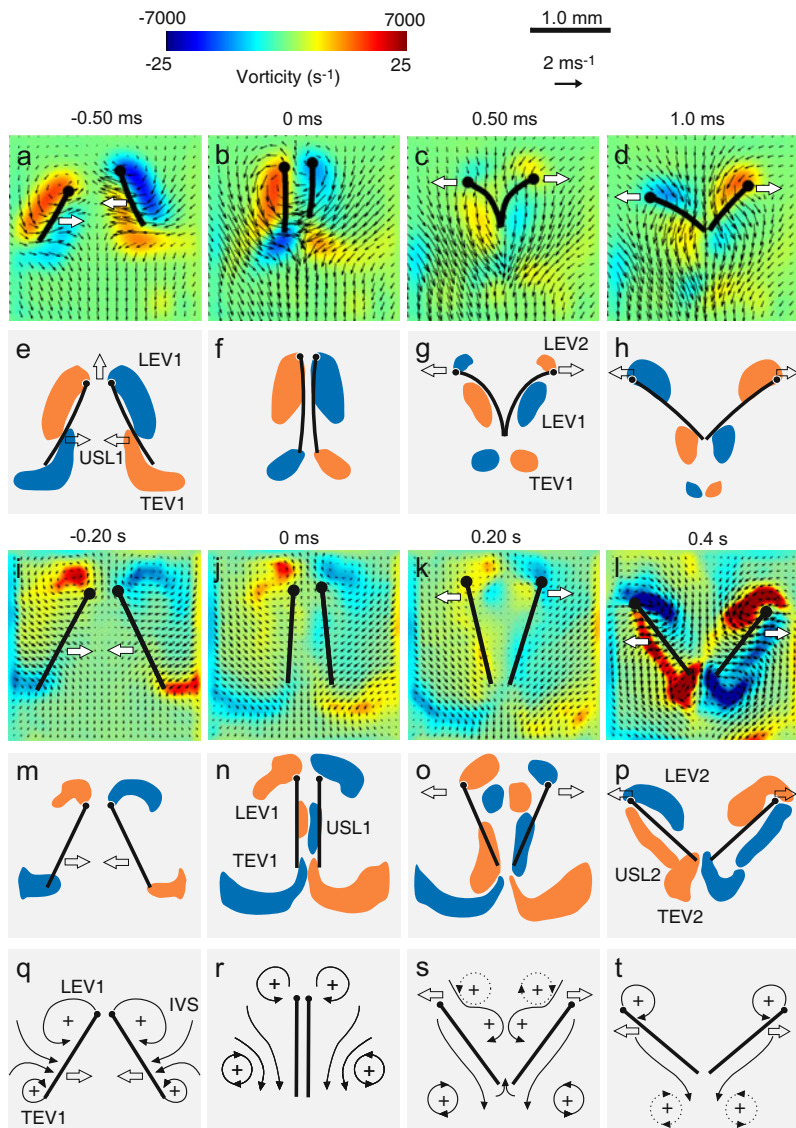


Fig. 4 Vorticity measurements and vortex reconstruction during dorsal wing-wing interaction. **a-h** Data from flexible wings of a fruit fly and **i-t** data measured in a rigid robotic model wing mimicking wing motion of a fruit fly. The wake is visualized at the center of force at approximately 0.6 wing length and the values above and below the vorticity color coding bar refer to the fruit fly and the mechanical wing, respectively. Wing motion refers to the time at which the wings reverse their flapping direction (0 ms). LEV, leading edge vortex; TEV, trailing edge vortex; USL, under shear layer of fluid; IVS, inter-vortex stream. The numbers 1 and 2 indicate vortical structures during upstroke and downstroke, respectively.

3.4 The Significance of Wing Elasticity: Fruit Fly and Fruit Fly Model Wings

Up to now, we have considered chordwise elastic wing bending as a mechanism that allows to keep the wing's structural integrity during dorsal wing-wing interference. Rigid wings do not allow wing clapping, and thus chordwise and spanwise bending is required. Early studies suggested that chordwise wing bending accelerates air more gently around the leading edge at the beginning of the downstroke, lowering power requirements and enhancing vortex stability. The benefit, however, is dubious because rigid wings should reinforce the low pressure region in the opening cleft and thus the induction of a leading edge vortex. We investigated this issue by comparing the wake structure produced by flapping fruit fly wings (elastic wings) with the wake of a robotic, model wing in the shape of a fruit fly (rigid wing), using DPIV. These data highlighted a novel mechanism for vortex control in insect flight.

For the comparison between rigid and elastic wing aerodynamics, we limited the measured 17 DPIV images during dorsal stroke reversal to 4 characteristic phases. These DPIV vorticity fields are shown in figure 4a-h for the tethered flying fruit fly and in figure 4i-t for the fruit fly model wing flapped by the mechanical apparatus (robotic wing). In both cases, the wings interact via the clap-and-fling mechanism and yield comparable stroke kinematics at a similar Reynolds number of 124. Since rigid wing aerodynamics is less complex, we start with a description of DPIV data in figure 4i-l, the reconstruction of the vortices in figure 4m-p and the schematics of flow condition in figure 4q-t. In rigid wings, the upstroke LEV stays attached to the wing until the wings clap. During rotation, the wing moreover generates a trailing edge vortex (TEV). Upstroke LEV and TEV accelerate fluid towards the wing, producing an inter-vortex stream (IVS) that enhances induced velocity of the fluid. Fractions of the IVS kinetic energy are recycled via the wake-capture mechanism. At wing flap, the LEVs of both wings are shed but remain close to the leading edge (Fig. 4j,n,r). Subsequently, the LEVs quickly dissipate and broadly vanish within 0.4 s.

Although elastic wings of the fruit fly exhibit similar vortex development and IVS, the fate of their upstroke LEV and TEV is different compared to rigid wing aerodynamics. In elastic wings, the upstroke LEV is trapped under the cambered, ventral wing surface and moves chordwise from the leading to the trailing wing edge during the wing's fling motion (Figs 4c,g, 5a). Figure 5b and d shows that while travelling in a chordwise direction, the trapped upstroke LEV loses vorticity and sectional kinetic energy within approximately 0.8 ms. These decreases amount to approximately 66% of the initial value, estimated at the time of vortex shedding. Immediately before the wings start to separate for the downstroke, camber is negligible and LEV vorticity and vortex energy are minimum. The upstroke LEV eventually fuses with the start vortex produced at the trailing edge while the wings slowly separate. This vortex fusion is due to similar spin of upstroke LEV and downstroke TEV and transiently reinforces vorticity of the upstroke LEV. This effect is shown as an increase in vorticity and sectional blade energy in figure 5b,d.

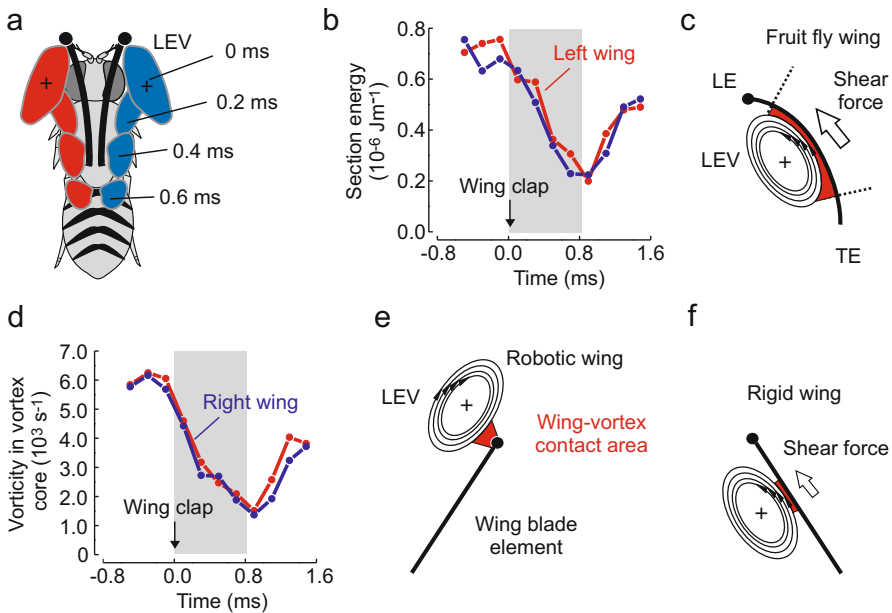


Fig. 5 Leading edge vortex travelling at fruit fly wings. **a** After wing flap, the LEV generated during the wing's upstroke travels chordwise from the leading to the trailing wing edge on the ventral wing surface. **b** Change in sectional energy of the blade at 0.5 wing length and **d** decay of vorticity of the LEV. Grey area indicates the fling period in which the wings separate after clapping. Numerical simulation on vortex development may not explain the observed decrease in **b** and **d**. **c,e,f** Three types of vortex degradation at the beginning of the wing's downstroke. In rigid robotic wings, the LEV remains near the wing's leading edge, whereas the LEV travels chordwise in fruit fly wings as shown in **c**. Shear forces potentially lower and thus recycle vortex energy. This mechanism might be reinforced by wing bending due to a larger wing-vortex contact area in **c** compared to a rigid wing in **f**. LE, leading wing edge; TE, trailing wing edge.

3.5 Lamb-Oseen Vortex Model

To tackle the steep loss of energy of the upstroke LEV, we modeled vortex development using the two-dimensional theoretical Lamb-Oseen vortex model (Lamb 1932). In this model, the space-time functions of vorticity and velocity depend on the initial circulation, the radial distance, the time, and the kinematic viscosity of $15 \times 10^{-6} \text{ m}^2 \text{ s}^{-1}$ and of $115 \times 10^{-6} \text{ m}^2 \text{ s}^{-1}$ for air (fruit fly) and oil (model wing), respectively. Using the equivalent radius of each identical vortex and the corresponding vorticity on the vortex borderline, we calculated the initial circulation for the whole vortex using the measured DPIV vorticity data.

Without energy dissipation in the fluid, the Lamb-Oseen model predicts constant circulation, although vortex size increases with time. Preliminary comparisons between the theoretical data, DPIV vorticity data of the fruit fly and data from the model wing altogether suggest that the upstroke LEV loses more energy

than a vortex free of close-by surfaces. This finding fuels the assumption that part of the vortex energy is transferred to the wing and recycled during flapping wing motion. Integration of the LEV energy loss to the wing surface suggests that the animal might save a significant amount of muscle mechanical power output for flight by vortex energy recycling. Preliminary calculation shows that vortex recycling may account for 10-20% of the induced power requirements, which are the costs of producing a vertical momentum opposite to gravity. The contribution of heat dissipation to the temporal development of LEV is still under investigation.

3.6 Wing-Vortex Interaction in Fruit Fly Wings

The recycling of energy from the inter-vortex stream of a flapping robotic model was first described by Dickinson et al. (Dickinson et al. 1999). Their study demonstrates that the efficacy of the wake capture mechanism strongly depends on rotational timing and the wing's angle of attack at the beginning of each halfstroke. For example, advanced wing rotational timing, in which the wing completes its rotation at the end of the half stroke, produces a pronounced wake capture effect compared to delayed wing rotation, at which the wing starts to rotate at the beginning of the following halfstroke. At the latter condition, wing-IVS interaction occurs at negative angles of attack and thus produces unfavorable negative lift (Lehmann 2008, Birch and Dickinson 2003). The wake capture mechanism functions in rigid wings and does not require any chord- or spanwise deformations of the biofoil.

Depending on stroke kinematics and wing elasticity, we found three types of wing-LEV interaction during clap-and-fling wing motion. Figure 5e shows the characteristic location of the upstroke LEV after shedding from a rigid, robotic model wing. We reconstructed this position from our DPIV measurements in figure 4j-t. Under this condition, the upstroke LEV (LEV1) remains close to the wing's leading edge with small wing-vortex contact area and quickly dissipates during wing rotation. The sign of vorticity in the developing LEV for the wing's downstroke (LEV2) is opposite to the upstroke LEV (LEV1), thus the upstroke LEV potentially hinders and delays leading edge vortex development in the opening cleft during the downstroke (see chapter 3.3).

By contrast, in flapping fruit fly wings, the upstroke LEV is trapped by the ventral surface of the cambered wing while the vortex travels chordwise. The camber thereby likely reinforces LEV energy transfer and thus potentially increases energy transfer efficiency because of the large wing-vortex contact area (red, Fig. 5c). As a consequence of the energy transfer, shear forces might accelerate the wing in the direction of the downstroke, in turn lowering the energetic requirements to overcome wing drag (profile drag) at the early moment of the half stroke. This mechanism is very similar to the function of a conveyer belt. Without chordwise, elastic deformation of the wing, we hypothesize a less effective energy transfer because the wing-vortex contact area is supposed to be smaller in a rigid wing (Fig. 5f).

4 Conclusions

Energy recycling from trapped leading edge vortices is a novel mechanism in flapping insect flight and adds to the list of other lift-enhancing aerodynamic mechanisms which have been described previously. Vortex trapping compares to the wake capture effect in single flapping wings because both mechanisms appear to be valuable for lift enhancement and power reduction. In contrast to the wake-capture effect that has been discovered and quantified in rigid, robotic model wings, however, vortex trapping apparently requires suitable wing motion patterns and wing elasticity - important prerequisites to energetically benefit from such aerodynamic mechanisms. Despite preliminary data on numerical vortex models, caution must still be applied when comparing the efficacy of vortex trapping with other rotational-based power-reducing mechanisms such as swirl-removal by the hindwings of four-winged insects (Lehmann 2010).

Altogether, wing-wake interactions in flapping flight may not only shape the evolution of maneuverability and agility in flying animals but may also improve the endurance of the next generation of man-made flapping aerial devices such as biomimetic micro air vehicles.

Acknowledgments. This book chapter reports results from projects “Experimental evaluation of forces and fluid structures during maneuvering flight of flies, using biomimetic robotics” and “Fluid phenomenon and body control of flying insects during aerodynamically-induced perturbations” to FOL, funded by the National-Priority-Program SPP1207 “Impact of fluid flows in nature and technology” of the German Science Foundation DFG.

References

- Birch, J.M., Dickinson, M.H.: Spanwise flow and the attachment of the leading-edge vortex on insect wings. *Nature* 412, 729–733 (2001)
- Birch, J.M., Dickinson, M.H.: The influence of wing-wake interactions on the production of aerodynamic forces in flapping flight. *J. Exp. Biol.* 206, 2257–2272 (2003)
- Brackenbury, J.: Wing movements in the bush cricket *Tettigonia viridissima* and the mantis *Ameles spallanziana* during natural leaping. *J. Zool. Lond.* 220, 593–602 (1990)
- Brodsky, A.K.: Vortex formation in the tethered flight of the peacock butterfly *Inachis io* L (Lepidoptera, Nymphalidae) and some aspects of insect flight evolution. *J. Exp. Biol.* 161, 77–95 (1991)
- Cooter, R.J., Baker, P.S.: Weis-Fogh clap and fling mechanism in *Locusta*. *Nature* 269, 53–54 (1977)
- Daniel, T.L., Combes, S.A.: Flexible wings and fins: bending by inertial or fluid-dynamic forces? *Integ. Comp. Biol.* 42, 1044–1049 (2002)
- Dickinson, M.H., Lehmann, F.-O., Sane, S.: Wing rotation and the aerodynamic basis of insect flight. *Science* 284, 1954–1960 (1999)
- Dickinson, M.H., Palka, J.: Physiological properties, time of development, and central projection are correlated in the wing mechanoreceptors of *Drosophila*. *J. Neurosci.* 7, 4201–4208 (1987)
- Egelhaaf, M., Borst, A.: Motion computation and visual orientation in flies. *Comp. Biochem. Physiol.* 104A, 659–673 (1993)

- Ellington, C.P.: The aerodynamics of hovering insect flight. IV. Aerodynamic mechanisms. Phil. Trans. R. Soc. Lond. B 305, 79–113 (1984)
- Ennos, A.R.: The importance of torsion in the design of insect wings. J. Exp. Biol. 140, 137–160 (1988)
- Fry, S.N., Sayaman, R., Dickinson, M.H.: The aerodynamics of free-flight maneuvers in *Drosophila*. Science 300, 495–498 (2003)
- Götz, K.G.: Course-control, metabolism and wing interference during ultralong tethered flight in *Drosophila melanogaster*. J. Exp. Biol. 128, 35–46 (1987)
- Kern, R., van Hateren, J.H., Egelhaaf, M.: Representation of behaviourally relevant information by blowfly motion-sensitive visual interneurons requires precise compensatory head movements. J. Exp. Biol. 209, 1251–1260 (2006)
- Lamb, H.: Hydrodynamics. Dover, New York (1932)
- Lehmann, F.-O.: When wings touch wakes: understanding locomotor force control by wake-wing interference in insect wings. J. Exp. Biol. 211, 224–233 (2008)
- Lehmann, F.-O., Gorb, S., Nazir, N., Schützner, P.: Elastic deformation and energy loss of flapping fly wings. J. Exp. Biol. 214, 2949–2961 (2011)
- Maybury, W.J., Lehmann, F.-O.: The fluid dynamics of flight control by kinematic phase lag variation between two robotic insect wings. J. Exp. Biol. 207, 4707–4726 (2004)
- Nalbach, G.: Extremely non-orthogonal axes in a sense organ for rotation: behavioral analysis of the dipteran haltere system. Neurosci. 61, 149–163 (1994)
- Saharon, D., Luttges, M.W.: Dragonfly unsteady aerodynamics: The role of the wing phase relationship in controlling the produced flows. AIAA J. 89-0832, 1–19 (1989)
- Sane, S.: The aerodynamics of insect flight. J. Exp. Biol. 206, 4191–4208 (2003)
- Sherman, A., Dickinson, M.H.: Summation of visual and mechanosensory feedback in *Drosophila* flight control. J. Exp. Biol. 207, 133–142 (2004)
- Srygley, R.B., Thomas, A.L.R.: Unconventional lift-generating mechanisms in free-flying butterflies. Nature 420, 660–664 (2002)
- Sun, M., Tang, J.: Unsteady aerodynamic force generation by a model fruit fly wing flapping motion. J. Exp. Biol. 205, 55–70 (2002)
- Taylor, G.K.: Mechanics and aerodynamics of insect flight control. Biol. Rev. 76, 449–471 (2001)
- Weis-Fogh, T.: Quick estimates of flight fitness in hovering animals, including novel mechanisms for lift production. J. Exp. Biol. 59, 169–230 (1973)

Experimental Quantification and Numerical Simulation of Unsteady Flow Conditions during Free Flight Maneuvers of Insects

Andrei Shishkin, Peter Schützner, Claus Wagner, and Fritz-Olaf Lehmann

Abstract. This study aimed to numerically simulate aerodynamic forces produced by wing motion of small fruit flies maneuvering freely inside a flight chamber. The kinematic data were derived from high-resolution, high-speed video measurements, tracking fluorescent markers on head, body and wings of the animal. We constructed a geometrical model of the fly and applied the kinematic data to simulate free flight. Based on the calculated velocity and pressure fields, we evaluated vorticity and flight forces. Our numerical simulation confirmed experimentally predicted lift enhancing mechanisms such as the leading edge vortex, rotational circulation and wake capture, and thus appears to be a potent tool to study the impact of body motion on forces and moments during the various forms of flight maneuvers.

1 Introduction

Flying insects are famous for their impressive and unexcelled maneuvering capabilities during territorial and chasing behaviors, rapid avoidance reactions and escape responses. Uncovering the underlying physical principles of these behaviors is a challenging task due to the high dynamics and complexity of unsteady aerodynamic force production in flapping flight. Over the past decade, the mechanisms of force production in insects have been the subject of some rigorous theoretical and experimental investigations, revealing several novel lift enhancing aerodynamic mechanisms such as the leading edge vortex, rotational circulation and wake

Andrei Shishkin · Claus Wagner

Fluid Systems, Institute of Aerodynamics and Flow Technology, German Aerospace Center, Bunsenstr. 10, 37073 Göttingen, Germany

e-mail: {Andrei.Shishkin,Claus.Wagner}@dlr.de

Peter Schützner · Fritz-Olaf Lehmann

Biofuture Research Group, Institute of Neurobiology, University of Ulm, Albert-Einstein-Allee 11, 89081 Ulm, Germany

e-mail: {Peter.Schuetzner,Fritz.Lehmann}@uni-ulm.de

capture (Dickinson et al. 1999). The majority of these investigations used mechanical wings flapped by a robotic apparatus (Dickinson et al. 1999, Ellington et al. 1996, Maybury and Lehmann 2004) or computational models (Kliss et al. 1989, Wang 2000, Sun et al. 2007), and was performed under hovering flight condition, in which the induced wake only depends on the wings' own motions.

In a freely flying animal, by contrast, the production of vorticity and the shedding of vortical structures in each stroke cycle depend on additional factors such as wake components produced in a preceding half stroke or preceding stroke cycles, flow components resulting from force generation of wings flapping in close distance, changes in fluid velocity at the wings due to the animal's body motion, and external disturbances in the surrounding air. Altogether, these components determine the instantaneous flow regime around a flapping insect wing and thus lift and drag production (Lehmann 2008, Sane 2003). Ramamurti and Sandberg (2007) investigated the significance of body motion on force production and frictional damping using three-dimensional computational fluid dynamics simulations (CFD). They applied their programming code to the rapid turning behavior in fruit flies, termed flight saccades. The authors found that the additional flow components due to body rotation produce pronounced drag on the flapping wings that limits turning speed and effectively brakes rotational movements (FCT, flapping counter torque). Similar results were reported for turning flight of birds (cockatoos, Hedrick et al. 2007, 2009), highlighting that frictional damping coefficients for roll and yaw are 4 to 6-fold higher in these animals than in airplanes.

The dominant role of frictional damping due to body motion further contrasted a previous study on rotational damping in which mechanical wings mimicked free flight kinematics of fruit flies during saccadic turning (Fry et al. 2003). In the latter study, the authors ignored body motion during their physical simulation and thus falsely concluded that turning behavior is dominated by inertial moments of the animal body and not by frictional damping due to wing drag. Behavioral studies on tethered fruit flies flying in a virtual-reality flight simulator later demonstrated that low frictional damping overloads the visually-controlled feedback-loop during maneuvering flight, potentially causing body instabilities in free flight (Hesselberg and Lehmann 2007). The modifications in local flow condition at flapping wings, moreover, change with increasing advance ratio, which is the ratio between forward speed of the animal and wing flapping velocity. In fruit flies, this ratio varies between zero at hovering flight and approximately 0.53 at maximum forward velocity (1.22 ms^{-1} , wing flapping velocity = 2.29 ms^{-1}), altering magnitude and direction of local air flow at the different flight modes. Consideration of wing kinematics and body movements is thus a key factor to understand aerodynamic force production in freely maneuvering animals (Fontaine et al. 2009, Ristroph et al. 2009, Schützner and Lehmann 2007).

This book chapter focuses on research funded by the National-Priority-Program SPP1207 of the German Science Foundation, presenting an approach towards the fundamental question of how body motion in an insect alters wake structure and unsteady aerodynamic force production. This is demonstrated by high-speed video measurements on wing and body motion of freely maneuvering 1.2 mg fruit flies

Drosophila and simulation of flow conditions and forces using an elaborated three-dimensional CFD modeling approach.

2 Experimental Approaches – High-Speed Video Tracking Technology

To reconstruct wing motion of freely maneuvering fruit flies *Drosophila melanogaster*, we developed an experimental setup that consists of a cylindrical free-flight arena, three high-speed video cameras, an infrared light laser trigger, an infrared light sensitive camera, and commercial software packages. In the following paragraphs, we summarize the main features of the experimental components and describe how we derived temporally resolved kinematics of wings and body in three dimensions using self-written software.

2.1 Tracking of Fluorescent Markers in a Free Flight Arena

All experiments were conducted in a 62 mm wide cylindrical free-flight arena with 70 mm diameter. To allow the animals to visually orientate inside the arena, the cylinder was made from Plexiglas and surrounded by a back-light illuminated cyan-black random dot pattern (Fig. 1). The upper end of the flight chamber was closed with a glass plate but equipped with several small lateral holes. The holes were filled with foam, allowing the exchange of air between chamber and the environment. In the middle of the arena, we mounted an upright tube filled with moist tissue that served both as a water dispenser and a launch pad for the flies. Before placing the flies into the arena, we marked head, body, and wings with fluorescent dye during low temperature anesthetization of 4°C on a Peltier stage. Each marker had a mass of approximately 0.1 μg and a diameter of approximately 200 μm . Since the mass of a fruit fly wing amounts to only 3 μg , we limited the number of wing markers to the wing tip and the trailing edge, in order to avoid wing bending due to inertial effects. To minimize motion blur of the fluorescent markers on the captured video images, a ring of 48 ultraviolet light-emitting diodes produced short 60 μs light pulses, which were synchronized with three high-resolution, high-speed video cameras. We scored the significance of UV light on visual orientation and vision capability by scoring tethered flying flies in their ability to track a visual target inside a virtual-reality, closed-loop flight simulator. Although we measured a small degradation in performance during UV light illumination, all flies were capable to actively control the visual object displayed inside the simulator.

The three high-speed cameras were mounted with an inter-camera angle of 120° above the arena that allowed us to track flies inside a volume of approximately 9900 mm³ at 3500 Hz frame capture rate. At the fly's 200 Hz wing stroke frequency, the latter value yields a temporal resolution of approximately 17.5 video frames per wing stroke cycle or 9 frames per half stroke. The cameras were also equipped with optical filters matching the emitted orange-red light from the fluorescent markers and automatically triggered by the flying animal using an infrared light path. We

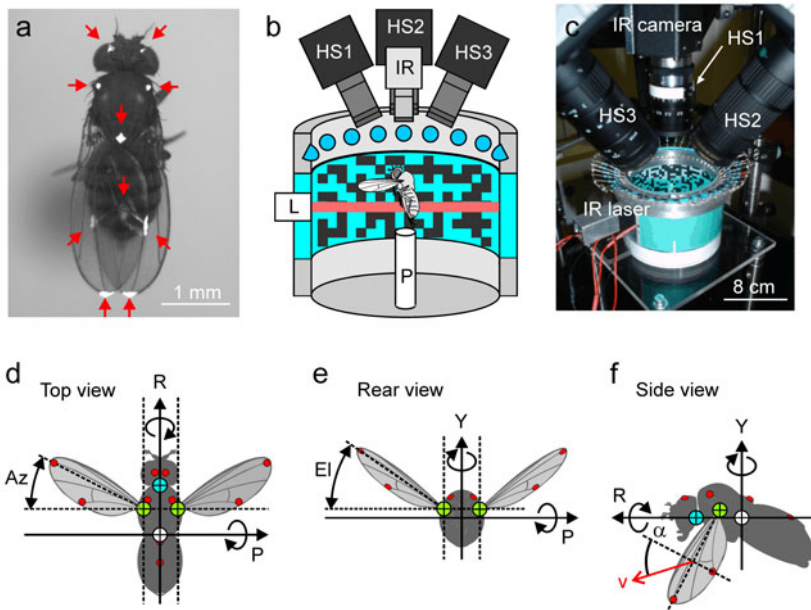


Fig. 1 Experimental setup for high-speed video recording in freely flying fruit flies. **a** Red arrows indicate fluorescent markers painted on head, body and wings of a fruit fly. **b** Sketch of the free-flight arena. UV light-emitting diodes (blue) stimulate fluorescent markers shown in a. HS, high-speed camera 1 to 3; IR, infrared sensitive camera; L, infrared laser; P, starting platform. Drawing is not to scale. **c** Image of the experimental setup. **d-f** Thorax axes and wing angles. Red dots indicate fluorescent markers. Center of body mass (white), center of head rotation (blue) and wing hinges (green) are derived from the fly's morphology. Az, wing azimuth; El, wing elevation; α , wing's geometric angle of attack, with respect to wing velocity vector v ; Y, vertical yaw axis; P, horizontal pitching axis; R, horizontal roll axis.

constructed the light path employing a horizontally orientated infrared laser sheet, an infrared-sensitive camera and motion detector software. The camera lens was equipped with an infrared filter and a computer continuously recorded the infrared images with a frame rate of approximately 20 Hz. Software analyzed the images online and generated a hardware trigger signal for the high-speed cameras whenever a fly crossed the laser sheet. To further increase the frequency of flight bouts within the recording time, we starved the flies one hour before placing them into the free-flight arena, in which they remained up to 6 hours.

2.2 Three-Dimensional Reconstruction of Wing Motion

The quality of computational models of flapping flight critically depends on the precision with which wing and body kinematics is measured in the freely maneuvering animal. It is less challenging to reconstruct markers on the fly body because those

markers are comparatively large and only move at a low speed during flight. By contrast, tracking azimuth and elevation angles of an oscillating wing including its angle of attack from small dye markers is more difficult and requires elaborated data processing. In particular, the precise reconstruction of fast kinematic maneuvers, such as speed and timing of wing rotation at the stroke reversals, is critical for force generation due to rotational circulation and wake capture enhancement (Dickinson et al. 1999). Markers on wings may, moreover, be masked by the fly body or may disappear on the video images because of their small size and thus low fluorescence intensity. At the dorsal stroke reversal, fluorescent markers of tip and trailing wing edges even fuse during physical wing-wing contact, making the application of automatic tracking procedures more complicated (see second chapter of this book on insect flight).

We coped with the above problems by application of commercial video software that enhanced the visibility of the markers. The markers were subsequently tracked in each video frame using software developed in Matlab. To match corresponding video pixels in frames of all three high-speed video cameras, we applied a direct linear transformation algorithm, calibrated with a target at six distances from the cameras. The calibration target was mounted horizontally and displaced by a micro-manipulator in 2.0 mm equidistant steps inside the measurement volume (Hedrick 2008). We repeated this procedure before and after the experiments to ensure high precision of the three-dimensional reconstruction.

The captured video frames were enhanced removing image noise and increasing image contrast by the box blur tool and image enhancement tool in VirtualDub, respectively. The image-processing procedure conserved the brightness gradient from the border to the center of each marker that improved position tracking of the marker center. The tracking software routine was developed under Matlab and automatically scored the position of each marker according to the marker's center of area (Hedrick 2008). The algorithm provided subpixel acuity of position estimates and greatly enhanced the quality of the data. Missing data points due to occlusion of fluorescent markers were interpolated applying separate spline functions to each coordinate value. The Matlab fit functions were also used for a 10-fold upsampling procedure of the position data. The latter step helped to smooth out high accelerations of the wing's rotational velocity during the stroke reversals due to the sparse number of data samples (2-3 data). During stroke reversals, the wing's angle of attack changes by approximately 90° at an angular speed of approximately 90,000° s⁻¹.

We did not filter the wing position data (tips and trailing edges) because low pass filters produced pronounced motion artifacts in the data set. By contrast, we removed digitization noise from the body position data using a zero-phase one-dimensional digital filter. It was applied separately for each x/y/z coordinate as an unweighted running average with a time window size of a quarter mean wing beat period (approximately 1.25 ms).

We expanded the set of measured markers by a set of virtual body markers that were reconstructed from the fruit fly's morphology. From anatomical drawings (Demerec 1965), we estimated the position of the wing hinges, the fly's center of

gravity, and the center of head rotation with respect to the three fluorescent markers on the thorax. The distances between these points were expressed in relative units and absolute values scaled according to the animal's size. We further reconstructed the longitudinal axis of wing rotation by a method developed in a side project of this SPP1207 investigation (Lehmann et al. 2011). From the extended data set, we calculated various flight parameters such as yaw-, pitch- and roll angles of the body, horizontal and vertical flight directions, wing azimuth, elevation and angle of attack including their temporal derivatives in both the global and the fly body framework.

3 Experimental Results from 3D-Reconstructions

Fig. 2 shows typical flight traces of four categories of flight maneuvers: level flight with constant forward velocity (Fig. 2a), a saccadic flight turn during climbing flight (Fig. 2b), backward flight with reorientation and subsequent forward acceleration (Fig. 2c), and take-off behavior from a starting platform (Fig. 2d). The data in Fig. 3 represent the corresponding wing and body motions underlying the flight sequence in Fig. 2a and have been used for the flow simulation described in the second part of this book chapter. Fig. 4 summarizes body velocity and orientation parameters of non-categorized flight behaviors from 170 fruit flies and flight sequences (32673 video frames), without scoring takeoff maneuvers. The histograms indicate that fruit flies prefer to fly at a mean forward flight speed ranging from 0.2 to 0.3 ms^{-1} , but occasionally even fly backwards (negative values, Fig. 4a). Total flight speed is the vector sum of forward, sideward and vertical velocities and amounts to a maximum of approximately 0.7 ms^{-1} . This value is equal to 57% of the maximum flight capacity estimated in flies flying freely under optomotor stimulation (Mronz and Lehmann 2008). Fig. 4e and f shows the relationship between forward velocity and yaw orientation of the longitudinal body axis of the animal. These data highlight the

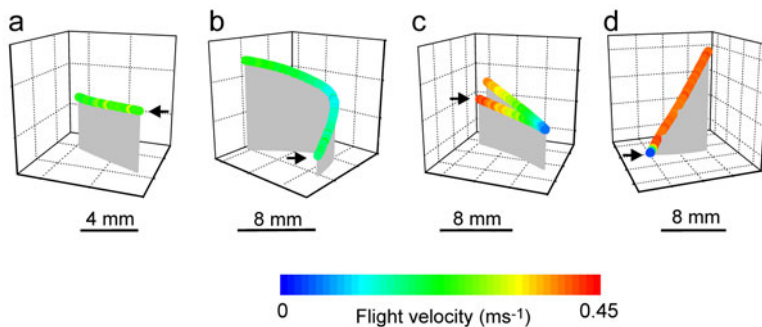


Fig. 2 Body motion (center of mass) during four types of flight maneuvers. **a** 28 ms sequence of level flight at low forward velocity. **b** 99 ms sequence of saccadic climbing flight. **c** 108 ms sequence of a backward/forward flight with reorientation maneuver during hovering. **d** 43 ms sequence of a takeoff maneuver. Arrow indicates flight start of the recorded path and grey area projects the flight trace into the horizontal.

remarkable aerial capacity of fruit flies to independently control body orientation and flight direction. For example: data points that are lined up horizontally indicate flies changing flight direction, while keeping their yaw orientation constant. By contrast, data points that are lined up vertically indicate flight maneuvers in which flies rotate around their vertical axis without changing flight direction.

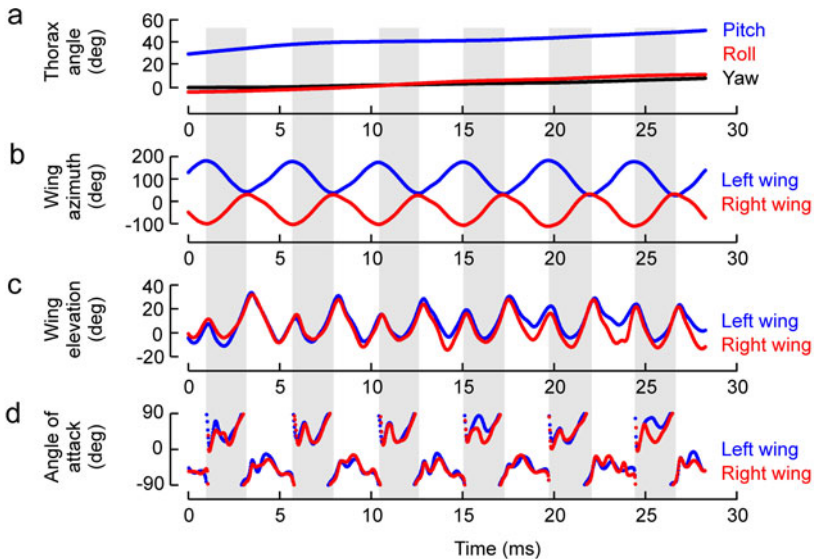


Fig. 3 Time-resolved body and wing angles of the flight sequence shown in Fig. 2a. **a** Yaw-, pitch-, and roll angles of the thorax, where negative values indicate counter-clockwise (yaw, roll) or nose-down (pitch) angles. **b** Wing azimuth in the horizontal. **c** Wing elevation with respect to the vertical. **d** Geometric angle of attack of both wings with respect to the oncoming flow. This angle considers wing and body motion. The kinematic parameters (except for the angle of attack) are plotted with respect to the external (global) coordinate system. Grey area indicates the downstroke.

4 Numerical Simulations of the Free-Flight Induced Flow

A main objective of the presented study is to conduct computations of the flow around a freely flying fruit fly (*Drosophila melanogaster*) based on the measured kinematics plotted in Fig. 2a. A 3D-visualization of the experimentally obtained kinematics is depicted in Fig. 5, where the curves reflect the trajectories of the markers on the fly body and the wings. While the traces of the markers on the body show a nearly linear flight path, those located on the wing tips and trailing edges produce complicated curves.

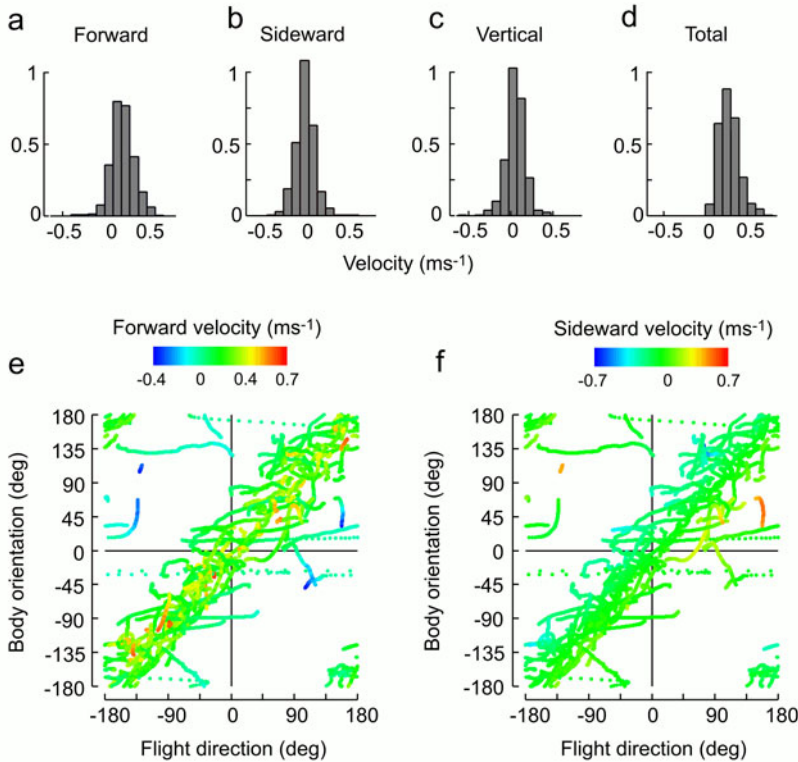


Fig. 4 Body dynamics in freely flying fruit flies. **a-d** Velocity distributions plotted as normalized histograms. Data show forward-, sideward-, and vertical velocity, including their vector sum (total translational velocity). **e-f** Flight direction in the horizontal plotted against angular orientation (yaw) of the fly body. Data are plotted from 32673 video frames recorded during 170 flight sequences of approximately 170 flies.

4.1 Numerical Method

The Arbitrary Lagrangian Eulerian (ALE) formulation of Navier-Stokes equations allows to simulate flows in computational domains with moving boundaries. Expressed in terms of the dimensionless incompressible Navier-Stokes equations it reads:

$$\frac{\partial \mathbf{u}}{\partial t} + ((\mathbf{u} - \mathbf{u}_{mesh}) \cdot \nabla) \mathbf{u} = \frac{1}{Re} \nabla^2 \mathbf{u} - \nabla p, \quad \nabla \cdot \mathbf{u} = 0, \quad (1)$$

where \mathbf{u} and p are the velocity and pressure fields, respectively, Re is the Reynolds number and \mathbf{u}_{mesh} is the mesh deformation velocity. Equations (1) depend on the time-dependent coordinates $\mathbf{x}(t)$ and the mesh velocity $\mathbf{u}_{mesh} = \dot{\mathbf{x}}(t)$. Both functions are unknown but can be reconstructed using information from the moving boundaries. For each time step Eq. (1) is solved in steps with the following procedure:

- a** – find the smooth functions $\mathbf{x}(t)$ and \mathbf{u}_{mesh} ;
- b** – perform the mesh deformation using $\mathbf{x}(t)$ for a given time step and recalculate the fields needed for the step (c);
- c** – finally, solve the conventional Eulerian Navier-Stokes equations on the deformed mesh.

For the flow simulations presented below we used the standard ALE solver implemented in the open-source OpenFOAM toolkit. The mesh motion velocity \mathbf{u}_{mesh} needed for step (a) is determined solving the Laplace equation:

$$\nabla \cdot (\gamma \nabla \mathbf{u}_{mesh}) = \mathbf{0}, \quad (2)$$

in which the diffusivity factor γ controls mesh deformation. The moving boundaries are the surfaces of the modeled fly body and the wings. Thus, the positions of the boundaries needed to solve Eq. (2) follow the fruit fly kinematics shown above.

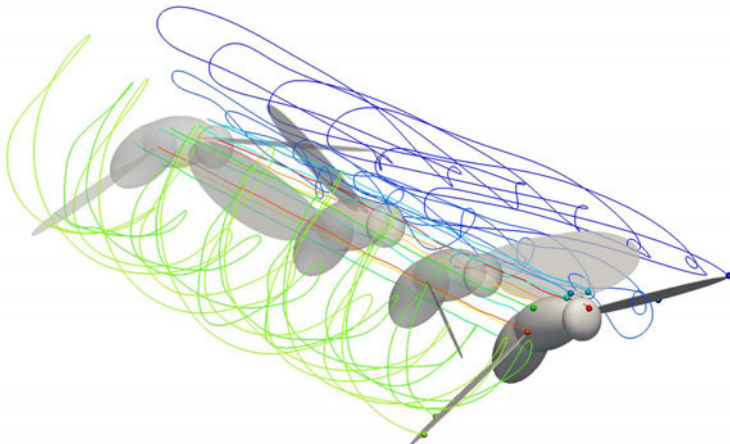


Fig. 5 Visualization of the *Drosophila*'s free-flight kinematics used in the numerical simulations. The different lines show times traces of different markers painted on the fly's body and wings.

To develop a geometric model suitable for the flow computations, the anatomical shape of the fruit fly, the measured kinematics and computational requirements were taken into account. The resulting geometry of the fly model (Fig. 6a) consists of three solid parts: the first is the body, consisting of head, thorax and abdomen, and the others are the two wings. With this approach, we were able to independently simulate the measured kinematics of body and wings using the same algorithm.

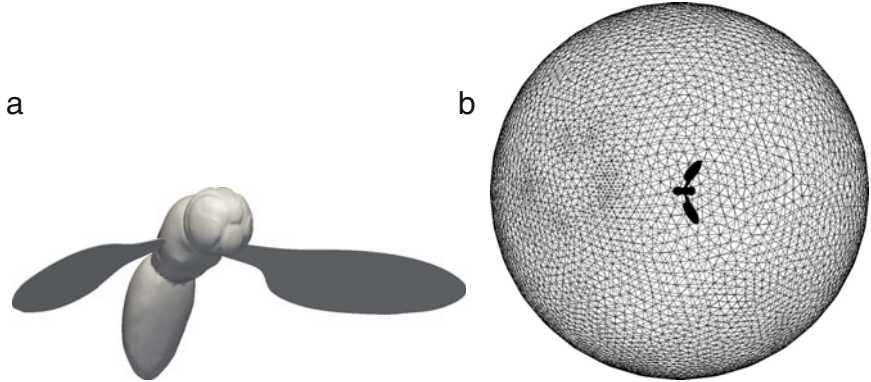


Fig. 6 Fruit fly model (a) and surface mesh of the computational domain (b).

4.2 Implementation of Measured Fruit Fly Kinematics

The motion of a rigid body is defined through the coordinates $\mathbf{x}_0(t)$ of a point on the body and an orthogonal matrix $\mathbf{O}(t)$ which describes the rotation of the body around the center of rotation $\mathbf{x}_0(t)$. Thus, for any point \mathbf{x} on the rigid body the equation of motion $\mathbf{x}(t)$ reads:

$$\mathbf{x}(t) = \mathbf{x}_0(t) + \mathbf{O}(t)(\mathbf{x}(t_0) - \mathbf{x}_0(t_0)), \quad (3)$$

where t_0 is a certain fixed time, \mathbf{x}_0 is a fixed point on the body and $\mathbf{O}(t)(=\mathbf{O}(\mathbf{x}_0,t))$ is an orthogonal matrix, which does not depend on \mathbf{x} . By substitution of t and t_0 by t_{n+1} and t_n , respectively, subtraction of $\mathbf{x}(t_n)$ from Eq. (3), and after dividing by $\Delta t = t_{n+1} - t_n$, we obtain the Dirichlet boundary conditions for Eq. (2):

$$\mathbf{u}_{mesh}^{(n+1)}(\mathbf{x}) = \frac{\mathbf{x}^{(n+1)} - \mathbf{x}^{(n)}}{t_{n+1} - t_n} = \frac{\mathbf{x}_0^{(n+1)} - \mathbf{x}_0^{(n)} + \mathbf{O}^{(n+1)}(\mathbf{x}^{(n)} - \mathbf{x}_0^{(n)})}{t_{n+1} - t_n}, \quad (4)$$

where the superscript (n) stands for the quantities taken at time t_n .

To determine the time-dependent vector \mathbf{x}_0 and the matrix \mathbf{O} for each solid part of the model we used the kinematics of the three markers on each part. For example, considering that $\mathbf{x}_b(t)$, $\mathbf{x}_t(t)$ and $\mathbf{x}_e(t)$ are the time series of the coordinates of the wing base, wing tip and wing edge markers, respectively, we take $\mathbf{x}_0 = \mathbf{x}_b$. We constructed, moreover, an orthonormal basis of vectors $\{\mathbf{e}_i(t), i = 1, 2, 3\}$ using the Gram-Schmidt orthogonalization of the sequence $\mathbf{x}_e - \mathbf{x}_b$, $\mathbf{x}_t - \mathbf{x}_b$ and $(\mathbf{x}_e - \mathbf{x}_b) \times (\mathbf{x}_t - \mathbf{x}_b)$. We consider the matrix $\mathbf{E}(t) = (\mathbf{e}_1(t), \mathbf{e}_2(t), \mathbf{e}_3(t))$ comprised by the vectors $\{\mathbf{e}_i(t); i = 1, 2, 3\}$ and the matrix

$$\mathbf{O}(t) = \mathbf{E}(t)\mathbf{E}(t_0)^T, \quad (5)$$

where t_0 denotes the initial time, and the superscript T stands for matrix transposition. Due to orthogonality of the unit vectors $\mathbf{e}_i(t)$, $i = 1, 2, 3$, the matrix $\mathbf{O}(t)$ is

orthogonal, i.e. $\mathbf{O}\mathbf{O}^T = \mathbf{I}$, where $\mathbf{I} = (\sigma_{i,j})$ is the identity matrix. The identity in Eq. (3) can be proven by straightforward calculations (it is sufficient to validate the expression for $\mathbf{x} = \mathbf{x}_0 + \mathbf{e}_i, i = 1, 2, 3$). Thus, the vector $\mathbf{x}_0(t)$ and the matrix $\mathbf{O}(t)$ needed for the mesh motion boundary conditions (4) are constructed.

The boundary conditions Eq. (4) force the points on the moving surfaces to keep their local positions on the surface during the motion. Another type of the mesh motion boundary conditions is represented by the following equation:

$$\left(\mathbf{u}_{mesh}^{(n+1)}(\mathbf{x}) - \frac{\mathbf{x}_0^{(n+1)} - \mathbf{x}^{(n)} + \mathbf{O}^{(n+1)})(\mathbf{x}^{(n)} - \mathbf{x}_0^{(n)})}{t_{n+1} - t_n}, \mathbf{n}^{(n+1)}(\mathbf{x}) \right) = 0, \quad (6)$$

where (\cdot, \cdot) is the scalar product, $\mathbf{n}^{(n+1)}(\mathbf{x}) = \mathbf{O}^{(n+1)}\mathbf{n}^{(n)}(\mathbf{x})$ is the surface normal at point \mathbf{x} . Under the conditions Eq. (6) the mesh motion velocity may have an additional component tangential to the surface. In other words, surface points can "slip" on the surface. These boundary conditions are more flexible than those defined by Eq. (4) and resist high mesh deformation, but they can be applied only to smooth surfaces.

Both types of mesh motion boundary conditions described above were implemented and used as appropriate.

4.3 Computational Details

To conduct numerical simulations of incompressible flow induced by a fruit fly during free flight, we used a second order accurate finite volume method that solves the incompressible Navier-Stokes equations on unstructured grids. The measured kinematics were transformed to mesh motion boundary conditions (as discussed above) and the spherical computational domain of radius $R = 20\text{mm}$ shown in Fig. 6b was defined. The *Drosophila* model is located in the center of this sphere moving with the flight speed of the fly's center of gravity. The wing length of the fruit fly model equals $\approx 2.5\text{mm}$. Characteristic wing length and wing velocity yielded a Reynolds number of approximately 130.

Due to the high amplitudes of the wing strokes depicted in Fig. 5, it is not possible to simulate the measured fruit fly maneuvers by deforming a single moving mesh. After a certain number of time steps the mesh deformation produces some degenerated mesh cells that prevent an accurate solution of the Navier-Stokes equation. To overcome this, new meshes were occasionally generated and the flow fields of the previous time step were interpolated on these new meshes before the simulation was continued. The meshes with between 3.5 and 5 million tetrahedral cells were generated with the open-source mesh generator Netgen and the number of meshes needed for one wing stroke varied between 25 and 30.

So far, only the flow simulation for which a disembodied *Drosophila* model was assumed, covers more than one complete wing stroke. In this simulation, the body kinematics define the motion of the computational domain while the wings follow the measured wing kinematics. The simulated time interval of 8 ms covers more

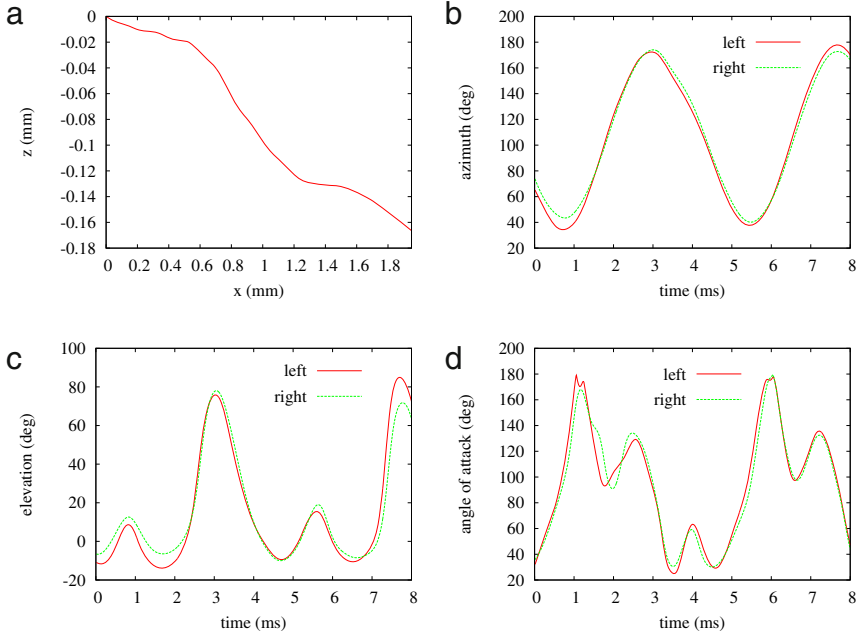


Fig. 7 Kinematics used in the numerical simulations. **a** The trace of the center of gravity of a fruit fly in xz -plane. **b** Azimuth, **c** elevation and **d** angles of attack of the two wings.

than 1.5 wing strokes. For simplicity, the data of the measured kinematics were orthogonally transformed such that the z -axis remains directed opposite to the gravity force, while the center of gravity of the fruit fly is initially placed at the origin of the coordinate system. Thus, during the simulated flight the center of gravity moves forward-and-down along the xz -plane with small fluctuations in y -direction as shown in Fig. 7a. The other parameters presented in Fig. 7 are the azimuth, i.e. the angle between the projection of wing base-tip vector on the (horizontal) xy -plane and the positive x -direction, the elevation (reflecting the angle between the base-tip vector and the xy -plane) and the angle of attack (AoA) which is the angle between the wing plane and xy -plane. These parameters slightly differ from the respective measured parameters due to some simplification made for the sake of being able to conduct flow simulations and, particularly, the use of a solid *Drosophila* model.

Since the local maxima and minima of the azimuth in Fig. 7b define the start of each half stroke, the time interval can roughly be divided into the following phases: the time segment 0 to 1 ms corresponds to the downstroke, 1 to 3 ms - to the up-stroke, 3 to 5.5 ms - to the downstroke and 5.5 to 7.5 ms - to the upstroke again. Variations in elevation angle and, even more, the angles of attack (see Fig. 7c and d, respectively) are more complex reflecting local extrema within the half stroke intervals. This is mainly due to the changing angular velocities during wing rotation, which peak at 1 ms, 1.7 ms, and 2.5 ms.

5 Free-Flight Induced Flow Fields

Fig. 8 shows streamlines calculated at different times during the upstroke (1.7 – 3 ms) and downstroke phase. The data suggest rather simple flow structures at the end of the upstroke (0 – 3 ms). By contrast, the flow becomes more vortical at 4.2 ms, when the upstroke-induced flow structures start to interact with the vortices generated during the downstroke. As a consequence, the dynamic shedding of trailing edge vortices and wing-wake interactions generate a highly complex flow field in flapping flight.

The streamlines of the velocity vectors projected on a selected plane are presented in Fig. 9. Although the 2D graphs do not show the full complexity of the flow, they give an impression of the developing wake structure. The isosurfaces of pressure and vorticity shown in Figs 10 and 11 suggest that the developing flow during the upstroke affects the surrounding fluid only in the vicinity of the wings, where the isosurfaces of the pressure and vorticity magnitude are concentrated. At $t = 3$ ms a wake region starts to develop downstream the wings. During downstroke (up to $t \approx 0.55$ ms) stable regions characterized by higher and lower pressure values move with the wings. At the first half of downstroke (Fig. 9, $t = 4.2$ ms), trailing edge vortices are shed, while the large pressure gradients produced in the wake region

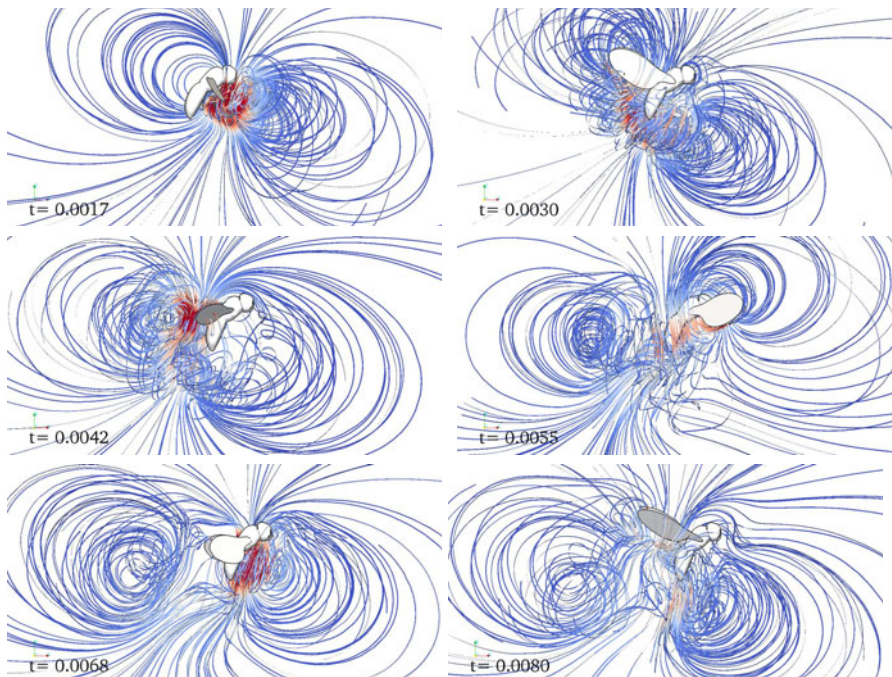


Fig. 8 The computed flow around the fruit fly visualized with 3D streamlines for different moments during the stroke cycle.

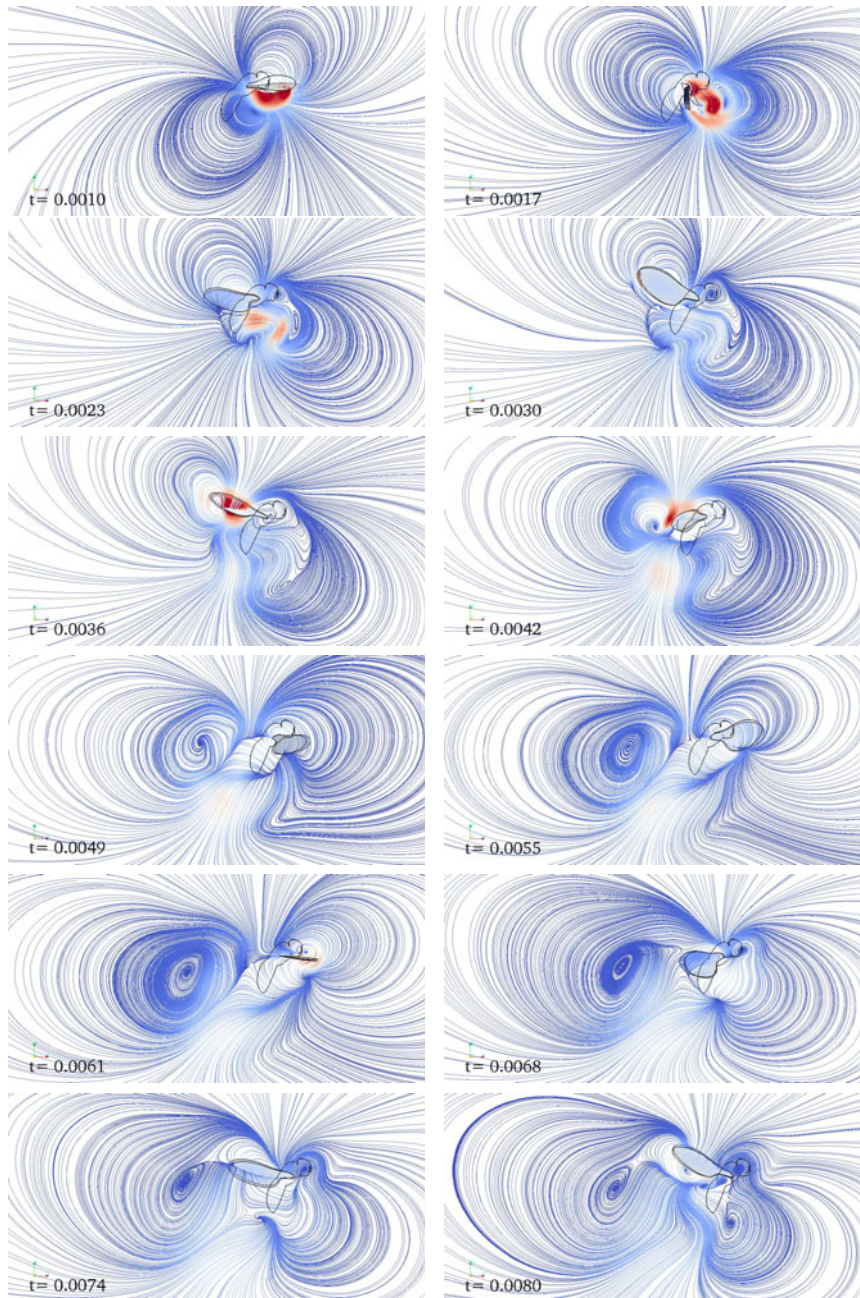


Fig. 9 2D view of the predicted streamlines around the fruit fly wing at different times of the stroke cycle.

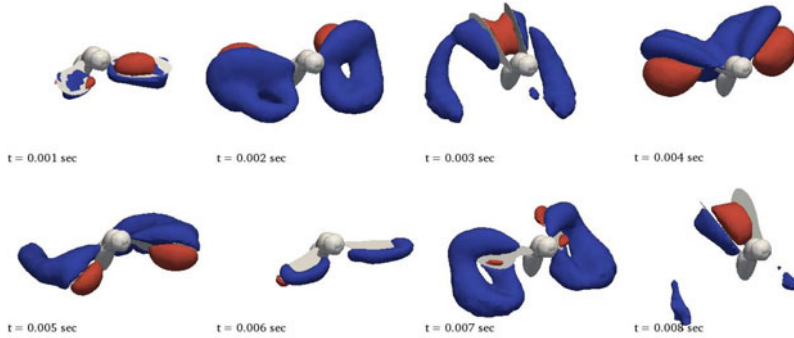


Fig. 10 Predicted isosurfaces of lower (blue) and higher (red) relative pressure field ($p \sim \pm 10\text{ Pa}$) for different times of the stroke cycle.

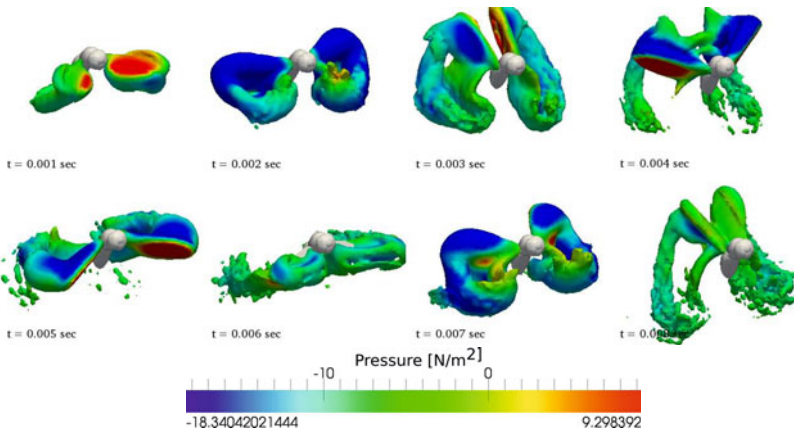


Fig. 11 Predicted isosurfaces of the vorticity magnitude (4000 s^{-1}) coloured with the pressure value at different times of the stroke cycle.

persist. They are later reused during the upstroke (Fig. 9, $t = 6.8\text{ ms}$ to 8 ms). The vorticity isosurfaces (Fig. 11, $t = 4\text{ ms}$ and $t = 5\text{ ms}$) also highlight regions with high vorticity and low pressure being attached to the leading edges of the wings (Fig. 12). LEV shedding is not observed at the down- upstroke transition in Fig. 9. We suppose that the complex wing kinematics, especially the changes in angle of attack, prevents LEVs from being shed during the stroke reversals.

Moreover, we calculated the aerodynamic force vector \mathbf{F} acting on the wings that splits into the pressure and shear components as follows:

$$\mathbf{F} = \underbrace{-\rho \iint_S p \mathbf{n} dS}_{\text{pressure component}} + \underbrace{\iint_S \mu [\nabla \mathbf{u} + (\nabla \mathbf{u})^T] \cdot \mathbf{n} dS}_{\text{shear component}}, \quad (7)$$

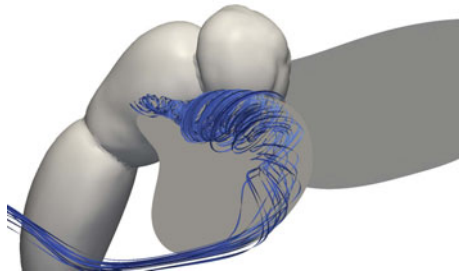


Fig. 12 Streamlines of LEV-induced flow downstream the leading edge during the wing's downstroke.

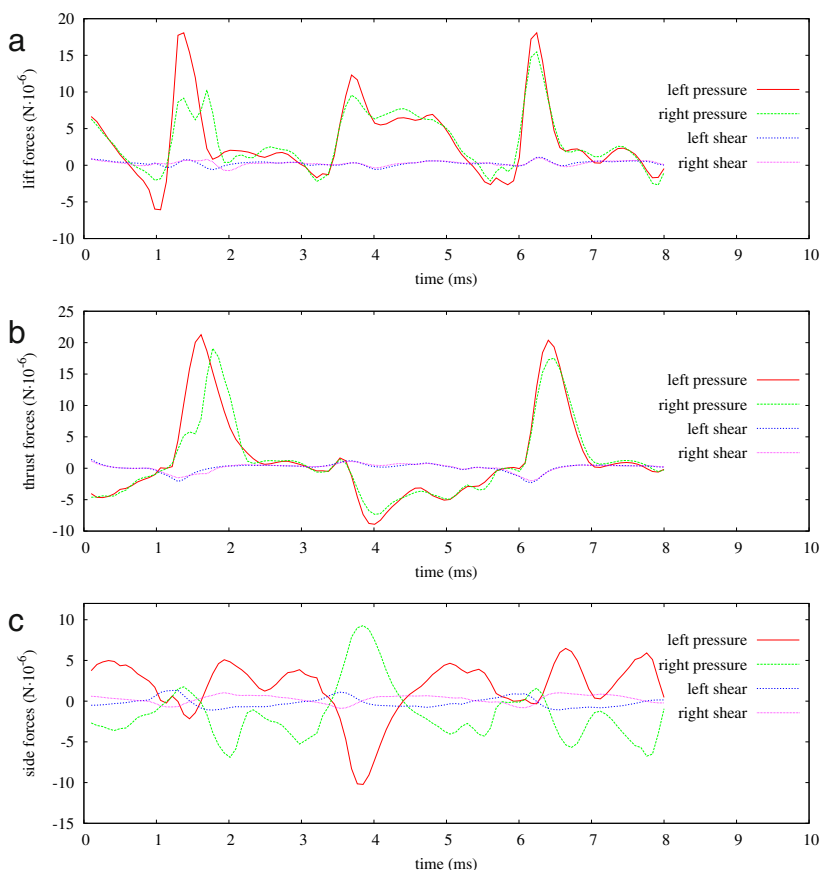


Fig. 13 Aerodynamic forces acting on the fruit fly's wings. **a** lift, **b** thrust and **c** lateral forces.

where S denotes the wing surface with normal \mathbf{n} , and ρ and μ are density and dynamic viscosity of air, respectively. The pressure force component is directed orthogonal to the wing plane, while the shear component acts tangentially. For further analysis each force component is decomposed by projection on vertical (z), forward (x) and side (y) directions to determine the lift, thrust and side forces, respectively.

Fig. 13 shows the resulting aerodynamic lift and thrust as pressure and shear components. The data indicate that pressure force always exceeds shear force during wing flapping. In general, shear forces are comparatively small and only amount to approximately 10% of the fly's body weight.

The pressure contributions on lift and thrust shown in Fig. 13 are correlated with the elevation angles and the angles of attack. Lift and thrust transiently increase at the stroke reversals at $1 - 1.5\text{ ms}$ and $6 - 6.5\text{ ms}$, when rotational acceleration of the wings is maximum. At times $1.5 - 3.0\text{ ms}$ and $6.5 - 8.0\text{ ms}$, the forces do not change much. During the downstroke (Fig. 13, $t \approx 4 - 6\text{ ms}$) lift decreases, while thrust increases.

6 Conclusions

Our three-dimensional numerical simulations of the flow around the wings of freely flying fruit flies demonstrate highly-dynamic and complex vortical flow structures in insects. Detailed analyses of pressure- and shear forces suggest that the leading edge vortex, rotational circulation and wake capture tremendously contribute to aerodynamic force production in the insect. A comprehensive and comparative numerical analysis of the contribution of each of these force enhancing mechanisms is still under investigation, including an analysis on the impact of wing elasticity on forces and moments. Moreover, a future goal of this project is to define similarity criteria of flight parameters that allow us to classify and group the maneuvers within the entire dataset. Eventually, these criteria are prerequisites in order to conduct profound statistics on wing kinematics and CFD data, and to understand the fluid dynamic features underlying the physical mechanisms of aerial maneuvering in insects.

Acknowledgments. This book chapter reports results from projects “Experimental evaluation of forces and fluid structures during maneuvering flight of flies, using biomimetic robotics” and “Experimental quantification and numerical simulation of unsteady flow conditions during free flight maneuvers of insects” to CW and FOL, funded by grants LE905/8-2 and WA1510/13-2 of the DFG National-Priority-Program SPP1207 “Impact of fluid flows in nature and technology”.

References

- Demerec, M.: Biology of *Drosophila*, pp. 368–419. Hafner Publishing Company, London (1965)
- Dickinson, M.H., Lehmann, F.-O., Sane, S.P.: Wing rotation and the aerodynamic basis of insect flight. *Science* 284, 1954–1960 (1999)
- Ellington, C.P., Van Berg, C.D., Willmott, A.P., Thomas, A.L.R.: Leading-edge vortices in insect flight. *Nature* 384, 626–630 (1996)
- Fontaine, E.I., Zabala, F., Dickinson, M.H., Burdick, J.W.: Wing and body motion during flight initiation in *Drosophila* revealed by automated visual tracking. *J. Exp. Biol.* 212, 1307–1323 (2009)
- Fry, S.N., Sayaman, R., Dickinson, M.H.: The aerodynamics of free-flight maneuvers in *Drosophila*. *Science* 300, 495–498 (2003)
- Hedrick, T.L.: Software techniques for two- and three-dimensional kinematic measurements of biological and biomimetic systems. *Bioinsp. Biomim.* 3 (2008), doi:10.1088/1748-3182/3/3/034001
- Hedrick, T.L., Usherwood, J.R., Biewener, A.A.: Low speed maneuvering flight of the rose-breasted cockatoo (*Eolophus roseicapillus*). II. Inertial and aerodynamic reorientation. *J. Exp. Biol.* 210, 1912–1924 (2007)
- Hedrick, T.L., Cheng, B., Deng, X.: Wingbeat time and the scaling of passive rotational damping in flapping flight. *Science* 324, 252–255 (2009)
- Hesselberg, T., Lehmann, F.-O.: Turning behaviour depends on frictional damping in the fruit fly *Drosophila*. *J. Exp. Biol.* 210, 4319–4334 (2007)
- Lehmann, F.-O.: When wings touch wakes: understanding locomotor force control by wake-wing interference in insect wings. *J. Exp. Biol.* 211, 224–233 (2008)
- Lehmann, F.-O., Gorb, S., Nasir, N., Schützner, P.: Elastic deformation and energy loss of flapping fly wings. *J. Exp. Biol.* 214, 2949–2961 (2011)
- Kliss, M., Sompas, C., Luttges, M.W.: Stable vortex structures: A flat plate model of dragonfly hovering. *J. Theor. Biol.* 136, 209–228 (1989)
- Maybury, W.J., Lehmann, F.-O.: The fluid dynamics of flight control by kinematic phase lag variation between two robotic insect wings. *J. Exp. Biol.* 207, 4707–4726 (2004)
- Mronz, M., Lehmann, F.-O.: The free-flight response of *Drosophila* to motion of the visual environment. *J. Exp. Biol.* 211, 2026–2045 (2008)
- Ramamurti, R., Sandberg, W.C.: A computational investigation of the three-dimensional unsteady aerodynamics of *Drosophila* hovering and maneuvering. *J. Exp. Biol.* 210, 881–896 (2007)
- Ristroph, L., Berman, G.J., Bergou, A.J., Wang, Z.J., Cohen, I.: Automated hull reconstruction motion tracking (HRMT) applied to sideways maneuvers of free-flying insects. *J. Exp. Biol.* 212, 1324–1335 (2009)
- Sane, S.: The aerodynamics of insect flight. *J. Exp. Biol.* 206, 4191–4208 (2003)
- Schützner, P., Lehmann, F.-O.: High-speed analysis of wing and body motions in flying *Drosophila* using fluorescent markers. In: Proceedings of the International Symposium on Flying Insects and Robots, Monte Verit, Switzerland, August 12–17, pp. 103–104 (2007)

- Sun, M., Wang, J., Xiong, Y.: Dynamic flight stability of hovering insects. *Acta Mech. Sin.* 23, 231–246 (2007)
- Wang, Z.J.: Two dimensional mechanism for insect hovering. *Phys. Rev. Lett.* 85, 2216–2219 (2000)

Barn Owl Flight

Thomas Bachmann, S. Blazek, T. Erlinghagen, W. Baumgartner, and H. Wagner

Summary

Owls (*Strigiformes*) are nocturnal birds of prey that are known for their silent flight. For a long time, the underlying mechanisms were not well understood. In a comprehensive study, we have characterized the flight apparatus of one representative of owls, the barn owl (*Tyto alba pratincola*), to advance beyond the phenomenological description provided so far. The barn owl wing is adapted to slow flight as indicated by a low wing loading, an elliptical shape, a high camber and a specific thickness distribution. Further, feather specializations can be found: 1.) serrations at the leading edge of the wing, 2.) a velvety dorsal surface texture, and 3.) fringes at the inner vanes of remiges. Quantitative characterizations of these structures revealed that serrations had a uniform shape, but the length depended on their position on the wing. The velvety dorsal surface texture differed between the inner and outer vanes which is a consequence of different functions (air flow control, friction reduction). The fringes were observed to merge into neighboring feather vanes by gliding into grooves at the lower wing surface to create a smooth airfoil. Besides anatomical data, material properties and wearing effects of feather keratin of rachises and barbs were obtained.

1 Introduction

Wings of barn owls (*Tyto alba pratincola*) are equipped with several anatomical specializations that either influence noise production or control the air flow around

Thomas Bachmann

Technische Universität Darmstadt, Institute for Fluid Mechanics and Aerodynamics,
Petersenstraße 30, 64287 Darmstadt, Germany
e-mail: bachmann@sla.tu-darmstadt.de

S. Blazek · T. Erlinghagen · W. Baumgartner · H. Wagner
RWTH Aachen University, Institute for Biology II, Mies-van-der-Rohe-Straße 15,
52056 Aachen, Germany
e-mail: {blazek,werner,wagner}@bio2.rwth-aachen.de,
thomas.erlinghagen@rwth-aachen.de

the wing during flight. Although these specializations have been mentioned in earlier reports, a precise quantitative description has been missing so far. We have conducted a comprehensive and interdisciplinary study in which the wings and feathers of barn owls were characterized anatomically, morphometrically and biomechanically. In the following, the wing and its characteristics will be described from the macroscopic to the microscopic levels.

The wing of a bird can be described in terms of its aerodynamic and geometric parameters such as wing span, area and chord. The profiling is determined by the thickness and camber distributions, the chord length and nose radius. From a biological point of view, the wing is characterized by the topography of the remiges (primaries and secondaries), the different rows of coverts and the alula. Primaries, secondaries and the appended coverts are associated with the underlying skeleton by which the wing can be divided into a hand part (primaries) and an arm part (secondaries) (Figure 1).

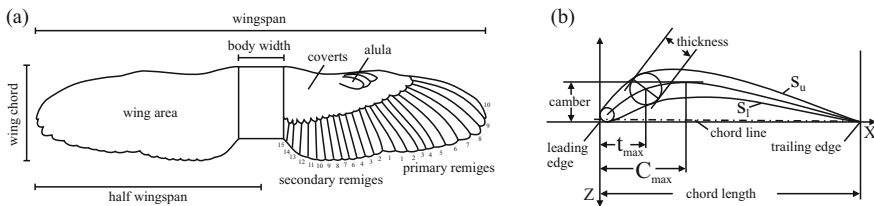


Fig. 1 Wing and feather terminology. (a) The wing of a bird is characterized by its geometry (left) and anatomical topography (right). (b) The wing profile is determined by the chord length and the thickness (t) and camber (C) distributions.

The material was collected from the barn owl colony of the Institute for Biology 2 at the RWTH Aachen University. This colony consists of North American barn owls (*Tyto alba pratincola*). Pigeons (*Columba livia*) served as reference for material property measurements and were provided by a local breeder. All studies were conducted under a permit by local authorities (Landespräsidium für Natur, Umwelt und Verbraucherschutz Nordrhein Westfalen (LANUV), Recklinghausen, Germany).

2 Free-Flight Studies and Wing Fixation

The wing of a bird is highly dynamic expressed by varying wing geometries at different flight styles. By changing the posture of the skeleton elements, the bird is able to change area and camber of the wing. In a first step of understanding the flight of owls, we examined the wing geometry of barn owls in gliding-flight position using two different approaches. In the first approach, wings of dead barn owls were fixed in gliding-flight position and subsequently digitized using computed

tomography and photogrammetry. A detailed description of the methods is given elsewhere [1, 3, 4, 5]. This approach yielded high spatial resolution data. However, although attention was paid to the fixation process to guarantee an almost natural arrangement of the bones and feathers [1, 4], the fixed wings may differ from that of living owls. Earlier studies suggested that even carefully prepared, fixed wings do not precisely reflect the geometry of spread wings of living birds. For example, Biesel et al. [8] found an overestimation of camber in pigeons when using dead specimens. Therefore, it seemed necessary to use two independent methods for the reconstruction of the owls' wing geometry. To obtain the wing geometry under free-flight conditions, two barn owls were raised by hand and trained to fly a predefined path. With this method, we were able to reconstruct the natural wing geometry. Although we took care that the paths were similar (Figure 2) slight changes from trial to trial cannot be excluded.

The wing geometry during gliding flight was obtained from photographs taken with a photogrammetric setup combined with laser sheets. While the birds flew through the laser sheets, a trigger activated the cameras and the upper and lower wing surfaces were captured simultaneously. The owls started and landed at a given position. In this situation the owls flapped their wings for the first ~50% of the distance, then shifted to gliding flight for 25 – 30% before moving into a breaking motion (Figure 2), indicated by high angles of attack, spread alulae, and small rigorous flapping movements. The images were taken at the end of the gliding phase before a movement of the alulae was detected.

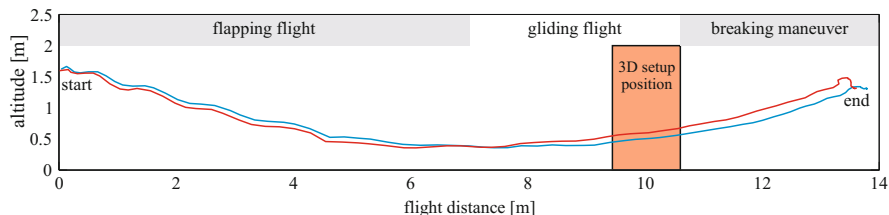


Fig. 2 Two flight paths of one barn owl (*Tyto alba*) individual over a distance of 14 m. The different flight styles within this distance are highlighted. Photogrammetric measurements took place after 10 m.

3 Morphometry of Wings

Three-dimensional reconstructions from the free-flight experiments and the digitized fixed wings (Figure 3) were analyzed with respect to aerodynamic parameters such as half wingspan, chord, area, camber line, and thickness distribution. Additionally, aspect ratio and wing loading were calculated.



Fig. 3 Example images of fixed barn owl wings investigated. (a) Photograph. (b) 3D reconstruction of bones, skin and feather rachises of remiges and the alula (CT data). (c) Surface scan using photogrammetrical techniques. Note that all images depict the same wing.

The following data refer to measurements on ten fixed wings from six barn owl individuals from both sexes. Wings of barn owls are characterized by a large wing area (705.7 cm^2 +/- SD of 78.9) in relation to the body mass (464.8 g +/- SD of 15.2) that results in a very low wing loading (33.0 N/m^2 +/- SD of 2.3) compared to other similar sized birds [1, 4]. The calculated aspect ratio of the owl wing is 6.89 (+/- SD of 0.18). Span and chord influence the planform of a wing. The chord of barn owl wings is constant over most parts of the span at the fully extended wing. At the wing tip (outermost 30% of span) a round taper shortens the chord. Hence, the barn owl wing appears almost elliptically. This unique wing geometry in combination with the low wing-loading enables the barn owl to maintain lift even at low flight velocities (2.5-7 m/s) [22].

Computer-aided analyses of the profiles of fixed wings were compared with the wing profiles obtained in free flight. Each surface scan or reconstructed wing was analyzed with respect to the maximum values of thickness and camber and their chordwise position within the wing. The data showed that the wing can be divided into two parts: the arm part of the wing which spans from the body to the wrist and the hand part that reaches from the wrist up to the wing tip. The hand part of the wing is mainly composed of overlapping remiges (primaries), which results in a thin, low cambered plate [1, 4].

As previously stated, differences between the wings of living animals and anesthetized/dead animals can be observed [8]. These studies, however, were done on pigeons and the upper wing surface was only measured in low spatial resolution. The lower wing surface was reconstructed using thickness distribution data of anesthetized birds. Thus, to validate and generalize previous findings as well as furthering the understanding of the silent flight, the wing morphometry of gliding barn owls was measured.

In the following, preliminary data on the wing morphometry of two animals, one male (blue) and one female (red) aged 2.5 and 4 years, are shown and compared to the data collected on 3 fixed wings.

The chord length in gliding flight was similar for the two living specimens. By contrast, the wings of the dead animals had a longer chord (Figure 4). The difference of less than 10% may be due to different individual body sizes.

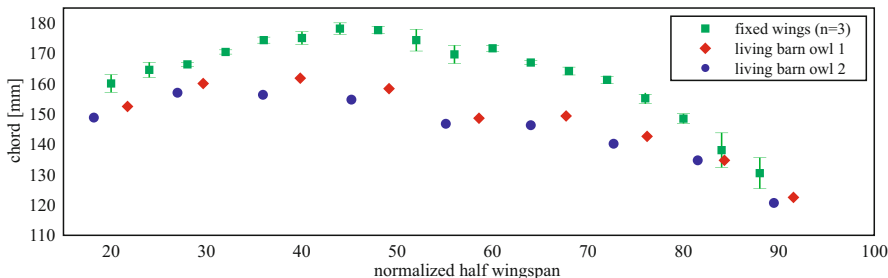


Fig. 4 Chord length of fixed ($n=3$, mean \pm s.d.) and living barn owl wings

The most interesting observation from an aerodynamic point of view was that the maximum camber was similar in the fixed wings and the wings measured during gliding flight (Figure 5). In both approaches the camber was around 13% at the shoulder and flattened out towards the wing tip. The agreement was very good between 0% and 50% of the half wingspan. Beyond 50% towards the wing tip, the data of the free-flight scattered and the values were larger than the data from the fixed wings. This may be due to the fact that the wing becomes very thin towards the tip and only feathers are found there. The camber is extremely influenced by movements of the feathers and their position relative to each other. The living bird can precisely position its feathers during flight, much better than at any manually attempt of fixing wings from dead specimens.

The data on the location of maximum camber (Figure 5b) showed a similar agreement between the wings from living barn owls and fixed specimens. Maximum camber laid around 50% of chord length at the shoulder and then shifted slightly towards the leading edge, reaching about 40% at the wrist. In the distal wing part, the data between the living and the fixed wings differed. Again, this may be due to the fact, that small difference in feather posture may have a large influence in the thin wing regions. Additionally, the fixed wings were digitized under quiescent air and, thus, the air flow did not affect the geometry which may explain our findings. Interestingly, the position of maximum camber in the arm part of the wing laid in close proximity to the point where the coverts of the lower wing surface ended. Here, the wing is extremely thin because it is mainly formed by remiges alone.

The normalized maximum thickness decreased from proximal to distal (Figure 5c). Over the entire half wingspan, exempting the wrist area, the fixed wings were, in relation to the chord, about 3% thicker than the wings from living owls. One reason for this may be the influence of the airflow during gliding and the resulting forces acting onto the wing. For example, Carruthers et al. [11] demonstrated that feathers on the wing of step eagles can bend to passively adapt to changing wind conditions, suggesting that in a stable position of gliding flight the constant air stream will increase the stability of the airfoil and decrease its thickness.

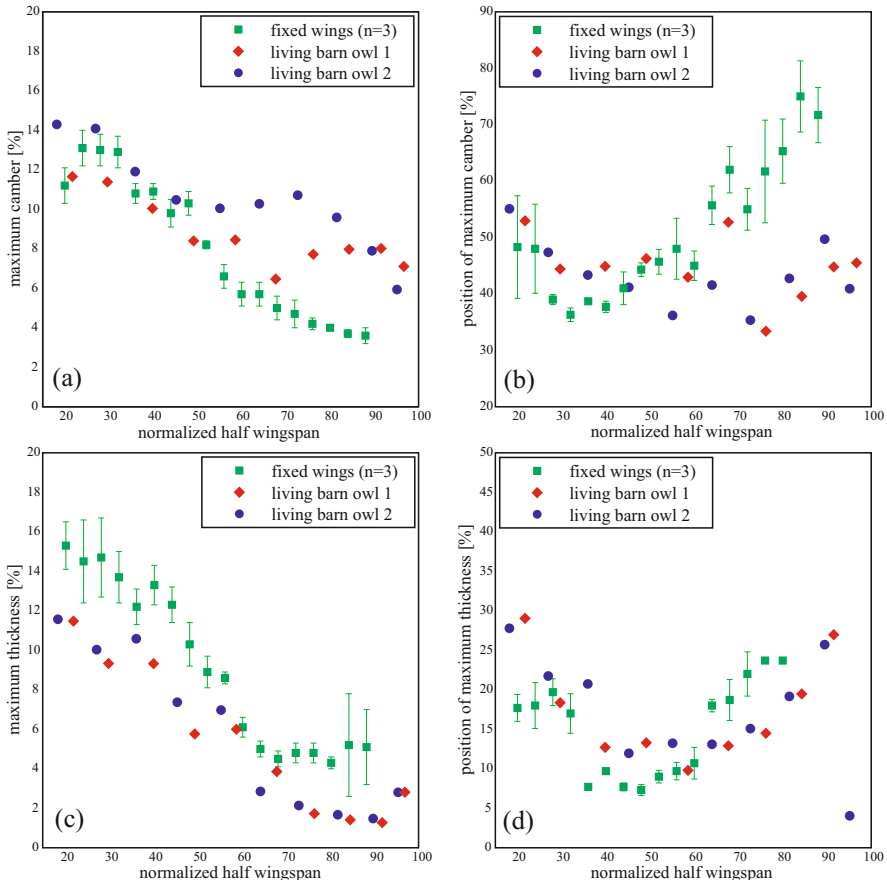


Fig. 5 Aerodynamic parameters of fixed ($n=3$, mean \pm s.d.) and living barn owl wings. Distribution of the maximum camber (a) and maximum thickness (c) (normalized by the chord length) and their chordwise position ((b), (d), 0% = leading edge) along the half wingspan are shown.

The location of the normalized maximum thickness followed the same pattern at the wings from living owls and fixed specimens (Figure 5d). The location of the maximum thickness was related to the location of bones of the forearm and the hand parts. In the hand part of the wing, the rachises of the feathers were an important determinant of the location of maximum thickness. The relation to body structures suggests that the ability of the owl to manipulate thickness location is limited. In the spread wing, the forearm moves closer to the leading edge. By contrast, folding the wing leads to the thickest point of the wing being moved backwards, while the angle at which it progresses towards the leading edge and the wrist joint steepens.

Overall, the comparison of wing from living owls and fixed specimens shows that the data relating to the camber overlaps to a high degree in the proximal wing region, whereas in the distal region the data differs. To validate the above statements, more data on wing geometry of living owls are necessary.

4 Flight Feathers

Feathers are the main aerodynamic components of a bird's wing. They consist of a hollow central shaft and two laterally attached vanes. The vanes are formed by parallel oriented barbs that branch off from either side of the rachis. Each barb repeats more or less this construction plan. Hook and bow radiates emerge laterally from the barb shaft. Tiny hooklets of the hook radiates cling into grooves formed by the bow radiates to form a flexible, lightweight and securing connected surface (Figure 6). Each feather is anchored into the skin of the bird. The geometry, surface texture, and edge characteristics of each feather influence the aerodynamic performance of the assembled wing. A quantitative morphometric characterization of wing feathers of the barn owl may be found at Bachmann et al. [3]. The large wing area of barn owl wings is a result of large remiges. The feathers appear filigree, pliant and translucent, which is caused by a reduced number of radiates compared to other birds. The few connection points between neighboring barbs lead to a flexible vane.

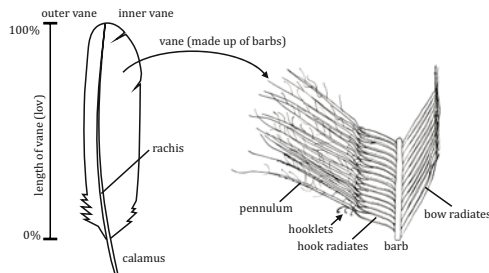


Fig. 6 Structure of a typical barn owl feather. The feather is composed of a central shaft (rachis) and laterally attached vanes. Tiny hooklets of the hook radiates cling into grooves of the bow radiates of neighboring barbs to create a closed and securely connected vane.

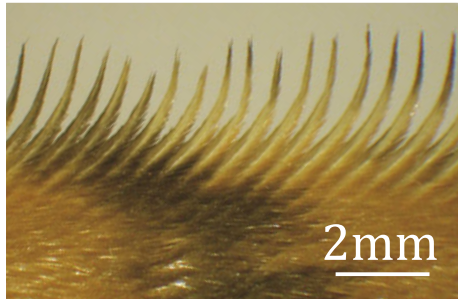
4.1 Plumage Specifics

Barn owls evolved several feather specifics that are associated with flow control and noise reduction during flight.

The leading edge of the 10th primary and the 10th greater primary covert is serrated [1, 3, 5]. Barb endings separate and bend upwards to form the hooked structure (Figure 7). As these feathers build the leading edge of the wing, serrations act as a passive mechanism to control the flow around the distal wing. By creating small turbulences that travel chordwise over the wing, flow separation is shifted to

higher angles of attack, lift is enhanced, and the noise that is generated by the wing is reduced [16, 19, 21, 27]. However, the serrations may only work properly at high angles of attack, because the stagnation point at the leading edge possibly prevents a circulation within the size of the serration in normal cruise flight conditions. By contrast, at critical flight maneuvers such as landing, take-off or striking, the serrations significantly reduce flight noise of owls.

Fig. 7 Serrations at the leading edge of the 10th primary of a barn owl



In the last years high-resolution imaging techniques have become available that allow the morphometrical characterization and reconstruction in 3D [5]. The 3D investigation of serrations revealed that the curvature and the taper of the serrations are similar along the leading edge. However, the length differs significantly. While longest serrations (2.7 mm) are located in central regions of the leading-edge vane, smallest serrations (1.8 mm) are found at the feather's tip. As the serrations are shorter at the tip of the feather and as the tapering is equal in all serrations, the distally located serrations have a rounded tip [5].

The rachis of the 10th primary is curved, resulting in different leading-edge angles towards the free stream direction. Consequently, different angles of the serrations towards the air-flow direction are found. In central regions of the feather the inclination angle of the serration is almost perpendicular to the air flow (82-91°). At basal parts of the feather, serrations point towards the air flow (74°), whereas they bend away at distal parts (113°) [5]. The distal wing of the barn owl resembles a slightly cambered plate over which the air flow normally tends to separate, especially at low-speed flight. We speculate that the turbulent boundary layer, induced by the serrations, may prevent a separation and increase lift. The variability of length, spacing, and orientation of serrations along the leading edge may be due to the taper of the distal wing of the barn owl. In this way serrations possibly maintain a constant excitation of the air flow along the distal wing.

A second specific of the barn owls' plumage is the velvety dorsal surface of each feather (Figure 8). Elongations of the hook radiates, so called pennula, form this fluffy texture by their number [3]. The digitization of this texture using confocal laser scanning microscopy suggested some possible functions [1]. The velvety surface can be found on the inner as well as on the outer vane. As the feathers have an imbricate arrangement within the spread wing, some areas are

subjected to the air flow and some areas are covered by neighboring feathers. The thickness and the porosity of the velvety structure differ significantly between covered and uncovered areas. In covered areas, the velvety structure is thicker and has a higher porosity. The pennula are long and bend at the surface to create a friction reducing texture. Most friction between feathers occurs in covered areas. Due to the parallel orientation of the barbs, a high frequent noise would be produced without the covering surface when adjacent feathers rub against each other during beating of the wings. We suggest that owls evolved elongated pennula to cover the barb shafts and, thus, effectively reduce friction noise of feathers.

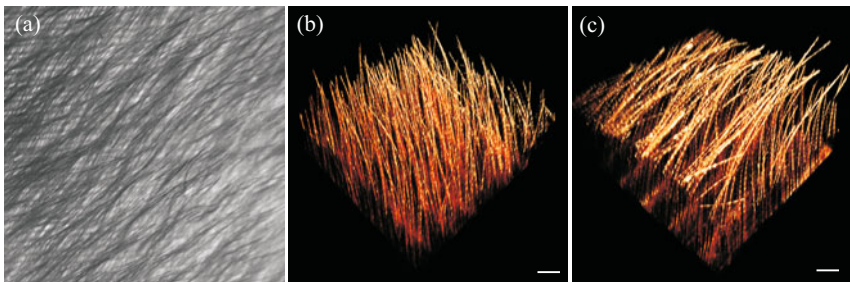


Fig. 8 Velvety surface texture of barn owl feathers. (a) Photograph (inner vane). (b) 3D visualization of the outer vane (subjected to the flow field). (c) 3D visualization of the inner vane (covered by neighboring feathers). Scale bars represent 100 μm .

The outer vane and small parts of the inner vane are subjected to the air flow during flight. Here, the surface texture is differently developed. The pennula are shorter and due to a lesser inclination angle oriented towards the barb shafts. Thus, the structure is thinner and has a lesser porosity compared to the structure of covered areas [1]. The tips of the pennula point into the air flow creating a rough and porous surface of the feather. Functionally, the increased roughness influences the air flow around the wing. This was shown experimentally by comparing two different wing models in wind tunnel experiments [17, 18]. The wing geometry of the model resembled that of the barn owl. While one wing model had a smooth and clean surface, the other one was equipped with velvet on the upper side. For Reynolds numbers similar to the barn owl flight and moderate angles of attack, the size of the separation bubble that occurred on the upper wing surface was reduced significantly and shifted towards the leading edge of the wing. Consequently, the air flow around the barn owl wing was stabilized by the velvety surface texture [17, 18].

Finally, fringes that border the inner vane of each remex are a further specialization of barn owls' feathers [1, 3, 4, 6] (Figure 9). The tips of the barbs of the inner vane are separated due to a loss of hooklets of the hook radiates. Thus, the connection of the barbs is no longer maintained. The radiates bend towards the barb shafts to support the formation of fringes.

Fig. 9 Photograph of fringes at the inner vane of a barn owl's 10th primary. Note that all inner vanes of barn owls' remiges are fringed.



Modern imaging techniques combined with morphometry measurements and air-flow experiments demonstrated that fringes merged into neighboring feather vanes by gliding into the grooves at the lower wing surface. The grooves were formed by the parallel orientation of the barb shafts. This is a new finding that suggests a hitherto unknown function of the fringes. Until now it was claimed that small vortices which occur at the trailing edge of the wing due to different velocities of the upper and lower streams are delayed by the fringes [14]. The existence of fringes along the complete inner vane and not only at the trailing edge of the wing was interpreted as a mechanism to reduce noise during fluttering, because single feathers separate on the upstroke to let the air flow through the wing [14, 21]. In this case, each feather acts as a small airfoil and has its own trailing edge where noise needs to be reduced. However, our flight analyses of barn owls revealed that the remiges hardly separate during normal cruise flight. By contrast, the wing surface seemed to be formed out of a single membrane. The remiges were in close contact. High-speed video analysis of an artificial wing equipped with natural owl feathers showed a merging effect of two neighboring feathers induced by the fringes. The orientation and density of fringes corresponded to the orientation and density of adjacent barb shafts. Thus, the fringes could easily fit between the barb shafts. This effect was even enhanced by the pressure gradient between upper and lower wing surface. As the feathers are air-transmissive [24], the fringes were sucked into the neighboring feather vane. This effect resulted in a smooth wing surface without any sharp edges where noise might be generated [23].

4.2 Material Properties of Rachises

Material properties of feather keratin, more precisely Young's modulus, were determined with nanoindentation and two-point bending tests. Rachis and barb specimens of remiges were investigated. The methods are described in detail in Bachmann et al. [2].

Flight feathers bend and twist under aerodynamic loads. The elastic modulus (Young's modulus, E) and the geometry of the cross section of rachises, more precisely the second moment of area (I), are responsible for the flexibility of feathers [2]. Young's modulus and the second moment of area were obtained quantitatively to test whether the feathers of barn owls underwent an adaptation in stiffness. Two

independent methodological approaches were used (two-point bending tests, nanoindentation) to determine Young's modulus. Pigeons' (*Columba livia*) remiges were taken as a reference as these birds are of comparable body mass but differ in flight speed and flight style.

No significant variation in Young's modulus was detected between the two species. By contrast, in both species differences of E between proximal and distal feather regions were found with the distal end of the feather having a higher Young's modulus. The overall values for E varied between 4.2 (feather base) and 6.3 GPa (feather tip) [2].

The geometry of the rachises is the second parameter that influences the flexibility of feathers. In general, the rachis is a hollow shaft of dense keratin filled with a foam-like structure, the medullary cells (air filled cells). Dorsal and ventral parts of the rachis' cortex are typically thickened in comparison to lateral parts where the radiates branch off. A transversal septum – a keratinous membrane structure – spans centrally between the dorsal and ventral cortex.

In barn owls, the cortex is smooth on the inner as well as on the outer contour. The transversal septum is reduced and only present between 30% and 50% of the rachis length. Here, the origin of the septum results in a ventral spine running distally along the inner sidewall. The second moment of area is largest at the calamus where highest bending moments are present due to the long lever arm. From here, I decreases rapidly towards the tip of the feather. The cross sectional geometry of pigeons' remiges is slightly different. The transversal septum is well developed and the inner dorsal cortex is mechanically stabilized by ridges that follow the longitudinal geometry of the rachis. Although the cross sectional geometry has a richer structural appearance, the second moment of area was lower in pigeons compared to barn owls [2].

The geometry and the elasticity of the rachis result in a beam structure that is resistant to dorsal and ventral forces. When the load exceeds a critical value, feathers deflect by twisting. As the feather is a dead structure, the bending behavior under aerodynamic loads acts as a passive flow control for the wing. Due to the pressure gradient of the upper and lower wing surfaces, the feathers will bend depending on the air-flow velocity. While the feather has a natural curvature at low flight-speeds and thus the wing is cambered, the feathers bend upwards and straighten as the flight speed increases. Consequently, the wing gets less cambered at higher air-flow velocity. This passive flow control seems to adjust lift to ensure that only as much lift as needed is produced to maintain the altitude.

To visualize the bending behavior of barn owl remiges, a hybrid wing consisting of an artificial leading-edge (carbon reinforced polymer) and real barn owl feathers at the trailing edge was built. This artificial wing was subjected to different air flow velocities (3, 5, 7 m/s) in an Eiffel-type wind tunnel at the Institute for Fluid Mechanics and Aerodynamics (TU Darmstadt). The angle of attack was initially constant at 6°. During the experiment, the upper wing surface was digitized with a laser distance sensor (AM 200-500, Allsens Messtechnik, Dreieich, Germany). The results are shown in Figure 10. Under quiescent air condition, the artificial wing had a normalized camber of 12.2% with the maximum camber at

47% chord length, which is equivalent to a gliding barn owl. With increasing air-flow speed, the feathers straightened themselves, the camber decreased (9.2% at $v_{max}=7$ m/s) and the position of maximum camber was shifted towards the leading edge of the wing (37% at $v_{max}=7$ m/s).

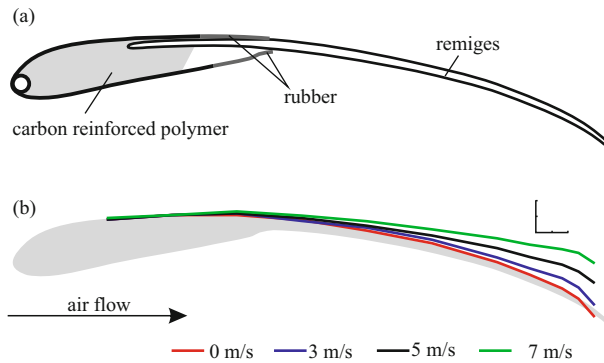


Fig. 10 Bending behavior of remiges. (a) A hybrid wing, consisting of an artificial leading edge (carbon reinforced polymer) and real barn owl remiges at the trailing edge was built. The profiling resembles that of a living barn owl at 40% half wingspan. The sealing was maintained using flexible rubber. (b) The deflection of the remiges was measured at a constant angle of attack (6°) and different airflow velocities (color coded) in an Eiffel-type wind tunnel. Scale bars represent 1 cm each.

4.3 Wearing Processes of Barn Owl Feather Keratin

Wings of birds are constantly exposed to wearing factors such as aerodynamic turbulences, UV-radiation, degradation by bacteria, and collision with obstacles and aerosols. Over time these abrasions influence the flight performance of birds. Degradations and abrasions of the feathers are compensated by replacing the feathers periodically (molt). The process is time consuming for the animal and requires a lot of resources [12, 26, 32]. Only a small amount of the extra demand arises from the production of feather proteins. The main factor is the loss of heat by reducing the insulation layer. Most species of birds with body masses under 1 kg replace their feathers annually. Heavier species spread their molt cycle over two or more years [30]. With respect to its mass, the barn owl weighing 400-500 g, belongs to the former class. However, the barn owl has an untypical molting cycle of 2-3 years [31]. The feathers are replaced one by one sequentially [29]. This incomplete molting pattern is typically for species that rely on their ability to fly for feeding [22]. Rhower [30] pointed out that many small owls are crepuscular or nocturnal hunters, causing less abrasion effects from ultraviolet-radiation exposure [7]. This statement might be true for barn owls from North America, Africa and Australia. But, barn owls from North England and Scotland show activity all day long, meaning that their feathers are exposed to a higher dosage of UV-radiation. Contrary to expectations, these barn owls show the same molting pattern

as the rest of their conspecifics [31]. In the context of this study, the influence of feather wearing on the aerodynamic properties and noise reduction are important. Thus, it was interesting to study wearing processes of feathers and to investigate possible adaptations against abrasion.

A feather is composed of keratin molecules [10] that are additionally stabilized by disulfide bonds [25]. The pigmentation of the feather is caused by situated melanin embedded between the keratin fibrils [13]. Former studies showed an increase of abrasion resistance of melanized feathers [9]. Thus, melanin influences the hardness of the keratin. One important wearing factor of keratin is the ultraviolet radiation (wavelength of 300-400 nm). When keratin is exposed to UV-light, the bonds between proteins are destroyed [28]. This also leads to a cleavage of the disulfide bonds, which changes the protein structure and reduces the stiffness of the keratin [15].

Barn owl feathers were subjected to UV-B radiation to examine the effect on the material properties. An UV-B radiation box with 3 Philips UVB Broadband (/12) Phototherapy lamps was build. A cluster of 6 fans created a constant air flow through the box by which the inside temperature stayed constant at 27.5°C. By exposing the barn owl specimens for 164 hours, we simulated an insolation of 2 years corresponding to the mean insolation of UV-B radiation in Germany (1.15 kwh/m²). The reflection spectra of the feather specimens were analyzed before and after the radiation exposure. A spectroradiometer (Spektroradiometer CS-2000, Konica Minolta, Japan) was used to measure the reflections in a wavelength range of 380 nm to 780 nm. The measurement area was illuminated by 10 lamps (Accentline, Philips, Germany). A luminosity sensor (Digilux, AS 501, Optronik, Germany) was installed behind the feather specimens to control the stability of the lightning conditions (14.3 W/m²).

In our preliminary results, the reflection spectra of the two samples (untreated and UV-B irradiated) show comparable results (Figure 11). In the range of 380 nm, both samples have the same reflection intensity. But, towards higher wavelengths, the UV-B treated samples had a higher relative intensity of reflection.

The outer vanes showed a weaker reflection at wavelength of 380 nm to 560 nm (Figure 11), probably due to melanin inclusion. Bleaching effects were visible after the UV-B treatment. If colors were fading, this led to an increase of the reflected light.

The exposure of the inner vane specimen to UV-B radiation led to a decrease of reflection in the spectral range of 380 nm to 425 nm. Beyond 426 nm the spectra of the two different samples (untreated and UV-B irradiated) have very similar and constant values of about 0.42 (Figure 12). This part of the feather is white which indicates a low level of situated melanin. White surfaces show a constant reflection of all wavelengths. Looking at the spectra after UV-B-wearing, a decrease between the wavelengths of 380 nm and 425 nm is visible, which is described in the literature as yellowing [20]. These changes were observed as side effects of the UV treatment. They came along with a decrease of the bending resistance. Future experiments will show how these effects are valuable indicators for wear and how much the flight performance of the owl is influenced by the UV-B induced aging process.

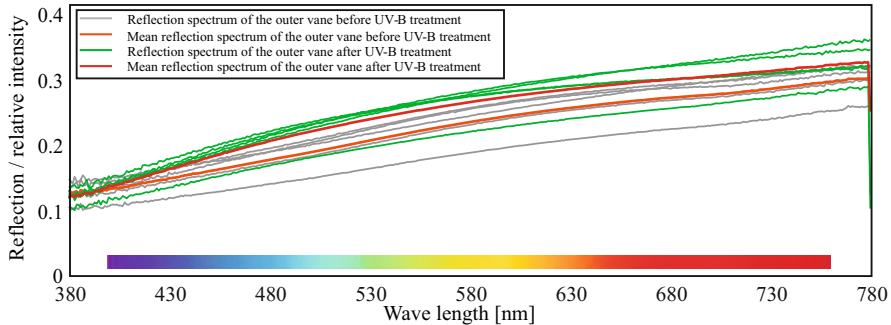


Fig. 11 Reflection Spectra of feathers. The grey lines represent the reflection spectrum of the outer vane before the UV-B treatment. The orange line stands for their mean value. The reflection spectrum of the outer vane specimen is represented by the green lines, whereas the mean value is shown by the red line. n=5.

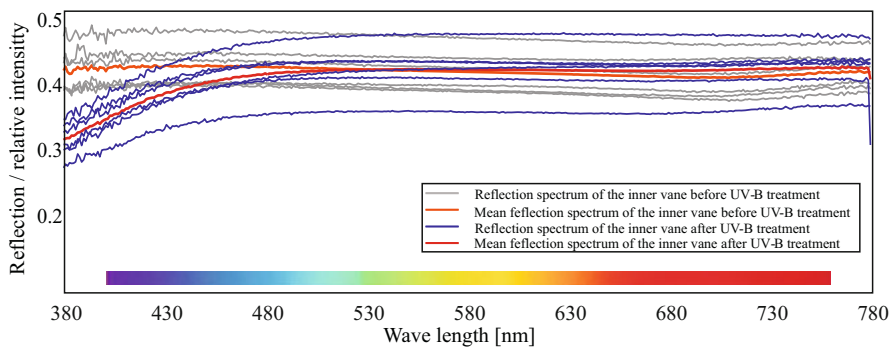


Fig. 12 Comparison of reflection spectra, 380 nm to 780 nm, of the inner vane before and after the UV-B radiation. The reflection spectra before the exposure to the UV-B radiation are represented by the grey lines with an orange line for their mean. The spectra after the treatment are blue. The red line stands for the mean of the reflection spectra. n=5.

Earlier studies have shown that melanin is involved in the hardness of keratin [9]. Consequently, UV-B treatment should have a higher impact on the outer vane, which is highly melanized. The dark coloration of the outer vane leads to a higher UV-B absorption. With the degradation of the keratin, the bending resistance of the outer vane should decrease. The inner vane will not be affected that much due to a low amount of melanin and the resulting high reflectivity.

Our preliminary data provide a basis for further experiments towards an understanding of degrading processes induced by the environment. In a next step, we plan to investigate changes in the material properties of feather keratin. The bending resistance will be determined before and after UV-B radiation to measure the mechanical effects of UV-radiation on the material. Finally, we can use the obtained data to interpret their impact on the molting cycle of barn owls.

5 Conclusion

The combined biological and engineering investigations (see chapters by Winzen et al. and by Friedl et al.) on owl flight have increased our understanding of the adaptations in barn owls for a silent and low-speed flight. New insights have been revealed through an integrative approach progressing from a macroscopic to a microscopic description, and by a synergy created by the combination of data from biological and engineering disciplines. This approach allowed us to draw conclusions about the underlying mechanisms and, thus, advance beyond earlier attempts.

In summary, the following depiction of the owls' silent flight emerged: First, the flight noise is reduced by the ability to fly very slowly. Second, the wing geometry in combination with the surface and edge specifics enable the barn owl to produce much lift without intense beating of the wings. Third, the porous and pliant plumage, and the velvety surface of the feathers reduce friction noise and dampen occurring sounds. However, a number of unresolved questions have been identified that are briefly described in the following.

One issue concerns the real camber of the bird's wing in flight. Earlier data had indicated that fixation leads to an increase in camber [8]. We have fixed our wings carefully and compared their camber with that measured in gliding flight of living owls. The results were alike. Specifically, we measured a camber of over 10%, which is much higher than typically used in wings of aircraft. It will be a challenge for the future to investigate whether this large camber is a specific adaptation of owls to low-speed flight and low Reynolds numbers or whether other, faster flying birds have similar high-cambered wings. Answers to this question may also be found by constructing three-dimensional artificial wings and testing their properties in wind tunnel experiments.

Fringes at the inner vane of the remiges were not in the focus of early investigations. Possible functions, apart from turbulence reduction devices, were not proposed yet. In our study, a new approach with a hybrid wing has already yielded interesting new insights. This approach is certainly just at the beginning, but the hope is that by creating more and specific hybrid wings, many new functions may be discovered. Thus, this approach should be continued in the future.

A largely unresolved issue concerns the question how birds are able to maintain a stable flight, although feathers are continuously changing through wear. This means that an additional safety factor is necessary in bird flight which should take the changes induced by wear into account. It will be a challenge to determine this safety factor and how it affects flight, positively or negatively.

All in all, the novel methods applied in the studies reported here allowed a detailed characterization of morphometrical, behavioral and biomechanical properties of the flight apparatus of owls. This knowledge could be applied to the construction of aircraft wings. However, it should be kept in mind that the implementation of owl characteristics to another case might work ineffectively, since the operating conditions in terms of flow conditions and Reynolds numbers differ significantly between aircraft and birds. Smart adaptations may be required

for any successful realization of owl inspired noise reduction and this will inevitably require robust scaling laws. The biological data provided here may serve as the basis for such smart adaptations. In the long run, this hopefully leads to noise reduction of aircraft or any kind of objects subjected to a flow field.

References

1. Bachmann, T.: Anatomical, morphometrical and biomechanical studies of barn owls' and pigeons' wings. PhD thesis at RWTH Aachen University (2010)
2. Bachmann, T., Emmerlich, J., Baumgartner, W., Schneider, J.M., Wagner, H.: Flexural stiffness of feather shafts: geometry rules over material properties. *J. Exp. Biol.* (accepted, 2012)
3. Bachmann, T., Klän, S., Baumgartner, W., Klaas, M., Schröder, W., Wagner, H.: Morphometric characterisation of wing feathers of the barn owl (*Tyto alba pratina*) and the pigeon (*Columba livia*). *Front. Zool.* 4, 23 (2007)
4. Bachmann, T., Mühlensbruch, G., Wagner, H.: The barn owl wing: An in-spiration for silent flight in the aviation industry? In: SPIE, vol. 7975 (2011)
5. Bachmann, T., Wagner, H.: The three-dimensional shape of serrations at barn owl wings: towards a typical natural serration as a role model for biomimetic applications. *J. Anat.* 218(6), 192–202 (2011)
6. Bachmann, T., Wagner, H.: Silent owl wings. In: Encyclopedia of Nanotechnology. Springer, Heidelberg (2012)
7. Bergman, G.: Why are the wings *Larus f. fuscus* so dark? *Ornis Fennica* 59(2-3), 77–83 (1982)
8. Biesel, W., Butz, H., Nachtigall, W.: Erste Messung der Flügelgeometrie bei frei gleitfliegenden Haustauben (*Columba livia* var. *Domestica*) unter Benutzung neu ausgearbeiteter Windkanaltechnik und der Stereophotogrammetrie. *Biona Report* 3. Gustav Fischer Verlag (1985)
9. Bonser, R.H.C.: Melanin and the abrasion resistance of feathers. *Condor* 97(2), 590–591 (1995)
10. Brush, A.H.: Feather keratin – analysis if subunit heterogeneity. *Corap. Biochem. Physiol.* 48, 661–664 (1974)
11. Carruthers, A.C., Thomas, A.L.R., Taylor, G.K.: Automatic aeroelastic devices in the wings of a steppe eagle *Aquila nipalensis*. *J. Exp. Biol.* 210, 4136–4149 (2007)
12. Chilgren, J.: Body Composition of Captive White-Crowned Sparrows during Postnuptial Molt. *Auk* 94(4), 667–688 (1977)
13. Filshie, B.K., Rogers, G.E.: An electron microscope study of the fine structure of feather keratin. *J. Cell Biol.* 13(1), 1–12 (1962)
14. Graham, R.: The silent flight of owls. *J. Roy. Aero. Soc.* 38, 837–843 (1934)
15. Inglis, A.S., Lennox, F.G.: Studies in Wool Yellowing: Part IX: Irradiation with Different UV Wavebands. *Text. Res. J.* 35(2), 104–109 (1965)
16. Ito, S.: Aerodynamic influence of leading-edge serrations on an airfoil in a low Reynolds number – A study of an owl with leading-edge serrations. *J. Biomech. Sci. Engin.* 4, 117–123 (2009)
17. Klän, S.: Experimental Analysis of the flow over an owl-based wing geometry. Berichte aus der Strömungstechnik. Shaker Verlag GmbH (2011)

18. Klän, S., Bachmann, T., Klaas, M., Baumgartner, W., Wagner, H., Schröder, W.: Experimental analysis of the flow field over a novel owl-based airfoil. *Exp. Fluids* 46(5), 975–989 (2008)
19. Kroeger, R., Gruschka, H., Helvey, T.: Low speed aerodynamics for ultra-quiet flight. *AFFDL* 71-75, 1–55 (1971)
20. Launer, H.F.: Effect of Light Upon Wool: Part IV: Bleaching and Yellow-ing by Sunlight. *Text. Res. J.* 35(5), 395–400 (1965)
21. Lilley, G.: A study of the silent flight of the owl. *AIAA Paper* 98-2340 (1998)
22. Mebs, T., Scherzinger, W.: *Die Eulen Europas*. Frankh-Kosmos Verlag (2000)
23. Moreau, D.J., Brooks, L.A., Doolan, C.J.: On the aeroacoustic tonal noise generation mechanism of a sharp-edges plate. *JASA Expr. Lett.* (2011)
24. Müller, W., Patone, G.: Air transmissivity of feathers. *J. Exp. Biol.* 201, 2591–2599 (1998)
25. Murozono, S., Murayama, K., Akahane, K.: Soluble proteins from fowl feather keratin. III. Isolation and characteristics of some calamus proteins. *J. Biochem.* 82(1), 53–58 (1977)
26. Murphy, M.E., King, J.R.: Energy and Nutrient Use during Moult by White-Crowned Sparrows *Zonotrichia leucophrys gambelii*. *Ornis Scand.* 23(3), 304–313 (1992)
27. Neuhaus, W., Bretting, H., Schweizer, B.: Morphologische und funktionelle Untersuchungen über den lautlosen Flug der Eule (*Strix aluco*) im Vergleich zum Flug der Ente (*Anas platyrhinchos*). *Biol. Zentralbl.* 92, 495–512 (1973)
28. Nicholls, C.H., Pailthorpe, M.T.: Primary Reactions in the Photoyellowing of Wool Keratin. *J. Text. Inst.* 67(11), 397–403 (1976)
29. Piechocki, R.: Über die Großgefieder-Mauser von Schleiereule und Waldkauz. *J. Orn.* 102(2), 220–225 (1961)
30. Rohwer, S., Ricklefs, R.E., Rohwer, V.G., Copple, M.M.: Allometry of the duration of flight feather molt in birds. *PLoS Biology* 7(6), e1000132 (2009)
31. Taylor, I.: Barn Owls, pp. 108–110. Cambridge University Press, Cambridge (1994)
32. West, G.C.: Bioenergetics of captive willow ptarmigan under natural conditions. *Ecology* 49(6), 1035–1045 (1968)

Flow Field Analysis and Contour Detection of a Natural Owl Wing Using PIV Measurements

Andrea Winzen, Stephan Klän, Michael Klaas, and Wolfgang Schröder

Abstract. A technical three-dimensional wing model based on the geometry of the wing of a barn owl was designed to investigate the aerodynamic characteristics of this wing, which is known to be perfectly adapted to the requirements of silent flight. This wing model possesses the basic geometry of the barn owl wing. To understand the impact of the owl-based shape plus the owl-specific anatomic elements on the flow field and to further analyze the characteristic flow field that enables the owl to fly at low speeds and thus silently, a prepared natural owl wing was investigated in a wind tunnel. Measurements using particle-image velocimetry were performed on the model and on the natural wing to investigate characteristic flow phenomena such as separation, transition, and reattachment. Additionally, changes of the geometry, i.e., the maximum chord line-to-upper surface distance normalized by the chord length and the deflection of the natural owl wing, are described and discussed in detail to understand the resulting fluid-structure interaction. Unlike the rigid model, the natural owl wing possesses a high flexibility leading to a mutual influence of the wing structure and the surrounding flow field. This has to be investigated to understand the complex physical mechanisms that allow the highly efficient flight of the owl.

1 Introduction

Air traffic has been increasing continuously during the last decades. Therefore, the number and size of airports has grown considerably to be able to handle the increasing number of landings and take-offs. This development will lead to an increased number of people that live in the direct vicinity of airports and thus are exposed to

Andrea Winzen · Stephan Klän · Michael Klaas · Wolfgang Schröder
Institute of Aerodynamics, RWTH Aachen University,
Wüllnerstraße 5a, 52062 Aachen, Germany
e-mail: a.winzen@aia.rwth-aachen.de
<http://www.aia.rwth-aachen.de>

air-traffic noise. Therefore, noise reduction of airplanes, especially during the landing phase is one of the major goals of future aircraft design. The dominant source of air traffic noise during the landing phase is the so-called airframe noise. Amongst others, e.g., fuselage and landing gear, the noise produced by the high-lift devices contributes significantly to the airframe noise. Since the barn owl is well known for its silent flight, a deep understanding of the noise reduction mechanisms of the barn owl wing and the technical application of these mechanisms on new wing configurations might help to reach the goal of noise reduction.

Many owl species adapted to their habitat and living conditions and have developed hunting strategies that require them to fly silently [11], [16]. The barn owl uses a highly accurate acesthesia to detect and localize its prey. Thus, it is necessary to fly quietly, on the one hand to avoid any kind of noise disturbing the localization of the prey and on the other hand to prevent the prey to be warned by noise emitted by the owl. Three special adaptations that have been developed by owls to fly silently have been identified by Graham [6]. These special features include the leading-edge serrations, the velvet-like surface structure, and the trailing-edge fringes. Also, the geometry of the wing possesses an exceptional shape.

Since the barn owl approaches its prey at a moderate speed of 2.5 m/s to 7.5 m/s [13], i.e., at Reynolds numbers of 30,000 to 90,000 based on a mean chord length of approximately 180 mm in the region of the arm pinion, the low flight velocity is the key feature of the silent flight of the owl. According to Carmichael [4], flow phenomena such as complete separation or a separation bubble, i.e., local separation, are likely to occur in this Reynolds number regime, leading to decreasing lift and increasing drag. The barn owl uses different optimization strategies to be able to operate at these low Reynolds numbers. As far as the airfoil cross section of the wing is concerned, the barn owl wing is characterized by a large camber and a position of the maximum thickness of the airfoil close to the leading edge. Being designed for low-speed gliding flight, the wing size of the barn owl is also much higher than for other birds of comparable size and weight [1] and possesses an almost elliptical planform. As shown by Klän et al. [9], the high camber in connection with the drip nose geometry of the three-dimensional wing model leads to an extended suction area on the upper side of the wing. The separation bubble caused by the adverse pressure gradient on the suction side of the wing model decreases the aerodynamic performance due to intense vortex shedding at the downstream end of the bubble and the corresponding pressure fluctuations [15].

Some of the special features of the owl wing, i.e., the leading-edge serrations, the velvet-like surface structures, and the trailing-edge fringes, may reduce the size of the separation bubble. The findings of Klän et al. [10] show that the size and position of the separation bubble is changed significantly when artificial surface structures imitating the natural wing surface are applied on the clean wing geometry. Furthermore, the analysis of the spatial two-point correlation of the velocity fluctuations perpendicular to the wall v' shows that the surface structures also influence the size and the distance between two consecutive vortices shed at the downstream end of the separation bubble. Video recordings of barn owls in free gliding flight show fluttering feathers on the suction side of the wing. This indicates the presence of a

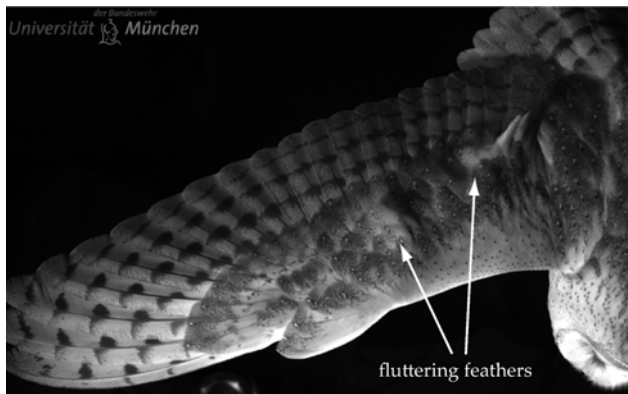


Fig. 1 Snapshot of a movie of a barn owl in gliding flight at $Re \approx 60,000$ ([5]). The lifted surface feathers indicate the presence of an unstable flow condition, i.e., a separation bubble.

separation bubble in the region of high camber, i.e., the arm region as shown by the stand-up feathers displayed in fig. 1 [5].

In this work, the three-dimensional wing model representing the basic geometry of an owl wing is compared to a natural owl wing concerning the corresponding flow field including flow phenomena such as separation and reattachment. Note that in contrast to the rigid three-dimensional wing model, the natural owl wing possesses a high flexibility, resulting in a movement as well as a change of geometrical shape of the wing depending on the flow condition such as angle of attack and Reynolds number.

The work is structured as follows. Firstly, the construction process of the 3D wing model based on the geometry of natural owl wings is described. Afterwards, the experimental setup and the measurement technique are presented. Subsequently, the results of the measurements of the wing model and the natural owl wing are analyzed and discussed. A brief description of the flow field on the three-dimensional wing model is given. Additionally to the flow field, structural deformations are analyzed for the natural owl wing. Finally, a conclusion and a brief outlook are given on the upcoming investigations.

2 Experimental Setup and Measurement Technique

Construction of the 3D Wind Tunnel Models

Measurements performed by Nachtigall and Klimbingat [14] and Biesel et al. [2] showed that the geometry of the owl wing differs from other birds or technical airfoils regarding the planform and the thickness of the wing. To understand the impact of the special adaptations of the owl wing on its aerodynamic performance, a clean technical wing model was designed and afterwards equipped with the owl-specific

structures, i.e., the velvet-like surface structure and the leading-edge serrations as described in detail by Klän et al. [9]. Therefore, only a brief summary is given here.

Surface scans of two dead barn owls were performed to obtain three-dimensional digital models of the wing. For this procedure, the wings were placed in a position that resembled gliding flight, based on photographs and videos of owls in this phase of flight. The twist was neglected for the construction of the wing model because it was assumed to be less than 3° [12]. Since the cross sections derived from the scanning procedure did not satisfy the requirements of a wind tunnel model due to roughness of the surface caused by sticking out feathers, the surface of each cross section was smoothed. Subsequently, the cross sections were decomposed into a thickness distribution and a camber line. A least square fit was used for the coefficients of the thickness distribution and the camber line to adjust the leading edge and the chord length in spanwise direction to obtain a smooth surface. Finally, a spanwise correction factor based on Biesel et al. [2] was introduced to correct the spanwise distribution of the maximum camber. This was necessary since it is well known that the shape of living and dead bird wings are different due to the drying and contraction of muscles, tendons, and tissue. The final geometry of the three-dimensional wing model is shown in fig. 2.

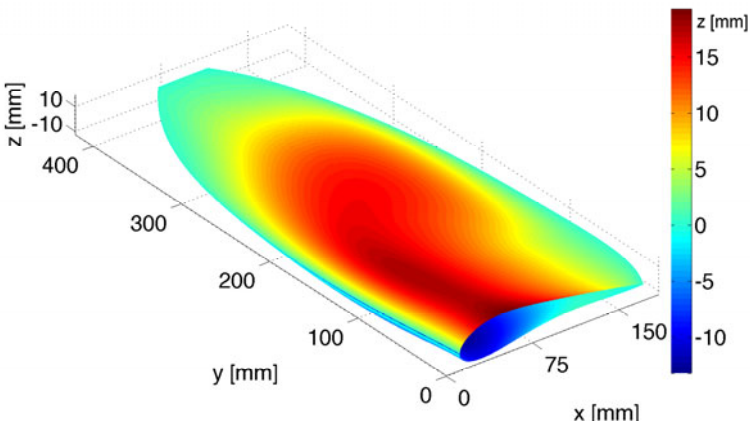


Fig. 2 Three-dimensional geometry of the final wing model [9]

Experimental Setup and Test Facilities

To provide an undisturbed flow at the wing tip, a wind tunnel with a large test cross section was required. The measurements were performed in a low-speed wind tunnel with a test section width of 1200 mm and a maximum free-stream velocity of approximately 60 m/s. Both measurement campaigns were performed in the same wind tunnel. Note that the chord length of the three-dimensional model and the natural owl wing vary significantly in spanwise direction. Thus, the corresponding

Reynolds numbers were calculated based on the averaged chord length of the inner 40 % span because this area provides approximately 50% of the lift under the assumption that the wing possesses a nearly elliptical lift distribution. The resulting average chord length was $c = 178$ mm and the Reynolds numbers were chosen to $Re_c = 4 \cdot 10^4$, $6 \cdot 10^4$, $1 \cdot 10^5$, and $1.2 \cdot 10^5$, which corresponds to free stream velocities of approximately $u_\infty = 3.5$, 5.3, 7.5, and 10.5 m/s. All measurements were performed at angles of attack of $\alpha = 0^\circ$, 3° , and 6° , respectively. The free stream turbulence level was $Tu \leq 0.3\%$. The flow on the ground plate was tripped by a 0.5 mm wire to ensure a turbulent boundary layer so that transitional effects do not interfere with the flow of the model or the natural wing.

The flow field was analyzed using 2D-2C particle-image velocimetry (PIV). The measurement plane was parallel to the mounting plate of the wind tunnel, i.e., normal to the center plane of the wing, and aligned with the flow direction. Only the suction side was recorded and analyzed. Four spanwise positions were measured for both configurations. For the 3D wing model, measurements were performed at $2y/b = 0.1$, 0.2, 0.3, and 0.4, whereas measurement planes for the natural owl wing were $2y/b = 0.3$, 0.5, 0.7, and 0.9. For both configurations, a PCO.4000 camera, a NewWave Solo 200XT Nd:YAG double-pulse laser, and an ILA MiniPIV-Synchronizer were used. 1500 images for the 3D model and 1000 images for the natural owl wing were recorded at a sampling frequency of 2 Hz. The post-processing was done using the VidPIV software of ILA GmbH. The size of the final interrogation window was $24\text{ px} \times 24\text{ px}$ with an overlap of 50 %. This leads to a vector spacing of $\Delta x_{vector} \approx 0.096$ mm or $\Delta x_{vector}/c \approx 0.0005c$. The experimental setup for the measurements of the natural owl wing is presented in fig. 3, showing the natural wing mounted on a flat plate in the test section of the wind tunnel.



Fig. 3 Experimental setup for the PIV measurements of the natural owl wing in the open test section low speed wind tunnel.

3 Results

As mentioned above, the structural build-up of the natural wing results in a high flexibility leading to an oscillatory bending and twisting motion as well as deformation of the feathers and bone structure. Thus, the maximum chord line-to-reference line distance normalized by the chord length and the deflection of the natural owl wing due to the flow field are discussed and analyzed to investigate the influence of the deflection on the occurring flow phenomena. The reference line is the detected contour line of the wing averaged over 1000 images. Firstly, the flow field around the 3D wing model is discussed focusing on the size of the laminar separation bubble at different spanwise positions. Secondly, the flow phenomena that occur in case of the natural owl wing are analyzed. That is, the laminar-to-turbulent transition, the flow separation, and the size of the turbulent structures are discussed. Subsequently, the change of the geometry and the deformation of the wing due to the aerodynamic loads is investigated.

3.1 Three-Dimensional Wing Model

An extensive analysis of the 3D wing model can be found in Klän [8]. Therefore, only a brief summary of the most important flow phenomena is presented. Figure 4 shows a three-dimensional view of the wing model and the corresponding flow field at various freestream conditions at spanwise positions $2y/b = 0.1, 0.2, 0.3$, and 0.4 . This overview gives an idea of the spanwise distribution of the separation bubble, which is indicated with the white solid lines. The white dashed lines indicate the extrapolated shape of the separation.

The separation bubble only occurs in the arm section of the wing span, i.e., only the inner 50 % of the wing. Thus, the flow is attached over the entire chord length for the outer half of the span. Moreover, it can be concluded from fig. 4 that the separation bubble possesses a three-dimensional shape. Note that no complete separation was found for the investigated freestream conditions. The described flow field shows a high susceptibility to the changes of the flow conditions, for example the size of the separation bubble increases drastically and thus extends to higher spanwise and chordwise positions at both Reynolds numbers shown in fig. 4 when the angle of attack is increased. Since the owl is assumed to be perfectly adapted to its flight conditions, it can be concluded that the presented flow field can not be characteristic for the owl. As described above, all special adaptations of the natural owl wing were removed and only the characteristic geometry was used to manufacture this technical wing model. Thus, it can be concluded that the application of the mentioned adaptations, i.e., the leading-edge serrations, the velvet-like surface structures, and the trailing-edge fringes must have a considerable influence on the flow field [9]. Furthermore, the structural build-up of the wing, i.e., the bone and feather structure is not mimicked by the wing model.

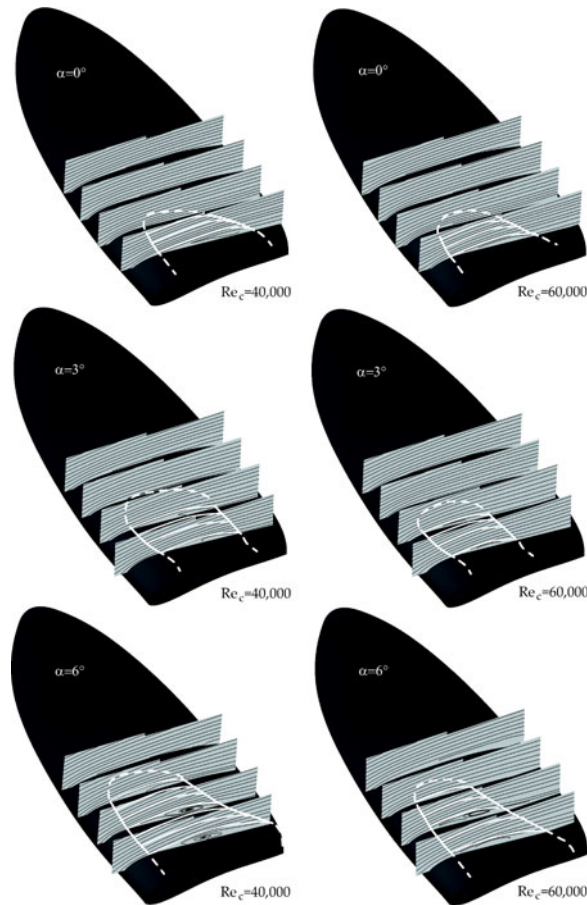


Fig. 4 Flow field of the clean 3D-wing shown by streamlines for $\alpha = 0^\circ$, 3° , and 6° at $Re_c = 40,000$ (left) and $Re_c = 60,000$ (right). Measuring planes located at $2y/b = 0.1$, 0.2 , 0.3 , and 0.4 . The white dashed lines indicate the extrapolated size of the separation bubble (Klän [8]).

3.2 Natural Owl Wing

In contrast to the measurement described in the previous section, the most important attribute of the natural owl wing is its flexibility caused by the build-up of the wing by single feathers and the properties of the feathers themselves. In particular, the interaction of the feathers with the surrounding flow field can not be simulated with the artificial wing model. These properties lead to deflections of the natural wing superimposed with local deformations such as surface buckling, representing an intricate task that was analyzed through instantaneous PIV measurements.

Flow Field

Different means of analysis were used to investigate the occurring flow structures on the suction side of the wing profile. Spatial two-point correlations were performed for the velocity fluctuations u' in the freestream direction and v' perpendicular to the flow direction, respectively. The two-point correlation of the wall-normal velocity fluctuations was calculated by

$$r_{vv} = \sqrt{\frac{\overline{v'(x)v'(x + \Delta x)}}{u_\infty^2}} \quad (1)$$

where u_∞ denotes the freestream velocity. The distribution of the local maxima and minima in this two-point correlation indicates the average streamwise extent of a shed vortex and the distance between two consecutive vortices [7].

Additionally, the time averaged Reynolds shear stresses, which are defined as $-\overline{u'v'}/u_\infty^2$ and the streamwise development of its maxima were analyzed. As described by Yuan et al. [17], the distribution of the shear stresses is a measure for the momentum transfer into the boundary layer. The criterion from [3] was used to detect the point of transition onset. That is, the transition onset is determined as the point where a significant rise of the shear stress above the noise level is detected.

The spanwise position at $2y/b = 0.3$ was chosen for the analysis because the results of the investigation of the clean wing model as shown in fig. 4 indicate the presence of a separation bubble at this location at higher angles of attack. Figures 5(a) to 5(c) show the averaged velocity field at $Re_c = 40,000$ for the three investigated angles of attack. No separation is found for $\alpha = 0^\circ$, whereas for $\alpha = 3^\circ$ flow separation occurs at approximately $x = 75$ mm. The point of separation is shifted further upstream to $x = 50$ mm for $\alpha = 6^\circ$. No reattachment is found for both cases, i.e., the flow is fully separated. This contradicts the findings for the clean wing model where a separation bubble is present for $\alpha = 6^\circ$ at this spanwise position, whereas no separation is found for $\alpha = 3^\circ$ as shown in fig. 4. At $Re_c = 60,000$ no separation is found for all investigated angles of attack, which agrees with the results for the clean wing model. Generally, no separation bubble was found for all investigated flow conditions, i.e., Reynolds number, angle of attack, and spanwise position. The flow was either attached or fully separated with no flow reattachment between the separation point and the trailing-edge.

Figures 6(a) to 6(c) show the distribution of the Reynolds shear stresses for $2y/b = 0.3$. Note that in fig. 6(c) the flow field at $Re_c = 60,000$ is not shown because the quality of the PIV measurements was not sufficient to offer reliable data. Comparing the point of the transition onset, it can be concluded that the chordwise position of the transition onset is approximately the same for the three angles of attack. Note that for $Re_c = 40,000$ and $\alpha = 0^\circ$ the raise in Reynolds shear stress occurs at approximately $x/c = 0.5$ and is as such different to the transition point for $\alpha = 3^\circ$ and $\alpha = 6^\circ$. From figs. 6(a) to 6(c) it can be concluded that the location of the transition onset depends on the Reynolds number but it is almost independent of the angle of attack for all investigated cases. This distribution is different from the

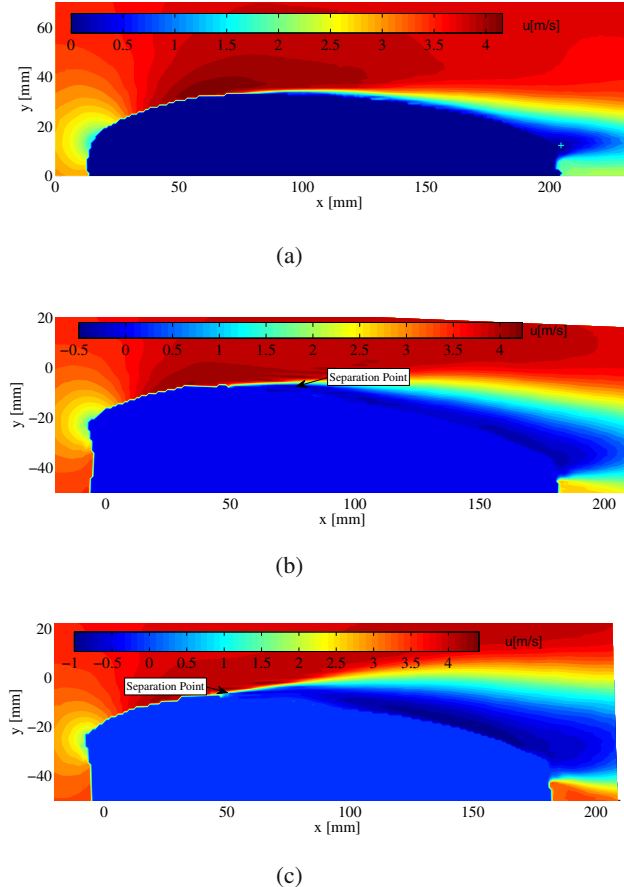


Fig. 5 Average velocity field at spanwise position $2y/b=0.3$ for $Re_c = 40,000$ for $\alpha = 0^\circ$ (top), $\alpha = 3^\circ$ (middle), and $\alpha = 6^\circ$ (bottom). The velocity distribution is displayed color coded from -1 m/s to 4 m/s

findings for smooth wing profiles where the transition onset is shifted with changing angle of attack as presented by Klän [8]. This leads to the assumption that the special adaptations of the natural owl wing might influence the flow field in such a way that the location of transition onset is kept at the same location at the upper side of the wing for changing angle of attack.

The findings of Klän [8] show that the distribution of the maximum Reynolds shear stresses is strongly influenced by the surface structures of the wing. The transition onset is shifted significantly compared to the clean wing geometry due to the applied artificial surface structures. According to Klän et al. [10] the change in size and location of the separation bubble is assumed to be caused by a redistribution of the kinetic energy in the reverse flow region. The size of the vortices shed at the end

of the separation bubble is reduced which leads to an enhanced mixing between the free shear layer and the back flow.

Note that the measurement of the Reynolds shear stresses was not possible very close to the surface of the wing for $Re_c = 100,000$ and $Re_c = 120,000$ at higher angles of attack because of bright reflections in the PIV images. Thus, the values of the Reynolds shear stresses shown in figs. 6(b) and 6(c) measured at a higher normal distance to the wall are small in comparison to the measurements performed at $\alpha = 0^\circ$. In this Reynolds number range, the maximum shear stress is located at approximately $y/\delta = 0.2$ where y represents the wall-normal coordinate and δ is the local boundary layer thickness. Due to the bright reflection above the wing, no seeding particle movement could be detected to calculate the corresponding velocities and velocity fluctuations near the surface. A measurement of the Reynolds shear stresses was only possible at the outer region of the local boundary layer. Therefore, the maximum Reynolds shear stresses were not captured by the measurements. Nevertheless, it can be concluded that the flow experienced laminar to turbulent transition because the corresponding distribution displayed in figs. 6(b) and 6(c) show a characteristic feature of the flow transition by the distinct increase in Reynolds shear stresses.

Figures 7(a) and 7(c) show the spatial two-point correlation r_{vv} of the wall-normal velocity fluctuations for $Re_c = 40,000$ at $2y/b = 0.3$. The reference position was located approximately 3 mm above the surface within the boundary layer at $x_{RP} = 150$ mm. It can be concluded from figs. 6(a) and 6(c) that the reference position is located behind the transition onset, i.e., in a region that is characterized by turbulent flow. Comparing the size of the turbulent structure for the different angles of attack, it is clearly visible that structures are smaller at $\alpha = 0^\circ$ where no flow separation occurs in contrast to $\alpha = 6^\circ$ where the flow is fully separated. The integral turbulent length scale Λ provides a measure of the extent of the region over which velocities can be assumed correlated, e.g., the size of the eddies carrying the energy of the turbulent motion. For $\alpha = 0^\circ$ $\Lambda \approx 8.5$ mm for $y/\delta = 0.85$. The values increase at increasing angle of attack, i.e., $\Lambda \approx 11.3$ mm for $y/\delta = 0.51$ at $\alpha = 3^\circ$ and $\Lambda \approx 12.2$ mm for $y/\delta = 0.49$ at $\alpha = 6^\circ$.

Geometry of the Natural Wing

The distance ratio D which is defined as the maximum distance of the chord line to the reference line normalized by the chord length and the deflection of the upper surface of the natural owl wing were analyzed using the laser light reflection line to determine its shape and position in the PIV images. The distance ratio D is defined as:

$$D = \frac{\Delta y_{max}}{x_{LE} - x_{TE}} \quad (2)$$

where Δy_{max} describes the maximum distance of the reference line to the chord line. The quantity x_{LE} denotes the x-coordinate of the leading-edge, x_{TE} represents the x-coordinate of the trailing-edge, respectively. Figure 8(a) shows the

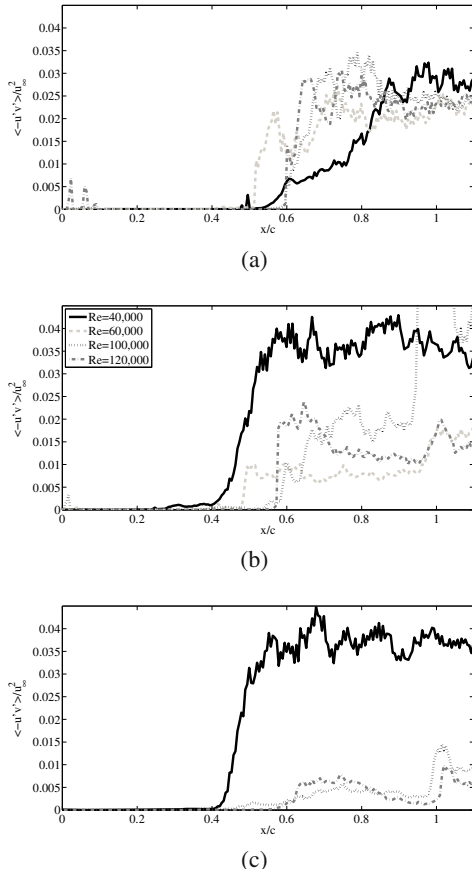


Fig. 6 Reynolds shear stress distribution at spanwise position $2y/b=0.3$ for $\alpha = 0^\circ$ (top), $\alpha = 3^\circ$ (middle), and $\alpha = 6^\circ$ (bottom).

comparison of the reference line for the four investigated Reynolds numbers at $\alpha = 0^\circ$ for $2y/b = 0.5$. The shapes of the reference lines are very similar in the leading-edge region due to the stiffness of the bone structure. For increasing chord length, the reference lines differ only in a small range. Also, the location of the maximum value of D is almost identical for all analyzed cases. The change in freestream velocity results in a change of aerodynamic forces acting on the wing by altering the pressure distribution. For constant angle of attack, the change in pressure distribution is mainly caused by the increasing freestream velocity. In case of the flexible wing, the changing pressure distribution seems to cause a reduction of the distance ratio D , i.e., a straightening of the wing. Assuming that the weight of the owl does not change during gliding flight, the increasing lift force caused by the altered pressure distribution might be negligible for the required force equilibrium of weight and lift. Thus, the straightening of the wing might be a passive control mechanism

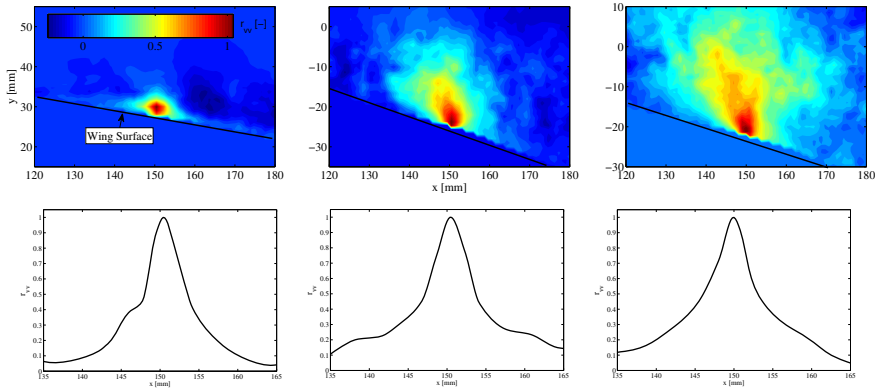


Fig. 7 Spatial two-point correlation r_{vv} of the wall-normal velocity fluctuations at a spanwise position of $2y/b=0.3$ for $Re_c = 40,000$ with $x_{RP}=150$ mm for $\alpha = 0^\circ$ (top left), $\alpha = 3^\circ$ (top middle), and $\alpha = 6^\circ$ (top right), and the corresponding distribution of r_{vv} along the wing surface for $\alpha = 0^\circ$ (bottom left), $\alpha = 3^\circ$ (bottom middle), and $\alpha = 6^\circ$ (bottom right). The distribution of r_{vv} is displayed color coded from 0 to 1.

adjusting the lift force when the Reynolds number is increased. The same trend is clearly visible for the two other investigated angles of attack shown in figs. 8(b) and 8(c). In contrast to $\alpha = 0^\circ$ the position of the maximum value of D is shifted upstream at increasing angle of attack.

Figure 8(c) displays the reference line at $\alpha = 6^\circ$. In comparison to $\alpha = 0^\circ$ and $\alpha = 3^\circ$, the portion of the chord length that shows a similar shape of the reference lines for all Reynolds numbers is decreased. Also, the change in the value D is significantly higher than for $\alpha = 0^\circ$ and $\alpha = 3^\circ$. Thus, the effect due to the change in pressure distribution caused by the change in freestream velocity seems to increase with increasing angle of attack.

Hence, the change of the shape of the reference lines depends on the Reynolds number. The change between $Re_c = 40,000$ and $Re_c = 100,000$ is high in comparison to the change between $Re_c = 100,000$ and $Re_c = 120,000$. This trend can be found for all angles of attack. It is most distinct for $\alpha = 6^\circ$. It can be concluded that the flexibility of the wing is limited due to the structural build-up and that a change in aerodynamic forces does not alter the distance ratio D and the chord length significantly when the limit is reached. The same trends concerning the change of shape of the contour can also be found at other investigated spanwise positions.

Additionally, the deflection of the trailing-edge was investigated. The term *deflection* is defined as the distance in the direction normal to the wing surface between the averaged reference line and the instantaneous position of the contour line. The trailing-edge deflection was calculated for the maximum chord position for which the contour could still be detected for all investigated combinations of angle of attack and Reynolds number. Note that this 'virtual trailing-edge' is not the trailing-edge of the wing but located at smaller chordwise positions due to the limitations of

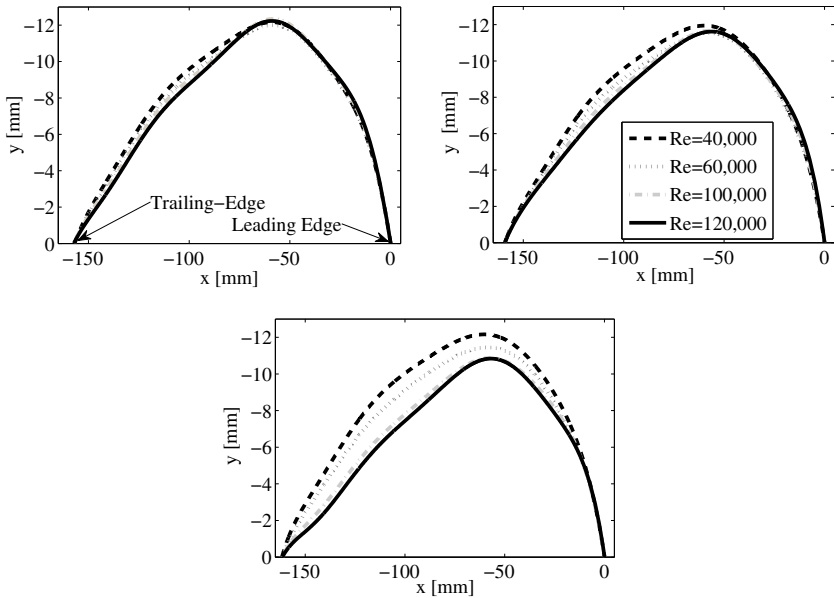


Fig. 8 Reference lines for $Re_c = 40,000$ to $Re_c = 120,000$ at $\alpha = 0^\circ$ (top left), $\alpha = 3^\circ$ (top right), and $\alpha = 6^\circ$ (bottom)

the image processing routine. Figure 9(a) gives an overview on the deflections for increasing Reynolds numbers for the three angles of attack at $2y/b = 0.5$. The deflections increase for increasing Reynolds number, i.e., higher freestream velocity. This trend can be explained by the increasing aerodynamic forces acting on the wing due to the altered pressure distribution. In fig. 9(b) the deflections are displayed for the four investigated Reynolds numbers as a function of the angle of attack. In all cases the deflections decrease with increasing angle of attack.

Combining the results for the distance ratio D and the deflection of the wing, an opposite development is found. At increasing Reynolds number, i.e., freestream velocity, the values of D of the wing decrease while the corresponding deflections increase. The increased kinetic energy of the flow due to the increased freestream velocity has to be absorbed by the wing. This absorption is performed by the straightening of the wing and thus decreasing the lift force on the one hand and the increasing oscillatory bending and twisting motion of the wing on the other hand. In contrast, when only the angle of attack is increased which leads to a change in pressure distribution without a significant raise in the kinetic energy of the flow, the distance ratio D of the wing is reduced absorbing a higher portion of the flow kinetic energy. Therefore, the amplitude of the deflection decreases at increasing angle of attack. Additionally, when the angle of attack is increased, the pressure distribution is changed leading to a reduction of aerodynamic forces acting at higher chordwise positions resulting in a decrease of the occurring deflections.

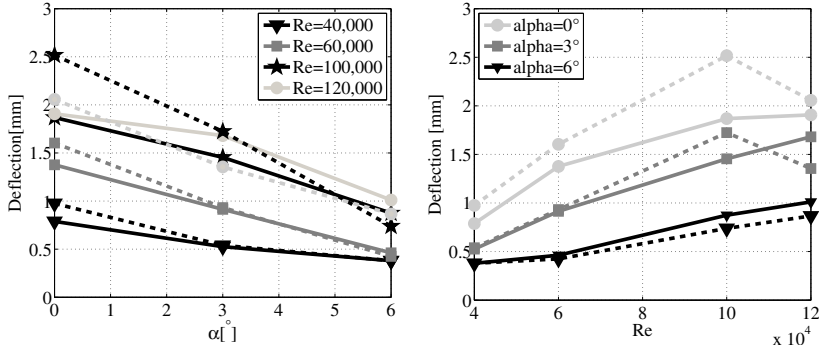


Fig. 9 Deflection at $2y/b=0.5$ for constant Reynolds numbers for $\alpha = 0^\circ$, $\alpha = 3^\circ$, and $\alpha = 6^\circ$ (left), deflection at $2y/b=0.5$ for constant angles of attack for $Re_c = 40,000$, $Re_c = 60,000$, $Re_c = 100,000$, and $Re_c = 120,000$ (right). Dashed line: upward deflection; solid line: downward deflection.

Table 1 Values and position of maximum value of D for $2y/b = 0.5$ and $Re_c = 40,000$

Parameter		Unit		
Angle of attack α	°	0	3	6
Maximum D ^a	%	7.75	7.51	7.50
x - position of maximum D	mm	58.73	59.99	61.06
x/c - position of maximum D	-	0.37	0.38	0.38

^a As calculated by eq.2.

When taking the flow structures into account, it can be concluded from figs. 7(a) to 7(c) that the size of the flow structures on the suction side of the wing does not dominate the structural movement, i.e., the deflections. The size of the turbulent structures characterized by the integral turbulent length scale develops in the opposite direction, meaning that the size of the structures increases at increasing angle of attack whereas the deflections decrease. Thus, the flow field on the upper wing side at the given spanwise position does not directly induce the corresponding bending and twisting motion of the wing. One reason could be that the flow structures on the pressure side of the wing might dominate the wing movement. Also, due to the structural build-up of the wing, the deflections might originally be caused by the flow structures at another spanwise position. Additionally, the wing tip vortex also induces a bending interacting with the twisting, which is described by the deflections. Finally, the flow field downstream of the wing also influences the structural movement and thus, the deflections.

Since the measurements were performed at a frequency of only 2 Hz, no conclusions on the frequency of the wing deformation or the turbulent flow structures can be drawn. Therefore, it is necessary to conduct measurements at higher sampling

frequencies to be able to correlate the wing movement with the corresponding flow structures. To further investigate the occurring fluid-structure interaction mechanism, simultaneous PIV measurements of the upper and lower side at high sampling frequencies will be performed on the natural owl wing. Additionally, measurements of the wing tip vortex as well as the wake will be conducted.

4 Summary and Conclusion

In the present investigation, the flow field of a clean wing model which possesses the geometry of an owl wing and a natural owl wing were analyzed. The analysis focused on the influence of the high flexibility of the natural wing resulting in an intricate fluid-structure interaction.

The flow field of a three-dimensional clean wing based on the geometry of a natural owl wing was briefly described and the dominant flow structures were presented. The wind tunnel model possesses a large thickness and a thick nose in the arm section. The flow field of such a wing geometry is characterized by the occurrence of a separation bubble over the inner 50% of the span.

Subsequently, the flow field of a prepared natural owl wing at similar spanwise positions was analyzed. In contrast to the rigid technical wing model, the natural owl wing possesses a flexible structure caused by the build-up of feathers and bones, which causes a oscillatory bending and twisting motion of the wing and a change of geometry due to the acting aerodynamic forces. The flow field was analyzed using the Reynolds shear stress distribution and the two-point correlation of the velocity components normal to the flow direction. The averaged velocity field showed fully separated flow for higher angles of attack and fully attached flow at lower angles of attack and higher Reynolds numbers. No separation bubble was visible for all investigated cases. Additionally, it was found that unlike the clean wing model [8] the transition onset depends on the Reynolds number but was kept at the same location for increasing angle of attack.

The analysis of the wing geometry showed a clear dependence of the wing shape on the freestream conditions. For increasing freestream velocity, i.e., Reynolds number the distance ratio D is decreased while the movement of the wing characterized by the amplitude of the deflections is increased. The altered pressure distribution leads to increasing aerodynamic forces acting on the wing. Assuming that the required lift is constant during gliding flight the reduction of the value of D might indicate a passive lift control mechanism adjusting the lift to the increased flight velocity. In connection with the increasing deflections the decrease of the distance ration D might be caused by a redistribution of the kinetic energy of the flow since the wing has to absorb the additional kinetic energy. Note that for increasing angles of attack the value of D is also increased while the deflections diminish. For a constant kinetic energy the resulting reduction of the values of the distance ratio D induces smaller deflections. Using the two-point correlation to investigate the size of the flow structures on the suction side of the wing, it was found that the size of turbulent structures increase with increasing angle of attack. Thus, it was concluded that these structures are not the dominant source for the wing deflections.

To further analyze the occurring fluid-structure interaction simultaneous PIV measurements of the upper and lower side of the natural owl wing at high frequencies are required. Also, measurements of the wing tip vortex and the wake structures will be performed to locate the source of the wing movement.

References

1. Bachmann, T., Klän, S., Baumgartner, W., Klaas, M., Schröder, W., Wagner, H.: Morphometric characterisation of wing feathers of the barn owl *tyto alba pratincola* and the pigeon *columbia livia*. *Frontiers in Zoology* 4.23 (2007), doi:10.1186/1742-9994-4-23
2. Biesel, W., Butz, H., Nachtigall, W.: Erste Messungen der Flügelgeometrie bei frei gleitfliegenden Haustauben (*columbia livia* var. *domestica*) unter Benutzung neu ausgearbeiteter Verfahren der Windkanaltechnik und der Stereophotogrammetrie. *Biona-Report* 3, 139–160 (1985)
3. Burgmann, S., Schröder, W.: Investigation of the vortex induced unsteadiness of a separation bubble via time-resolved and scanning PIV measurements. *Experiment in Fluids* 45(4), 675–691 (2008), doi:10.1007/s00348-008-0548-7
4. Carmichael, B.H.: Low reynolds number airfoil survey. *NASA CR-165803* (1981)
5. Friedl, A.: Video recordings of a natural flying barn owl. Personal Communication (2009)
6. Graham, R.R.: The silent flight of owls. *Journal of the Royal Aeronautical Society* 38, 837–843 (1934)
7. Kim, J., Moin, P., Moser, R.: Turbulence statistics in fully developed channel flow at low reynolds number. *Journal of Fluid Mechanics* 177, 133–166 (1987)
8. Klän, S.: Experimental analysis of the flow over an owl-based wing geometry. Ph.D. thesis, RWTH Aachen University, Aachen, Germany (2010)
9. Klän, S., Bachmann, T., Klaas, M., Wagner, H., Schröder, W.: Experimental analysis of the flow field over a novel owl based airfoil. *Experiments in Fluids* 46, 975–989 (2008), doi:10.1007/s00348-008-0600-7
10. Klän, S., Bachmann, T., Klaas, M., Wagner, H., Schröder, W.: Surface structure and dimensional effects on the aerodynamics of an owl-based wing model. Submitted to *European Journal of Mechanics B - Fluids* (2011)
11. Lilley, G.M.: A study of the silent flight of the owl. In: 4th AIAA/CEAS Aeroacoustics Conference, AIAA 98-2340 (1998)
12. Liu, T., Kuykendoll, K., Rhew, R., Jones, S.: Avian wing geometry and kinematics. *AIAA Journal* 44(5), 954–963 (2006)
13. Mebs, T., Scherzinger, W.: *Die Eulen Europas*. Franckh-Kosmos Verlag (2000)
14. Nachtigall, W.: Der Taubenflügel in Gleitflugstellung: Geometrische Kenngrößen der Flügelprofile und Luftkrafterzeugung. *Journal of Ornithology* 120(1), 30–40 (1979), doi:10.1007/BF01647339
15. Sandham, N.D.: Transitional separation bubbles and unsteady aspects of aerofoil stall. *The Aeronautical Journal* 112, 395–404 (2008)
16. Thorpe, W.H., Griffin, D.R.: Lack of ultrasonic components in the flight noise of owls. *Nature* 193, 594–595 (1962)
17. Yuan, W., Khalid, M., Windte, J., Radespiel, R.: An investigation of low-reynolds-number flows past airfoils. In: 23rd AIAA Applied Aerodynamics Conference, AIAA-2005-4607, Toronto (2005)

Shape and Deformation Measurement of Free Flying Birds in Flapping Flight

Wolf Thomas, Konrath Robert, Erlinghagen Thomas, and Wagner Hermann

Abstract. This paper describes a new approach for wing shape determination of free flying birds during flapping flight. The optical based measurement method called "image pattern correlation technique" (IPCT) is described as well as modifications of this technique in order to measure wing surfaces formed by feathers. Furthermore a newly developed camera driving system is introduced, which enables a movement of the surface measurement system synchronized with a bird. The application of this system to free flying barn owls is described together with high resolution surface results, obtained during free flapping flight of the bird.

1 Introduction

Birds have long been admired by mankind for their ability to move freely through the air and they therefore inspired humans to think about flying themselves. Hence, it is hardly surprising that the basics of the modern flight were learnt by looking at birds' flight.

At the end of the 19th century, Otto Lilienthal started to look at birds flight in a more scientific way. He was fascinated by the elegance of the flight of birds' and observed the kinematics of their free flight (Lilienthal, 1889). He also performed wing profile measurements using wings of dead birds. For the investigation of aerodynamic parameters of profiles he performed measurements using a whirling arm. By comparing the results obtained with a flat plate with the results of the curved bird wing profiles he realized that the cambered profile produces more lift compared to the plate. Based on this knowledge the Wright brothers started the

Wolf Thomas · Konrath Robert
German Aerospace Center, Institute of Aerodynamics and Flow Technology,
Department Experimental Methods
e-mail: thomas.wolf@dlr.de

Erlinghagen Thomas · Wagner Hermann
RWTH Aachen University, Institute of Biology II, Aachen, Germany
e-mail: thomas.erlinghagen@rwth-aachen.de

development of profiles using whirling arms and wind tunnels (Padfield, et al., 2003). This finally lead to the development of technical profiles, used in modern aircrafts.

The actual used technical profiles have been well examined, quite apart from any measurements with bird wings. The reasons for the lack of knowledge concerning bird flight results from the difficulties in carrying out measurements on adaptive wing shapes together with the complex kinematics and problems related to performing measurements on living animals.

One important part in aerodynamics is the shape of the wing. Looking at the simplest flight configuration of birds, the gliding flight, we can still find open questions. The bird wing profiles given in (Oehme, 1968; Nachtigall, et al., 1985; Pennycuick, 1982; Liu, et al., 2004) were measured using narcotised and dead animals. Therefore the applicability to real flight conditions is questionable. Nachtigall also realized a difference between the gliding values obtained using wing preparations and the gliding values observable in free flight (Nachtigall, et al., 1985). Therefore, Nachtigall, Butz and Biesel developed a measurement setup for the estimation of the wing shape during gliding flight in a wind tunnel, (Biesel, et al., 1985). However, the resolution was limited and they only measured the gliding flight case for certain velocities.

The flapping mode of birds was also of interest in bird flight research. Measurements were performed using birds in wind tunnels (e.g. by Tobalske et al.; 1996, 1999, 2007; Park, et al., 2001; Muijres, et al., 2012), but the result in wing shape is usually restricted to estimations of the position of a few points (e.g. wingtip) and therefore not sufficient for further aerodynamic analysis. Measurements of the kinematics were also performed in free flight, with cameras attached to flying birds (Taylor, et al., 2007) but this only led to qualitative results.

Hence, especially for the flapping flight case, the time dependent wing shape is actually not known. Therefore, this paper describes a measurement method which was developed for the estimation of the wing shape of a bird during flight. Together with the technique, a measurement setup for flapping flight is presented with first results obtained during flapping flight of barn owls (*Tyto alba*).

2 The Barn Owl

The barn owl (*Tyto alba*) is one of the most widely spread avian predators of small mammals worldwide, with approximately 30 subspecies. It can be found on all continents except Antarctica. Even though barn owl populations have decreased in central Europe due to agricultural activity by humans, the extent of distribution speaks for the success of physical and behavioural adaptation of the species (Parry-Jones, 2006).

The species is mostly active in twilight, can however be observed during daylight or night-time as well.

To support hunting with little illumination the owl relies heavily on auditory input, detecting even faint noises made by their prey animals when moving through the underbrush. The eyes however have also been adapted to work well under low light conditions. When hunting the owl flies at low altitudes until a

target is spotted, then it drops, talons first towards the ground. To increase the chances of a successful hunt, it is important for the owl to fly at low speeds so the opportunity for detecting prey, before the owl has passed by, is maximized. For this purpose the barn owl has wings with low aspect ratio and rounded tips. Low aspect ratio wings produce high amounts of lift at low speeds and increase the manoeuvrability. This is also an advantage for the owl when moving through densely wooded areas, where no clear flight paths are available. The slowness of movement also benefits the barn owl by creating less noise than faster movement would produce. This increases the owl's ability to detect its prey by reducing the background noise, which might mask the noises made by the prey, while simultaneously giving the prey less warning of its approach, thus reducing the chance of evasive movements.

In addition, the wings of the barn owl have three distinctive structures, which have previously been associated with noise reduction: comb like structures at the leading edge of the wing, which gradually split the air stream, velvety structures, which reduce the noise of feathers rubbing together while moving, and trailing edge fringes, which help to reunite upper and lower air stream after they have passed over the wing (Graham, 1937).

3 Measurement Techniques

The basic principle of the used measurement techniques is photogrammetry. In order to apply photogrammetry to an unknown surface, at least 2 pictures from different viewing positions are required (Kraus, 2004). Therefore a multi-camera-system has been used to observe each side of the bird's wings. The applied camera systems have to be calibrated for each measurement campaign. The inner (focal length, principal point etc.) and outer camera parameters (position, orientation) are determined during the calibration process (Sun, et al., 2006).

Using these parameters, the lines of sight (rays) can be calculated for each point in the images. If corresponding points can be identified within the measurement pictures, it is also possible to derive the 3D position of the points using triangulation. In most applications only easily recognisable points are determined.

For a high resolution measurement of surfaces the correspondences of a whole image area are needed. Therefore, an automated identification process is necessary to provide this information. In the following a correlation based approach for image matching is presented.

The principle of IPCT

In the present project DLR applies the cross correlation technique in order to identify/find corresponding points in two images of a stereoscopic setup. The correlation algorithm is a standard method for matching tasks in signal and image processing with which the displacement between 2 signals or images can be determined. In the current method, a quasi-random dot pattern is applied to the surfaces which allow an unambiguous assignment of corresponding points making the correlation technique very robust.

The principle of image correlation is graphically shown in Fig. 1. The first image on the left presents the search image f . The smaller image in the middle shows the template t . Both images can be seen as a gray level intensity function of their image coordinates $f(x, y)$ and $t(xt, yt)$. The idea is to find the position of the template t within the image f by a multiplication of their intensities. Hence the template t is shifted to each position x and y of the search image f , and the sum of the intensity product is calculated for each position. The normalized sums are called correlation coefficients (Eq. 1).

The diagram on the right of in Fig. 1 shows the correlation coefficients with respect to the applied shift of the template.

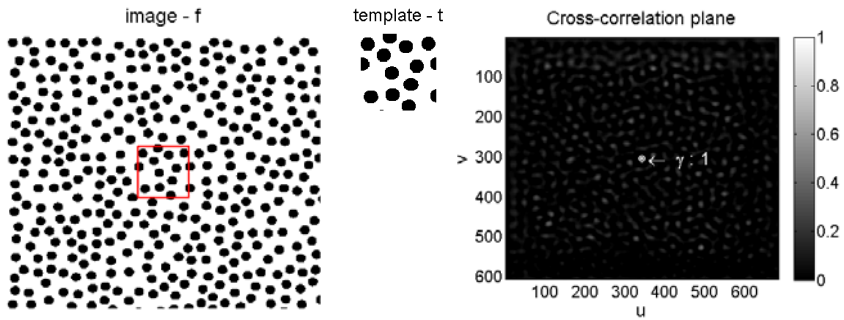


Fig. 1 Principle of correlation; left: Search image, middle: Image section - template, right: Calculated cross - correlation plane with peak

The maximum correlation coefficient can be found in the middle of the correlation plane and represents the position of the template within the image f when no shift is applied.

The applied algorithm is the normalized cross correlation (Lewis):

$$\gamma(u, v) = \frac{\sum_{x,y} [f(x,y) - \bar{f}_{u,v}] [t(x-u,y-v) - \bar{t}]}{\{\sum_{x,y} [f(x,y) - \bar{f}_{u,v}]^2 \sum_{x,y} [t(x-u,y-v) - \bar{t}]^2\}^{0.5}} \quad (1)$$

f and t are the intensity functions of the image and the template, respectively $\bar{f}_{u,v}$ is the mean of $f(x, y)$ in the area below the template and \bar{t} is the mean of the template t . By using the normalized correlation, the effect of inhomogeneous illumination can be minimized. In addition the maximum correlation coefficient for congruence of template and image section is set to 1. In Fig. 1, an idealized case is shown where the template is a part of the image f , no distortion occurs and no camera noise is present. Therefore a correlation coefficient of one is achieved.

However when measuring curved surfaces, these assumptions are not valid. Due to the different positions and viewing angles of the cameras with respect to the measurement object, local distortions as well as scaling effects appear within the obtained stereo images.

In Fig. 2 on the left an example for a small distortion of the search-image f is given. The originally regular grid shown in the image on the right, visualizes the applied distortion in the image. The template t , shown in the middle of Fig. 2, is still extracted from the undistorted rectangular image.

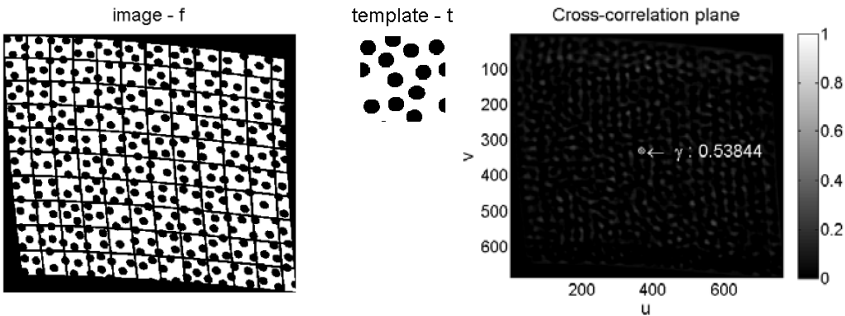


Fig. 2 Influence of distortion; left: Distorted search image; middle: Image section - template; right: Calculated cross - correlation plane with peak

In this case of moderate distortions, the maximum correlation coefficient is reduced to about half of the ideal value. This example shows the sensitivity of the correlation to effects like shear or scaling of the images.

In Fig. 3 stereo measurement pictures of an owl wing are shown. It is obvious that there is a much higher disparity between both pictures than in the example in Fig. 2. Therefore a direct correlation of these pictures would lead to wrong results.

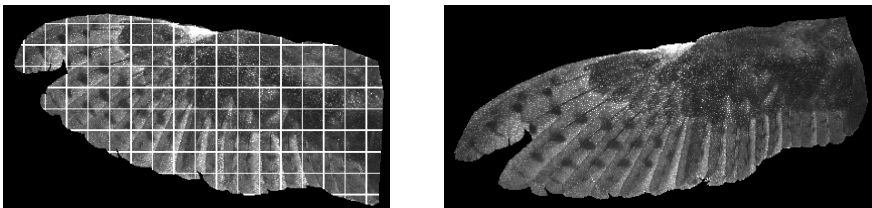


Fig. 3 Measurement pictures obtained from 2 different cameras in stereo viewing condition, in the left image a rectangular grid is applied

Hence a different approach was used for the performed matching process. A set of corresponding points was determined manually. By using these points, an initial transformation function between the pictures was calculated. Afterwards one picture is transformed using this transformation function. In Fig. 3 on the left, together with the obtained measurement image, a rectangular grid is shown. The same measurement picture is shown after the transformation in Fig. 4 on the left hand

side. Evidently the grid seems to be distorted, but the picture shows a similarity to the measurement picture obtained by the second camera, presented on the left of Fig. 4 (and Fig. 3).

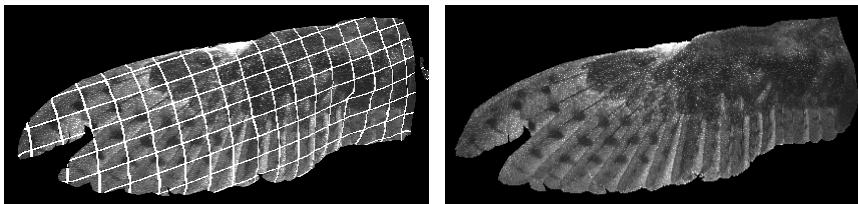


Fig. 4 Measurement pictures obtained from 2 different cameras in stereo viewing conditions, left image is warped using point correspondences

The left hand side of Fig. 4 shows the image transformed with the final transformation field. By using the manual selected points an initial transformation field is calculated. The transformed picture is then correlated with the second stereo measurement picture and, by using the newly calculated correspondences, the transformation field is refined. The calculation is performed in a pyramidal manner, from low to high spatial resolution.

Adaptation to a bird's wing

For the application of correlation-based matching algorithms an unambiguous texture or pattern on the surface of interest is needed, to provide a unique correlation coefficient maximum. For a high spatial resolution the structure or pattern has to provide enough information to enable the use of small image sections during the matching process.

Prior to the experiments with living birds, experiments using a wing preparation were performed. It was shown that the natural texture of the barn owl is not sufficient for high resolution measurements if correlation is applied during the matching process.

Therefore a projection technique is used to apply a high resolution pattern on the bird's wing surface. The technique had been used, prior to these tests, for vibration measurements (Konrath, et al., 2004). For the bird flight test, a high power white light projector was used. The projector was modified and equipped with an aperture. Therefore it was possible to enhance the depth of field. The dot pattern was applied to a mask (gobo) which was situated within the projector optic. By changing the gobo, different patterns could be projected, which enabled the adaptation of the projection to several distances. Fig. 5 presents the projected high resolution pattern within a free flight test. The good contrast, obtained on the upper wing surface, can clearly be seen.

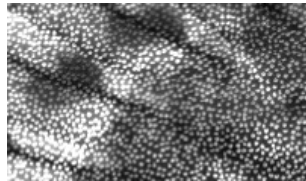


Fig. 5 Picture of the projected dot pattern on upper wing surface

3 Free Flight Experiments

Within the first part of the project, measurements of the gliding flight of birds were performed. Therefore, a static setup was placed within the flight path of the free flying bird. By using this setup it was possible to determine several wing profiles of birds during gliding flight. For the gliding flight investigation a female barn owl was used (Wolf, et al., 2010).

However, for flapping flight analyses, full flapping sequences are required in order to get insights into the kinematics and the changes of the wing morphology during a single period. A measurement of a full flapping sequence at high resolution is not possible with the gliding flight setup used here, because the measurement area is too small.

Therefore several ideas were developed for flapping flight investigations. The option adopted by DLR was to move the camera setup together with the free flying bird, leading to a setup as described below.

Moving camera setup

The free flight tests were performed at RWTH Aachen University using two different barn owls (male and female). Hence the design is based on the flying properties of barn owls. Barn owls have a flying speed of 5-7 m/s, a span of about 75 cm and a wing-beat frequency of about 5 Hz.

It was also necessary to anticipate the wing movement to optimize the camera parameters. Therefore, observations from the gliding flight tests were used together with videos, as a qualitative input.

Therefore, only a rough estimation of the wing movement was used as input for the development of the setup. Nevertheless, by using these first estimations a digital camera mock-up was designed by DLR. Parameters like depth of focus and observed area are calculated depending on the used cameras, camera positions, lenses and aperture. Fig. 6 shows the developed digital mock-up with the planned bird position. It was estimated that a minimum of 8 cameras is required to cover the movement of the wing during a wing beat cycle.

For camera support a double frame construction was developed, which enables the mounting of the cameras in front of and behind the bird. This was needed because we observed a large variation of the angle of attack in the wing tip region.

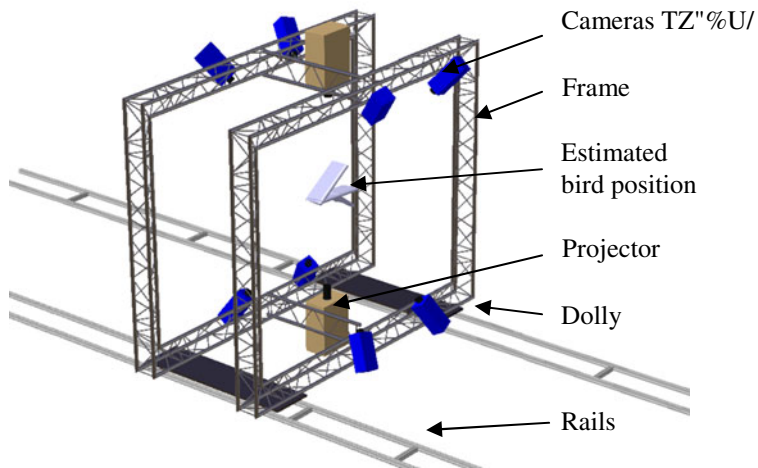


Fig. 6 Draft moving camera system

Therefore this approach was used to achieve a sufficient angle of view for the different camera systems during a whole wing beat cycle. For recording data, high speed cameras were chosen, (Phantom V12 Cameras as well as PCO - Dimax Cameras) with applied frame rates between 450 and 6000 Hz. Fig. 6 also presents the projectors for the dot - pattern, one for each side. The final test setup is shown in Fig. 7 on the left. During the tests the frame was mounted on a dolly - rail - system, provided by the company "Rail and Tracking Systems" (situated in Karlsruhe), shown in Fig. 7 on the right hand side.

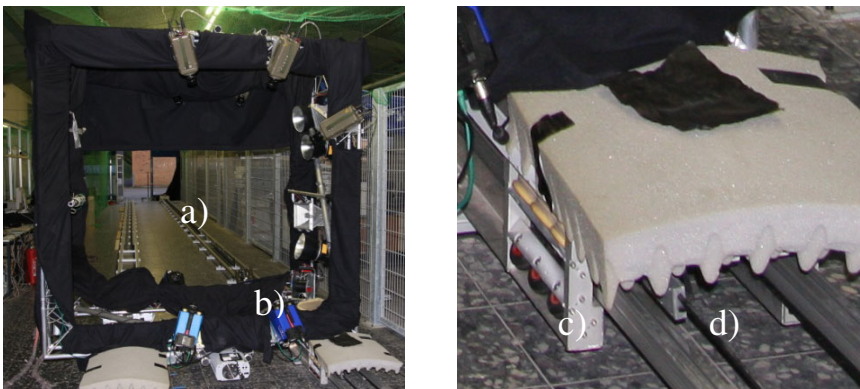


Fig. 7 Left: Free flight test setup; right: Detailed view of the dolly; a) Rail track; b) Frame construction; c) Dolly with wheels; d) Tow rope and rails

Two rail tracks of length 25 m length were used for frame support (Fig. 7., a). The movement of the frame was achieved by using a tow-rope, attached to one dolly shown in Fig. 7 c. The rope was driven by an electric motor, situated at the end of the rail track. Therefore the main sound source of the setup was not directly next to the bird and it was possible to minimize the sound level by using insulation.

The second dolly was not used for acceleration, supporting only the weight of the frame. In the end the adopted setup was able to accelerate the frame in about 5 s to speeds up to 12 m/s. For the deceleration another 5 m were needed. In addition, 5 m were used as a safety margin so that the resulting measurement section had a total length of about 10 m.

The control of the system was supplied by a *LabView* program. By use of *LabView* the acceleration and deceleration signals were generated. We applied defined acceleration ramps to achieve constant conditions for better habitation of the birds. The start of the acceleration was triggered by a light barrier which was situated in front of the perch and was connected to the *LabView* computer. The trigger signal for the cameras was also provided by the program. Therefore it was possible to define delays between driving the set up and recording start of the cameras.

In addition to the *LabView* program, there was a manual control to adjust the maximum set up speed. This device was used for the fine adjustment of the speed while the birds were flying within the measurement section.

The test procedure

The perch together with the bird were put in front of our measurement system, while the bird trainer moved to the end position of the driving system. The bird was than stimulated using food and started flying towards the trainer. After flying through the light barrier of our setup, the driving system, which was situated round about 2-3 m in front of the bird, starts to accelerate. In the middle of our driving track, the camera frame reaches nearly the velocity of the bird and the bird was situated near by the measurement position. The frame velocity was then slightly adapted manually to obtain a longer measurement time. At about 5 m before the end of the track, we placed a switch which automatically decelerated the system. While deceleration took place, the bird was perched on the trainer's arm and received a reward.

4 Results

In this chapter the obtained data from a typical flight are given. The data shows a case were the male barn owl was flying. Within the chosen flight a whole wing beat sequence was recorded. The weight of the chosen bird was approximately 400 g. The results are given together with a time stamp t. The bird had entered the measurement volume fully at time t = 0 s.

A resulting upper wing surface image of this flight is shown in Fig. 8. One can see the wing surface during the down-stroke. It can clearly be seen that the wing tip is pointing downwards with a negative angle of attack, while the proximal wing section has a positive geometric angle of attack.

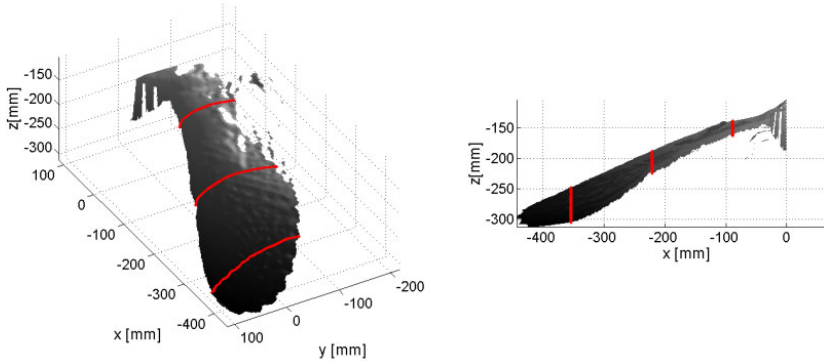


Fig. 8 An example of wing surface during down stroke at $t = 0,074$ s; left: Overview; right: Rear view

The calculated surface is obtained by using the upper front cameras. Therefore the resolution at the proximal trailing edge section is very low, which was caused by the camber of the profile and the related angle of view for the front cameras.

Important is the definition of the used coordinate system. The x direction shows the span wise coordinate with the wing root at $x = 0$ mm. The y coordinate points towards the direction of flight and the z direction is aligned vertically. The origin of the coordinate system is defined during the calibration process. Therefore we aligned the z plane in the ideal observation position of the cameras. The z-value of the wing root in Fig. 8 indicates that the owl was not flying at an ideal altitude such that the rear upper cameras were not able to capture the whole wing surface at time $t = 0,074$ s.

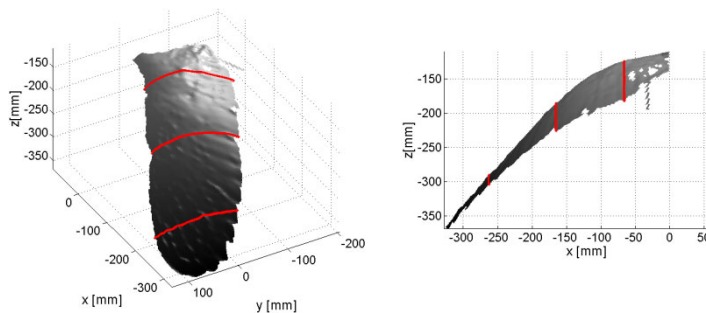


Fig. 9 An example of wing surface during down stroke $t = 0,026$ s; left: Overview; right: Rear view

Fig. 9 presents the upper wing surface at the end of the down stroke at the turning point. There it can be seen that the span wise angle of the wing reaches about 45° and the wing tip is situated at $z = -350$ mm. Due to these low z values corresponding to an enhanced camera-object-distance (for the upper cameras), this led to a lower resolution of the measurement setup in the wing tip region. Therefore the details of the feathers can hardly be seen.

Much more detail can be seen in Fig. 10. Note, the coordinate system for the next figures are turned, for better viewing angles. The wing surface is presented during the upstroke at the time $t = 0.18$ s. The feather structure at the wing tip can be seen clearly. The z coordinate shows that the wing is now close to the ideal flying position and the owl is gaining altitude between $t = 0.026$ s and $t = 0.18$ s.

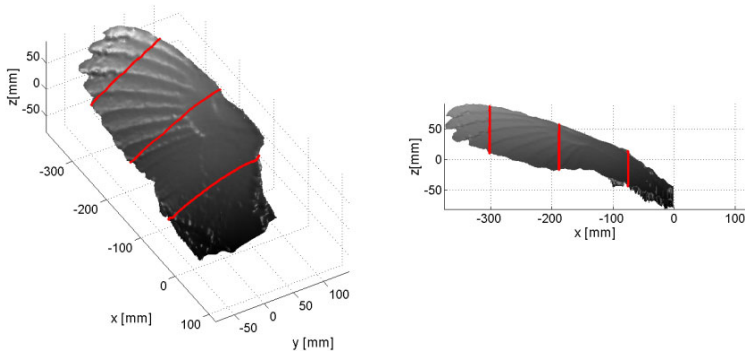


Fig. 10 An example of wing surface during up stroke at $t = 0.18$ s; left: Overview; right: Rear view

Fig. 10 shows the high geometric angle of attack within the wingtip region. Compared with the down stroke cases, two main changes can be seen along with the change of the angle of attack. First, the sweep angle of the wing which is lower with the down stroke. Second, the primary feathers are overlapping.

Fig. 11 shows the owl wing at the beginning of the down stroke. The wing is strongly swept forward and is stretched in span wise direction. Due to the stretching of the wing towards the wing tip, small ripples along the surface are developing, which can also be seen in Fig. 11.

In Fig. 12 a set of profiles, calculated by combinations of upper and lower surface results together, is presented. We can see the high angle of attack, especially at the wing tip region, as well as the steps at $\eta = 0.9$ which are caused by an overlapping of the feathers.

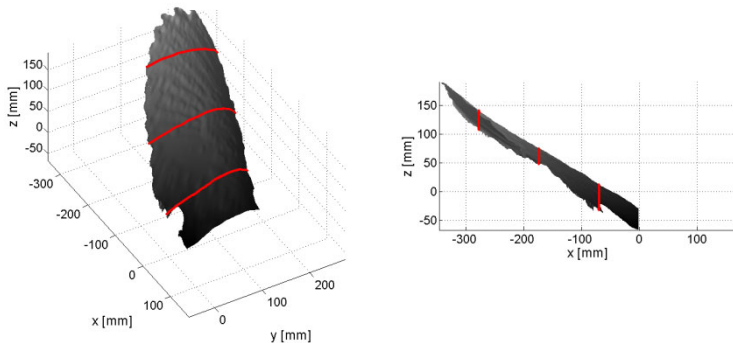


Fig. 11 An example of wing surface during begin of down stroke at $t = 0,26$ s; left: Overview; right: Rear view

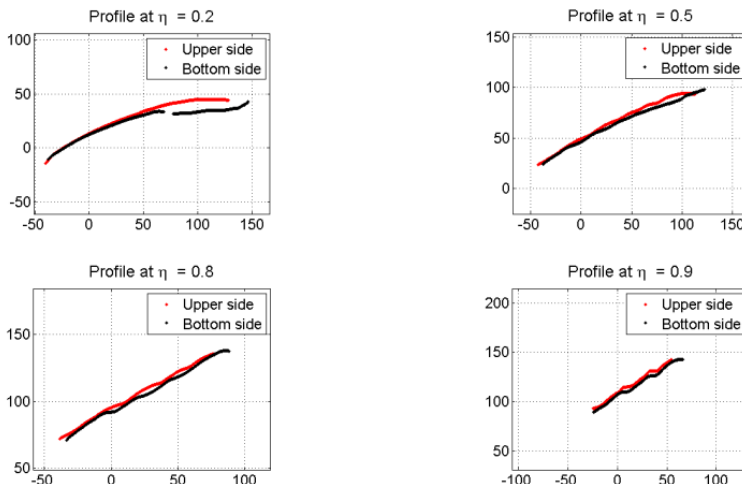


Fig. 12 Profiles derived from the wing surface measurement, η is the normalized spanwise coordinate

5 Summary / Outlook

The image pattern correlation technique has been successfully adapted to measurements of wings of birds. A new system projecting a fine random dot pattern enabled high resolution surface measurements of freely flying birds. Furthermore, new software was developed which is able to cope with the strong wing deformations and motions. The software is based on manually determined

correspondences which enable an initial warping of the stereo images. Afterwards the correlation function is applied in an iterative manner and used for refinement of the transformation function between the pictures. This leads finally to a point-to-point relation between both pictures and therefore to a pixel-wise resolution. Due to the initial warping process, the robustness of the surface calculation against noise and blurred pictures is enhanced.

Next step in the software development will be an automatization of the process for finding initial point correspondences. It is also planned to implement a detection of surface steps. By knowing the position of the steps, it should be possible to enhance the performance of the measurement system at regions with overlapping feathers. We are also planning to detect the wing edges of upper and lower wing surfaces to compensate for the displacement between upper and lower camera system.

The first measurements using a moving setup were performed in Aachen University. The moving setup, developed by DLR-Göttingen, was applied in these measurements and demonstrated its ability to deliver measurement pictures of barn owls during flapping flight. With this setup it was therefore possible to record several flapping sequences.

However, during the first tests the camera positions were chosen using a rough movement estimation of the birds. During the evaluation of the obtained data it was noticed that the bird was not perfectly situated in the measurement volume during flapping sequences. Therefore, the next step is to refine the positioning of the cameras with respect to the measured movement of the birds. The data obtained with these first measurements should be used for this optimisation.

Another point for improvement is the measurement volume. It should be increased by use of new projectors which provide a higher depth of focus. Together with enhanced training of the birds this should lead to the recording of more flapping flight sequences which can be processed entirely.

Acknowledgments. This study was funded by the German Research Foundation (DFG) within the priority program SPP-1207, "Nature Inspired Fluid Mechanics".

The measurements were performed in cooperation with the University of the Armed Forces (UniBW) Munich and the authors would like to thank Alexander Friedl for his contributions during the free flight measurement campaign in Aachen.

References

- Biesel, W., Butz, H., Nachtigall, W.: Erste Messung der Flügelgeometrie bei frei gleitfliegenden Haustauben (*Columba livia* var. *domestica*) unter Benutzung neu ausgearbeiteter Verfahren der Windkanaltechnik und der Stereophotogrammetrie. *Biona Report 3*, 139–160 (1985)
- Graham, R.: The silent flight of owls. *Journal of the Aerodynamic Society* 38, 837–843 (1937)
- Konrath, R., et al.: The projected pattern correlation technique for vibration measurements. In: 6th International Conference on Vibration Measurements by Laser Techniques, Italy, Ancona (2004)
- Kraus, K.: Photogrammetrie Bd. 1. Auflage, vol. 7. Walter de Gruyter, Berlin (2004)

- Lewis, J.P.: Fast Normalized Cross Correlation,
[http://scribblethink.org/Work/nvisionInterface/nip.html#foo
t263](http://scribblethink.org/Work/nvisionInterface/nip.html#foot263)
- Lilienthal, O.: Der Vogelflug als Grundlage der Fliegekunst. R. Gaertners Verlagsbuchhandlung, Berlin (1889)
- Liu, T., et al.: Avian Wings. In: 24th AIAA Aerodynamic Measurement, AIAA 2004-2186, Portland (2004)
- Muijres, F.T., et al.: Vortex wake, downwash distribution, aerodynamic performance and wingbeat kinematics in slow-flying pied flycatchers. *Journal of the Royal Society Interface* 2012 9, 292–303 (2012)
- Nachtigall, W., Klümbingnat, A.: Messung der Flügelgeometrie mit der Profilkamm Methode und geometrische Flügelkennzeichnung einheimischer Eulen. *Biona Report* 3, 45–86 (1985)
- Oehme, H.: Der Flug des Mauerseglers (*Apus apus*). *Biologisches Zentralblatt*, Bd. 87, 3 (1968)
- Padfield, G.D., Lawrence, B.: The birth of flight control: An engineering analysis of the Wright brothers' 1902 glider. *The Aeronautical Journal*, Paper No. 2854 (2003)
- Park, K.J., Rosen, M., Hedenstrom, A.: Flight kinematics of the barn swallow (*Hirundo rustica*) over a wide range of speeds in a wind tunnel. *The Journal of Experimental Biology* 204, 2741–2750 (2001)
- Parry-Jones, J.: Understanding Owls. David & Charles, Brunel House (2006)
- Pennycuick: The Flight of Petrels and Albatrosses. *Philosophical Transactions of the Royal Society of London* 300(1098) (1982)
- Sun, W., Cooperstock, J.R.: An empirical evaluation of factors influencing camera calibration accuracy using three public available techniques. *Machine Vision and Applications* 17, 51–67 (2006)
- Taylor, G.K., et al.: Flight control mechanism in birds of prey. *American Institute of Aeronautics and Astronautics*, 2007-39 (2007)
- Tobalske, B.W., Dial, K.: Flight kinematics of black-billed magpies and pigeons over a wide range of speeds. *The Journal of Experimental Biology* 199, 263–280 (1996)
- Tobalske, B.W., et al.: Three-dimensional kinematics of hummingbird flight. *The Journal of Experimental Biology* 210, 2368–2382 (2007)
- Tobalske, B.W., Peacock, W.L., Dial, K.P.: Kinematics of flap bounding flight in the zebra finch over a wide range of speeds. *The Journal of Experimental Biology* 202, 1725–1739 (1999)
- Tucker, V., Cristian, P.: Aerodynamics of gliding flight in a falcon. *J. Exp. Biol.*, Bd. 5 (1970)
- Wolf, T., et al.: Measuring shape of bird wings during flight. In: 14th International Symposium on Flow Visualization - ISFV14, Daegu, Korea, June 21-24 (2010)

A Discussion on Vortex Growth and Saturation in Dragonfly-Inspired Flight

David E. Rival, Alex Widmann, and Cameron Tropea

Abstract. This report is devoted to examining vortex formation and interactions as they occur with isolated and tandem pitching and plunging airfoils. Motivation for understanding such flow phenomena is inspired from dragonflies, which exhibit a wide range of acrobatic flight maneuvers, possibly interesting for the realization of flapping drones known as Micro Air Vehicles (MAVs). Experimental investigations are described in which the kinematics of the forefoil and hindfoil could be independently varied, attaining any combination of pitch and plunge movements up to reduced frequencies of approximately $k=0.3$ in forward flight. Furthermore, the Reynolds number in these studies was varied between $Re=3000$ (hover) and $Re=30000$ (forward flight). Particle Image Velocimetry (PIV) was used to extract information on leading-edge vortex (LEV) and trailing-edge vortex (TEV) circulation, which in turn was useful in examining the growth rate and saturation often referred to as formation number. The following results will be presented: the effect of airfoil kinematics on LEV and TEV development; the influence of hindfoil interaction on the vortex formation and lift generated by the forefoil; and a quantification of the vortex interaction found in the hover condition. Finally, some thoughts regarding a new model of vortex growth will be discussed.

1 Introduction

Numerous biological studies of dragonfly flight have been performed suggesting specific wing kinematics and phasing are responsible for the insect's exceptional maneuverability [1-3]. The studies considered here, which attempt to extract the salient

David E. Rival · Alex Widmann · Cameron Tropea
Institute of Fluid Mechanics and Aerodynamics,
Technische Universität Darmstadt, Germany

David E. Rival
Department of Mechanical Engineering, University of Calgary, Canada

Cameron Tropea
Center of Smart Interfaces, Technische Universität Darmstadt, Germany

features pertaining to vortex formation associated with dragonfly-like flight, have been carried out at a realistic Reynolds-number and reduced-frequency range, which in turn is also relevant to the development of flapping Micro Air Vehicles (MAVs). The associated vortex dynamics of these strongly separated flows have been examined using vortex-tracking, pressure-integration and control-volume methods. To a lesser extent, direct force measurements and URANS-based numerical simulations have also been used to support the findings. At first the formation and manipulation of leading-edge vortices (LEVs) and trailing-edge vortices (TEVs) for a single airfoil have been examined using non-sinusoidal kinematics and the theory of optimal vortex formation. Results show that the development of the LEV can be modified without the need for a spanwise flow, contrary to previous conjectures. In a similar fashion, the TEV can be reduced or even completely mitigated through the superposition of a quick-pitch motion near the bottom of the stroke.

Subsequently, the studies of tandem configurations in cruise conditions revealed that the vortex-formation process for the forefoil is strongly influenced by the placement of a hindfoil in its wake, be it static or moving. In strong agreement with observations made on live dragonflies, airfoil configurations with specific out-of-phase kinematics of approximately 60° were found to generate net thrust. The mechanism for this thrust production was identified as the formation of a leading-edge suction bubble on the hindfoil induced by the passing of the forefoil LEV. Similarly, the passing forefoil TEV was found to induce a vortex on the hindfoil, which in turn helped reduce power consumption on the upstroke. Finally, time-resolved PIV investigations into tandem hovering identified a beneficial interaction at 90° in which the forefoil TEV interacted with the development of the hindfoil LEV. This aerodynamic mechanism in turn adjusted the strength and positioning of the hindfoil TEV, thus affecting thrust and power consumption. This result agrees with observations in nature and analogous force measurements for three-dimensional flapping wings, suggesting again that a spanwise flow is not necessarily required for efficient vortex control but rather a result of the evolutionary restrictions in nature towards root-flapping flight.

The current paper looks to connect the concept of optimal vortex formation for the series of studies discussed above. By gradually introducing increasingly more complex interactions, i.e. from isolated cases to tandem-cruise flight and finally to tandem hovering, the reader will be able to develop an appreciation for the factors influencing vortex growth and its ultimate saturation, as presented in a preliminary model at the end.

2 Experimental Methods

A test rig, as shown in Figure 1, was developed to reproduce dragonfly-like flight with a bulk two-dimensional flow in the wind tunnel. Two pairs of linear actuators are controlled separately to facilitate pitch and plunge motions. The test rig is mounted into a wind tunnel to simulate cruise conditions or can be mounted in a hover chamber to model hover conditions using acrylic glass plates, as shown in Figure 2. Two *Dantec Dynamics* PIV systems have been used for these various studies: one conventional system (15Hz) and one high-speed system (1000Hz). The conventional system utilized a 135mJ *Litron* Nd:YAG dual cavity laser and two 10-bit *Flow-Sense*

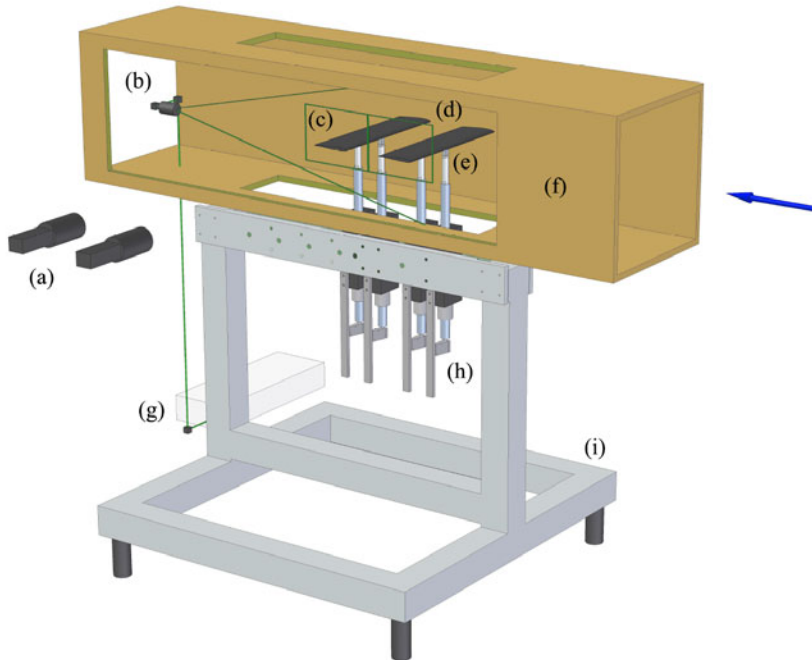


Fig. 1 Experimental setup in wind tunnel with flow direction from right-to-left: (a) CCD cameras, (b) beam expander, (c) PIV image frames, (d) wall-spanning carbon fibre profile, (e) embedded piezo-electric force sensors, (f) test-section, (g) laser head, (h) linear motors with linkage system and (i) base structure.

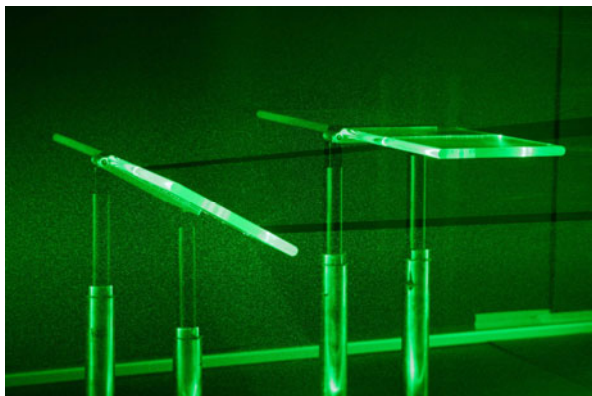


Fig. 2. Acrylic glass plates in tandem arrangement; note minimal shadows emitted from leading and trailing edges allowed for excellent optical access during PIV measurements.

2M CCD cameras. The high-speed system was based on a 22mJ *Litron* dual-cavity Nd:YLF laser synchronized with two *Phantom V12* high-speed cameras.

3 Results

3.1 Vortex Formation for an Isolated Airfoil

The influence of stroke kinematics on the characteristics of LEVs and TEVs has been investigated for forward-flight conditions. During the downstroke the shear layer at the leading edge rolls up into a vortex, grows and eventually detaches. When the reduced frequency is varied between $0.05 < k < 0.3$ different types of vortex shedding are observed, as described by Rival and Tropea [4]. For values of $k < 0.15$ dynamic stall causes shedding of multiple alternating vortices from the leading and trailing edges during one stroke cycle, corresponding to a typical bluff-body von Karman street. For values of $k \approx 0.2$, transition from the Karman-type shedding can be observed: one LEV and one TEV are shed per stroke cycle, forming a distinct vortex pair. Only minimal differences between equivalent pure-pitching and pure-plunging motions are observed and can be attributed to the large displacement of the shed vortices during the plunging motion. The strength of these shed vortices and therefore their circulatory contribution to lift depends strongly on the level of stall prevailing on the airfoil. Larger angles of attack promote the occurrence of dynamic stall and higher peak values in lift hysteresis can be achieved. These peak values can be attributed to well-developed LEVs.

In order to take advantage of LEV formation through unsteady lift augmentation, it is beneficial to prolong the vortex growth stage and delay detachment via careful airfoil kinematics. In Rival et al. [5], the effect of various plunging kinematics for a single airfoil has been compared to a sinusoidal reference case, as shown in Figures 3 and 4. The results are considered in light of the concept of optimal vortex formation presented by Dabiri [6]. This concept suggests universality for vortex development, where the formation number T^* reaches values of $T^* \approx 4.4$ at vortex detachment (saturation). T^* is given in its general form as $T^* = C\Gamma(\Delta U L)^{-1}$, with Γ as the measured circulation, ΔU as the shear layer velocity difference, $L=2c$ (c – chord) as the characteristic length and C as a vortex generator constant. For the given case the vortex generator constant was set to $C=1$.

In Figure 5 it is found that LEV circulation increases continuously until a maximum value is reached and saturation/detachment occurs late in the downstroke. For kinematics crossing the dynamic stall angle at higher speeds the shear layer feeding into the LEV is strengthened. Depending on the timing of the maximum feeding velocity LEV circulation can be augmented and its formation can be prolonged. Formation times in the range of $4.4 < T^* < 5.0$ were observed for all experiments and were found to be in agreement with the concept of optimal vortex formation. The results suggest that LEVs can be stabilized by a progressive strengthening of the feeding layer. By making slight adjustments to airfoil plunging kinematics significantly higher lift values can therefore be achieved.

Kelvin's law demands that with accumulating bound vorticity on the leading edge, counter-rotating vorticity must be discharged at the trailing edge. For increased LEV

circulation, more counter-rotating circulation emanates from the trailing edge and rolls up into the TEV as soon as the LEV detaches and convects over the airfoil. According to Katz and Plotkin [7] substituting a distinct TEV with a wake is advantageous for lift production. One particular phenomenon detrimental to both lift and drag is the large separation after a LEV has detached. To avoid this, a quick reattachment of flow over the airfoil surface is favorable. The technique applied to avoid both detrimental effects is a fast pitching motion at a late stage of the downstroke. A quick pronation and a subsequent supination are superposed to the oscillating wing movement. Prangemeier et al. [8] investigate this type of motion and reveal the aerodynamic mechanisms. During pronation the interaction of the airfoil and the forming TEV cause a drastic reduction in TEV circulation. The described pitching motion thus provides a technique to reduce drag and increase lift simultaneously, while maintaining LEV growth.

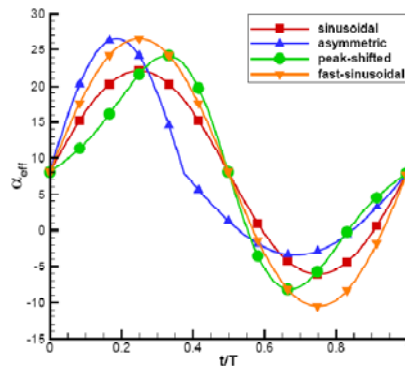


Fig. 3 Variation of airfoil kinematics

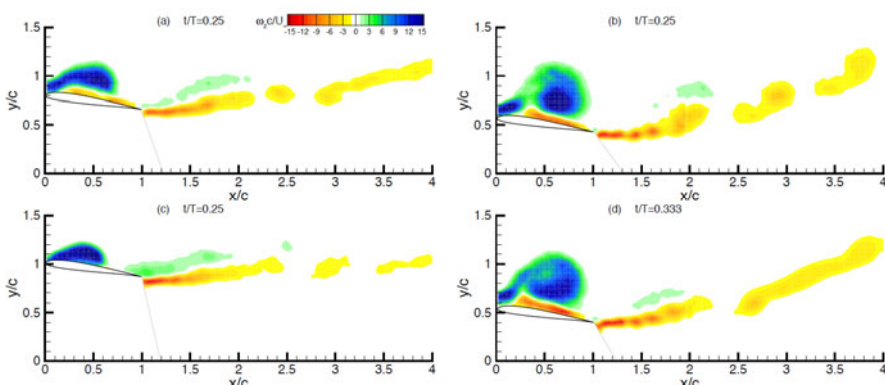


Fig. 4 Vorticity production during the downstroke for (a) sinusoidal, (b) asymmetric, (c) peak-shifted and (d) fast-sinusoidal cases.

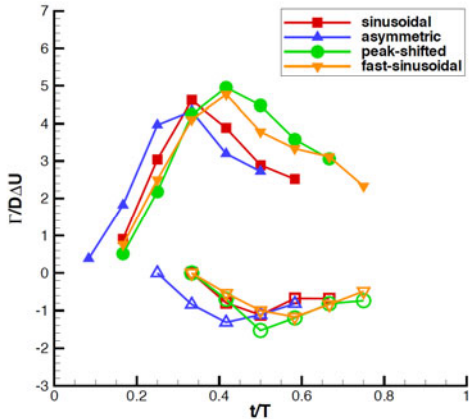


Fig. 5 Development of LEV and TEV circulation (formation number).

3.2 Influence of Tandem Configuration on Vortex Formation

Although kinematic adjustments are useful to control LEV and TEV formation for an isolated airfoil, the ability to extract vortical energy with the presence of a second wing pair is particular to dragonfly flight. Tandem arrangements of wings allow an interaction of the hindwing pair with the oncoming vortices shed from the forewing pair. A configuration consisting of an oscillating forefoil and a fixed hindfoil was studied by Rival et al. [9]. It allows the hindfoil to extract vortical energy from the wake of the forefoil so as to generate thrust. The mutual interaction associated with a moving tandem configuration was also considered by Rival et al. [10].

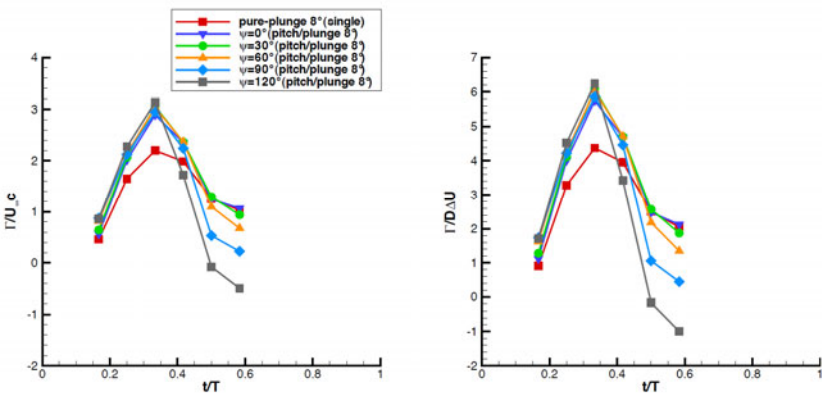


Fig. 6 Development of LEV circulation (left) and equivalent formation time (right) as a function of period for the various tandem-airfoil configurations.

It was found that the overall aerodynamic behavior of the tandem wing configuration under forward flight conditions is dictated by the interaction of the hindfoil with the oncoming vortices from the forefoil, which in turn is sensitive to the flapping phase. The behavior of the forefoil in tandem arrangement compared to a single airfoil remains almost unchanged. However, as observed in Figure 6 (left), the tandem arrangement has the effect of strengthening the LEV over the forefoil. When the equivalent formation time is plotted in Figure 6 (right), an increase in the formation number to $T^* > 6$ clearly identifies the manipulation of the limiting vortex-formation process through temporal and spatial variation of the feeding shear layer, as discussed by Dabiri [6].

3.3 Vortex Formation in Tandem Hover Conditions

Of particular interest in the study presented by Rival et al. [11] are the aerodynamic mechanisms occurring in dependence of airfoil phasing and the associated mean values for lift and thrust in one stroke cycle. As for cruise conditions, lift and thrust forces on the forefoil are unaffected. In strong contrast, the forces produced by the hindfoil show a strong dependency to phasing (vortex interaction). The peaks in thrust are explained by a pair of counter-rotating TEVs shed from the hindfoil. These vortex pairs establish a reverse von Karman street and thus a jet is produced. In Figure 7, the trajectories and non-dimensional circulation for one of these thrust-producing TEVs are presented. One can observe that the interaction of the airfoil pair causes a variation in vortex growth and pinch-off, again suggesting that the stabilization (or release) of such vortices is highly controllable. This mechanism controlling thrust corresponds very well to the findings of Azuma and Watanabe [2] and suggests that the dominant aerodynamic mechanism in tandem-wing hovering is two-dimensional in nature.

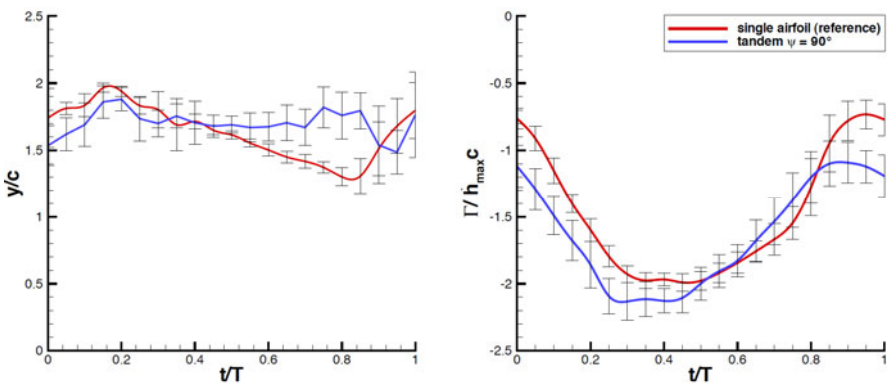


Fig. 7 Trajectories (left) and non-dimensional circulation (right) of downstroke TEV from single airfoil and tandem configuration with 90° phase angle.

3.4 Development of a Vortex-Growth Model

The high formation numbers in tandem airfoil experiments indicate that the vortex formation process and its associated scaling with a characteristic length scale has not yet been properly understood. Vortex growth and the accumulation of vorticity are intrinsic to the process of vortex formation. To study this behavior uncoupled from geometric and kinematic constraints a setup without inherent length scales has recently been developed. A Dielectric-Barrier-Discharge (DBD) actuator is mounted near the edge of a flat plate in quiescent air. By applying an alternating high voltage across two electrodes, one exposed to the flow, the other embedded beneath a dielectric layer, ambient air in vicinity of the electrodes is ionized. The ions are accelerated by a Coulomb force and collide with uncharged molecules causing a planar wall-jet. The roll-up of the jet into a distinct vortex and its convection is monitored with the high-speed PIV system. Vortex diameter and circulation are calculated and related to shear-layer (wall jet) properties. Its convective speed is determined by tracking the vortex center. The jet velocities depend on the DBD actuator's operating voltage and the vortex convection speed. The experimental arrangement is depicted in Figure 8.

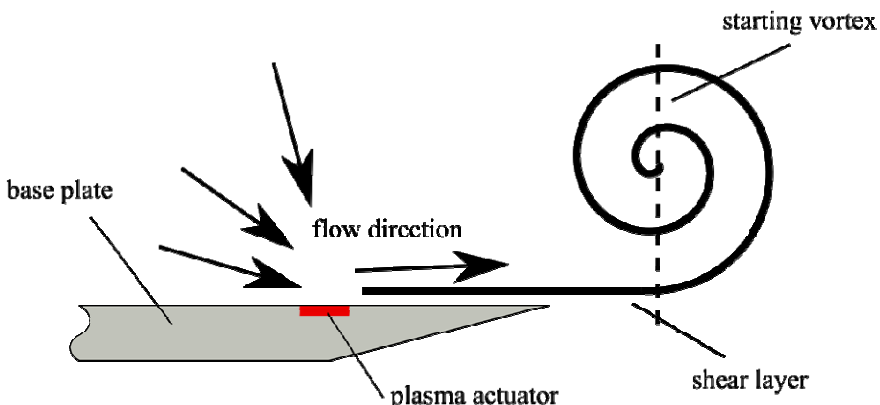


Fig. 8 Vortex generation using a dielectric barrier discharge plasma actuator mounted at the trailing edge of a flat plate in quiescent air.

With increasing vortex convection speed the relative velocity of the shear layer gradually decreases, i.e. the mass flux from the shear layer feeding the forming vortex diminishes. Some preliminary measurements for vortex circulation are depicted in Figure 9 for four different shear-layer velocities (cases A-D). As can be expected higher shear-layer velocities yield higher values of vortex circulation. As the radius of the vortex core increases with time a plateau is gradually reached (indicated by broken lines) and no further growth is observable.

The growth rate of the unconstrained vortex in the current model is described as the mass flow transferred from the shear layer into the forming vortex, following the suggestions of Kaden [12] and taking the vortex convection speed into

account. A comparison between the theoretical model (solid lines) and measurements in Figure 9 indicates good agreement until vortex saturation/detachment begins. The prediction of this saturation limit can be made using local characteristics of the vortex and shear layer and will be published in the near future [13].

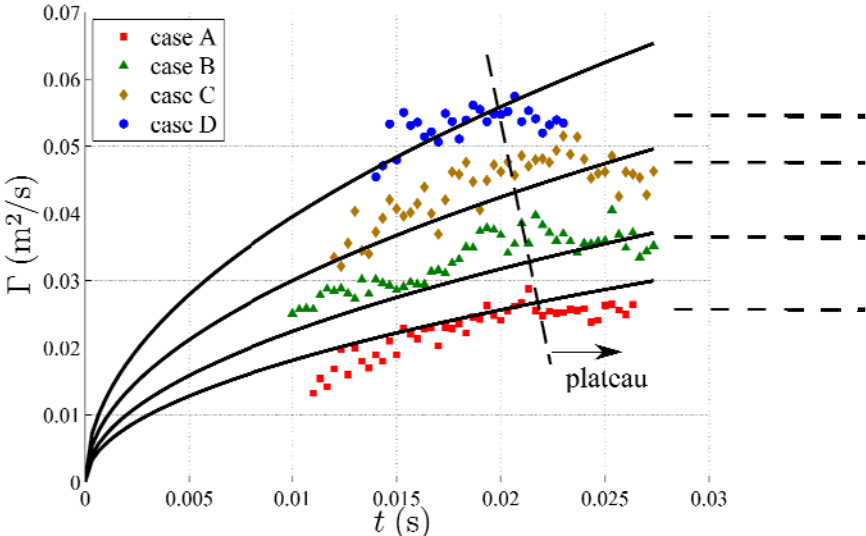


Fig. 9 Vortex strength for increasing shear-layer velocities (cases A-D) together with predictions by the proposed growth model (solid lines). The dashed line marks the approximate onset of the vortex growth plateau.

4 Conclusions and Outlook

The studies reviewed in this paper allow for a deeper insight into the vortex-growth and saturation mechanisms associated with isolated and tandem airfoil configurations for both forward flight and hover. The flow field is dominated by vortical structures whose interactions with the airfoils determine lift and thrust characteristics. Vortices emerging from a single airfoil can be stabilized and manipulated by means of kinematics only. Small variations affecting vortex development may promote beneficial or detrimental aerodynamic effects. This finding suggests that spanwise flow is not a requirement for vortex stabilization and supports the arguments by Thomas et al. [3] that vortices in dragonfly flight are primarily two-dimensional in nature. When examining tandem cases in cruise conditions, the hindfoil was found to be sensitive to airfoil phasing, while the forefoil demonstrated only a weak dependency. However, the presence of the hindfoil had the effect of substantially increasing the forefoil LEV circulation, this contradicting the basic premise of a universal formation time. Completely different mechanisms for lift and thrust generation in hover were identified. TEV

growth and detachment were also found to be altered (delayed) by the presence of a second airfoil.

While the concept of optimal vortex formation provided by Dabiri [6] is applicable to single airfoils, formation numbers of forefoil LEVs are increased drastically in tandem arrangements; the hindfoil affects the upstream positioned forefoil shear layer. This observation suggests that the mechanisms of vortex growth and detachment in flapping flight have yet to be understood and therefore limit our ability to manipulate such vortices in a targeted way. To this end a new experimental setup has been developed in which vortex formation isolated from inherent length scales and external influences can be observed. The results lead to a model of vortex growth and saturation, which is governed by a flux of mass from the shear layer into the forming vortex.

References

1. Alexander, D.E.: Unusual phase relationships between the forewings and hindwings in flying dragonflies. *Journal of Experimental Biology* 109, 379–383 (1984)
2. Azuma, A., Watanabe, T.: Flight Performance of a Dragonfly. *Journal of Experimental Biology* 137, 221–252 (1988)
3. Thomas, A.L.R., Taylor, G.K., Srygley, R.B., Nudds, R.L., Bomphrey, R.J.: Dragonfly flight: free-flight and tethered flow visualizations reveal a diverse array of unsteady lift-generating mechanisms, controlled primarily via angle of attack. *Journal of Experimental Biology* 207, 4299–4323 (2004)
4. Rival, D., Tropea, C.: Characteristics of Pitching and Plunging Airfoils Under Dynamic-Stall Conditions. *Journal of Aircraft* 47(1), 80–86 (2010)
5. Rival, D., Prangemeier, T., Tropea, C.: The influence of airfoil kinematics on the formation of leading-edge vortices in bio-inspired flight. *Experiment in Fluids* 46(5), 823–833 (2009)
6. Dabiri, J.O.: Optimal Vortex Formation as a Unifying Principle in Biological Propulsion. *Annual Review of Fluid Mechanics* 41, 17–33 (2009)
7. Katz, J., Plotkin, A.: Low-Speed Aerodynamics. Cambridge University Press, Cambridge (2001)
8. Prangemeier, T., Rival, D., Tropea, C.: The manipulation of trailing-edge vortices for an airfoil in plunging motion. *Journal of Fluids and Structures* 26(2), 193–204 (2010)
9. Rival, D., Manejev, R., Tropea, C.: Measurement of parallel blade-vortex interaction at low Reynolds numbers. *Experiments in Fluids* 49(1), 89–99 (2010)
10. Rival, D., Hass, G., Tropea, C.: Recovery of Energy from Leading- and Trailing-Edge Vortices in Tandem-Airfoil Configurations. *Journal of Aircraft* 48(1), 203–211 (2011)
11. Rival, D., Schoenweitz, D., Tropea, C.: Vortex interaction of tandem pitching and plunging plates: a two-dimensional model of hovering dragonfly-like flight. *Bioinspiration and Biomimetics* 6(1), 16008 (2011)
12. Kaden, H.: Aufwicklung einer unstabilen Unstetigkeitsfläche. *Ingenieur-Archiv* 2, 140–168 (1931)
13. Sattari, P., Rival, D., Martinuzzi, R., Tropea, C.: Evolution and scaling of a start-up vortex from a two-dimensional shear layer. *Physics of Fluids* (under review)

Part III

**Flow Control in Fish, Dolphins
and Seals**

Station Holding of Trout: Behavior, Physiology and Hydrodynamics

Horst Bleckmann*, A. Przybilla, A. Klein, A. Schmitz,
S. Kunze, and Christoph Brücker

Abstract. Trout commonly experience unsteady flows such as those caused by a stationary object exposed to running water. Instead of avoiding these flows, trout often use flow fluctuations for station holding. The behaviors associated with station holding are entraining, Kármán gaiting and bow wake swimming. We investigated the swimming behavior of trout in the vicinity of a stationary or moving 2-D shaped cylinder. To uncover the sensory modalities used for station holding, we studied the behavior of intact trout and of trout whose lateral line system was partially or totally impaired in the light or under infrared illumination. We also studied the activity of the axial red swimming muscles of entraining, Kármán gaiting and bow wake swimming trout and the neuronal processing of vortex information in the hindbrain of fish. Further studies showed that small motions of the caudal and/or pectoral fins are necessary to stay in preferred areas irrespective of the unsteadiness imposed by the wake of an object. Computational Fluid Dynamics simulations were carried out to uncover the forces that allow trout station holding with a minimum of energy expenditure.

1 Introduction

Reophilic fishes are constantly exposed to running water. Both, swimming upstream and station holding, require energy to overcome drag. While flows that display chaotic fluctuations repel fishes (Enders et al., 2003), flows that have

Horst Bleckmann · A. Przybilla · A. Klein · A. Schmitz
Institute of Zoology, University of Bonn, Poppelsdorfer Schloss
53115 Bonn, Germany
e-mail: Bleckmann@uni-bonn.de

S. Kunze · Christoph Brücker
Technical University of Freiberg, Freiberg, Germany

* Corresponding author.

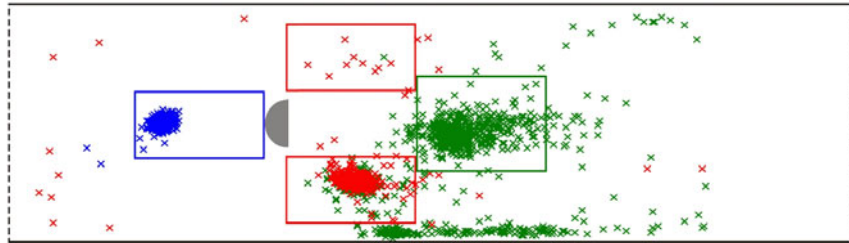


Fig. 1 Swimming behavior of trout exposed to a D-shaped cylinder (grey half circle, diameter 5 cm). The working section (width 28 cm, length 100 cm, water height 28 cm) of the flow tank, shown in top view, was delineated within the flow tank by an upstream and downstream net (vertical dashed lines). Bulk flow (42 cm s^{-1}) was from left to right. Head locations of trout are plotted every 2 s (900 data points for each individual). Each colour represents one animal. Red rectangles: entraining zones [defined by Liao (2003) as two 7 cm x 15 cm rectangular regions on either side of the cylinder]. Blue rectangle: bow wake zone (size 7 cm x 15 cm). Green rectangle: Kármán gait zone (size 7 cm x 15 cm). All experiments were done in the light. Figure taken from Przybilla et al. (2010).

predictable fluctuations can attract fishes (for a comprehensive review see Liao, 2007). To save energy fishes either exploit regions of reduced flow or harness the energy of environmental vortices. For this, fishes especially exploit flow fluctuations caused by rocks, roots or boulders (Sutterlin and Waddy, 1975). Sutterlin and Waddy (1975), Liao et al. (2003), Montgomery et al. (2003), and Przybilla et al. (2010) investigated how trout interact with unsteady flow regimes in a defined laboratory environment (flow tank). At Reynolds numbers ($Re > 140$), flow behind a bluff 2-D body, such as a stationary D-shaped cylinder (hereafter referred to as cylinder), not only alters the water velocity and pressure gradients in the vicinity of the cylinder but also generates a staggered array of discrete, periodically shed columnar vortices of alternating sign (Kármán vortex street, Vogel 1983). Trout exposed to the flow fluctuations caused by a cylinder either position their head (body) downstream of and close to one of the sides of the cylinder without touching it (entraining, Przybilla et al. 2010) or swim directly in the vortex street displaying a swimming kinematic that synchronises with the shed vortices (Kármán gaiting, Liao et al. 2003). Another observation is that entraining fish angle their body away from the cylinder and the bulk flow direction. For station holding, trout also use the high-pressure, reduced-flow bow wake zone in front of the cylinder (Liao et al., 2003). The preference of trout for certain areas in a flow tank is not only individual specific (for an example see Fig. 1) but may even change on a daily basis for a given individual (Przybilla, 2012). In addition, swimming behavior of trout in the light may differ from swimming behavior in the dark (Liao et al., 2003; Przybilla, 2012).

Besides the still open questions of fluid mechanics of flow control for entraining fish we still do not know how trout find and select a location in a river or creek that allows them to save energy? Furthermore, after having found such a location

which sensory cues enable them to control their position there? Potential systems involved in station holding are the visual system (during day time and in clear water) and the acoustic, vestibular and lateral line system (during day and night time). Under light conditions and in clear water the visual system allows rheophilic fish to stay at a fixed location relative to the object used for entraining, bow wake swimming or Kármán gaiting. Since running water that impinges on an object causes sound waves, acoustic cues may serve the same function. The vestibular system informs fish about any active and passive movements in all three dimensions of space (Popper et al., 2003). Thus, this system may help fish to sense and avoid unwanted body displacements. With the aid of the lateral line fish can detect minute water motions and pressure gradients (for a review see Bleckmann, 1994; Montgomery et al., 1995). Therefore if visual input is poor the lateral line may be the most important sensory system used by fish for microhabitat selection and station holding.

2 Flow Control during Entrainning

Liao et al. (2003) studied the flow control of station holding trout during Kármán gaiting. Kármán gaiting trout exploit the energy of discrete vortices as well as the average reduced velocity in the Kármán street. Motivated by the study of Liao et al. (2003), Pzybilla et al. (2010) studied the entraining behaviour in more detail. During entraining, considerably long sequences could be observed where trout had a stretched-straight body posture with the pectoral fins not extended and the body and tail fin showing no motions (no-motion sequences). These sequences were interrupted by sequences of irregular body and/or pectoral and tail fin motions (motion sequences), where trout need to adapt to unsteady flow fluctuations. From a fluid mechanical standpoint, no-motion sequences are only possible if the sum of all forces acting on the trout cancel to zero. Fig. 2 illustrates the forces affecting a trout while entraining, assuming a straight body profile. We separated the force components along the fish body in a drag and lift force in analogy to the flow around an airfoil angled to the flow (this angle is named the angle of attack or pitch angle). The drag force F_{drag} is pointing in the direction of the mean flow U_0 upstream of the fish's nose, the lift force F_{lift} is perpendicular to F_{drag} . The fish feels an incoming flow that is already affected by the presence of the cylinder, therefore the streamlines in this region have an angle of α to the horizontal. This leads to the resulting total force F_{outside} that would drive the fish away from the cylinder. However, there is an additional suction force F_{inside} , which is directed towards the cylinder due to the reduction of pressure in the gap between the fish's body and the cylinder where the flow is accelerated. In a no-motion phase during entraining, the trout can keep a stable entraining position only if the force F_{outside} , which depends on the pitch angle, is cancelled out by the counteracting suction force F_{inside} , which depends on the position of the fish's body relative to the cylinder. Thus, at a specific position next to the cylinder and for a specific pitch angle β the sum of the forces cancel to zero. If so, a fish can maintain its position without active body or

fin movements. The validity of this hypothesis has been shown by computational fluid dynamic (CFD) simulations of the flow around a fish body next to a cylinder and a plate for different pitch angles. The results show that the forces are highly reduced when (i) the trout hold station at a certain position next to the cylinder and (ii) when it maintains a certain pitch angle (Przybilla et al., 2010).

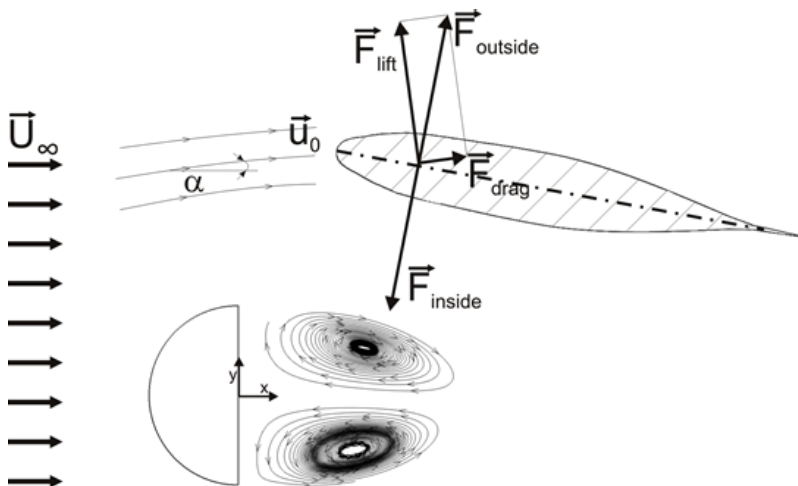


Fig. 2 Sketch of the principal forces acting on a trout while entraining next to a flow disturbance caused by a cylinder (from Przybilla et al., 2010). The virtual components of the lift and drag forces are added in the same way they would act on a pitched 2-D airfoil. The sum of the drag and lift forces results in an outward directed force $F_{outside}$. Due to the presence of the cylinder, fluid is accelerated in the gap between fish body and cylinder and wake, thus pressure is reduced in this region. Consequently, an additional force component is pointing towards the cylinder (F_{inside}), which is balancing the outward directed force. The sum of all forces cancels to zero, when the fish is in a perfect position relative to the cylinder and has the perfect pitch angle.

Behavioral observations showed that entraining trout ($N=8$) extended their pectoral fins more often ($72.9 \pm 30.9\%$, total observation time 858 s) than trout ($N=5$) swimming in steady flow ($8.6 \pm 10.4\%$, total observation time 462 s). Intact trout ($N=3$) that tended to entrain covered a distance of 37.18 ± 10.12 m in the flow tank (observation time 30 minutes), while the same trout after pectoral fins amputation covered a distance of 75.5 ± 47.2 m. This indicates that trout use their fins to adjust their body position and pitch angle as a corrective manoeuvre while entraining (Przybilla, 2012). It is argued that such correcting manoeuvres are necessary due to the unsteady character of the cylinder wake flow. These manoeuvres for fine-tuning of the pitch angle β (pitch control) during entraining are not only performed with the pectoral fins but also with the tail fin.

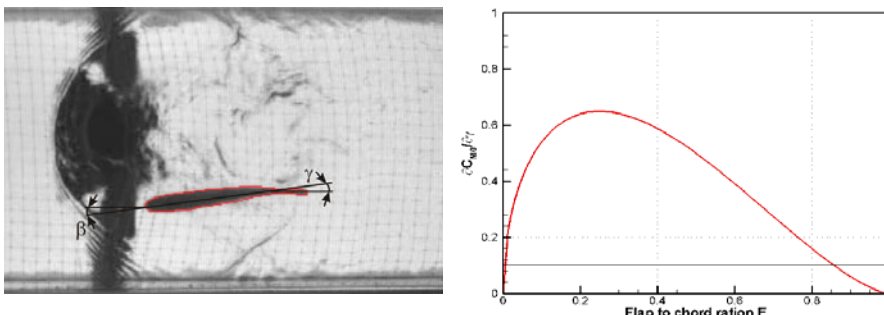


Fig. 3 Left. Ventral image of an entraining trout adapting its tail fin to balance the forces and pitching moment. The angle γ is the fin angle against the body. Right. Rate of change of zero flap moment coefficient C_{M0} over flap deflection angle γ for a plane flap airfoil at different flap-to-cord ratios E . Figure taken from Przybilla et al. (2010).

Again, aerodynamics may help to understand the role of the tail fin in pitch control as shown by Brücker (2006). He considered the body of the fish as the shape of an airfoil and the tail of the fish as a hinged flap, the chord length representing the total fish length L_C and the hinged flap length L_F representing the tail fin measured from the peduncle to the trailing edge of the fin. Thus, the hinged airfoil is characterized by the flap-to-chord length ratio $E = L_F / L_C$ and the flap deflection angle γ . For such a simplified airfoil, the solution of Glauert (1927) describes the rate of change of pitching moment of the foil as a function of E as follows:

$$\frac{\partial C_{M0}}{\partial \gamma} = -2\sqrt{E - (1-E)^3} \quad (1)$$

This equation demonstrates that $\partial C_{M0} / \partial \gamma$ is maximum at approximately $E=0.2$ (cf. Fig. 3). In other words, the rate of change of pitching moment and therefore the change of pitch angle β with small changes of flap deflection angle γ is highest at a flap-to-chord ratio of 0.2. Not surprising, a value of $E=0.2$ is typical for the fin-to-body length ratio in trout. Therefore, entraining trout are assumed to efficiently correct the pitch angle β by small adjustments of the tail fin angle γ .

3 Activity of Axial Swimming Muscles

As already mentioned above, rheophilic fish may prefer flows with predictable fluctuations over uniform currents to save energy (Cook and Coughlin, 2010; Taguchi and Liao, 2011). In steady flow, station holding trout activate their red axial swimming muscles in a rostro-caudal sequence. However, Kármán gaiting trout only activate their anterior axial red swimming muscles, a finding based on the analysis of only a few tail beat cycles (Liao, 2004). Since the activity of the axial red swimming muscles of trout has never been correlated with the preferred microhabitats while trout were swimming for longer periods of time in unsteady flow, we exposed trout ($N = 6$) to the

flow altered by a cylinder (diameter 5 cm) for three hours. We quantified the 3-D swimming coordinates of trout while continuously recording the activity of their axial red swimming muscles (for an example see Fig. 4). Our data show that muscle activity was significantly reduced not only during Kármán gaiting (as expected, Liao 2004), but also during bow wake swimming and entraining (an exemplary result is shown in Fig. 5). Since a high correlation exists between muscle activity and oxygen consumption (Cooke et al., 2004), our study helps to explain while entraining, bow wake swimming and Kármán gaiting trout save locomotory energy.

4 Importance of the Lateral Line System in Flow Control

The smallest functional unit of the lateral line is the neuromast, a sensory structure that occurs freestanding on the skin (superficial neuromasts) and in subepidermal fluid filled canals (canal neuromasts). Lateral line information reaches the central nervous system via the anterior, middle and posterior lateral line nerves (Northcutt, 1989). Lateral line nerves show ongoing activity even if no stimulus is present (Mogdans and Bleckmann, 1999; Münz, 1989). Adequate lateral line stimuli are low frequency (1-100 Hz) water movements (superficial neuromasts) and pressure gradients (canal neuromasts) (Bleckmann, 2007). Lateral line afferents terminate in the Medial Octavolateralis Nucleus (MON) of the medulla. From there, lateral line information is relayed to the midbrain Torus semicircularis and finally to the di- and telencephalon (Wullimann, 1998).

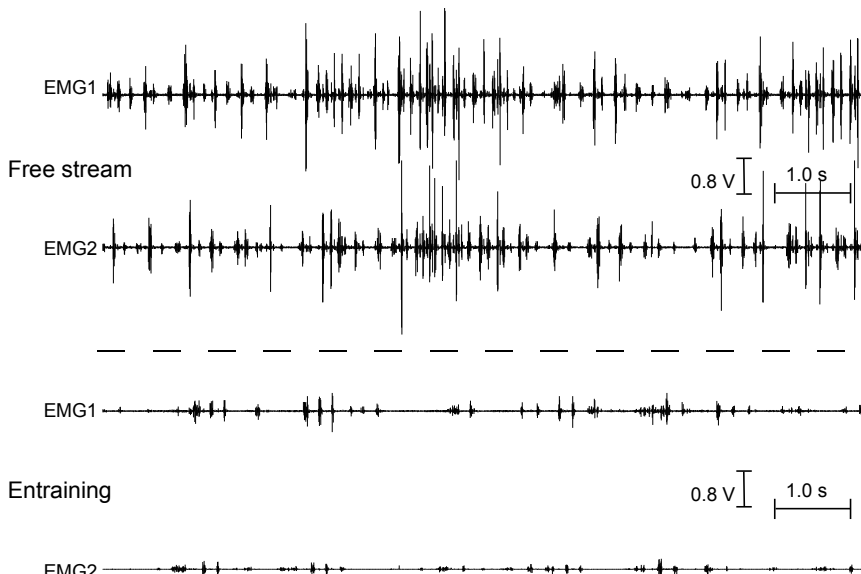


Fig. 4 Representative electromyograms recorded from the left (EMG 1) and right (EMG 2) red swimming muscles of a station holding trout while swimming in free stream (top) and during entraining (bottom). Flow velocity was 48 cm s^{-1} .

Fish use lateral line information for the detection of prey, predators, and conspecifics, for intraspecific communication and for rheotaxis (Bleckmann, 1994). Since many fish have up to several thousand SNs on each body side (e.g. Beckmann et al., 2010; Coombs et al., 1988), researchers originally assumed that lateral line information is also important for sensory feedback during locomotion. Contrary to this assumption, the performance of fish swimming freely in uniform flow remained unaffected when the lateral line was blocked (Dijkgraaf, 1963; Kesel et al., 1989). However, according to a recent study fish use hydrodynamic sensing to modulate the amplitude of undulatory swimming (McHenry et al., 2010).

If swimming in steady flow hardly requires lateral line input, at least manoeuvring through unpredictable and unsteady flow may benefit from the ability to sense minute changes in the hydrodynamic environment. For instance, unpredictable flow fluctuations destabilize entraining or swimming trajectories and thus may increase the cost of locomotion. To address this question, researchers compared the swimming behavior of intact and lateral line ablated trout in unsteady flow. A bilateral denervation of the posterior lateral line nerve reduced the degree to which trout entrained on objects when visual cues were omitted (Sutterlin and Waddy, 1975). Kármán gait kinematics changed when the lateral line was blocked, indicating that hydrodynamic feedback was used to alter motor output (Liao, 2006).

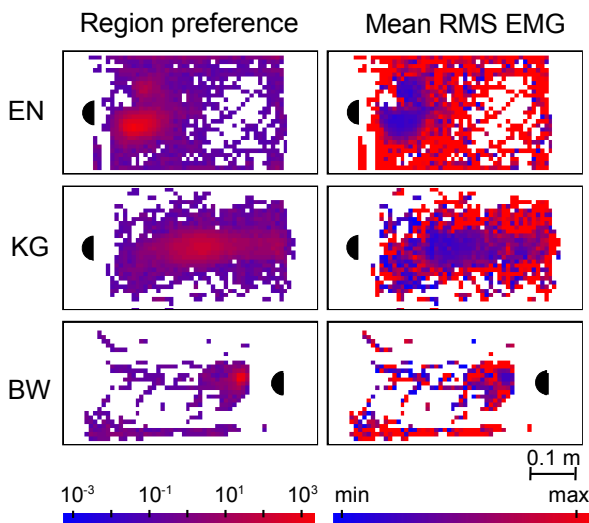


Fig. 5 Color coded region of preference (left) and mean RMS EMG-amplitudes (right) as a function of space. Note that trout preferred areas in the flow tank that allowed fish to reduce muscle activity. Bulk flow velocity was $48 \text{ cm} \cdot \text{s}^{-1}$ (EN, entraining), $28 \text{ cm} \cdot \text{s}^{-1}$ (KG, Kármán gaiting and BW, bow wake swimming).

Surprisingly, trout still show entraining, bow wake swimming and Kármán gaiting in complete darkness (Liao, 2006). They even do so when the lateral line system is blocked although in this case trout that tend to Kármán gait in the light now prefer entraining. The flow fluctuations caused by a cylinder exposed to running water are unsteady but still fairly predictable (Vogel 1983). This may be the reason why trout continued to hold station even if neither their visual nor their lateral line system provided sensory information. To make things less predictable, we confronted trout with the water movements caused by a cylinder that was moved perpendicular to bulk flow direction. Albeit moving, such a cylinder continues to shed vortices (Fig. 6).

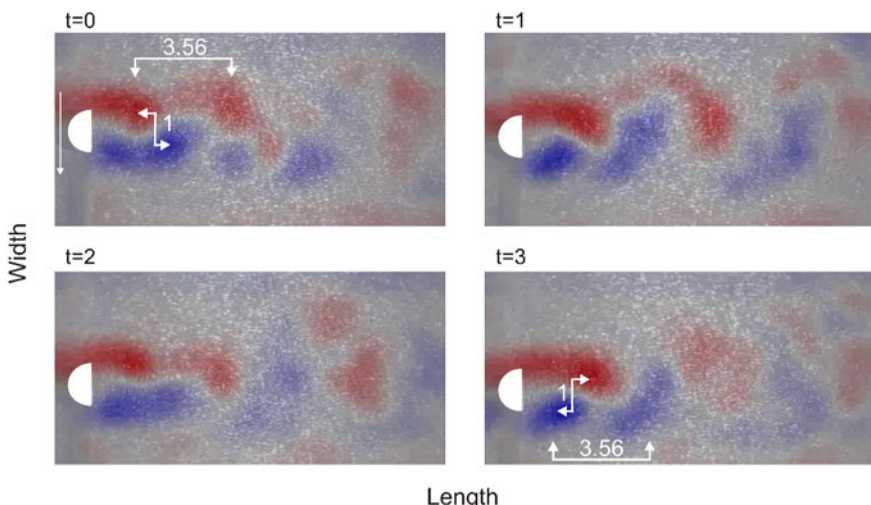


Fig. 6 Water flow in the vicinity of a cylinder (white hemi-circle) that moved with a velocity of 1 cm s^{-1} three cm perpendicular to bulk flow direction (as indicated by the vertical white arrow in $t = 0$). The size of each measurement plane is $24 \times 43 \text{ cm}$ (width x length); pictures are separated by 1 s. Note the vortices of alternating sign (red = clockwise, blue = counter-clockwise) downstream of the cylinder. The distance between successive vortices on each side of the vortex street and the distance between the central lines of the two alternating rows of vortices remained (Vogel, 1983) at a ratio of approximately 1:3.6 (white lines and arrows at $t = 0$ and $t = 3$) indicating a stable Kármán vortex street. Flow was from left to right.

4.1 Effect of Blocking the Lateral Line

To learn whether trout are able to follow a moving cylinder while entraining, Kármán gaiting or swimming in the bow wake zone, the cylinder was moved perpendicular to bulk flow direction with a velocity of 1 cm s^{-1} . In some experiments, visual and/or lateral line information was restricted by using infrared (IR) illumination and/or by pharmacologically (Kaus, 1987) or surgically (cutting the posterior lateral line nerves

bilaterally) (c.f. Sutterlin and Waddy, 1975) blocking the lateral line. Intact station holding trout generally followed the movements of the cylinder, but sometimes moved away from it to then immediately repositioning themselves after the cylinder movement had come to a halt (re-positioning instead of a successful station holding trial). Intact trout performed $48.9 \pm 21.8\%$ successful station-holding trials in the light and $41.8 \pm 28.7\%$ in the dark. Trout followed the cylinder movements whether they were entraining, Kármán gaiting or swimming in the bow wake zone (for examples see Figs. 7, 8). Trout ($N=5$) treated with streptomycin were still able to follow the cylinder in the light. However, under IR illumination successful station holding trials dropped to $2.0 \pm 2.7\%$. Thus, without visual cues lateral line information is needed if the object used for station holding is moving.

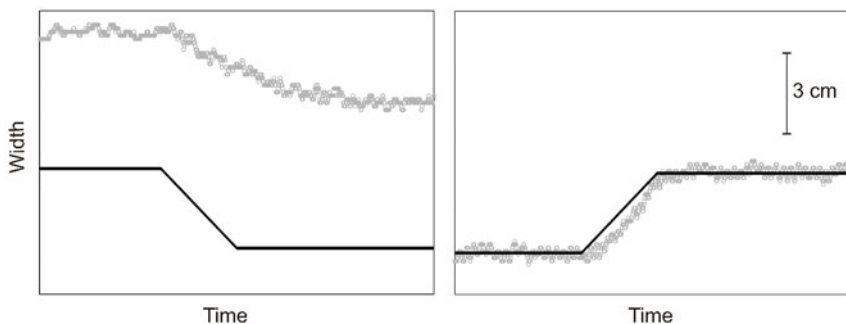


Fig. 7 The position of trout (grey, the snout served as a reference point) in the flow tank. Black lines indicate the position of the cylinder. The x-axis represents time, the y-axis the width of the working section of the flow tank. Flow was from left to right. The trout in the left graph was entraining, that in the right graph was swimming in the bow wake zone. Note that trout followed the cylinder movement. Data points are separated by 1 s.

4.2 Effect of Ablated Telencephalon

As has been shown, intact trout use visual, acoustic (most likely) and lateral line information for station holding in the vicinity of an object (Liao, 2006; Przybilla et al., 2010). The neural substrate used by fish for entraining, bow wake swimming or Kármán gaiting has not yet been uncovered. Most likely medullary and perhaps midbrain circuits are involved in these behaviors. However, since all sensory systems of fish project to the dorsal telencephalon (for a review see Wullimann, 1998) forebrain areas may also be involved in microhabitat selection. To address this question, we compared the spatial behavior of intact trout with that of trout whose telencephalon was ablated.

Removal of the telencephalon had no obvious influence on the swimming behavior of trout, irrespective of whether trout were exposed to the flow regimes caused by an upstream plate (length 12 cm, height 10 cm, thickness 5 cm; $N=4$) or cylinder ($N=1$). Telencephalon ablated trout continued to entrain, but sometimes also used the high-pressure, reduced-flow bow wake zone in front of the cylinder.

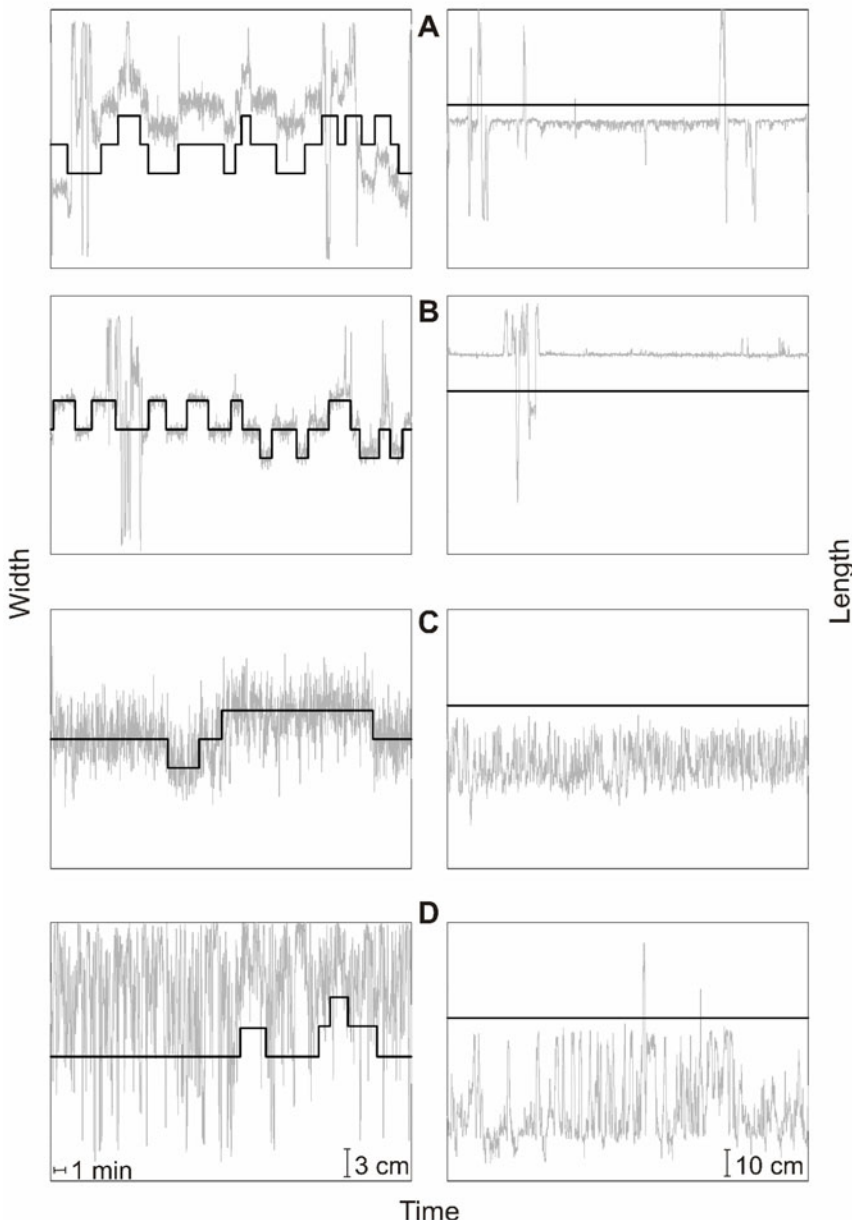


Fig. 8 The positions of trout (grey, snout served as reference point) in the flow tank. The y-axis represents the width (left) and length (right) of the working section, the x-axis represents time. Black line: position of cylinder. Flow was from top to bottom. In the cases shown intact trout were swimming in the entraining (A) and bow wake zone (B). Note that intact trout held their position relative to the cylinder even if the cylinder was moving. C, D. Movements of two streptomycin treated trout. Data points are separated by 1 s.

4.3 Medullary Recordings

Behavioral data have shown (see above) that manoeuvring through unsteady and non-uniform flow in the dark requires fish to sense minute changes in their hydrodynamic environment. This is not surprising given that the lateral line is highly sensitive to water motions and local pressure gradients (see above). According to several studies (for a review see Liao 2007), one type of stimulus fish encounter in their natural habitat are the vortices shed by inanimate objects exposed to running water (Vogel, 1983) as well as the vortex motions found behind a swimming fish (e.g. Bleckmann et al., 1991; Blickhan et al., 1992; Brücker and Bleckmann, 2007). Primary lateral line afferents that innervate superficial neuromasts are sensitive to vortex motions. Consequently, the amplitudes of their spike train frequency spectra peak at the vortex shedding frequency (Chagnaud et al., 2007). Thus, the fish brain not only receives vortex information (see also Chagnaud et al., 2006), but should also be able to determine the frequency with which an object sheds vortices. Assuming that fish can measure bulk flow velocity (a possible correlation mechanism to determine bulk flow from the lateral line system has been discovered by Chagnaud et al. 2009), they should also be able to calculate the size of an upstream object (Yang et al., 2011; Klein et al. 2011). If stimulated with a vortex street, 20 out of 31 MON units responded with bursts of spikes whose frequency matched the vortex shedding frequency (for one example see Fig. 9). Thus, both primary lateral line afferents and secondary lateral line units encode certain aspects of a vortex street. The representation of the vortex shedding frequency was better in MON units than in primary lateral line afferents (Klein and Bleckmann, unpublished). Thus central mechanisms lead to an improved signal-to-noise ratio.

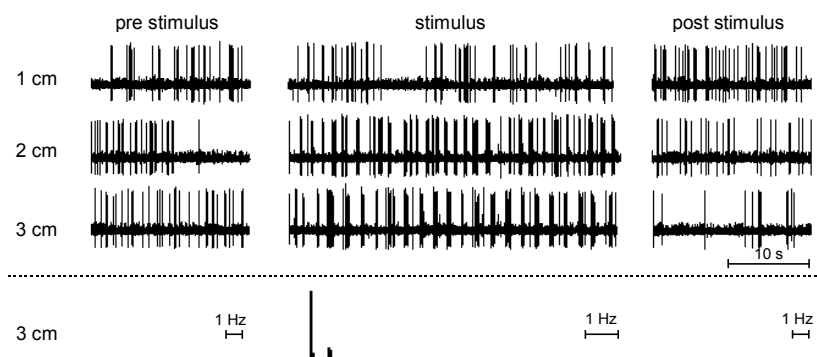


Fig. 9 Responses of a MON unit to uniform flow (left and right) and to the vortex motions caused by a cylinder of 1, 2, and 3 cm diameter (middle). Flow velocity varied between 6 and 7 cm s^{-1} . Note that the activity of the unit was fairly regular in uniform flow. Bottom: Spectral composition of the neuronal responses. The peak in the middle spectrum at 0.56 Hz was close to the measured vortex shedding frequency (0.63 Hz).

4.4 Dynamics of Body-Surface Pressure Distribution

The last part addresses further aspects that might be important for a highly efficient flow control in station holding fish. As previously stated (above), a complex situation occurs when trout are exposed to unsteady flow conditions along their body caused by wake vortices, turbulences or large-scale flow currents that affect the pressure distribution around the body of the fish. For hydrodynamic sensory systems like the lateral line it may be difficult to distinguish external flow signals from the flow signals generated by the fish's own body movements. Therefore, we need to understand the flow conditions during undulatory swimming, before we can speculate about possible adaptations of the peripheral lateral line (Coombs et al., 1988; Schmitz et al., 2008), especially in the caudal part of the body.

Experiments were carried out in the lab using a silicone membrane, which was actuated to move in an undulatory motion pattern (see Fig. 10). The membrane was mounted on a transverse and was placed within a water channel. PIV measurements were taken for different flow conditions and undulatory frequencies, details are given in (Kunze and Brücker, 2011). A complete presentation of the pressure field along an undulating membrane is given in Fig. 10. It shows that there is a dynamic variation of positive and negative pressure gradients along the body contour. Accordingly, the lateral line of a swimming fish is continuously stimulated with the frequency of trunk undulation. The pressure field is controlled by the amplitude change occurring from the head to the tail fin. How these excitations are separated from external flow signals is still not known.

In addition to the oscillating pressure gradient cycle there is a well-defined oscillatory cycle of transition to turbulence and re-laminarisation that prevents flow separation and offers thrust generation in an elegant way. The RMS-values of velocity and the measured boundary layer profiles in Kunze and Brücker (2011) demonstrate that transition to turbulence is triggered in the boundary layer at the windward side of the wave crest. The calculated pressure fields allow one to identify a pressure maximum in this region that causes transition to turbulence. This is due to a flow deceleration at the windward side of the wave crest caused by the positive pressure gradient. Further downstream, flow undergoes re-laminarisation in the region of the leeward side of the wave crest where fluid is accelerated again.

What happens to the sensory detection when this cycle is disturbed by external pressure or flow fluctuations? Typical disturbances consist, for example, of vortex structures left in the wake of a fish (Brücker and Bleckmann, 2007). Therefore, we studied the impact of the undulating wall with a 2-D vortex structure and the interaction within the wave cycle in a towing experiment. The visualizations (cf. Fig. 11) demonstrate that trout may gain maximum thrust from the pressure field of the vortex when the undulatory wave-type motion is controlled so that the vortex center is always close to the leeward side of the wave crest.

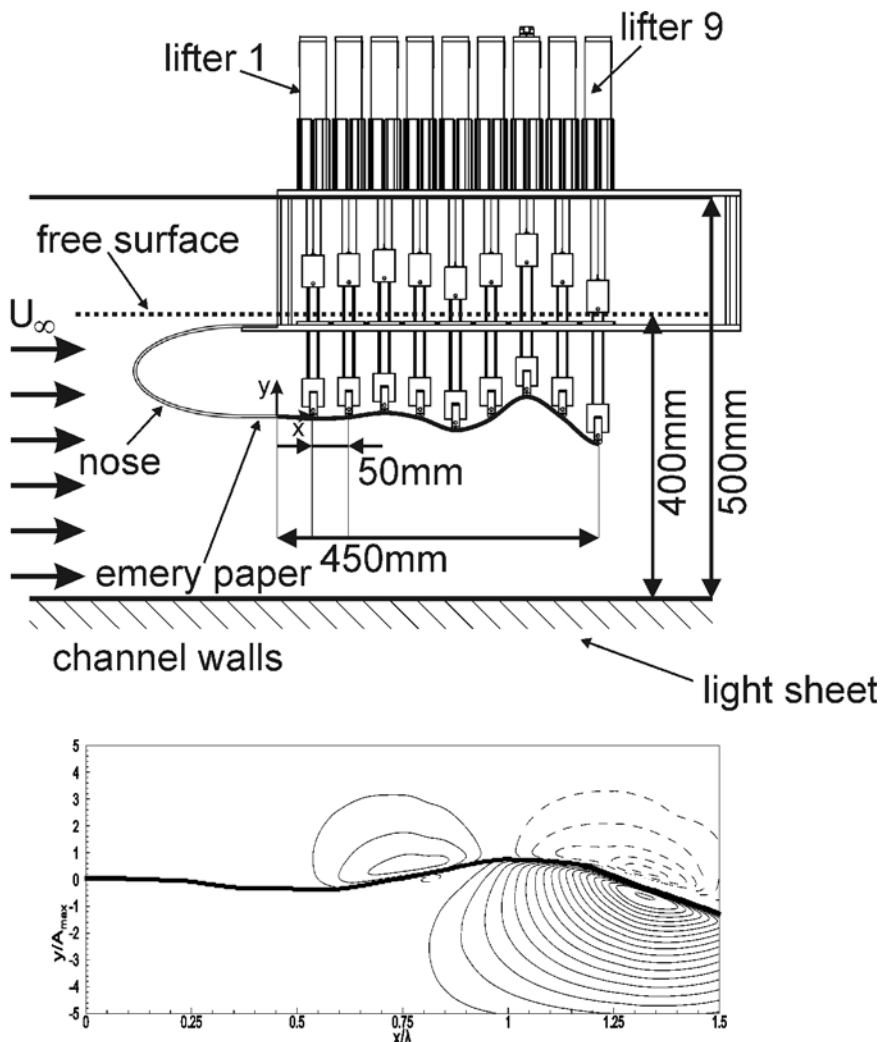


Fig. 10 Top: experimental flow studies with an undulating membrane, actuated with 9 lifter motors; Bottom: pressure distribution along the undulating membrane (thick black line) for one time instant of the motion, dashed lines shows contours of negative pressure (relative to ambient pressure), continuous lines show contours of positive pressure. Figure from Kunze and Brücker (2011).

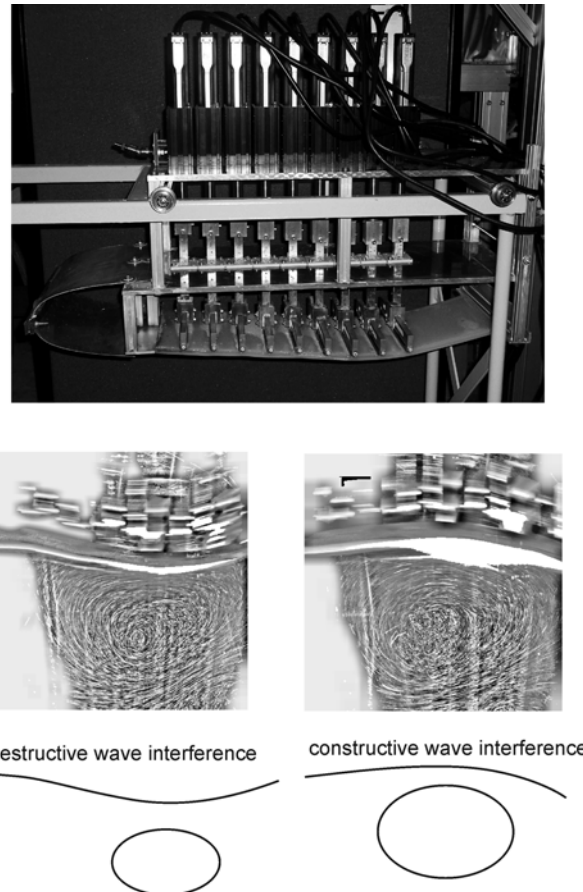


Fig. 11 Top: picture of the membrane device on the rolling traverse, which is put in the water tank and towed from right to the left with a constant velocity while undulating with a preset frequency. Before the membrane was started to move, a vortex was generated in the tank that stayed at a defined position for longer times. After vortex generation, the undulating membrane was started to move over the vortex with the towing traverse; experiments were repeated with different phase-shift of undulatory frequency and traverse motion over the vortex. Center: visualization of wall-vortex interaction when towing the undulating membrane model from right to left over the stationary vortex structure (left: phase shift such that the membrane crest hits the vortex; right: phase shift such that the membrane rolls over the vortex with its valley). Note that fish may gain maximum thrust from the pressure field of the vortex when the undulatory wave-type motion is controlled so that the vortex center is always close to the leeward side of the wave crest. Then, there is a constructive wave interaction contributing to the thrust producing pressure distribution on the membrane. Figure from Kunze (2011).

5 Conclusions

As has been shown (e.g. Liao et al., 2003; Przybilla et al., 2010 and this study) undulatory swimming fish exhibit a wide variety of mechanisms that contribute to energy savings and energy harvesting in natural environments as well as in controlled laboratory conditions. During daytime and in clear water vision is the dominant sense used for station holding. However, during nighttime and in murky waters fish need lateral line input for spatial orientation, at least if hydrodynamic conditions are unpredictable. But which hydrodynamic information is essential for station holding in unpredictable flow? Only further experiments in which fish that are exposed to unpredictable and unsteady flow regimes are studied, promise to shed insight into the sensory information fish need for station holding in complex hydrodynamic environments if visual cues are not available. The peripheral lateral line of rheophilic fish species can be quite different (e.g. Beckmann et al., 2010; Engelmann et al., 2002). To find possible peripheral adaptations to complex hydrodynamic environments more cross-disciplinary studies are needed where the lateral line will be stimulated with quasi natural flow fluctuations while recording from peripheral and central units. We should try to uncover the brain areas that allow fish to cope with unsteady flow fluctuations. If we stimulate the lateral line with complex stimuli (e.g. a vortex street), responses should be correlated with PIV measurements to uncover the temporal and/or spatial stimulus parameters to which a unit is most sensitive (Chagnaud et al., 2006). Qualitative descriptions such as average water velocity or vorticity may not be sufficient.

Up to now nearly all electrophysiological studies have been done with immobilized fish. Unfortunately such fish will not experience a natural stimulus situation. In unsteady flow, both the body and the fins of a fish will be displaced by the flow fluctuations. To counteract these displacements, a fish must perform certain fin and body movements. Both, passive and active body and fin movements will stimulate the lateral line receptors. Superimposed on the neuronal activity caused by active and passive movements (Palmer et al., 2003) is the neuronal activity caused by externally generated flow fluctuation. Whether and how fish distinguish between these two events is not clear. A freely swimming fish will also activate its efferent lateral line system. This in addition will determine the lateral line information that reaches the brain. We suggest to record peripheral and central lateral line responses from freely swimming fish (Palmer et al., 2003). In addition, we should study species that prefer different hydrodynamic environments. In so doing we may learn how the spatial arrangement of lateral line neuromasts influences signal processing and signal filtering. For example, the question remains how fish can sense and distinguish prey-related vortex structures from natural turbulent fluctuations. Further CFD studies might help to analyze the interference of self-propulsion effects and external flow disturbances on the boundary layer flow around the fish's body and the pressure distribution along the lateral line. This is subject of ongoing research in our group.

Acknowledgements. We thank our graduate students Jan Winkelkemper, Simon Kranz and Felix Kaldenbach who contributed to the electrophysiological experiments. We are grateful to Vera Schlüssel and Joachim Mogdans for carefully reading and commenting on the manuscript. Funding was provided by the DFG (SPP 1207, BI 242/12 and BR 1494/10), which is greatly acknowledged here.

References

- Beckmann, M., Eros, T., Schmitz, A., Bleckmann, H.: Number and distribution of superficial neuromasts in twelve common European cypriniform fishes and their relationship to habitat occurrence. *Intern. Rev. Hydrobiol.* 95, 273–284 (2010)
- Bleckmann, H.: Reception of hydrodynamic stimuli in aquatic and semiaquatic animals. In: Rathmayer, W. (ed.) *Progress in Zoology*, vol. 41, pp. 1–115. Gustav Fischer, Stuttgart (1994)
- Bleckmann, H.: Peripheral and central processing of lateral line information. *J. Comp. Physiol. A* 194, 145–158 (2007)
- Bleckmann, H., Breithaupt, T., Blickhan, R., Tautz, J.: The time course and frequency content of hydrodynamic events caused by moving fish, frogs, and crustaceans. *J. Comp. Physiol. A* 168, 749–757 (1991)
- Blickhan, R., Krick, C., Breithaupt, T., Zehren, D., Nachtigall, W.: Generation of a vortex-chain in the wake of a subundulatory swimmer. *Naturwissenschaften* 79, 220–221 (1992)
- Brücker, C., Bleckmann, H.: Vortex dynamics in the wake of a mechanical fish. *Exp. Fluids*, 799–810 (2007)
- Chagnaud, B.P., Bleckmann, H., Engelmann, J.: Neural responses of goldfish lateral line afferents to vortex motions. *J. Exp. Biol.* 209, 327–342 (2006)
- Chagnaud, B.P., Bleckmann, H., Hofmann, M.: Kármán vortex street detection by the lateral line. *J. Comp. Physiol. A* 193, 753–763 (2007)
- Cook, C.L., Coughlin, D.J.: Rainbow trout *Oncorhynchus mykiss* consume less energy when swimming near obstructions. *J. Fish Biol.*, 1–8 (2010)
- Cooke, S.J., Thorstad, E.B., Hinch, S.G.: Activity and energetics of free swimming fish; insights from electromyogram telemetry. *Fish Fisheries* 5, 21–52 (2004)
- Coombs, S., Janssen, J., Webb, J.F.: Diversity of lateral line systems: evolutionary and functional considerations. In: Atema, J., Fay, R.R., Popper, A.N., Tavolga, W.N. (eds.) *Sensory Biology of Aquatic Animals*, pp. 553–593. Springer, New York (1988)
- Dijkgraaf, S.: The functioning and significance of the lateral line organs. *Biol. Rev.* 38, 51–106 (1963)
- Enders, E.C., Boisclair, D., Roy, A.G.: The effect of turbulence on the cost of swimming for juvenile Atlantic salmon (*Salmo salar*). *Can. J. Fish. Aquat. Sci.* 60, 1149–1160 (2003)
- Engelmann, J., Hanke, W., Bleckmann, H.: Lateral line reception in still- and running water. *J. Comp. Physiol. A* 188, 513–526 (2002)
- Glauert, H.: Theoretical relationships for an aerofoil with hinged flap. *Aero. Res. Cttee. R and M*, 1095 (1927)
- Kaus, S.: The effect of aminoglycoside antibiotics on the lateral line organ of *Alocheilus lineatus* (Cyprinodontidae). *Acta Otolaryng (Stockh)* 103, 291–298 (1987)
- Kesel, A., Blickhan, R., Nachtigall, W.: Ablation of posterior lateral line organ. Does it effect steady swimming. In: Elsner, N., Singer, W. (eds.) *Dynamics and Plasticity in Neuronal Systems*, p. 265. Georg Thieme, Stuttgart (1989)
- Klein, A., Bleckmann, H.: Determination of object position, vortex shedding frequency and flow velocity using artificial lateral line canals. *Beilstein. J. Nanotechnol.* 2, 276–283 (2011)

- Kunze, S.: Untersuchungen zur Strömungs-Struktur Interaktion an dynamisch bewegten, flexiblen Oberflächen. Dissertation TU Freiberg, Freiberg (2011)
- Kunze, S., Brücker, C.: Flow control over an undulating membrane. *Exp. Fluids* 50, 747–759 (2011)
- Liao, J.C.: Neuromuscular control of trout swimming in a vortex street: Implications for energy economy during the Kármán gait. *J. Exp. Biol.* 207, 3495–3506 (2004)
- Liao, J.C.: The role of the lateral line and vision on body kinematics and hydrodynamic preference of rainbow trout in turbulent flow. *J. Exp. Biol.* 209, 4077–4090 (2006)
- Liao, J.C.: A review of fish swimming mechanics and behaviour in altered flows. *Phil. Trans. R Soc. Lond. B* 362, 1973–1993 (2007)
- Liao, J.C., Beal, D.N., Lauder, G.V., Triantafyllou, M.S.: The Kármán gait: Novel body kinematics of rainbow trout swimming in a vortex street. *J. Exp. Biol.* 206, 1059–1073 (2003)
- McHenry, M.J., Michel, K.B., Stewart, W., Müller, U.K.: Hydrodynamic sensing does not facilitate active drag reduction in the golden shiner (*Notemigonus crysoleucas*). *J. Exp. Biol.* 213, 1309–1319 (2010)
- Mogdans, J., Bleckmann, H.: Peripheral lateral line responses to amplitude modulated hydrodynamic stimuli. *J. Comp. Physiol. A* 185, 173–180 (1999)
- Montgomery, J., Coombs, S., Halstead, M.: Biology of the mechanosensory lateral line in fishes. *Rev. Fish Biol. Fisheries* 5, 399–416 (1995)
- Montgomery, J.C., Macdonald, F., Baker, C.F., Carton, A.G., Ling, N.: Sensory integration in the hydrodynamic world of rainbow trout. *Proc. R Soc. Lond. B (Suppl.)*, 195–197 (2003)
- Münz, H.: Functional organization of the lateral line periphery. In: Coombs, S., Görner, P., Münz, H. (eds.) *The Mechanosensory Lateral Line Neurobiology and Evolution*, pp. 285–298. Springer, New York (1989)
- Northcutt, R.G.: The phylogenetic distribution and innervation of craniate mechanoreceptive lateral lines. In: Coombs, S., Görner, P., Münz, H. (eds.) *The Mechanosensory Lateral Line Neurobiology and Evolution*, pp. 17–78. Springer, New York (1989)
- Palmer, L.M., Giuffrida, B.A., Mensinger, A.F.: Neural recordings from the lateral line in free-swimming toadfish, *Opsanus tau*. *Biol. Bull.* 205, 216–218 (2003)
- Popper, A.N., Fay, R.R., Platt, C., Sand, O.: Sound detection mechanisms and capabilities of teleost fish. In: Collin, S.P., Marshall, N.J. (eds.) *Sensory Processing in Aquatic Environments*, pp. 3–38. Springer, Heidelberg (2003)
- Przybilla, A.: The swimming behavior of rainbow trout, *Oncorhynchus mykiss*, in turbulent water flow, p. 257. Dissertation. Faculty of Mathematics and Natural Sciences. University of Bonn, Bonn (2012)
- Przybilla, A., Kunze, S., Ruder, A., Bleckmann, H., Brücker, C.: Entrainment trout: A behavioural and hydrodynamic analysis. *J. Exp. Biol.* 213, 2976–2986 (2010)
- Schmitz, A., Bleckmann, H., Mogdans, J.: Organization of the superficial neuromast system in goldfish, *Carassius auratus*. *J. Morphol.* 269, 751–761 (2008)
- Sutterlin, A.M., Waddy, S.: Possible role of the posterior lateral line in obstacle entrainment by brook trout (*Salvelinus fontinalis*). *J. Fish Res. Bd. Canada* 32, 2441–2446 (1975)
- Taguchi, M., Liao, J.C.: Rainbow trout consume less oxygen in turbulence: the energetics of swimming behaviors at different speeds. *J. Exp. Biol.* 214, 1428–1436 (2011)
- Vogel, S.: Life in moving fluids. The physical biology of flow. Princeton University Press, Princeton (1983)
- Wullimann, M.F.: The central nervous system. In: Evans, D.H. (ed.) *The Physiology of Fishes*, pp. 245–282. CRC Press, New York (1998)
- Yang, Y., Klein, A., Bleckmann, H., Liu, C.: Artificial lateral line canal for hydrodynamic detection. *Applied Physics Letters* 99, 023701 (2011)

Learning from Dolphin Skin – Active Transition Delay by Distributed Surface Actuation

Andreas Pätzold, Inken Peltzer, and Wolfgang Nitsche

Abstract. The goal of this project was the development of an active laminarisation method in order to reduce skin friction drag. Laminar-turbulent boundary layer transition on unswept two-dimensional wings is mainly caused by Tollmien-Schlichting (TS-) waves. Based on an actively driven compliant wall as part of the wing's surface, a method for attenuation of these convective instabilities was developed. Different arrangements of piezo-membrane actuators were investigated with an array of highly sensitive surface flow sensors and appropriate control strategies. Spanwise differentiated and streamwise cascaded actuation were used as well as inclined wall displacement. The onset of transition could be shifted downstream by 100mm or six average TS-wave lengths. Additionally, the investigation of the boundary layer flow downstream of the active wall area and an efficiency estimation are presented in this contribution.

1 Introduction

Depending on the Reynolds number, transition can cause a tenfold increase in skin friction. Since friction drag accounts for 50% of an aircraft's overall drag, even a slight delay of laminar-turbulent transition towards a wing's trailing edge promises a significant improvement. TS-instability waves, which are small, frequency-dependent velocity fluctuations, are responsible for transition on many two-dimensional flow configurations. Their streamwise amplification can be reduced by some kind of damping.

Natural role models provide motivation for the development of TS-damping methods. Dolphins are well-known for their low overall drag, which results, amongst other mechanisms, from a combination of body shape and their specific skin properties [4]. By a certain muscle contraction, blood pressure or temperature

Andreas Pätzold · Inken Peltzer · Wolfgang Nitsche

Technische Universität Berlin, Institut für Luft- und Raumfahrt, Marchstr. 12, 10587 Berlin
e-mail: andreas.paetzold@TU-Berlin.de

variation, these marine mammals are able to control local damping and compliancy of their surface. By coupling the oscillating boundary layer flow instabilities to the damping surface, an energy transfer from the flow into the structure stabilises the boundary layer. The first to demonstrate this effect was Gaster in 1988 [5]. Later Carpenter designed compliant coatings for transition delay and developed an anisotropic plate-spring model of the surface [2]. One example is depicted in Figure 2(b). Maximum transition delay was obtained for one defined combination of spring constant, damping coefficient and alignment relative to the flow direction.

The requirements for transition delay on an aircraft's wing differ from water flows, because Reynolds number and relevant pressure forces are not comparable. The goal of the research project was the transfer of adjustable dolphin's skin properties to a wing in wind tunnel experiments by means of active wave control.

In the course of the project, required active wall properties were determinated out of base flow investigation. Slot actuator arrays proved to be unsuitable for producing clean counter waves. Only with piezo-polymer membrane actuators transition could be delayed. Since first unimorph type actuators could not be cascaded well, more compact cymbal type actuation elements were developed. At the same time, signal-to-noise ratio was improved and structural plus electronic coupling between sensors and actuator elements was removed. Newly developed model predictive control algorithms were applied.

2 Principle of Active Wall Damping

Dynamic stabilisation of transitional boundary layers has proved to be an effective method of drag reduction in past research [8, 10, 9, 3]. Destructive interference of naturally occurring boundary layer instabilities (TS-waves) and artificial counter waves resulted in a significant delay of transition. While manipulating the fluctuation profile of the boundary layer, the mean velocity distribution remains unmodified, see Figure 2(a). The counter waves were generated by discrete actuation strips with intermediate sensors on the wing. In the project, the locally restricted actuation method was meant to be extended towards large continuous 'active compliant wall' areas. Besides the enlargement of the actuation area, and thereby laminar flow region, the power consumption decreases.

For the determination of appropriate wall deflections, the detection of oncoming TS-waves upstream of the active wall was required, see Figure 1. The active wall consisted of several streamwise actuator elements which are linked by one common and continuous surface membrane. Up to five actuator elements were cascaded within one average TS-wave length. By deflection at different nodes, convective travelling counter waves were generated and TS-control was not constricted to a discrete position. The actuator-induced velocity fluctuation v' was then transformed

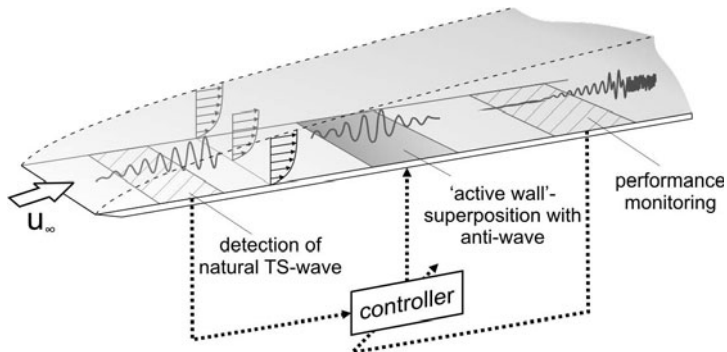


Fig. 1 General Principle of an Active Controlled Wall for TS-wave Damping

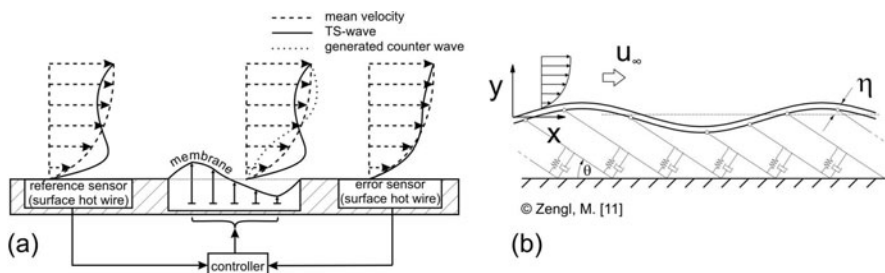


Fig. 2 Distributed Surface Actuation Mode;
 (a) Destructive Interference of TS-wave with Artificial Travelling Wave;
 (b) Model of an Anisotropic Compliant Wall, according to Zengl [11]

into a streamwise component u' by the flow itself. Figure 2(a) illustrates the working principle. Downstream surface sensors as well as flow field measurements with movable probes served for monitoring of the damping performance.

Because there were no sensors at the membrane, the controller had to compute counter wave signals for each actuator element in real time out of one upstream located, global reference sensor. For this purpose, an open-loop model predictive controller was developed and described in the associated contribution by Nikolas Goldin ("Chair of Measurement and Control" (MRT) at Technische Universität Berlin), [7]. It allowed direct damping as well as biomimetic damping of TS-waves. With direct damping, counter waves were calculated as inversion of the TS-wave over the active wall, which was estimated from the upstream measurements. With the biomimetic approach, the active wall area simulated compliant wall properties taken from literature [1, 2] and numerical investigations. The wall model as part of the control law corresponded to compliant wall properties. By altering its coefficients, it was possible to investigate different compliancy and damping parameters without touching the experimental setup.

3 Experimental Setup

All experiments were conducted in a low turbulence wind tunnel which was equipped with flow temperature control. An unswept two-dimensional wing model with a modified NACA0008 airfoil and a chord of $c = 1300\text{mm}$ was deployed. It featured a perturbation slot for the generation of artificial boundary layer instabilities at a chord position of $x = 300\text{mm}$.

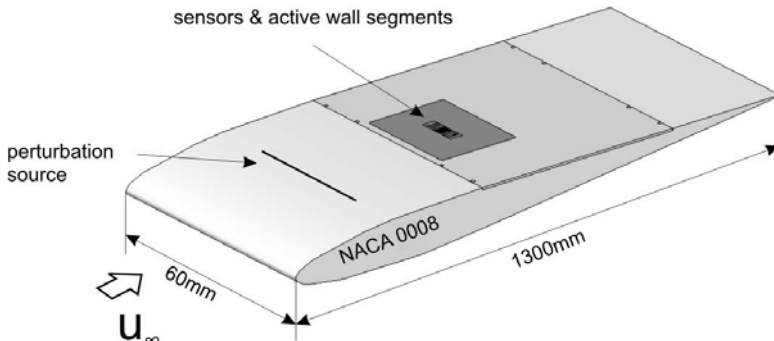


Fig. 3 Wing Model with Perturbation Source and Module for Sensors and Active Wall

Because the superposition principle only works within the linear regime of transition, very sensitive surface hot wire sensors were deployed. These surface-mounted hot wires ($\varnothing = 5\mu\text{m}$) allowed for the detection of the very small velocity fluctuations of TS-waves. They generated negligible surface roughness and provided a high signal to noise ratio as well as a 40kHz cut-off frequency at the used overheat ratio of 1.7. Figure 4 demonstrates that the sensors were not calibrated but adjusted for equal sensitivity. For this purpose a forced turbulent boundary layer was generated.

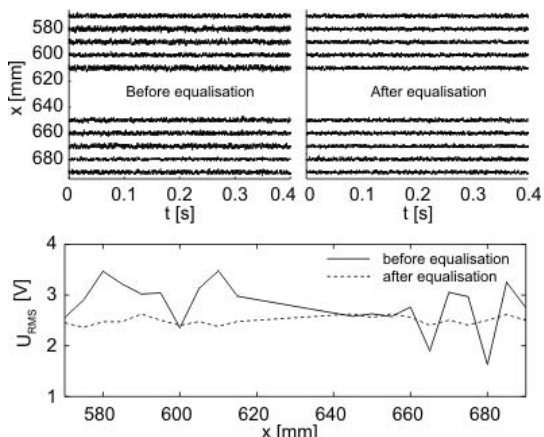


Fig. 4 Forced Turbulent Boundary Layer for Equalisation of Surface Hot Wire Sensor Output

Signals were captured and amplified via Constant Temperature Anemometry (CTA) modules with subsequent signal-conditioning units. They were processed by a real time application on a Digital Signal Processing (DSP) system, which calculated the required counter waves. A multi-channel high voltage amplifier produced the signals for driving the actuator.

All actuation devices were developed in collaboration with "Department of Microsystems Engineering" (IMTEK) at the University of Freiburg [6]. In the first part of the project, unimorph actuators were used. Due to their piezo-polymer composite structure, these beams converted alternating voltage signals into wall-normal deflections. More compact actuator elements were developed within the course of the project. These miniaturised cymbal-type actuators, that were used for all presented experiments, are described in detail in Daniel Haller's contribution.

4 Wind Tunnel Experiments

Wind tunnel experiments were conducted at a freestream velocity of $u_\infty = 24,5 \text{ m/s}$, a flow temperature of $T = 297 \text{ K}$ and angles of attack around $\alpha = 0^\circ$. This corresponds to a local Reynolds number of $Re_x \approx 1 \cdot 10^6$. The base flow was investigated with a single calibrated hot wire probe. Figure 5(a) shows the distribution of freestream velocity at $y = \delta_{99}$. With the convection velocity of TS-waves being approx. 35% of the local freestream velocity, one can determine the available calculating time for given distances between sensors and actuators. Boundary layer thickness δ_{99} and its steep increase at $x = 700 \text{ mm}$, due to the transition process, can be seen in Figure 5(b). Transition also went along with a typical decrease of the shape factor H_{12} at the same position. The amplified frequency range of TS-waves within the transition region is depicted in Figure 5(c). This means, that actuators had to cope with instable fundamental modes between 200Hz and 500Hz.

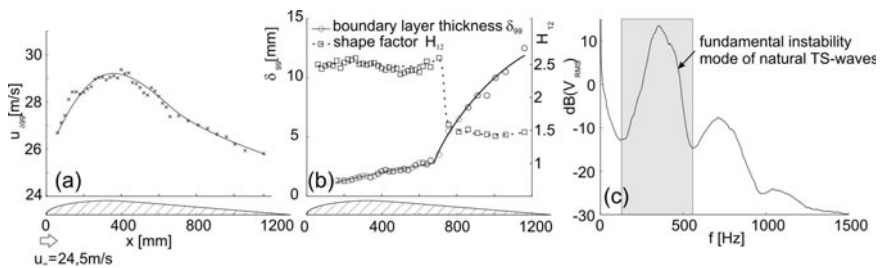


Fig. 5 Base Flow Conditions for $u_\infty = 24,5 \text{ m/s}$;
 (a) Local Distribution of Freestream Velocity for $y = \delta_{99}$;
 (b) Boundary Layer Thickness δ_{99} and Shape Factor H_{12} ;
 (c) Power Spectral Density within Transition Region ($x=650 \text{ mm}$; $y=0,1 \text{ mm}$)

According to these requirements, actuators were developed and integrated into the test wing. Different actuator arrangements were tested. The first configuration was an active wall with wall-normal membrane deflection for damping of two-dimensional TS-waves (4.1). The second experiment utilised a similar surface, but with inclined actuation (4.2). A cascade of three active wall segments was meant to maximise transition delay (4.3). Finally, spanwise differentiated actuator elements for attenuation of oblique TS-waves were used (4.4).

4.1 Active Wall for Damping of Two-Dimensional TS-Waves

Five single actuator elements were combined to an active wall with a streamwise dimension of $x = 30\text{mm}$. The distance between streamwise adjacent actuator elements was $\Delta x = 5\text{mm}$. In this way, the membrane could be displaced at five nodes within one TS-wave length. Each element acted on a membrane span of $z = 50\text{mm}$, see Figure 6(a). The membrane center was located at $x = 650\text{mm}$ within the linear TS-amplification stage. A total of 20 surface hot wires was distributed upstream and downstream of the membrane, as shown in Figure 6(b).

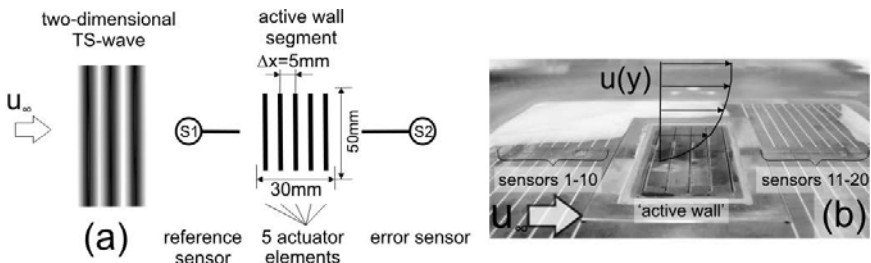


Fig. 6 Attenuation of Two-dimensional TS-waves;
 (a) Active Wall Configuration with Five Streamwise Actuator Elements;
 (b) Setup With Surface Hot Wire Sensors and Active Wall Actuator Integrated into Test Wing

Direct and biomimetic TS-damping schemes were tested with this setup. Figure 7 shows the effects of direct damping for different number of actuator elements in operation. As the streamwise development of boundary layer fluctuations shows in Figure 7(a), adding more elements improved damping quality. With the whole active wall moving, a maximum damping of local TS-amplitudes by 83,6% was obtained. It took a distance of 30mm behind the membrane until the lowest fluctuation levels were observed. Obviously, the introduced travelling waves needed this way for their conversion into a TS-counter wave within the boundary layer. In frequency domain, the best damping rate equaled 15,7dB at a position downstream of the actuator, see Figure 7(b).

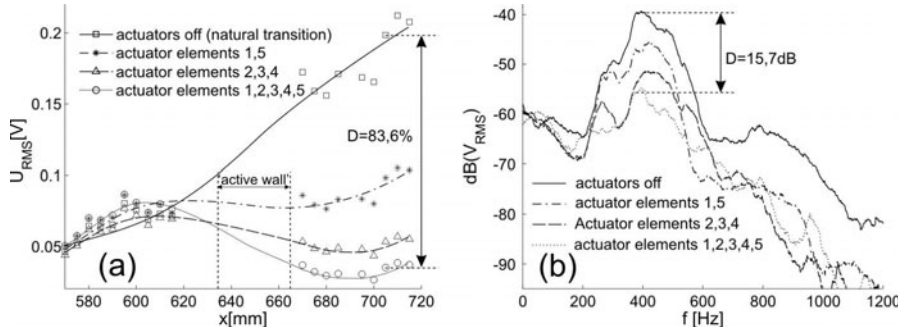


Fig. 7 Different Actuator Operating Modes;
(a) Streamwise TS-amplification;
(b) Error Sensor Power Spectra ($x=705\text{mm}$)

Although re-amplification started shortly after the actuator position, the damping effect was still visible far downstream. According to Figure 8(a), the reduction of instability fluctuations occurred up to a wall distance of $y \approx 2.5\text{mm}$. Figure 8(b) shows the transition location in terms of surface RMS-values for the cases of natural amplification of TS-waves and for TS-damping. This dataset was acquired by 20 surface hot wires and one moveable single hot wire probe. The latter was kept at the wall distance with maximum fluctuation amplitudes for each chord position.

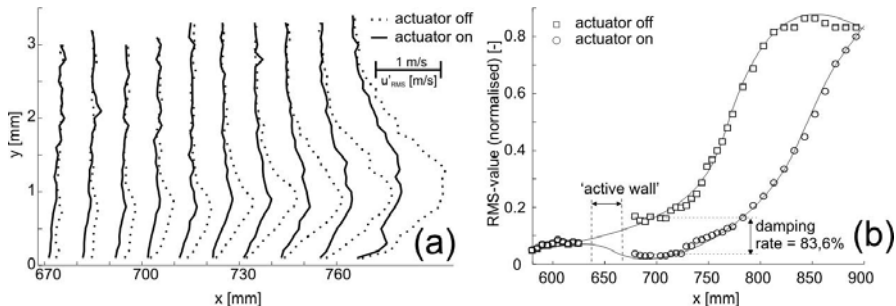


Fig. 8 Flow Field Downstream of Active Wall;
(a) Fluctuation Velocity Profiles;
(b) TS-amplification in Terms of Wall Fluctuation

The whole transition process was delayed downstream by $\Delta x \approx 100\text{mm}$ or six average TS-wave lengths.

Figure 9 illustrates ten snapshots of the active wall's deformation during control of TS-waves. Within 2ms one typical counter wave was transported across the membrane area. Peak deflection amplitudes of $y_m = \pm 20\mu m$ were generated, which corresponded to 0,6% of local boundary layer thickness δ_{99} . These deflection snapshots were derived from the computed controller output and the pre-identified actuator model. The reliability of the actuator model was verified by laser vibrometer measurements before.

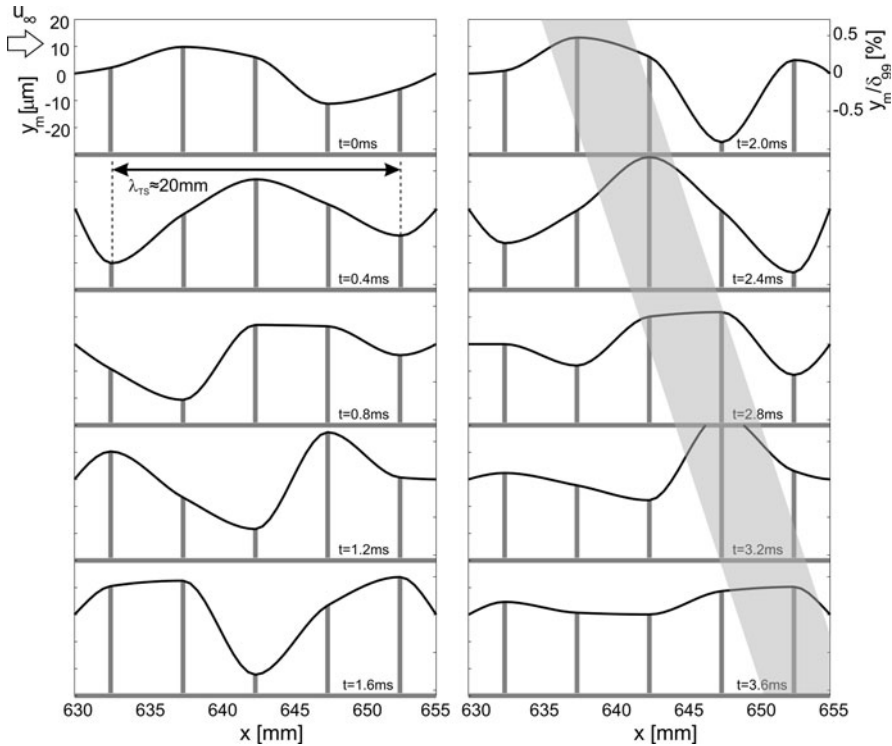


Fig. 9 Snapshots of Membrane Displacement During TS-wave Control

4.2 Inclined Actuation and Performance Estimation

Carpenter and Morris [2] have shown the advantage of so-called anisotropic compliant walls over isotropic ones concerning transition delay. An optimised anisotropic compliant surface according to Figure 2(b) generated a negative Reynolds stress which allowed complete laminarisation, when the whole wing surface was covered by it.

Its motion was planned to be emulated by an active wall segment with five inclined actuation elements, see Figure 10. With active wall actuation, improved damping rates rather than full laminar flow till the trailing edge were expected because only a very small amount of the wing's surface was covered by the membrane. The anisotropic wall structure suggested by Carpenter made a 'stiffness' angle of $\Theta \approx 30^\circ$ to the vertical. To achieve a similar effect, the designed active wall structure in Figure 10 featured a complementary 'compliance' angle of $\Theta_{act} = 60^\circ$. It provided a wall-normal and wall-parallel combined displacement ($u' + v'$) rather than only a wall normal displacement v' .

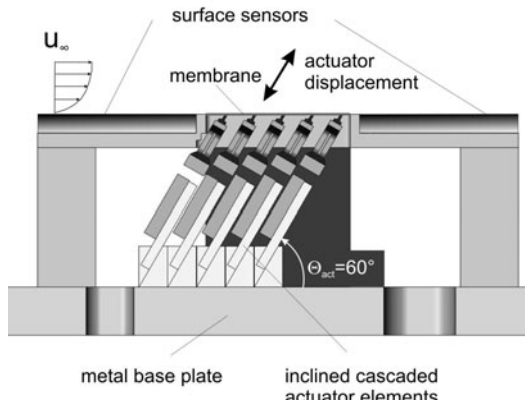


Fig. 10 Active Wall Configuration With Inclined Actuator Elements

Achievable damping rates with the inclined array of cymbal actuators showed a slight improvement compared to wall-normal actuation. With direct damping, 85,4% of local amplitude reduction was possible, see Figure 11(a). The frequency domain can be used for evaluation of the damping success. Dominating parts of the TS-wave packages can be identified in Figure 11(b) between 200 and 500 Hz at a sensor position 15mm downstream of the active wall. This fundamental mode of unstable TS-frequencies is followed by a second harmonic peak in the range between 600 and 1000Hz. The fundamental mode was damped by 16,7dB. Due to mode coupling, the second harmonic instabilities disappeared nearly completely.

Inclined actuation seemed to be more effective than wall-normal actuation, since the required input voltages of $U_{RMS} = 13,5V$ were similar.

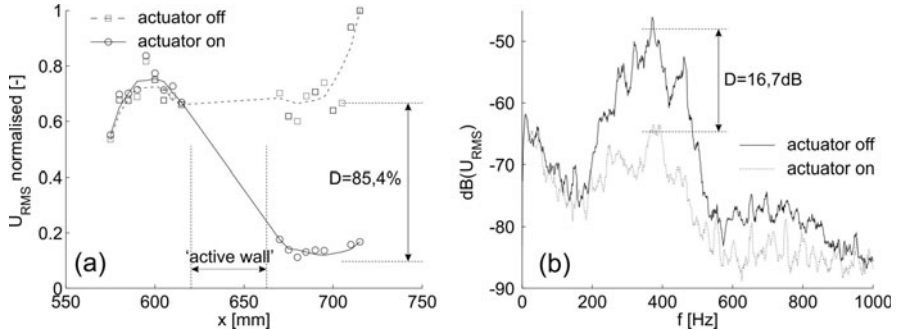


Fig. 11 Transition Delay with Inclined Actuator Elements;
(a) Damping Rate;
(b) Error Sensor Power Spectral Density

A maximum local skin friction reduction by approx. $\Delta \tau_w \approx 1 \text{Nm}^{-2}$ between $750 \text{mm} \leq x \leq 950 \text{mm}$ on a span of $z_{act} = 50 \text{mm}$ was derived from measured boundary layer velocity profiles, see Figure 12(a). For a freestream velocity of $u_\infty = 24.5 \text{ms}^{-1}$ the benefit added up to $P = u_\infty \cdot z_{act} \cdot \int \Delta \tau_w dx = 0.2 \text{W}$.

On the other hand, the time-dependent apparent power consumption of the actuator was determined. This running product of measured voltage and current is illustrated in Figure 12(b). The time-averaged amount of apparent power consumption was $|S| = U_{RMS} \cdot I_{RMS} = 137 \text{mVA}$ for each of the five actuator elements. Overall, an apparent power of 685mVA was observed. Additional overhead consumption was not considered because measurement electronics were not optimised for this purpose yet.

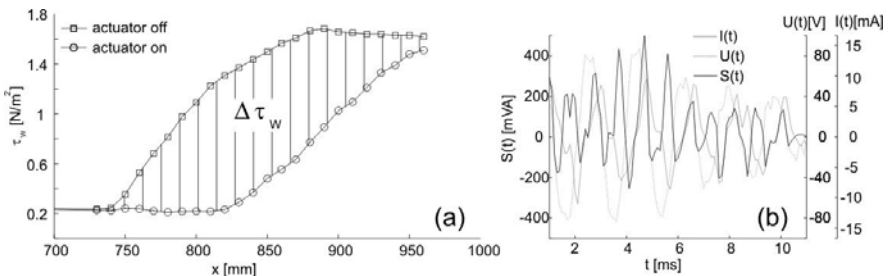


Fig. 12 Efficiency Estimation;
(a) Local Distribution of Skin Friction for Wing Center Line ($z=0$); (b) Power Consumption of Single Actuator Element During AWC

In summary, power efficiency of $\frac{P_{out}}{P_{in}} = 0.29$ at these low flow speed experiments may seem not entirely satisfying. With comparable damping rates at Mach 0.7, the potential of absolute skin friction reduction grows by a factor of 60, while energy consumption seems not to increase significantly [3].

4.3 Streamwise Repeated Actuation

An experimental setup with three active wall segments, which were cascaded in streamwise direction is shown in Figure 13(a). Amplification in streamwise direction was mostly affected by the first actuation segment in operation. With segments 2 and 3 added, only minor further transition delay was observed, see Figure 13(b). There seem to be two reasons for that behaviour. First of all, the spanwise range of $\Delta z = 50\text{mm}$ that was influenced by the active walls was too small. Unaffected TS-waves contaminated the re-amplification, beginning at the first active wall's edges. Therefore, actuation elements with a broader span would be necessary.

Second, mainly three-dimensional TS-waves remained in the boundary layer after the primary damping stage. The following active wall segments were not able to dampen these. Therefore, spanwise differentiated actuation is required.

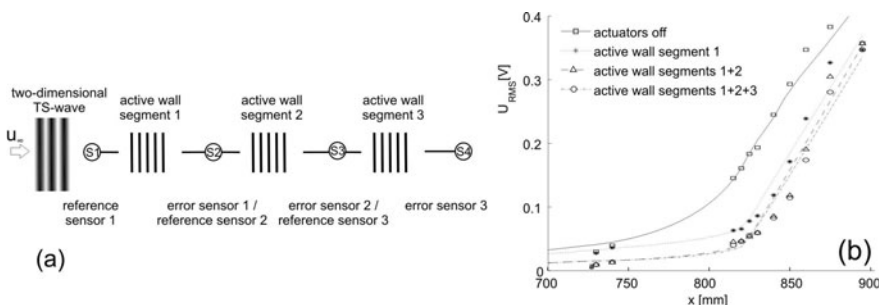


Fig. 13 Streamwise Extension;
 (a) Arrangement of Three Cascaded Active Walls;
 (b) TS-amplification

4.4 Spanwise Differentiated Actuation

For demonstrating the damping of three-dimensional TS-waves, two active wall segments were arranged in spanwise direction. Each consisted of three single actuator elements. This setup was able to generate spanwise differentiated counter waves. A smooth phase transition between the two rows is ensured by the flexible membrane. The whole active wall covered an area of $\Delta x \times \Delta z = 20\text{mm} \times 110\text{mm}$. Figure 14 displays the setup. A perturbation source with spanwise distributed slots was integrated into the wing's nose. Oblique travelling TS-waves could be generated by spanwise phaseshifted excitation with loudspeakers.

RMS-values of two parallel rows of surface sensors were analysed. Each row was located in the centerline of the corresponding actuation segment. Figure 15 demonstrates that both spanwise segments obtained comparable damping results. No dynamic coupling in z-direction resulted from the mechanical crosslink of the actuation segments by the membrane. So, both spanwise actuation segments were driven by independent control algorithms which saved calculation time.

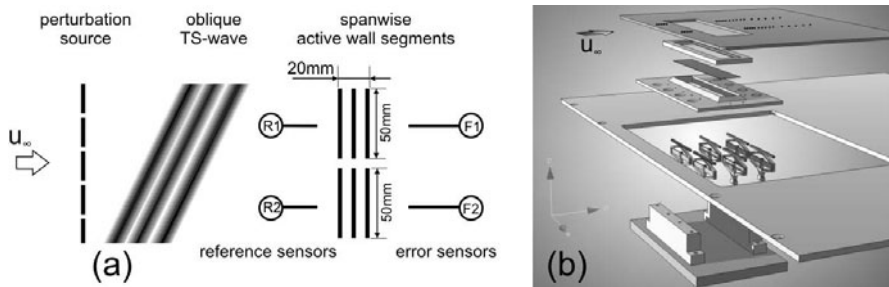


Fig. 14 Damping of Oblique TS-waves;
(a) Spanwise Distributed Arrangement;
(b) Actuator Design with Surface Sensors

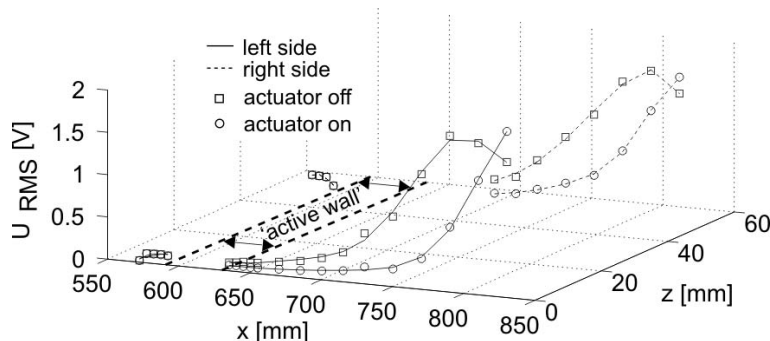


Fig. 15 Spanwise Delay of TS-amplification

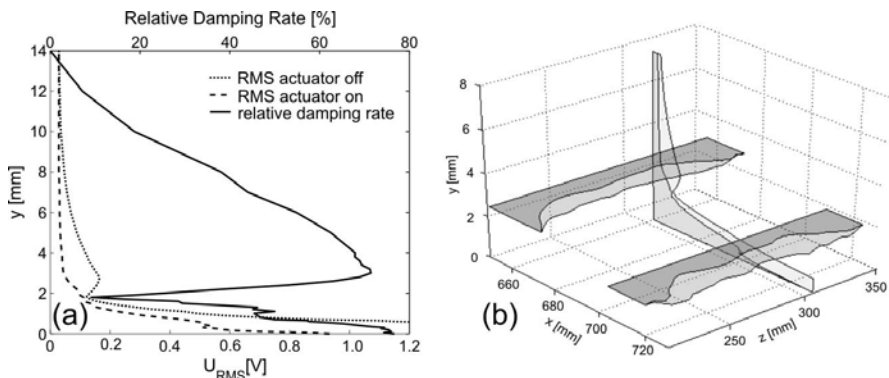


Fig. 16 Downstream Effect of Spanwise Distributed Actuation;
(a) Fluctuation Profiles and Damping Rate for $z=305\text{mm}$;
(b) Vertical and Spanwise Damping Rates

Furthermore, the distributions of velocity fluctuations and relative damping rate within the boundary layer were measured with a movable hot wire probe and plotted in Figure 16. At $z = 305\text{mm}$, which was in the centerline of the right actuation segment, damping rates varied between $D = 0$ and $D = 76\%$, depending on the wall distance, see Figure 16(a). Additional spanwise damping results can be observed for a wall distance of $y = 2,5\text{mm}$ in Figure 16(b). Damping rates were constant across the active wall area, even at the small gap between the spanwise segments.

5 Conclusions

A novel approach of active transition delay for low-speed wind tunnel experiments was developed. Distributed surface actuation was used on a unswept wing model. A five-stage 'active compliant wall' in combination with model predictive control algorithms was able to attenuate local instability amplitudes by 85,4% or 16,7dB. Transition was shifted towards the wing's trailing edge by $\Delta x \approx 100\text{mm}$. Inclined actuation had slight advantages over wall-normal actuation. The method's benefit is expected to improve with increasing Mach-numbers. Damping of three-dimensional TS-waves was successfully demonstrated. Future work would include an active wall for combined damping of two-dimensional and three-dimensional TS-waves. With increasing processing power, multi-channel actuator arrays become possible. An even broader range of optimal control could be realised in future in-flight experiments with pre-identified controller models.

Acknowledgements. This research project was funded by the German Research Foundation (DFG) within the framework of the priority program SPP 1207 "Strömungsbeeinflussung in Natur und Technik".

References

1. Carpenter, P., Garrad, A.: The hydrodynamic stability of flow over Kramer-type compliant surfaces. Part 1. Tollmien–Schlichting instabilities. *Journal of Fluid Mechanics* 155, 465–510 (1985)
2. Carpenter, P., Morris, P.: The effect of anisotropic wall compliance on boundary-layer stability and transition. *Journal of Fluid Mechanics* 218, 171–223 (1990)
3. Engert, M., Pätzold, A., Becker, R., Nitsche, W.: Active Cancellation of Tollmien-Schlichting Instabilities in Compressible Flows Using Closed-Loop Control. In: Morrison, J.F., Birch, D.M., Lavoie (eds.) IUTAM Symposium on Flow Control and MEMS. IUTAM Bookseries, pp. 319–331 (2008)
4. Fish, F., Lauder, G.: Passive and Active Flow Control by Swimming Fishes and Mammals. *Annu. Rev. Fluid Mech.* 38, 193–224 (2006)
5. Gaster, M.: Is the Dolphin a Red Herring? Turbulence Management and Relaminarisation. In: Liepmann, H.W., Narasimha, R. (eds.) IUTAM Symposium, Bangalore, India, pp. 285–304 (1988)
6. Haller, D., Pätzold, A., Losse, N., Peltzer, I., Nitsche, W., King, R., Woias, P.: A Piezo-polymer based movable wall for active cancellation of flow instabilities across airfoils. *Journal of Intelligent Material Systems and Structures* 22(5), 465–478 (2011)

7. King, R., Aleksic, K., Gelbert, G., Losse, N., Muminovic, R., Brunn, A., Nitsche, W., Bothien, M.R., Moeck, J.P., Paschereit, C.O., Noack, B.R., Rist, U., Zengl, M.: Model predictive flow control. In: 38th Fluid Dynamics Conference and Exhibit, AIAA 2008-3975, Seattle, Washington, June 23-26, pp. 2008–3975 (2008)
8. Milling, R.W.: Tollmien-Schlichting wave cancellation. *Physics of Fluids* 24, 979–981 (1981)
9. Opfer, H., Evert, F., Ronneberger, D.: On the potential and limitations of boundary-layer stabilization via active wave cancellation. In: Notes on Numerical Fluid Mechanics and Multidisciplinary Design. NNM, vol. 86, pp. 219–230. Springer (2003)
10. Sturzebecher, D., Nitsche, W.: Active Cancellation of Tollmien-Schlichting Instabilities on a Wing Using Multi-channel Sensor Actuator Systems. *International Journal of Heat and Fluid Flow* 24, 572–583 (2003)
11. Zengl, M., Rist, U.: Linear stability investigations of flow over yawed anisotropic compliant walls. In: Schlatter, P., Henningson, D.S. (eds.) *Proceedings of the Seventh IUTAM Symposium on Laminar-Turbulent Transition*, Stockholm, Sweden. IUTAM Bookseries, vol. 18, pp. 601–604. Springer, Berlin (2009)

Development and Fabrication of Active Microstructures for Wave Control on Airfoils

Daniel Haller, Sebastian Neiss, Michael Kroener, and Peter Woias

Abstract. Transition of an airfoil's boundary layer from the laminar to the turbulent flow regime increases the overall drag of an airplane significantly. The major origin of this transition are Tollmien-Schlichting (TS) waves. Similar to the dolphin's skin, a system that is capable to dampen TS waves locally is proposed here. A surface wave can interfere destructively with TS waves and thus delay transition towards the edge of the airfoil. For this purpose, an actuator array is combined with a thin membrane. The presented actuators were developed and improved continuously so that all requirements for the dampening of TS waves are fulfilled. Several actuators are cascaded in a compact manner and combined with a membrane and an array of sensors. The system has proven in wind tunnel experiments to be capable of dampening TS waves successfully and delaying transition.

1 Introduction

Transition of an airfoil's boundary layer increases skin friction which has a major influence on an airplane's overall drag. Delaying the point of transition towards the wing edge promises a significant decrease of the drag thus reducing the airplane's fuel consumption. The major origin of transition are boundary layer instabilities, so-called Tollmien-Schlichting (TS) waves [13]. These velocity instabilities are denoted as waves because they exhibit a wavelike behavior with a spectrum of different frequencies. TS waves are the first phenomenon in the process of transition. Their streamwise amplification ends up in a fully turbulent flow [12]. Dampening of the TS waves thus enables to keep a laminar boundary layer and delay transition.

A nature role model for the dampening of TS waves is given by the dolphin's skin. Its viscoelastic properties allow the dolphin to retain a mostly laminar

Daniel Haller · Sebastian Neiss · Michael Kroener · Peter Woias
University of Freiburg, Department of Microsystems Engineering
Georges-Köhler-Allee 102, D-79110 Freiburg, Germany
e-mail: sebastian.neiss@imtek.uni-freiburg.de

boundary layer around its body reducing the overall drag [1]. The dolphin can furthermore control the elastic properties of the skin by regulating the blood flow in the dermal papillae [2].

The goal of this project was the development of a system that mimics the dolphin's skin properties in order to dampen TS waves on an airfoil. A passive control of the boundary layer seems unfeasible and active systems are more promising [7]. Thus, an actively driven system with actuators and sensors has been developed. The working principle of the proposed system is shown in Figure 1. TS waves are subjected to the principle of superposition. Incoming TS waves are measured using surface hot-wire sensors. A corresponding counter wave is generated on a flexible membrane at several nodes on the membrane using an array of micromechanical actuators. The counter wave is calculated using a model-predictive control and the resulting TS wave dampening is measured using another set of sensors that is located downstream with respect to the actuator array.

This concept of an active wall has proven to be suitable to dampen TS waves and delay transition. Piezoelectrically actuated unimorph bending actuators were used in first experiments. However, only two of such actuators can be cascaded which limits the number of nodes on the membrane and thus the capabilities of the system [9]. A new generation of actuators is presented here that overcomes the present limitations.

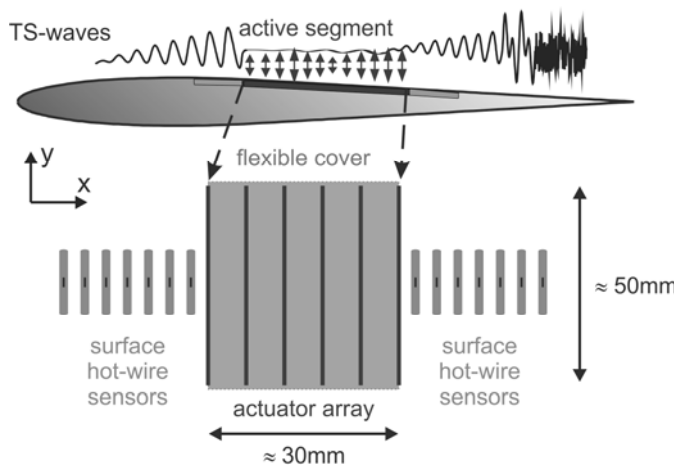


Fig. 1 Schematic of the basic setup for active cancellation of TS waves [8].

2 Development of a Cymbal actuator

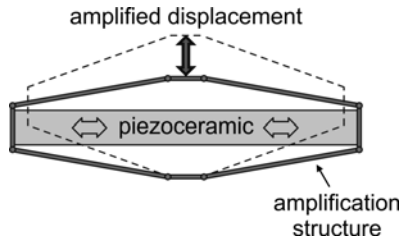
The requirements on the actuator characteristics were determined in previous experiments. There are additional demands on the actuator that are given by the application.

1. A successful TS wave dampening with two actuators was achieved with a displacement of up to $50 \mu\text{m}$ [9]. This displacement is taken as requirement for the static displacement of actuators that are developed for this application. To obtain this displacement, the maximal amplitude of the driving voltage is set to 150 V by the available power amplifiers.
2. There must not be any resonance frequencies in the frequency range of the TS waves. The change of 180° in the actuator's phase response would make control extraordinary difficult. Consequently, no resonance frequencies are allowed in the frequency range between 200 Hz and 600 Hz which is the frequency range of the investigated TS waves.
3. The membrane has to be displaced over a spanwide width of 50 mm at each actuation node on the membrane (see Figure 1).
4. The actuator thickness is limited to 6 mm in streamwise direction. This makes it possible to implement a stacked system with five actuation nodes on the membrane within one wavelength of the investigated TS waves (see Figure 1).

2.1 Basic Actuator Design and Fabrication

An actuator design that meets the given geometrical requirements is the so-called Cymbal structure. This design was proposed by [5] and a schematic of the basic working principle is shown in Figure 2. Actuation is provided by a ceramic with piezoelectric properties. The ceramic generates a small horizontal strain as response to an electrical field that is applied between the front and back electrodes. The cymbal-shaped structure that is bonded to the ceramic thereby generates an amplified vertical displacement.

Fig. 2 Schematic of the basic structure of a Cymbal actuator. Small horizontal strain of the piezoceramic is amplified by the cymbal-shaped structure into a vertical movement [9].



The actually developed Cymbal structure is much more complex compared to this simple geometry. The final design of the developed actuator with all relevant dimensions is shown in Figure 4. The interactions between the different dimensions make it impossible to obtain the optimal design analytically. Therefore, the design process relies on numerical FEM simulations that are performed with COMSOL Multiphysics 3.5a. Displacement and eigenfrequencies are optimized

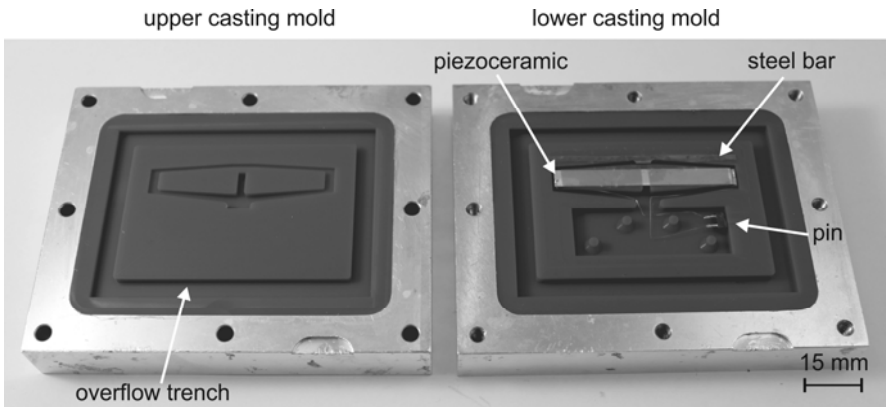


Fig. 3 Actuator casting molds with inserted piezoceramic and steel bar. After the electrodes are connected to the pins, the mold is filled with epoxy resin [10].

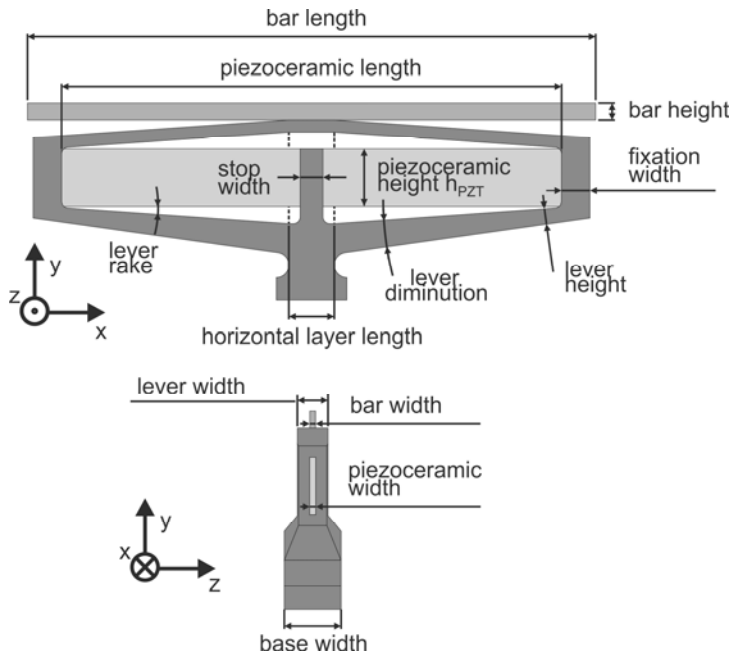


Fig. 4 Simulation model of the final design of the Cymbal actuator with all relevant dimensions

with the help of parametric studies for the single dimensions. The structure exhibits three relevant eigenmodes that are shown in Figure 5. Besides the expected upstroke mode of the whole structure, there are two additional tilting modes. In one of those two modes, the bar performs a strong tilting motion but the actuator

does not. In the second mode, the whole actuator is in a tilting motion. An important aim of the simulations is to find a device with increased eigenfrequencies of these three modes with values higher than 600 Hz. However, this typically involves an increase of the actuator's stiffness and consequently a reduction of the displacement.

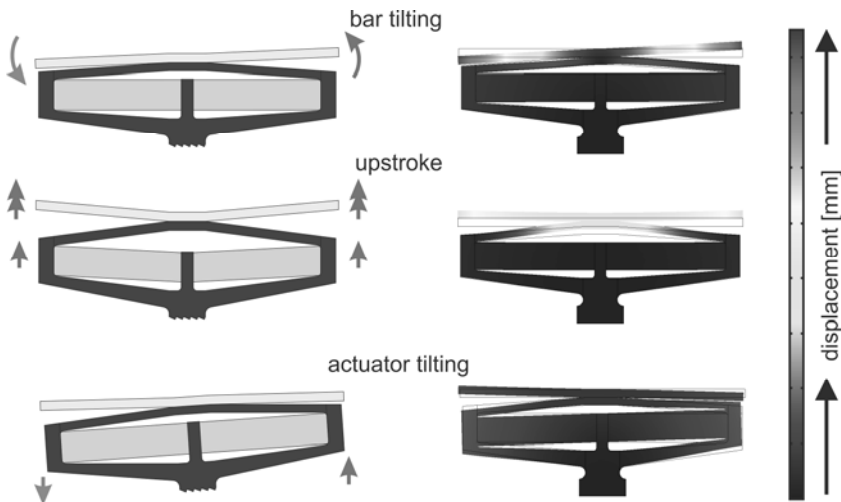


Fig. 5 Listing of all relevant eigenmodes for the designed Cymbal actuator; left: sketch of the eigenmodes; right: FEM simulations of the eigenmodes [10]

The actuators are fabricated in piezo-polymer-composite technology. Structures and devices are fabricated in this technology using an insert casting process of a two-component epoxy resin. In a first step, a silicone mold (Elastosil 4624, Wacker) as shown in Figure 3 is made from an aluminum master mold. The piezoceramic (Vibrit 1100, Johnson Matthey) and the steel bar are inserted into the mold. After the ceramic's electrodes are connected to the pins, both parts of the mold are filled with liquid, two-component epoxy resin (Stycast 2057, Emerson & Cuming). The actuator can be removed from the mold after the polymer is cured in the closed mold for 12 hours at room temperature. More detailed information on the fabrication process can be found for example in [6] and [11].

2.2 Development Process and Actuator Behavior

The final design that is shown in Figure 4 and Figure 5 is the result of a design process with several versions of actuators. The different development steps are shown in Figure 6.

The first design that is shown in Figure 6(a) comprises only two lever arms. It was intended to use the ceramic itself to displace the membrane at the actuation nodes. However, the displacement of this design was too small and the ceramic exhibits a strong bow caused by the non-symmetrical design.

The second design that is shown in Figure 6(b) comprises a full structure with four lever arms. This design generates a static displacement of $73 \mu\text{m}$ at an actuation voltage of 150 V and all resonance frequencies are higher than 600 Hz . Although this design thus meets the requirements, new problems occurred which make this design unsuitable for the use in wind tunnel experiments. The actuator exhibits a fourth resonance mode in which the piezoceramic is in a strong out-of-plane motion. Moreover, the resonance frequency of this mode is around 400 Hz which can lead to a device failure during normal operation due to fraction of the piezoceramic.

In the third design that is shown in Figure 6(c), two changes were implemented to overcome this problem. A second ceramic layer increases the stiffness and the actuation force of the piezoceramic and a mechanical stop limits the ceramic's out-of-plane movement. The two ceramics are glued together with the help of a hot press. Connecting the electrodes is more complicated in this process but the additional stiffness as well as actuation force lead to an increased reliability and thus compensates for the increased production effort. In addition to the two design changes, a steel bar is integrated for the displacement of the membrane over the required width of 50 mm . Polymer bars have shown a too low stiffness to deflect the membrane and cannot provide a homogeneous displacement over the whole width. The steel bar is cut using wire electrical discharge machining (EDM). However, a strong influence of the bar tilting resonance mode is observed in this design.

This last drawback was cancelled in the final design that is shown in Figure 6(d). The mechanical stop is glued to the piezoceramic which increases the tilt stiffness significantly. Although gluing the stop to the ceramic reduces the actuator displacement, the achieved value still meets the requirements.

Figure 7(a) shows the measured static displacement of the final actuator's displacement at different actuation voltages. The static displacement is $65 \mu\text{m}$ without attached membrane at a driving voltage of 150 V and it is only reduced by $5 \mu\text{m}$ when a membrane is attached to the steel bar. The nonlinear increase of displacement with increasing actuation voltage is caused by nonlinear, large-signal piezoelectric effects, namely elastostriiction and electrostriction [15].

The measured resonance frequencies of the final actuator design are 800 Hz for the bar tilting mode, 960 Hz for the upstroke mode, and 1380 Hz for the actuator tilting mode. Figure 7(b) shows the actuator displacement in the frequency range from 100 Hz to 600 Hz for three different values of the driving voltage. The peaks of displacement are caused by harmonic distortions at $1/2$ and $1/3$ of the upstroke resonance frequency. They are caused by the piezoelectric hysteresis that leads to an actuation with additional harmonics of the actuation frequency. More detailed information about harmonic distortions and how they can be suppressed can be found in [3].

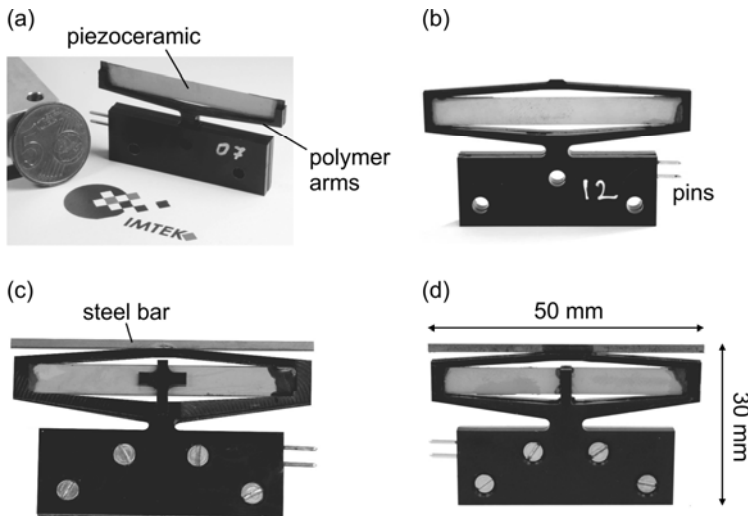


Fig. 6 Different development steps of the Cymbal actuator with design (a) to (d) [10]

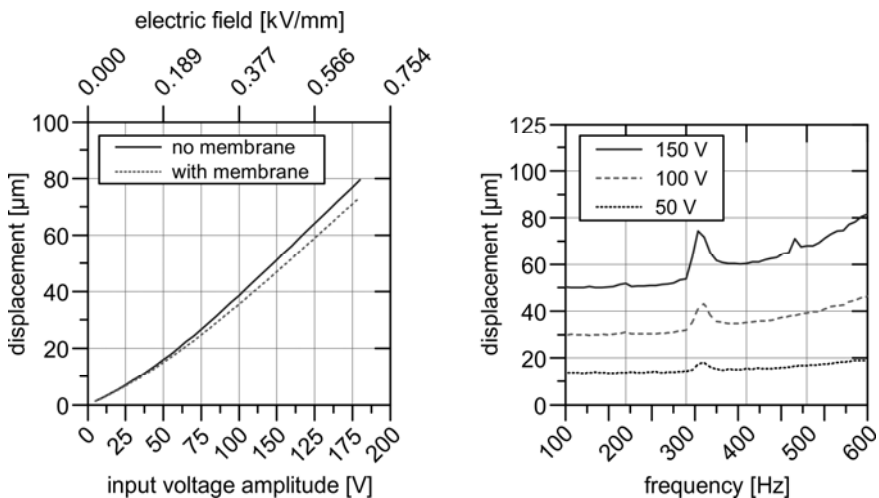


Fig. 7 Measured characteristics of the final design of the Cymbal actuator; left: static displacement [10]; right: frequency response in the working range

Concluding this section, the final version of the Cymbal actuator fulfills all requirements. The base width is only 5 mm, all resonance frequencies are higher than 600 Hz, the steel bar generates a homogeneous displacement of a membrane, and the maximal displacement is larger than 50 μm . Therefore, the actuator can be integrated into an active wall and a complete system for the cancellation of TS waves.

3 System Implementation

The developed Cymbal actuator fulfills all requirements for successful dampening of TS waves that have been defined based on previous experiments. In the next step, they were integrated with sensors and a membrane into a complete system. Hot wire sensors were used in the first tests and have proven to be suitable to measure TS waves [9, 14]. 100 µm thin silicone membranes with outer dimensions of 30×56 mm² and 18×111 mm² were used to generate the surface wave.

3.1 Streamwise Cascaded Actuators

Figure 8 shows the complete system with five streamwise cascaded actuators. Such a system allows the generation of a surface wave with five deflection nodes within one wavelength of the investigated TS waves.

The five single actuators are mounted on an aluminum bar which is placed on a brass mount at a distance of 6 mm between each other. The aluminum bar allows to align the steel bar of the single actuators horizontally.

The silicone membrane is fabricated in a casting process. An aluminum mold is filled with liquid, two-component silicone (Elastosil 4642, Wacker). Excess silicone is stripped off with a doctor blade to obtain the dedicated membrane thickness of 100 µm and a membrane size of 30×56 mm². The cured silicone membrane is pre-strained by 10 % and then fixed in an aluminum mount. The actuator's steel bars are glued to the membrane to enable downward and upward deflection of the membrane.

Additionally, surface hot wire sensors are welded on a printed circuit board (PCB) that has an opening for the membrane. Ten sensors are located with a distance of 5 mm between each other both, upstream and downstream of the active wall segment. The PCB is laminated into an aluminum insert of the model airfoil (NACA008) and the brass mount is fixed with screws to the PCB.

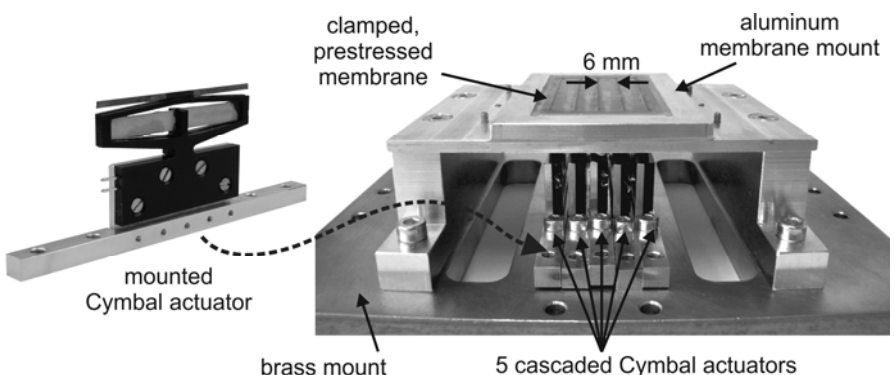


Fig. 8 System with five streamwise cascaded Cymbal actuators and silicone membrane [10]

3.2 Spanwise Cascaded Actuators

In a real environment, TS waves do not only travel streamwise but also spanwise. Consequently, a spanwise actuator arrangement was implemented to test the system's capability for the dampening of these so-called 3D TS waves.

Figure 9 shows the system that was developed for this purpose. The previous requirements on the system remain the same. It is especially necessary to use a continuous, flexible membrane. However, the big calculation effort of the control makes it impossible to use more than six actuators at a time. Therefore, two rows of each three actuators were placed on a bigger brass mount. The distance between the actuators is 6 mm in streamwise direction and 5 mm between the bar ends in spanwise direction. Accordingly, only the membrane size was increased to $18 \times 111 \text{ mm}^2$ and the previously described casting process could still be used for the fabrication.

Furthermore, the sensor arrangement was changed to measure the behavior of 3D TS waves (see Figure 10). The total number of sensors is now 20 and only five sensors are placed in each row upstream of the active wall segment while each row is made of 15 sensors downstream of the active wall segment. The distance between the sensors 1-10 is 5 mm, 10 mm between the sensors 11-16, and 20 mm between the sensors 16-20. Therewith, the monitored area downstream of the active wall segment is increased drastically which makes it possible to examine the process of transition more precisely after the air stream has passed the active wall segment.

The integration into the model airfoil is the same as for the streamwise cascaded setup. The PCB is laminated into the airfoil's aluminum insert and the active wall segment is fixed to the PCB with screws.

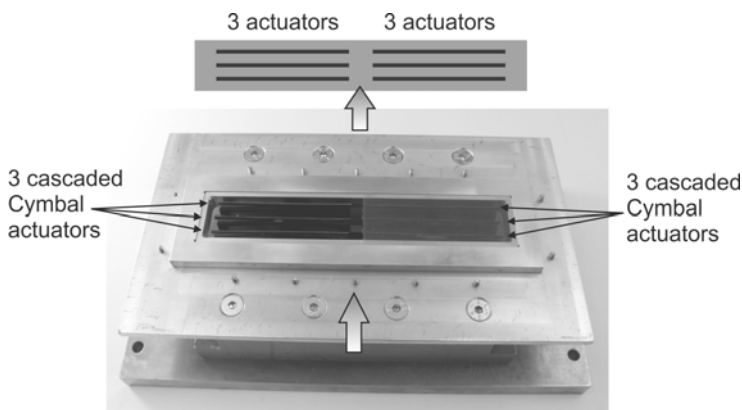


Fig. 9 Spanwise cascaded arrangement with 3x2 Cymbal actuators and attached membrane

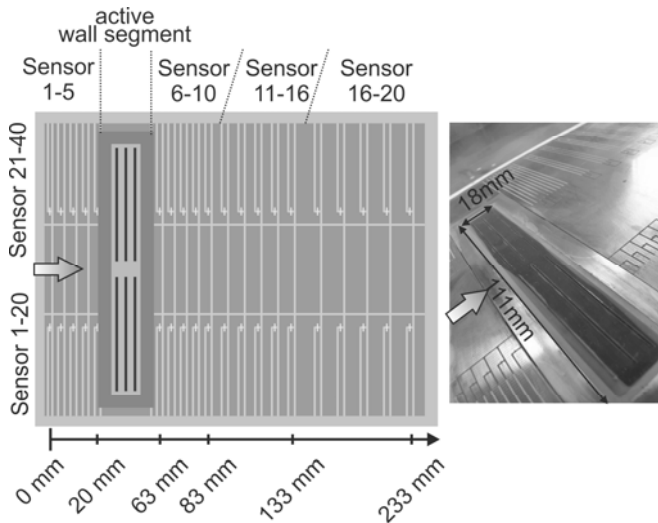


Fig. 10 PCB layout and sensor distribution for the analysis of 3D TS waves

3.3 Anisotropic Wall

A further improvement of the system's dampening performance is predicted by simulations for an anisotropic wall setup [4]. In this setup, the actuators are not mounted vertical but inclined. This gives an additional motion of the membrane towards the air stream over the active wall segment.

The actuator setup is shown in Figure 11. Five actuators are inclined by an angle of 30° to the vertical axis and fixed on the brass mount with a distance of 6 mm. For this purpose, only the aluminum bar for the actuators was changed compared to the streamwise cascaded setup.

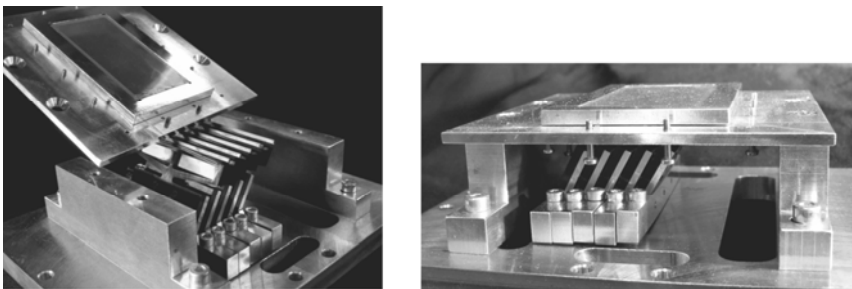


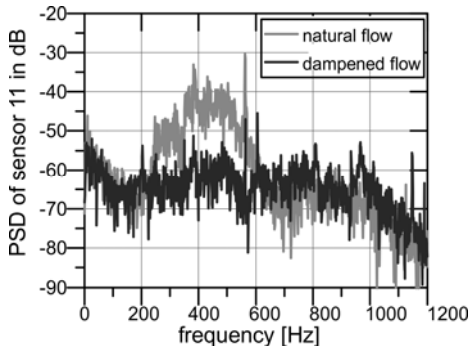
Fig. 11 System with 5 inclined, streamwise cascaded Cymbal actuator and silicone membrane which form an anisotropic wall.

3.4 Wind Tunnel Experiments

A detailed description of the wind tunnel experiments and the results can be found in Goldin's chapter in this book.

Figure 12 shows the measured power spectral density (PSD) with the streamwise cascaded setup. The spectrum is measured with the first sensor downstream of the active wall segment which is located at a distance of 15 mm from the membrane. The streamwise cascaded setup leads to a TS wave dampening of 80%. During the actual experiments, the maximal actuator displacement was only in the range of 25 μm .

Fig. 12 Measured power spectral density of natural and damped flow at a distance of 10 mm after the active wall segment measured with the streamwise cascaded setup [10].



The setup with spanwise cascaded actuators has proven to be suitable to dampen natural 2D TS waves with superposed, artificial 3D TS waves in the wind tunnel experiments. A dampening of 70% was achieved and the actuator displacement was again only in the range of 25 μm .

The experiments with the anisotropic wall setup show a slight increase of the system's performance compared to the vertical, streamwise cascaded setup. TS wave dampening of 85% was achieved. As for the other two setups, the necessary actuator displacement was only in the range of 25 μm .

4 Conclusions

A system for a novel approach to actively control the boundary layer of an airfoil was developed. Piezoelectrically driven Cymbal actuators provide a compact actuation with large actuation force combined with a sufficiently large displacement. The actuators were developed and constantly improved in a computer-aided design process. The final actuator design fulfills all requirements for the use in a TS wave dampening system. A maximal static displacement of 50 μm can be achieved at a driving voltage of 150 V. The relevant resonance frequencies of the device were tuned to values higher than 700 Hz by different stiffening measures. Problems that occurred during the development process were successfully eliminated by appropriate countermeasures. The piezo-polymer-composite fabrication

technology has proven to be suitable for the fabrication of the actuators. At the same time, it allows for fast design changes.

The developed actuators were integrated into a complete system that is suitable to actively control the boundary layer on an airfoil. For this purpose, a membrane casting process was developed which allows the fabrication of thin silicone membranes with a homogeneous thickness. The necessary surface hot wire sensors were integrated into the system with the help of a PCB technology.

Wind tunnel experiments show that the developed systems are capable to dampen 2D and 3D TS waves. High dampening of up to 85% was achieved in wind tunnel experiments with a model airfoil. The actuator's dynamic characteristics are well suited for the application. At the same time, the maximal displacement was only 25 µm which is far below the actuator's capabilities.

Acknowledgments. We gratefully acknowledge funding by the German Research Foundation (DFG) within the framework of the priority program SPP 1207 “Strömungsbeeinflussung in Natur und Technik”.

References

1. Alekseeva, T.E., Semenov, B.N.: Hydrodynamic drag of the dolphin. *J. Appl. Mech. and Tech. Phys.* 12, 326–329 (1973)
2. Babenko, V.V.: Some hydrodynamic peculiarity of dolphins swimming (Russian title: Nekotorye gidrodinamičeskie osobennosti pla-vanija del'finov). *Bionika* 3, 19–26 (1969)
3. Biancuzzi, G., Haller, D., Lemke, T., Wischke, M., Goldschmidtboeing, F., Woias, P.: A Dynamic Linearization Concept for Piezoelectric Actuators. *IEEE Trans. on Ultrason., Ferroelectr. and Freq. Control* 58, 689–697 (2011)
4. Carpenter, P.W., Morris, P.J.: The effect of anisotropic wall compliance on boundary-layer stability and transition. *J. Fluid. Mech.* 218, 171–223 (1990)
5. Dogan, A., Uchino, K., Newnham, R.: Composite piezoelectric transducer with truncated conical endcaps “cymbal”. *IEEE Trans. on Ultrason., Ferroelectr. and Freq. Control* 44, 597–605 (1997)
6. Friese, C., Woias, P., Goldschmidtboeing, F.: Piezoelectric Microactuators in Polymer-Composite Technology. In: Proc. IEEE Transducers Conf., Boston, USA (2003)
7. el Hak, M.G., Tsai, H.M.: Transition and turbulence control. World Scientific, Singapore (2006)
8. Haller, D., Hempel, J., Paetzold, A., Losse, N., Peltzer, I., Nitsche, W., King, R., Woias, P.: A piezo-actuated closed loop MEMS system for active delay of transition. In: Proc. IEEE Transducers Conf., Denver, USA (2009)
9. Haller, D., Paetzold, A., Losse, N., Neiss, S., Peltzer, I., Nitsche, W., King, R., Woias, P.: Piezo-Polymer-Composite unimorph actuators for active cancellation of flow instabilities across airfoils. *J. Intel. Mater. Syst. and Struct.* 22, 465–478 (2011)
10. Haller, D., Paetzold, A., Goldin, N., Neiss, S., Goldschmidtboeing, F., Nitsche, W., King, R., Woias, P.: Cymbal type piezo-polymer-composite actuators for active cancellation of flow instabilities on airfoils. In: Proc. IEEE Transducers Conf., Beijing, China (2011)

11. Just, E., Bingger, P., Woias, P.: Piezo-Polymer-Composite Actuators - A New Chance for Applications. In: Proc. ACTUATOR Conf., Bremen, Germany (2004)
12. Kachanov, Y.S.: Physical mechanisms of laminar-boundarylayer transition. *Annu. Rev. Fluid Mech.* 26, 411–482 (1994)
13. Schlichting, H., Gersten, K.: Boundary-Layer Theory, 8th edn. Springer, New York (2000)
14. Sturzebecher, D., Anders, S., Nitsche, W.: The surface hot wire as a means of measuring mean and fluctuating wall shear stress. *Exp. in Fluids* 31, 294–301 (2001)
15. Wischke, M., Haller, D., Goldschmidtboeing, F., Woias, P.: Assessing the elastostiction and the electrostriction parameter of bulk PZT ceramics. *Smart Mater. and Struct.* 19, 085003 (2010)

Learning from Dolphin Skin – Drag Reduction by Active Delay of Transition: Flow Control by Distributed Wall Actuation

Nikolas Goldin and Rudibert King

Abstract. Control strategies for laminar flow control above a surface are investigated. A flexible membrane displaced by multiple piezo-polymer composite elements is used as actuator in wind-tunnel experiments. Direct methods of damping Tollmien-Schlichting waves are compared to a biomimetic approach imitating the damping mechanisms of a compliant skin. In both cases, model predictive control algorithms are applied to control the multi-bar actuator segments. For the biomimetic approach, reduced models of compliant surfaces are developed and parametrized by direct optimization and according to numerically generated optimal wall properties. Damping results of up to 85% RMS value are achieved.

1 Introduction

In order to reduce the drag of an airfoil, one possible solution is to delay the onset of turbulence. As laminar flow induces much less drag than a turbulent one, this has the potential to greatly reduce the wing's overall drag. The delay of the transition to turbulent flow which is already achieved by passive means such as the design of the airfoil's shape can be increased further by active flow control, i.e., using active elements to directly influence dynamic processes in the flow. The dynamics of the flow which need to be affected are the Tollmien-Schlichting (TS) waves, unstable modes of the boundary-layer which can trigger the transition to turbulence by their growth. Damping these TS waves delays transition, thus reducing drag.

Two approaches to damping TS waves are used here. The first is the direct damping method. This method consists of generating a matching counterwave which mitigates the TS wave by negative superposition. The second is the biomimetic damping

Nikolas Goldin · Rudibert King

Fachgebiet Mess- und Regelungstechnik, TU Berlin, Hardenbergstr. 36, 10623 Berlin
e-mail: {nikolas.goldin, rudibert.king}@tu-berlin.de

method, which instead prescribes a certain dynamic for the wing's surface. This dynamic is adapted from dolphin skin, whose elasticity and structure are suspected to be beneficial for the animal's drag.

The active flow control method used in this investigation uses wall-bounded measurements from sensors placed upstream in the flow to calculate an actuation signal which affects the flow. However, due to the convective nature of Tollmien-Schlichting waves, a closed control loop can not be formed. In the terminology of control theory the damping of TS waves corresponds to an open-loop control problem, mostly a disturbance feedforward compensation. According to the definitions proposed by Gad-El-Hak [4], this strategy represents a reactive, open-loop flow control method.

2 Experimental Setup

Experiments are conducted in a closed Göttinger-type wind tunnel at a free stream velocity of $U_\infty = 25\text{ms}^{-1}$. In the measurement section, a NACA0008 wing segment is fixed, spanning the width of the tunnel. The angle of attack of the wing segment is variable. In the following, we will use the coordinates x for streamwise, y for wall-normal and z for spanwise position.

In a removable aluminum insert in the wing segment, the actuators and sensors are mounted. The actuators consist of a variable number of piezo-polymer-composite Cymbal actuation elements, which displace steel actuation bars glued to a pre-stretched silicone membrane [5, 6]. The sensors are surface mounted hotwire anemometers. Multiple sensor positions are available in front of and behind each actuation segment. Sensor placement on the actuation segments is not possible.

Different actuator configurations are tested. The most basic one consists of two actuation bars displacing a single membrane. More complex configurations with more bars per membrane (five bars, straight and inclined) and multiple actuators side-by-side (three bars times two) and placed behind each other (five bars times three with multiple membranes) are also investigated. These configurations are visualized in Fig. 1.

The configuration with inclined actuation elements mimics the motion of the surface of an anisotropic compliant wall, as found on the dolphin [8] and calculated by

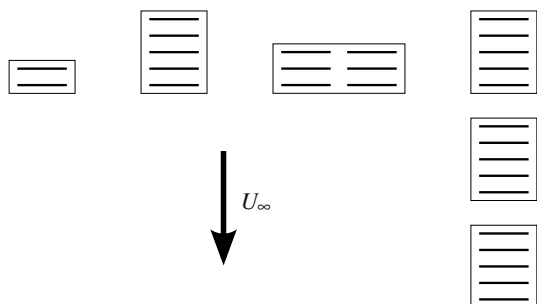


Fig. 1 Actuator setups. Actuation bars are represented by horizontal lines, with the membrane indicated as a box. From left to right: two-bar, five-bar, side-by-side and cascaded configuration.

Carpenter [3]. The actuation elements are mounted with an angle of 60° to the horizontal. While Carpenter uses a fibre angle of 60° , which corresponds to an actuator angle of 30° , this was not technically feasible. 60° was the lowest angle attainable with the used construction method.

The side-by-side configuration is used to investigate the damping of oblique TS waves using a single large membrane stretched over actuation elements in both stream and spanwise direction. The cascaded configuration serves the investigation of the possibility of using multiple actuation patches to prolong the laminar region even further. The use of multiple patches of actuation allows the placement of sensors between the patches, which is not possible when using a continuous membrane.

More details about the actuators can be found in this book's chapter by D. Haller et al., details about the experimental setup in the chapter by A. Pätzold et al.

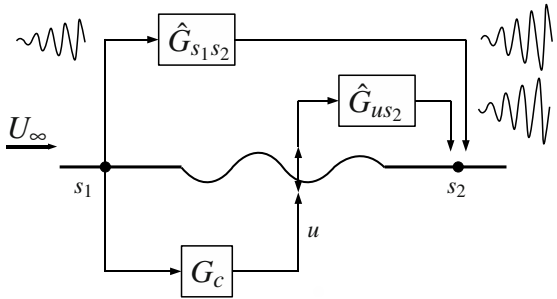
3 Direct Damping Scheme

The direct damping scheme is the prevailing active flow control method for damping TS waves [1]. It utilizes the fact that TS waves are a linear phenomenon. Thus, two different TS waves can be superposed. Therefore, by generating a counterwave which is exactly the negative of an incoming TS wave, both are destroyed.

This is an open-loop control problem, as we will now argue. We do this as there is some confusion of terminology in the literature. TS waves are convective phenomena appearing in distinct wave packets. The wave packets form due to small disturbances. In general, two different wave packets are not correlated with each other. They share the same frequency range, determined by the unstable frequencies of the flow, but other than that, information about one wave packet is of no help in predicting the next one. The wave packets convect in the direction of the flow, and there is no noticeable upstream effect. As there are no sensors on top of the actuator, wave packets can be sensed upstream or downstream of the actuator only. Upstream information can be used in a feedforward, open-loop configuration. In a closed control loop, a comparison of the actuated flow to a reference value (the unperturbed mean flow in this case) would be used to calculate the actuation input. As the wave generated by the actuator travels downstream and has no upstream effect, only the downstream sensor senses the actuated flow. But as the wave packets are uncorrelated, this information can not be used to calculate a useful control input to counteract the next wave packet. Therefore, no closed-loop structure makes sense for the damping of TS waves. The only way the downstream sensor can be used in a meaningful way is as a gauge of the control's effectiveness, fed back for adaptive control strategies, where the feedforward control law is adapted according to the measurements of the downstream sensor. However, this is not closed-loop control. The closest analogue in control theory is a disturbance feedforward or disturbance variable compensation.

To generate the fitting counterwave, models of both the flow and the actuator's influence on the flow have to be identified. Both models refer to the same downstream sensor as output (see Fig. 2). As the superposition principle holds for TS waves in the linear region, the expected signal at s_2 is the sum of both model's outputs. An optimal control law with respect to damping could be found by demanding the signal at s_2 to be zero. Thus, the perfect control law would be $G_{co} = -\hat{G}_{us2}^{-1}\hat{G}_{s_1s_2}$. As the resultant controller has to obey causality, a G_c which approximates the properties of the unrealizable perfect controller G_{co} in the relevant frequency range is to be derived. Contrary to most control problems, here the phase response of the controller is of utmost importance, as a counterwave which misses the necessary phase is obviously useless or even harmful.

Fig. 2 Direct damping, block diagram. Signals refer to the sensors s_1, s_2 and actuation u . The models of the flow $\hat{G}_{s_1s_2}$ and of the actuation effect \hat{G}_{us2} both use s_2 as output. An optimal controller would be G_{co} with $\hat{G}_{us2}G_{co} = -\hat{G}_{s_1s_2}$



As the TS wave takes a certain time to convect from the upstream sensor s_1 to the actuator, the actuator does not need to start working immediately once a wave packet is detected. There is a certain delay time, during which the information about the incoming wave packet is available before the actuator needs to act on this information. Therefore, the control algorithm cannot only determine the displacement the actuator needs to generate right now, but also a trajectory of displacements it will need to generate in the near future. This additional information can be utilized to increase control performance by using a model predictive control algorithm.

This is sketched in Fig. 3. To this end, the delay part of the flow transfer function $\hat{G}_{s_1s_2}$ is written separately, giving $\tilde{G}_{s_1s_2} = \tilde{G}_{s_1s_2} \cdot e^{-s \cdot t_{d,flow}}$. A trajectory can be generated with any length up to $\bar{H}_p = (t_{d,flow} - t_{d,act})/T_s$, where $t_{d,act}$ is the delay part of the actuation model $\hat{G}_{us2} = \tilde{G}_{us2} e^{-s \cdot t_{d,act}}$, and T_s the sampling time of the implementation. The delay time of the actuator reduces \bar{H}_p , as the generated signal needs to be shifted by this delay. If a smaller prediction horizon $H_p < \bar{H}_p$ is used, $t_{d,y} = (\bar{H}_p - H_p)T_s$ marks the time span of unused information. The relationships between the different delay times are sketched in Fig. 4.

The transfer function $(\mathbf{G}_t)_i = e^{-s \cdot (H_p T_s - iT_s)}$, $i = 0, \dots, H_p$ is used for generating a vectorial trajectory from the scalar input. Then a vectorial reference input for signals at s_2 for the model predictive controller controlling the actuator would be $\underline{r}_p = -\mathbf{G}_t e^{-s \cdot t_{d,y}} \tilde{G}_{s_1s_2} s_1$.

Fig. 3 Sketch of the trajectory generation for flow delay time $t_{d,flow}$, actuator delay time $t_{d,act}$ and maximal prediction horizon $\bar{H}_p T_s$. At the actual sampling instant k , the value $y(k)$ is measured at the position of sensor 1, while the estimated signal at sensor 2 is given by $\tilde{G}_{s_1 s_2} y(k - t_{d,flow})$ in the Laplace domain.

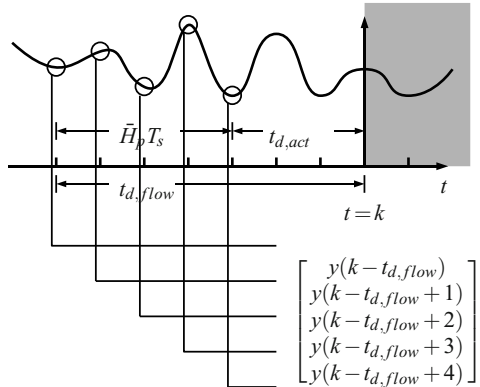
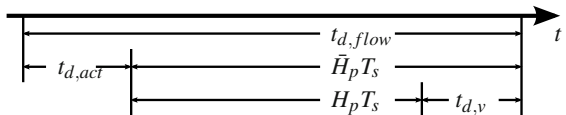


Fig. 4 Relationships of the delay times.



Model predictive control (MPC) is an optimization based control method, where the control goal is given by an optimization criterion depending on the errors and control inputs over a prediction horizon H_p . Before the optimization criterion can be stated, the notation of the MPC needs to be introduced. More detailed information can be found in [7]. We assume our actuation effect model \hat{G}_{us_2} is given as a discrete-time state-space model of the form

$$\underline{x}(k+1) = \mathbf{A}\underline{x}(k) + \underline{u}(k) \quad (1)$$

$$\underline{y}(k) = \mathbf{C}\underline{x}(k) \quad (2)$$

with states $\underline{x} \in \mathbb{R}^{n_x}$, inputs $\underline{u} \in \mathbb{R}^{n_u}$ and outputs $\underline{y} \in \mathbb{R}^{n_y}$. Based on this model, predictions of the future development of the state and outputs can be made, subject to a known initial state and assumptions on the future inputs. For example, given the knowledge of $\underline{x}(k)$ and $\underline{u}(k)$, the model (1) yields the prediction for $\underline{x}(k+1)$, and with (2) also for $\underline{y}(k+1)$. As this prediction is based on the known initial state at k , this prediction will be written as $\underline{y}(k+1|k)$. This can of course be repeated for further predictions, here up to the prediction horizon H_p . These predictions are stacked in the vector $\underline{y}_p = (\underline{y}^T(k+1|k), \underline{y}^T(k+2|k), \dots, \underline{y}^T(k+H_p|k))^T$. Likewise, the future values of \underline{u} are stacked in $\underline{u}_p = (\underline{u}^T(k), \underline{u}^T(k+1), \dots, \underline{u}^T(k+H_p))^T$.

With these vectors and a vector r_p of future reference values as shown above, the cost functional for the optimization is $J = (r_p - \underline{y}_p)^T (r_p - \underline{y}_p) + \underline{u}_p^T \mathbf{R}_p \underline{u}_p$, where \mathbf{R}_p is a block diagonal matrix consisting of weight matrices $\mathbf{R} \in \mathbb{R}^{n_u \times n_u}$ on the main diagonal. While in the constrained case MPC generally depends on an online optimization of the criterion, this is not feasible for the small sampling times necessary in the case of TS damping. Therefore, constraints are neglected here for control

design. This allows the algebraic solution of the optimization, resulting in a MPC implementation which can be computed by a matrix multiplication (see [7]). The result of this multiplication is the optimal input vector for all times up to $k + H_p$. Of this vector, the first part $\underline{u}^T(k)$ is implemented. In the next timestep, the optimization is repeated, and the new first part is applied, and so on ad infinitum.

For the prediction and optimization, the MPC requires the actual state of the system. If possible, this state is measured or estimated from measurements. In this case, no measurements of the immediate state above the compliant wall is possible, and calculating the actual state from wave packets that have already reached the downstream sensors is impossible. Therefore, the identified model is used instead, simulating the system state from the inputs. Generally this would be problematic, as any error or drift in the model could amplify over time. However, as the modeled process is almost memoryless because a given wave packet will convect away from the sensor and does not influence any further measurements, this is not the case here. With this setup, the closed control loop of the MPC can be computed offline and becomes a single feedforward control function which calculates the inputs from a trajectory of future reference values.

Because the cost functional of the MPC is formulated in the time domain, it is not possible to apply frequency weights in an integrated way, as is the case, e.g., for H_∞ control. In order to penalize the use of frequency ranges for the MPC, the system model is expanded by adding additional outputs to the system, which consist of filters amplifying the true output signal in a frequency range that is to be penalized. By prescribing a reference of zero for these outputs, the application of actuation energy in these frequencies enters the cost functional through the output weight. This is mainly used for two purposes. Firstly, to penalize high frequency output. Because the resonance frequency of the piezo elements is only slightly above the TS frequencies, the actuators might otherwise be driven at their resonance, which not only distorts their output but also heats them up, leading to reduced lifetime. Secondly, low frequency outputs are penalized. While these have no influence on the flow, as neither the actuator nor the flow react to them it is better to avoid them, as an output saturation is used to protect the actuators. A larger low frequency output can drive the outputs close to or into the saturation, thus blocking the output of the higher frequency parts of the signal.

The weight matrices of the cost functional are chosen such that the output signals remain inside the saturation bounds of the actuator for a characteristic test signal. The prediction horizon is chosen as large as possible, i.e., $H_p = \tilde{H}_p$, when not barred from doing so due to calculation time constraints.

4 Biomimetic Damping Scheme

The hypothesis that a compliant surface can help to reduce the drag of a body has been numerically validated in multiple studies [2, 3]. One limiting factor for the usefulness of this effect for practical applications is that the parameters of the compliant

wall need to fit to the flow conditions. A wall that can reduce drag for, e.g., one flow speed can increase drag for other speeds. A biological system, such as a dolphin, can change the elasticity of its surface by controlling muscle tension, blood pressure or temperature. It is hypothesized that this might serve as a means to delay flow transition in case of a dolphin. For this technical setup, a different approach is chosen. The actively displaceable wall actuator is used instead to mimic the behaviour of a compliant wall. This is achieved by controlling the wall to generate a prescribed displacement velocity. The prescribed displacement velocity is calculated according to a model \mathbf{G}_w of a compliant wall, using the flow state above the actuator as estimated from upstream sensor measurements as inputs and the resulting displacement velocity of the modeled compliant wall as outputs.

This allows for testing of different types of compliant walls without altering any physical components of the test setup. Likewise, an adaption to a changing flow speed would be straightforward. Different walls are realized by using a different wall model, which is just a change in the control software. Therefore, multiple wall properties can be tested rapidly, even allowing a limited optimization of the wall's properties in the experiment.

Two approaches of finding a wall model \mathbf{G}_w which dampens TS waves are followed. The first is the experimental approach, where model structures and parameters are proposed, then tested and refined in the wind tunnel. The second is the numeric approach, where wall structures and parameters which are known to be beneficial to drag reduction from numerical investigations found in the literature are used. These models are converted to reduced models which can be calculated in real-time and also tested in the wind tunnel.

The control problem for this application is similar to the direct damping case, but computationally more demanding, as the outputs of the actuator model $\hat{\mathbf{G}}_{ud}$ are the displacement velocities of each bar, as opposed to the result of the actuation as measured by one downstream sensor in the direct damping case. This makes the system model for biomimetic damping a $n_u \times n_u$ model, as opposed to a $1 \times n_u$ model for the direct damping approach, where n_u is the number of actuator elements. As predictions with this model need to be calculated in real time and as sampling rates of typically 5 kHz are used, this increased model size is a decisive factor in the choice of prediction horizon and other parameters.

The actuator model is identified experimentally. Pseudo random binary (PRBS) and wave signals are used as inputs for the actuators and their displacement velocity is measured using a laser vibrometer. The model is identified using the prediction error method.

MPC is used in the same way as for the direct damping scheme, using the delay of the flow transfer function to generate a trajectory of reference values. The reference values in this case are the displacements generated by the wall model, i.e., the response of the simulated wall to the flow. The MPC generates the actuator inputs such that this reference is tracked as close as possible.

Preliminary experiments were conducted to determine the basic properties of the wall model most suitable for TS wave damping. Different model structures, i.e., differential equations, linking the estimated flow conditions to the generated reference

output were used with parameters manually optimized for damping. This way, a model structure for the wall was found which (i) matches the expectations for a mechanical model, (ii) is solvable in real-time and (iii) allows a damping of TS waves with suitable parameters.

The resulting model uses a spatial discretization of the actuated wall with one element per actuation bar. The inputs of the model are the flow states above each element, the outputs are the resulting displacement velocities of the surface at each element. Thus the model is $n_u \times n_u$, as pictured in Fig. 5.

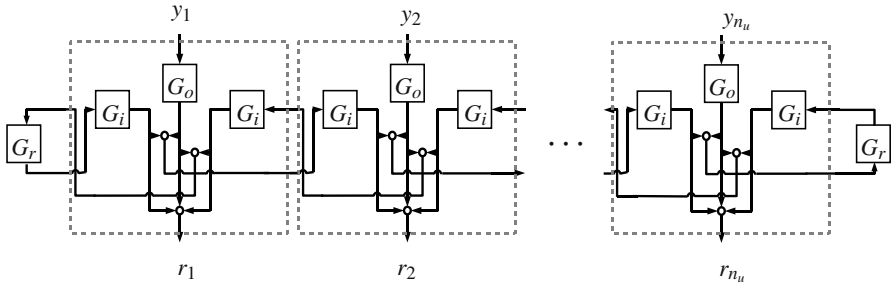


Fig. 5 Block diagram of the one-dimensional wall model.

The outer and inner transfer functions G_o and G_i determine the properties of the model \mathbf{G}_w . The outer transfer functions are chosen to be (linear) second order while the inner transfer functions are second order with deadtime. As the wall is in essence a spring-damper system, this second order behaviour corresponds well with the intuition how the wall should move. The deadtime component in the inner transfer function is necessary because the distance between two elements is large enough that the travel time of a wave in the wall medium can become important. The reflection transfer function G_r can be used when modeling the behaviour of finite compliant wall patches, where fixed boundary conditions can cause a reflection of a wave. Note that this greatly increases the order of the resulting model, thus increasing calculation time. In the following, G_r is always set to zero. For a wall with elements stretching in two directions, the model can be extended easily. Here, it is necessary to note that the structure of the model prohibits waves from changing direction other than at the reflection transfer function. This prohibits unphysical behaviour not wanted in the model and also avoids the formation of closed loops inside the wall, which would raise the model order significantly, making the model useless for real-time experiments.

The model transfer function \mathbf{G}_w , written for a two dimensional wall, where instead of G_i we have separate G_{ix} and G_{iz} , with n_{ux} elements in x -direction and n_{uz} elements in z -direction are

$$(\mathbf{G}_{ix})_{i,j} = G_{ix}^{|i-j|}, \quad i, j \in \{1, \dots, n_{ux}\} \quad (3)$$

$$(\mathbf{G}_w)_{i,j} = G_o G_{iz}^{|i-j|} \mathbf{G}_{ix}, \quad i, j \in \{1, \dots, n_{uz}\} \quad (4)$$

where the elementary transfer functions are

$$G_o(s) = \frac{K_o \omega_o^2}{\omega_o^2 + 2D_o \omega_o s + s^2}, G_{ix}(s) = \frac{K_{ix} \omega_{ix}^2}{\omega_{ix}^2 + 2D_{ix} \omega_{ix} s + s^2} e^{-st_{ix}}, G_{iz}(s) = \frac{K_{iz} \omega_{iz}^2}{\omega_{iz}^2 + 2D_{iz} \omega_{iz} s + s^2} e^{-st_{iz}}.$$

The inputs of this model are the estimates of the flow state above each element. This estimate is based on the black-box model of the flow $G_{s_1 s_2} = \tilde{G}_{s_1 s_2} \cdot e^{-s \cdot t_{d,flow}}$, consisting of a delay free part $\tilde{G}_{s_1 s_2}$ and a delay part. This initial model is identified based on two sensors. Then, the delay time of the model is modified in order to produce the flow state at a different position s_3 . While this is a simplification of the flow's dynamics, for small distances from the sensor position it is feasible. Comparing the modified model's performance for a prediction s_3 with a real measurement at s_3 shows that the modified models generated by this approach perform on a level comparable with models identified directly for a pair of sensors. Hence, this can be used for predicting the flow state at positions where no sensors are available. Using the delay free part $\tilde{G}_{s_1 s_2}$, the delay time from sensor s_1 to the first actuation element position t_{df1} and the delay time from element to element t_{df2} , the flow model is

$$(\mathbf{G}_f)_i = \tilde{G}_{s_1 s_2} e^{-s(t_{df1} + (i-1)t_{df2})}, \quad i \in \{1, \dots, n_{ux}\}. \quad (5)$$

As cross-flow speeds are small in the linear flow region where the actuator is placed, one such model is used for each row of actuators with no coupling between the rows.

To find parameters for the wall model, the experimental approach and the numerical approach are used. To experimentally find parameters suitable for damping, the properties of the successful direct damping controller are used as a starting point. While the models used for the derivation of the direct damping controller include the flow coupling of the actuators, which the wall model does not, it is still possible to compare them based on the actuation outputs. Therefore, the wall transfer functions are first chosen such that the frequency content of the outgoing actuation signal of the wall control matches the actuation signal of the direct damping control as closely as possible for a given incoming TS wave. This can be done in offline simulations, and thus can be optimized automatically. From this starting point, the parameters are varied manually in the online experiment to achieve the best possible damping with this model structure.

The numerical approach is based on optimal damping parameters which were numerically calculated by other researchers. Two well known papers by Carpenter & Garrad [2] and Carpenter & Morris [3] are chosen as data source.

As the models in the literature are calculated for different flows, they are first non-dimensionalized and then re-dimensionalized with the parameters of the performed wind-tunnel experiments. The wall models for which Carpenter calculated optimal damping parameters are partial differential equations, which cannot be solved in real-time to calculate the wall's appropriate response to an incoming TS wave. Therefore, the wall model (3,4) is used to approximate these models. This is achieved by simulating the partial differential equation models' responses to different pressure inputs and using the simulation results to identify parameters for the wall transfer functions. The simulation is performed using MATLAB's ode45

solver for the temporal solution while the spatial derivatives are calculated using the pseudospectral method. The identification is performed with the MATLAB implementation of the prediction error method.

5 Results

Direct Damping

In order to measure the damping effect of both methods, the root mean square (RMS) value of sensor signals downstream of the actuators is calculated. This gives a measure of the remaining disturbances in the flow. Additionally, the spectra of the same sensor signals are investigated. In both cases, the unactuated, natural, flow is compared to the actuated flow.

First damping tests were carried out with the two-bar actuator configuration [5]. The main advantage of using only two bars is that the actuation elements can be manufactured in unimorph shape, which allows actuators with a higher displacement. The direct damping with the unimorph actuators achieved a 84% reduction in RMS value at a sensor 25 mm behind the actuator.

More recent experiments were performed with five-bar actuators. These utilize cymbal-structure actuator elements. While the maximum displacement of the cymbal actuator elements is lower than that of the unimorph elements, their smaller size allows the placing of these elements in bigger arrays. As more actuator elements are available, less amplitude is necessary for each single element. While the peak displacements for the unimorph elements is about $24\mu\text{m}$, for the actuator with five cymbal elements they are $15\mu\text{m}$.

The damping results with the five-bar actuator are comparable to the damping results with the two-bar actuator. About 83% RMS reduction are achieved. One difference to the 2-bar actuator case is that the damping of the lower frequency TS waves (250-350Hz) is much better than with the 2-bar actuator, which had a very small effect on these frequencies (cf. [5]). As the amplitude of TS waves in this area is smaller than in the main frequency range, this better behaviour does not influence the RMS damping value significantly. The freqency spectrum of natural and damped flow is pictured in Fig. 6.

The effect on the RMS value downstream of the actuator is shown in Fig. 7. Here, a hotwire probe mounted on a movable traverse is used to measure the RMS values of the flow far downstream of the actuator. For this, the probe is kept at a constant distance of 0.5 mm above the surface of the wing segment. As the shape of the amplification curve is slightly distorted due to different surface roughnesses and other experimental impurities, the distance by which the curve is shifted varies according to where it is measured. Mainly it lies between 80 mm and 100 mm.

The measurements with the 5-bar actuator is repeated with a variant of the actuator which uses the same actuation elements, only mounted inclined. This is a way to mimic the motion of anisotropic compliant walls. Results with the inclined

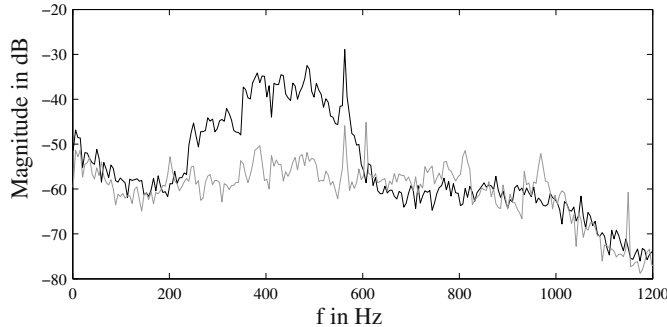


Fig. 6 Frequency spectrum of natural and damped flow at a sensor 25 mm behind the actuator, using five-bar actuator. Natural, unactuated flow (black) vs. damped flow (grey).

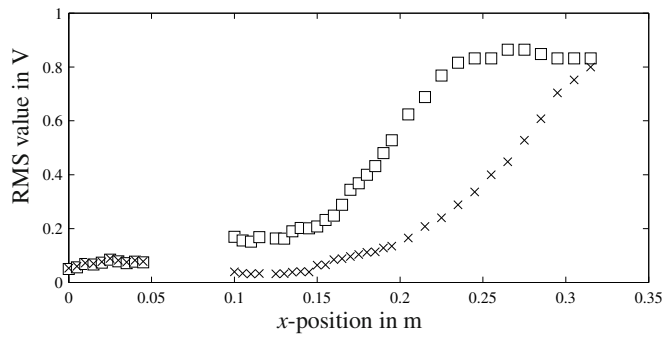


Fig. 7 RMS values over x -position for natural and damped flow, using five-bar actuator. Actuator position between 50 and 100 mm. The RMS curve is shifted by 80 to 100 mm.

actuation elements are almost identical to the results with upright actuation elements. Using the direct damping method, an RMS damping of 85% is achieved. While the displacements in y -direction are smaller than using the upright actuator elements, the required voltage is the same in both cases (on average 13.5V amplitude). This is to be expected, as a part of the displacement goes in x -direction with the inclined actuation elements.

In order to check the robustness to variations of U_∞ , three different experiments are conducted. First, individual controllers are derived for five different flow speeds to ascertain that the actuators can function in the frequency range necessary for this speed. Then, a controller derived for one speed (22ms^{-1}) is tested for the other speeds. This shows that the controller is still working for small variations of U_∞ , but losing its effect for larger variations and even adding to the RMS value for too large variations. A third experiment uses the same controller, but varies the delay part of the actuation according to the flow speed. With this adaptation, the controller works for all the tested speeds. The RMS values and damping rates are shown in Fig. 8.

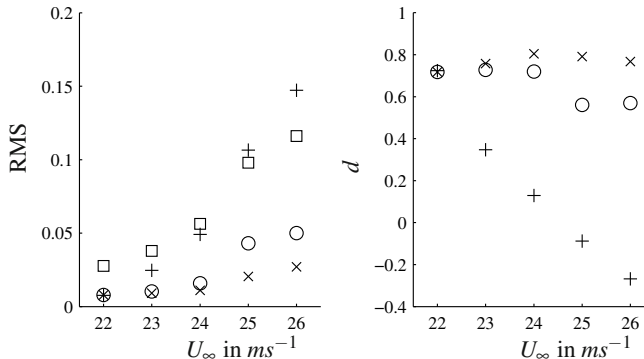


Fig. 8 On the left RMS values of different speeds for three experiments. On the right corresponding damping ratios d . Symbols are: natural flow (\square), controller for each speed (\times), unadapted controller (+) and delay-adapted controller (\circ).

Tests with a side-by-side configuration consisting of two rows of three bars each, under a single, large membrane are used to investigate the damping of oblique TS waves. As the natural flow in the used wind tunnel is very close to the two dimensional case, artificial oblique TS waves are created. A loudspeaker is used to generate waves from a slit in the wing surface. This loudspeaker is connected to the left and right side of the slit by different length tube segments, generating the same signal on both sides, but with different time delay.

The identification of the actuators shows no coupling between the two rows of actuators, which allows the use of two independent controllers. This reduces the calculation load for control. The damping of oblique waves is tested for different frequencies. Damping results were identical to those attained without added oblique waves. In order to characterize the damping at spanwise locations not directly behind the actuator, a hotwire probe on a movable traverse is used to measure damping in z -direction. This is visualized in Fig. 9.

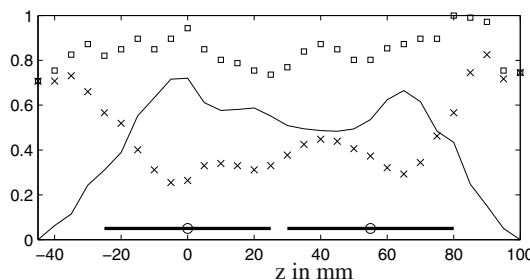
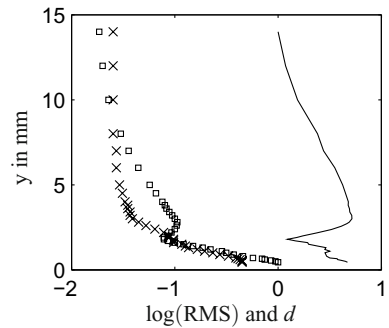


Fig. 9 Damping results in different spanwise positions, 30mm behind the actuator. Natural RMS value (\square) and damped RMS value (\times) are plotted normalized. Damping quotient $d = (1 - RMS_{damp}/RMS_{nat})$ is the continuous line. Actuation bar width (thick line) and sensor position (\circ) are indicated.

The damping effect is best directly behind the sensors. To the side, the effect is reduced as the TS waves at that spanwise position are not necessarily identical to those at the sensor position. With the shown spanwise sensor distance of 55 mm, the lowest damping between the sensors is 48%. The damping directly behind the right sensor is 66% in this case. This number is not as high as the damping ratios measured before as it is based on measurements with a hotwire probe above the wall. Higher damping ratios are seen at the wall when using surface hotwires. With different wall-normal positions, the results vary as the RMS values varies, as shown in Fig. 10. The damping away from the wall is best at the maximum of the RMS value, where the probe in Fig. 9 was positioned, but is still better at the surface hotwires. As the probe in Fig. 10 can not be safely brought that close to the wall, this is not a part of this dataset.

Fig. 10 Damping results, profile in wall-normal direction. Natural RMS value (\square) and damped RMS value (\times) are plotted normalized and logarithmic, damping quotient $d = (1 - \text{RMS}_{\text{damp}}/\text{RMS}_{\text{nat}})$ is the continuous line.



The cascaded actuator configuration is used to investigate the possibility of increasing the shift of transition by adding sensors and actuators behind each other. The actuators are controlled independently from each other. This way, the remaining TS waves which start to grow again after the first actuator can be damped again by the second actuator and so on. Fig. 11 shows the RMS over x -position plots for this configuration.

While the additional actuators manage to reduce the RMS values further and add to the shift, their effect is not as pronounced as could be expected. This is due to the steeper slope of the damped RMS curves. The reason for this effect is the three dimensionality of the flow. While the flow in the linear region is mostly two-dimensional, with growing TS waves three-dimensional effects increase. As we are damping the TS waves only behind the actuator, TS waves to the side of our measurement plane still increase in size. Their three-dimensional effect are affecting the flow behind the second and third actuator from the side, adding disturbances that these actuators had no chance of reducing. In order to improve results, the cascaded structure would need to be combined with the side-by-side configuration. It is expected this would generate a broader region of damped TS waves. In the center, the cascaded damping could be investigated without disturbances from the side.

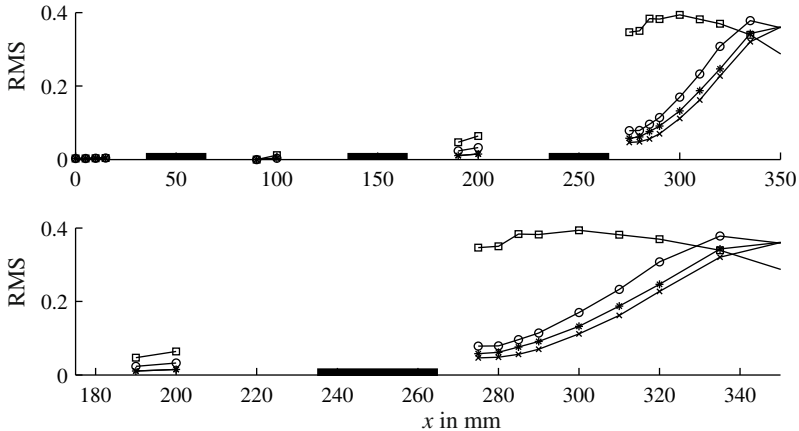
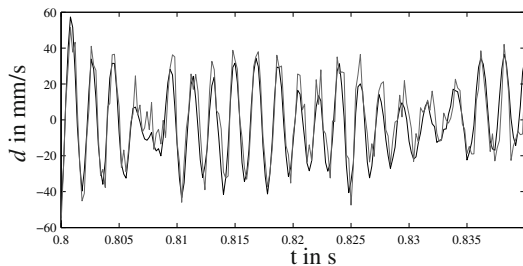


Fig. 11 RMS values over streamwise position. Natural flow (\square), damped flow with one actuator (\circ), damped flow with two actuators (*) and damped flow with all three actuators (\times). The first plot shows the whole measurement region, the second is a magnified view showing only the second half. Actuator positions are indicated by black lines.

Biomimetic Damping

In order to prescribe the desired elastic behaviour to the wall, it is necessary to control the displacement of the actuation bars. Dynamic trajectories with frequency content around the TS frequencies need to be followed without phase shift. The actual trajectory following performance is measured with the same vibrometer used for the actuator identification. The fit¹ between commanded reference and measured displacement velocity is about 42%. As seen in Fig. 12, most of the disagreement between the two signals is in the maximal amplitude, where the additional high frequency noise of the vibrometer measurement further reduces the fit value. As the phase of the signal is matched, this behaviour is sufficient for damping.

Fig. 12 Trajectory following of the actuation bars, shown for the middle-left bar of the 3×2 configuration. Reference trajectory (black) is a measured flow signal, following displacement velocity d (grey) is measured by vibrometer.



¹ For two scalar discrete time series x_1, x_2 we define the fit as $1 - (\|x_1 - x_2\| / \|x_2 - \text{mean}(x_2)\|)$.

In preliminary experiments with the two bar unimorph actuator, it was found that for a simple wall with a fixed delay between the two bars and second order dynamics with a cutoff frequency of $\omega = 500\text{Hz}$ yield the best damping results, 84%. Based on these experiments, the wall model for the five bar wall is derived.

The five bar actuator is then used to optimize the damping parameters of the wall model. While the larger parameter space gives more degrees of freedom, it also complicates the optimization process. With the best parameter set found ($K_o = 0.9, \omega_o = 900\text{Hz}, D_o = 0.5, K_{ix} = 0.6, \omega_{ix} = 300\text{Hz}, D_{ix} = 0.7, t_{ix} = 0$), 81% damping are achieved.

The inclined actuation elements are slightly less effective than the upright actuation elements. This is mainly due to problems in attaining a good system identification for the actuator, as the measurement of the displacement of the actuation bars is done by laser vibrometer. This vibrometer depends on the reflection of a laser beam off the actuation bar and measures only the displacement velocity in y -direction. The signal quality is much higher using the actuation elements only moving perpendicular to the surface than using the inclined actuators, which led to a better model and thus better trajectory following. With the same parameters as the previous experiment, 70% damping are achieved.

Experiments with the side-by-side configuration show that any coupling in the behaviour of the actuator bars across the sides is in a very high frequency range which does not influence the flow. Therefore both rows of actuators can be controlled independently from each other. Moreover, the influence of the wall transfer functions in z -direction are found to be detrimental. This suggests that the chosen extension of the wall model for two dimensional walls is too simple. A solution more tailored to the flow, utilizing transfer functions not in z -direction but diagonal, might be more suitable.

The second approach of finding parameters by converting numerically found optimal parameters does not produce any damping results. While the fitting of the numerical data to the simplified model structure produces very promising results as the found dynamics are of second order in good approximation, none of the resulting models achieved any damping in the experiment.

6 Conclusions

The damping of natural multi-frequency TS waves with the membrane based actuator was successful, with reductions in RMS value of around 85%. The delay of transition is visible in the RMS values. Because the shape of the amplification curve changes, an absolute value for the shift cannot be given. Mainly it is between 80 and 100 mm for an actuation segment of 30 mm length.

The use of the membrane actuator as an artificial compliant wall is feasible with an ordinary differential equation based wall model. The wall model is successfully parametrized for damping, achieving damping values comparable to the direct damping. The wall model with parameters calculated from numerical data does not achieve any measurable damping.

Acknowledgements. This work was supported by the Deutsche Forschungsgesellschaft (DFG) as part of SPP 1207 “Strömungsbeeinflussung in Natur und Technik”.

References

1. Baumann, M., Nitsche, W.: Investigation of active control of Tollmien-Schlichting waves on a wing. In: Henkes, R., van Ingen, J. (eds.) *Transitional Boundary Layers in Aeronautics*, pp. 89–90. KNAW (1996)
2. Carpenter, P.W., Garrad, A.D.: The hydrodynamic stability of flow over Kramer-type compliant surfaces. Part 1. Tollmien-Schlichting instabilities. *J. Fluid Mech.* 155, 465–510 (1985)
3. Carpenter, P.W., Morris, P.J.: The effect of anisotropic wall compliance on boundary-layer stability and transition. *J. Fluid Mech.* 218, 171–223 (1990)
4. Gad-el-Hak, M.: Flow control: passive, active, and reactive flow management. Cambridge Univ. Pr. (2000)
5. Haller, D., Paetzold, A., Losse, N., Neiss, S., Peltzer, I., Nitsche, W., King, R., Woias, P.: Piezo-polymer-composite unimorph actuators for active cancellation of flow instabilities across airfoils. *J. Intel. Mat. Syst. Str.* 22(5), 465–478 (2011), doi:10.1177/1045389X10395794
6. Haller, D.: Piezo-Polymer-Composite Actuators - Design, Nonlinear Characterization and Application for Active Cancellation of Flow Instabilities. PhD thesis, IMTEK, Universität Freiburg (2011)
7. King, R., Aleksic, K., Gelbert, G., Losse, N., Muminovic, R., Brunn, A., Nitsche, W., Bothien, M.R., Moeck, J.P., Paschereit, C.O., Noack, B.R., Rist, U., Zengl, M.: Model predictive flow control. In: 4th AIAA Flow Control Conference, AIAA Paper 2008-3975 (2008)
8. Pavlov, V.V.: Dolphin skin as a natural anisotropic compliant wall. *Bioinsp. Biomim.* 1, 31–40 (2006)

Linear-Stability Investigations for Flow-Control Experiments Related to Flow over Compliant Walls

Marcus Zengl and Ulrich Rist

Abstract. Results of linear stability calculations and direct numerical simulations for flow-control experiments are presented. Good agreements between measurements and simulations are shown. Furthermore, the linear stability of the flow over the experimental wing section is investigated. Hereby, also the use of isotropic and anisotropic compliant materials is assessed. The prevailing surface-based compliant-wall model of Carpenter was extended to yaw angles, pressure gradients and oblique-traveling disturbances. The influence of the yaw angle is demonstrated for an anisotropy angle of 75° . Also transient-growth of instabilities over the compliant wall was investigated, since the eigenvalue spectrum of the compliant-wall problem turned out to be sensitive to truncation errors. For the parameters investigated, the maximum transient growth of the compliant-wall case is in the same order as the growth of the rigid-wall case.

1 Introduction

For flow-control experiments we investigate the flow of a $1.3m$ long wing section in a wind tunnel. The experiments are conducted by Pätzold et al. at the ILR of the TU-Berlin. The aim of the flow-control experiment is to dampen Tollmien-Schlichting (TS) waves by actively actuating a wall using different control mechanisms. These experiments are inspired by the use of compliant coatings in order to dampen or even inhibit flow instabilities that lead to laminar-turbulent transition. Earlier water tunnel and towing tank experiments found in literature have shown that satisfying transition delays can be achieved. However, since the fluid of the experiment is air, an adequate compliant material does not exist for this purpose. This can be pointed out e.g. by the mass ratio of the compliant coating to the fluid which is in the order of one for the common coatings in water. Therefore, the wall of the wing

Marcus Zengl · Ulrich Rist

Institut für Aerodynamik und Gasdynamik, Pfaffenwaldring 21, 70550 Stuttgart, Germany
e-mail: {marcus.zengl, ulrich.rist}@iag.uni-stuttgart.de

section is actively actuated in the present experiment to imitate the behavior of a compliant coating. This has the advantage, that all thinkable material properties can be investigated.

2 Numerical Simulation of the Boundary Layer over the Wing Section

In order to investigate the stability properties of the wing section in the wind tunnel a direct numerical simulation (DNS) of the boundary layer flow was carried out. The key feature of this simulation is that its free-stream and inflow boundary condition (BC) was chosen using the measured free-stream velocity distribution. Therefore, the simulation depends on a high quality of the measurements. This distribution was quantified in one Prandtl tube and two hotwire measurement campaigns. A 9th-order polynomial was then fitted to have the least squares difference to the measurement points and applied for the free-stream velocity of the simulation. The respective free-stream velocities are plotted in Fig. 1 over the downstream coordinate.

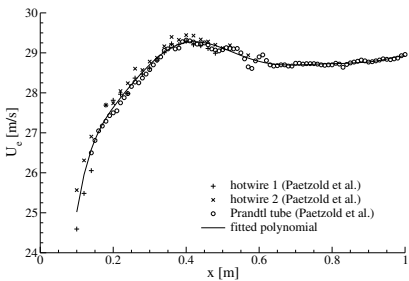


Fig. 1 Comparison of free-stream velocity between experiment and DNS

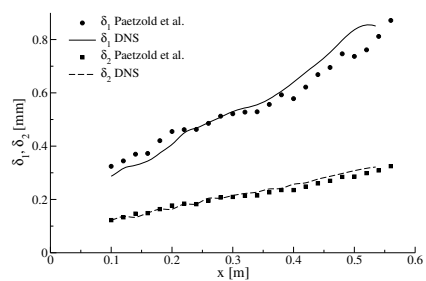


Fig. 2 Comparison of displacement and momentum thickness between experiment and DNS

Furthermore, velocity profiles were measured by Pätzold et al. at different streamwise positions using a hotwire. The wall-normal spacing of the measurements was 0.1 mm. The inflow velocity profile was chosen such that the momentum thickness matches the momentum thickness of the measurements and that the shape factor matches the local pressure gradient.

To cross-check the simulation data with the experiment, the velocity profiles and integral quantities of the boundary layer were compared. In Fig. 2 the comparison of the displacement and momentum thickness is plotted versus the streamwise coordinate for the laminar part of the boundary layer. Here, the boundary layer thickness is in the order of a millimeter. Keeping in mind that the boundary layer is very thin, the experimental and numerical data is in good agreement.

To further scrutinize the agreement of experimental measurements and numerical investigations, a comparison of controlled disturbances was conducted. For this

purpose a two-dimensional TS-wave of 500Hz was forced by a blowing and suction slot in the front part of the wing section. Downstream the disturbances in the boundary layer were measured by Pätzold et al. using hotwire anemometry at different streamwise locations and wall-normal positions. The measurement data were then evaluated by the authors. Since the time signal of the forcing was measured simultaneously, the phase of different wall-normal measurements could be related. The voltage fluctuations were converted to velocity fluctuations and then Fourier transformed. This permits to extract the eigenfunctions of the generated TS-wave as well as the quantification of the background disturbances. According results are plotted in Fig. 3. The eigenfunctions of the linear stability theory are scaled in their amplitude to match the experimental curves best.

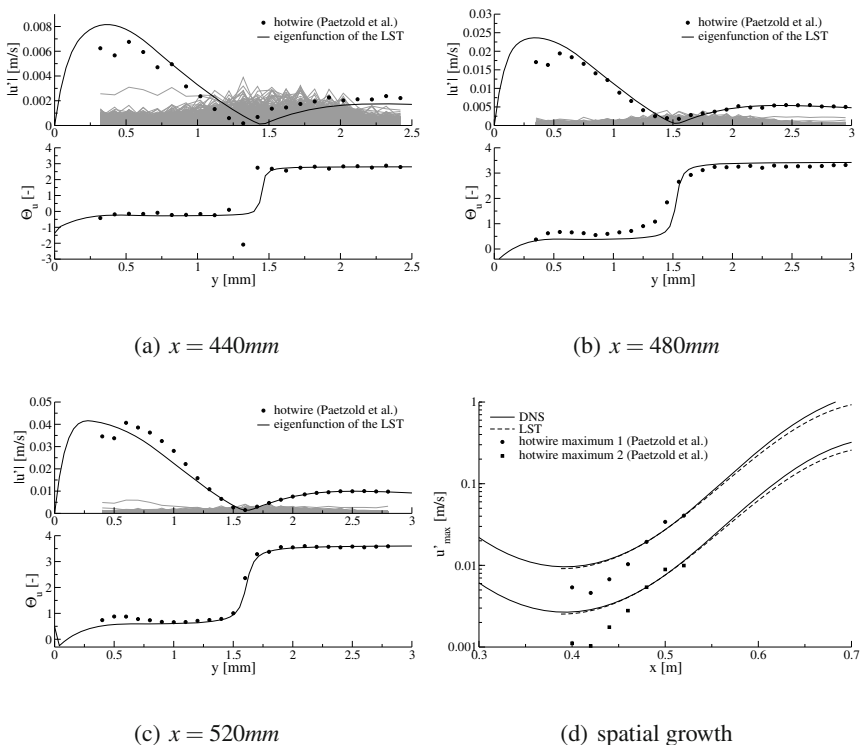


Fig. 3 Comparison of disturbance amplitude and phase at different positions as well as the spatial growth of a TS-wave with a frequency of 500Hz between the experiment and linear stability calculations

The amplitude and phase of the forced TS-wave are plotted versus the wall-normal coordinate in Fig. 3(a) for $x = 440\text{mm}$. The amplitudes of the other resolved frequencies are plotted in gray as a reference to get an idea of the disturbance background. The magnitudes of both, the background disturbances and the forced

TS-wave, are of the same order. The amplitude and phase of the forced disturbance do not match well to the linear stability results.

At $x = 480\text{mm}$ the agreement between experiment and LST is much better. This is plotted in Fig. 3(b). Here the background disturbances are a magnitude smaller than the forced TS-wave. The amplitude only deviates at the points closest to the wall. The region closest to the wall is very sensitive to small vibrations of the hotwire, because here the velocity gradient is highest. Also the mean velocity is very low so that free convection could deteriorate the results. In the region of the phase shift, small differences in the phase can be ascribed to the low amplitude ratio with respect to the background noise in this region.

In Fig. 3(c) is the comparison for $x = 520\text{mm}$. The amplitude of the forced wave is further increased with respect to the background disturbances. In the outer region amplitude and phase are in good agreement with the eigenfunction of the LST. In the inner region the amplitude distribution is different. This is a sign for three-dimensionality. The two-dimensional wave is unstable to three-dimensional disturbances and deforms. Shortly downstream of this location, the laminar flow breaks down making comparisons to the linear theory futile.

In Fig. 3(d) a comparison of the streamwise disturbance-amplitude development between the measured disturbance, DNS and LST is shown. Two criteria were used to define the amplitude. One is the inner maximum of the amplitude distribution, and the other is the outer maximum. The amplitudes of the LST and DNS were scaled to match at the point where the eigenfunctions matched best. Small deviations between LST and DNS are due to nonparallel effects.

The comparison of the controlled disturbance shows that a qualitative comparison is feasible. Keeping in mind that the presented disturbance measurements are in the order of 0.03% of the free-stream velocity, while the displacement thickness is in the order of 0.6mm the comparison to the experiment is satisfactory. The baseflow of the DNS can be used to calibrate and design flow control algorithms. Also it enables us to investigate the potential of different compliant-wall parameters.

3 Extended Anisotropic Wall Model

Inspired by the compliant skin of delphinidae a surface-based model of a compliant wall is implemented in the linear stability theory. Pavlov[6] investigated the skin of harbor porpoise and came to the result that its compliant skin not only behaves anisotropic but also its dermal ridges make an angle to the surface stream line. Carpenter et al. developed an anisotropic compliant wall model[3], and implemented it in a framework for two-dimensional disturbances. In our implementation the anisotropic wall model of Carpenter is extended to account for three-dimensional disturbances and a yaw angle of the material. Furthermore, our implementation is suited for flows with pressure gradients, because an inflection point of the streamwise velocity is not assumed at the wall.

The solution of the linear stability equations—the Orr-Sommerfeld and the Squire equation—using our extended anisotropic wall model differs from the

solution for a rigid wall. The boundary condition of the Orr-Sommerfeld equation contains the variable of the Squire equation. Therefore, the classic way of solving the Orr-Sommerfeld equation first and then solving the Squire equation to obtain the eigenfunction is not feasible. Both equations are coupled and have to be solved in combination.

In Fig. 4 is a sketch of the extended anisotropic compliant wall model. A flexible plate is bound to a rigid base with stiffeners. Springs and dampers are attached to the stiffeners. These form an angle θ to the base and an angle ψ to the flow direction. A sectional sketch of the deformed wall is shown in Fig. 5. The cross section has the angle ψ to the flow direction. Note the longitudinal stretch of the flexible plate which is visible by varying distances between its attachment points to the stiffeners. This stretch is induced by the differential motion of the swivel arms, leading to a restoring force to the original form.

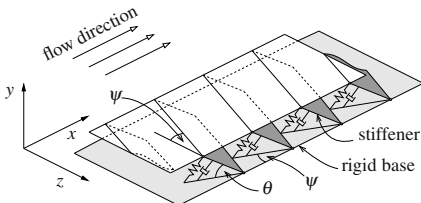


Fig. 4 Sketch of the compliant-wall model

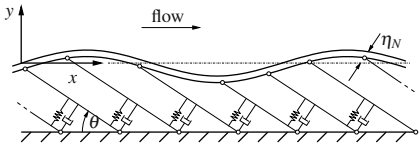


Fig. 5 Sectional view of the wall model

The wall parameters can be reduced to the non-dimensional quantities

$$C_m^{(v)} = \frac{\rho_m b_m U_\infty}{\rho v}; \quad C_k^{(v)} = \frac{K_m v}{\rho U_\infty^3}; \quad C_b^{(v)} = \frac{E_m b_m^3 U_\infty}{12(1-v_m^2)\rho v^3}; \quad C_i^{(v)} = \frac{E_m b_m}{\rho v U_\infty}. \quad (1)$$

These coefficients account for the *mass ratio* C_m , *spring stiffness* C_k , *flexural rigidity* C_b , and the *induced tension* C_i in the plate, caused by the differential motion of the swivel arms. The wall parameters are reflected by *Young's modulus* E_m , *Poisson's ratio* v_m , *plate density* ρ_m , *plate thickness* b_m , and the *spring stiffness* K_m . The flow parameters are reflected by *fluid density* ρ , *kinematic viscosity* v and the *reference velocity* U_∞ . The parameters for the calculations presented in this paper are listed in Table 1. Since there is an abundance of possible parameters the present wall parameters were taken from Carpenter[3]. They were optimized to reduce the amplification of TS-waves, while flow-induced surface instabilities (FISI) are kept stable.

4 Numerical Implementation of the Linear Stability Equations

For the solution of the Orr-Sommerfeld and Squire-equation we use two numerical schemes. One scheme formulates the equations as a boundary value problem. These are then solved with a *shooting method*. The other scheme formulated the

Table 1 Compliant wall parameters of the investigated compliant materials

material	θ	ψ	$C_m^{(v)}$	$C_k^{(v)}$	$C_b^{(v)}$	$C_i^{(v)}$
1	0°	0°	1.464×10^4	4.443×10^{-5}	1.208×10^{12}	—
2	60°	0°	2.211×10^3	7.405×10^{-6}	1.529×10^9	2.814×10^3
3	75°	0°	5.777×10^2	1.983×10^{-6}	2.281×10^7	6.152×10^2
4	75°	36°	5.777×10^2	1.983×10^{-6}	2.281×10^7	6.152×10^2
5	75°	54°	5.777×10^2	1.983×10^{-6}	2.281×10^7	6.152×10^2
6	75°	90°	5.777×10^2	1.983×10^{-6}	2.281×10^7	6.152×10^2

equations as an eigenvalue problem. Here the eigenvalues of a matrix are solved, so we will refer to it as *matrix method*. Both schemes have their specific advantages and disadvantages. The shooting method solves for one eigenvalue/mode using an initial guess. Its computational expense is proportional to the number of used discretization points. It suits well to calculate eigenvalues and eigenfunctions with a high accuracy. Also it can be used to calculate “three-dimensional” stability diagrams, i.e. diagrams with varying parameters *streamwise wavenumber* α , *spanwise wavenumber* β and streamwise location x in a matter of minutes to high accuracy. The matrix method solves for all eigenvalues at the same time. This ensures that no instability mode can be missed. Its computational expense is proportional to the number of discretization points to the power of three. It suits well to calculate transient growth of disturbances. Also its eigenvalues can be used as an initial guess of the shooting method.

The “shooting-method” The stability equations are formulated as in [5, sect. 2.5.2]. This has the advantage that the baseflow appears in the equations only with its first derivative. In the free-stream the three base solutions of parallel flow which decay towards infinity are prescribed. The six first-order equations are then integrated from the free-stream to the wall using a standard Runge-Kutta scheme. The baseflow of the semi-steps is interpolated using a cubic spline. Hence the baseflow can also be non-equidistant. Since the three integrated base solutions grow towards the plate with different growth rates, truncation errors of the slower growing solution grow with higher rates and pose a numerical problem. This problem is overcome by a technique proposed by[4]. After a given number of Runge-Kutta steps the three base solutions are orthonormalized to eliminate the numerical errors. At the wall the base solutions are then combined to fulfill two of the three boundary conditions. The residual of the third boundary condition is then minimized using common root-finding techniques, such as the Newton-Raphson or the Müller method. Note that for these two methods the residual of the boundary condition must be an analytic function of the eigenvalue α or ω that is solved for, but the phase of this complex quantity can be arbitrary if no special precautions are taken. Therefore, we scale the phase of the residual with the phase of the disturbance pressure at the wall. This creates a very good convergence behavior. The trade-off is that the shooting method does not converge to Squire-modes, because their disturbance pressure is zero at the

wall. Using the shooting method one can solve for both, the spatial amplification or the temporal amplification using the same algorithms.

The “matrix method” For the matrix method the stability equations are posed as an eigenvalue problem. The equations are formulated in v and ω_y constituting the Orr-Sommerfeld and Squire-equation. We use a pseudospectral collocation method for discretization, using Chebyshev-Gauss-Lobatto points. Special attention has been paid to the calculation of the differentiation matrices. Since the equations contain the fourth derivative, truncation errors have to be avoided wherever possible. The differentiation matrices were set up using the recursion formula of Welfert[10, eq. 7] for the off-diagonal elements, and the “negative sum trick” of Baltensperger[1] for the diagonal elements. The differentiation matrices are afterwards transformed using the rational mapping that is described in Schmid & Henningson[8, sect. A.4]. Currently, incorporating the compliant wall only the temporal model is implemented in the matrix scheme. Even though the temporal problem states a linear generalized eigenvalue problem, the eigenvalue appears in the compliant-wall BC quadratically. Therefore, we linearize the boundary condition, e.g.[9]. The resulting generalized eigenvalue problem is then solved using the QZ-algorithm.

A comparison of the current implementation to Carpenters results[3] is shown in Fig. 6. The neutral stability curve is plotted versus the Reynolds number based on displacement thickness Re_{δ_l} . Results for a rigid wall, an anisotropic compliant material, i.e. $\theta = 0$, and two anisotropic compliant materials are presented. The neutral stability curves are in very good agreement, and validate the present numerical scheme. Note that not only the area encircled by the neutral stability line is reduced, the maximum amplification rate is also smaller. Using anisotropic materials the amplification of TS waves can be reduced even more than using isotropic materials. A typical eigenvalue spectrum incorporating the compliant wall is shown in Fig. 7. The open and filled symbols denote eigenvalues of the matrix method. The filled symbols are eigenvalues found by the shooting method. Note that the shooting method does

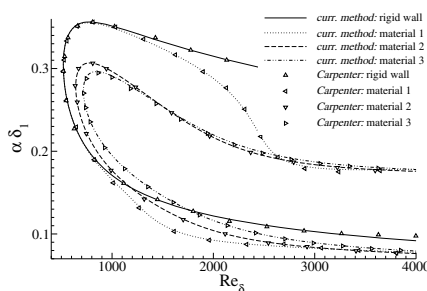


Fig. 6 Comparison of neutral-stability curves.

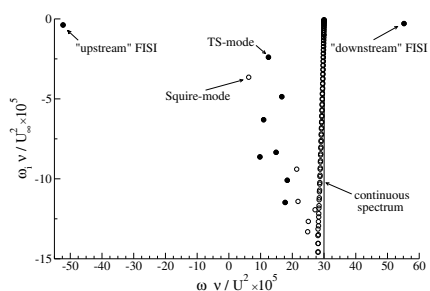


Fig. 7 Eigenvalue spectrum for Blasius flow over material 2 with $Re_{\delta_l} = 1000$, $\alpha = 30 \times 10^{-5} \frac{U_\infty}{v}$ and $\beta = 65 \times 10^{-5} \frac{U_\infty}{v}$.

not converge for the continuous spectrum, since there the residual of the boundary condition is not zero at a discrete location.

5 Further Stability Investigations of the Experimental Setup

Stability calculations of the experimental flow were carried out to investigate how far a compliant wall would be able to delay or even inhibit laminar-turbulent transition. Here, again the optimized parameters of Carpenter were used. Note that Pätzold et al. actuate the wall in a small region, and that the following diagrams apply to the case where the surface of the whole wing section is actively actuated. Hence they are somewhat idealized. Values of $U_\infty = 24.5 \frac{m}{s}$ and $v = 1.54 \times 10^{-5} \frac{m^2}{s}$ were used for the non-dimensionalization of the wall parameters.

Since the Squire-theorem does not apply for growing boundary layers over compliant walls, we have to account for three-dimensional disturbances as well. The maximum spatial amplification rate and the N -factor (i.e. $-\int \alpha_i dx$) is given in Table 2 for the calculations of the different materials. Considerable reduction of both the maximum growth rate as well as the N -factor are achieved by applying the compliant surfaces.

Table 2 Maximum spatial amplification rate and N -factor for the experimental setup

material	θ	ψ	$\max(-\alpha_i) [m^{-1}]$	N
rigid	—	—	9.66×10^{-2}	6.6
1	0°	0°	9.14×10^{-2}	5.4
2	60°	0°	4.31×10^{-2}	2.1
3	75°	0°	4.21×10^{-2}	2.0

Fig. 8 shows a “three-dimensional” spatial stability diagram of the flow in the present experiment. In the spatial model, we prescribe the *angular frequency* ω and the *spanwise wavenumber* β for a given velocity profile at the streamwise location x and solve for the complex *streamwise wavenumber* α . The three quantities x , α and β form the coordinates of the stability diagram. Contours of the *spatial amplification rate* α_i are shown for different slices of the unstable region. The neutral stability surface is pictured with lines of constant spanwise wavenumber β . Since wall and flow are symmetric the stability diagram is also symmetric. It can be seen, that the maximum amplification rate is located at $\beta = 0$. The unstable region is closed at large x , due to the favorable pressure gradient in the rear of the wing section. However, in the wind tunnel experiment the flow becomes turbulent before the end of the unstable region.

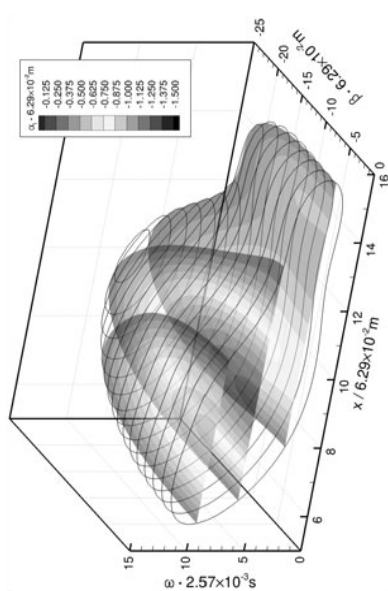


Fig. 8 Spatial stability diagram for the experimental setup with rigid wall.

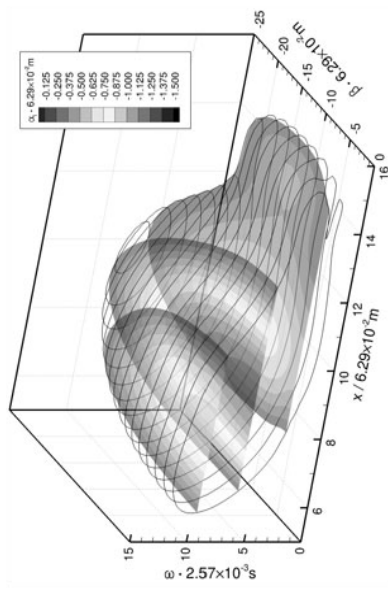


Fig. 9 Spatial stability diagram for the experimental setup with material 1.

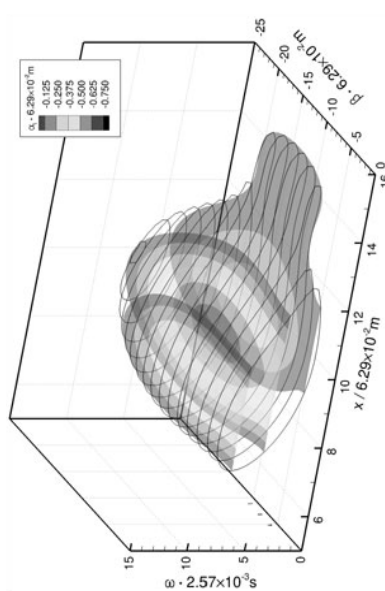


Fig. 10 Spatial stability diagram for the experimental setup with material 2.

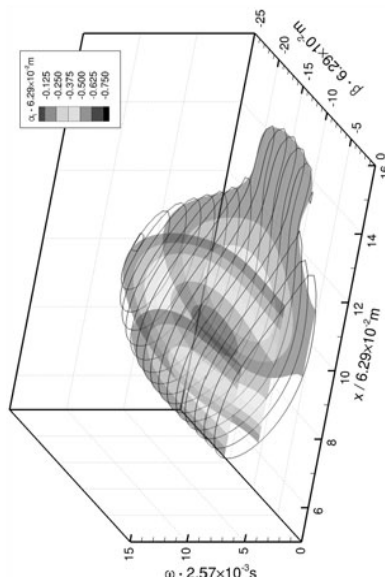


Fig. 11 Spatial stability diagram for the experimental setup with material 3.

Fig. 9 shows a stability diagram for the isotropic material. The unstable region is hardly reduced with respect to the rigid case and the maximum amplification rate is slightly lower. However, the maximum N -factor is reduced from 6.6 down to 5.4. Depending on the disturbance level of the wind tunnel, this reduction could already inhibit the breakdown to turbulence.

When using an anisotropic compliant material, the TS-instability could be further reduced. The stability diagrams for $\theta = 60^\circ$ and $\theta = 75^\circ$ are shown in Fig. 10 and 11 respectively. Here, the unstable region and the amplification rate for two-dimensional waves is significantly reduced. The unstable region for oblique-traveling waves is larger than the one for two-dimensional waves and the maximum amplification rate is located at $\beta \neq 0$. The N -factor is reduced to 2.1 and 2.0 respectively. In the wind tunnel of Pätzold et al. this N -factor leads to inhibition of laminar-turbulent transition. In cases of high free-stream disturbances the breakdown scenario will be different to the rigid-wall case.

The stability diagrams impressively demonstrate that anisotropic compliant walls have a higher potential than isotropic compliant walls to delay or even inhibit laminar-turbulent transition. In case one could actuate the wall of the whole wing section, it would be possible to keep the flow laminar over the entire wing section.

6 Effect of Yawing the Anisotropic Material

It is still not verified if the compliant skin of delphinidae really helps to delay laminar-turbulent transition. Inspired by the work of Pavlov[6] we investigated the effect of yawing the anisotropic material with respect to the flow direction. Pavlov found out that the structures in the epidermis—so-called dermal ridges—make an angle to the flow direction. The effect of this angle was previously unclear. Starting from the materials 2 and 3 we investigated the influence of the yaw angle on the stability properties of the Blasius boundary layer. The results of yawing the material 2 can be viewed in [11]. In this case, the TS-wave with the highest amplification moves from a two-dimensional wave to an oblique-traveling wave. The higher the yaw angle, the higher its spanwise wavenumber. At some yawing angle a FISI becomes unstable traveling in the opposing direction of the TS-wave.

Here we want to show different stages of turning material 3 in more detail. In Fig. 12 a temporal “three-dimensional” stability diagram of the Blasius boundary layer is shown. The neutral stability surface is displayed by lines of constant β . The neutral stability line for $\beta = 0$ is drawn thicker to get an impression how two-dimensional disturbances are affected. Sections of constant α are shaded with contours of the temporal amplification rate. The stability diagram is symmetric with the maximum amplification rate located at $\beta = 0$.

For a yaw angle $\psi = 36^\circ$ the stability diagram is plotted in Fig. 13. The diagram is clearly asymmetric with highest amplification for right-traveling waves. The maximum amplification rate is slightly higher than in the unyawed case. However, two-dimensional waves are more stable.

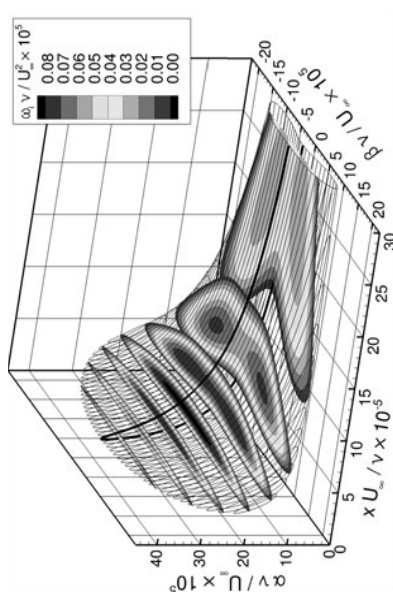


Fig. 12 Stability diagram for Blasius boundary layer over material 3.

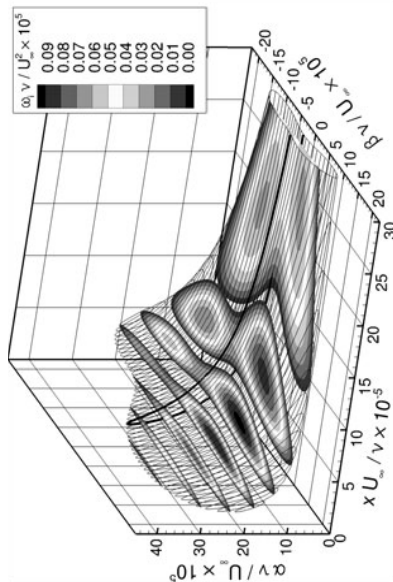


Fig. 13 Stability diagram for Blasius boundary layer over material 4.

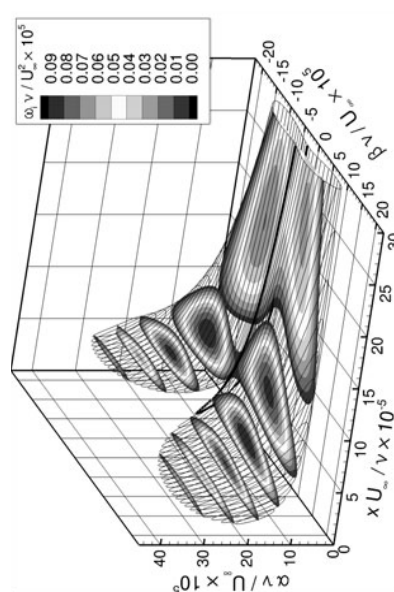


Fig. 14 Stability diagram for Blasius boundary layer over material 5.

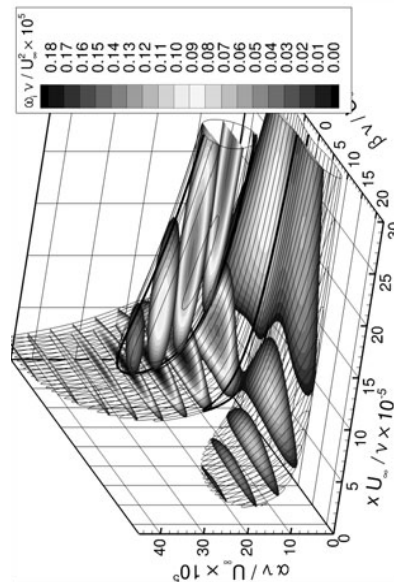


Fig. 15 Stability diagram for Blasius boundary layer over material 6.

With a yaw angle of $\psi = 54^\circ$ two-dimensional waves are significantly more stable. This can be viewed in Fig. 14. Now left-traveling waves are about as amplified as right-traveling waves. The stability diagram has a “symmetry-like” appearance.

Increasing the yaw angle further leads to a destabilization of a FISI-mode. A second unstable region caused by the FISI develops for $\theta = 60^\circ$ as well as for $\theta = 75^\circ$. This can be observed in Fig. 15 for $\psi = 90^\circ$. Here the FISI mode become unstable for two-dimensional waves first. Note that the FISI can become absolutely unstable. It is sufficient to make sure that it is temporally stable at all times to prevent this case which leads to premature transition. For material 6 the amplification rates are significantly higher than for material 3. While turning of the material first promoted right-traveling TS-instabilities, it now promotes left-traveling TS-instabilities.

We conclude that the behavior of the instabilities when yawing the anisotropic material is case dependent. There seems to be no general rule how the single modes are affected. Note that the TS-mode for material 5 and 6 is a formidable example of the invalid Squire-theorem, because it first becomes unstable for oblique waves. It becomes clear that oblique-traveling waves must be taken into account for all stability investigations of compliant walls.

7 Transient Growth of Disturbances over Compliant Walls

One distinguishes between the asymptotic stability for long times and the transient stability for short times[7]. Disturbances which are asymptotically stable do not necessarily have to be monotonically stable. Thus, one can imagine disturbances that are asymptotically stable, but grow *transiently* to high amplitudes which cause laminar-turbulent transition. When using the compliant wall model in the LST we encountered a high sensitivity of the eigenvalues to truncation errors. It was previously unclear if this high sensitivity is due to the numerical scheme, discretization or a matter of the physical problem. If the high sensitivity of the problem is caused by the physics, this will be a sign of a high transient growth.

In comparison to the rigid-wall case, a compliant wall causes additional instability modes. In Fig. 7 a typical eigenvalue spectrum of the Blasius boundary layer is plotted for $Re_{\delta_l} = 1000$, $\alpha = 30 \times 10^{-5} \frac{U_\infty}{v}$ and $\beta = 65 \times 10^{-5} \frac{U_\infty}{v}$ and the compliant material 2. One can see two additional modes, which we name “downstream” and “upstream” FISI-mode. These modes have a high wall deformation with respect to their amplitudes, and can have negative phase speeds or phase speeds that are faster than the free-stream velocity. Furthermore, one can see Squire-modes in the spectrum since we solve the Squire-equation in combination with the Orr-Sommerfeld-equation. These also exist for the rigid wall case, but are mostly not solved for, because it can be shown that they are always stable.

To investigate the transient growth of disturbances over compliant walls, we use the method in Schmid and Henningson[8, sect. 4.4]. By superimposing the calculated instability modes we can determine the transient energy of arbitrary disturbances. We use an energy norm that also incorporates the energy of the moving wall. With some linear algebra, we can optimize disturbances to have the maximum

growth within a certain time span τ . Transient energy developments are plotted exemplarily in Fig. 16 for $Re_{\delta_l} = 1000$, $\alpha = 30 \times 10^{-5} \frac{U_\infty}{v}$, $\beta = 65 \times 10^{-5} \frac{U_\infty}{v}$, and a rigid wall. For the three time transients the energy grows highly in magnitude. At the time τ where the initial disturbance was optimized for, the curves touch the curve $G(t)$ tangentially. The curve $G(t)$ is the envelope of all curves. Its maximum exhibits the maximal possible transient growth.

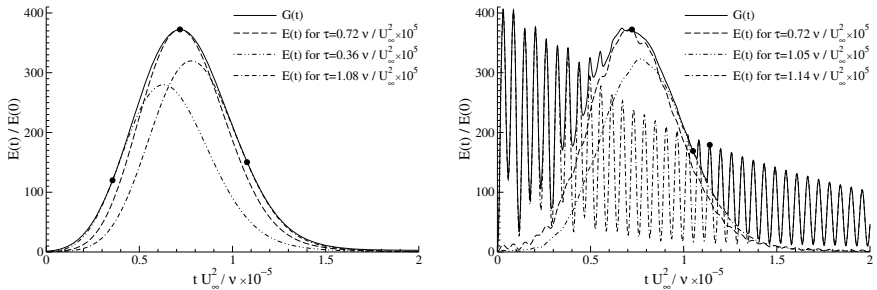


Fig. 16 Time transients of optimal disturbances for Blasius flow over rigid wall with $Re_{\delta_l} = 1000$, $\alpha = 30 \times 10^{-5} \frac{U_\infty}{v}$ and $\beta = 65 \times 10^{-5} \frac{U_\infty}{v}$.

Fig. 17 Time transients of optimal disturbances for Blasius flow over material 2 with $Re_{\delta_l} = 1000$, $\alpha = 30 \times 10^{-5} \frac{U_\infty}{v}$ and $\beta = 65 \times 10^{-5} \frac{U_\infty}{v}$.

In Fig. 17 three transient energy developments are shown for the material 2. The transient behavior has changed dramatically. The envelope $G(t)$ features strong oscillations in wide parts. The curve for $\tau = 0.72 \times 10^5 \frac{v}{U_\infty^2}$ shows a similar development as in the rigid-wall case except for a waviness of the curve. For $\tau = 1.14 \times 10^5 \frac{v}{U_\infty^2}$ the transient of the energy shows high oscillations and the curve is very close to the envelope in large parts. The frequency of this oscillation correlates with the beat frequency of the two FISI-modes. Since the two modes have a very similar eigenfunction—having their energy in the same wall-normal region—they are non-orthogonal with respect to the energy norm.

This shows that there exists another mechanism for the transient growth of disturbances. Both mechanisms coexist; in different regions either one of them prevails. In Fig. 18(a) contours of the maximum of $G(t)$ are plotted versus α and β for the rigid wall. This plot is in excellent agreement with Schmid & Henningson[8]. The maximum energy growth and its location is listed in Table 3 for the cases we present here. These values for the rigid wall are accurate to 0.2% with respect to the values of Butler and Farrell[2].

In Fig. 18(b) contours of the maximum of $G(t)$ are plotted versus α and β for the anisotropic material 2. The contour plot has changed slightly with respect to the rigid wall case. The location of the maximum transient growth and its magnitude are hardly effected. For large streamwise and spanwise wavenumbers the mechanism of the two interfering FISI prevails. However, the magnitude of this mechanism is in

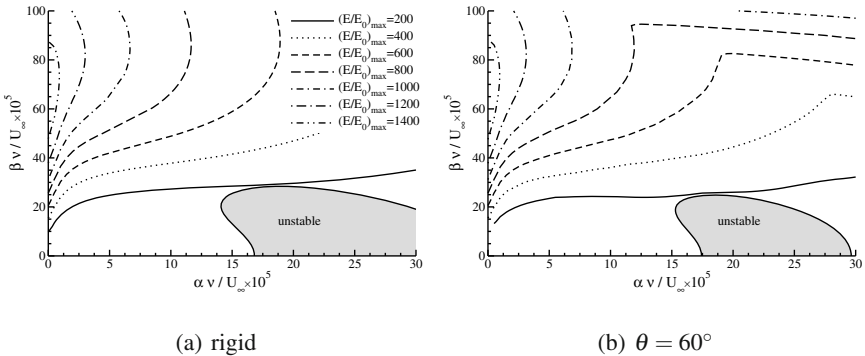


Fig. 18 Comparison of the maximum transient growth in the Blasius boundary layer at $Re_{\delta_1} = 1000$ for rigid wall and material 2.

Table 3 Maximum transient growth and its location

material	G_{\max}	$\alpha(G_{\max}) \left[\frac{U_{\infty}}{V} \right]$	$\beta(G_{\max}) \left[\frac{U_{\infty}}{V} \right]$
rigid	1515	0	6.51×10^{-4}
2	1521	0	6.53×10^{-4}

the same order as the classic one. This leads to the conclusion, that the described sensitivity of the eigenvalues to truncation errors is a numerical problem rather than a physical phenomenon. In cases the asymptotic stability can be reduced to low N-Factors by using compliant walls, the effect of transient growth can become an important factor.

8 Conclusion

We have simulated the boundary layer flow over the wing section of the current experiment using direct numerical simulation. The quantitative comparison of the integral quantities of the boundary layer and the comparison of the disturbance development of a forced Tollmien-Schlichting wave has been successful. An extension of Carpenters anisotropic compliant-wall model has been devised and the current numerical schemes are in perfect agreement to results in literature. Investigations of the stability of the flow in the experiment show that if it was possible to actuate the wall of the whole wing imitating the behavior of a compliant coating, laminar-turbulent transition could be inhibited. The introduced yawing of the material with respect to the fluid direction has the effect that the different instability modes are affected in their promoted propagation direction. The results of the calculations show that the Squire theorem is *not satisfied*. Also the the most unstable wave can be a three-dimensional one. We conclude that in-depth stability investigations of

compliant walls must take three-dimensional instabilities into account. Though we found an additional mechanism of transient growth for compliant walls, we have only encountered cases where the energy growth is in the same order as for the rigid wall.

Acknowledgements. The authors gratefully acknowledge the financial support by Deutsche Forschungsgemeinschaft (DFG) under the research grant Ri680/18.

References

- [1] Baltensperger, R., Trummer, M.R.: Spectral differencing with a twist. *SIAM J. Sci. Comput.* 24, 1465–1487 (2002), doi:10.1137/S1064827501388182
- [2] Butler, K.M., Farrell, B.F.: Three-dimensional optimal perturbations in viscous shear flow. *Phys. Fluids A* 4(8), 1637–1650 (1992), doi:10.1063/1.858386
- [3] Carpenter, P.W., Morris, P.J.: The effect of anisotropic wall compliance on boundary-layer stability and transition. *J. Fluid. Mech.* 218, 171–223 (1990), doi:10.1017/S0022112090000970
- [4] Godunov, S.K.: Numerical solution of boundary-value problems for systems of linear ordinary differential equations. *Uspehi. Mat. Nauk.* 16(3(99)), 171–174 (1961)
- [5] Mack, L.M.: Boundary-layer linear stability theory. In: Special Course on Stability and Transition of Laminar Flow, AGARD report, vol. 709 (1984)
- [6] Pavlov, V.V.: Dolphin skin as a natural anisotropic compliant wall. *Bioinspir. Biomim.* 1(2), 31–40 (2006), doi:10.1088/1748-3182/1/2/001
- [7] Schmid, P.J.: Nonmodal stability theory. *Annu. Rev. Fluid. Mech.* 39(1), 129–162 (2007), doi:10.1146/annurev.fluid.38.050304.092139
- [8] Schmid, P.J., Henningson, D.S.: Stability and Transition in Shear Flows. Applied Mathematical Sciences, vol. 142. Springer, New York (2001)
- [9] Tisseur, F., Meerbergen, K.: The quadratic eigenvalue problem. *SIAM Rev.* 43(2), 235–286 (2001), doi:10.1137/S0036144500381988
- [10] Welfert, B.D.: Generation of pseudospectral differentiation matrices I. *SIAM J. Numer. Anal.* 34(4), 1640–1657 (1997), doi:10.1137/S0036142993295545
- [11] Zengl, M., Rist, U.: Linear stability investigations of flow over yawed anisotropic compliant walls. In: Schlatter, P., Henningson, D.S. (eds.) *Proceedings of the Seventh IUTAM Symposium on Laminar-Turbulent Transition*, Stockholm, Sweden. IUTAM Bookseries, vol. 18, pp. 601–604. Springer, Berlin (2009), doi:10.1007/978-90-481-3723-7_110

Analysis of the Relation between Skin Morphology and Local Flow Conditions for a Fast-Swimming Dolphin

Vadim Pavlov, Donald Riedeberger, Ulrich Rist, Ursula Siebert

Summary. The dolphin skin close to the anisotropic compliant wall design could potentially reduce the friction drag. The goal of this work was to study the relation between local flow conditions around dolphin model and parameters of skin morphology relevant in flow/skin interface. Three-dimensional CAD models presenting authentic geometry of fast-swimming common dolphin *Delphinus delphis* and low-swimming harbor porpoise *Phocaena phocaena* were constructed. CFD study of the flow parameters were carried out for the natural range of dolphin swimming velocities. The results of this study allow to conclude that the streamwise variability of the dolphin skin structure appears to be associated with the streamlined body geometry and corresponding gradients of the velocity and pressure rather than with specific local Re numbers. The hypotheses on different optimal conditions for potential drag-reducing properties of dolphin skin are proposed.

1 Introduction

The basic idea of biomimetics or bionics is to develop new technologies based on highly effective and specialized solutions found in nature. Fast moving animals are usually optimized for efficiency by evolution. Since marine top predators move within a high density and therefore high drag and high buoyancy medium,

Vadim Pavlov · Ursula Siebert
Institute of Terrestrial and Aquatic Wildlife Research,
University of Veterinary Medicine Hannover, Foundation, Werftstr. 6, 25761 Büsum
e-mail: pavlov.v.v@gmail.com

Donald Riedeberger · Ulrich Rist
Institute of Aerodynamics and Gas Dynamics, University of Stuttgart,
Pfaffenwaldring 21, 70550 Stuttgart

their need for efficient drag reduction mechanisms appears quite evident. Modern engineering designs of marine and air transport vehicles make use of streamlined shapes to reduce the form or pressure drag while several solutions aimed at reducing friction drag came from the study of sea animals.

Dolphins are one of the most famous examples of extreme adaptations to drag reduction. Interest in the understanding of a dolphin's hydrodynamics was initiated by Sir J Gray who published his analysis of a dolphin's energetics with unexpected outcome, later called Gray's paradox [1]. Assuming a fully turbulent flow Gray came to the conclusion that a dolphin should possess either enormously powerful muscles (seven times more power per unit mass than any other mammalian) or must be capable of maintaining laminar flow by some extraordinary means. In the late 1950s the aerodynamicist Max Kramer claimed that a dolphin ensured a low level of friction drag by maintaining laminar flow over most parts of its body. The dolphin's skin having an unusually ordered inner structure was considered to be a natural compliant wall effectively suppressing the growth of Tollmien-Schlichting waves in the transition region of the flow, Kramer [2], [3]. This suppression delays the transition from laminar to turbulent flow in the boundary layer thus decreasing the friction drag. Kramer proposed the drag-reducing properties of a dolphin's skin as a solution of Gray's paradox and initiated numerous investigations of the structure and function both of dolphin skins and compliant walls.

The structure of the dolphin skin presents morphological adaptations which appeared as a result of 50 millions year of evolution of cetaceans. A thick layer of skin covers the body of dolphins and streamlines his skeleton and muscles. The skin surface is smooth, hairless and elastic. Skin glands are absent with little exceptions only and the number of layers of the epidermis is reduced compared to other mammals, Sokolov [4].

The structure of the dolphin skin and the blubber layer is highly organized and complex (Parry [6], Sokolov [5], Aleyev [7], Haun et al. [8], Pershin [9], Toedt et al. [10], Hamilton et al. [11]). Unlike the chaotic arrangement for terrestrial mammals, the dermal ridges in cetaceans' skins are arranged in a highly ordered manner. This feature of dolphins' skin inspired suggestions of its possible relation with the flow direction (Sokolov [4], Palmer & Weddell [12], Purves [13], Surkina [14]). In addition, variable blood pressure in capillary vessels in the papillary and sub-papillary layers can modify the range of mechanical properties of the dolphin skin, Pershin [9].

The mechanical properties of dolphin skins related to species, position on the body, degree of training, and physical condition was investigated by Babenko et al. [15] or Toedt et al. [10], for instance. They found that the modulus of elasticity E was lower in the middle of the common dolphin compared to more anterior and posterior sections of the body [16]. For a freshly captured bottle-nosed dolphin, E was higher than for the same animal after training, when the dolphin was calm. The higher value of the modulus of elasticity was interpreted to better correspond to the condition of high-speed swimming [15]. The elastic properties of the integument are particularly dependent on the deeper layer of thick blubber. The

blubber layer is highly resilient, with E-modulus similar to biological rubbers (e.g. Pabst et al. [17]).

Experimental studies of living dolphins did, however, not confirm Gray's superposition about fully laminar flow of swimming dolphin. Direct measurements of turbulence by means of transducers attached to the dolphin's body as well as visualization studies of the flow of swimming dolphins indicated turbulent boundary layers over the most part of the body (Romanenko [18], Rohr et al. [19]). Nevertheless, the level of turbulence measured in the boundary layer of swimming dolphins was significantly lower compared with the flow over a rigid or solid model of the dolphin (Romanenko [18]).

The state-of-the-art view of dolphin hydrodynamics assumes a number of simultaneous adaptations, e.g. to unsteady velocity and pressure gradients from accelerating water over the body, skin tension and micro vibrations, shedding of the superficial layer of epidermis as well as skin damping, which provides additional boundary layer stabilization for the swimming dolphin (Gray [1], Haider & Lindsley [20], Ridgway & Carder [21], Babenko & Carpenter [22], Romanenko [18], Nagamine et al. [23]).

Considerable progress has also been achieved in the theoretical modeling and understanding of compliant walls and the current level of knowledge assumes a substantial delay of laminar-turbulent transition as well as drag reduction in a turbulent boundary layer by appropriately designed compliant walls (Gad-el-Hak [24], Choi et al. [25], Carpenter et al. [26]). According to these a two-layer anisotropic compliant wall which comes close to the actual dolphin's skin structure possesses the best drag-reducing properties (Sokolov [26], [4], Palmer & Weddell [12], Grosskreutz [28], Stromberg [29], Carpenter & Morris [30], Yeo [31]).

At the same time, the mechanism of dolphin skin/flow interaction is still unclear. There are several objective reasons: First, there is still a considerable lack of quantitative data of potentially drag-reducing features of dolphin skin morphologies. Second, these were rarely considered in connection to the local flow properties. The goal of this work is to study the relation between local flow conditions around dolphin model and parameters of skin morphology relevant in flow/skin interface.

2 Methods

Scheme of Sampling

The scheme of sampling was elaborated both for study of skin morphology and parameters of the flow simulated around the dolphin model. As the goal of the study was to compare the flow/skin interface in regions which are characterized by different Reynolds numbers, two parts of the body were selected for that purpose. The first is the dorsal fin that presents a typical wing-like shape and is built of symmetrical cross-sections. The second is limited by the tip of the melon on the head on one side and the position between dorsal fin and genital slit on the other side. Both regions present smooth streamlined bodies with similar geometry at different size. For the comparative purpose in both regions the sampling was done in 20 points located on equal intervals along a line on the body surface. The

dimensionless scheme of sampling allowed comparison of the flow/skin interface for the different parts of the dolphin body.

Skin Morphology and Morphometry

The skin samples of 4x4x4 mm³ in size were fixed in 10% formalin, dehydrated and embedded by the Technovit 7100 media. Both vertical cross-sections and sections parallel to the skin surface were made with the thickness of 7 µm. Sections were dried and stained by hematoxylin-eosin for the general picture and aldehyde-fuchsin to reveal the elastic fibers in dermis layer of the skin.

All measurements of the skin features on the histological sections were done with a measurement system including an Olympus CK X41 microscope and morphometry software. The images of skin sections were captured by the video camera, calibrated, and saved in JPG file format. On the vertical cross sections of the skin the following parameters were measured:

1. Height of the epidermis (HEP), mm
2. Height of the dermal papillary layer (HDP), mm
3. Height of the subpapillary layer of dermis (HSL), mm
4. Thickness of the dermal ridges (TDR), mm
5. Thickness of the epidermal ridges (TER), mm

The angle between the dermal ridges direction and the long axis of the body was measured on sections parallel to the skin surface. The average values of all morphological parameters were calculated based on three repeated measurements.

CAD Modeling

A full-scale, three-dimensional CAD model of a common dolphin *Delphinus Delphis* was constructed with SolidWorks software. For the common dolphin the measurements and photos of the body of a newly stranded animal were used. All measurements were taken according to the standard protocol of postmortem examination (Kuiken and Hartmann 1993). Laser scanning data of the rigid model of the same species held at the German Oceanographic Museum in Stralsund were used for correction of the dolphin's body geometry. The resulting model presents an authentic geometry of an adult female common dolphin of 1.94 m length.

Additionally, a three-dimensional geometry of a by-caught harbour porpoise was obtained by an Atos V7 optical scanning system by IGS Development GmbH. Scanned data were processed with the GOM software and exported in CAD format as a set of cross-sections. The resulting model built with the SolidWorks software presents an authentic geometry of a sub-adult male harbor porpoise of 1.1 m length.

For both species models of fins were constructed separately using photos of fin outlines as well as cross-sectional measurements of fins and joined to the models of the bodies. A straightened body position, which corresponds to the gliding phase of the dolphin's swimming cycle, was chosen for the CFD study.

CFD Study

The flow around the dolphin and porpoise model was studied with the FloWorks software. The flow parameters along with both sampling lines on the common dolphin were measured for the range of natural swimming velocities. The calculations were done under the following conditions: Static pressure 101325 Pa, temperature 20° C, turbulence intensity 0.1%, and turbulent length scale of 3.44E-04 m. The velocity in X direction (along long axis of the model) varied from 2 to 8 m/sec at fixed 0 m/sec for the velocity both in Y and Z direction. FloWorks uses the finite volume method to solve the Reynolds-averaged Navier-Stokes equations, implementing the $k - \epsilon$ turbulence model.

The numerical simulation of laminar-turbulent transition on the same model of common dolphin using the empirical γ - Re_0 transition model was carried out by Donald Riedeberger [32] at IAG, Stuttgart University. The finite-volume code STAR-CCM+ was used with a RANS formulation and SST-k- ω closure together with similar boundary conditions as prescribed before. Simulated swimming speed varied in the range from 0.25 to 5 m/sec, with the turbulent intensity ranging from 0.25% to 5%.

Model of the Flow/Skin Interface

The simplified model of the flow/skin interface includes the angle ϕ formed by the velocity vector on the outer edge of the boundary layer and the plane of the dermal ridges. The angle α formed by the dermal ridges with the Y-axis was used for the calculation of a 2D vector of dermal ridges. Then a 3D vector a of the dermal ridges was obtained by the projection of the 2D vector on the surface of the 3D model (Pavlov 2003).

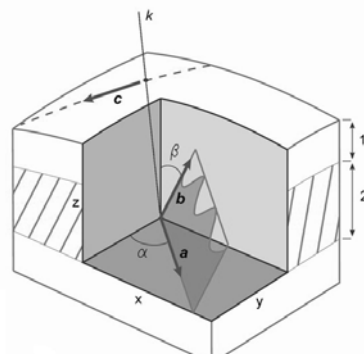


Fig. 1 Definitions of angles of the dolphin skin structures, used for the calculation of the angle ϕ .

The angle β formed by the dermal papillae with the Z-axis as well as the vector normal to the fin surface was used for the calculation of a 3D vector b of the dermal papillae. Vectors a and b were used for the calculation of the local spatial orientation of the plane of the dermal ridges in the data points (figure 1). The velocity vector c at the same points on the fin surface was used for the calculation of

the angle ϕ between the plane of the dermal ridges and a line corresponding to the local flow direction:

$$\sin \phi = \frac{|(y_b \cdot z_a - z_b \cdot y_a)x_c + (x_b \cdot z_a - z_b \cdot x_a)y_c + (x_b \cdot y_a - y_b \cdot x_a)z_c|}{\sqrt{(y_b \cdot z_a - z_b \cdot y_a)^2 + (x_b \cdot z_a - z_b \cdot x_a)^2 + (x_b \cdot y_a - y_b \cdot x_a)^2} \cdot \sqrt{x_c^2 + y_c^2 + z_c^2}}$$

where a – ridges vector, b – papillae vector, and c – velocity vector.

3 Results

Hydrodynamics

The streamlined body of the common dolphin has a complex shape that resembles a body of revolution in the region from blowhole to the leading edge of the dorsal fin only. The head of the dolphin, especially the external morphology of the melon and the beak affects the flow and forms specific gradients of the velocity and pressure in that region. This part of the dolphin's body looks important in sense of flow control and formation of specific flow patterns around the dolphin body. The rear part of the dolphin's body, approximately 1/3 of the body length is flattened starting from the genital area to the tail flukes. To avoid the influence of natural turbulators like eye or blowhole, the position of the sampling line was defined to lie on the plane oriented at 45 degrees to the plane of symmetry of the dolphin body. This part of the body was found to show more homogeneous (i.e. less gradients in circumference direction), representative flow on the main body compared to other areas in the CFD simulation thus verifying the approach. For the dorsal fin the shape of the sampling line is close to a conventional airfoil shape. The cross-section of the dorsal fin made at the mid of the wing span is close to the NACA 63-015A and GOE 459 symmetrical airfoils. The main difference occurs at the thickened trailing edge of the fin.

The similarity in shape between fin and body section leads to a resemblance of gradients of the flow parameters in both regions (figure 2). The obvious difference in pressure gradient on the last third of the dolphin's body that associated with the strokes of the tail fin.

The results of the flow simulations obtained with Flowworks show a shift of the transition zone in frontward direction as well as a reduction of the laminar regions with increasing speed of swimming from 2 to 8 m/sec. For the minimal speed of swimming the laminar region on the upper part of the body reaches the dorsal fin position that corresponds approximately to the half of the body length. For the maximal speed of 8 m/sec this region is reduced to the position of the pectoral fins that is less than one third of the body length.

While preliminary simulations in STAR-CCM+ with a low turbulence environment verified the above results, detailed study of the transition on the common

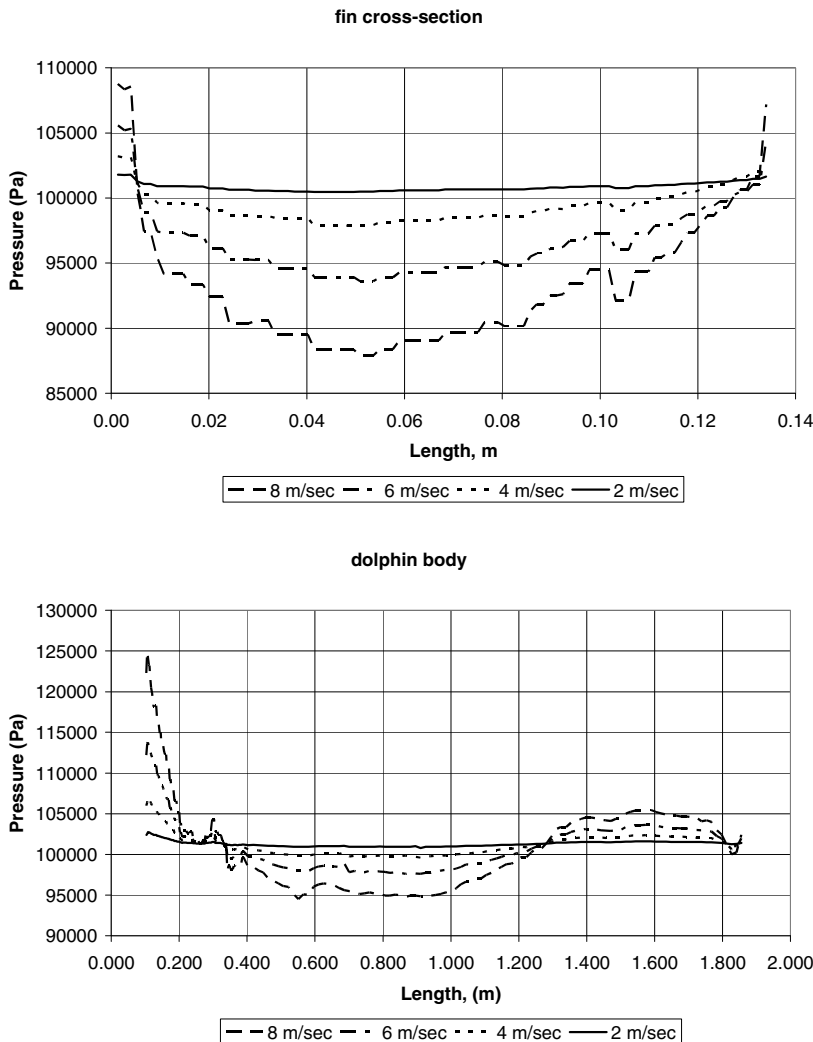


Fig. 2 Pressure distribution along the cross-section of the dorsal fin (upper graphics) and body of the common dolphin (lower graphics) calculated for the range of dolphin swimming velocities.

dolphin model carried out by Riedeberger has shown that for the cruising speed of swimming around 3 m/sec in a moderate 1% turbulence-intensity environment the flow around the dolphin is mainly turbulent with limited laminar regions at the front of the head (figures 3, 4). The influence from the fin appendices on the main body pressure distribution was found to be of negligible impact. Estimations of possible surface drag reduction due to a downstream shift of transition were as high as 25 %.

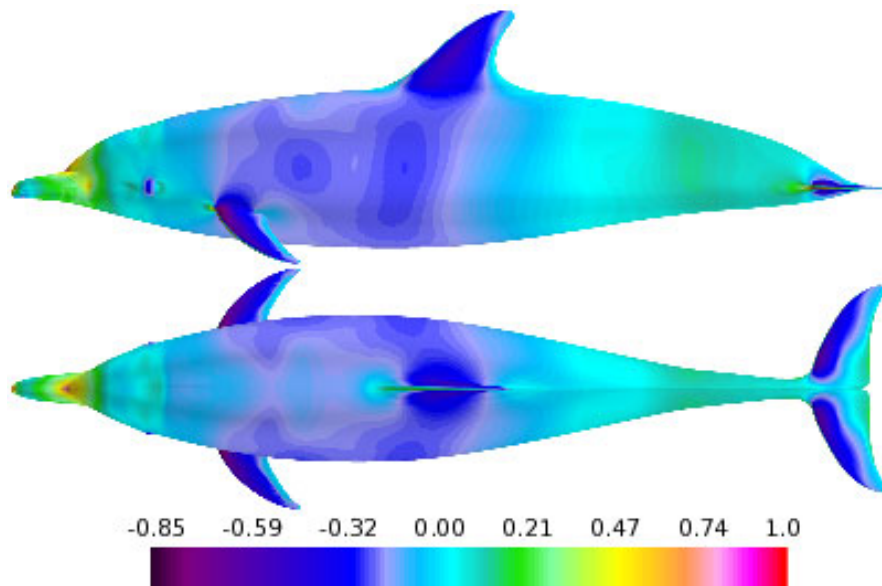


Fig. 3 Distribution of pressure coefficient C_p for free-stream velocities of $u_\infty = 1.0$ m/s, side (upper) and top (lower) projection, turbulence intensity $Tu = 1\%$

4 Skin Morphology

Skin parameters of the common dolphin were compared in two locations, on the dorsal fin and on the body of the animal. Difference in mean values of thickness of dermis and epidermis ridges, height of the subpapillary layer, as well as angle ϕ was found significant at $p < 0.05$. The significance of difference in mean values of the height of dermal papillary layer as well as total height of epidermis was found lower, at $p > 0.05$.

A sketch of the different skin three-dimensional structures for both sampling lines is presented in Figure 5. The height of the composite upper layer of skin which presents the biological analog on to an anisotropic compliant wall in engineering is similar at both locations. The difference in three-dimensional structure is related to the density and dimensions of the dermal ridges as well as their orientation with respect to the flow direction.

At similar velocity gradient the distribution of the skin parameters is not uniform along the fin and the body of the dolphin. The skin parameters HEP, HDP, and HSL which make up the “compliant wall of the dolphin” correlate with the velocity gradient and smoothly decrease in caudal direction in both regions (figure 6). This relation stands out stronger for HEP and HDP and is weaker for the HSL parameter. Apart of that, the thickness both of dermal and epidermal ridges is negatively

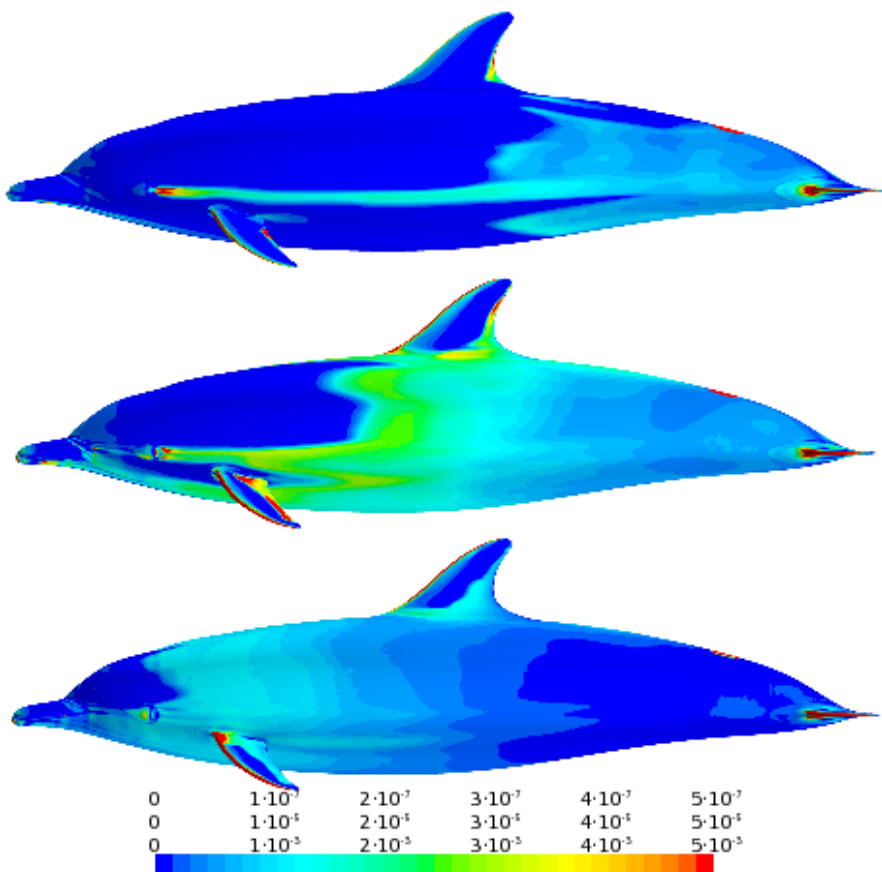


Fig. 4 Turbulent kinetic energy k for free-stream velocities of $u_\infty = 0.25$ (upper), 1.0 (mid) and 2.5 m/s (lower), turbulence intensity $Tu = 1\%$.

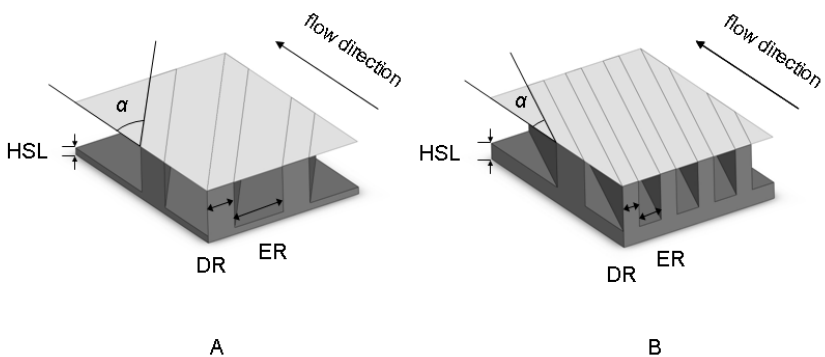


Fig. 5 Sketch of three-dimensional structure of dolphin skin. A – on dorsal fin. B – along body.

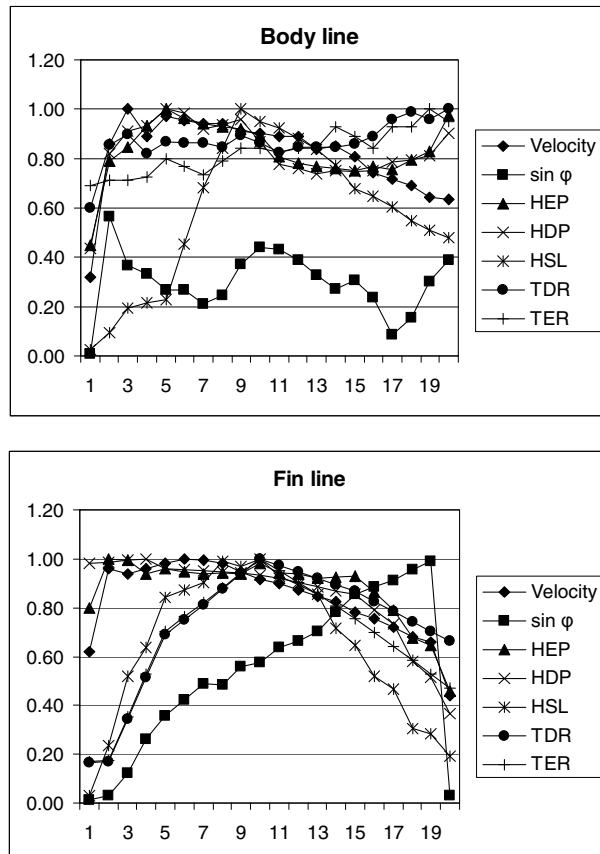


Fig. 6 Variability of the flow and the skin structure parameters along two sampling lines. Data are normalized from 0 to 1.

correlated with the chord-wise velocity distribution. This correlation is stronger on the dorsal fin compared with the body region.

Data obtained for the dorsal fin of the common dolphin can be compared with the previous results of the study for the dorsal fin of a harbor porpoise *Phocaena Phocaena*. As the cross-sections of the fins are close to conventional airfoils, the hypothesis of a possible relation between skin morphology parameters and derivatives of the functions of cross-sectional geometry was examined. For that purpose a curve fits of cross-sections of the dorsal fins were done with CurveExpert 1.4 by Daniel Hyams. The chord-wise thickness distribution $Z(X)$ was interpolated by a 4th degree polynomial fit with the following coefficients for the common dolphin: $a = -1.20E-03$, $b = 3.49E-03$, $c = -3.23E-04$, $d = 1.12E-05$, and $e = -1.77E-07$. For the cross-section of the harbor porpoise the appropriate coefficients were: $a = -9.50E-01$, $b = 3.21E+00$, $c = -4.37E-01$, $d = 2.36E-02$, and $e = -4.79E-04$.

For the common dolphin it was found that $\sin \phi$ has a negative correlation with the 1st derivative of Z(X) function significant at $p<0.05$. This correlation revealed to be lower for the harbor porpoise. The difference in this correlation between two species is related with a less ordered arrangement of the dermal ridges on the dorsal fin of the harbor porpoise. The first two parameters of skin layer composition, HEP and HDP, have positive correlation with the 1st derivative of Z(X) significant at $p<0.05$ in both species, while for the HSL this correlation was found to be low.

Table 1 Correlations between skin morphology parameters and derivatives of the functions of cross-sectional geometry of the dorsal fin of common dolphin. Marked correlations are significant at $p < .05000$, N=20 (Casewise deletion of missing data).

	1st drv	2nd drv	Pressure	$\sin \phi$	HEP	HDP	HSL
1st drv	1.00	-0.97	-0.03	-0.77	0.50	0.72	-0.12
2nd drv	-0.97	1.00	-0.14	0.82	-0.30	-0.54	0.31
Pressure	-0.03	-0.14	1.00	-0.19	-0.75	-0.56	-0.87
$\sin \phi$	-0.77	0.82	-0.19	1.00	-0.09	-0.31	0.24
HEP	0.50	-0.30	-0.75	-0.09	1.00	0.94	0.64
HDP	0.72	-0.54	-0.56	-0.31	0.94	1.00	0.50
SPL	-0.12	0.31	-0.87	0.24	0.64	0.50	1.00

Table 2 Correlations between skin morphology parameters and derivatives of the functions of cross-sectional geometry of the dorsal fin of harbor porpoise. Marked correlations are significant at $p < .05000$, N=20 (Casewise deletion of missing data).

	1st drv	2nd drv	Pressure	$\sin \phi$	HEP	HDP	HSL
1st drv	1.00	0.56	0.55	-0.21	0.67	0.80	-0.08
2nd drv	0.56	1.00	-0.29	-0.44	0.92	0.78	0.71
Pressure	0.55	-0.29	1.00	0.08	-0.19	0.09	-0.85
$\sin \phi$	-0.21	-0.44	0.08	1.00	-0.25	-0.11	-0.19
HEP	0.67	0.92	-0.19	-0.25	1.00	0.94	0.64
HDP	0.80	0.78	0.09	-0.11	0.94	1.00	0.38
SPL	-0.08	0.71	-0.85	-0.19	0.64	0.38	1.00

5 Discussion

The challenge in biomimetics studies of natural phenomena is the complexity of the biological objects. As a rule, any biological structure is multifunctional by its nature and serves different functions. The main task in modeling of useful effects of a biological system is to reveal the variables that define the most part of the system behavior. In highly specialized systems showing an extremity in adaptation to (a) specific function(s), the number of significant variables can be limited, that

helps in modeling the biological phenomenon. The dolphin skin differs from the skin of terrestrial mammals by an unusually ordered inner structure and a considerably simplified composition with reduced glands, hairs, and layers of the epidermis. These peculiarities of the dolphin skin were considered as adaptation to the life in the water which are potentially able to decrease the friction drag.

The choice of parameters relevant for the flow/skin interface is facilitated if one considers the dolphin skin as natural analogue of anisotropic compliant walls. The latter have ordered inner structure and have a good potential in decreasing friction drag. In the general case, the wall matrix is reinforced by the aligned elements (fibers or voids) making the inner structure of the wall ordered [28]. The structure of the anisotropic wall is arranged so that rather than being displaced up and down by the fluctuating pressure it is displaced sideways as well making a substantial angle to the vertical, thereby generating a negative Reynolds shear stress on the compliant surface [30].

The first group of selected morphological parameters includes parameters of skin composition, i.e. the total height of the skin, as well as the height of two basic layers of skin. This corresponds to the basic design of a two-layer anisotropic compliant wall by Carpenter. The angle ϕ presents the angle between flow direction and dermal ridges as an analogue to the ordered elements in the compliant wall matrix. The second group of parameters consists of the thickness of the ordered elements and distance between them. The parameters of this group can be considered as the next step from the two-dimensional case of an anisotropic compliant wall to the more complex three-dimensional one.

For a better understanding the correlations between local flow parameters and skin structure at two different locations having similar shape but different Reynolds numbers, i.e., the body and dorsal fin of the dolphin, were compared. Additionally, the results for the dorsal fin were compared with the previously obtained data for the harbor porpoise. The last comparison aimed to reveal possible differences in the flow/skin interface in fast-swimming (common dolphin) and low-swimming (harbor porpoise) species.

The data obtained show obvious correlations between parameters of the two-dimensional skin composition and relative gradients of the velocity and pressure. This correlation was found similar for the dolphin body and the fin, having different ranges of Re number. A similar relationship was also observed for the parameters of the three-dimensional structure of the skin. Apart from that, the relation between the angle ϕ and pressure and velocity gradients was found to be non-linear.

The results of this study allow to conclude that the stream-wise variability of the dolphin skin structure appears to be associated with the streamlined body geometry and corresponding gradients of the velocity and pressure rather than with specific local Re numbers. The difference in results for the dolphin's body and cross-section of the dorsal fin can be related to the degree of specialization of these two regions. The dorsal fin having a wing-like shape presents an extremum in hydrodynamic function while the fin cross-sections are close to conventional symmetrical airfoils. Apart from the body region, the relation between airfoil geometry and surface structure is presented clearer there. All morphological

parameters including the angle ϕ correlate with the 1st derivative of the interpolated cross-sectional geometry.

Comparison of this correlation between common dolphin and harbor porpoise has shown that it is stronger for the first species. This distinction could reflect the difference in hydrodynamic performance, as the common dolphin is recognized to be a fast swimmer, while the harbor porpoise has an approximately half as large average-speed of swimming. To check if the difference in the flow/skin interface refers to the potential drag reduction rather than the taxonomic features, an additional study of species with different swimming performance is needed.

Theoretical and experimental studies of compliant walls have shown that drag can be minimized by delaying the transition from laminar to the turbulent flow and by stabilization of the turbulent flow in the boundary layer. Potentially, a dolphin skin close to the anisotropic compliant wall design could reduce the friction drag in both ways. Meanwhile, the potential drag-reducing effect depends considerably on the external flow conditions, such as initial flow velocity and turbulence level.

A general question of possible friction-drag reduction by the skin of a swimming dolphin can be posed as follows: Which flow conditions is it optimized for? Dolphins use a variety of swimming speeds and modes, the cruising speed is normally within the range of 1-4 m/sec, while the top speed of the burst can reach up to 8-10 m/sec. During swimming the active phase can be interspersed with gliding phases which anticipate different flow regimes and mechanisms of boundary-layer stabilization.

From the point of view of optimization of energy expenditures, two hypotheses on potential drag-reducing properties of dolphin skin can be proposed. The first assumes that the skin is optimized for the cruising motion with moderate speed of swimming 1-4 m/sec in low depth with relatively high initial turbulence. The fact, that dolphins spend most of their time moving with moderate speed speaks in favor of this supposition. An alternative hypothesis, based on the “cheetah hunting strategy” [33], anticipates extreme energy expenditure for a short-time period with a chance to catch a prey and compensate energy losses. Following this idea, the dolphin skin could be optimized for the reduction of friction drag during fast swimming at moderate or high depth with relatively low initial turbulence.

6 Outlook

The next step in the study of the flow/skin interface in dolphins is getting the complete distribution of skin morphology and flow parameters all over the body of the dolphin. The complex geometry of dolphins presents a variety of specific local flow conditions that gives an opportunity to verify the relation between skin structure and local flow parameters obtained in the ongoing study. An important prerequisite for a future study is the variability of the swimming performance and Re numbers of different species that allows carrying out comparative studies of the potential drag-reducing properties of dolphin skin.

From the point of numerical simulation the next steps would include a more detailed understanding of the marine turbulent environment to more accurately account for the reality in simulation boundary conditions. Furthermore unsteady effects on transition location due to swimming body motion would enable more insight to the phenomena whereas a comparative study of the possibilities of available turbulence modeling approaches can shed more insight in the limitations of simulation and in the end enable more precise answers to drag-reduction capabilities of modeled compliant walls.

Acknowledgements. Our thanks go to Dr. Vincent, Dr. Dabin, Dr. Doremus, and Dr. Jensen for their help with dolphin morphology, and to the staff of the Labor für Orthopädie und Biomechanik for their help with laser scanning the dolphin model. We also thank Dr. Benke for the opportunity to work on a dolphin model in the German Oceanographic Museum in Stralsund.

References

- [1] Gray, J.: Studies in Animal Locomotion VI. The Propulsive Powers of the Dolphin. *J. Exp. Biol.* 13, 192–199 (1936)
- [2] Kramer, M.O.: Boundary Layer Stabilization by Distributed Damping. *J. Amer. Soc. Nav. Eng.* 72, 25–33 (1960a)
- [3] Kramer, M.O.: The Dolphins' Secret. *New. Sci.* 7, 1118–1120 (1960b)
- [4] Sokolov V.E.: Integument of mammals. Nauka, Moscow (in Russian) (1973)
- [5] Sokolov, V.E.: Some Similarities and Dissimilarities in the Structure of the Skin Among the Members of the Suborders Odontoceti and Mysticeti (Cetacea). *Nature* 185, 745–747 (1960)
- [6] Parry, D.A.: The Swimming of Whales and a Discussion of Gray's Paradox. *J. Exp. Biol.* 26, 24–34 (1949a)
- [7] Aleyev, Y.G.: Nekton. Junk, The Hague (1977)
- [8] Haun, J.E., Hendricks, E.W., Borkat, F.R., Kataoka, R.W., Carder, D.A., Chun, N.K.: Dolphin Hydrodynamics: Annual Report FY 82. NOSC* TR935. SSC San Diego, CA (1983)
- [9] Pershin, S.V.: Fundamentals of hydrobionics. Sudostroyeniye, Leningrad (1988) (in Russian)
- [10] Toedt, M.E., Reuss, L.E., Dillaman, R.M., Pabst, D.A.: Collagen and elastin arrangement in the blubber of common dolphin (*Delphinus delphis*). *Am. Zool.* 37, 56A (1997)
- [11] Hamilton, J.L., McLellan, W.A., Pabst, D.A.: Functional Morphology of Harbor Porpoise (*Phocoena phocoena*) Tailstock Blubber. *Amer. Zool.* 38, 203A (1998)
- [12] Palmer, E., Weddell, G.: The relation between structure, innervation and function of the skin of the bottlenose dolphin (*Tursiops truncatus*). *Proc. Zool. Soc. Lond.* 143, 553–568 (1964)
- [13] Purves, P.E.: The Structure of the Flukes in Relation to Laminar Flow in Cetaceans. *Z. Sdugertierkd* 34, 1–8 (1969)
- [14] Surkina, R.M.: Structure and function of the skin muscles of dolphins. *Bionika* 5, 81–87 (1971) (in Russian)

- [15] Babenko, V.V., Koslov, L.F., Pershin, S.V., Sokolov, V.Y., Tomilin, A.G.: Self-adjustment of Skin Dampening in Cetaceans in Active Swimming. *Bionika* 16, 3–10 (1982) (in Russian)
- [16] Babenko, V.V.: Investigating the Skin Elasticity of Live Dolphins. *Bionika* 13, 43–52 (1979) (in Russian)
- [17] Pabst, D.A., McLellan, W.A., Gosline, J.G., Piermarini, P.M.: Morphology and Mechanics of Dolphin Blubber. *Amer. Zool.* 35, 44A (1995)
- [18] Romanenko, E.V.: Fish and Dolphin Swimming. Pensoft, Sofia (2002)
- [19] Rohr, J., Latz, M.I., Fallon, S., Nauen, J.C., Hendricks, E.W.: Experimental Approaches Towards Interpreting Dolphin-stimulated Bioluminescence. *J. Exp. Biol.* 201, 1447–1460 (1998)
- [20] Haider, M., Lindsley, D.B.: Microvibrations in Man and Dolphin. *Science* 146, 1181–1183 (1964)
- [21] Ridgway, S.H., Carder, D.A.: Features of Dolphin Skin with Potential Hydrodynamic Importance. *IEEE Eng. Med. Biol.* 12, 83–88 (1993)
- [22] Babenko, V.V., Carpenter, P.W.: Dolphin hydrodynamics Flow Past Highly Compliant Boundaries and in Collapsible Tubes. In: Carpenter, P.W., Pedley, T.J. (eds.), ch. 13, pp. 293–323. Kluwer, Dordrecht (2003)
- [23] Nagamine, H., Yamahata, K., Hagiwara, Y., Matsubara, R.: Turbulence modification by compliant skin and strata-corneas desquamation of a swimming dolphin. *J. Turb.* 18, 1–25 (2004)
- [24] Gad-el-Hak, M.: Compliant coatings: a decade of progress. *Appl. Mech. Rev.* 49, 147–157 (1996)
- [25] Choi, K.S., Yang, X., Clayton, B.R., Glover, E.J., Atlar, M., Semenov, B.N., Kulik, V.M.: Turbulent drag reduction using compliant surfaces. *Proc. R. Soc. A* 453, 2229–2240 (1997)
- [26] Sokolov, V.E.: Structure of the integument of some cetaceans. *Byulleten' Moskovskogo Obshestva Ispitatelyj Prirody Otdel Biologii* 60, 45–60 (1955) (in Russian)
- [27] Carpenter, P.W., Davies, C., Lucey, A.D.: Hydrodynamics and compliant walls: does the dolphin have a secret? *Curr. Sci.* 79, 758–765 (2000)
- [28] Grosskreutz, R.: Wechselwirkungen zwischen turbulenten Grenzschichten und weichen Wänden. *MPI für Strömungsforschung und der AVA Göttingen Mitt* 53 (1971)
- [29] Stromberg, M.W.: Dermal–epidermal relations in the skin of bottlenose dolphin (*Tursiops truncatus*). *Anat. Histol. Embryol.* 18, 1–13 (1989)
- [30] Carpenter, P.W., Morris, P.J.: The effect of anisotropic wall compliance on boundary-layer stability and transition. *J. Fluid Mech.* 288, 171–223 (1990)
- [31] Yeo, K.S.: The hydrodynamic stability of boundary-layer flow over a class of anisotropic compliant walls. *J. Fluid Mech.* 220, 125–160 (1990)
- [32] Riedeberger, D., Rist, U.: Numerical simulation of laminar-turbulent transition on a dolphin using the γ -Reθ model. In: Nagel, W.E., Kröner, D.B., Resch, M.M. (eds.) *High Performance Computing in Science and Engineering 2011: Transactions of the High Performance Computing Center, Stuttgart (HLRS)*, Springer, Berlin (2011)
- [33] Aguilar Soto, N., Johnson, M.P., Madsen, P.T., Diaz, F., Dominguez, I., Brito, A., Tyack, P.: Cheetahs of the deep sea: Deep foraging sprints in short-finned pilot whales off Tenerife (Canary Islands). *Journal of Animal Ecology* 77, 936–947 (2008)

Hydrodynamic Perception in Pinnipeds

Wolf Hanke, Sven Wieskotten, Benedikt Niesterok, Lars Miersch,
Matthias Witte, Martin Brede, Alfred Leder, and Guido Dehnhardt

Abstract. The vibrissal system of pinnipeds such as harbor seals (*Phoca vitulina*) or California sea lions (*Zalophus californianus*) serves not only for the detection and identification of objects by direct touch, but also detect and analyze water movements (hydrodynamic stimuli). These two species represent two different types of vibrissae, one with an undulated outline (harbor seal) and one with a smooth outline (sea lion). In our recent set of studies, we analyzed the hydrodynamic stimuli generated by stationary fish and by escaping fish, and tested the ability of pinnipeds to analyze artificial hydrodynamic stimuli that share certain features with natural hydrodynamic stimuli. Biomechanical studies of isolated vibrissae in a flow tank show different signal-to noise ratios for the two species that are consistent with their different performance in behavioral experiments, and can be explained by fluid-structure interactions.

1 Introduction

The aquatic environment poses special challenges to the sensory systems of animals that need to orient and perform vital activities therein. Given that the operating range of the visual system is generally severely limited by absorption and scattering of light, and quite often reduced to virtually zero in deep waters or waters rich in suspended matters, aquatic animals have refined other senses, such as chemoreception and mechanoreception including the sense of touch, hearing, and hydrodynamic perception.

Wolf Hanke · Sven Wieskotten · Benedikt Niesterok · Lars Miersch · Guido Dehnhardt
Rostock University, Institute for Biosciences, Chair of Sensory and Cognitive Ecology,
Albert-Einstein-Strasse 3, 18059 Rostock, Germany
e-mail: {wolf.hanke, guido.dehnhardt}@uni-rostock.de

Matthias Witte · Martin Brede · Alfred Leder
Rostock University, Chair of Fluid Mechanics, Albert-Einstein-Strasse 2, 18059 Rostock
e-mail: {matthias.witte2, martin.brede}@uni-rostock.de,
alfred.leder@uni-rostock.de

Hydrodynamic perception is herein defined as the reception and analysis of water movements other than sound. These water movements are thus defined by the feature of not propagating through the water as a wave by alternating compression and decompression of the medium. They are termed hydrodynamic stimuli.

Hydrodynamic perception has developed several times independently during evolution in both invertebrates (animals without a backbone) and vertebrates (animals with a backbone). The oldest taxa of vertebrates, that is the various groups commonly subsumed as fishes, are primarily aquatic. They share the lateral line sensory system that measures water movements using hair cells. The lateral line is also present in amphibians. Reptilians sometimes have hydrodynamic sensory systems, but on a different morphological basis; no hydrodynamic sensory systems have been described in birds.

In mammals, hydrodynamic sensory systems have only recently been described (Dehnhardt et al., 1998; Dehnhardt et al., 2001). They are present at least in pinnipeds (seals and sea lions) (Dehnhardt et al., 1998; Gläser et al., 2011), insectivores (Catania et al., 2008), and rodents (Hanke, 2010). These mammalian hydrodynamic sensory systems are based on vibrissae, also known as whiskers or sinus hairs. Vibrissae are present in almost all mammals and have originally developed to sense and analyze items by direct touch (cf. Carvell and Simons, 1990; Ling, 1977).

The present work specifically deals with hydrodynamic perception in harbor seals (*Phoca vitulina*) and California sea lions (*Zalophus californianus*). These two species are typical representatives of the two major groups of pinnipeds: the harbor seal belongs to the true seals, while the California sea lion belongs to the eared seals. True seals are adapted to an aquatic life style to a larger extent than eared seals, which tend to be more amphibious (although both catch their prey under water). The vibrissae of both groups are (with few exceptions among the true seals) different in shape: the vibrissae of true seals have an undulated outline, while the vibrissae of eared seals are smooth (Fig. 1).

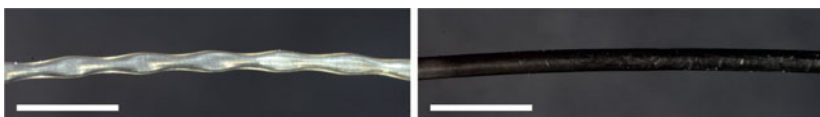


Fig. 1 A harbor seal vibrissa showing the typical undulated shape (left), and a California sea lion vibrissa. Scale bars 5 mm.

It was known from earlier behavioral studies that both species are able to sense hydrodynamic stimuli caused by an oscillating sphere (hydrodynamic dipoles) while at rest (Dehnhardt and Mauck, 2008; Dehnhardt et al., 1998; Dehnhardt et al., 2004). It was also known that harbor seals can detect and follow hydrodynamic trails (Dehnhardt et al., 2004; Dehnhardt et al., 2001). Hydrodynamic trails are hydrodynamic stimuli left behind by animals, for example by prey, that have passed by at an earlier point in time (cf. Hanke et al., 2000); they can last for at

least a minute and contain information that allows to discriminate between different trail generators to a certain degree (Hanke and Bleckmann, 2004). Harbor seals can follow hydrodynamic trails generated by artificial objects which are in the same order of magnitude as the trails generated by swimming fish (Dehnhardt et al., 2001; Hanke, 2001; Hanke et al., 2000) and hydrodynamic trails generated by other seals (Schulte-Pelkum et al., 2007).

Further questions that need to be addressed concern the properties of hydrodynamic stimuli that are of ecological relevance to the harbor seal, specifically the water movements caused by swimming or stationary fishes, and the ability of harbor seals to discriminate between different objects by means of the hydrodynamic stimuli that they cause.

2 Experiments on Hydrodynamic Stimuli Produced by Fish

2.1 Stationary Fishes

To investigate the water flow generated by stationary fishes, a total of three flounders (*Platichthys flesus*), two European eels (*Anguilla anguilla*), and three rainbow trout (*Oncorhynchus mykiss*) were used. Flounders and eel were obtained from local commercial fishery. Trout were obtained from the state research facility for aquaculture (Landesforschungsanstalt für Fischereiwirtschaft), Born am Darss, Germany.

Hydrodynamic stimuli were quantified using Digital Particle Image Velocimetry (Westerweel, 1997; Willert and Gharib, 1991). Depending on the expected flow speed and on the size of the field of view, one of two solid state lasers was used: a 0.5 W DPSS-Laser Entertainer 500 (Quantum physics, Newcastle, UK) or a 10 W OPSL Laser Coherent Taipan (Coherent, Santa Clara, CA, USA). Lasers were used in continuous mode. Seeding particles were neutrally buoyant polyamide particles colored with titan disulfide (Vestosint 1141, Degussa AG, Marl, Germany). High speed PIV images were recorded with a Phantom V12 camera (Vision Research, Wayne, NJ, USA). The behavior of the experimental animals was additionally monitored with a camcorder (Sony XLS-1 or Sony DCR).

Analysis of the particle image velocimetry data was performed with the PIV software DaVis 7.2 (Lavision GmbH, Göttingen, Germany) and with custom made scripts in Matlab 6.5 (The Mathworks, Natick, MA, USA).

We found that stationary fishes produced significant amounts of water currents by breathing (Bublitz et al., 2010; and Bublitz et al., in preparation). In all three species, breathing currents usually exceeded the water flow produced by fin movements after the fish had adapted to the measuring situation. Furthermore, they differed in strength relative to body weight, being the strongest in flounders. Breathing currents were oriented in different directions depending on the species: upwards into the water column in flounders, laterally in trout, and downwards in eels.

2.2 Fast-Starting Fishes

Fast starts are flight reactions of fish that occur in reaction to startling stimuli such as simulated predator attacks. The fast starts that accelerate the fish the most are initialized by a C-shaped bend of the body and are termed C-starts (Webb, 1975, 1976). Fast-starting trout were, due to the spatial extent of the generated water movements, investigated in an indoor pool ($3\text{ m} \times 1.4\text{ m}, *0.5\text{ m L*W*H}$, water level 0.3 m) made from planks and pond liner. Two horizontal laser light sheets were generated by a 10 W OPSL laser equipped with a beam splitter and cylinder lenses. The light sheets were coupled into the water via mirrors and Perspex screens to avoid any influence of surface waves. They were adjusted to the same height in the water column. This way shadows cast by the fish's body were avoided. PIV data were recorded with a Phantom V12 camera set to a frame rate of 1000 fps and a shutter time of 0.5 ms. Additionally, particle image velocimetry data were taken in multiple planes using a specially designed rotating mirror drum. The mirror drum allows for PIV recordings in 12 planes in fast succession (e. g. 12 planes within 48 ms or 4 planes within 16 ms).

We found that in accordance with an earlier study on a different fish species (the bluegill sunfish *Lepomis macrochirus*, Tytell and Lauder, 2008) the C-starting trout produced at least two jets of water flow, one by the tail fin (termed jet 1) and one by the midbody (termed jet 2) (Niesterok, 2011). Figure 2 shows an example of a C-start in a trout (body length 25 cm) with the two jets that have developed at $t=146\text{ ms}$. They constitute travelling vortex rings. Further analysis showed that they differ in shape, in duration, and in their direction with regard to the escape trajectory of the escaping fish (Niesterok et al., in preparation). We conclude that a fish-eating predator would greatly benefit from being able to discriminate between the two types of vortex rings.

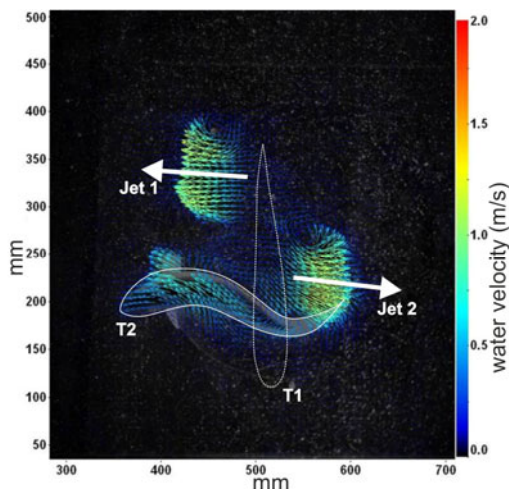


Fig. 2 Typical PIV measurement of a C-start in a trout. Outline of trout indicated at times $T1=0\text{ s}$ and $T2=0.146\text{ s}$; two water jets travelling in opposite directions are depicted at $T2$.

3 Experiments on Perceptual Abilities of Pinnipeds

The ability of pinnipeds to analyze hydrodynamic stimuli was quantified in harbor seals and a sea lion using artificial hydrodynamic stimuli that share certain features with fish-generated water movements.

3.1 Experiment 1: Moving Direction of an Artificial Fin

In experiment 1, the ability of harbor seals to identify the moving direction of an artificial fish fin was quantified (Wieskotten et al., 2010a).

3.1.1 Material and Methods

Hydrodynamic stimuli were generated inside an experimental box (1.8 m * 2.0 m * 1.3 m, L*W*H) that was mounted within the animal's pool. The water level inside the box was between 1.0 and 1.2 m. The hydrodynamic stimuli were generated by dragging a paddle that closely mimicked the shape of a fish fin (5 cm * 7 cm width*height) through the water in one of two directions: from the left to the right, or from the right to the left (viewed from the seal's perspective).

While the hydrodynamic stimulus was being generated, the harbor seal waited in the water outside the experimental box. The harbor seal was equipped with a flexible eye mask to prevent vision and with headphones that generated pink acoustic noise to prevent hearing. After the hydrodynamic stimulus had been generated and the stimulus generator had been removed from the water, the headphones (but not the eye mask) were removed and the harbor seal was allowed to swim into the experimental box up to its foreflippers through a circular gate in the front wall of the box (diameter 40 cm). There it encountered the hydrodynamic trail left by the paddle.

Between the time of stimulus generation and the time when the seal was allowed to swim into the box, a delay of 5 to 50 s was introduced. This way, the seal encountered hydrodynamic trails of different age.

The seal was trained to indicate the moving direction of the paddle (left to right or right to left) by pressing one of two small plastic spheres (response targets) that were mounted outside the experimental box on either side of the circular door. Correct responses were rewarded with pieces of fish.

Flow was measured using a 0.5 W DPSS laser (Entertainer 500, Quantum Physics, Newcastle, UK), a video camera mounted above the pool (DMK 801, The Imaging Source, Bremen, Germany), and Vestosint 1101 seeding particles. Analysis was performed in MatLab 6.5.

3.1.2 Results

Figure 3 shows a visualization of the hydrodynamic trail during a behavioral experiment. A horizontal illuminated layer in the experimental box was recorded in top view. The left panel shows the trail approximately 5 s after the paddle had been

moved through the water. Then the seal entered the experimental box and probed the trail (right panel). It responded very quickly: in all cases where flow visualizations allowed to measure the time between when the seal hit the trail and when it made its decision, it was below 0.5 s. Additional PIV measurements in an indoor setup allowed for a better resolution of the parameters of the hydrodynamic trail.

We found that the harbor seal could discriminate between the two moving directions of the paddle for at least 35 s (Wieskotten et al., 2010a). The hydrodynamic trail showed features similar to a fish trail: it contained flow velocities in the same range of magnitude as would be expected of a swimming fish, counter-rotating vortices approximately as large as the trail generating fin, and a jet of water flow between the vortices (reversed in direction in comparison with a swimming fish, as this experiment used a drag wake rather than a thrust wake). The positions at which the seal decided on the moving direction were consistent with the hypothesis that the rotation direction of the vortices and/or the direction of the jet were analyzed by the seal (Wieskotten et al., 2010a).

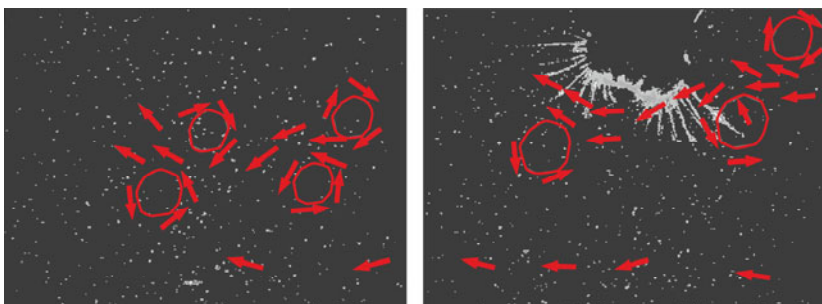


Fig. 3 PIV measurements of hydrodynamic stimulus while the harbor seal detects the moving direction of an artificial fish fin. Top view into the experimental box. Water flow direction and vortex structures indicated by red lines and arrows. Left: the trail of the fin that passed from right to left 5 s earlier; right: the harbor seal (snout and vibrissae illuminated by the light sheet) probes the trail. Based on Wieskotten et al. 2010a.

3.2 Experiment 2: Influence of Glide Phases on Trail Following

Harbor seals that set out to follow the hydrodynamic trails of swimming fish often face the problem that the fish does not swim continuously, but performs burst phases alternating with glide phases (burst-and-glide-swimming) (Blake, 1983). This swimming style yields an energetic advantage (Weihs, 1974) but has also been hypothesized to reduce hydrodynamic stimuli that could lead to detection by a predator. We investigated the hypothesis that the vibrissal system of harbor seals is suitable to follow the trail of a fish-like object that switches from burst into glide mode, while the trail following performance and reliability is reduced.

3.2.1 Material and Methods

In this experiment (Wieskotten et al., 2010b), hydrodynamic trails that incorporated both burst phases and glide phases were generated using a remote controlled miniature submarine. The miniature submarine was 0.64 m long and 0.13 cm in diameter. It was driven by a propeller. One person, the operator, steered the submarine in a water depth of 0.3 m to 1.0 m at a speed of approximately 2 ms^{-1} on varying swimming paths, 8 to 10 m long. A second person, the experimenter, handled the harbor seal. The swimming paths were unpredictable both to the harbor seal and to the experimenter (double blind experiment).

In half of the experiments, the submarine's motor ran continuously, generating a hydrodynamic trail. In the other half of the experiments, the motor was switched off after a distance of 3 to 5 m (randomized), and the submarine was allowed to glide on. This way a hydrodynamic trail composed from the burst phase and the glide phase, at least 8 m long in total, was generated.

While the stimulus was being generated, the harbor seal waited at a station close to the experimenter. It was equipped with an eye mask and headphones with pink noise to prevent vision and hearing. After stimulus generation, when the submarine's motor had been switched off and did not produce acoustic cues any more, the headphones were removed from the harbor seal. The harbor seal, still wearing the eye mask, was asked to follow the hydrodynamic trail. Successful trail following was immediately signaled to the seal by a whistle and was rewarded with fish after the seal had returned to the starting station.

The hydrodynamic stimulus produced by the submarine was measured using PIV in an outdoor pool ($5 \text{ m} * 2 \text{ m} * 1 \text{ m}$, L*W*H). The water was seeded with Vestosint 1101 (Degussa AG, Marl, Germany), and PIV images of size $32 \text{ cm} * 24 \text{ cm}$ were taken in a horizontal plane. The submarine was steered through the plane on a horizontal path so that its midline was met by the measurement plane. Recordings of the propelled (burst-mode) as well as the gliding (glide-mode) submarine were taken for 30 s.

3.2.2 Results

We found that harbor seals, using their vibrissal system, are still able to follow the trail of a fish-like object when it switches from burst- into glide mode, however the reliability of the trail following (the percentage of correctly followed trails) can be reduced as compared to the same object in burst mode.

Flow measurements demonstrated that the submarine trails shared specific features with fish trails and that the trails of gliding submarines in glide-mode differed from those in burst-mode as expected. Trails in burst-mode lasted longer (water velocities 50 mm*s^{-1} after 15 s) and were wider (40 cm after 15 s) than those in glide-mode ($<40 \text{ mm*s}^{-1}$, width 25 cm, after 15 s). Flow direction was reversed at the point of transition from burst- to glide mode.

Despite these differences, the harbor seal followed both burst-mode trails and trails with transition from burst- to glide-mode, albeit success rate for the latter was significantly reduced at intermediate time delays.

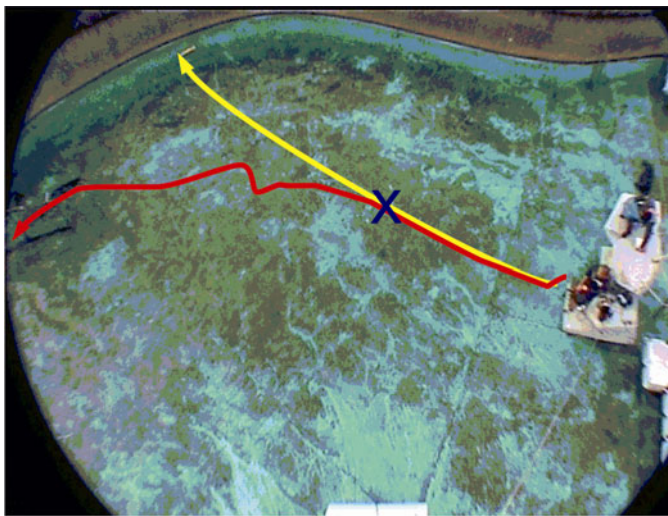


Fig. 4 Example of a trail following experiment where the harbor seal lost the trail as a consequence of a switch from the burst to the glide phase. Experimental pool viewed from above. Yellow: path of the submarine, red: path of the seal; blue cross: switching point. On the right, at the starting points of the paths, the experimenter and the submarine pilot are sitting on two experimental platforms. Modified after Wieskotten et al., 2010b.

We conclude that gliding phases in swimming fish can reduce the risk of being detected and tracked by a predator using the hydrodynamic trail, but on the other hand the vibrissal system of harbor seals is able to cope with this strategy to a large degree.

3.3 Experiment 3: Discrimination of Hydrodynamic Stimuli Caused by Objects of Different Size or Shape

3.3.1 Material and Methods

A harbor seal was trained to work in the experimental box described under experiment 1. Hydrodynamic stimuli were now generated by objects of different size (Experiment 3a) or different shape (Experiment 3b) (Wieskotten et al., 2011). The objects were vertically oriented paddles and rods of 30 cm length with different cross-sectional shapes. For the size discrimination study, flat paddles of width 2 cm, 3 cm, 4 cm, 5 cm, 6 cm, 7 cm, and 8 cm were used. For the shape discrimination study, flat paddles (object type 1), flat paddles with undulated edges (object type 2), cylinders with round cross section (object type 3) and cylinders with triangular cross sections (object type 4) were used, which were originally of the same size (4 cm wide), and were modified in size in another set of experiments for control purposes (2cm, 4 cm, 5 cm and 7 cm wide). All objects were moved on a horizontal circular path, in one direction (from left to right from the seal's point of

view), at speeds between 0.25 and 0.85 ms⁻¹. Speeds, sizes and shapes were presented in randomized orders. For details, see (Wieskotten et al., 2011).

The hydrodynamic trails generated by the objects were visualized and measured using the same methods as in Experiment 2.

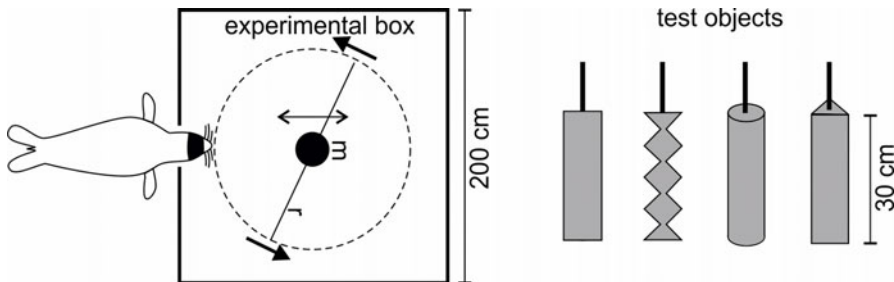


Fig. 5 Setup. Left, the experimental box in top view, being entered by the seal through the gate. m motor, r rotor that moves the test objects on a circular path (indicated by dashed circle and arrows) Right, the four different types of test objects (flat paddle, undulated paddle, cylinder, and triangular cylinder).

We measured the harbor seal's ability to discriminate size differences relative to three different sized standard paddles at constant speed and at randomized speed, and the ability of the seal to discriminate objects of different shape. The size discrimination ability was measured by assessing the psychometric functions (see e. g. Gescheider, 1976), i. e. the percentage of correct decisions as a function of the size difference. The ability of the seal to discriminate objects of different shape was measured as percentage of correct responses after the seal had learned to respond by pressing one of two response targets (compare experiment 1).

3.3.2 Results

We found that a harbor seal, using its mystacial vibrissae to investigate the hydrodynamic trail of a moving object, can discriminate size differences of 2.8 to 3.2 cm in this kind of objects when objects move at the same speed. Since in the case of constant object speed the water velocity in the wake clearly depended on the object size, providing a possible cue to the seal, we repeated the test using different object speeds to reduce the information available to the seal. The seal could then still discriminate objects with a size difference of 4.1 to 4.3 cm, presumably utilizing the size of the vortices within the wake (Wieskotten et al., 2011).

In the shape discrimination task, the harbor seal was able to discriminate the flat paddle from the cylindrical, triangular and the undulated paddle, as well as the cylindrical from the undulated paddle, as long as the paddles presented were of the same width. If the width of the paddles was changed in pseudo-random order, the seal could still discriminate flat from triangular paddles. We conclude that seals possess the sensory abilities and learning abilities to discriminate the trails left by fish of different size and different species to a certain degree.

3.4 Experiment 4: Detection of Vortex Rings by a Stationary Harbor Seal

In ongoing experiments, we investigate the ability of harbor seals to discriminate between different vortex rings produced by a vortex ring generator (Krüger, Wieskotten, Miersch, Dehnhardt and Hanke, in preparation). This way, the complex hydrodynamic stimuli of former experiments are reduced to a single element that is relatively stable, reproducible, and can be modified in a controlled way. Vortex rings have also been observed in the hydrodynamic trails of fish (Hanke and Bleckmann, 2004; Hanke et al., 2000; Nauen and Lauder, 2002; Niesterok et al., 2011; Tytell and Lauder, 2008).

3.4.1 Material and Methods

Two vortex ring generators were constructed from acrylic glass, polyethylene and PVC. Each vortex ring generator consists of a cube (20 cm * 20 cm * 20 cm) with two openings (14 cm * 14 cm) on opposing sides. On top of the cube, a Perspex tube (diameter 10 cm) with a plunger is mounted. The plunger is driven inside the tube by a linear motor (LinMot, NTI AG, Dresden, Germany). The two openings are covered with plates that are either closed or contain an aperture that produces the vortex ring when water is expelled by moving the plunger. In a typical application, one plate is closed and the one on the opposing side has an aperture. The vortex ring generator is then rotated so that the vortex ring travels either towards the animal or away from it. This way, the motor noise does not inform the animal whether a vortex ring is to be expected or not.

Vortex rings were produced using apertures of 20 mm diameter. In the first set of experiments, the harbor seal's ability to perceive the direction from where a vortex impinges on the mystacial vibrissae was tested. To this end the two vortex ring generators were mounted on a horizontal semicircle made from aluminum frame (diameter 1.4 m). The harbor seal was trained to position its head in the center of the semicircle. The vortex ring generators were in subsequent experimental sessions moved along the semicircle from either side of the animal (60 degrees to the left and 60 degrees to the right) towards the position straight ahead of the animal (0 degrees). Where the two vortex generators came too close to each other to be mounted, they were replaced by one vortex generator with an asymmetric aperture that served the same purpose. The animal was trained to indicate the direction from which a vortex ring impinged on its vibrissae. The percentage of correct choices per angular position was recorded and the resulting function was interpolated to obtain the minimum angle that the harbor seal can hydrodynamically perceive.

Flow was measured using a PIV system consisting of a 10 W OPSL laser and a Phantom V12 high speed camera.

3.4.2 Results

The vortex ring generator is suitable to generate vortex rings similar to those observed in fast starting fish (see above). The harbor seal is able to reliably detect a vortex ring of low flow velocity in calm water, but the influence of turbulence

needs to be investigated further. The harbor seal can reliably discriminate the direction from where a vortex ring impinges at angles from clearly less than 15 degrees to the left or to the right.

3.5 Experiment 5: Hydrodynamic Trail Following in Another Pinniped Species, the California Sea Lion

Hydrodynamic trail following had so far only been demonstrated in one pinniped species, the harbor seal (*Phoca vitulina*), representing one of the two major groups of pinnipeds, the true seals. The other major group of pinnipeds, the eared seals, possess a highly developed vibrissal system as well. However, their vibrissae look completely different. While the vibrissae of most true seals like the harbor seal have an undulated structure (Dehnhardt and Mauck, 2008; Ginter et al., 2010; Hanke et al., 2010), those of eared seals are smooth in outline. As we had reason to believe that this feature influences the performance in hydrodynamic trail following (Hanke et al., 2010; Miersch et al., 2011), we tested trail following performance in a species of eared seals, the California sea lion (*Zalophus californianus*) (Gläser et al., 2011).

3.5.1 Material and Methods

Trail following experiments with a California sea lion (Gläser et al., 2011) were performed in the Zoo Duisburg, Germany, where the animal lived in a group of sea lions in a pool of 230 m². The same remote controlled miniature submarine and similar eye masks as in the recent harbor seal study (Wieskotten et al., 2010b) were used. The sea lion was trained to follow the hydrodynamic trail generated by the submarine while blindfolded. 209 hydrodynamic trails of length 1 m to 6 m with different curvature were generated and the sea lion was asked to follow them after delays (time between the start of the submarine and the animal) of up to 7 s. Hydrodynamic trails were quantified using PIV as in (Wieskotten et al., 2010b).

3.5.2 Results

We found that the sea lion was able to follow the hydrodynamic trails reliably regardless of their length and curvature. However, the time delay between the start of the submarine and the animal had a significant effect on the trail following performance. In contrast to harbor seals, the sea lion was unable to follow this kind of hydrodynamic trails after a delay of 7 s (Gläser et al., 2011).

Flow measurements showed that after 7 s the hydrodynamic trail still contained water velocities higher than 50 mm*s⁻¹ (Gläser et al., 2011). By contrast harbor seals can follow the hydrodynamic trails of the same type for at least 20 s, corresponding to water velocities close to 20 mm*s⁻¹ (Wieskotten et al., 2010b).

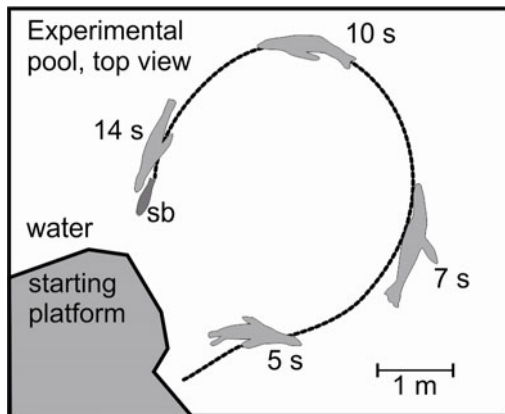


Fig. 6 Example of hydrodynamic trail following in a California sea lion. Experimental pool in top view. The submarine (sb) started at the platform and was driven on the path indicated by the dashed line. The blindfolded California sea lion followed the path and was in the depicted positions at the times indicated in the figure ($t=0$ s is the starting time of the submarine). Based on Gläser et al., 2011.

4 Biomechanics of Pinniped Whiskers

Behavioral results (experiments 2 and 4) as well as fluid mechanical considerations (Hanke et al., 2010; Witte et al., this volume) lead to the assumption that the specialized undulated structure of harbor seal vibrissae reduces hydrodynamic noise in the actively swimming animal as compared to the sea lion vibrissae. We tested this hypothesis further by comparing the forces exerted at the base of both vibrissa types in laminar and turbulent flow (Miersch et al., 2011).

4.1 Material and Methods

Three vibrissae of different length from a harbor seal and three vibrissae of comparable length from a California sea lion were used for the study. The vibrissae were, one at a time, mounted in a tube-shaped piezoelectric transducer at their bases and exposed to laminar water flow between 15 and 55 cm s^{-1} . The water flow was generated by means of a rotational flume (diameter 124 cm). In each of the measurements, part of the time a hydrodynamic signal was generated by inserting an aluminum cylinder into the flow in front of the vibrissa. This way, the vibrissa was exposed to a von Kármán vortex street with known vortex shedding frequency.

The piezoceramic transducer generated a charge proportional to the momenta present at the base of the vibrissa. This signal was transformed to a voltage by a charge amplifier and digitized using a data acquisition card and LabView (both National Instruments, Austin, TX, USA). The signal was filtered and analyzed for its frequency content via FFT in LabView. The signal-to-noise ratio was calculated as the wanted signal (the amplitude of the signal at the vortex shedding

frequency of the aluminum cylinder) and the noise, that is the signal still produced after removal of the aluminum cylinder, for example by vortices shed from the vibrissa.

4.2 Results

The vibrissae of both types were able to pick up the frequency of the von Kármán vortex street produced by the aluminum cylinders. In both types, vibrations were also induced by the laminar flow in the absence of the aluminum cylinder. These vibrations were, however, one order of magnitude lower in the harbor seal vibrissae than in the sea lion vibrissae. Consequently, in harbor seal vibrissae the signal-to-noise ratio was much higher (+7dB on average) than in sea lion vibrissae (-9dB on average) (Miersch et al., 2011). We also discuss the idea that the vibrations of sea lion vibrissae in laminar flow do not necessarily have to be interpreted as noise, but could also constitute a carrier frequency that is modulated by the wanted signal.

5 Discussion

The studies outlined here represent an advance in our understanding of hydrodynamic perception in pinnipeds. Starting with the knowledge that the harbor seal (a true seal) and the California sea lion (an eared seal) can sense hydrodynamic dipoles of very low intensity using their whiskers, and that harbor seals can also sense and follow aged hydrodynamic trails, we analyzed the harbor seal's abilities in more detail, quantified the sea lion's ability to follow hydrodynamic trails, and identified a fluid dynamical mechanism that can explain the harbor seal's apparent advantage over the sea lion in the case of the actively moving animal. Furthermore we quantified two classes of water movements generated by fish that are potentially of great value to piscivorous animals that need to detect prey and discriminate between different species, sizes, and motions using hydrodynamic stimuli.

The harbor seal is the best studied species in this respect to date. Harbor seals can not only detect water movements with high sensitivity, but also analyze moving direction, size and shape of a hydrodynamic trail generator to a certain degree. We have so far used artificial stimuli that mimic natural, that is fish-generated stimuli in certain respects: (1) artificial fish fins that leave a vortex trail of similar dimensions, vortex diameters and water velocities as a fish in a confined experimental box, (2) remote controlled miniature submarines that generate hydrodynamic trails of larger dimensions similar to a natural hunting situation, (3) rods and paddles that were driven along a circular path in a confined experimental box that allowed for testing a large number of different sizes and shapes, generating complex vortex trails, and (4) vortex rings that are similar to the vortex rings produced by single tail flicks of fish. The resulting thresholds for directional, size and shape discrimination (Krüger et al., 2011; Wieskotten et al., 2010a; Wieskotten et al., 2011) represent a conservative estimate for the harbor seal's abilities. However, since sensory systems of animals are often highly adapted to the most relevant

stimuli they encounter, experiments with live fish as stimulus generators are being conducted.

The sea lion, being even more sensitive to hydrodynamic dipole stimuli than the harbor seal while at rest, is to our current knowledge less well adapted to follow hydrodynamic trails, although an extension of the study to more individuals and better models of natural hydrodynamic stimuli would be desired (Gläser et al., 2011). We provide a fluid dynamical explanation for the underlying mechanism based on the shape of the vibrissae (see also Witte et al., this volume). A sensory biological explanation lies in the observation that sea lions inhabit less turbid waters than harbor seals do and can more often resort to their visual system.

Important topics in our current research include the questions how the different vibrissae of an animal interact, and what role the animal's head movements may play in the sensing process (active sensing).

Acknowledgments. This work was supported by the DFG (SPP 1207: Ha4411/8, De538/9, Le713/22) and by a grant of the Volkswagen Foundation to GD. The authors thank various members of the SPP as well as Profs. Paul Nachtigall and George Lauder for enlightening discussions.

References

- Blake, R.W.: Functional design and burst-and-coast swimming in fishes. *Canad. J. Zool.* 61, 2491–2494 (1983)
- Bublitz, A., Dehnhardt, G., Hanke, W.: Water movements from stationary fishes and their relevance to prey detection by marine mammals. In: Conference of the European Cetacean Society, Stralsund (2010)
- Bublitz, A., Dehnhardt, G., Hanke, W.: Breathing currents of stationary fish and their possible relevance to prey detection (in preparation)
- Carvell, G.E., Simons, D.J.: Biometric analyses of vibrissal tactile discrimination in the rat. *J. Neurosci.* 10, 2638–2648 (1990)
- Catania, K.C., Hare, J.F., Campbell, K.L.: Water shrews detect movement, shape, and smell to find prey underwater. *Proc. Natl. Acad. Sci. USA* 105, 571–576 (2008)
- Dehnhardt, G., Mauck, B.: Mechanoreception in secondarily aquatic vertebrates. In: Theissen, J.G.M., Nummela, S. (eds.) *Sensory Evolution on the Threshold: Adaptations in Secondarily Aquatic Vertebrates*, pp. 295–314. University of California Press, Berkely (2008)
- Dehnhardt, G., Mauck, B., Bleckmann, H.: Seal whiskers detect water movements. *Nature* 394, 235–236 (1998)
- Dehnhardt, G., Mauck, B., Hanke, W.: Hydrodynamic perception in seals. In: Ilg, U., Bühlhoff, H.H., Mallot, A. (eds.) *Dynamic Perception*, Akademische Verlagsgesellschaft Aka GmbH, Berlin (2004)
- Dehnhardt, G., Mauck, B., Hanke, W., Bleckmann, H.: Hydrodynamic trail following in harbor seals (*Phoca vitulina*). *Science* 293, 102–104 (2001)
- Gescheider, G.A.: *Psychophysics. Method and Theory*. Lawrence Erlbaum Associates, Hillsdale (1976)
- Ginter, C.C., Fish, F.E., Marshall, C.D.: Morphological analysis of the bumpy profile of phocid vibrissae. *Mar. Mamm. Sci.* 26, 733–743 (2010)

- Gläser, N., Wieskotten, S., Otter, C., Dehnhardt, G., Hanke, W.: Hydrodynamic trail following in a California sea lion (*Zalophus californianus*). *J. Comp. Physiol. A* 197, 141–151 (2011)
- Hanke, W.: Hydrodynamische Spuren schwimmender Fische und ihre mögliche Bedeutung für das Jagdverhalten fischfressender Tiere. PhD thesis, p. 121. Institut für Zoologie. Rheinische Friedrich-Wilhelms-Universität, Bonn (2001)
- Hanke, W.: Sensorische Grundlagen des Beutefangverhaltens aquatischer Säuger - Sensory basis of prey capture in aquatic mammals. Habilitation thesis. Institute for Biosciences. Rostock University, Rostock (2010)
- Hanke, W., Bleckmann, H.: The hydrodynamic trails of *Lepomis gibbosus* (Centrarchidae), *Colomesus psittacus* (Tetraodontidae) and *Thysochromis ansorgii* (Cichlidae) measured with Scanning Particle Image Velocimetry. *J. Exp. Biol.* 207, 1585–1596 (2004)
- Hanke, W., Brücker, C., Bleckmann, H.: The ageing of the low-frequency water disturbances caused by swimming goldfish and its possible relevance to prey detection. *J. Exp. Biol.* 203, 1193–1200 (2000)
- Hanke, W., Witte, M., Miersch, L., Brede, M., Oeffner, J., Michael, M., Hanke, F., Leder, A., Dehnhardt, G.: Harbor seal vibrissa morphology suppresses vortex-induced vibrations. *J. Exp. Biol.* 213, 2665–2672 (2010)
- Krüger, Y., Wieskotten, S., Miersch, L., Dehnhardt, G., Hanke, W.: Perception of vortex rings by stationary harbour seals (*Phoca vitulina*). Flow sensing in air and water. University of Bonn (2011)
- Ling, J.K.: Vibrissae of marine mammals. In: Harrison, R.J. (ed.) *Functional Anatomy of Marine Mammals*, pp. 387–415. Academic Press, London (1977)
- Miersch, L., Hanke, W., Wieskotten, S., Hanke, F.D., Oeffner, J., Leder, A., Brede, M., Witte, M., Dehnhardt, G.: Flow sensing by pinniped whiskers. *Phil. Trans. R Soc. B* 366, 3077–3084 (2011)
- Nauen, J.C., Lauder, G.V.: Quantification of the wake of a rainbow trout using three-dimensional stereoscopic particle image velocimetry. *J. Exp. Biol.* 205, 3271–3279 (2002)
- Niesterok, B.: Hydrodynamics and kinematics of fast starts in teleost fish and their ecological meaning for predator-prey interactions. Institute for Biosciences. Rostock University, Rostock (2011)
- Niesterok, B., Dehnhardt, G., Hanke, W.: Hydrodynamic patterns from fast starts in rainbow trout and their possible relevance to predator-prey interactions (2011) (in prep.)
- Schulte-Pelkum, N., Wieskotten, S., Hanke, W., Dehnhardt, G., Mauck, B.: Tracking of biogenic hydrodynamic trails in a harbor seal (*Phoca vitulina*). *J. Exp. Biol.* 210, 781–787 (2007)
- Tytell, E.D., Lauder, G.V.: Hydrodynamics of the escape response in bluegill sunfish, *Lepomis macrochirus*. *J. Exp. Biol.* 211, 3359–3369 (2008)
- Webb, P.W.: Acceleration performance of rainbow trout *Salmo gairdneri* and green sunfish *Lepomis cyanellus*. *J. Exp. Biol.* 63, 451–465 (1975)
- Webb, P.W.: Effect of size on fast-start performance of rainbow trout *Salmo gairdneri*, and a consideration of piscivorous predator-prey interactions. *J. Exp. Biol.* 65, 157–177 (1976)
- Weihs, D.: Energetic advantages of burst swimming of fish. *J. Theor. Biol.* 48, 215–229 (1974)
- Westerweel, J.: Fundamentals of Digital Particle Image Velocimetry. *Meas. Sci. Technol.* 8, 1379–1392 (1997)

- Wieskotten, S., Dehnhardt, G., Mauck, B., Miersch, L., Hanke, W.: Hydrodynamic determination of the moving direction of an artificial fin by a harbour seal (*Phoca vitulina*). *J. Exp. Biol.* 213 (2010a)
- Wieskotten, S., Dehnhardt, G., Mauck, B., Miersch, L., Hanke, W.: The impact of glide phases on the trackability of hydrodynamic trails in harbour seals (*Phoca vitulina*). *J. Exp. Biol.* 213, 3734–3740 (2010b)
- Wieskotten, S., Mauck, B., Miersch, L., Dehnhardt, G., Hanke, W.: Hydrodynamic discrimination of wakes caused by objects of different size or shape in a harbour seal (*Phoca vitulina*). *J. Exp. Biol.* 214, 1922–1930 (2011)
- Willert, C.E., Gharib, M.: Digital particle image velocimetry. *Exp. Fluids* 10, 181–193 (1991)

On the Wake Flow Dynamics behind Harbor Seal Vibrissae – A Fluid Mechanical Explanation for an Extraordinary Capability

Matthias Witte, Wolf Hanke, Sven Wieskotten, Lars Miersch, Martin Brede, Guido Dehnhardt, and Alfred Leder

Abstract. While hunting for prey in dark and turbid water the harbor seals use their mystacial vibrissae to follow the hydrodynamic trails left by prey fish. Sensing the minute velocity fluctuations in the trail is a challenge. In our research study we will answer the questions how mean and oscillating drag and lift forces are affected by the special body shape of the vibrissa and how the vortex structure in the wake is formed by a vibrissa to suppress self induced vibrations from the wake. For this purpose the wake flow of a harbor seal vibrissa was investigated by Stereo-Micro-PIV and with a detailed 3D direct numerical simulation. Using the proper orthogonal decomposition the most energetic structures of the wake flow could be extracted and evaluated.

1 Introduction

Having passed a long evolutionary process biological organisms and species are nearly perfectly adapted to their natural habitat. One experiment has demonstrated the ability of harbor seals (*Phoca vitulina*) to detect minimal water movements caused by an oscillating sphere (Dehnhardt et. al., 1998). Furthermore these animals are able to track hydrodynamic trails without any optical or acoustical information (Dehnhardt et al., 2001). These two experiments prove that the harbor seal is able to obtain essential sensorial input exclusively with the help of their vibrissae (which are also called whiskers).

The vibrissae are placed around the snout and above the eyes and are highly sensitive to mechanical stimuli. The density of myelinated nerve fibers at the base of a hair is approximately ten times higher (Hyvärinen 1989) compared with those of a cat or a rat. The design of the mechanical suspension of the hair protects the nerve fibers from being overstrained on the one hand and can amplify very small forces at the same time. These two features result in the ability of the harbor seal to detect velocity fluctuations down to a few micrometers per second.

While hunting for prey in dark and turbid water the seal is positioning his whiskers in an abducted position. It assumes a swimming speed in the order of

meters per seconds and is then able to detect and track the hydrodynamic trails caused by prey fish. During the hunt the seal is turning its head periodically to both sides to locate and track the hydrodynamic trail. The trail itself consists of vortices shed from prey fish. These vortices meet the vibrissae resulting in very small vortex induced vibrations. For a successful trail following these vibrations have to be detected with a high signal to noise ratio.



Fig. 1 Head of a harbor seal with whiskers at the Marine Science Center in Rostock/Warnemünde

From the fluid mechanical point of view we have to keep in mind that the vibrissa itself could induce a classical Kármán vortex street. This will happen even at a swimming speed of only 0.5 meters per second because the Reynolds number relating to the hydrodynamic diameter D_h of the vibrissa is already high enough.

$$\text{Re} = \frac{U_\infty \cdot D_h}{\nu} \quad (1)$$

$$D_h = \frac{4 \cdot A}{U_c} \text{ with area } A \text{ and circumference } U_c \quad (2)$$

The effect of a self induced Kármán vortex street on the vibrissa would be dramatic. The resulting vortex induced vibrations from the vortex street would mask the small signals from hydrodynamic trail vortices and corrupt the trail following capability of the seal. As a matter of fact measurements of the vibration forces in homogeneous flow on the vibrissa by Miersch et al. 2011 (see also the preceding paper by Hanke et al.) show, that self induced vibration by a vortex street is largely reduced at a harbor seal vibrissa.

The surface geometry of a harbor seal vibrissa was obtained from digital photography of a series of vibrissae from adult animals. Details can be inferred from Hanke et al., 2010. The cross section of a vibrissa is nearly elliptical, with a

varying ratio of the semi-axes along the centerline. A closer look shows that the main axes of the ellipses defining the 3D contour are not perpendicular to the span wise axis of the vibrissa. For the two describing ellipses with the most extreme axes ratios the parameters are given in table 1. Here the semi-axes a and b and the angle of attack is defined as α for the first and correspondingly the semi-axes k and l and the angle β for the second defining ellipse in which M defines the distance between them.

Table 1 Geometry parameters

ϕ	:	M/mm	a/mm	b/mm	k/mm	l/mm	α [°]	β [°]
$\bar{\phi} = \frac{1}{M} \cdot \sum_{i=1}^M \phi_i$		0.91	0.59	0.24	0.47	0.29	15.27	17.6
$\phi' = \sqrt{\frac{1}{M-1} \cdot \sum_{i=1}^M (\phi_i - \bar{\phi})^2}$		0.138	0.049	0.053	0.055	0.057	9.04	9.73
\overline{D}_h	-		0.65		0.7		-	-
			0.68					

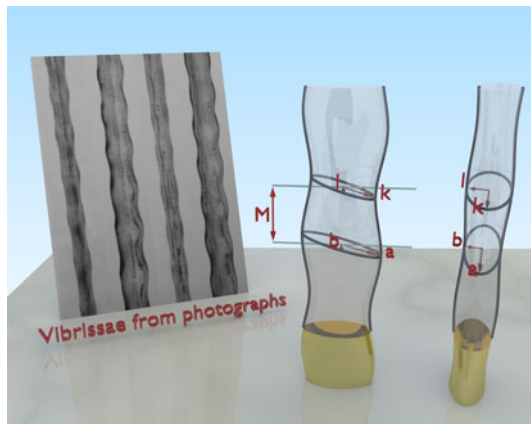


Fig. 2 Parameters of a vibrissa extracted from photographs

Now, with the knowledge of the 3D surface geometry of the vibrissa the interaction of the geometry and the wake flow structure and subsequently the influence on vortex induced vibrations (VIV) can be studied. VIV is a well known phenomenon in modern engineering and is still a topic of ongoing research (Bearman, 1998; Bearman, 2009; Bearman and Owen, 1998; Owen et al., 2001; Scruton, 1965; Williamson and Govardhan, 2004; Williamson and Govardhan, 2008; Zdravkovich 1981). The original idea to avoid VIV of bluff bodies was presented by Scruton (1965) and is commonly known as the Scruton helix. This structure shows an increased drag as the main disadvantage.

Other ideas are based on cylinders with a cross section of a half ellipse and a wavy trailing edge (Tombazis and Bearman, 1997) or with a rectangular cross section and a wavy leading edge (Bearman and Owen, 1998) or with a circular cross section with varying diameter along the centerline (Owen et al., 2001). The drag reduction of the latter structure was determined to be approximately 40%, which was the best result so far.

To clarify the mechanism of VIV-suppression the focus of the present investigation was put on the structure and the dynamics of the wake flow of the vibrissa and on the resulting lift and drag forces. For our investigations we performed experiments using particle image velocimetry in a stereoscopic arrangement and a numerical simulation with a direct, 3D calculation of the Navier-Stokes equations.

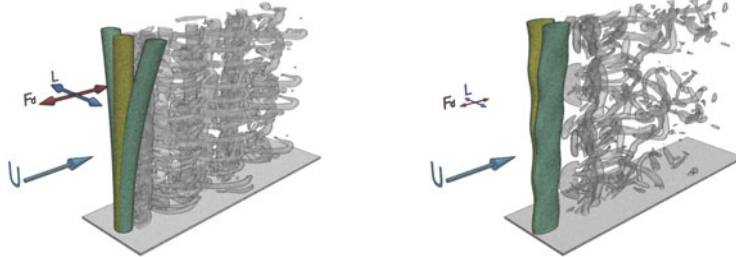


Fig. 3 Sketch of the Kármán vortex street behind a infinite circular cylinder at $Re = 500$ with high fluctuating lift and drag forces; light green shows the cylinder without any deflection; dark green shows the cylinder with a high deflection caused by the fluctuating forces (VIV)

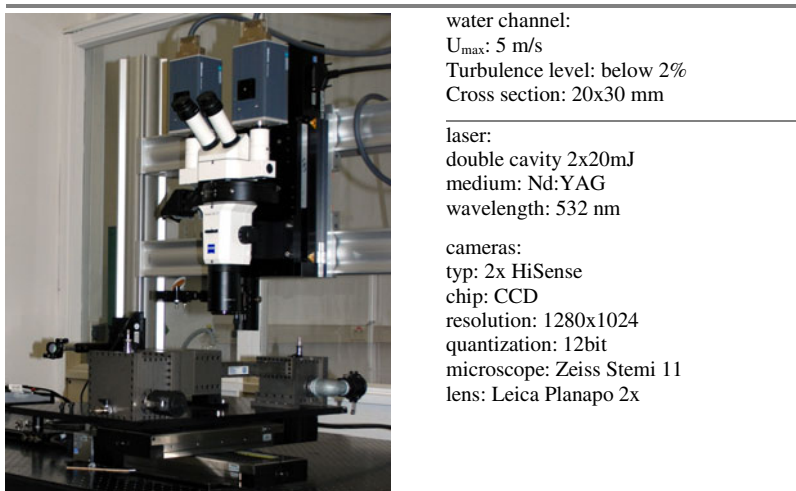
Fig. 4 Sketch of the wake flow of a vibrissa at $Re = 500$ with very low fluctuating lift and drag forces and a disturbed wake flow; light green shows the vibrissa without any deflection; dark green shows the vibrissa with only very low deflection caused by the fluctuating forces (VIV)

2 Experimental and Numerical Methods

2.1 Stereo-PIV Measurements

For the experimental part the Particle Image Velocimetry (PIV) technique in a stereoscopic arrangement was used to allow the observation of the 3D movement of the flow.

Because of the small hydraulic diameter of the original vibrissa (Tab. 1) the Stereo-PIV system had to be set up as a microscopic system resembling a Stereo-Micro-PIV (Brede et. al. 2008). Further general information on Stereo-Micro-PIV measurements is given in Nguyen and Wereley (2002).

Table 2 Parameters Stereo-Micro-PIV system**Fig. 5** Stereo-Micro-PIV setup

PIV analysis (DANTEC Flow Manager):

interrogation size: 32x32 pixel

overlap: 50%

adaptive correlation with deforming windows

peak validation: 1.5 + local neighborhood

water channel:
 U_{max} : 5 m/s
 Turbulence level: below 2%
 Cross section: 20x30 mm

laser:
 double cavity 2x20mJ
 medium: Nd:YAG
 wavelength: 532 nm

cameras:
 typ: 2x HiSense
 chip: CCD
 resolution: 1280x1024
 quantization: 12bit
 microscope: Zeiss Stemi 11
 lens: Leica Planapo 2x

The measurement campaign on natural vibrissae from adult animals took place in the water channel for micro flows at the Chair of Fluid Mechanics at the University of Rostock. The camera system, the microscope and the water channel system were mounted on a three axis traversing system. As seeding polyamide particles with a size of approximately $5\mu\text{m}$ were used. Along the centerline (z -axis) of the vibrissa 13 measurement planes with a distance $\Delta z/D_h=0.42$ (0.31mm) were observed to cover the wake flow behind the vibrissa. For the calculation of Reynolds stresses and the mean flow field a series of 500 velocity fields at each plane were used. The two in-plane and the third out of plane velocity component were computed using a third order image distortion model.

2.2 Numerical Simulation of the Wake Flow

In addition to the experimental investigation using the Stereo-PIV approach a numerical simulation of the flow was performed. The Navier-Stokes equations were solved with the public source code OpenFOAM (GPL)(OpenCFD, Caversham, Reading, UK) based on the finite volume method. The hexahedral mesh was designed with the help of ICEM-CFD, based on the parameters for a single vibrissa as given in Tab. 1.

$$\int_V \left(\frac{\partial(\rho \cdot u_i)}{\partial t} + \frac{\partial(\rho \cdot u_i \cdot u_j)}{\partial x_j} \right) dV = \int_V (\rho \cdot K_i) dV + \int_V \left(\frac{\partial \sigma_{ji}}{\partial x_j} \right) dV \quad (3)$$

$$\sigma_{ji} = -p \delta_{ji} - \frac{2}{3} \cdot \eta \cdot D_{xx} \cdot \delta_{ji} + 2 \cdot \eta \cdot D_{ji} \quad (4)$$

$$\int_V \left(\frac{\partial \rho}{\partial t} + \frac{\partial(\rho \cdot u_i)}{\partial x_i} \right) dV = 0 \quad (5)$$

The equations of motion for an incompressible fluid (3) together with the constitutive law (4) and the continuity equation (5) were solved directly without any assumption on turbulence. Due to the fact that no turbulence model was used all turbulent scales had to be resolved. The mesh design was based on an O-grid topology around the vibrissa and locally refined in normal and in circumferential direction. The final mesh comprised a total number of mesh elements of approximately 8 million. Cyclic boundaries for the top and bottom patches were used to avoid end effects which would corrupt the spanwise periodicity of the primary vortex structure. To reduce the numerical dissipation only second order schemes were used for the discretization of the governing equations. Different grid nodes were chosen in which velocity and pressure information were captured at each time step.

This allows the computation of characteristic parameters from the results at representative points such as the local frequency spectrum or the convergence quality of the computed solution. At every fifth time step data were written on pressure and shear stresses at the surface of the vibrissa to calculate the unsteady lift and drag forces.

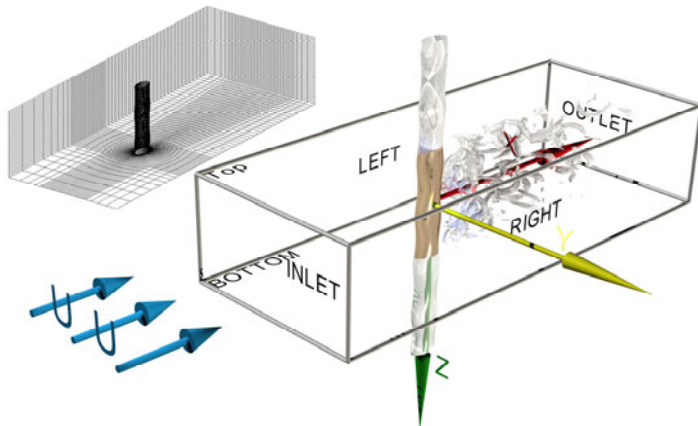


Fig. 6 Mesh topology

Table 3 Boundary conditions for the numerical simulations

mesh dimension:	$-10 \leq X/D_h \leq 15; -5 \leq Y/D_h \leq 5; -4 \leq Z/M \leq 4$ $-\pi/2 \leq Z/D_h \leq \pi/2$ for cylinder calculations
boundary conditions:	
inlet:	$U_\infty = \frac{Re \cdot v}{D_h}; \frac{\partial p}{\partial n} = 0$ for $Re = 500$
outlet:	$\frac{\partial u_i}{\partial n} = 0; \frac{\partial p}{\partial n} = 0$ or $p = 0$
vibrissa:	$u_i = 0; \frac{\partial p}{\partial n} = 0$
left & right:	$u_i \cdot n_i = 0; \frac{\partial p}{\partial n} = 0$
top & bottom:	all cyclic

For an in depth view into the dynamics of the wake flow of the vibrissa a proper orthogonal decomposition (POD) was performed. The covariance matrix for the POD was generated by the velocity and the pressure fields of the complete domain which were written at every fiftieth time step.

To test the sensitivity of the wake of the vibrissa to a variation of the geometry two modified vibrissa contours were computed. The two variants of the surface geometry differ in the angle of attack of the describing ellipses and in the length of the spanwise periodicity from the original vibrissa.

Table 4 Variations of the original vibrissa for the numerical simulations

variants	M	a	b	k	l	$\alpha [^\circ]$	$\beta [^\circ]$
1	0.91	0.59	0.24	0.47	0.29	0	0
2	1.82	0.59	0.24	0.47	0.29	0	0

2.3 Proper Orthogonal Decomposition

The power of modern 3D time resolving experimental techniques and the increasing performance of parallel computing technology results in an overwhelming amount of fluid flow data. The challenge is to collect the significant part information from the data. The common strategy in the past was to analyze the mean velocity and Reynolds stress distribution as well as frequency spectra at certain points in the flow field. A greatly improved approach is offered by the proper orthogonal decomposition (POD) which is also known in the literature as Karhunen-Loéve decomposition or PCA. The fundamentals of this method were given independently by Karhunen already in 1946 and Loéve in 1956. The POD allows it to find an access to the chaotic system of turbulence with the help of

statistical methods. The aim of the POD is to identify the coherent periodic structures in a highly unsteady flow and separates them from the rest. Reynolds and Hussain (1972) suggested separating the velocity field into three parts, a mean part, a coherent periodic part and an incoherent part which describes the irregular velocity fluctuations in an unsteady flow.

$$\mathbf{u}_i = \bar{\mathbf{u}}_i + \tilde{\mathbf{u}}_i + \mathbf{u}'_i \quad (6)$$

The POD method may be able finding a reasonable border between the irregular part of motion and the coherent and periodic structures, which also contain most of the flow energy. The transfer of the mathematical ideas into the field of turbulent flows was first presented by Lumley et al. (1967). With the introduction of the snapshot method by Sirovich (1987) the POD became applicable to experimental and numerical fluid flow data.

$$\{\mathbf{u}(\mathbf{x}, t_m)\}_{m=1}^M := \sum_{i=0}^M \mathbf{m}_i(\mathbf{x}) \cdot \mathbf{a}_i(t_m) \text{ with } \mathbf{a}_0 = 1 \quad \mathbf{m}_o = \bar{\mathbf{u}} \quad (7)$$

$$\mathbf{u}(\mathbf{x}, t_m) = \mathbf{u}_0(\mathbf{x}) + \mathbf{u}'(\mathbf{x}, t_m) \quad (8)$$

$$\mathbf{u}'(\mathbf{x}, t_m) = \sum_{i=1}^M \mathbf{m}_i(\mathbf{x}) \cdot \mathbf{a}_i(t_m) \quad (9)$$

The idea of POD is to calculate a new representation of a given snapshot ensemble, e.g. from experimental data or numerical simulation in terms of a Galerkin approximation. The basis of the Galerkin approximation is an ensemble of spatial modes \mathbf{m}_i (7). The quantity in m could be a velocity or pressure distribution or any other quantity. Each mode is linearly independent. The Galerkin approximation can be interpreted as a separation of the field into spatial eigenfunctions or modes $\mathbf{m}_i(\mathbf{x})$ and the corresponding time coefficients $\mathbf{a}(t_m)$ and can be obtained by variational calculus. The core element of the POD is the covariance matrix of the snapshot ensemble:

$$\mathbf{C}_{ij} = \frac{1}{M} \int_{\Omega} \mathbf{u}'(\mathbf{x}, t_i) \mathbf{u}'(\mathbf{x}, t_j) d\Omega \quad (10)$$

The covariance matrix (10) contains all information on the turbulent character of the unsteady flow. The trace of the matrix represents the accumulated turbulent kinetic energy of the domain over the measurement time. To calculate the POD modes and the time coefficients an eigenvalue problem of the covariance matrix has to be solved.

$$\mathbf{C}b^{[i]} = \lambda_i \mathbf{b}^{[i]} \quad (11)$$

$$\mathbf{m}_i = \frac{1}{\sqrt{M \cdot \lambda_i}} \sum_{m=1}^M b^{[i]}(t_m) [\mathbf{u}(\mathbf{x}, t_m) - \bar{\mathbf{u}}(\mathbf{x})] \quad (12)$$

The POD modes can be computed using the eigenvectors and eigenvalues using equation (12). The time coefficients are the projection of each snapshot onto the POD modes.

$$\mathbf{a}_i(t_m) = \int_{\Omega} (\mathbf{m}_i \cdot [\mathbf{u}(\mathbf{x}, t_m) - \bar{\mathbf{u}}(\mathbf{x})]) d\Omega \quad (13)$$

More information on POD can be inferred from Holmes et al. (1997) and Noack (2006).

3 Experimental and Numerical Results

The first results were obtained from Stereo-Micro-PIV measurements on a single original vibrissa. With an average hydraulic diameter of 0.74 mm the resulting Reynolds number was 300, approximately. The time averaged flow field was created from an array of 13 measurement planes which were placed along the centerline of the vibrissa. 500 PIV snapshots from each plane were used to compute the time averaged flow field.

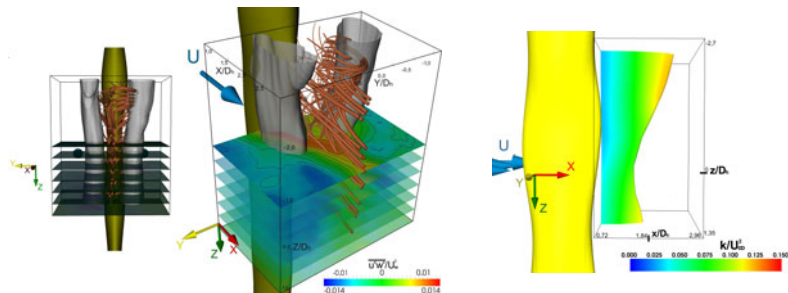


Fig. 7 Three dimensional streamline reconstruction in the wake of a vibrissa, grey isosurfaces: vortex core reconstruction using λ_2 criterion (Jeong and Hussain 1995), color planes: Reynolds shear stress $u'w'/U_\infty^2$; horizontal planes also depicting the spacing of the measurement planes

Fig. 8 Isosurface of the velocity component $u/U_\infty^2 = 0$; color: normalized turbulent kinetic energy

The reconstructed streamlines (Fig.7) which were calculated from the time averaged flow field demonstrate that the primary vortices are affected and deformed by the three dimensional surface geometry of the vibrissa. The vortex cores in the steady state flow field visualized here with the λ_2 criterion resemble those of an infinite cylinder but are slightly curved additionally. The recirculation area (Fig.8)

is also affected by the geometry of the vibrissa and is modulated periodically along the centerline. Particularly interesting is the distribution of the Reynolds stresses. A comparison of the Reynolds stresses from the vibrissa wake flow with numerical data from the infinite cylinder shows a significant deviation between both of them due to the 3D motion in the wake of the vibrissa. We would like to emphasize that the analysis of Reynolds stresses from Stereo-Micro-PIV is very challenging and can be affected by image noise, disturbances and uncertainties due the limitation of the stereo angle.

Table 5 Maximal and minimal amplitudes of the Reynolds stresses from the vibrissa wake flow ($Re = 300$) obtained with stereo micro-PIV compared with the results for the infinite cylinder from the numerical study at $Re = 500$ and with the experimental results for axial shear layers (Leder 1991 and 1992)

	vibrissa	cylinder (double sided shear layers)	axial shear layers
$\overline{u'^2}/U_\infty^2$	0.14	0.21	0.09
$\overline{v'^2}/U_\infty^2$	0.1	0.46	0.09
$\overline{w'^2}/U_\infty^2$	0.12	0.048	0.09
$\overline{u'v'}/U_\infty^2$	-0.057 ; 0.045	-0.13 ; 0.125	± 0.004
$\overline{u'w'}/U_\infty^2$	-0.014 ; 0.014	-0.008 ; 0.012	± 0.004
$\overline{v'w'}/U_\infty^2$	-0.019 ; 0.021	-0.01 ; 0.0098	± 0.004

The extremal amplitudes of the Reynolds stresses allow a classification of the governing flow regime. The values given in Table 5 indicate that the wake of the vibrissa exhibits features of both, axial and double sided shear flows but is neither pure axial shear flow nor pure double sided shear flow. The shortcomings of Stereo-Micro-PIV and other PIV techniques hamper a detailed analysis of the unsteady spatial structure of the flow. With modern parallel computing the numerical simulation offers a feasible way to obtain missing informations.

In Fig.9 a snapshot from the numerical simulation is presented. The flow regime of the infinite cylinder at $Re = 500$ which is given here for comparison shows the typical B-mode structure (Brede et al., 1996; Williamson 1996). The lateral shear layers roll up and form Kármán vortices which are connected by rib like vortex structures which are commonly known as secondary vortices. The onset of vortex formation starts closely to the cylinder. The unsteady flow topology in the wake of the vibrissa is considerably more complex. Neither Kármán vortices nor secondary vortices can be observed. An important fact is that the onset of vortex

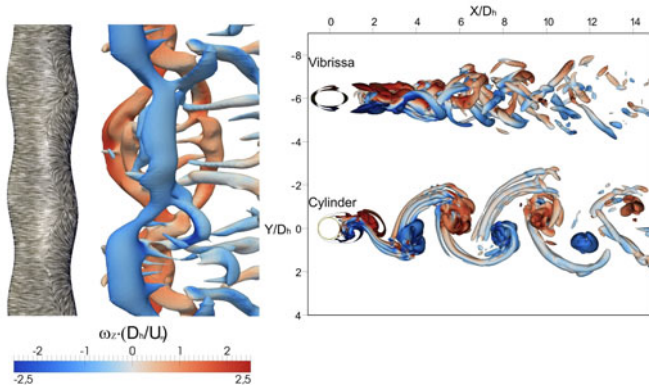
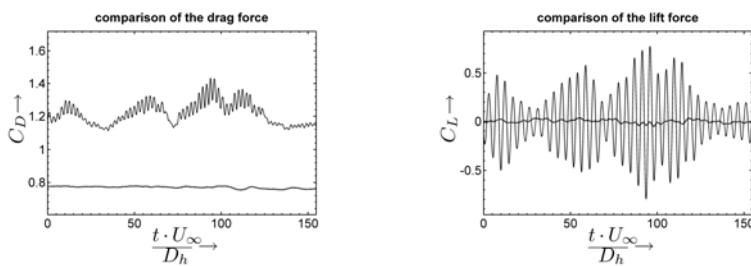


Fig. 9 Snapshot from the numerical simulations for a vibrissa (Table 1) and a circular cylinder with similar hydraulic diameters at $\text{Re} = 500$. color: cross stream vorticity ω_z ; iso-surfaces: normalized $Q = 0.5$ criterion (Hunt et al., 1988); left side: LIC pattern (Cabral and Leedom, 1993) showing the shear stress vector field at the surface of the vibrissa

formation is shifted downstream in contrary to the cylinder wake. From the top view it is visible that the shear layers in the wake of the vibrissa eventually do roll up on both sides of the wake and do form primary vortex segments. The gap between the vibrissa and the first vortices is clearly visible. Interestingly segments showing opposite rotation are being shed at the same time but at different locations along the centerline of the vibrissa. This results in a spanwise periodicity of the shedding of two undulation periods M (see Table 1). The LIC surface flow pattern generated from the shear stress vector on the surface of the vibrissa shows that the separation line of the flow is significantly curved. This feature has been seen previously on engineering drag reduction solutions which were based on curved separation lines but in an arbitrary form.



solid line: cylinder; dashed line: vibrissa solid line: cylinder; dashed line: vibrissa

Fig. 10 Time history of the drag and lift coefficients from the numerical simulations

Table 6 Mean values and standard deviation of lift and drag coefficients from the numerical simulations

	cylinder	vibrissa	vibrissa (V1)	vibrissa (V2)
$\overline{C_D}$	1.218	0.769	0.762	0.767
$\overline{C_L}$	-	-	-	-
$\sqrt[2]{\overline{C'^2_D}}$	0.064	0.0065	0.0032	0.0017
$\sqrt[2]{\overline{C'^2_L}}$	0.292	0.0173	0.0163	0.007

The impact of the vibrissa type vortex structure on the resulting lift and drag forces is tremendous. In the case of a circular cylinder the time history of the lift and drag coefficients is dominated by the Kármán vortex street. The frequency analysis of the lift coefficient of the cylinder shows a strong peak at $Sr = 0.21$.

In the case of the vibrissa-type shedding however the lift and drag coefficients are nearly unaffected by vortex shedding as depicted in Fig. 10. This applies to both the original and the vibrissa with modified parameters. The mean value of the drag coefficient presented in Table 6 is reduced by approx. 40 % for all three variations of the vibrissa. The reduction of the fluctuating drag (r.m.s) reaches around 90% for the original vibrissa and about 97 % for variation 2 and is in accordance with Miersch et al. (2011) and Hanke et al. (2010). The reduction of the fluctuating lift (r.m.s) is at least 94 % compared to the cylinder. This can be explained by the downstream shift of the vortex formation onset which detaches the periodical pressure minima of the vortices from the surface of the body. The r.m.s of the lift coefficient of the circular cylinder is in a good compliance with experimental results published by Norberg (2002).

From the time averaged flow field it is obvious that the recirculation area depicted in Fig. 11 is strongly affected by the geometry of the vibrissa. In the case of the original and the first variation of the vibrissa the recirculation area is partially separated from the vibrissa and has a huge gap along the centerline. The second variation V2 with larger M looks more like the results from the Stereo-Micro-PIV experiment. Here the recirculation area is not separated from the vibrissa. The recirculation area of all three vibrissae extends downstream to a distance of approx. three hydraulic diameters and therefore is twice as long as that of a circular cylinder. The distribution and the extremal amplitudes of the Reynolds stresses (Table 7) show the same significant differences to the cylinder wake as those taken from the experiment (Table 5). For a better understanding of the wake flow topology and the effects especially to the resulting lift and drag forces a POD analysis was performed.

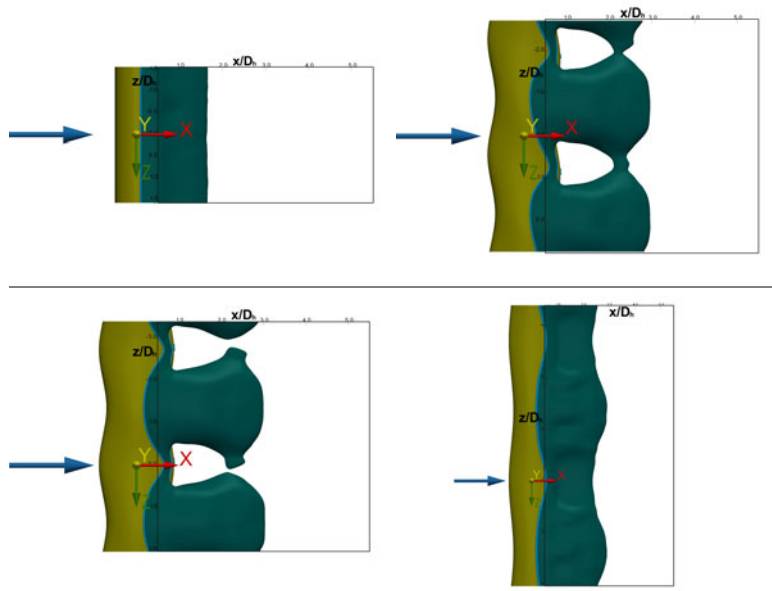


Fig. 11 Iso-surface of the recirculation area $u/U_{\infty} = 0.0$ top row: cylinder and original vibrissa; bottom row: vibrissa (V1) and vibrissa (V2)

Table 7 maximal and minimal amplitudes of the Reynolds stresses from the numerical simulations at Re 500

	cylinder	vibrissa	vibrissa (V1)	vibrissa (V2)
$\overline{u'^2}/U_{\infty}^2$	0.21	0.104	0.102	0.095
$\overline{v'^2}/U_{\infty}^2$	0.46	0.18	0.174	0.214
$\overline{w'^2}/U_{\infty}^2$	0.048	0.079	0.076	0.08
$\overline{u'v'}/U_{\infty}^2$	-0.13 ; 0.125	-0.072 ; 0.072	-0.074 ; 0.065	-0.075 ; 0.078
$\overline{u'w'}/U_{\infty}^2$	-0.008 ; 0.012	-0.034 ; 0.034	-0.03 ; 0.03	-0.024 ; 0.024
$\overline{v'w'}/U_{\infty}^2$	-0.01 ; 0.0098	-0.021 ; 0.021	-0.019 ; 0.02	-0.044 ; 0.039

From the spatial arrangement of the POD modes and the frequency spectrum of the corresponding time coefficient an in-depth view into the wake dynamics is feasible.

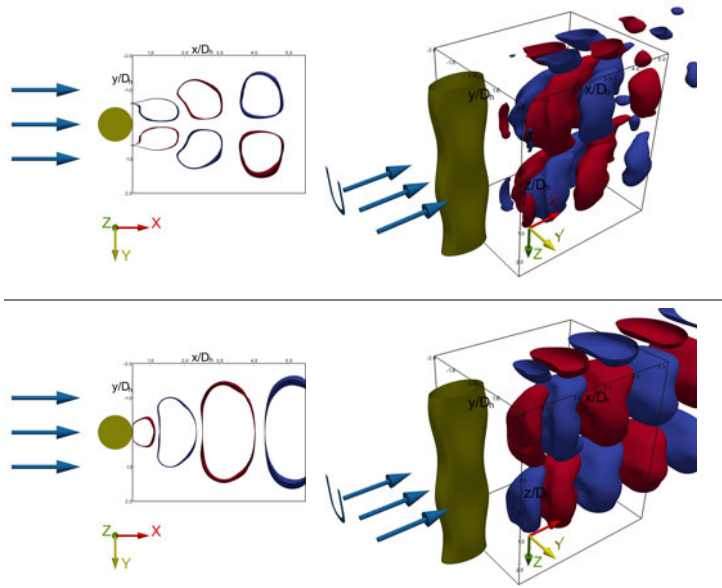


Fig. 12 POD comparison cylinder vs. vibrissa (numerical data); top row: POD mode m_{1u} ; bottom row: POD mode m_{1v} (iso-surface value ± 0.05)

The first two POD modes from the cylinder and vibrissa wake flow presented in Fig. 12 describe the convective transport of the most energetic structures. For the cylinder this is always the formation and transport of the Kármán vortices. The POD modes for the cylinder are nearly two dimensional and symmetrical to the x-z layer. The first modes for the vibrissa flow however are completely three dimensional and periodical along the centerline. As seen previously in the unsteady snapshot (Fig. 9) the primary vortex segments of opposite rotation occur on both sides of the vibrissa at the same time.

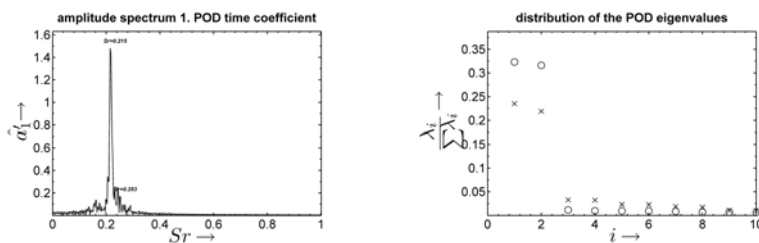


Fig. 13 Left: frequency spectrum a_1 for the wake of the vibrissa, Right: eigenvalue spectrum from POD on velocity (right); cylinder (o) and vibrissa (x)

Using spectral analysis of the time coefficients we can obtain information on the periodic frequency of the most dominant structures in the flow (Fig.13). Both the cylinder wake and the vibrissa wake show a dominant frequency of Sr 0.21. Additionally, the eigenvalue spectrum supplies information on distribution of the turbulent kinetic energy over the POD modes and the different flow structures respectively. The Kármán vortex street which is described by the first two POD modes incorporates approx. 65% of the turbulent kinetic energy. The energy content of the primary vortex street behind the vibrissa only approx. 44%.

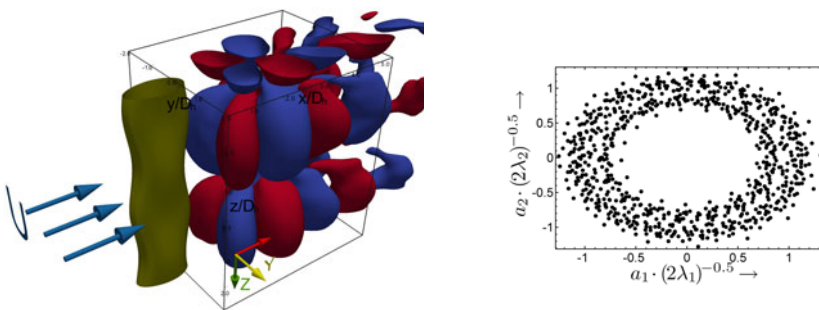


Fig. 14 Left:POD mode m_{1p} of the pressure field of the vibrissa flow (iso-surface value ± 0.05); Right: phase reconstruction from the first two time coefficients

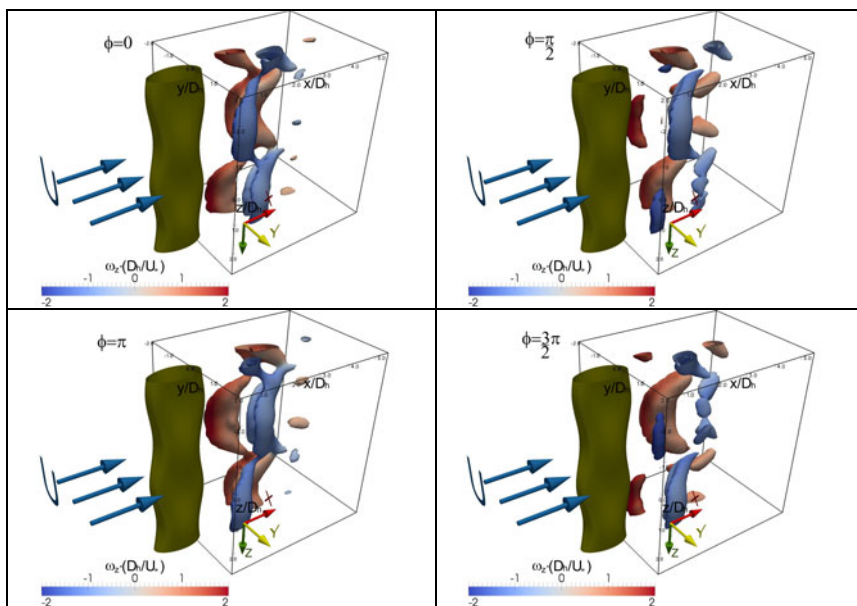


Fig. 15 Vortex core structures for four phases of the phase averaged flow field (iso-surface: normalized $Q = 0.5$); color: cross stream vorticity ω_z ; $\Delta\phi = \pi/2$; starting with $\phi=0$ from left to right and from top to bottom

The POD analysis of the pressure field in Fig.14 can now explain the extreme reduction of the fluctuations of the lift and drag forces on the vibrissa which is essential to the capability as a sensitive vortex sensor. The resulting lift and drag forces can be defined as the integral of the pressure and shear forces over the surface of the body. Furthermore, the POD modes can be interpreted as the fluctuation of the underlying mean field. In contrast to the modes of a circular cylinder wake the first two POD modes of the pressure field of the vibrissa flow are found to be periodic in spanwise direction with alternating signs. The pressure distribution on the vibrissa surface along the span for the left side of the wake is repeated on the right side with a spanwise shift. In combination with nearly pure harmonic first time coefficients it is obvious that the pressure forces on the left half of the vibrissa are always compensated by the forces on the right side so that the fluctuation of the lift force is minimal. The same effect causes the low level of fluctuations of the drag coefficient. Furthermore we used the first two time coefficients to compute the phase averaged flow field behind the cylinder and the vibrissa. The phase of each snapshot from the flow can be computed from the two time coefficients as given in Eq. 14.

$$\phi_{1-2} = \arctan\left(\frac{a_2}{a_1} \cdot \frac{\sqrt{\lambda_1}}{\sqrt{\lambda_2}}\right) \quad (14)$$

The results for the phase averaged flow field based on the POD analysis allows the reconstruction of coherent unsteady 3D vortex structures in the wake of the vibrissa (Fig.15). Due to the averaging process all small scale fluctuations, particularly from random noise are removed. The resulting vortex structure shown in Fig.13 exhibits a dominant frequency of $Sr = 0.21$ which is close to that of an infinite cylinder at the same Reynolds number. One observation found again here which was discussed previously (Fig.9) is that primary vortex segments are being shed with opposite rotation at both sides of the vibrissa at the same time with a spanwise shift. This is in contrast to circular cylinder wake flow characteristics. It is

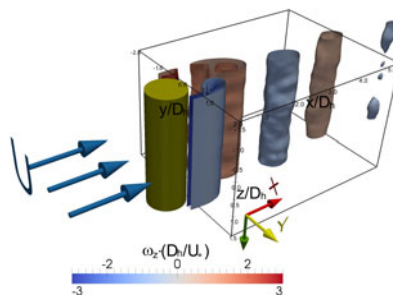


Fig. 16 vortex core structures from the phase averaged flow field of the cylinder visualized by normalized Q (iso-surface value of normalized Q = 0.5); color: cross stream vorticity ω_z ; phasing $\phi=0$

also obvious that the original rotation axis of the vortices in z direction changes downstream into a rotation around the x-axis (Fig.14 phasing $\phi=\pi/2$). Simultaneously a breakup of the structures occurs, also very rapidly compared with the vortices in the wake of the cylinder (Fig.15 and Fig.16).

4 Conclusions

The ability of the harbor seal to detect turbulent water movements caused by swimming fishes or other objects is still amazing and has raised questions within the fluid mechanics community on drag and fluctuating lift reduction and on VIV. In this study it was found that the wavy surface geometry of a harbor seal vibrissa is extremely effective in damping the fluctuating lift and drag forces by 90% compared to an infinite cylinder. The Reynolds stresses obtained by Stereo-Micro-PIV experiments were the first indications of a new kind of a wake flow, combining features of axial and double sided shear layer flows. Extensive 3D numerical simulation complemented the experimental data and allowed a detailed insight into the unsteady vortex structure in the wake of vibrissa-shaped bodies.

Using proper orthogonal decomposition the physical mechanisms behind the reduction of the fluctuating lift and drag have been identified. Reductions of approx. 90% compared to the forces on a circular cylinder are achievable. In particular it was shown by phase averaged flow field analysis that the primary vortex structure is completely different from that of circular cylinders. The primary vortex formation in the wake of the vibrissa occurs further downstream and the breakdown of the vortex structures is faster than in the cylinder wake. The results from the experimental and numerical investigation raises the opportunity that the design characteristics of the vibrissa will be a biomimetic blueprint for the future design of wake sensors, building, bridges, towers or other objects wherever the aerodynamics of vortex induced vibrations is concerned. To verify that the basic principles of the vortex structure in the wake of vibrissa-shaped bodies will also hold at higher Reynolds numbers wind tunnel investigations are being performed at present.

References

- Bearman, P.W.: Developments in the understanding of bluff body flows. JSME International Journal Series B-Fluids and Thermal Engineering 41(1), 103–114 (1998)
- Bearman, P.W.: Understanding and predicting vortex-induced vibrations. Journal of Fluid Mechanics 634, 1–4 (2009)
- Bearman, P.W., Owen, J.C.: Reduction of bluff-body drag and suppression of vortex shedding by the introduction of wavy separation lines. Journal of Fluids and Structures 12(1), 123–130 (1998)
- Brede, M., Eckelmann, H., Rockwell, D.: On secondary vortices in the cylinder wake. Physics of Fluids 8(8), 2117–2124 (1996)

- Brede, M., Witte, M., Leder, A., Miersch, L., Dehnhardt, G.: Stereo- μ PIV investigation of the separated flow behind a 3D shaped vibrissae from an aquatic mammal. In: 14th Int. Symp. on Applications of Laser Techniques to Fluid Mechanics, Lisbon, Portugal (2008)
- Cabral, B., Leedom, L.: Image vector fields using line integral convolution. In: International Conference on Computer Graphics and Interactive Techniques (1993)
- Dehnhardt, G., Mauck, B., Bleckmann, H.: Seal whiskers detect water movements. *Nature* 394(6690), 235–236 (1998)
- Dehnhardt, G., Mauck, B., Hanke, W., Bleckmann, H.: Hydrodynamic trail-following in harbor seals (*Phoca vitulina*). *Science* 293(5527), 102–104 (2001)
- Hanke, W., Witte, M., Miersch, L., Brede, M., Oeffner, J., Michael, M., Hanke, F., Leder, A., Dehnhardt, G.: Harbor seal vibrissa morphology suppresses vortex-induced vibrations. *Journal of Experimental Biology* 213(15), 2665–2672 (2010)
- Holmes, P.J., Lumley, J.L., Berkooz, G., Mattingly, J.C., Wittenberg, R.W.: Low-dimensional models of coherent structures in turbulence. *Physics Reports-Review Section of Physics Letters* 287(4), 338–384 (1997)
- Hunt, J.C.R., Wray, A.A., Moin, P.: Eddies, streams and convergence zones in turbulent flows. *Studying Turbulence Using Numerical Simulation Databases* (1988)
- Hyvärinen, H.: Diving in darkness: whiskers as sense organs of the ringed seal (*Phoca hispida saimensis*). *Journal of Zoology* 218(4), 663–678 (1989)
- Jeong, J., Hussain, F.: On the Identification of a Vortex. *Journal of Fluid Mechanics* 285, 69–94 (1995)
- Leder, A.: Dynamics of fluid mixing in separated flows. *Physics of Fluids A* 3(7), 1741–1748 (1991)
- Leder, A.: Abgelöste Strömungen, Physikalische Grundlagen. Vieweg-Verlag, Braunschweig, Wiesbaden, 214 S (1992) ISBN 3-528-06436-6
- Lumley, J.L., Yaglom, A.M., Tatarski, V.I.: The Structure of Inhomogeneous Turbulent Flows. In: Atmospheric Turbulence and Radio Propagation, Nauka, pp. 166–178 (1967)
- Miersch, L., Hanke, W., Wieskotten, S., Hanke, F.D., Oeffner, J., Leder, A., Brede, M., Witte, M., Dehnhardt, G.: Flow sensing by pinniped whiskers. *Philosophical Transactions of the Royal Society B-Biological Sciences* 366(1581), 3077–3084 (2011)
- Nguyen, N.-T., Wereley, S.T.: Fundamentals and Applications of Microfluidics. Artec House, Boston (2002)
- Noack, B.: Niederdimensionale Galerkin Modelle für laminare und transitionelle freie Scherströmungen. *Habilitation thesis* (2006)
- Norberg, C.: Fluctuating lift on a circular cylinder: review and new measurements. *Journal of Fluids and Structures* 17(1), 57–96 (2003)
- Owen, J.C., Bearman, P.W., Szewczyk, A.A.: Passive control of vortices with drag reduction. *Journal of Fluids and Structures* 15(3-4), 597–605 (2001)
- Reynolds, W.C., Hussain, A.K.M.: Mechanics of an Organized Wave in Turbulent Shear-Flow.3. Theoretical Models and Comparisons with Experiments. *Journal of Fluid Mechanics* 54, 263 (1972)
- Scruton, J.C.: On the wind-excited oscillations of stacks, towers and masts. In: *Proceedings of the Symposium on Wind Effects on Buildings and Structures*, pp. 798–836 (1965)
- Sirovich, L.: Turbulence and the Dynamics of Coherent Structures.1. Coherent Structures. *Quarterly of Applied Mathematics* 45(3), 561–571 (1987)
- Tombazis, N., Bearman, P.W.: A study of three-dimensional aspects of vortex shedding from a bluff body with a mild geometric disturbance. *Journal of Fluid Mechanics* 330, 85–112 (1997)

- Williamson, C.H.K.: Three-dimensional wake transition. *Journal of Fluid Mechanics* 328, 345–407 (1996)
- Williamson, C.H.K.: Vortex dynamics in the cylinder wake. *Annual Review of Fluid Mechanics* 28, 477–539 (1996)
- Williamson, C.H.K., Govardhan, R.: Vortex-induced vibrations. *Annual Review of Fluid Mechanics* 36, 413–455 (2004)
- Williamson, C.H.K., Govardhan, R.: A brief review of recent results in vortex-induced vibrations. *Journal of Wind Engineering and Industrial Aerodynamics* 96(6-7), 713–735 (2008)
- Zdravkovich, M.M.: Review and Classification of Various Aerodynamic and Hydrodynamic Means for Suppressing Vortex Shedding. *Journal of Wind Engineering and Industrial Aerodynamics* 7(2), 145–189 (1981)

Part IV

**Flow Control in Human
Swimmers**

Experimental and Numerical Investigation of the Unsteady Flow around a Human Underwater Undulating Swimmer

Stefan Hochstein, Steffen Pacholak, Christoph Brücker, and Reinhard Blickhan

Abstract. Underwater undulatory swimming describes one of the fastest modes of human aquatic locomotion. The human swimmer can be considered as natural paradigm for technical segmented linkage systems used in robotics that must compensate its anatomical limitations through sophisticated kinetics. In order to reveal and evaluate such mechanisms the flow around and behind the swimmer was measured by time-resolved particle image velocimetry (TR-2D-PIV) and simulated by computational fluid dynamics (CFD). In comparison to fish, despite of joint asymmetries the swimmers used undulatory waves characterized by very similar absolute amplitude distributions along the body but at much higher Strouhal numbers. The observed 3D-patterns revealed in the CFD helps us to newly interpret experimental findings. Both the experimental flow field as well as that obtained from CFD document the effect of flow preformation and vortex re-capturing. We propose that the use of high Strouhal numbers facilitates the re-capture of vortices unavoidable due the disadvantageous geometry of the human swimmer.

1 Introduction

To maximize their swimming speed human swimming athletes successfully copy strategies from fish locomotion such as undulatory underwater swimming after start and turn. Since the Olympic Games in Moscow in 1980 swimmers began to prolong the phase of swimming under the water surface applying undulatory swimming in

Stefan Hochstein · Reinhard Blickhan
Friedrich-Schiller-Universität Jena, Institute of Sport Science, Motion Science,
Seidelstr. 20, 07749 Jena, Germany
e-mail: stefan.hochstein@uni-jena.de

Steffen Pacholak · Christoph Brücker
Bergakademie TU Freiberg, Institute of Mechanics and Fluid Dynamics,
Lampadiusstr. 4, 09599 Freiberg, Germany

order to reduce wave drag. The fact, that the former competition rules required per lane ($50m$) only one complete arm stroke above water resulted over the next few years in underwater swimming phases up to $40m$ by some specialized athletes. Because athletes spent more time under water than above water the international swimming foundation, FINA, regulated (1998 for butterfly swimming) the maximum underwater phase to $15m$ in order to restore a more spectator friendly swimming style and to prevent "dive challenges".

In the Olympic Games in Atlanta in 1996 the Russian swimmer Denis Pankratov swam during his new $200m$ butterfly world record the first $15m$ (with underwater undulatory motion) even faster than all other swimmers including all crawl swimmers. Due to the advantageous resistance conditions and the usage of multiple muscle groups the undulatory underwater swimming motion describes one of the fastest modes of human locomotion in water. Correspondingly, this swimming style moved into the focus of sport scientists.

Following the line of research on fish locomotion in experimental biology the research of swimming biomechanics evolved from the pure observation of swimmer's kinematic to a basic flow dynamic approach [1].

The undulatory motion, also called dolphin kick, is characterized by a body wave traveling through the body from the finger tip to the toe. The rhythmic and periodic changes of the body shape induce the propulsive forces necessary for locomotion. In addition this motion determines active drag [7]. Swimmer's general goal is both to maximize the propulsion and to minimize drag. More precisely, depending on swimming distance the major focus varies between maximization the thrust for maximum swimming speed (short distance) and optimization of efficiency (middle and long distance). In contrast to passive drag (during gliding or towing a non-swimming subject through the water) active drag takes modifications induced by the propulsive motions into account. As to the intertwining of drag and propulsion in underwater undulatory swimming there is no satisfactory method for a direct experimental determination of active drag while swimming. Only for front crawl swimming it is possible to judge active drag by the MAD-system (Measure Active Drag, [12, 25]).

The human body represents a non-smooth multi body linkage system with restricted flexibility. These anatomical limitations constrict apparently a fast and effective underwater motion and prohibit swimming with a symmetric motion pattern. In previous research the characterization of undulatory underwater swimming mainly based on the described kinematics which indicated that the velocity of undulatory underwater swimmer is determined by the shape and velocity of the propulsive waveform [7, 16, 30]. In general, swimmers have the possibility of variation of the propulsive wave velocity and to vary the wavelength along the length of an undulatory swimming body [3].

Like in *subcarangiform* and *anguilliform* swimmers in human undulatory swimming the propulsion is distributed along the body. The cranial segments like upper body and arms may contribute to propulsion but the main part of the thrust is in consequence of the leg motion. The motion of the swimmer as a whole (amplitude, amplitude distribution along the body, frequency, propulsive wave, and body

wavelength) has to be coordinated in such a sequenced manner that the oscillation of each body segment which produces the propulsive impulse accelerate the water mass pedally and minimize active drag. In addition net rotational momentum during a cycle must vanish.

Both experimental methods as well as numerical methods can be used to judge drag and propulsion. In the context of human locomotion the experimental quantification of flow poses considerable hurdles and by now the investigations and methods are still in early stages.

Only a few methods to visualize and quantify flow have been so far applied to human swimming. They range from the observation of natural or injected air bubbles [1] to the orientation of tufts attached to the swimmers body [9, 24]. Recently Particle Image Velocimetry (PIV) which has been evolved into one of the standard methods for flow visualization in fish locomotion over the last couple of years (e.g. [14, 20]) has been applied to the hand stroke of crawl swimmers [17, 18] and in our studies to the dolphin kick [10, 11, 19].

The group around Matsuuchi monitored the flow of swimmers in a water tunnel and was focused on hand area for front crawl swimming [17] or feet region and wake for undulatory motion [19]. The small window of observation (below $0.4m \times 0.4m$) reduces requirements for illumination which is also facilitated by a low capturing rate of $15Hz$ (time between double images: $1ms$) which is too slow to demonstrate fast unsteady vortex structures in a chronological sequence. By subtracting the steady flow from the observations, flow and especially vortex patterns were extracted. They pointed out that during the stroke in front crawl swimming a strong counter clockwise vortex was generated above the back of the hand as soon as a pair of vortex and a jet flow in the wake after the down stroke for undulatory motion.

A much more detailed information about the relation between the swimmers motion and his performance is possible by computational fluid dynamics (CFD). Using CFD the human dolphin kick was simulated by Cohen et al. for one female and one male swimmer in prone position (three kick cycles, [33]) and by von Loebbecke et al. for one male swimmer in supine position (six kick cycles, [6]). The body shape was determined using a body scan and the kinematics were obtained by a video camera. Both studies only focused on swimmer's wake and displayed vortex rings after the down stroke for prone position and after the up stroke for supine position, but without a validation by an experimental validation. The down stroke produces a much larger thrust than the up stroke [6, 33].

Contrary to von Loebbecke et al. and Cohen et al. which focused on the specific enhancement of the human swim efficiency our study has also the approach is to understand the mechanism of flow preformation and flow re-capturing transferring these results to robotic underwater propulsion. This study represents the first attempt to reconstruct the total flow field in the sagittal plane of a human swimmer using two dimensional time resolved Particle Image Velocimetry (2D-PIV) with an adequate temporal resolution (250Hz) [10].

2 Material and Methods

2.1 Experimental Setup

In an indoor pool (length x width x depth: 20m x 8m x 0.5–2m) two female national swimmers swam undulatory motion in prone position. The swimmers performed across approximately 15m underwater with their preferred undulation frequency starting swimming in the low water area from a standing position, accelerating themselves within the following 10m to reach the deep water area and swimming with maximum speed through the camera recording window (Fig. 1). To neglect the effects of wave drag [27, 34] it was requested to swim at a depth of about 0.8–1m under the water surface.

Swimming in still water allowed the swimmers to display their preferred swimming technique, and the signal-to-noise ratio in the flow visualization was maximum in the absence of turbulence and flow gradients induced by the flow tank [20]. The recorded flow field in the pool fixed frame of reference is exclusively generated by the swimmer.

The flow generated by the swimmer was visualized using a two-dimensional particle image velocimetry (2D-PIV) and polyamide seeding particles (Degussa, Vestosint 1121, diameter 100 μm), with density similar to water. A Nd:YLF laser (Litron LDY 303, wavelength $\lambda = 527\text{nm}$, maximum output energy 20mJ @ 1kHz) illuminated the particles in the swimmers' sagittal plane by a laser light sheet. Using a laser guiding arm and a cylindrical lens, the laser beam (1.5mm diameter) was widened to a laser sheet with the width of 1m and a thickness of 3cm and deflected by a mirror to create a vertical laser light sheet in the swim direction parallel to the pool wall (Fig. 1).

In most applications small observation windows (e.g. 0.4m x 0.4m or smaller) fulfill the requirements for analyzing smaller objects. Thereby the light intensity, reflected from the particles, is sufficient to identify the path of the particles. To visualize the flow around the human swimmer and in its wake it is necessary to

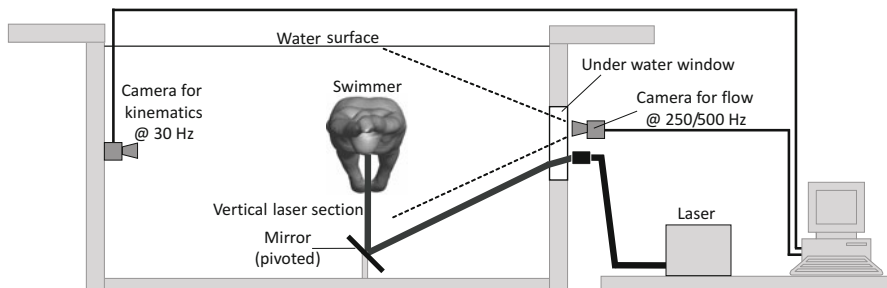


Fig. 1 Schematic setup (cross section of the pool). To generate a vertical laser section the laser beam passed an underwater window, was expanded and reflected by a mirror. Two opposing positioned cameras recorded the particle motion (right; Phantom V12.1) and swimmer's motion (left; Basler A602fc), respectively.

illuminate an observation window of at least $1m \times 1m$ by simultaneously strongly expanding laser beam. Thus, the light intensity is at the lower limit. Furthermore, such PIV experiments on living humans require extreme safety requirements.

To protect the eyes and skin swimmers wore laser protection glasses (Laservision Protector L-08K, filter type 13) and a speed-suit (Adidas Jetconcept suit woman), respectively. The laser protection glasses removed the green wavelength of the laser. Each Swimmer performed some preliminary experiments to adjust the swimming direction centrally (sagittal level) across the laser sheet. The differences between the middle line of the body surface and the vertical laser section were 5–15% of the hip width. A high speed camera (Phantom V12, Vision Research, Wayne, USA) recorded images of 1280×800 pixels at a frequency of 250 and $500Hz$ perpendicular to the laser light sheet. A $1m \times 1m$ calibration target with 10×10 regularly distributed white dots was used for calibration. The methods and the data post-processing in detail were quite similar to those in previous experiments described in Hochstein and Blickhan [10].

The experimental setup was approved by the German technical control board (TÜV Rheinland Industrie Service, KS-07/7048) and the ethics committee of the University of Jena. The subjects were informed about the methods, aims, risks, and safety regulations of the study and gave their written informed consent prior to participation.

The recorded images were imported in DynamicStudio 3.14. (Dantec Dynamics, Skovlunde, Denmark) and calibrated with respect to space and time. After using a median filter (7×7 pixels) the static background was removed by subtraction of a 7×7 pixels median filter. For the vector field calculation a cross-correlation algorithm was used (multi pass mode decreasing: $2 \times (256^2, 50\% \text{ overlap}) \rightarrow 2 \times (32^2, 50\% \text{ overlap})$) and post-processed by a moving average filter (5×5). Finally, the vector field was smoothed (5×5 linear smoothing filter) and exported to Tecplot 360 2011 (Tecplot Inc., USA) for further graphical postprocessing.

For the kinematical analysis anthropometric data such as body length L (distance from fingertips to the toes of the outstretched arms and feet), segmental length, and circumference were measured. Swimmer's motion was recorded at $30Hz$ using six encapsulated LED marker (positioned at the wrist, shoulder, hip, knee, ankle, and toe joint) and a video camera (Basler A602fc, provided by K. Reischle and M. Buchner) in an underwater housing perpendicular to the swimmer's sagittal plane. The horizontal and vertical positions of the LED markers were tracked using WinAnalyse V2.1.1. (Mikromak, Berlin, Germany) and post processed in MATLAB 2009b (The MathWorks Inc., Natick, USA) to calculate the joint angles as well as kinematic parameters, e.g. Strouhal number

$$St = \frac{A_{toe} \cdot f}{v} \quad (1)$$

where A_{toe} is the peak-to-peak amplitude of the toe, f the stroke frequency, and v the swimming speed.

2.2 Mathematical and Numerical Model

The best swimmer of the subjects (female, personal best 200m butterfly: 2:14,12; 793 FINA points) was used as template for creating a realistic geometry. Her silhouette (Fig. 2a) was scanned by a 3D body scanner from four different spatial directions and saved into a stereolithography (STL) datafile (Fig. 2b). A smoothing algorithm (Delauney Triangulation, [4, 22]) was used to reconstruct hidden and missing areas and to reduce redundant surface structures and not required details like swim suit and face composition to enhance the calculation speed.

To transfer the motion obtained from the human swimmer to the simplified silhouette (Fig. 2d) it is necessary to indicate the main marker points of human swimming body (wrist, shoulder, hip, knee, ankle and toe) and to divide the body into ten parts located between the marker points for body anterior and posterior side (Fig. 2c, [21]). The exact position of each marker point was detected by the body scans. The moving function of each pivot was created by the measured kinematics from the scanned female swimmer. As the human body represents a multi body linkage system the motion of each body segment strongly depends on the motion of the adjacent segments. As the shoulder represents the smallest vertical oscillation along the body [10] the shoulder joint was selected as reference point. From there the time course of all pivot points were calculated by rotation matrices and the joint angles obtained from kinematics [21].

The governing equations of mass- and momentum conservation in fluid dynamics, the Navier-Stokes-Equations, are solved in the open source CFD program Open-

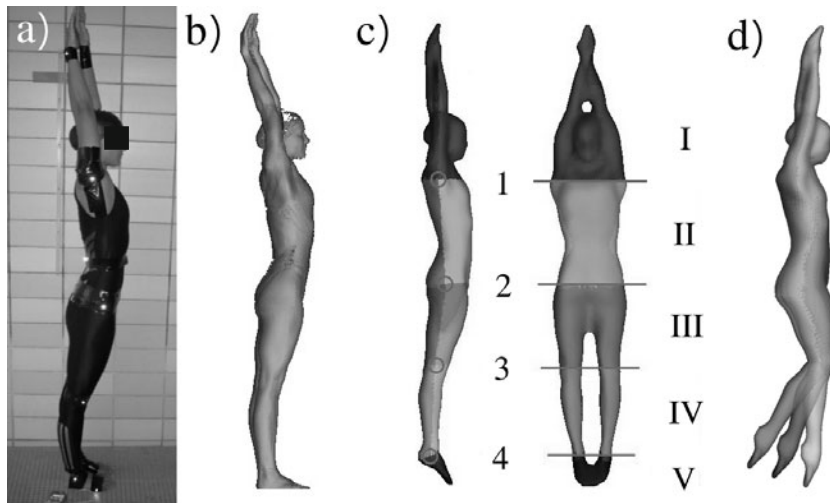


Fig. 2 Schematic representation for the generation of a realistic swimmer silhouette: a) human swimmer, b) scanned data, and d) modified surface model for several motion phases. c) The axis of rotation (1 shoulder, 2 hip, 3 knee, 4 ankle) define the ten segments (I head/arm, II upper body, III thigh, IV shank, and V feet) for both anterior and posterior side.

FOAM for an incompressible, newtonian fluid with constant density [8, 28]. Base for a highly resolved final mesh of one million tetrahedral cells was a rough block mesh refined and adapted to the swimmer's surface by the tool SnappyHexMesh. The boundary conditions and initial values for the system of partial differential equations are shown in Fig. 3. To these boundary conditions the movement functions obtained from the swimmers were added.

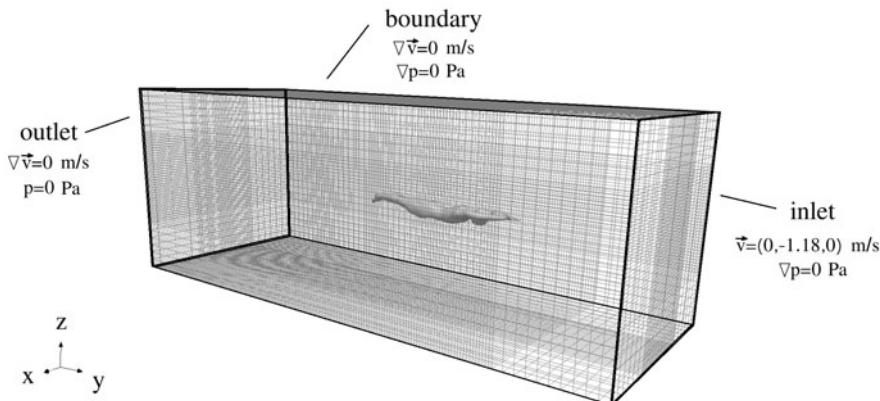


Fig. 3 Boundary conditions at calculation mesh: fluid intake (inlet), fluid cleanout (outlet) and remaining boundaries (boundary) with included initial values. The mesh with the fine resolution near the swimmers surface is not pictured for a better visualization of the calculation domain.

3 Kinematics and Asymmetric Amplitude Distribution

The kinematics of human swimmer swimming undulatory motion show similarities to fish locomotion, e.g. with respect to the length-specific amplitude of the "end-effector", length-specific body wavelength, and the amplitude distribution. On the other hand in human swimming the Strouhal numbers are much higher (range 0.8–1.0) than for fish or dolphin and clearly above the optimum range (0.2–0.35) documented for efficiently swimming and flying animals [23, 26]. These large Strouhal numbers are not only a result of the swimmers' ambition to swim with maximum velocity (thrust). While briefing the swimmer to swim efficient there is no significant difference in Strouhal number compared to maximum swimming. The dimensionless forward speed in terms of body length per stroke period ($\tilde{v} = v/(L \cdot f)$) in human undulatory swimming is about 0.25 (without fins, [10]) and 0.5 (with fins, [29]), respectively. In comparison to humans dolphins ($\tilde{v} = 0.9$, [32]) are more efficient swimmers. The durations of the up and down strokes are about the same (ratio of up to down stroke: 1.08 ± 0.06 and 1.04 ± 0.05 for the two subjects). There are intra-cyclic velocity variations during the stroke cycle and during the half-cycles. The average velocity of the center of mass (approximated by the motion of the hip joint) is slightly different during the up and down stroke phases.

In fish swimming, most species swim with a symmetric amplitude (e.g. [14]). Their deflection is symmetric about the sagittal plane with caudally rising amplitudes. However, some marine swimmers also use an asymmetric amplitude distribution, for example those swimming close to the water surface such as dolphins [32], and thereby realize very high swimming speeds.

Not only the amount of the amplitude (in body length) of the "end-effector" toe ($A_{\text{toe}}/L = 0.22$ for the two subjects) but also the distribution of the absolute deflection along the body of the human underwater undulatory swimmers is rather similar to that observed in *subcarangiform* or *carangiform* fish (Fig. 4a; e.g. [2, 5, 15, 31]). The total amplitude distribution along the body increases quadratic from hand to toe (Fig. 4a). This is surprising as due to morphologic limitations the joints within the human linkage system cannot move symmetrically. In fact, the dorsal and ventral part of the deflection along the body and therefore the envelope of the deflection are highly asymmetric with respect to the swimmers stretched position (Fig. 4b). Some joints are deflected rather symmetric (hand, hip, and ankle) and some very asymmetric (shoulder, knee, and toe) related to the swimmers stretched position. Despite this asymmetry during straight horizontal swimming the net vertical forces during a cycle must vanish. Furthermore, to avoid rotation the net rotational moment during a cycle must be zero [5].

Conform to the results of von Loebbecke et al. [33] the results of CFD studies show that the down stroke produces a much larger thrust than the up stroke in human undulatory swimming. In part this can be traced back to an adaptation to swimming near to the surface. During the up stroke, more energy is "lost" to the surface wave than in the down stroke. Furthermore the anatomical and morphological asymmetry (e.g. muscle distribution) of the human musculoskeletal system allows or rather causes the down stroke to be more powerful than the up stroke. Furthermore, human swimmers alter the shape of legs and feet during up and down stroke (more opened or more closed).

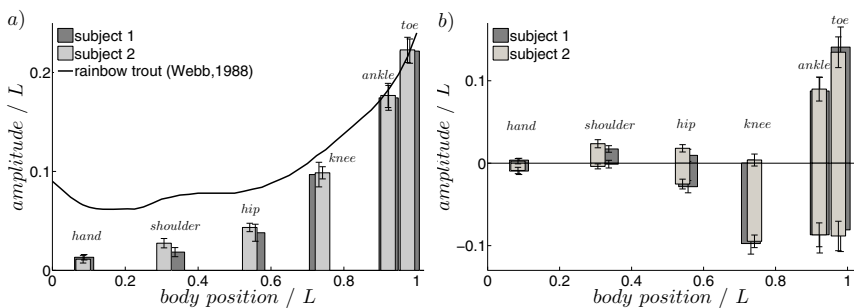


Fig. 4 Amplitude distribution (mean \pm SD) along swimmer's body (both normalized by body length L : distance from fingertip to toe of the outstretched arms and feet) for both subjects: a) absolute total deflection and b) dorsal and ventral deflection with respect to swimmer's stretched position (Fig. 5c). The solid line in a) represents the amplitude distribution of a rainbow trout [35].

Results of Videler and Kamermans [32] document the similarities between dolphin swimming and human swimming presented here. Dolphins decelerated during the up stroke and accelerated during the down stroke and both half-cycles have nearly equal durations similar to the human swimming presented here. Calculations of the thrust forces during both half-cycles in dolphins revealed that there are net resistive forces during the up stroke and net propulsive forces during the down stroke phase. Although the thrust forces during the up and down stroke were different the forward velocity of the dolphins was hardly affected [32]. This points towards differences in drag during both phases which may also play a role in human swimming.

4 Flow Visualization and Flow Pattern around a Human Swimmer

4.1 Experimental Flow

The presented experimental method of flow visualization using PIV in combination with human swimmer demonstrate for the first time the unsteady flow around the human swimmer and in its wake while swimming underwater undulatory motion. Except for areas located dorsal to the upper body in the shadow of the laser light sheet this approach allows to reconstruct the flow pattern around the total human swimmer in contrast to previous approaches which were able to investigate only small details of the motion (e.g. hand, see Chap. 1). The first results of flow visualization and the unsteady flow around a human swimmer [10] indicate that the flow pattern around a human swimmer is highly complex. Especially, it was not possible to identify a simple and stable flow pattern in the wake.

The amount and size of the vortices produced in the head region depends on swimmer's level of performance and technique. Swimmers with poor technique and large deflections in arm and shoulder region generate two larger counter rotating vortices ventral below the head with a resulting jet flow. In contrast a small vortex was separated when the swimmer perform only small vertical oscillation in arm and head (Fig. 5c). Consequential these swimmers avoid large vortex separation and initialize already the undulatory pump. Furthermore, larger separation areas are introduced by an immoderate high head position. Despite of the segmentation of the human body and the restricted range of motion of the joint angles the human swimmer is able to reproduce the undulatory pump (Fig. 5a,b,d) and use it for propulsion. The largest vortex separation occurs in the leg region especially around knee, ankle, and toe by reason of the edges and the undulatory movement of the lower limbs. These vortices were partly reabsorbed (e.g. vortex dorsal of the shank, Fig. 5a,b,c). Both in experimental and numerical results these vortex pair with the jet (Fig. 5c,d) is clearly more distinct after the down stroke than after the up stroke [10].

The missing stable flow pattern in the wake of the swimmer may be due to the selected central sagittal observation slice. The numerical results show that the vortex structures in the wake are positioned in slices parallel to the swimmer's central sagittal plain (Fig. 6a, Fig. 7c). It has to be mentioned that the feet in the numerical

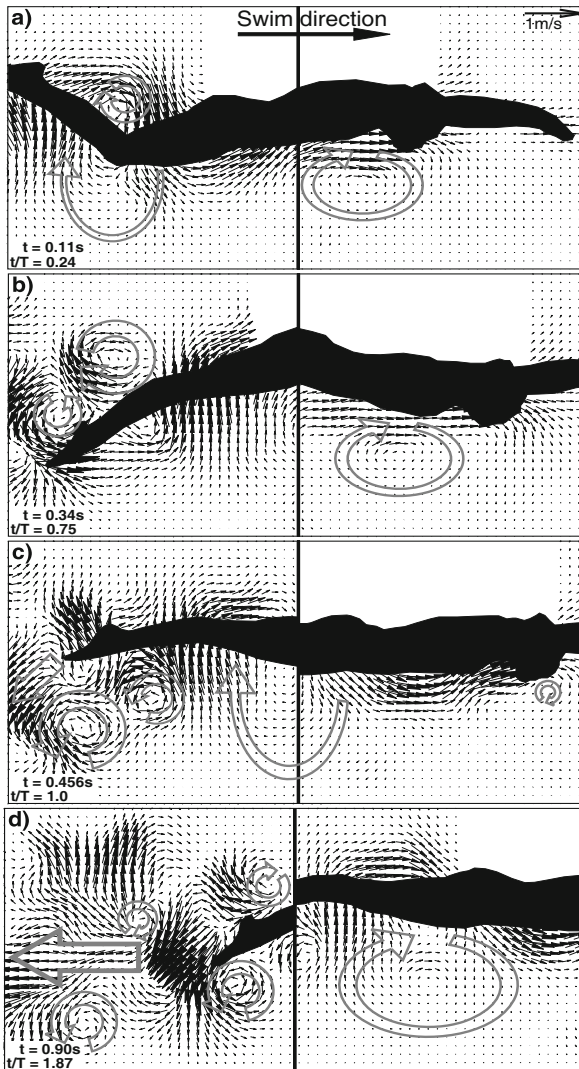


Fig. 5 Composed flow field (black arrows) generated during dolphin kicks in a still water fixed window of $2m \times 1m$ at certain points of the swimming period. The kick cycle starts when the swimmer is in its stretched position ($t = 0$) and ends after a complete period ($t = T = 0.455s$). Each subimage is a combination (divided by the vertical black bar) of the same phase of the kick cycle. In each case the right part of the subimage is two complete periods before the left part. a) Begin of the down stroke. Vortex separation dorsal of the knee. b) End of the down stroke. The vortex at the shank rotates fixed to the pool reference frame. c) End of a kick cycle (swimmer's stretched position). The feet kick into the vortex and destroy it (vortex re-capturing, [10, 11]). Two counter rotating vortices generated after the down stroke behind the feet induced a jet flow (gray arrow). d) One kick later. The flow behind the swimmer is directed backwards (bold gray arrow).

simulations are closed all the time and thus approach a more fin-like function. In real swimming the distance between the legs and feet varies during the kick cycle (more opened in the down stroke and more closed in the up stroke). Therefore some of the differences between the experimental and numerical flow field may be due to the variation of the shape of the legs during a kick cycle.

4.2 Numerical Simulation

Different unsteady structures were identified during calculation of the undulatory dolphin kick. All structures are visualized with a modified Q -Criterion.

Conventional criteria like Q -Criterion [13] and λ_2 -Criterion, that detect areas with higher flow rotation than shear, are not suitable for vortex visualization of transient and fast diffusing structures of weaker intensity (Fig. 7a). Adapting the standard Q -Criterion by the magnitude of relative vortex velocity leads to a new visualization method, the modified Q -Criterion, for vortex evolution and interaction over time (Fig. 7b,c). A comparison of unsteady structures at calculation after period one and six (Fig. 7b,c) shows differences in intensity and displacement. The initial horse-shoe vortices (Fig. 7b left) from gliding phase were not observed. The remaining ring vortices are generated by up (upper ring) and down stroking feet (lower ring) in the first period. Using the modified Q -Criterion, identifies a huge area of vortex interaction in swimmer's wake for the sixth period (Fig. 7c). The ring vortices of the current up and down stroke merge with remaining structures of previous motion cycles into two longitudinal vortices per up and down direction.

Comparing numerical results with experimental findings for same phases of the period shows some similarities in vortex generation and transport. The vortex structures near the knee are conform. Even flow properties near body surface are similar. The vortex near the shank and feet after the legs moved down from the maximum upper transversal excursion in the experiments are in agree with the CFD results. At maximum lower excursion there are similarities at the ventral flow patterns. At the end of the stroke cycle some unsteady structures are dorsally shown in experiments

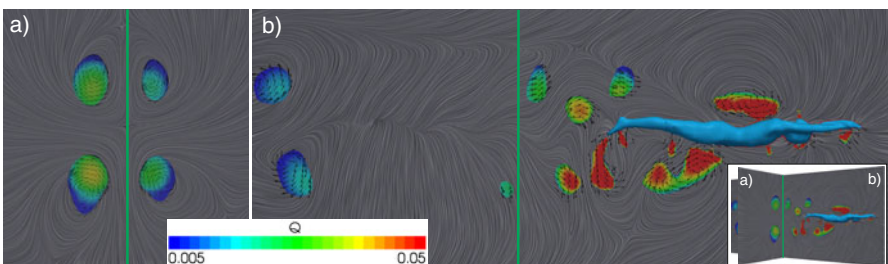


Fig. 6 Visualization of vortex structures (modified Q -Criterion) generated by the swimmer in two perpendicular planes: a) back view and b) side view, see icon in the right edge. In each case the solid green vertical lines represent the slice plane.

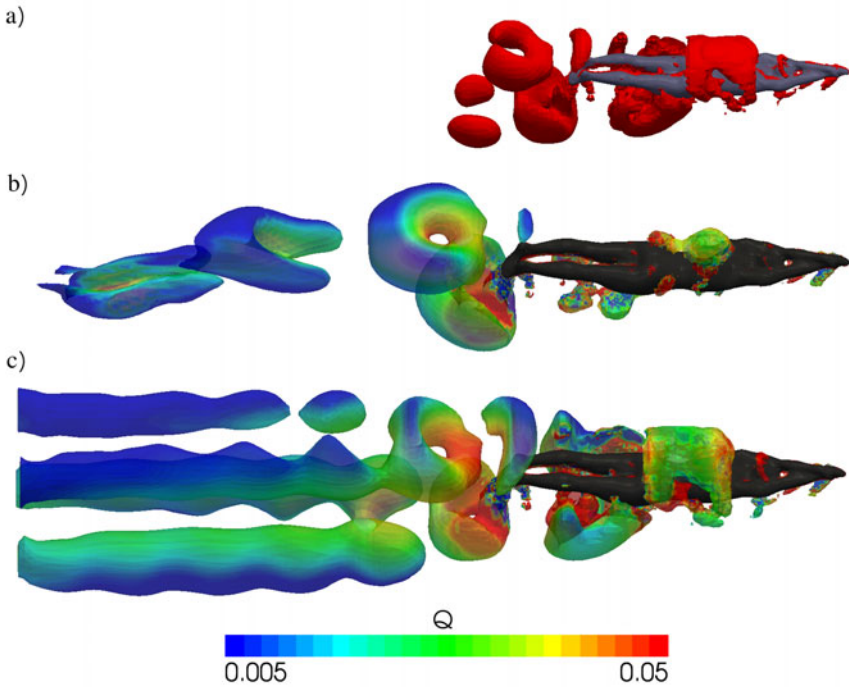


Fig. 7 Visualization of unsteady structures for a) a discrete value ($Q = 0.5 \text{ s}^{-2}$) with standard Q -Criterion and b) for a steady interval of Q with modified Q -Criterion at logarithmic scaling. The superposition of the vortex rings of several periods causes a vortex merging in the wake c) after period one. There is an increasing intensity of vortex structures around the entire swimmers body from period one to period six.

and numerics. Differences in the flow intensity near the feet may be due to closed feet position in numerics and varying feet distance in the experiment.

5 Flow Preformation and Vortex Re-capturing

During the underwater phase after start and turn elite swimmer typical perform six till eight underwater dolphin kicks. Per kick they cover a distance of about a fourth of the body length ($\bar{v} = v/(L \cdot f) = 0.25$). Only the hands interact unaffected with the flow field in front of the swimmer. Depending on the part of the body the flow is affected by the previous caudal body segments and by the flow generated up to four kick before (flow preformation). In experimental observations at least two to three periods are visible to analyze the interaction of the prior preformed flow field and the flow just created by the interaction between the body motion and the water. For numerical results the first ten dolphin kicks were calculated.

In the context of a energy recovery strategy the pedal body parts interact with caudally produced vortices to reuse a fraction of the kinetic energy of rotation of the

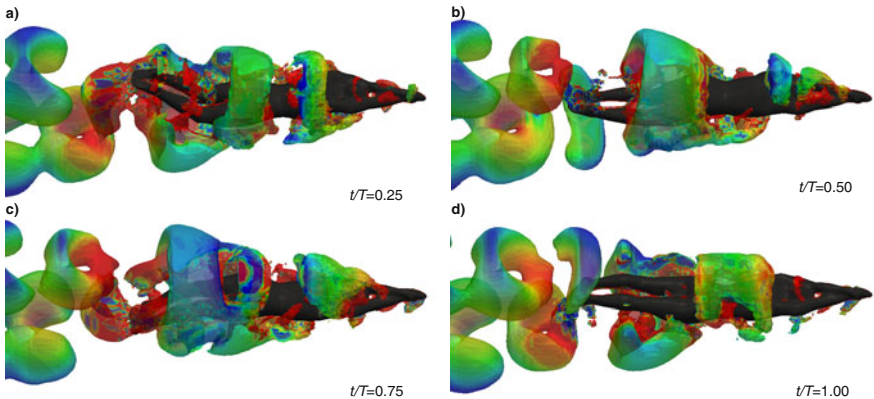


Fig. 8 Vortex re-capturing at swimmers surface and vortex merging at the wake visualized with the modified Q -Criterion at logarithmic scaling ($0.005 \leq Q \leq 0.05$) for period six at different points of the period t/T . The vortex transport of unsteady structures from the shoulder (a) to the hip (b) and increasing intensity into ring (c) and horse-shoe vortices (d) is pictured.

vortex to increase the swimming speed and thus to enhance the propulsion (vortex re-capturing, [10, 11]). As described, vortices are mainly generated in the leg region caused by flexion and extension of the hip, knee, and ankle joint. In part, cranially generated vortices rotated on the spot with respect to the pool fixed reference system. The swimmers pass these vortices and interact thereafter with them. For example, due to knee flexion a vortex is generated dorsal to the shank (Fig. 5a). This vortex rotates while swimmer moves past it (Fig. 5b,c) and later the feet kick into the vortex and destroy it (Fig. 5d). Hence, a constructive usage of flow preformation and vortex re-capturing is suggested which is conducive to minimize the energy loss due to vortex separation and as a result enhances efficiency.

In contrast to the experimental results displaying only a sagittal slice of the complete flow field the numerical simulations present in addition information about the complete 3D flow field. This provides new possibilities for global monitoring of energy recovery strategies such as vortex re-capturing. Due to the opposite movement of arms and shoulder a vortex structure is generated in the shoulder region and transported along the body surface to the hip (Fig. 8a). While the hip moves up this vortex structure is extended into a horse-shoe vortex and increases intensively when the legs lower. Meanwhile the down stroking feet release an upper vortex ring which merges with previous upstroke rings into two longitudinal vortices in the wake over time (Fig. 8b). At maximum lower excursion of legs and feet the lower vortex ring is released to join with earlier down-stroke-ring (Fig. 8c) into two other longitudinal vortices (Fig. 7c). The intensity of this unsteady structure increases with every period (Fig. 7) with subsequently increasing dorsal and ventral interaction between vortices at the front and back side. Horse-shoe vortices grow up and extend to ring vortices around the swimmer (Fig. 7b,c).

6 Conclusion and Outlook

Despite of the segmentation of human body and the restricted conditions concerning the joint angles the human swimmer is able to reproduce the undulatory pump and use it for propulsion. It could be experimentally demonstrated that the flow preformation in a caudal part of the body allows the principally usage of the vortex structures generated at the body downstream for strategies like vortex re-capturing (illustrated by the measured vortex structures). We propose that the high Strouhal numbers used by the human swimmers facilitate this process. It does represent a measure to increase efficiency in presence of unavoidable vortex separation at the level of distal joints.

The optimization of the motion relevant in sport swimming can indicate whether and how motion patterns can be used for the compensation of the anatomical disadvantages (segmentation and body shape). Segmented linkage systems are used in robotics and thus, especially in amphibious systems, an adaptation of the body shape to the requirements of swimming is limited. Especially for larger systems mechanical, structural, or technical constraints exist to imitate fish like motion.

The simulations revealed besides agreements some unexpected 3D aspects. In order to further validate the modeling it will be necessary to perform experiments with the laser sheet shifted from the central sagittal plane and in the transversal plane. New techniques for illumination making this possible are on the way.

In future, by modification of the coordination it can be analyzed whether selective motion strategies can enhance or reduce thrust (formation of the incoming flow, constructive superposition of the fluid) or affect efficiency (destructive energy-recovering superposition), and to what extent limitations of the human locomotor system prevents an optimum utilization. Furthermore, it is necessary to investigate the sensitivity of thrust and efficiency with respect to variation of the motion pattern (cause and effect) and if robust strategies can be identified.

The numerical calculations allow to estimate the pressure distribution and thereby the net forces on each body segment and the torques on each joint. Torques and motions can be used to feed muscle driven models in order to obtain proper activation patterns. In contrast to the human swimmer the virtual swimmer (numerical simulation) is able to move with symmetrical joint excursions. It should be analyzed how to which extent the flow pattern differs between symmetric and asymmetric motion. It cannot be excluded that the asymmetry of human motion is beneficial for the usage of unsteady effects.

These steps should improve the fluid mechanical understanding for an efficient and thrust orientated undulatory underwater locomotion and clarify to which extent these strategies are applicable for humanoid machines.

Acknowledgements. The authors greatly acknowledge the support from the "Deutsche Forschungsgemeinschaft" (DFG) in the Priority Program SPP 1207: "Nature-Inspired Fluid Mechanics" within the project: "Active use of unsteady effects at human swimming", BL 236/17-1 & 17-2 and BR 1494/11-1 & 11-2.

Furthermore the authors wish to express their thanks to the swimmer and the Institute of Sports and Sports Sciences at the University of Heidelberg for allowing us to use

their indoor pool for this investigation. Furthermore we would like to thank Klaus Reischle and Markus Buchner (University of Heidelberg), Hans-Wolfgang Döttling (Olympic Center Rhein-Neckar) for their help and support in the experimental trials as well as Maren Witt and Steffen Kerner (IAT Leipzig) allocating the body scanner. Without Horst Bleckmann (University of Bonn), Cam Tropea, and David Rival (University of Darmstadt) taking the risk of allocating the PIV system to us this investigation would not have been possible.

References

1. Arellano, R., Terrés-Nicoli, J.M., Redondo, J.M.: Fundamental hydrodynamics of swimming propulsion. In: Vilas-Boas, J.P., Alves, F., Marques, A. (eds.) Proceedings of the Xth Congress of Biomechanics and Medicine in Swimming, pp. 15–20 (2006)
2. Bainbridge, R.: The speed of swimming of fish as related to size and to the frequency and amplitude of the tail beat. *Journal of Experimental Biology* 35(1), 109–133 (1958)
3. Batty, R.S.: Locomotion of plaice larvae. In: Symposium of the Zoological Society of London, vol. 48, pp. 53–69 (1981)
4. Bowyer, A.: Computing dirichlet tessellations. *The Computer Journal* 24, 162–166 (1981)
5. Cheng, J.Y., Blickhan, R.: Bending moment distribution along swimming fish. *Journal of Theoretical Biology* 168(3), 337–348 (1994)
6. Cohen, R.C.Z., Cleary, P.W., Mason, B.R.: Simulations of dolphin kick swimming using smoothed particle hydrodynamics. *Human Movement Science* (2011) (in press)
7. Connaboy, C., Coleman, S., Sanders, R.H.: Hydrodynamics of undulatory underwater swimming: A review. *Sports Biomechanics* 8(4), 360–380 (2009)
8. Ferziger, J.H., Peric, M.: Computational Methods for Fluid Dynamics. Springer, Berlin (2002)
9. Hay, J.G., Thayer, A.M.: Flow visualization of competitive swimming techniques: The tufts method. *Journal of Biomechanics* 22(1), 11–19 (1989)
10. Hochstein, S., Blickhan, R.: Vortex re-capturing and kinematics in human underwater undulatory swimming. *Human Movement Science* 30(5), 998–1007 (2011)
11. Hochstein, S., Blickhan, R., Reischle, K., Kunze, S., Brücker, C.: Swimming like a fish? first evidence of vortex re-capturing. In: Duarte, A., Cabri, J., Barreiros, J. (eds.) European Workshop on Movement Sciences, p. 89. Faculdade de Motricidade Humana, Lisbon (2009)
12. Hollander, A.P., de Groot, G., van Ingen Schenau, G.J., Toussaint, H.M., de Best, H., Peeters, W., Meulemans, A., Schreurs, A.W.: Measurement of active drag during crawl arm stroke swimming. *Journal of Sports Sciences* 4(1), 21–30 (1986)
13. Hunt, J.C.R., Wray, A., Moin, P.: Eddies, stream and convergence zones in turbulent flows. In: 2. Proceedings of the 1988 Summer Program, pp. 193–208. National Aeronautics and Space Administration, Ames Research Center, Moffett Field, CA (1988)
14. Lauder, G., Tytell, E.: Hydrodynamics of undulatory propulsion. In: Fish Biomechanics, vol. 23, pp. 425–468. Elsevier (2005)
15. Liao, J.C.: Swimming in needlefish (belonidae): anguilliform locomotion with fins. *Journal of Experimental Biology* 205(18), 2875–2884 (2002)
16. Lighthill, M.J.: Mathematical biofluidynamics. SIAM Pub., Philadelphia (1975)
17. Matsuuchi, K., Miwa, T., Nomura, T., Sakakibara, J., Shintani, H., Ungerechts, B.E.: Unsteady flow field around a human hand and propulsive force in swimming. *Journal of Biomechanics* 42(1), 42–47 (2009)

18. Matsuuchi, K., Muramatsu, Y.: Investigation of the unsteady mechanism in the generation of propulsive force while swimming using a synchronized flow visualization and motion analysis system. In: Klika, V. (ed.) Biomechanics in Applications, pp. 389–408. InTech (2011)
19. Miwa, T., Matsuuchi, K., Shintani, H., Kamata, E., Nomura, T.: Unsteady flow measurement of dolphin kicking wake in sagittal plane using 2c-piv. In: Vilas-Boas, J.P., Alves, F., Marques, A. (eds.) Proceedings of the Xth Congress of Biomechanics and Medicine in Swimming, pp. 66–68 (2006)
20. Müller, U.K., Smit, J., Stamhuis, E.J., Videler, J.J.: How the body contributes to the wake in undulatory fish swimming flow fields of a swimming eel. *Journal of Experimental Biology* 204, 2751–2762 (2001)
21. Pacholak, S., Rudert, A., Brücker, C.: Numerical study of human dolphin swimming. In: Brenn, G., Holzapfel, G.A., Schanz, M., Steinbach, O. (eds.) PAMM 82nd Annual Meeting of the International Association of Applied Mathematics and Mechanics. Technische Universität Graz, Graz (2011)
22. Shewchuck, J.R.: A two dimensional quality mesh generator and delauney triangulator. Technical report, Carnegie Mellon University Pittsburgh (1995)
23. Taylor, G.K., Nudds, R.L., Thomas, A.L.R.: Flying and swimming animals cruise at a strouhal number tuned for high power efficiency. *Nature* 425(6959), 707–711 (2003)
24. Toussaint, H.M.: An alternative fluid dynamic explanation for propulsion in front crawl swimming. In: Sanders, R., Hong, Y. (eds.) Applied Program: Application of Biomechanical Study in Swimming, pp. 96–103. The Chinese University of Hong Kong, Hong Kong (2000)
25. Toussaint, H.M., Beelen, A., Rodenburg, A., Sargeant, A.J., de Groot, G., Hollander, A.P., van Ingen Schenau, G.J.: Propelling efficiency of front-crawl swimming. *Journal of Applied Physiology* 65(6), 2506–2512 (1988)
26. Triantafyllou, M.S., Techet, A.H., Zhu, Q., Beal, D.N., Hover, F.S., Yue, D.K.P.: Vorticity control in fish-like propulsion and maneuvering. *Integrative and Comparative Biology* 42(5), 1026–1031 (2002)
27. Vennell, R., Pease, D., Wilson, B.: Wave drag on human swimmers. *Journal of Biomechanics* 39, 664–671 (2006)
28. Versteeg, H.K., Malalasekera, W.: An Introduction to Computational Fluid Dynamics. Harlow Pearson Education Limited (2007)
29. Videler, J.J.: Fish swimming movements: a study of one element of behaviour. *Netherlands Journal of Zoology* 34, 170–185 (1985)
30. Videler, J.J.: Fish swimming. Chapman and Hall, London (1993)
31. Videler, J.J., Hess, F.: Fast continuous swimming of two pelagic predators, saithe (*pollockius virens*) and mackerel (*scomber scombrus*): A kinematic analysis. *Journal of Experimental Biology* 109, 209–228 (1984)
32. Videler, J.J., Kamermans, P.: Differences between upstroke and downstroke in swimming dolphins. *Journal of Experimental Biology* 119(1), 265–274 (1985)
33. von Loebbecke, A., Mittal, R., Mark, R., Hahn, J.: A computational method for analysis of underwater dolphin kick hydrodynamics in human swimming. *Sports Biomechanics* 8(1), 60–77 (2009)
34. Vorontsov, A.R., Rumyantsev, V.A.: Propulsive Forces in Swimming. In: Biomechanics in Sport, 1st edn., vol. 1, pp. 184–204. Blackwell Science Ltd., Oxford (2000)
35. Webb, P.W.: Steady swimming kinematics of tiger musky, an esociform accelerator, and rainbow trout, a generalist cruiser. *Journal of Experimental Biology* 138, 51–69 (1988)

Part V

**Flow Control with Aid of
Compliant Walls, Airfoils,
Wave-Like Riblets**

Influence of Wave-Like Riblets on Turbulent Friction Drag

René Grüneberger, Felix Kramer, Erik Wassen, Wolfram Hage,
Robert Meyer, and Frank Thiele

Abstract. This article reports on a numerical and experimental study of the turbulent drag on riblet surfaces, where the trapezoidal riblet grooves were formed in a wave-like sinusoidal or zigzag pattern. The aim was to enhance the drag-reducing capabilities of conventional, straight riblet grooves by an additional contribution that originates from the induced oscillating lateral flow component. By means of a comprehensive parameter study in an oil channel at Re between 10,000 and 30,000 and DNS simulations at $Re_\tau = 180$, suitable waveform parameters are sought, with which wave-like riblets produce a drag reduction larger than that of their straight counterparts. For a riblet cross-section shape that is known to be optimal for straight grooves, no such beneficial drag modification could be demonstrated. With a riblet groove cross-section different from the optimum shape, an augmented attainable drag reduction in comparison to straight riblet grooves was found within a certain range of the waveform amplitude. The improvement amounts up to 1.3%-points in terms of drag reduction. Wave-like riblets with reduced riblet height never outperformed the drag reduction of straight riblet grooves of optimal cross-section form, but exhibit a similar drag reduction in the best cases investigated. It is shown that this favourable influence on the riblet-modified turbulent drag persists under a mild misalignment of the riblets to the main flow direction.

1 Introduction

Triggered by the initial publications of Walsh [20, 21], the capability of microscopic grooves aligned parallel to the flow to lower the skin friction in turbulent boundary

René Grüneberger · Felix Kramer · Erik Wassen · Frank Thiele
TU Berlin, Müller-Breslau-Str. 8, D-10623 Berlin
e-mail: {rene.grueneberger, felix.kramer}@cfd.tu-berlin.de,
{erik.wassen, frank.thiele}@cfd.tu-berlin.de

Wolfram Hage · Robert Meyer
DLR, Institut für Antriebstechnik, Abteilung Triebwerksakustik,
Müller-Breslau-Str. 8, D-10623 Berlin
e-mail: {wolfram.hage, robert.meyer}@dlr.de

layers has been extensively studied in the past. The optimal cross-section design for rectangular grooves was specified by Bechert [2] and a trapezoidally grooved profile was found as the best trade-off between the riblet's effectiveness and their mechanical strength and durability [3]. A drag reduction of 10% compared to a smooth surface was achieved experimentally with a rectangular groove cross-section of extremely thin ribs, whereas trapezoidal grooves attain approximately 8%.

Initially, riblets were intended for aircraft applications to save fuel, with their feasibility for that purpose confirmed in full-scale flight tests [19] as well as in normal service operation of a long-range aircraft [22]. From both investigations, a fuel consumption diminished by approximately 2% is reported. Hence, riblets are a fairly well-understood passive means of turbulent drag reduction, but rarely used, even in these days of increasing fuel prices. One-off attempts in the *America's Cup* yacht race in 1987 and 2010 remain the best-known examples.

To the present, the economic benefit of riblets on aircraft hulls is apparently outbalanced by the expenses of application, maintenance and removal of such coating. Potential remedies follow two paths: recently, an automated paint application technology was developed by Stenzel et al. [18], which allows for riblet grooves to be imprinted directly in a laquer coat, which is reported to reduce the application and removal costs for a riblet lining. The other option, upon which this work focuses, pursues the enhancement of the drag reduction achievable with riblets.

The combination of the drag reduction of conventional, straight riblet grooves with the much more potent effect of imposing an oscillatory lateral velocity component to the near-wall flow is a tempting idea. Results from numerical and experimental studies published by Wassen et al. [23], Kramer et al. [9, 10] and Grüneberger et al. [5] demonstrated, that generally a favourable superposition of both drag reducing techniques is possible. Here, the lateral velocity was generated in an active, energy-consuming fashion by tilting thin band-shaped ribs around their contact point at the wall to either side, thus emulating the oscillating wall technique. The actuating mechanism and its energy consumption renders this attempt impractical for application. More importantly, only a small increase in drag reduction under certain flow conditions could be achieved due to the limited lateral displacement of the rib tips, which prevented the production of sufficiently high velocity amplitudes.

An innovative three-dimensional riblet modification was proposed by Quadrio [17], which induces a periodic near-wall motion in a passive way by deflecting the riblet grooves in the lateral direction and arranging them in plan view in a wave-like pattern. This method avoids the limitation of the lateral displacement and is possibly capable of improving the performance of known two-dimensional riblet structures. In contrary to oscillating riblets, the desired periodic velocity component is generated as an oscillation in space, not time.

An LES of sinusoidal riblets was published by Peet et al. [15]. They investigated the friction drag on triangular riblet grooves with $h/s = 0.87$ in a channel flow at $Re_\tau = 180$ at a riblet width $s^+ = 21^1$. For straight riblet grooves, a drag reduction of 5.4%-points was found, which is in good agreement to measurements by other

¹ $(\cdot)^+$ values are nondimensionalised by the friction velocity $u_\tau = \sqrt{\tau_0/\rho}$ and v .

authors [2, 21]. A sinusoidal deflection with an amplitude of 18 wall units at a wavelength of 580 wall units resulted in a drag increase by 0.5%-points if compared to a smooth surface. An increased wavelength of 1080 wall units at an amplitude of 34 wall units led to an enhanced drag reduction of 7.4%, an improvement by 2%-points. In that contribution, only the friction drag was considered. More recently, Peet et al. [16] extended those investigations to infinitely thin ribs and rectangular riblet grooves and included the pressure drag which occurs in the sinusoidal configurations. Here, they computed 11.2% drag reduction for rectangular riblet grooves in baseline configuration and up to 14.6%-points if deflected with amplitudes of 34 wall units at a wavelength of 1080 wall units.

In an attempt to refine the previous research on riblet performance augmentation by inducing an oscillating lateral velocity component, experimental and numerical investigations were carried out on passive riblet structures with wave-like modified grooves. Preliminary results have already been published by Kramer in [11, 12].

In the experiments, the drag of test plates lined with riblets of sinusoidal or zigzag wave pattern are measured in an oil channel facility and compared to the drag on a smooth test plate of equal size that is exposed to the same flow. By a parameter variation of the channel flow velocity, the wave amplitude and wavelength, and the ratio of riblet height to width h/s , suitable parameters, under which wave-like grooves provoke a drag reduction larger than that of comparable straight riblets, shall be identified. The measurements are accompanied by DNS on trapezoidally shaped riblet grooves with a fixed ratio $h/s = 0.5$ at $Re_\tau = 180$. A parameter variation of the waveform amplitude and length similar to the experiments was conducted. A breakdown of the overall drag into its contributing parts provides a deeper insight into the flow affected by wave-like riblets.

2 Experimental Setup

The experiments were conducted in the Berlin oil channel operated by the DLR (German Aerospace Center). This test facility was designed and built specifically for friction drag measurements and the development of drag reducing surfaces. A comprehensive description of the channel, its instrumentation and flow characteristics is given by Bechert et al. [1].

This channel is of closed-circuit type with a rectangular cross-section of ca. 0.75m in height and 0.25m in width. Technical white oil with a density $\rho = 837\text{kg/m}^3$ and a kinematic viscosity $\nu = 1.19 \cdot 10^{-5}\text{m}^2/\text{s}$ at 20°C is used as a fluid. The oil channel can be operated in a range of $Re_{ch} = 8 \cdot 10^3 \dots 3 \cdot 10^4$, where Re_{ch} is based on the channel width and the bulk velocity u_b . The fluid level is mostly covered to avoid the entrainment of air bubbles. The test section is equipped with an adjustable upper lid to set the static pressure gradient $\partial p / \partial x \approx 0$ for each flow velocity.

In the test section, a riblet test plate and a smooth test plate serving as a reference are flush-mounted in the smooth channel walls opposite to each other. Both test plates are 500mm in length and have a width of 400mm. An extremely sensitive differential force balance provides means for the measurement of the sum and the

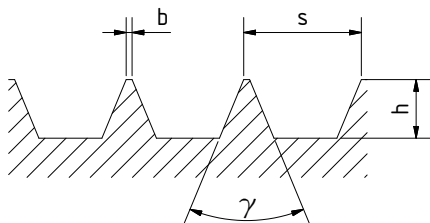


Fig. 1 Riblet cross-section profile with trapezoidal grooves

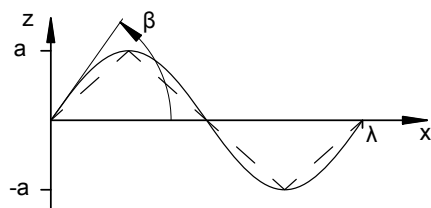


Fig. 2 Waveform plan view;
— sinus, - - - zigzag

difference of the drag forces on both test plates simultaneously. Correction functions are applied to those figures to account for flow inhomogeneities before the relative change in wall shear stress $\Delta \tau / \tau_0$ is calculated. As a rough estimate, those values $\Delta \tau / \tau_0$ are correct to within $\pm 0.3\%$ -points, or $\pm 0.003 \tau_0$. A detailed assessment of the measurement accuracy is provided by Grüneberger&Hage [6].

For the experimental results shown below, the drag-reducing properties of 46 individual riblet test plates were evaluated. Those test plates were produced from acrylic glass in a CNC milling process using purpose-made form cutters. All riblets used a trapezoidal groove cross-section according to figure 1 with a constant riblet spacing s of 3.2mm and a rib tip angle $\gamma = 30^\circ$. The elaborate production process ensures, that the riblet tip width b lies reliably within 0.03 ± 0.01 mm. All other geometric parameters, namely the rib height h , the waveform amplitude a , the wavelength λ and the waveform pattern (refer to fig. 2) were subject to variation. Figure 3 depicts an example of a test plate with sinusoidal riblet grooves.

The laterally-deflected riblet grooves were arranged in the flow direction with a zero point of the waveform positioned midway on the test plate and consecutive oscillation periods extending symmetrically in the up- and the downstream directions.

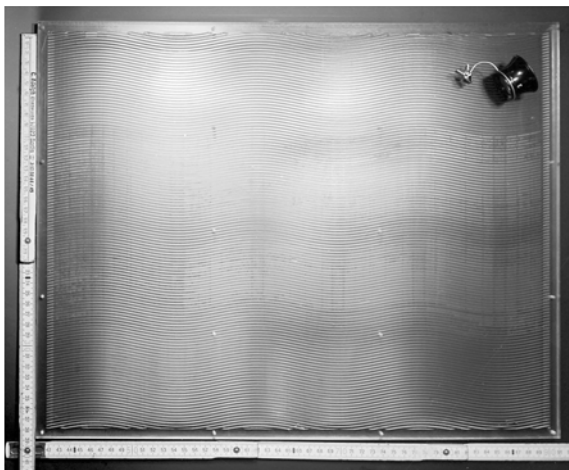


Fig. 3 Test plate with sinusoidally deflected riblet grooves

The expected values for the oscillation wavelength is of the same order of magnitude as the test plate length, which restricts the meaningful range of wavelengths that can be tested. For example, at $\lambda/s = 50$ and $s = 3.2\text{mm}$, three complete periods of oscillation can be arranged within the test plate length. Changing that parameter in the experiments will inevitably alter the number of periods, causing an additional effect on the average drag force due to more or less complete transition to a flow regime controlled by a lateral velocity component. For measurements on riblet grooves under a yaw angle, an additional set of test plates with grooves inclined to the flow direction was machined.

3 Numerical Setup

The simulations are performed using a fully turbulent channel at $Re_\tau = 180$ based on the channel half-height and the shear velocity u_τ , or $Re = 5750$ if calculated with the channel height and u_b ². The channel consists of two walls as illustrated in figure 4. The upper smooth wall serves as a reference to the opposing wall equipped with the riblet structure. The remaining sides of the channel are periodic faces. Their distance to each other is large enough to ensure significant decorrelation of the flow. Hence, the computational domain is larger than the “minimal flow unit” defined by Jiménez [8]. The domain size shown in figure 4 was used for all simulations at zero yaw angle.

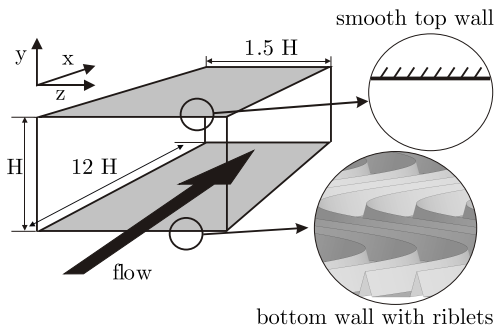


Fig. 4 Setup of the computational domain

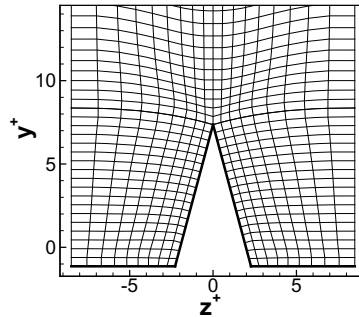


Fig. 5 Riblet segment with grid cells

In the presence of riblets, the channel height H can be specified in multiple ways. The present work defines it as the channel’s fluid volume divided by the area of the top wall. This definition is independent of the riblet structure itself and facilitates in terms of Reynolds’ number a comparison of different cross-section geometries better than arbitrarily choosing the rib tips or groove bottoms as the origin for a direct specification of H . The height definition used is equivalent to the distance between

² Following the traditional naming convention, the “height” in simulations corresponds to the “width” of the experimental channel.

the top wall and a virtual plane located in between the rib tips and groove bottoms at a position where the rib volume above this plane equals the fluid volume below.

The Navier-Stokes-equations are discretised using Finite Volumes in a cell-centered storage scheme, and solved by an algorithm that is second order accurate in space. The discretisation in time uses implicit backward differencing of second order. Within the applied *SIMPLE* algorithm [4], the generalised Rhie and Chow interpolation [14] avoids oscillations between the pressure and the velocity field. Incompressibility and a Newtonian fluid are presumed.

Each grid is structured having roughly 65 million cells. The cell size in the x -direction is eight wall units. The cell size in the y -direction starts at 0.5 wall units at the smooth wall, increases to 4.6 wall units at the channel center and reduces to approximately 0.5 wall units near to the riblet structure depending on its z -position. Between the ribs, the cell size in the z -direction is non-uniformly distributed starting at 0.5 at the rib walls, and growing to a maximum of 1.6 wall units in the center between two ribs. A sample of one riblet segment is illustrated in figure 5. Except for the sharp rib tips, the trapezoidal shape of the riblet grooves is comparable to the experiments with the same rib tip angle of 30° , $h^+ = 8.5$ and $s^+ = 17$, resulting in a ratio of height to width of 0.5. Using this setup, 32 riblet grooves fit into the domain side by side.

In the simulations at yaw angles other than zero, the driving pressure gradient is rotated accordingly such that the streamwise direction no longer coincides with the x -direction. To allow a similar decorrelation length in the new streamwise direction, the domain dimension is enlarged such that the width and the length are five times the channel height. Using the same grid segment as before, the total grid size increases to 90 million cells.

For all cases, the sinusoidal deflection of the riblet structure is realised by shearing the grid: the corners of the cells are shifted in the z -direction depending on their x -position. The length of the computational domain is kept constant for different wavelengths. To assure periodicity, the wavelengths are restricted to be a whole-number fraction of the channel length.

4 Drag Reduction of Straight Riblet Grooves

Straight riblets consisting of rectangular grooves and band-shaped thin ribs at different height-to-width ratios h/s were extensively investigated in the experiments by Bechert et al. [2] in the same facility as used for the present work, however for trapezoidal groove profiles, only shear stress measurements at $h/s = 0.5$ are available. Therefore, four different straight-grooved riblet geometries with trapezoidal cross-section shape and $h/s = 0.3, 0.5, 0.7$, and 0.9 were tested. By consecutive measurements at different channel velocities, the dimensionless spacing s^+ was varied between approximately 10 and 18 wall units. The results for $\Delta\tau/\tau_0$ are depicted in figure 6.

A single data point representing the baseline results from a DNS of grooves of $h/s = 0.5$ at $s^+ = 17$ is also plotted. It corresponds to a representative wall shear

stress derived from the total drag force on the riblet wall divided by their projected surface area and amounts to $0.932\tau_0$, or 6.82% drag reduction. Compared to the experimental data, this drag reduction is about 1%-point weaker. After the initial transient, the averaging to determine this figure was carried out for 1900 convective time units based on H and u_b , resulting in a statistical error of $\pm 0.2\%$ -points with a 67%-confidence interval [13].

Results from Bechert [2] for trapezoidal riblet grooves and $h/s = 0.5$ are given for comparison and are found in good agreement to the present experimental data. A third-order polynomial fit is applied to each measurement series to determine the minimum relative wall shear stress, i.e. the point of maximum drag reduction for a given configuration.

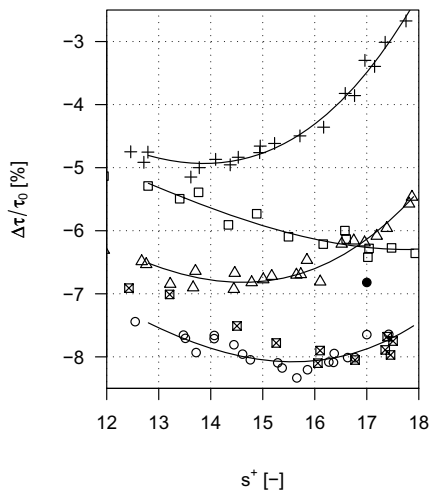


Fig. 6 Relative wall shear stress for straight trapezoidal riblet grooves with different h/s ; Exp: $\square h/s = 0.3$, $\circ h/s = 0.5$, $\triangle h/s = 0.7$, $+ h/s = 0.9$, — third-order interpolation
DNS: $\bullet h/s = 0.5$, $\blacksquare h/s = 0.5$, data from Bechert [2]

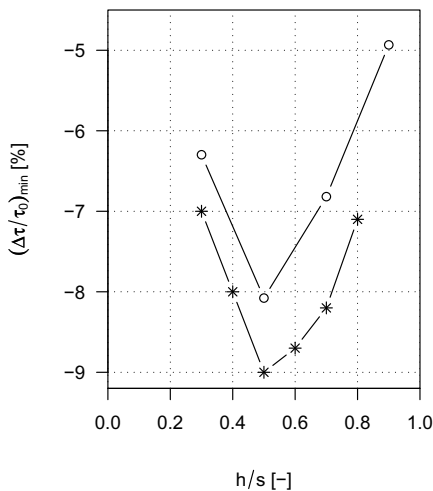


Fig. 7 Minimum relative wall shear stress for straight riblet grooves with different h/s ; Exp: \circ trapezoidal cross-section, $*$ rectangular cross-section from Bechert [2]

These values $(\Delta \tau / \tau_0)_{\min}$ for trapezoidal groove profiles are plotted in figure 7 versus the ratio of h/s . Likewise, the corresponding findings of Bechert [2] for rectangular groove profiles are displayed. The effect of the riblet groove cross-section design on the attainable drag reduction appears to be similar for rectangular and trapezoidal shapes, with an almost constant shift in $(\Delta \tau / \tau_0)_{\min}$ of ca. 1%-point, or $0.01\tau_0$. In both investigations, a groove configuration with $h/s = 0.5$ provided the highest drag reduction. Through these results, a plausible reference data set for trapezoidal riblet grooves and different riblet heights is established.

5 Effect of Amplitude and Wavelength

Starting with the optimal riblet height for straight grooves, $h/s = 0.5$, the amplitude and wavelength of sinusoidally-deflected riblet grooves were changed independently in a wide range to find a parameter combination that allows for an increase in drag reduction.

As an initial value, the configuration with a favourable influence on the shear stress value from the work of Peet [15], $\lambda/s = 51.4$, was used. For a moderate wavelength of $\lambda/s = 50$ in the experiments and $\lambda/s = 64$ in the simulations, the amplitude was altered between $0.3 \leq a/s \leq 4.0$. In figure 8, the relative drag change values found for a constant riblet width $s^+ = 17$ are charted as a function of the dimensionless amplitude $a^+ = a/s \cdot s^+$. The simulations are performed exactly at this riblet width. For the experimental results, intermediate values had to be calculated based on a third-order interpolation of the actual data points to enable a direct comparison. The error bars given in fig. 8 represent the 67% confidence interval for the numerical data and the estimated uncertainty in the oil-channel measurements respectively.

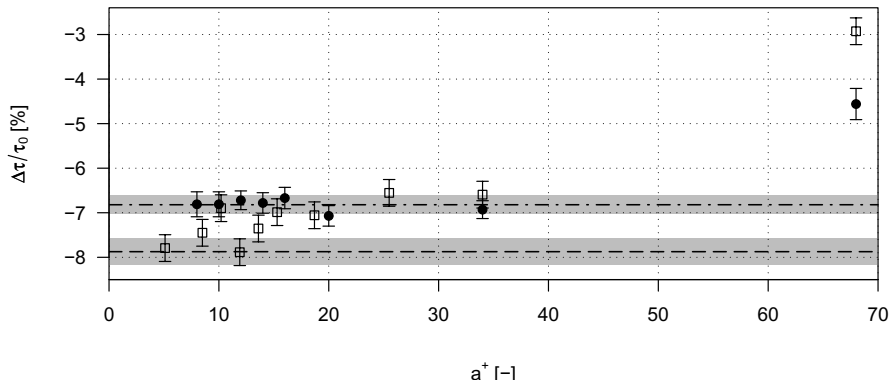


Fig. 8 Relative wall shear stress at $s^+ = 17$ for sinusoidal riblets with different amplitude, $h/s = 0.5$, shaded blocks and error bars indicate 67%-confidence interval;
Exp: $\square \lambda^+ = 850$, $--\Delta\tau/\tau_0$ of straight riblet grooves
DNS: $\bullet \lambda^+ = 1080$, $--\Delta\tau/\tau_0$ of straight riblet grooves

In the experiments, within the data range considered, no improvement of the drag reduction could be observed. Instead, for the smallest amplitude $a^+ = 4.7$, $\Delta\tau/\tau_0$ of straight and sinusoidally-deflected riblet grooves coincide. With increasing a^+ , the maximum drag reduction first lessens slightly but reaches the baseline value again at $a^+ \approx 11$. With a further increase in a^+ , the attainable drag reduction drops drastically.

These findings are supported by the DNS. Their straight-grooved baseline case at $s^+ = 17$ reached a wall shear stress of $0.932\tau_0$. Within the statistical uncertainty, this value is not altered by applying lateral amplitudes up to 34 wall units. Only at the

highest amplitude $a^+ = 68$ is an effect of the sinusoidal deflection observed, leading to an increase in wall shear stress if compared to straight riblets.

The DNS data allow for the total streamwise drag working on the riblet surface to be separated into three contributing parts, which are the shear force acting on the riblet groove bottom, the shear force acting on the ribs and the pressure force experienced by those surface parts of the ribs that are not aligned with the flow. Figure 9 illustrates how these individual forces, normalised by the corresponding drag on the smooth reference wall D_0 , change with increasing amplitudes of the oscillation. For all cases shown, the wavelength was kept constant at 1080 wall units, or $\lambda/s \approx 64$. In this breakdown, the fraction missing between the sum of the contributions and 1.0 corresponds to the drag reduction of the respective simulation. The shear drag on the ribs at over 65% is the major source of drag within the observed range of amplitudes. The groove bottom accounts for only 20 to 25% of the total drag. The pressure part is negligible for small values a^+ but rises to 10% of the drag at the largest amplitude.

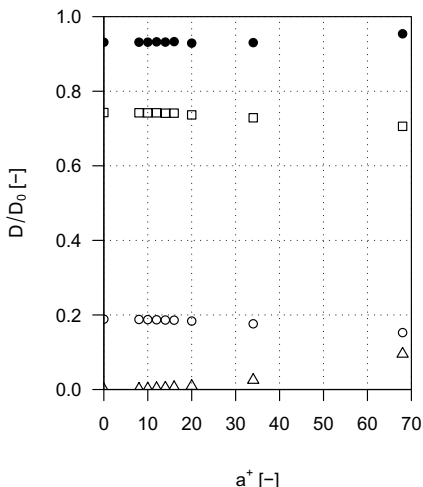


Fig. 9 Contributions of different drag components to overall drag;
DNS: \square friction drag on rib faces, \circ friction drag on groove valley floor, \triangle pressure drag, \bullet total drag

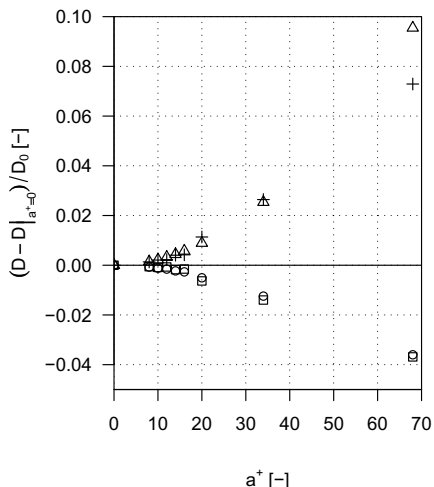


Fig. 10 Gain/reduction in drag components;
DNS: \square friction drag on rib faces, \circ friction drag on groove valley floor, \triangle pressure drag, $+$ negative sum of friction drag reduction

The changes in the individual drag sources due to an amplitude variation are isolated by subtracting the offset at zero amplitude from each drag component. The results are depicted in figure 10. The gain in pressure drag increases with increasing amplitude at a growing rate. The friction drag reduction is almost the same for the groove valley floor and the ribs, and their reduction is disproportionately correlated to the amplitude in a similar way as the pressure drag.

To compare the differences between the shear and the pressure drag changes quantitatively, the negative sum of the shear force reduction is also plotted. For a large portion of the amplitude range below $a^+ = 34$, the loss in friction is balanced by an increase in pressure drag, leaving the representative wall shear stress in fig. 8 unaffected. This is reasonable, since the flow is slowed by the increased static pressure in front of the misaligned surface parts belonging to the ribs. It is remarkable that a force equivalent up to $0.025D_0$ can be redistributed between shear drag and pressure drag without a change in overall drag reduction. If a weakening of the drag reduction as for $a^+ = 68$ is acceptable, more than $0.095D_0$ can be exploited for passive flow manipulation at small costs.

In the next step, with a constant moderate amplitude $a/s = 0.7$ in the experiments and $a^+ = 15$ for the simulations, the sine-function wavelength was varied from $\lambda/s = 10$ to 80. Due to the finite test plate length, the variation of this parameter is strongly restricted in the experiments. In figure 11, the experimental and numerical results for $\Delta\tau/\tau_0$ at $s^+ = 17$ are given as a function of $\lambda^+ = \lambda/s \cdot s^+$.

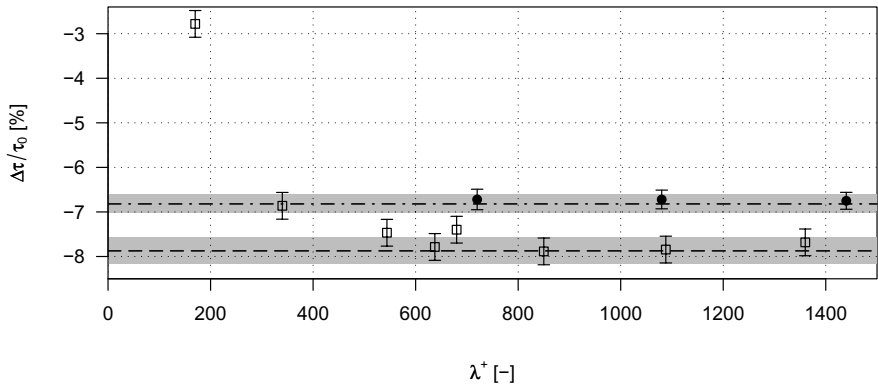


Fig. 11 Relative wall shear stress at $s^+ = 17$ for sinusoidal riblets with different wavelength, $h/s = 0.5$, shaded blocks and error bars indicate 67%-confidence interval;
 Exp: $\square a^+ = 15$, $--\Delta\tau/\tau_0$ of straight riblet grooves
 DNS: $\bullet a^+ = 12$, $--\Delta\tau/\tau_0$ of straight riblet grooves

It emerged, that for λ^+ larger than 600, the achievable drag reduction collapses to the corresponding value for conventional, straight riblet grooves. Reducing the wavelength in the experiments produced weaker drag reduction figures. Within the parameter range considered, no improvement relative to the drag reduction of straight riblets was achieved by sinusoidally-deflected riblet grooves with $h/s = 0.5$.

6 Variation of Waveform Pattern

As the desired lateral velocity component is generated in a passive manner, kinetic energy is extracted and converted from the downstream flow velocity. In general,

the efficiency thereby is determined by the waveform pattern with a sine-function as an obvious choice. According to fig. 9, within reasonable geometry parameters only minor drag contributions due to pressure drag are generated. Therefore, only a weak sensitivity of the wall shear stress to the actual waveform topology is expected. Producing test plates with sinusoidal riblet grooves with the high surface quality and precision needed for consistent measurements proved to be quite an intricate process due to the complex geometry description in the CNC programme. Using a zigzag waveform pattern instead of a sine function with identical values for a/s and λ/s , those challenges can be avoided. The effect on the wall shear stress was tested with two different geometry parameter sets.

The relative wall shear stress on sinusoidal and zigzag riblet grooves with $h/s = 0.5$, $a/s = 0.7$ and $\lambda/s = 37.5$ is depicted in figure 12. Both measurements coincide almost perfectly, but their minimum value is comparable to the corresponding baseline case of straight riblet grooves, indicating no influence of a lateral velocity component whatsoever.

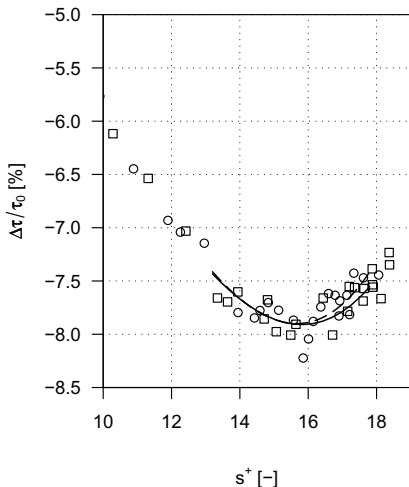


Fig. 12 Minimum relative wall shear stress for wave-like riblets with different waveform, $h/s = 0.5$, $a/s = 0.7$, $\lambda/s = 37.5$; Exp: \square sinus, \circ zigzag, —— interpolation sinus, --- dto. zigzag

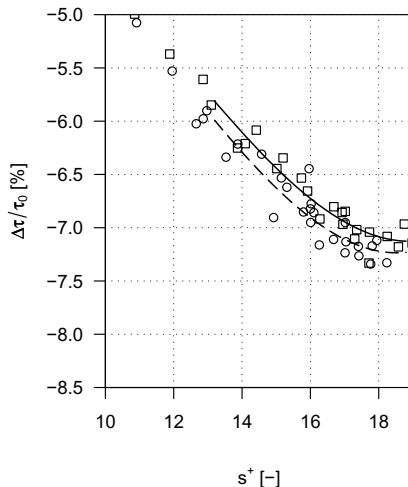


Fig. 13 Minimum relative wall shear stress for wave-like riblets with different waveform, $h/s = 0.3$, $a/s = 2.0$, $\lambda/s = 37.5$; Exp: \square sinus, \circ zigzag, —— interpolation sinus, --- dto. zigzag

Wave-like riblets with $h/s = 0.3$ reliably produce a drag reduction larger than straight riblets with an identical cross-section shape. This assessment of the waveform pattern was repeated with geometries $h/s = 0.3$, $a/s = 2.0$ and $\lambda/s = 37.5$. Here, the zigzag grooves achieved 7.2% drag reduction, while with sinusoidal riblets 7.1% were measured, an improvement by 0.9% and 0.8%-points over straight riblets.

The waveform pattern was hence demonstrated to be of minor importance for the additional drag reduction caused by a periodic lateral riblet deflection and a zigzag waveform pattern was used in further experiments.

7 Influence of the Riblet-Groove Cross-Section Shape

The investigations so far have concentrated on trapezoidal riblet groove profiles with a height-to-width ratio of 0.5. Here, even the smallest additional contribution by a lateral groove deflection would immediately pay off, but no such manipulation of the average wall shear stress could be accomplished, either in the experiments or in DNS.

The experimental investigation was then extended to ratios h/s other than 0.5, and an amplitude variation similar to section 5 performed on zigzag riblet grooves with $h/s = 0.3, 0.5, 0.7$, and 0.9 at amplitudes a/s between 0.5 and 1.5 (up to 3.0 for $h/s = 0.3$). The wavelength was kept constant at $\lambda/s = 37.5$. In figure 14, the minima of $\Delta\tau/\tau_0$ received in the measurements on 23 different test plates are plotted against the amplitude a^+ . The dashed lines represent the respective values for straight riblets. As already noticed at sinusoidally deflected grooves, an amplitude up to ca. 10 wall units is admissible also for zigzag riblets of $h/s = 0.5$ until their maximum drag reduction lessens. A similar behaviour was observed for slightly higher ribs at $h/s = 0.7$ with respect to a reduced baseline drag reduction of 6.8%. In both cases, no favourable influence on the wall shear stress could be demonstrated.

The results from measurements on geometries with considerably increased and reduced riblet heights of $h/s = 0.9$ and 0.3 render a different picture: for both riblet groove cross-sections, a decreased wall shear stress compared to straight riblets of the same profile was observed at several different amplitudes a/s .

For $h/s = 0.9$, the range of amplitudes that provoke an enhanced drag reduction extends from $a/s = 0.5$ to 1.5, with $a/s = 0.9$ as an optimal value. Here, the maximum drag reduction increases from 4.9% for straight riblet grooves to 5.5%. With shallow riblet grooves of $h/s = 0.3$, the range of advantageous amplitudes reaches from $a/s = 0.5$ to 2.5, the most effective modification of the friction properties is again obtained at $a/s = 0.9$. A maximum drag reduction by 7.6% is achieved, which compares to 6.3% measured for straight riblets. The difference in $(\Delta\tau/\tau_0)_{\min}$ amounts to 1.3%, which is four times larger than the measurement uncertainty.

For a detailed analysis of the effect of a lateral riblet groove deflection on the wall shear stress, the value $\Delta\tau/\tau_0$ measured on zigzag riblets is decomposed in the portion caused by the drag reduction of straight grooves and an additional contribution DC :

$$\frac{\Delta\tau}{\tau_0} = \left(\frac{\Delta\tau}{\tau_0} \right)_{\text{straight}} + DC \quad (1)$$

The function $\Delta\tau/\tau_0 = f(s^+)$ on zigzag and straight riblets is known at discrete points s^+ only, which had to be interpolated by linear segments in order to obtain equidistant nodes for the determination of DC . Figure 15 illustrates DC in

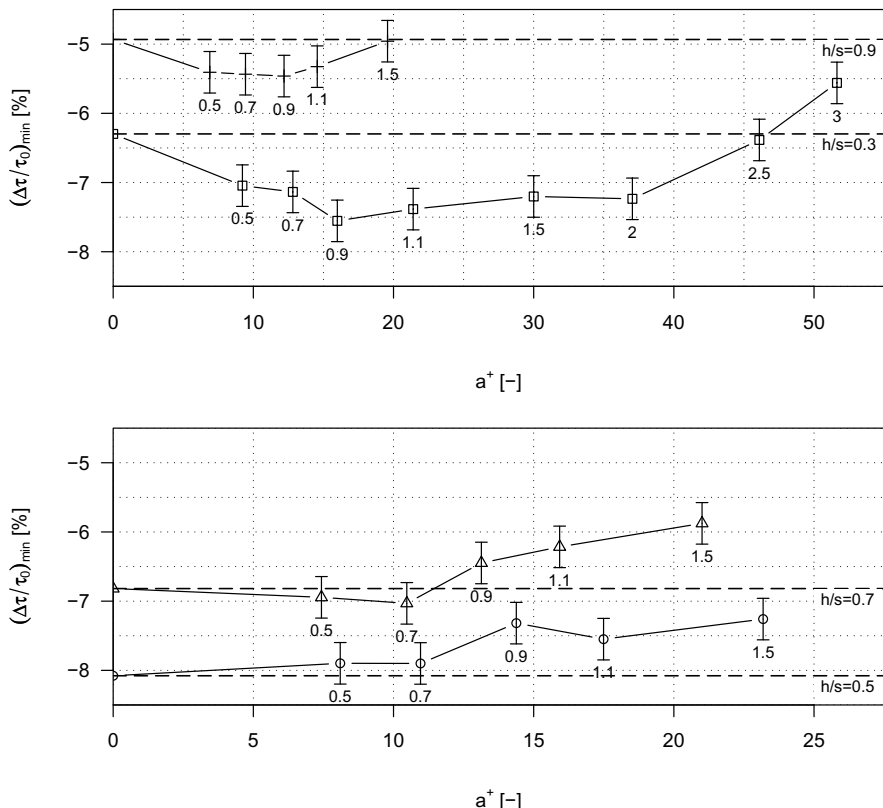


Fig. 14 Minimum relative wall shear stress for zigzag trapezoidal riblet grooves with different h/s , $\lambda/s = 37.5$; Exp: $\square h/s = 0.3$, $\circ h/s = 0.5$, $\triangle h/s = 0.7$, $+ h/s = 0.9$, $-- (\Delta\tau/\tau_0)_{min}$ of straight trapezoidal riblet grooves, figures indicate a/s

a grayscale as a function of the dimensionless riblet width and the amplitude a/s for the shallowest and deepest riblet grooves. As a second abscissa, the dimensionless riblet height h^+ is given. The dashed line marks the limit $DC \equiv 0$, beyond which the drag on zigzag riblets is larger than on straight riblets under equal flow conditions.

It can be noted that with both riblet profiles, a change in the wall shear stress properties of the order of 1%-point can be realised. The generation of an additional drag reducing contribution due to the introduction of a periodic lateral velocity component appears to be a tradeoff between the amount of that velocity component and the correlated additional drag reduction and the gain in pressure drag due to the riblet groove misalignment to the main flow direction.

At moderate amplitudes $a/s \approx 1$ and for riblet heights between five and eight viscous length units, the ribs are almost completely immersed in the viscous sublayer. Therefore, they can be arranged in a rather steep angle β to the main flow direction,

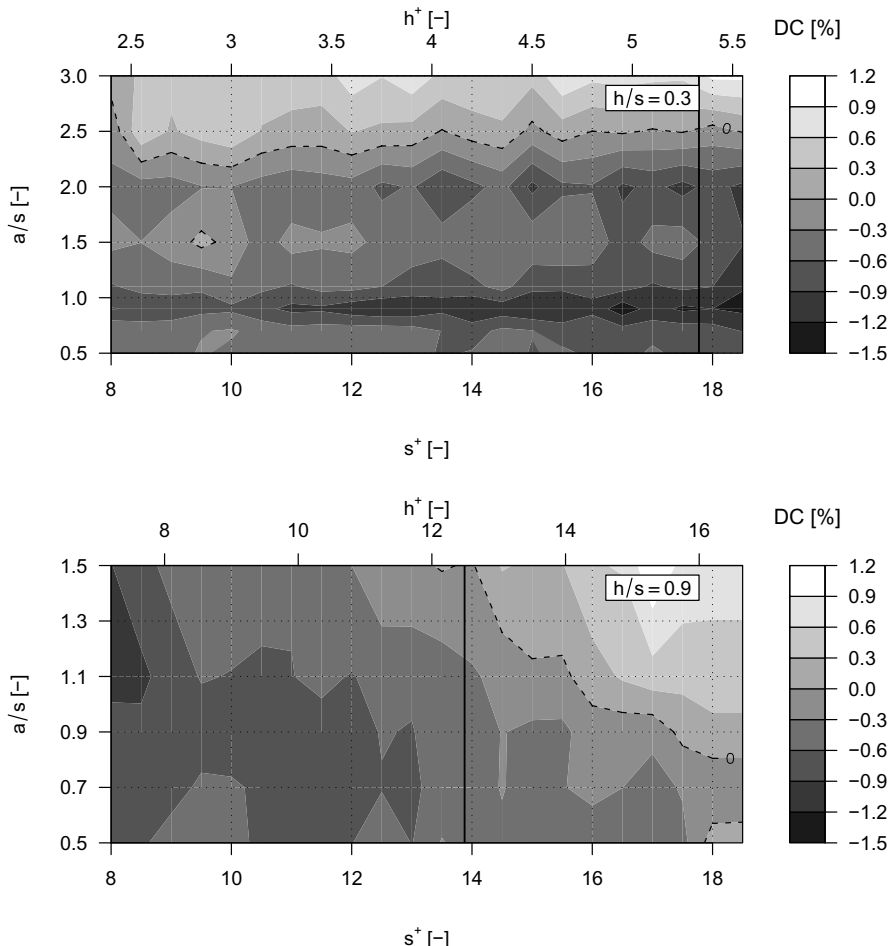


Fig. 15 Difference DC in relative wall shear stress between straight and zigzag riblet grooves; — s_{opt}^+ for straight riblet grooves, — — limit $DC \equiv 0$

creating an effective amount of lateral velocity. Its impact on the streamwise vortices provokes a decrease in surface friction that exceeds the inevitable increase in pressure drag. The beneficial range of a/s depends on h^+ . At $h/s = 0.3$, amplitudes $a/s \leq 2.0$ produce a decrease in wall shear stress compared to straight riblets for h^+ up to 5.5 wall units. Riblet heights h^+ larger than ca. eight wall units expose the rib tips to a higher streamwise velocity, leading to a stronger sensitivity to the riblet groove amplitude. At $h/s = 0.9$, h^+ can be variated within the channel Re -range in an interval $7 \leq h^+ \leq 16.5$. Above $h^+ = 12$, the value for feasible amplitudes declines as the increased parasitic drag outweighs the advantages of the lateral flow component.

The most advantageous combination of conventional riblets with the drag reduction related to a lateral velocity component is achieved when both mechanisms

reach their maximum effectivity under equal flow conditions. It emerges from figure 15, that DC is maximised for h^+ between five and eight wall units. The ideal riblet groove cross section should find its maximum drag reduction also at the same value h^+ . Therefore, shallow riblet grooves with $h/s = 0.3$ are more appropriate than those with $h/s = 0.9$ as they reach $(\Delta \tau/\tau_0)_{\min}$ at $s^+ \approx 17.8$, or $h^+ \approx 5.3$. This is illustrated in figure 15 by the marked positions s_{opt}^+ for the point of minimum wall shear stress of straight riblet grooves. For $h/s = 0.3$, this point coincides with the region of large values of DC , where at $h/s = 0.9$, the straight riblets reach their point of maximum drag reduction at large values of $h^+ \approx 12.5$, when the possible drag reducing contribution of the lateral deflection is already decreased or completely vanished.

8 Yaw-Angle Effect

It is known from different authors [7, 21], that the effectiveness of conventional riblets is adversely affected if the flow approaches under a yaw angle φ . According to Hage, Bechert&Bruse [7], the drag reduction of trapezoidal riblet grooves is diminished from 8.2% to 7.4% by a yaw angle of 10° . With measurements of zigzag riblets with two different amplitudes it was tested, whether the favourable effect of the wave-like modification on the attainable drag reduction described in section 7 persists under a mild misalignment of up to 10° .

With measurements on six test plates equipped with straight riblet grooves of $h/s = 0.5$, that were arranged under different angles $\varphi \leq 30^\circ$, a reference data set was established. In figure 16, the extreme values $(\Delta \tau/\tau_0)_{\min}$ derived from those experiments are compared with the re-evaluated data from Hage [7], measured in the same flow channel on a round pivotable riblet surface segment. The impact of the yaw angle was slightly underestimated in that data. This is believed to be an artefact of the different setups used, since the effective surface portion covered with riblets is smaller in the measurements of Hage [7]. The DNS data is in good agreement to both experimental assessments provided the riblet width used ($s^+ = 17$) does not differ much from the value s_{opt}^+ found in the oil channel. This is not the case for the largest yaw angle $\varphi = 30^\circ$.

The behaviour of wave-like riblets with reduced riblet height of $h/s = 0.3$ under yaw angle was investigated for amplitudes $a/s = 0.9$, which represents the optimal zigzag modification, and at $a/s = 2.0$ as a rather large amplitude that still produced significantly larger drag reduction than straight riblet grooves of equal shape. Figure 17 illustrates the data for $(\Delta \tau/\tau_0)_{\min}$ found on zigzag riblets under yaw along with the values for straight grooves of optimal shape $h/s = 0.5$ as a comparison.

The degradation of the drag reducing capability of zigzag riblets with $h/s = 0.3$ and $a/s = 0.9$ is similar to the characteristics observed in the reference case of straight riblets at $h/s = 0.5$. Up to a yaw angle of 10° , this zigzag configuration

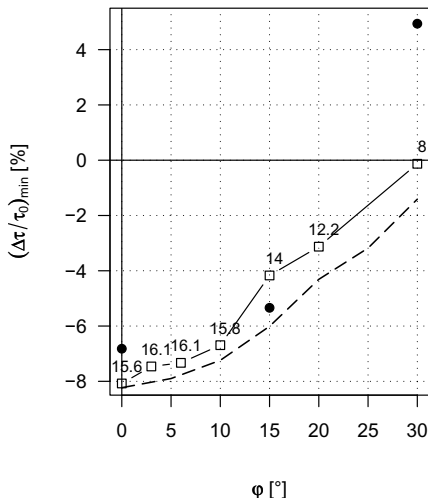


Fig. 16 Minimum relative wall shear stress for straight trapezoidal riblet grooves at different yaw angles;
Exp: \square $h/s = 0.5$, figures indicate s_{opt}^+
DNS: \bullet $h/s = 0.5$, $s^+ = 17$
— — Hage [7], $h/s = 0.5$

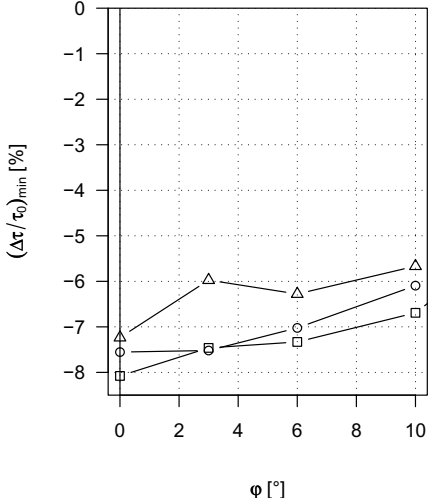


Fig. 17 Minimum relative wall shear stress for wave-like trapezoidal riblet grooves with $\lambda/s = 37.5$ at different yaw angles;
Exp: \square straight grooves $h/s = 0.5$, \circ zigzag grooves $h/s = 0.3$ $a/s = 0.9$, \triangle zigzag grooves $h/s = 0.3$ $a/s = 2.0$

yields a drag reduction that equals or exceeds the value observed for straight riblet grooves of $h/s = 0.3$ at zero yaw angle, indicating that the favourable modification of the friction properties by a lateral deflection is still present under moderate misalignment. On the other hand, no advantages in terms of a reduced wall shear stress arise from such wave-like riblet design.

9 Summary

A wave-like rather than straight arrangement of riblet grooves as a possible way to improve the performance of known riblet structures is occasionally discussed in the literature. The available findings so far are restricted to theoretical considerations such as Quadrio [17] or coarse LES by Peet [15, 16]. An enhancement of the achievable drag reduction of riblets would be of large practical impact, and so this passive flow control technique was studied in a combined numerical and experimental investigation.

A trapezoidal riblet groove profile with a rib tip angle of 30° as the most favourable cross-section shape for application was used throughout in the simulations and the measurements. Starting with the optimal ratio $h/s = 0.5$, a variation of the sinusoidal waveform amplitude and wavelength was conducted. This range

included a configuration similar to the one that achieved a drag reduction improvement in the work by Peet [15], but no such enhanced drag reduction was observed in our research. Instead, for a fixed wavelength and a moderate amplitude, a drag reduction comparable to that of straight riblet grooves was captured in the experiments. Larger amplitudes lead to an increase in drag. This observation is confirmed by the simulation, where in most cases the drag is unaffected by the wave-like riblet arrangement. Similar to the experiments, the largest amplitude created higher surface drag in comparison to straight riblet grooves.

By means of DNS, the overall drag was split into its three contributors, the friction drag on the rib faces and the groove valley floor plus the pressure drag acting on deflected rib parts. It was shown that within a wide parameter range for the deflection amplitude, most of the drag is generated by friction on the ribs, while the pressure drag stays negligible. Increasing the waveform amplitude results in a lowered friction drag, but this advantageous flow manipulation is almost exactly outweighed by the increase in pressure drag.

The experimental investigation was then extended to different ratios h/s smaller as well as larger than 0.5. For riblet grooves arranged in a zigzag fashion and values $h/s = 0.5$ and 0.7, again no beneficial influence of the lateral deflection was measured, but for shallow riblet grooves of $h/s = 0.3$ as well as for deep riblet grooves at $h/s = 0.9$, within an amplitude range of $0.5 \leq a/s \leq 2.5$ for shallow and $0.5 \leq a/s \leq 1.5$ for the deep grooves, a maximum drag reduction was detected that is considerably larger than that measured at straight grooves of the same cross-section shape. In both cases, the best results are achieved for amplitudes $a/s = 0.9$. The differences in $(\Delta\tau/\tau_0)_{\min}$ for straight and deflected riblets amount up to 1.3%-points for riblets of $h/s = 0.3$, but wave-like riblets never outperformed the drag reduction of standard riblets with optimal groove profile of $h/s = 0.5$. However, the maximum drag reduction of straight riblets of optimal design could almost be reached. This wave-like riblet modification might be of some interest for application, as a reduced riblet height will undoubtedly lead to a higher resistance to mechanical wear, an alleviation of manufacturing issues as well as a reduction of the weight per unit of area of a riblet coating thanks to its smaller sectional area.

Unlike tests under laboratory conditions, in application the riblet groove will seldom be perfectly aligned with the main stream direction. The shift in drag reduction for riblets under yaw has been considered for straight as well as for two wave-like riblet geometries. It was experimentally confirmed that wave-like riblets under misalignment exhibit no advantage or disadvantage compared to their straight equivalent and the additional drag reduction caused by the lateral deflection in some configurations persists up to yaw angles of 10°.

Acknowledgements. This research was funded by the German Science Foundation (DFG) within the scope of the priority programme “Nature-Inspired Fluid Mechanics” (SPP 1207). That financial support is gratefully acknowledged. The computational resources were provided by the North-German Supercomputing Alliance (HLRN). The authors thank Dr. Charles Mockett for his helpful comments on the manuscript.

References

1. Bechert, D.W., Hoppe, G., van der Hoeven, J.G.T., Makris, R.: The Berlin oil channel for drag reduction research. *Exp. Fluids* 12, 251–260 (1992)
2. Bechert, D.W., Bruse, M., Hage, W., van der Hoeven, J.G.T., Hoppe, G.: Experiments on drag-reducing surfaces and their optimization with an adjustable geometry. *J. Fluid. Mech.* 338, 59–87 (1997)
3. Bechert, D.W.: Surface for a wall subject to a turbulent flow showing a main direction of flow. United States Patent No. 5.971.326 (1999)
4. Caretto, L.S., Gosman, A.D., Patankar, S.V., Spalding, D.B.: Two calculation procedures for steady, three-dimensional flows with recirculation. In: Proceedings of the Third International Conference on Numerical Methods in Fluid Mechanics. Lecture Notes in Physics, vol. 19, pp. 60–68 (1973)
5. Grüneberger, R., Kramer, F., Hage, W., Meyer, R., Thiele, F., Wassen, E.: Experimental Investigation of Oscillating Riblets for Turbulent Drag Reduction. In: 17. DGLR-Fach Symposium der STAB, November 09-10, Berlin (2010) (to be published in NNFM)
6. Grüneberger, R., Hage, W.: Drag characteristics of longitudinal and transverse riblets at low dimensionless spacings. *Exp. Fluids* 50(2), 363–373 (2011)
7. Hage, W., Bechert, D.W., Bruse, M.: Yaw angle effects on optimized riblets. In: Thiede, P. (ed.) Proceedings of the CEAS/DragNet European Drag Reduction Conference, pp. 278–285 (2000) ISBN 3-540-41911-0
8. Jiménez, J., Moin, P.: The minimal flow unit in near-wall turbulence. *J. Fluid Mech.* 225, 213–240 (1991)
9. Kramer, F., Thiele, F., Wassen, E.: DNS of oscillating riblets for turbulent drag reduction. In: Proceedings of TSFP6, Seoul, June 22-24 (2009)
10. Kramer, F., Thiele, F., Wassen, E.: Investigation of oscillating riblets for turbulent drag reduction. In: Proceedings of KATnet II, Bremen, May 12-14 (2009)
11. Kramer, F., Grüneberger, R., Thiele, F., Wassen, E., Hage, W., Meyer, R.: Wavy riblets for turbulent drag reduction AIAA-paper 10-4583 (2010)
12. Kramer, F., Thiele, F., Wassen, E.: Wavy riblet design to reduce friction drag by inducing lateral oscillation. In: European Drag Reduction and Flow Control Meeting, Kiew, September 02-04 (2010)
13. Mockett, C., Knacke, T., Thiele, F.: Detection of initial transient and estimation of statistical error in time-resolved turbulent flow data. In: Proceedings of ETMM8, Marseille (2010)
14. Obi, S., Peric, M., Scheuerer, G.: Second-moment calculation procedure for turbulent flows with collocated variable arrangement. *AIAA Journal* 29(4), 585–590 (1991)
15. Peet, Y., Sagaut, P., Charron, Y.: Turbulent Drag Reduction using Sinusoidal Riblets with Triangular Cross-Section, AIAA paper 2008-3745 (2008)
16. Peet, Y., Sagaut, P., Charron, Y.: Pressure loss reduction in hydrogen pipelines by surface restructuring. *International Journal of Hydrogen Energy* 34(21), 8964–8973 (2009)
17. Quadrio, M., Luchini, P.: Method for reducing the viscous friction between a fluid and an object, International patent application PCT/EP2008/057622 (2008)
18. Stenzel, V., Wilke, Y., Hage, W.: Drag-reducing paints for the reduction of fuel consumption in aviation and shipping. *Progress in Organic Coatings* 70(4), 224–229 (2011)
19. Szodruch, J.: Viscous drag reduction on transport aircraft, AIAA-paper 91-0685 (1991)
20. Walsh, M.J.: Drag characteristics of V-groove and transverse curvature riblets. In: Hough, G.R. (ed.) *Viscous Flow Drag Reduction*. Progress in Astronautics and Aero-nautics, vol. 72. AIAA (1980)

21. Walsh, M.J., Lindemann, A.M.: Optimization and application of Riblets for Turbulent Drag Reduction, AIAA paper 1984-0347 (1984)
22. Warsop, C.: Current status and prospects for turbulent flow control. In: Thiede, P. (ed.) Proceedings of the CEAS/DragNet European Drag Reduction Conference, pp. 269–277 (2000) ISBN 3-540-41911-0
23. Wassen, E., Kramer, F., Thiele, F., Grüneberger, R., Hage, W., Meyer, R.: Turbulent Drag Reduction by Oscillating Riblets, AIAA paper 2008-4204 (2008)

Aerodynamics and Structural Mechanics of Flapping Flight with Elastic and Stiff Wings

Stephan Bansmer, Nadine Buchmann, Rolf Radespiel, Ralf Unger,
Matthias Haupt, Peter Horst, and Ralf Heinrich

Abstract. The flapping flight mechanism is expected to provide revolutionary operation capabilities for tomorrow's Micro Air Vehicles (MAV). The unsteady aerodynamics of the flapping flight is vastly different from traditional fixed-wing flyers. Boundary layers with moving laminar-turbulent transition, three-dimensional wake vortices and fluid-structure interaction with anisotropic wing structure are only a few examples for the challenging problems. To get basic understanding of these effects, the authors develop a computational method that is validated with boundary-layer measurements on flexible and inflexible, flapping wings in a wind-tunnel. The computational method solves the unsteady Reynolds-averaged Navier-Stokes equations and is combined with both transition prediction and fluid structure interaction capability. Using generic airfoils shapes inspired by seagulls and hawks, different aerodynamic, structural and kinematic effects are systematically analyzed on their influence on thrust and propulsive efficiency of the flapping flight mechanism. In particular, we demonstrate that a slight forward-gliding motion during the flapping downstroke can increase significantly thrust and efficiency. Wing elasticity however seems to lower the propulsive efficiency in the investigated cruise flight flapping case. Beyond, we show that the wake structure of 3D flapping wings generates an efficiency loss of about 10% compared to equivalent two-dimensional flapping cases.

1 Introduction

Inviscid aerodynamic theory of flapping flight goes back to THEODORSEN [1] and GARRICK [2], who investigated the phenomenon of aerodynamic flutter.

Stephan Bansmer · Nadine Buchmann · Rolf Radespiel
Institute of Fluid Mechanics, Technische Universität Braunschweig, Germany

Ralf Unger · Matthias Haupt · Peter Horst
Institute of Aircraft Design and Lightweight Structures,
Technische Universität Braunschweig, Germany

Ralf Heinrich
DLR Germany

THEODORSEN showed that depending on the flutter - i.e. flapping - frequency, the lift force oscillation has a phase lag with respect to the angle of attack oscillations. The theory is quite simple and nowadays still used for rough estimations of the lift and thrust distribution over one flapping cycle. The flapping flight of birds however takes place in a Reynolds-number range of 100000, where the viscous effects of boundary layers and eddy formation can not be neglected, i.e. the THEODORSEN theory might not give adequate results.

Eminently difficult seems to be the presence of laminar separation bubbles (LSB), which are a phenomenon at the laminar-turbulent transition, according to early observations by HORTON [3]. A pressure increase along the airfoil contour causes the oncoming laminar boundary layer to separate. The separated flow performs the transition process from laminar to turbulent flow following a gradual development of the primary instabilities from TOLLMIEN-SCHLICHTING instabilities towards KELVIN-HELMHOLTZ instabilities. The resulting turbulent fluctuations in the flow enhance momentum transport towards the wall, and the flow reattaches to the airfoil contour. The resulting region of circulating flow is called LSB. LSB's are usually not desired in airfoil design because they increase the pressure drag of the airfoil due to a higher displacement thickness level of the boundary layer.

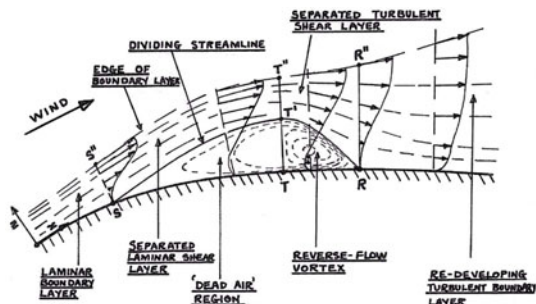


Fig. 1 Sketch of a Laminar Separation Bubble (LSB) by HORTON [3] (corrected).

Of course, there is no simple 'formula based' theory to cover the transitional flow over flapping airfoils. It can not be avoided to solve the Navier-Stokes equations. These equations are derived from the first principles of mass, momentum and energy conservation. Solving the Navier-Stokes equations without further simplifications can be very demanding since even small turbulent structures have to be discretized for the numerical schemes. To minimize the computational effort, RADESPIEL et al. [4] demonstrated that it is sufficient to solve the unsteady Reynolds-averaged Navier-Stokes (URANS) equations, which have to be coupled with a transition prediction method. In the present contribution, we will adopt this methodology and investigate the aerodynamics of naturally evolved airfoils. Seagull and hawk airfoils are used because these birds are known to be efficient flapping flyers, see chapter 2.

2D effects in chapter 6.1 and also 3D aerodynamics effects in chapters 6.3 and 6.4 are discussed. The common objective is to yield information on the propulsive efficiency η_p , given by

$$\eta_p = \frac{\int_0^T c_t U_\infty dt}{\int_0^T (c_d \dot{x} + c_l \dot{z} + c_m \dot{\phi} c) dt},$$

where c_l, c_d and c_m are lift, drag and moment coefficients, $\dot{x}, \dot{z}, \dot{\phi}$ are translational and rotational speeds of the airfoil, c is the chord length, T is the time of one flapping period and U_∞ the free-stream velocity. The determination of the thrust coefficient c_t is not trivial. Compared to conventional aircraft, drag and thrust of a flapping airfoil have to be separated artificially, because these forces are generated by an "all-in-one" integral system. To compute the thrust coefficient c_t , Windte [5] subtracted the static drag coefficient $c_{d,\text{stat}}$ of the airfoil at the mean angle of attack φ_0 from the force coefficient $c_d(t/T)$:

$$c_t = -c_d + c_{d,\text{stat}}(\varphi_0).$$

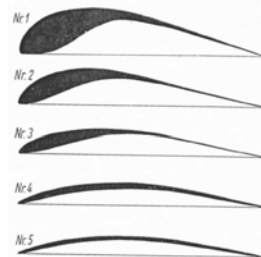
A further effect in bird's flapping flight is the non ridigity of the wing, namely the elasticity of the feathers. Their stiffness and mass properties are uncertainties in the understanding of birds flight. An experimental approach to assess the role of flexibility is cumbersome, a numerical approach is able to clarify the aeroelastic phenomena of flapping flight. For the simulation of such phenomena fully coupled with a flexible thin structure, a high qualitative and time resolved coupling scheme nowadays used for fluid-structure interaction problems is utilized [6]. The so-called partitioned coupling approach uses well-validated fluid as well as structural solvers, which are linked together within a simulation environment by the aid of flexible data transfer libraries [7]. For the flexible airfoil itself, a nonlinear finite element methodology is applied [8]. Here, the simulation environment is applied to a flexible airfoil and numerical flow computations are presented. The question arises how to improve the propulsive efficiency of the flapping airfoil motion by varying certain parameters on the structural side of the coupled fluid-structure system. As an answer parameter studies are accomplished, which focus on improving the propulsive efficiency of the flapping motion.

2 Airfoil Characteristics

Investigations of OEHME [9] on airfoil shapes of birds revealed that their design is different from conventional airfoils, see also figure 2. Most remarkable are a large maximum camber and further a position of maximum thickness located close to the leading edge. Obviously, the wing anatomy with the skeleton and muscles reasons the latter. The impact of this design is significant for the characteristics of thin airfoils in the vicinity of the wing tip, where the most of the thrust is produced during one flapping cycle.

From an aerodynamic point of view, a large airfoil thickness close to the leading edge is favorable, because the adverse pressure gradients along the upper surface can be kept reasonably small. This yields thin laminar separation bubbles with

Fig. 2 Comparative investigations on airfoil shapes of birds from OEHME [9]. Shown are five idealized bird wing sections, starting from the wing root.



low pressure drag losses. Furthermore, thin airfoils with their position of maximum thickness in the vicinity of the leading edge exhibit an increased nose radius, which increases the angle of attack range with attached flow. A large relative camber of 8 percent was measured by BILO using narcotized birds [10]. Observations in nature revealed that this value is usually smaller for gliding flight (approximately 4 percent), although in wind-tunnel experiments with living birds the maximum camber during one flapping stroke was found to vary from 8 to 12 percent.

Based on these design aspects, a new birdlike airfoil, the SG04, was developed, see figure 3. This profile represents the hand pinion of a seagull wing, and corresponds in its shape to section 3 in figure 2. Sections 4 and 5 of figure 2 are not used as an airfoil design inspiration, because these sections are only determined by the shape of feather tips. SG04 has a maximum thickness and a maximum camber of 4%, where the maximum camber is located at $x/c=40\%$. The aerodynamic design of the SG04 involves both aerodynamic analysis and inverse design according to the bubble ramp approach introduced by SELIG [11] to reduce the size of the laminar separation bubble for a broad range of angles of attack. Figure 4 shows the drag polar of the SG04 airfoil computed by FLOWer [24], a validated URANS-solver, and XFOIL. The e^N -method is used for transition prediction with the critical N factor of 10. Although XFOIL is a very simple tool to predict steady airfoil aerodynamics, its polar is in good agreement with the results of the more complex FLOWer solver. Additionally, the drag decomposition into friction and pressure drag is plotted, which are approximately in the same order of magnitude in this low Reynolds number range of 100,000. Considering the small pressure drag values, the design goal of the SG04 airfoil with small laminar separation bubbles is attained. To be able to compare the polar with a SD7003 airfoil at an equivalent Reynolds number, experimental data from SELIG [12] is added to the chart. Mainly reasoned by the higher camber, the SG04 polar is shifted to higher lift values and has therefore a smaller drag at the same lift performance. However, the disadvantage of thin airfoils is clearly visible with a decreased operational range of lift. At the Universität der

Fig. 3 Seagull SG04 airfoil shape

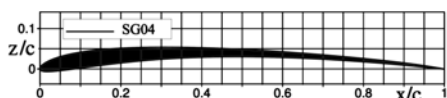
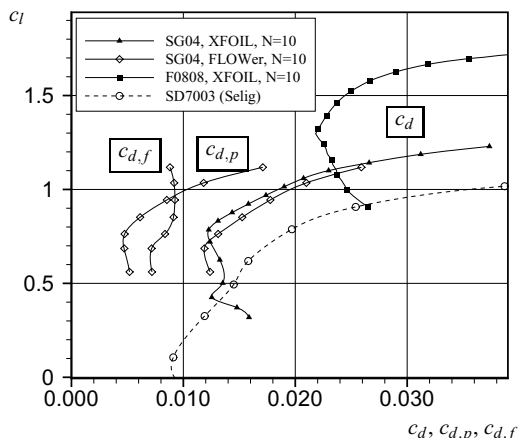


Fig. 4 Drag polar of the seagull SG04 airfoil and the hawk F0808 airfoil; $Re = 100000$, steady conditions and additional SD7003 data [12].



Bundeswehr München, the flapping flight of a hawk is measured by a stereoscopic setup of high-speed cameras. The feather pattern of the hawk is favourable for image pattern recognition techniques. Therefore, the optical flow technique is chosen to reconstruct the exact three-dimensional shape of the hawk-wing during one flapping cycle, see figure 5 on the left. To extract an airfoil out of the surface data taken in München, a cut A-A' in the y-z plane of the measurements reveals raw data for the new birdlike F0808 airfoil as illustrated on the right hand side of figure 5. This curve was then digitized with the open source software *engauge*. Afterwards the digitized data was adapted and analysed with the *XFOIL* code. Compared to the seagull SG04 airfoil, the hawk airfoil F0808 shows increased camber and thickness of 8%. The maximum thickness is located close to the leading edge. According to the large nose radius there is a large area of angles of attack for which the hawk airfoil does perform well, particularly at high angles of attack up to 15° , see also the polar in figure 4. In consequence, the F0808 has the advantage of a more extensive range of lift as the SG04 and even the SD7003. But the increased thickness and especially the larger nose radius entails a higher drag coefficient of the hawk airfoil.

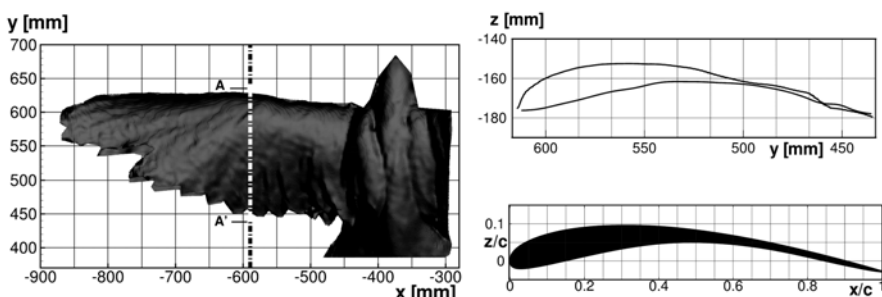


Fig. 5 Surface data (left) and cut in y-z plane of surface data at marked line (right)

3 Kinematics

The two-dimensional motion of an oscillating airfoil is combined of a plunging $z(t/T)$ motion and a pitching oscillation $\varphi(t/T)$ around the quarter chord for one flapping period $0 \leq t/T < 1$:

$$\begin{aligned} z(t/T) &= \hat{z} \cdot \cos(2\pi t/T) \\ \varphi(t/T) &= \hat{\varphi} \cdot \cos(2\pi t/T + \pi/2) + \varphi_0. \end{aligned} \quad (1)$$

The plunging motion alters the angle of attack (AoA), which acts on the airfoil in its moving frame of reference. In consequence, the geometric AoA $\varphi(t/T)$ is perceived as an effective angle of attack $\alpha_{\text{eff}}(t/T)$ from the airfoil, see figure 6. In the investigated parameter space of this contribution for instance, the geometric AoA is negative during the downstroke, however, the effective AoA is positive and thus a lift force is created, which has a component in upstream direction.

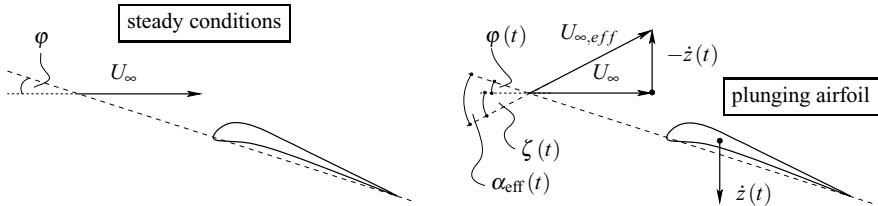


Fig. 6 The change from geometric φ to effective angle of attack $\alpha_{\text{eff}}(t)$ due to the plunging motion $\dot{z}(t)$.

Usually, the frequency of the flapping motion $f = 1/T$ is made non-dimensional using the equation

$$k = \frac{\pi f c}{U_\infty},$$

where k represents the reduced frequency, a measure for the aerodynamic unsteadiness of the flow. The inverse of k describes how far the undisturbed air passes the chord length c of the airfoil during one flapping cycle. For seagull and hawk flight conditions, k has values around 0.2 [13]. Furthermore, the pitch-plunge amplitude ratio λ is an important design parameter for efficiency:

$$\lambda = \frac{\hat{\varphi}}{\arctan(2k\frac{\hat{z}}{c})}.$$

The inviscid theory of Theodorsen states that the propulsive efficiency for different combinations of pitch and plunge motions remain approximately constant if the parameter λ is kept constant. Windte et al. [5] reports that a choice of $\lambda = 0.8$ guarantees high propulsive efficiencies at a reduced frequency of $k = 0.25$.

4 Numerical Methods

Flow Simulation

The numerical flow simulation approach is based on URANS solutions, which are coupled with a e^N transition-prediction method. The time-dependent mean flow is computed by solving the unsteady Reynolds-averaged Navier-Stokes equations. Linear stability analysis (LST) uses the velocity profiles of the RANS solution to predict waves due to Tollmien-Schlichting and Kelvin-Helmholtz instabilities. Their amplification rates are then used to predict the transition location using an integration scheme for mode amplitude ratios that takes unsteady flow effects into account. The largest amplitude exponents are finally compared with a critical N -factor in order to determine the transition location. Details of this approach can be found in RADESPIEL et al. [4].

Two different Navier-Stokes solvers are applied, TAU and FLOWer [14]. **TAU** requires unstructured meshes; its discretization scheme is a finite-volume approach. A second-order accurate central-difference scheme with scalar dissipation is applied to evaluate convective fluxes. Local time stepping, preconditioning and multigrid operations are performed to accelerate the computation. A second-order accurate implicit dual time stepping scheme is used for the time-accurate computations. The Menter two-layer k- ϵ -model [15] is chosen for the turbulence modeling. **FLOWer** requires block-structured meshes, which yields faster solution convergence.

For simulating a three-dimensional, flapping hawk wing, the TAU Mesh deformation tool using Radial Basis Functions (RBF) is applied [16, 17]. These functions are topology independent functions, whose values only depend on the distance from the origin. RBF are well suited for interpolation of scattered data like in our TAU simulation case with unstructured meshes.

Aeroelastic Simulation

An aeroelastic simulation combines the fluid with the structural analysis. For the structural part of this computation, a finite element model is generated, which is solved here with the commercially available simulation package ANSYS® [18]. The fluid flow interacts with the flexible structure on the wetted surface. Here, the so-called two-field approach is used, applying the Lagrangian multiplier method [19]. Both, the fluid and the structure, need to interchange data at the interface, i.e. the displacement field has to be transmitted from the structural to the fluid solver and the forces acting on the airfoil are transferred vice versa [20]. The coupled problem can be written in a matrix form as

$$\begin{aligned} \text{Fluid: } & \mathcal{F} & 0 & -\mathcal{M}_{ff} \\ \text{Structure: } & 0 & \mathcal{S} & \mathcal{M}_{sf} \\ \text{State Transfer: } & -\mathcal{M}_{ff} & \mathcal{M}_{fs} & 0 \end{aligned} \begin{bmatrix} u^T \\ u_s^T \\ \lambda \end{bmatrix} = \begin{bmatrix} 0 \\ f_s^T \\ 0 \end{bmatrix}, \quad (2)$$

where the fluid and structural operators \mathcal{F} and \mathcal{S} involve the solution of the fluid and structure problem, respectively. The nodal vectors u^T and u_s^T denote the

displacement field vectors on the fluid (subscript: f) and structural (subscript: s) interface Γ , respectively. The vector $\hat{\lambda}$ is the vector of discrete Lagrangian multipliers, which links the fluid and structure together. The vector f_s^Γ is the vector of external nodal forces on the structure, which have other sources than the forces caused aerodynamically by the fluid. The coupling matrices are calculated by integrating the product of the subdomains shape functions with those of the Lagrangian multipliers [21]. Without access to the matrices of each solver S or F the classical Richardson iteration can be used to find a solution of the system

$$\mathbf{u}_{s,k+1}^\Gamma = \zeta_{RI} \underbrace{\left(\mathcal{F}^{-1} \circ (\mathbf{f}_s^\Gamma - \mathcal{M}_{sf} \circ \mathcal{M}_{ff}^{-1} \circ \mathcal{F} \circ \mathcal{M}_{ff}^{-1} \circ \mathcal{M}_{fs} \circ \mathbf{u}_{s,k}^\Gamma) + (1 - \zeta_{RI}) \mathbf{u}_{s,k}^\Gamma \right)}_{\check{\mathbf{u}}_{s,k+1}^\Gamma}, \quad (3)$$

where ζ_{RI} is a user defined relaxation parameter. In each iteration a Dirichlet-Neumann step is invoked to get the displacement field of the fluid and structure on the interface, respectively. Here, a simple staggered scheme is used, with implies $\zeta_{RI} = 1.0$ and $k_{max} = 1$. With this iteration procedure, the time integration and equilibrium iteration of the coupled problem can be illustrated as shown in figure 7, where the time loop index is n and the iteration index is k . For the vector $\mathbf{u}_{s,k=0}^\Gamma$ a second order time accurate predictor is used based on the structural forces obtained in the previous time step [23]. Within the iteration control box a relaxation of the most recent computed structural displacement field $\check{\mathbf{u}}_{s,n+1}^\Gamma$ is conducted.

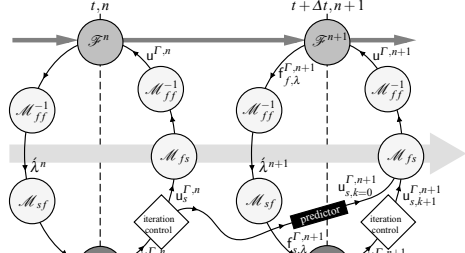


Fig. 7 Time integration and equilibrium iteration for the coupled problem [22].

5 Experimental Setup

PIV Measurements, Wind Tunnel and Motion Apparatus

To validate the numerical simulations, selected motion cases are investigated in wind-tunnel experiments. Of great interest is the velocity distribution of the boundary layer of the flapping airfoil, because it contains information on the transition location and turbulence intensity, which can be compared with computational data. The velocity and associated ensemble-quantities like the shear-correlation $\overline{u'w'}$ are measured by stereoscopic particle image velocimetry. The challenges of such measurements are described in [13].

The experiments are carried out at the low-speed Low Noise Wind Tunnel, see Figure 8. The inlet of the Eiffel-type tunnel is covered by a fleece mat 30 mm in thickness. Afterwards, the air passes a straightener made out of aluminum honeycombs, 14 mm in diameter and 200 mm in length and then finally through a fine-mesh woven screen. In the large settling chamber, small-scale turbulence is dissipated. A Boerger-type nozzle contracts the air at a 16:1 ratio. Consequently, the air has a very low turbulence level in the 400 x 600 millimeter sized test section. The wind tunnel is driven by a 4 kW, acoustically encapsulated, speed controlled three-phase asynchronous motor, which produces stable wind-tunnel speeds from 2 up to 20 meters per second. The diffusor is mounted on a rail system, which allows one to interchange modular test sections. The laboratory is lined with open-celled acoustic foam.

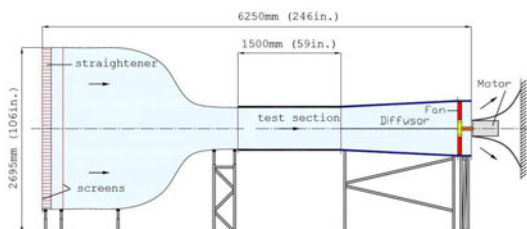


Fig. 8 Schematic of the low speed Low Noise Wind Tunnel.

In order to create a combined plunging and pitching motion of the airfoil as denoted by equation 1, a special Flapping Motion Apparatus is used. The apparatus synchronizes pitching and plunging motion with a mechanical gearing, depicted in Figure 9. A broad range of motion parameters can be adjusted: plunging amplitude from 0 to 0.1 meters, pitching amplitude from 0° to 25° , flapping frequency from 0 to 10 Hertz. Also three-dimensional motions can be created when using different plunging amplitudes at both wing tips. Additionally, a light barrier is mounted at the rig enabling the connected measurement systems to be triggered according to

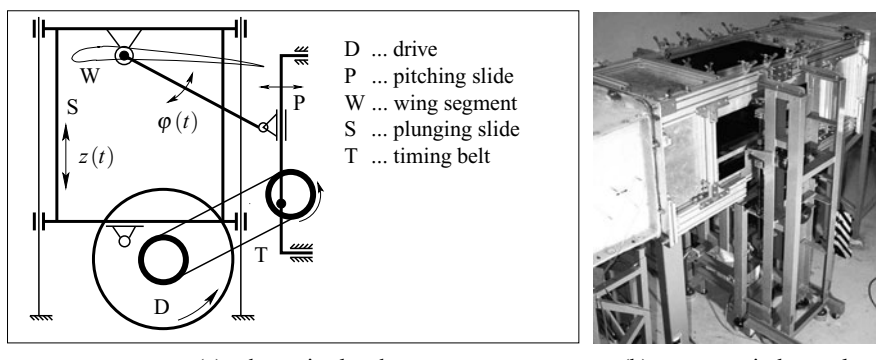


Fig. 9 Flapping Motion Apparatus

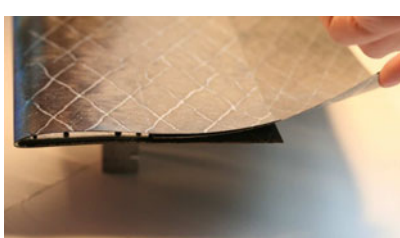
the operated flapping frequency. The estimated motion accuracy for the investigated validation cases is about 0.8 mm for the plunging motion and 0.2° for the pitching motion. These values are measured by capturing the airfoil position at a constant phase for 500 flapping cycles and determining its standard deviation.

The rigid SG04 wing segment used for the experimental investigations is made of a carbon-fabrics shell, which is reinforced by a closed-cell rigid foam. For a high bending stiffness, a carbon fiber spar is integrated. A top coat out of polyester resin provides a smooth surface. The mass of the rigid wing segment is 360 g.

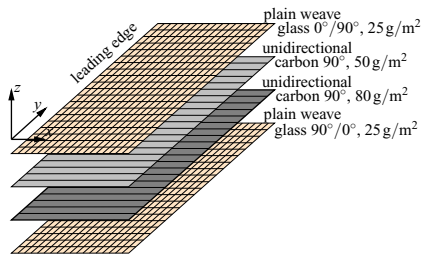
Elastic SG04 Airfoil

The elastic airfoil has to fulfill several requirements. The most important are that the area weight should be close to bird's feathers and that the deformation due to aerodynamic and inertia loads should be in same range, to consider both sources of deformation. Furthermore, the airfoil should have a nearly 2D behavior and a smooth surface shape for PIV measurements. A simple manufacturing is self-evident.

A design using carbon-reinforced plastic with a stiff forebody and an overlapping three-shell concept was found to be a reasonable approach for the flexible airfoil, figure 10a. The upper and lower shell are bonded together at the leading edge and prestressed to ensure continuous contact during a flapping period. The central shell is attached to a stiff spar also made by carbon fiber reinforced composites. At 65% of the chord length, the upper and lower shell are in contact with the central shell. A shell thickness of 0.15 mm and a layer structure according to Figure 10b give reasonable deflections of the trailing edge due to aerodynamic forces. The total mass of this lightweight design is 124 g including the metal parts, e.g. ribs for the wind-tunnel mounting.



(a) assembled airfoil



(b) ply lay up of shells

Fig. 10 Design of the elastic airfoil.

Feather Strips

The design with a single shell in span wise direction tends to deformation coupling in spanwise direction. As an alternative concept a spanwise segmented strip concept was realized. The segments are motivated by the bird's feather, which also avoid the spanwise mechanical couplings. Figure 11 shows the design parameter of a single

Fig. 11 Design parameters of a single featherstrip.

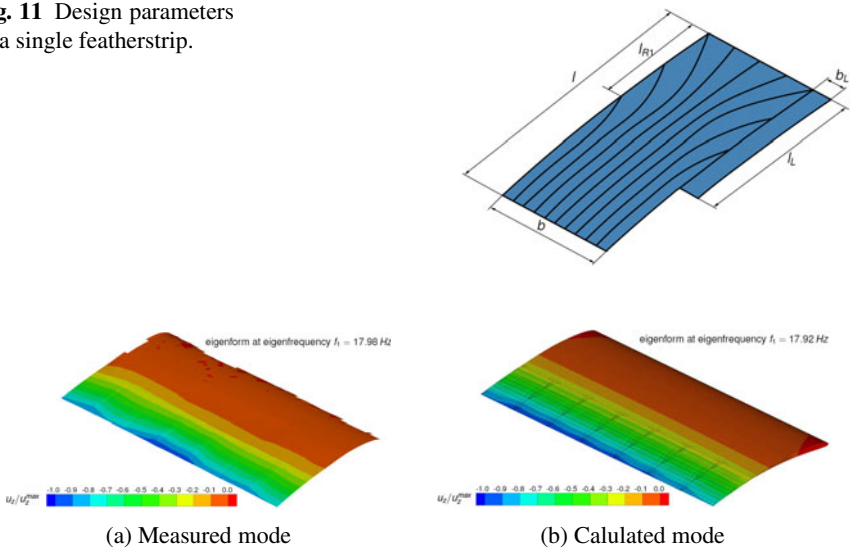


Fig. 12 Comparison of the eigenmodes of the featherstrip model.

strip. The black lines mark the paths of the carbon roving providing the stiffness. The aerodynamic surface is spanned by a thin glass fabric. As a result of parameter studies, the number of 7 rovings is optimal, to achieve the required stiffness and a low weight. The manufacturing and testing demonstrate the feasibility of such a bioinspired design. Figure 12 shows the accordance of the measured and calculated eigenmodes of the lowest eigenfrequency. The application of piezoceramic actuators extends this featherstrip concept to an airfoil with spanwise variable controllable camber.

6 Results

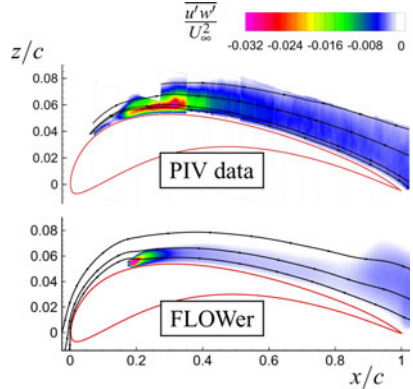
6.1 2D Rigid, Flapping Airfoil SG04

Validation of the URANS simulation with wind-tunnel data

A validation case for seagull cruise flight conditions (parameters: $Re = 10^5$, $k = 0.2$, $c = 0.2\text{m}$, $\varphi_0 = 4^\circ$, $\hat{\varphi} = 7.46^\circ$, amplitude of effective AoA $\Delta\alpha_{\text{eff}} = 4^\circ$, $\hat{z} = 0.1\text{m}$, $\lambda = 0.66$) is used to compare the computational result with experimental data on the basis of the distribution of the turbulent shear stress $\overline{u'w'}$, see figure 13. The turbulent shear stress characterizes the viscous momentum transport across the boundary layer and is used to detect regions of turbulent flow. During the downstroke, we found that the laminar-turbulent transition moves from the trailing edge to the leading edge and vice versa during the upstroke. At the mid of the downstroke $t/T = 0.25$, the transition is located at $x_t/c \approx 0.15$ and the computational result of $\overline{u'w'}$ agrees very

well with the experimental data. However, the magnitude of $\overline{u'w'}$ in the experiment is higher than the computational prediction, yielding higher turbulent kinetic energy in the experiment. This excess of turbulent kinetic energy needs more time to dissipate, and the relaminarization process starting at $t/T \approx 0.4$ takes longer than predicted by FLOWer. Further details can be found in [24] and [25].

Fig. 13 Comparison of the turbulent shear stress $\overline{u'w'}$ between computational prediction and experimental PIV data. Mid downstroke, $t/T = 0.25$; $\alpha_{\text{eff}} = 8^\circ$.



Thrust and Efficiency Increase due to Forward Gliding Oscillations

A parametric study with the URANS solver and fixed transition ($x_t/c = 0.1$) is performed to analyze the propulsive efficiency for different motion cases with high thrust capability, see table 1. The history of lift (c_l) and drag (c_d) coefficient over one flapping period is plotted in figure 14 for the motion-parameter case VI. $t/T = 0$ corresponds to the top dead center of the motion, thus the downstroke takes place during $0 \leq t/T < 0.5$. The URANS solution - plotted as a solid line - is compared to the result of the inviscid theory of Theodorsen/Garrick, drawn as a dash-dot-dot line. The lift coefficient peaks during the downstroke due to the high effective AoA (α_{eff} about 14°) in this phase. Furthermore, most thrust is produced ($c_d < -|c_{d,\text{stat}}|$) during the downstroke. This can be explained by the Knoller-Betz effect; the effective AoA is high during the downstroke, although the geometric AoA is less than 0° resulting in a component of the lift force, which is directed upstream and acts as thrust. The result also indicates the viscous effect of the boundary layer and eddy formation in the flow field. Particularly during the downstroke less lift and less thrust is generated than predicted by the inviscid theory.

Based on the history plots, time-averaged quantities like mean lift $\overline{c_l} = \frac{1}{T} \int_0^T c_l dt$ and mean thrust $\overline{c_t} = \frac{1}{T} \int_0^T c_t dt$ can be derived. Figure 15 depicts the propulsive efficiency η_p and the mean lift coefficient $\overline{c_l}$ over the mean thrust coefficient $\overline{c_t}$ for the motion cases I-VI at constant λ and increasing amplitude of the effective AoA (solid line with square dots). When the amplitude of the effective AoA $\Delta \alpha_{\text{eff}}$ is increased, the mean thrust increases but the propulsive efficiency decreases from 87%

Table 1 Flapping motion parameters

flapping case No.		I	II	III	IV	V	VI
REYNOLDS-number	Re	10 ⁵					
reduced frequency	k	0.2					
chord length	c	0.2 m					
lambda	λ	0,8					
phasediff. pitch/plunge	$\Delta\Psi$	90°					
mean AoA	φ_0	4°					
amplitude eff. AoA	$\Delta\alpha_{\text{eff}}$	4° 5° 6° 7° 8° 9°					
amplitude geom. AoA	$\hat{\varphi}$	16° 20° 24° 28° 32° 36°					
amplitude plunging	$\frac{\hat{z}}{c}$	0.91 1.17 1.44 1.75 2.10 2.50					

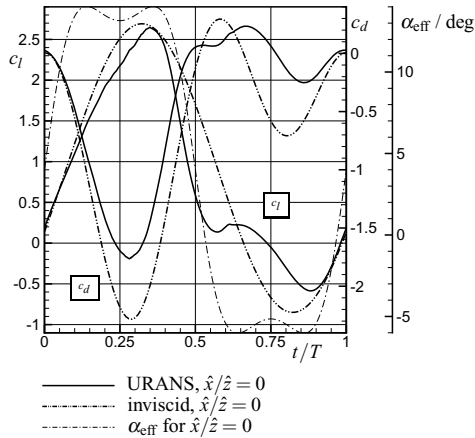


Fig. 14 History of lift and drag coefficient for one flapping period, comparison between inviscid and URANS solution, motion case VI, motion without gliding, $\lambda = 0.8$, $\Delta\alpha_{\text{eff}} = 9^\circ$.

to 70% in the investigated parameter space. The inviscid result (diamond points) predicts significantly higher efficiencies, because the viscous effect of the boundary layer and dynamic-stall vortices that are created for large amplitudes of the effective AoA, is not covered by this theory. The mean lift coefficient increases from 0.85 ($\Delta\alpha_{\text{eff}} = 4^\circ$) to 0.87 ($\Delta\alpha_{\text{eff}} = 6^\circ$), and decreases subsequently for increasing amplitudes of the effective AoA. This decrease can be explained by the onset of dynamic stall vortices.

Finally, the aerodynamic effect of an additional gliding motion $x(t/T) = \hat{x} \cdot \cos(2\pi t/T)$ in the direction of the free-stream velocity U_∞ is investigated. This gliding motion is superimposed on the motion cases I-VI. Figure 15 demonstrates that a small superimposed forward gliding motion during the downstroke (\hat{x}/\hat{z} about 1/8) yields significant increase in both efficiency and thrust production. This behavior is observed for small and large amplitudes of effective AoA ($\Delta\alpha_{\text{eff}} = 4^\circ$, 6° and 9°). One disadvantage of the superimposed forward gliding motion during the

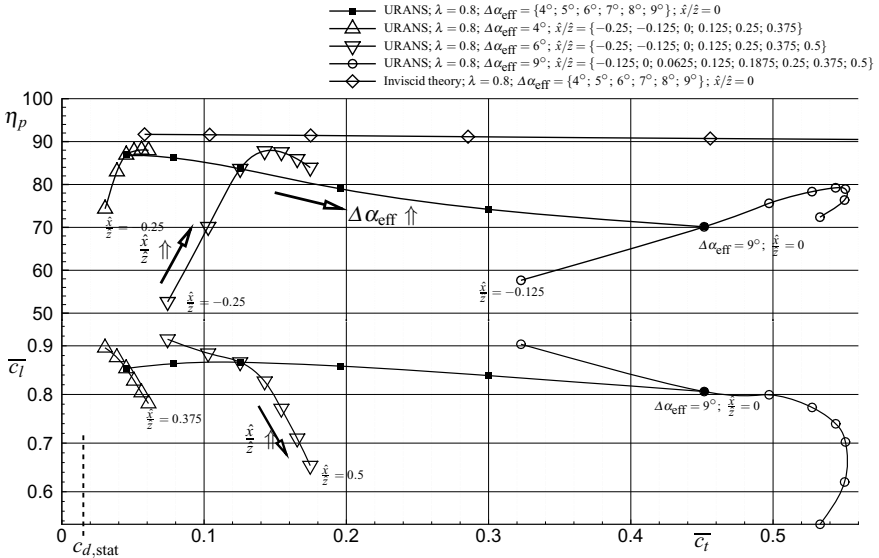


Fig. 15 Parametric study on the propulsive efficiency of the oscillating SG04 airfoil with $\lambda = 0.8$ and superimposed gliding oscillations $x(t) = \hat{x} \cdot \cos(\omega t)$, $c_{d,stat} = 0.015$ from airfoil polar.

downstroke is the reduction of the mean lift coefficient. Hereby, penalties of about $\Delta \bar{c}_l = 0.1$ are noticed. However, a superimposed backward gliding motion during the downstroke shows the potential for lift increase.

6.2 2D Flexible, Flapping Airfoil SG04

Validation

The comparison of simulations and experiment for the flexible airfoil is a challenge, because of the additional parameters of the structural model. Again, a validation case for seagull cruise flight conditions (parameters: $Re = 10^5$, $k = 0.2$, $c = 0.2\text{m}$, $\varphi_0 = 4^\circ$, $\hat{\phi} = 7.46^\circ$, amplitude of effective AoA $\Delta\alpha_{eff} = 4^\circ$, $\hat{z} = 0.1\text{m}$, $\lambda = 0.66$) is used to compare the computational result with experimental data. Figure 16 shows the simulated time history of the lift and pressure drag coefficient as well as the evolution of the transition location x_t^u of the upper airfoil side. The lift has its maximum during the downstroke shortly after the mid-downstroke although the highest effective AoA is reached at $t/T = 0.25 + i$ (i : period number). The mean lift over one period is $\bar{c}_l = 0.8802$. The highest negative drag, i.e. thrust, is reached shortly after the mid-downstroke but before the maximum lift is obtained. On the other hand the highest positive drag is obtained shortly before the mid-upstroke. The mean drag has a value of $\bar{c}_{d,p} = -0.0128$, i.e. thrust is generated during a flapping period. The propulsive efficiency is calculated to $\eta = 0.827$. The laminar-turbulent transition

Fig. 16 Lift, drag and transition location during two periods of motion

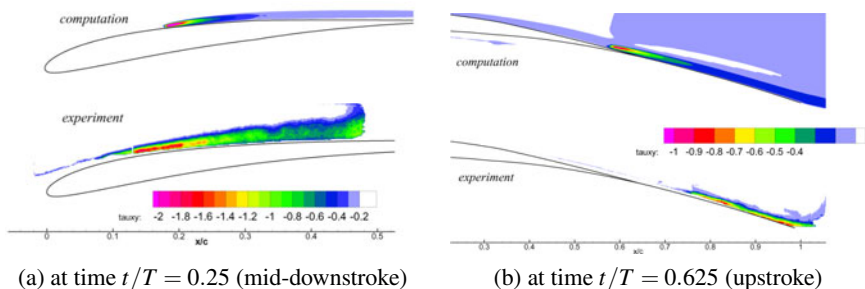
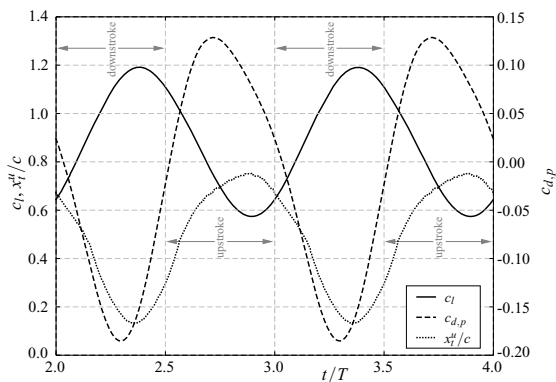


Fig. 17 Comparison of computational and experimental results in terms of the turbulent shear stress distribution around the airfoil at several time instances.

moves from the trailing edge towards the leading edge during the downstroke and vice versa during the upstroke, whereas it never reaches the last 30% of the rear part. The turbulent shear stress distribution is an adequate indicator for the transition from laminar to turbulent flow and is shown exemplarily in 17 for two discrete time points together with the distribution obtained with PIV in wind tunnel test campaigns. From the comparison it can be observed, that during the downstroke the calculated transition location lies slightly behind the experimentally found location, 17a. This indicates, that the change of x_t^d is not precisely resolved by the numerical scheme. During the upstroke the experimentally found transition location is again more downstream than numerically predicted, 17b. Such disagreement was already noticed for the rigid version of the airfoil and is likely caused by the modeling errors of the Menter's baseline turbulence model, see [24] for a thorough discussion. Furthermore, the airfoil deformation is measured in order to assess the predicted fluid-structure interactions. With two measurement techniques, the commercially available ARAMIS system and a custom made system described in [24], a complete airfoil surface deformation field could be determined at different phase angles. From these data, the deformation of the trailing edge d/c could be extracted, see

Fig. 18 Comparison of the deformation of the trailing edge between numerical computation and experimental results.

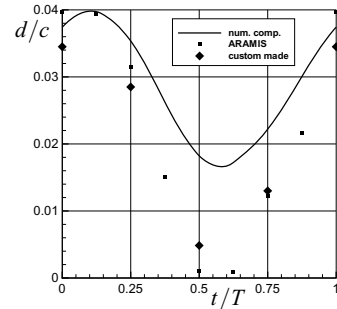


Figure 18. The plots reveal the largest deformation when the airfoil has passed the top dead center of the motion, i.e. the airfoil has then the smallest camber. During the downstroke the camber is continuously increasing until the bottom dead center is reached. This deformation behavior is a result of the partially counteracting forces of inertia and lift. From an aerodynamic point of view, this behavior is favorable because the downstroke is known to be the thrust producing part of the flapping cycle. According to the linear airfoil theory, increased camber means increased lift and consequently thrust due to the KNOLLER-BETZ effect. Also, the deformation behavior of the upstroke is aerodynamically advantageous because the decreasing camber reduces the drag of this configuration. The general deformation behavior is well-resolved with the numerical simulation. However, the numerical result predicts slightly higher deformations. The largest error is about 2 mm at bottom dead center. This discrepancy has two major sources. The first source is the accuracy of the model's jig-shape. Due to the use of orthotropic material for curved shells and the layer structure of figure 10b, manufacture-related initial stresses are unavoidable, which result in spanwise distortion. The deviation of the vertical trailing edge position due to the curvature of the structural model is temperature-dependent and is about 1.0 - 1.5 mm in the spanwise direction. This is even further intensified due to the anticlastic deformation of the trailing edge, which is non-negligible due to the geometry of the manufactured model (the span has twice the length of the chord). A second possible source of the discrepancy is the presence of the wind-tunnel walls, which are not modeled in the computations.

Variation of Airfoil Stiffness

The basic aeroelastic parameter is the stiffness, which is varied by the Young's modulus E . The major influence is given in the lift coefficient, which is shown in 19a, where Young's modulus is decreased compared to a reference value E_{ref} . This stiffness reduction is done for the whole structural airfoil model. The reduction of the stiffness goes along with a decrease of the lift level over the whole flapping period. This reduction reaches a similar value at the time points, when the lift has its minimum and maximum value. Thus, the pressure induced drag/thrust and therefore the propulsive efficiency are reduced. The decrease of the efficiency is caused by the

interaction of the aerodynamic forces and the deformation of the airfoil. Due to the reduction of the stiffness, the airfoil is more decambered during the thrust producing downstroke, 19b, which results in a decrease of the aerodynamic force vector, which is directed towards the inflow vector. Indeed, the airfoil is also decambered during the upstroke, 19b, but the additional trailing edge deformation is lower than that during the downstroke. This difference has a negative influence on the propulsive efficiency. The resulting mean lift and drag coefficients as well as the propulsive efficiency are summarized in Tab. 2. With the present structural configuration, a rigid airfoil would be even more advantageous in terms of the propulsive efficiency.

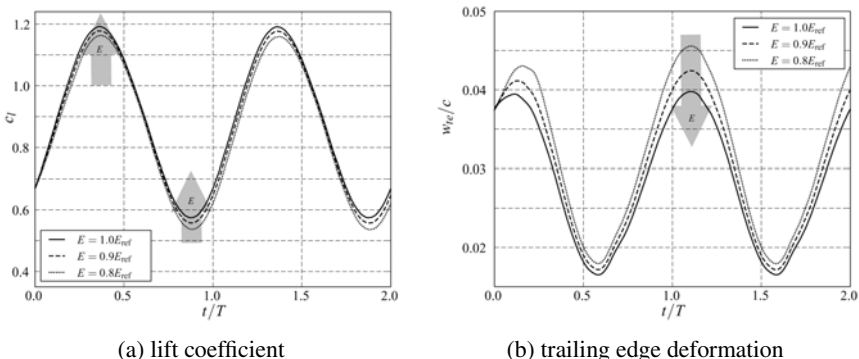


Fig. 19 Lift and trailing edge deformation over two periods of the flapping motion at different airfoil stiffness [22].

Table 2 Mean lift, drag and propulsive efficiency for Young's modulus variations

	Young's modulus E/E_{ref}			stiffness amplitude $\Delta E/E_{ref}$		
	1.0	0.9	0.8	0.0	0.2	0.4
mean lift \bar{c}_l :	0.880	0.869	0.850	0.880	0.886	0.887
mean pressure induced drag $\bar{c}_{d,p}$:	-0.0128	-0.0117	-0.0115	-0.0128	-0.0130	-0.0132
propulsive efficiency η :	0.827	0.780	0.713	0.827	0.850	0.862

Time Varying Stiffness Of The Airfoil

An approach for a better thrust and efficiency is to apply a time varying stiffness. From the biological point of view, this could be the case in bird flight due to the use of muscles. Thus, for the airfoil, the time dependent stiffness

$$E(t) = 0.5(E_{\max} - E_{\min}) \sin(2\pi f t) + 0.5(E_{\max} + E_{\min}), \quad (4)$$

is used, i.e. the airfoil becomes more stiff during the downstroke with the highest value of Young's modulus at the mid-downstroke and will be more flexible during the upstroke, where the minimal Young's modulus is reached at the mid-upstroke. Therefore, the decambering of the airfoil during the downstroke is counteracted, whereas the decambering is assisted during the upstroke. Initially, the mean value of Young's modulus is set to reference value, i.e. $0.5(E_{\max} + E_{\min}) = E_{\text{ref}}$ and the amplitude $\Delta E = E_{\max} - E_{\min}$ is subject to variation. From figure 20a it can be noticed, that the pressure induced drag coefficient generates during the downstroke more thrust, due to the higher aerodynamic force vector. Likewise, less drag is produced during the upstroke due to the decreased aerodynamic force vector, which is directed downstream. In summary, this behavior leads to an improvement of the mean pressure induced drag, see table 2. The mean lift \bar{c}_l is almost not affected by the time dependent airfoil stiffness, because the increase in maximum lift and the reduction of minimum lift with higher amplitudes of Young's modulus are in balance. Therefore, the propulsive efficiency is increased with higher stiffness amplitudes ΔE . Furthermore in 20b, the desired stiffening and flexibilization is seen in terms of the trailing edge deformation of the airfoil. During the downstroke the deformation is reduced, whereas for the upstroke the trailing edge shows a higher deformation.

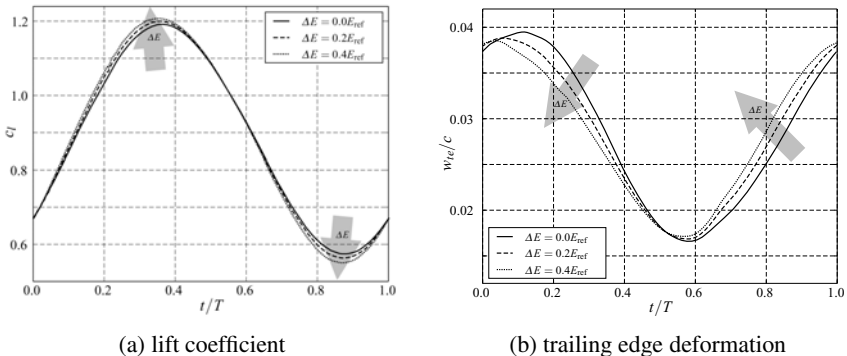
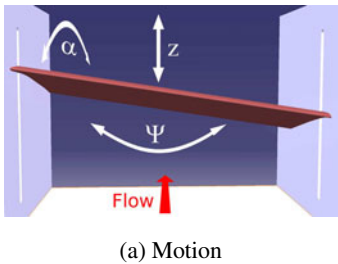


Fig. 20 Lift, pressure induced drag and trailing edge deformation over one periods of the flapping motion at different amplitudes of Young's modulus [22].

6.3 3D Flow over a Rigid, Flapping SG04 Wing Section

A three-dimensional flapping motion, which is composed of a plunging, pitching and rolling motion is investigated, see figure 21. Compared to the aerodynamics of two-dimensional flapping airfoils, there are two main differences to be taken into account. First, we will demonstrate that the spanwise variation of plunging amplitude will change the amplitude of effective AoA in spanwise direction, which will have an impact on the laminar-turbulent transition. Second, we will show that a variation of the amplitude of effective AoA in spanwise direction will create a



(a) Motion

		left side	right side
REYNOLDS number	Re	100000	
reduced frequency	k	0.25	
chord length	c	0.2 m	
mean AoA	φ_0	4°	4°
amplitude of geometric AoA	$\hat{\varphi}$	7.46°	7.46°
amplitude of effective AoA	$\Delta\alpha_{\text{eff}}$	0°	5.22°
plunge amplitude	\hat{z}	0.052 m	0.09 m
pitch-/plunge-amplitude ratio	λ	1	0.59
phase difference plunge/pitch	$\Delta\varphi$	90°	

(b) Motion Parameters

Fig. 21 Three-dimensional oscillating wing segment. The difference of the plunging amplitude between left and right side of the wing causes a roll motion.

spanwise variation of circulation resulting in streamwise wake vortices that lower the propulsive efficiency. However, the three-dimensional effect of wing tip vortices due to a finite span is suppressed by sidewalls.

Transition characteristics

The rolling motion of the wing segment effects the transition characteristics over one flapping period, see figure 22. The distribution of the wall shear stress c_f for $t/T = 0.375$ and the overlaid pressure distribution indicate a laminar separation bubble, whose spatial extension varies in spanwise direction. The absence of cross-flow instabilities and the fact that the tips of the wing segment are modeled as slip walls yield a nearly linear transition distribution in spanwise direction. The transitional behavior is further investigated and compared with experimental data for three spanwise sections (for $\Delta\alpha_{\text{eff}} = \{4.2^\circ; 2.7^\circ; 1.2^\circ\}$) in figure 23. In each of the three sections, the transition moves towards the leading edge during the downstroke and back towards the trailing edge during the upstroke motion. The smaller the amplitude of the effective angle of attack $\Delta\alpha_{\text{eff}}$, the less the transition moves along the airfoil surface. The transition locations computed by the TAU-code for the two different critical N -factors show only small differences of about 10%. Obviously, the transition is further downstream for the critical N -factor of 10. The experimental determined transition locations from the PIV measurements match well with the computational prediction. The approach to extract transition locations from PIV data is to analyze the turbulent shear-stress distribution in the boundary layer, see for instance the distributions in figure 13. The turbulent shear stress characterizes the viscous momentum transport across the boundary layer and is used to detect regions of turbulent flow. The transition location in the measurements is thus defined as the beginning of the turbulent wedge that starts from the shear layer of the LSB.

Fig. 22 Shear-stress distribution on the wing segment for $t/T = 0.375$, $k = 0.25$, $\text{Re} = 100000$, from TAU-computation. The negative values of shear stress and the overlaid pressure distribution indicate the presence of a laminar separation bubble, whose spatial extension varies in spanwise direction.

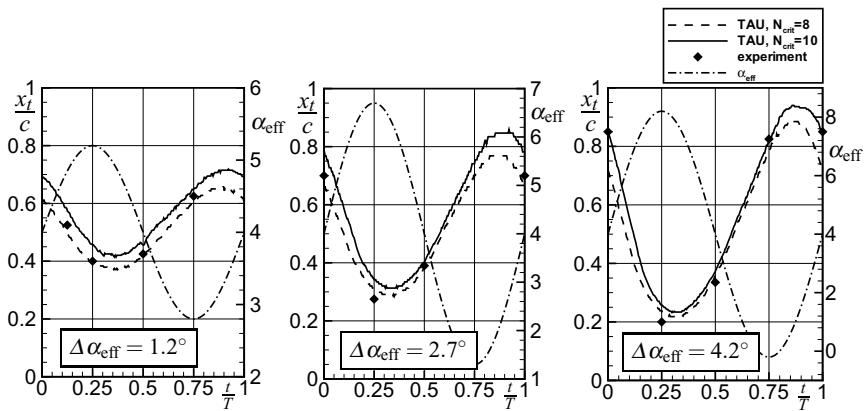
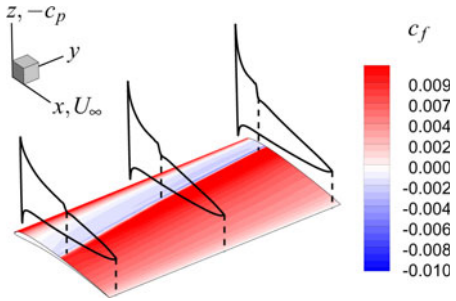
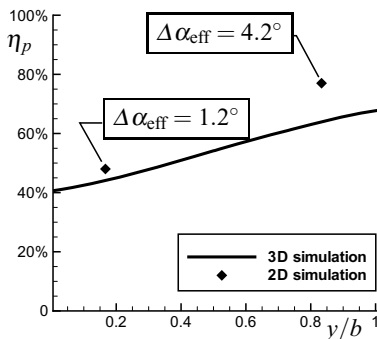


Fig. 23 Comparison of the transition locations over one flapping period with experimental PIV-data for three selected spanwise sections.

Efficiency loss due to streamwise vortices

Figure 24 shows the spanwise distribution of the propulsive efficiency for the three-dimensional TAU-computation. The efficiency is not constant along the span. On the side with large amplitudes of the effective AoA $\Delta\alpha_{\text{eff}}$ and low pitch-/plunge amplitude ratios λ ($y/b > 0.5$) the propulsive efficiency is larger. At two spanwise sections, the two-dimensional aerodynamics are computed, assuming the SG04 airfoil oscillates with the local motion of each wing section. Thus, the same distribution of the effective angle of attack over one flapping period is assured for each two-dimensional flapping case with its corresponding wing-section counterpart. The efficiencies of these two-dimensional reference cases are indicated as diamonds and demonstrate an efficiency loss of about 10% for the three-dimensional flapping airfoil. This is reasoned by the vortex dynamics in the wake of the wing segment. The unsteady part of the 3D wake is composed of start and stop vortices with a strength that varies in spanwise direction and in between these spanwise structures the

Fig. 24 Comparison of the propulsive efficiency for the two- and three-dimensional case.



formation of a streamwise vortex street takes place, so that conservation of vorticity is fulfilled. The energy to sustain these streamwise vortices finally decreases the propulsive efficiency.

6.4 3D Flow over a Flapping Hawk Wing

A generic 3D Model of a hawk wing based on the F0808 airfoil is simulated to perform a flapping motion with spanwise variation of pitch and plunge amplitude. Therefore a selected two-dimensional motion with good performance regarding thrust and propulsive efficiency of the hawk airfoil F0808 is translated into a three dimensional motion of the wing. The 3D motion is a pitching of the wing tip with an amplitude of effective AoA $\Delta\alpha_{\text{eff}} = 6^\circ$ which linearly decreases spanwise so that the wing root does not perform any pitch motion. A spanwise weighed plunging motion overlays this pitching motion of the wing with a phase shift of 90° , a reduced frequency of $k = 0.2$ and pitch-plunge amplitude ratio $\lambda = 0.8$, according to previous findings. Hence, the maximum torsion of the wing is placed in mid-upstroke and mid-downstroke, respectively. The wing root is not affected by the deformation. The 3D simulation of the hawk wing is done with the mesh deformation tool of TAU using RBF interpolation and the assumption of fully turbulent flow in the present computation. In mid-downstroke position a small three-dimensional effect can be seen, a trailing edge vortex, which does not appear in the same position of the two-dimensional motion, see figure 25. Beyond, a three-dimensional view reveals tip vortices of the deformed wing. The three-dimensional motion entails higher drag and lift reduction through the appearance of trailing edge and tip vortices, in addition to the spanwise decreasing motion. The energy to sustain this complex 3D vortex system lowers significantly both thrust and propulsive efficiency. The amplitudes of the lift and drag variations over one flapping period are therefore lower than in the corresponding 2D case, see figure 27.

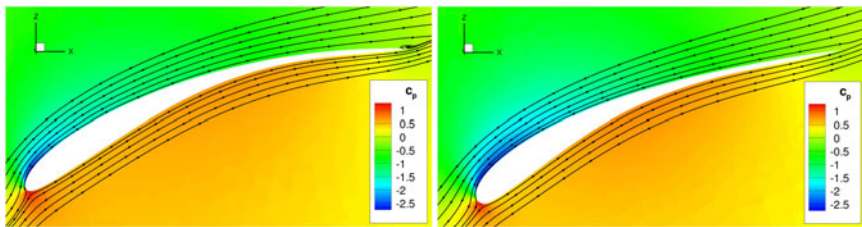


Fig. 25 Mid-downstroke of 3D motion, cut in y -plane at $y/b = 0.8$ (left) mid-downstroke of 2D motion (right)

Fig. 26 Tip vortices on deformed wing in mid-downstrokeposition

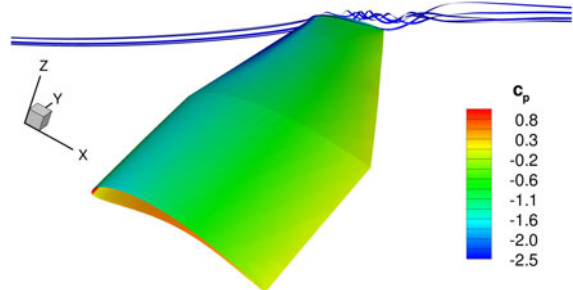
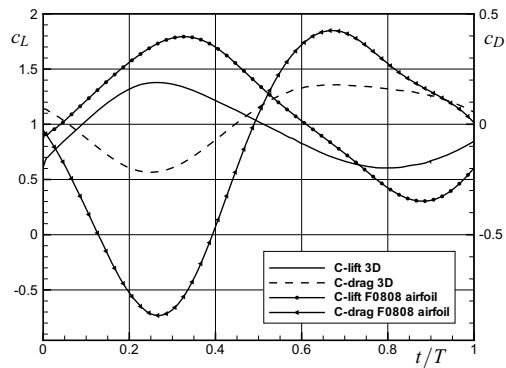


Fig. 27 Comparison of lift and drag coefficients of 2D and 3D simulation for one period



References

1. Theodorsen, T.: General theory of aerodynamic instability and the mechanism of flutter. NACA TM 496 (1935)
2. Garrick, I.: Propulsion of a Flapping and Oscillation Airfoil. NACA report No. 567 (1936)

3. Horton, H.: Laminar Separation Bubbles in Two and Three Dimensional Incompressible Flow. Departement of Aeronautical Engineering. Queen Mary College, University of London (1968)
4. Radespiel, R., Windte, J., Scholz, U.: Numerical and Experimental Flow Analysis of Moving Airfoils with Laminar Separation Bubbles. *AIAA Journal* 45(6), 1346–1356 (2007)
5. Windte, J., Radespiel, R.: Propulsive Efficiency of a Moving Airfoil at Transitional Low Reynolds Numbers. *AIAA Journal* 46(9), 2165–2177 (2008)
6. Unger, R., Haupt, M.C., Horst, P.: Coupling techniques for computational non-linear transient aeroelasticity. *Proceedings of the Institution of Mechanical Engineers, Part G: Journal of Aerospace Engineering* 222(4), 435–448 (2008)
7. Haupt, M., Niesner, R., Unger, R., Horst, P.: Coupling Techniques for Thermal and Mechanical Fluid-Structure-Interactions in Aeronautics. *PAMM* 5(1), 19–22 (2005)
8. Zienkiewicz, O.C., Taylor, R.L.: The finite element method for solid and structural mechanics, 6th edn. Elsevier Butterworth-Heinemann (2005)
9. Oehme, H.: Vergleichende Profiluntersuchungen an Vogelflügeln. Beiträge zur Vogelkunde, Band 16, Heft 1/6 (1970)
10. Bilo, D.: Flugbiophysik von Kleinvögeln; I. Kinematik und Aerodynamik des Flügelabschlages beim Haussperling (*Passer domesticus L.*) *Dissertation*, Zoologisches Institut der Universität München (1970)
11. Selig, M.: Low Reynolds Number Airfoil Design Lecture Notes. VKI Lecture Series, November 24–28. AVT Panel (2003)
12. Selig, M., Guglielmo, J., Broeren, A., Giguère: Summary of Low-Speed Airfoil Data, vol. 1. SoarTech Publications, Virginia Beach (1995)
13. Bansmer, S., Radespiel, R.: Validations of Unsteady Reynolds-averaged Navier-Stokes Simulations on Three-Dimensional Flapping Wings. *AIAA Journal* 50(1) (2012)
14. Kroll, N., Rossow, C.C., Schwamborn, D., Becker, K., Heller, G.: MEGAFLOW: A Numerical Flow Simulation Tool for Transport Aircraft Design. In: International Council of the Aeronautical Sciences, Toronto (2002); Paper No. 1105
15. Menter, F.: Two-Equation Eddy-Viscosity Transport Turbulence Model for Engineering Applications. *AIAA Journal* 32(8), 1598–1605 (1994)
16. Rendall, T.C.S., Allen, C.B.: Efficient mesh motion using radial basis functions with data reduction algorithms. *Journal of Computational Physics* 228, 6231–6249 (2009)
17. de Boer, A., van der Schoot, M.S., Bijl, H.: Mesh deformation based on radial basis function interpolation. *Computers and Structures* 85, 784–795 (2007)
18. ANSYS Inc., ANSYS 11.0 Documentation (2006)
19. Unger, R., Haupt, M.C., Horst, P.: Application of Lagrange multipliers for coupled problems in fluid and structural interactions. *Computers & Structures* 85(11–14), 796–809 (2007)
20. Gomes, J.P., Yigit, S., Lienhart, H., Schaefer, M.: Experimental and numerical study on a laminar fluid-structure interaction reference test case. *Journal of Fluids and Structures* 27(1), 43–61 (2011)
21. Unger, R.: Application of finite elements for computational aeroelasticity, CCF research report 2011-08, Cuvillier, Göttingen (2011)
22. Unger, R., Haupt, M.C., Horst, P., Radespiel, R.: Fluid-structure analysis of a flexible flapping airfoil at low-Reynolds number flow. *Journal of Fluids and Structures* (October 2011)

23. Piperno, S.: Explicit/implicit fluid/structure staggered procedures with a structural predictor and fluid subcycling for 2D inviscid aeroelastic simulations. *International Journal For Numerical Methods In Fluids* 25(10), 1207–1226 (1997)
24. Bansmer, S., Radespiel, R., Unger, R., Haupt, M., Horst, P.: Experimental and Numerical Fluid-Structure Analysis of Rigid and Flexible Flapping Airfoils. *AIAA Journal* 48(9), 1959–1974 (2010)
25. Bansmer, S.: Strömungsanalyse an einem zwei- und dreidimensional schlagenden Flügelsegment. Dissertation, Shaker Verlag (2011) ISBN: 978-3-8322-9892-0

Author Index

- Alt, Wolfgang 3
Babu, Sujin B. 25
Bachmann, Thomas 101
Bansmer, Stephan 331
Baumgartner, W. 101
Blazek, S. 101
Bleckmann, Horst 161
Blickhan, Reinhard 293
Böhm, Valter 3
Brede, Martin 255, 271
Brücker, Christoph 161, 293
Buchmann, Nadine 331
- Dehnhardt, Guido 255, 271
Engstler, Markus 43
Erlinghagen, T. 101
Fritzsche, Christoph 355
- Geyer, Thomas 355
Goldin, Nikolas 207
Grüneberger, René 311
- Hage, Wolfram 311
Haller, Daniel 193
Hanke, Wolf 255, 271
Haupt, Matthias 331
Heddergott, Niko 43
Heinrich, Ralf 331
Hermann, Wagner 135
Hochstein, Stefan 293
Horst, Peter 331
- Kaufhold, Tobias 3
King, Rudibert 207
Klaas, Michael 119
Klän, Stephan 119
Klein, A. 161
Kramer, Felix 311
Kroener, Michael 193
Krüger, Tim 43
Kunze, S. 161
- Leder, Alfred 255, 271
Lehmann, Fritz-Olaf 65, 81
Lobutova, Elka 3
- Meyer, Robert 311
Miersch, Lars 255, 271
- Neiss, Sebastian 193
Niesterok, Benedikt 255
Nitsche, Wolfgang 179
- Pacholak, Steffen 293
Pätzold, Andreas 179
Pavlov, Vadim 239
Peltzer, Inken 179
Pfohl, Thomas 43
Przybillia, A. 161
- Radespiel, Rolf 331
Resagk, Christian 3
Riedeberger, Donald 239
Rist, Ulrich 223, 239
Rival, David E. 149
Robert, Konrath 135

- Sarradj, Ennes 355
Schmeltzer, Christian 25
Schmitz, A. 161
Schröder, Wolfgang 119
Schützner, Peter 81
Shishkin, Andrei 81
Siebert, Ursula 239
Stark, Holger 25
Stellamanns, Eric 43

Thiele, Frank 311
Thomas, Erlinghagen 135
Thomas, Wolf 135
Tropea, Cameron 149

Unger, Ralf 331
Uppaluri, Sravanti 43
Voges, Danja 3
Wagner, Claus 81
Wagner, H. 101
Wassen, Erik 311
Widmann, Alex 149
Wieskotten, Sven 255, 271
Winzen, Andrea 119
Witte, Matthias 255, 271
Woias, Peter 193

Zengl, Marcus 223
Zimmermann, Klaus 3

Notes on Numerical Fluid Mechanics and Multidisciplinary Design

Available Volumes

Volume 119: Cameron Tropea and Horst Bleckmann (eds.): Nature-Inspired Fluid Mechanics – Results of the DFG Priority Programme 1207 “Nature-inspired Fluid Mechanics” 2006–2012. ISBN 978-3-642-28301-7

Volume 118: Tatsuo Maeda, Pierre-Etienne Gautier, Carl E. Hanson, Brian Hemsworth, James Tuman Nelson, Burkhard Schulte-Werning, David Thompson, and Paul de Vos (eds.): Noise and Vibration Mitigation for Rail Transportation Systems. ISBN 978-4-431-53926-1

Volume 116: Michael Klaas, Edmund Koch, and Wolfgang Schröder (eds.): Fundamental Medical and Engineering Investigations on Protective Artificial Respiration. ISBN 978-3-642-20325-1

Volume 115: Egon Krause, Yurii Shokin, Michael Resch, Dietmar Kröner, Nina Shokina (eds.): Computational Science and High Performance Computing IV. ISBN 978-3-642-17769-9

Volume 114: Piotr Doerffer, Charles Hirsch, Jean-Paul Dussauge, Holger Babinsky, and George N. Barakos (eds.): Unsteady Effects of Shock Wave Induced Separation. ISBN 978-3-642-03003-1

Volume 112: Andreas Dillmann, Gerd Heller, Michael Klaas, Hans-Peter Kreplin, Wolfgang Nitsche, and Wolfgang Schröder (eds.): New Results in Numerical and Experimental Fluid Mechanics VII – Contributions to the 16th STAB/DGLR Symposium Aachen, Germany 2008. ISBN 978-3-642-14242-0

Volume 111: Shia-Hui Peng, Piotr Doerffer, and Werner Haase (eds.): Progress in Hybrid RANS-LES Modelling – Papers Contributed to the 3rd Symposium on Hybrid RANS-LES Methods, Gdansk, Poland, June 2009. ISBN 978-3-642-14167-6

Volume 110: Michel Deville, Thien-Hiep Lê, and Pierre Sagaut (eds.): Turbulence and Interactions – Proceedings the TI 2009 Conference. ISBN 978-3-642-14138-6

Volume 109: Wolfgang Schröder (ed.): Summary of Flow Modulation and Fluid-Structure Interaction Findings – Results of the Collaborative Research Center SFB 401 at the RWTH Aachen University, Aachen, Germany, 1997–2008. ISBN 978-3-642-04087-0

Volume 108: Rudibert King (ed.): Active Flow Control II – Papers Contributed to the Conference “Active Flow Control II 2010”, Berlin, Germany, May 26–28, 2010. ISBN 978-3-642-11734-3

Volume 107: Norbert Kroll, Dieter Schwamborn, Klaus Becker, Herbert Rieger, Frank Thiele (eds.): MEGADESIGN and MegaOpt – German Initiatives for Aerodynamic Simulation and Optimization in Aircraft Design. ISBN 978-3-642-04092-4

Volume 106: Wolfgang Nitsche, Christoph Dobriloff (eds.): Imaging Measurement Methods for Flow Analysis - Results of the DFG Priority Programme 1147 “Imaging Measurement Methods for Flow Analysis” 2003–2009. ISBN 978-3-642-01105-4

Volume 105: Michel Deville, Thien-Hiep Lê, Pierre Sagaut (eds.): Turbulence and Interactions - Keynote Lectures of the TI 2006 Conference. ISBN 978-3-642-00261-8

Volume 104: Christophe Brun, Daniel Juvé, Michael Manhart, Claus-Dieter Munz: Numerical Simulation of Turbulent Flows and Noise Generation - Results of the DFG/CNRS Research Groups FOR 507 and FOR 508. ISBN 978-3-540-89955-6

Volume 103: Werner Haase, Marianna Braza, Alistair Revell (eds.): DESider – A European Effort on Hybrid RANS-LES Modelling - Results of the European-Union Funded Project, 2004–2007. ISBN 978-3-540-92772-3

Volume 102: Rolf Radespiel, Cord-Christian Rossow, Benjamin Winfried Brinkmann (eds.): Hermann Schlichting – 100 Years - Scientific Colloquium Celebrating the Anniversary of His Birthday, Braunschweig, Germany 2007. ISBN 978-3-540-95997-7

Volume 101: Egon Krause, Yurii I. Shokin, Michael Resch, Nina Shokina (eds.): Computational Science and High Performance Computing III - The 3rd Russian-German Advanced Research Workshop, Novosibirsk, Russia, 23–27 July 2007. ISBN 978-3-540-69008-5

Volume 100: Ernst Heinrich Hirschel, Egon Krause (eds.): 100 Volumes of 'Notes on Numerical Fluid Mechanics' - 40 Years of Numerical Fluid Mechanics and Aerodynamics in Retrospect. ISBN 978-3-540-70804-9

Volume 99: Burkhard Schulte-Werning, David Thompson, Pierre-Etienne Gautier, Carl Hanson, Brian Hemsworth, James Nelson, Tatsuo Maeda, Paul de Vos (eds.): Noise and Vibration Mitigation for Rail Transportation Systems - Proceedings of the 9th International Workshop on Railway Noise, Munich, Germany, 4–8 September 2007. ISBN 978-3-540-74892-2

Volume 98: Ali Gühan (ed.): RESPACE – Key Technologies for Reusable Space Systems - Results of a Virtual Institute Programme of the German Helmholtz-Association, 2003–2007. ISBN 978-3-540-77818-9

Volume 97: Shia-Hui Peng, Werner Haase (eds.): Advances in Hybrid RANS-LES Modelling - Papers contributed to the 2007 Symposium of Hybrid RANS-LES Methods, Corfu, Greece, 17–18 June 2007. ISBN 978-3-540-77813-4

Volume 96: C. Tropea, S. Jakirlic, H.-J. Heinemann, R. Henke, H. Hönliger (eds.): New Results in Numerical and Experimental Fluid Mechanics VI - Contributions to the 15th STAB/DGLR Symposium Darmstadt, Germany, 2006. ISBN 978-3-540-74458-0

Volume 95: R. King (ed.): Active Flow Control - Papers contributed to the Conference "Active Flow Control 2006", Berlin, Germany, September 27 to 29, 2006. ISBN 978-3-540-71438-5

Volume 94: W. Haase, B. Aupoix, U. Bunge, D. Schwamborn (eds.): FLOMANIA - A European Initiative on Flow Physics Modelling - Results of the European-Union funded project 2002 - 2004. ISBN 978-3-540-28786-5

Volume 93: Yu. Shokin, M. Resch, N. Danaev, M. Orunkhanov, N. Shokina (eds.): Advances in High Performance Computing and Computational Sciences - The Ith Khazakh-German Advanced Research Workshop, Almaty, Kazakhstan, September 25 to October 1, 2005. ISBN 978-3-540-33864-2

Volume 92: H.J. Rath, C. Holze, H.-J. Heinemann, R. Henke, H. Hönliger (eds.): New Results in Numerical and Experimental Fluid Mechanics V - Contributions to the 14th STAB/DGLR Symposium Bremen, Germany 2004. ISBN 978-3-540-33286-2

Volume 91: E. Krause, Yu. Shokin, M. Resch, N. Shokina (eds.): Computational Science and High Performance Computing II - The 2nd Russian-German Advanced Research Workshop, Stuttgart, Germany, March 14 to 16, 2005. ISBN 978-3-540-31767-8

Volume 87: Ch. Breitsamter, B. Laschka, H.-J. Heinemann, R. Hilbig (eds.): New Results in Numerical and Experimental Fluid Mechanics IV. ISBN 978-3-540-20258-5

Volume 86: S. Wagner, M. Kloker, U. Rist (eds.): Recent Results in Laminar-Turbulent Transition - Selected numerical and experimental contributions from the DFG priority programme 'Transition' in Germany. ISBN 978-3-540-40490-3

Volume 85: N.G. Barton, J. Periaux (eds.): Coupling of Fluids, Structures and Waves in Aeronautics - Proceedings of a French-Australian Workshop in Melbourne, Australia 3-6 December 2001. ISBN 978-3-540-40222-0

Volume 83: L. Davidson, D. Cokljat, J. Fröhlich, M.A. Leschziner, C. Mellen, W. Rodi (eds.): LESFOIL: Large Eddy Simulation of Flow around a High Lift Airfoil - Results of the Project LESFOIL supported by the European Union 1998 - 2001. ISBN 978-3-540-00533-9

Volume 82: E.H. Hirschel (ed.): Numerical Flow Simulation III - CNRS-DFG Collaborative Research Programme, Results 2000-2002. ISBN 978-3-540-44130-4

Nature-Inspired Porous Airfoils for Sound Reduction

Thomas Geyer, Ennes Sarradj, and Christoph Fritzsche

Abstract. Inspired by the results from acoustic measurements on flying owls and prepared owl wings that support the thesis of the silent flight of owls, measurements were conducted on technical airfoils made from open-porous, flow-permeable materials, characterized by their air flow resistivity, in an aeroacoustic wind tunnel. One major objective of these experiments is the identification of porous materials that enable a reduction of aeroacoustic noise. Both the generation of trailing edge noise and the generation of leading edge noise were investigated using microphone array technology and three-dimensional deconvolution beamforming algorithms. The highest trailing edge noise reduction per unit lift force can be achieved by using airfoils with medium to high air flow resistivities, while the highest leading edge noise reduction was measured for airfoils with low air flow resistivities.

1 Introduction

The aim of the research is the transfer of the mechanisms that enable the quiet flight of owls to technical applications. The adaptations leading to the reduced noise generation of the owl, which were identified by Graham in 1934 [11], are fringes at the trailing edge of the wings, a comb-like structure at the leading edge and a very soft downy upper surface of the feathers. The focus of the present study is on the last adaptation, the soft and flow-permeable plumage.

A significant part within the framework of the study is dedicated to the silent flight of the owls. In a first step, the air flow resistance of bird plumage was measured, and the results confirm that the plumage of owls has indeed a lower air flow resistance than that of non-silent flying birds. In a second step, the low noise generated by owls flying in gliding flight compared to the noise from non-silent flying birds was examined experimentally using two different approaches: “indoor”

Thomas Geyer · Ennes Sarradj · Christoph Fritzsche
Aeroacoustics Group, Brandenburg University of Technology Cottbus, Germany
e-mail: {thomas.geyer, ennes.sarradj}@tu-cottbus.de

measurements on prepared bird wings in an aeroacoustic wind tunnel [5] and “outdoor” measurements on flying birds [17].

The results from the wind tunnel measurements [5] indicate that the noise generated by owls is lower than that of other birds of prey, which is not only a consequence of their lower flight speed, but also a consequence of their special feather adaptations. Although the prepared wings were carefully chosen from a large set of specimen, and the aerodynamic performance was measured simultaneous to the acoustic measurements, the use of prepared wings is a severe limitation since the shape of the prepared wings does not necessarily represent the wing shape of a bird when flying under natural conditions.

Therefore, acoustic flyover measurements were performed on two silent flying bird species and three non-silent flying species [17]. This approach is way more complex, as it involves the determination of the flight trajectory and microphone array measurements with a moving-focus beamforming technique, but it has the advantage that the birds can be assumed to be flying according to their natural habit. Again, the results show that less noise is generated by flying owls than by non-silent flying birds both due to the adaptations of their wings and feathers and due to their lower flight speed.

Since airfoils are one basic technical application where the previous findings may be of use, a major part of the research is dedicated to measurements on open-porous, flow-permeable airfoil models in an aeroacoustic wind tunnel. A low aeroacoustic noise generation is one key parameter in the design of propellers, fans and wind turbines, and the use of airfoils made of porous materials may contribute to achieve this objective.

Different airfoil noise source mechanisms are investigated in the study. As a more or less direct consequence of the reduced noise generation at the wings of owls, measurements of airfoil trailing edge noise were performed on a large set of porous airfoils in comparison to a non-porous reference airfoil. The noise sources located at the trailing edge are due to the interaction of the turbulent boundary layer with the trailing edge and, to some extent, due to the vortex shedding if the trailing edge is not ideally sharp.

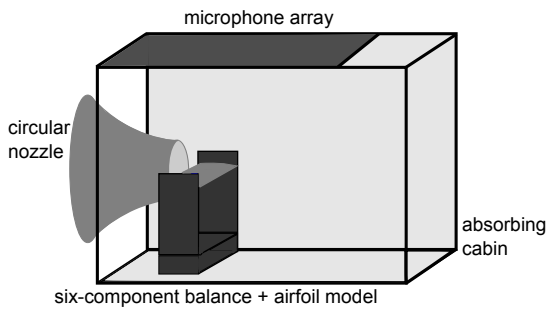
Owing to the promising results of these trailing edge noise measurements, in a further step the noise due to the interaction of incident turbulence with the leading edge of the porous airfoils was examined. Noise sources at the leading edge are dominant when the inflow contains considerable turbulence, with an intensity that exceeds that of the turbulent boundary layer developing along the airfoil surface.

Besides the noise generation of the porous airfoils, their aerodynamic efficiency has to be taken into account. To this end, the aerodynamic forces acting on the airfoils were measured simultaneously with the airfoil trailing edge noise measurements.

The basic questions that should be answered as a result of this research are:

- How does the porous consistency affect the noise generation at the trailing edge and leading edge of the airfoils?
- How does the porous consistency affect the aerodynamic performance?

Fig. 1 Schematic of the measurement setup in the aeroacoustic wind tunnel, including nozzle, absorbing cabin, microphone array and six-component balance with airfoil (for the measurement of airfoil leading edge noise, different turbulence generating grids may be mounted directly to the nozzle exit)



2 Experimental Setup

This section gives an overview on the setup that was used for the experimental study on the noise generated by porous airfoils in comparison to a non-porous reference airfoil.

Aeroacoustic Wind Tunnel. All measurements were performed in a small aeroacoustic open jet wind tunnel at Brandenburg University of Technology. The nozzle used for the experiments is circular and has an exit diameter of 0.2 m. The flow is characterized by a very low turbulence (in the order of 0.1 % at a flow speed of 20 m/s in front of the nozzle) and a low background noise (overall sound pressure level below 60 dB(A) for flow speeds up to 50 m/s, measured at 1 m distance at an angle of 90° to the nozzle axis).

During acoustic measurements, the test section is surrounded by a cabin whose side walls are equipped with an acoustic foam, thus providing a nearly anechoic environment for frequencies above 500 Hz. Additional information on the wind tunnel are given in [15]. Fig. 1 shows a schematic of the experimental setup.

For the measurement of airfoil leading edge noise, a noticeable inflow turbulence is required. In the present study, this turbulence was generated by the use of grids which can be mounted directly to the wind tunnel nozzle. However, such grids generate strong self noise, and hence efforts have to be made in order to separate the noise sources located at the grid (background noise) from the noise sources located at the airfoil leading edge which are to be analyzed.

Porous Airfoil Models. For the investigation of the noise generated by porous airfoils, a large set of different porous materials was used to manufacture two-dimensional airfoil models. The porous materials are characterized by their air flow resistivity r which was measured according to ISO 9053 [12].

The airfoils have an SD7003 shape with a chord length of 0.235 m and a span width of approximately 0.4 m. Due to manufacturing reasons, the trailing edge thickness of the porous airfoils was increased to 1.59 mm compared to 0.5 mm for the non-porous reference airfoil. The reference airfoil is equipped with a thin tripping tape at 10.6% of the chord [6] to enforce boundary layer transition and hence the existence of a turbulent boundary layer at the trailing edge.

Table 1 Materials used for the manufacturing of the airfoils (given is the air flow resistivity r)

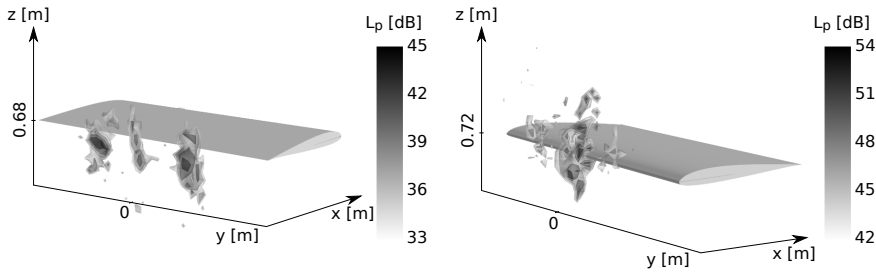
No	Name	Material	r [Pa s/m ²]
1	Reference	non-porous	∞
2	M&K felt, 0.36 g/cm ³	woolen felt	506,400
3	Porex	polyethylene granulate	316,500
4	M&K felt, 0.22 g/cm ³	woolen felt	164,800
5	Needlona felt, SO 2002	synthetic felt	130,200
6	ArmaFoam Sound	elastomer foam	112,100
7	Needlona felt, WO-PE 1958	woolen / synthetic felt	40,100
8	Arpro Porous 4025	expanded polypropylene foam	23,100
9	Reapor	porous glass granulate	16,500
10	Basotect	melamine resin-foam	9,800
11	Recemat	metal foam	8,200
12	Balzer RG 3550	polyurethane foam	4,400
13	Panacell 90 ppi	polyurethane foam	4,000
14	Panacell 60 ppi	polyurethane foam	3,600
15	M-Pore PU 45 ppi	polyurethane foam	1,500
16	M-Pore Al 45 ppi	metal foam	1,000
17	Panacell 45 ppi	polyurethane foam	700

Measurement of Aerodynamic Forces. Simultaneously to the measurement of the trailing edge noise, the lift and drag forces acting on the airfoils were measured using a six-component balance. The balance consists of six single point load cells and the resulting data were recorded using a National Instruments 24 Bit full bridge analog input module. All three aerodynamic forces acting on the airfoil (the lift force, the drag force and the side force), as well as the three moments (pitching moment, rolling moment and yawing moment) are then determined from the electrical signals from the load cells.

Microphone Array Measurements. The acoustic measurements of the present study were performed using a planar microphone array that consists of 56 flush-mounted 1/4th inch microphone capsules. The data were recorded with a sample frequency of 51.2 kHz and a measurement duration of 40 s using a National Instruments 24 Bit multichannel measurement system. The recorded data were Fast Fourier transformed in blocks with 4,096 samples per block, using a Hanning window. With 50 % overlap of these blocks the averaged cross-spectral matrix was calculated and then further processed using deconvolution beamforming algorithms.

Different deconvolution algorithms were considered for the analysis of the acoustic data within this study, including (1) the deconvolution approach for the mapping of acoustic sources, DAMAS [3], (2) the CLEAN-SC algorithm [18] and (3) the orthogonal beamforming, OB [16].

The different algorithms were applied to a fully three-dimensional source domain instead of a two-dimensional source map, thus resulting in three-dimensional



(a) Trailing edge noise measurement, (b) Leading edge noise measurement,
 $U_0 \approx 50$ m/s, 4 kHz octave band, OB $U_0 \approx 35$ m/s, 2 kHz octave band, CLEAN-SC

Fig. 2 Examples of three-dimensional beamforming sound maps, obtained from measurements at the non-porous reference airfoil, dynamic range 12 dB (Note that the flow speed U_0 is different in both cases.)

distributions of noise sources. Compared to conventional two-dimensional beam-forming, this method provides a better depth resolution, and hence sources positioned in front of or behind the usual two-dimensional mapping plane are localized more accurately. As an example, Fig. 2 presents sound maps obtained for both a trailing edge noise measurement, processed using the OB algorithm [9], and a leading edge noise measurement which was processed using CLEAN-SC [10].

Sound pressure level spectra were obtained from the beamforming results by integration over selected regions within the sound maps. For the present investigation of different noise source mechanisms, integration volumes were defined that contain only noise sources generated by the chosen mechanism, but no background noise sources.

No correction for the refraction of sound at the shear layer was applied due to the fact that the exact shape and thickness of the conical shear layer is not known. Additionally, an estimation of the resulting deviation of the noise source locations was found to be very small only.

Due to the compactness condition [2], which states that airfoil leading edge and trailing edge can only be regarded as independent noise sources if the chord length c_l equals at least one acoustic wavelength λ , results were only analyzed for frequencies larger than approximately 1.5 kHz.

3 Airfoil Aerodynamic Performance

This section contains a summary of the results from the aerodynamic measurements. The aerodynamic performance of the porous airfoils will basically be analyzed based on the lift force F_L and the drag force F_D only. Additional results can be found in [6, 9].

Fig. 3 shows the measured lift and drag forces of the porous airfoils at m different flow speeds U_0 at 8° angle of attack, normalized to the corresponding values of the

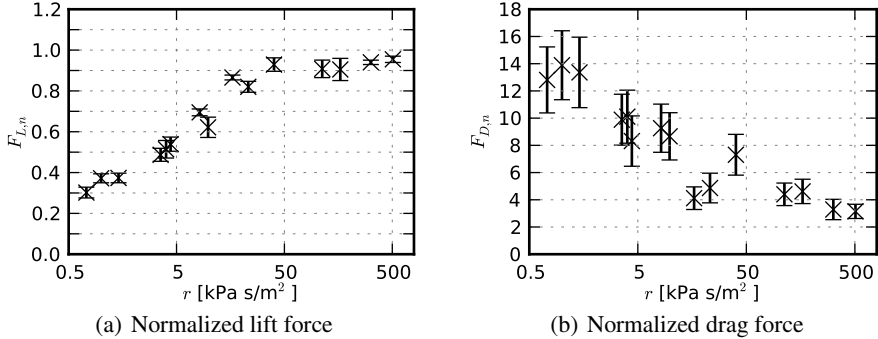


Fig. 3 Mean value and standard deviation of the normalized lift and drag forces $F_{L,n}$ and $F_{D,n}$ according to Eq. (1) as a function of air flow resistivity r of the porous materials at 8° angle of attack

non-porous airfoil at the same flow speed and averaged over the complete range of flow speeds between 25 m/s and 50 m/s:

$$F_{L,n} = \frac{1}{m} \sum_{i=1}^m \frac{F_L(U_{0,i})}{F_{L,\text{ref}}(U_0)} \quad \text{and} \quad F_{D,n} = \frac{1}{m} \sum_i^m \frac{F_D(U_{0,i})}{F_{D,\text{ref}}(U_0)}. \quad (1)$$

F_L and F_D are the measured lift and drag forces while $F_{L,\text{ref}}$ and $F_{D,\text{ref}}$ are the forces of the non-porous reference airfoil at the same flow speed U_0 . It can be seen from Fig. 3 that the porous airfoils generate less lift, but more drag than the reference airfoil. For increasing air flow resistivity r of the porous materials, the measured lift increases, while the drag decreases.

4 Airfoil Trailing Edge Noise

In a first step, the noise generated at the trailing edge of the airfoils from Tab. 1 will be analyzed. To this end, experiments were performed at a variety of flow speeds approximately between 25 m/s and 50 m/s and at angles of attack between -16° and 20° . However, only results for the zero angle of attack case are shown here, for additional information the reader is referred to [6].

Theory. Airfoil trailing edge noise is the dominant noise source in virtually non-turbulent flow. According to the basic theory by Ffowcs Williams and Hall [4], the far field intensity I of the sound generated by a turbulent flow over the edge of a half plane at zero angle of attack is given by

$$I = \frac{\rho \cdot k \cdot U^4 \cdot V^2 \cdot \gamma^2 \cdot \overline{D}}{\pi^3 \cdot c \cdot R^2 \cdot \ell^3}, \quad (2)$$

where ρ is the fluid density, $k = \omega/c$ is the wave number with the speed of sound c , γ is the normalized turbulence intensity inside the turbulent boundary layer, U is

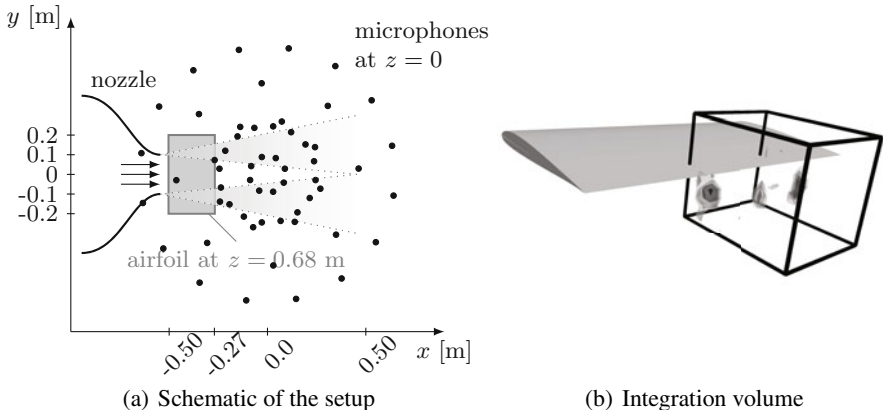


Fig. 4 Setup used for the trailing edge noise measurements and volume chosen for the integration of the corresponding noise source contributions (shown for a measurement at the reference airfoil, $U_0 = 50$ m/s, 4 kHz third octave band)

a typical fluid velocity, ℓ is the diameter of the turbulent eddy and R is the distance between the sound source at the edge and the field point (the "distance of the observer"). V is the volume of the turbulent eddy, which is assumed to be a cylinder of diameter 2ℓ centered on the edge of the half plane. The term \bar{D} is a simplified description for the source directivity. It may take values between zero and one.

The theory by Ffowcs Williams and Hall is often adapted in studies of airfoil trailing edge noise and airframe noise. The main conclusion drawn from their work is that trailing edge noise can be assumed to depend on the fifth power of the flow speed.

Acoustic Measurements. A schematic of the setup used for the trailing edge noise measurements is given in Fig. 4(a), while the volume for the integration of the corresponding trailing edge noise sources is presented in Fig. 4(b). The integration volume does not contain noise sources at the trailing edge or noise sources due to the interaction of the wind tunnel shear layers with the airfoil, but only noise sources due to the interaction of the turbulent boundary layer with the airfoil trailing edge.

In a first step, the measured trailing edge noise levels, obtained using the OB algorithm [16], are scaled based on the flow speed U_0 according to

$$L_{p,\text{scaled,TE},1} = L_p - 10 \cdot \log_{10} \left(\frac{U_0}{1 \text{ m/s}} \right)^{4.5} [\text{dB}]. \quad (3)$$

A scaling using the 4.5th power of the flow speed, instead of the fifth power as proposed by Ffowcs Williams and Hall, was for example also used by Oerlemans and Migliore [14]. The resulting third octave band sound pressure levels are given in Fig. 5 as a function of the chord based Strouhal number. Note that for clarity

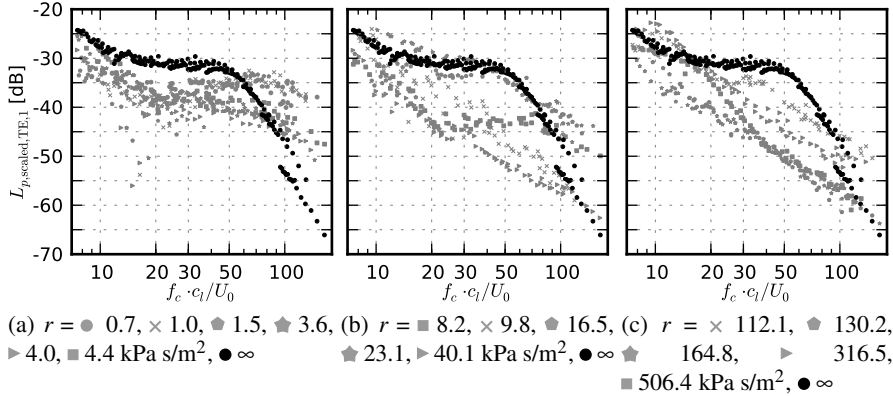


Fig. 5 Third octave band sound pressure level of the trailing edge noise of all airfoils from Tab. 1, scaled according to Eq. (3), for (from left to right) low, medium and high air flow resistivities

of the presentation only a subset of the third octave band sound pressure levels are depicted, additional results can be found in [9].

It is visible that the trailing edge noise of most porous airfoils is lower than that of the reference airfoil at medium Strouhal numbers. At high Strouhal numbers, the noise of porous airfoils with low air flow resistivities exceeds that of the reference airfoil. This is assumed to be a contribution of surface roughness noise, since the porous airfoils with low air flow resistivities have larger pores than materials with high air flow resistivities and hence a coarser surface.

In a second step, the aerodynamic performance of the airfoils is included in the analysis. The scaling used for the presentation of the results (Fig. 6) now employs both the flow speed and the lift forces that were measured simultaneously to the acoustic measurements according to

$$L_{p,\text{scaled},\text{TE},2} = L_p - 10 \cdot \log_{10} \left(\frac{U_0}{1 \text{ m/s}} \right)^{2.5} - 10 \cdot \log_{10} \left(\frac{F_L}{1 \text{ kg m/s}^2} \right) [\text{dB}]. \quad (4)$$

The use of the measured lift force for the scaling of trailing edge noise can be found in various aeroacoustic studies, such as the work of Lilley [13]. Thus, the aerodynamic efficiency of the porous airfoils is taken into account and the resulting scaled sound pressure levels represent the trailing edge noise generated by the corresponding airfoil per unit lift force. According to basic aerodynamic theory, the lift force is proportional to the square of the flow speed, $F_L \propto U_0^2$, and hence the approach given by Eq. (4) again includes a scaling with the 4.5th power of the flow speed. It is visible that, when the aerodynamic performance is considered, only those porous airfoils with medium and high air flow resistivities provide an alternative to a common airfoil in a technical application.

Turbulent Boundary Layer Characteristics. Hot-wire measurements in the turbulent boundary layer were performed on a subset of the airfoils from Tab. 1 using

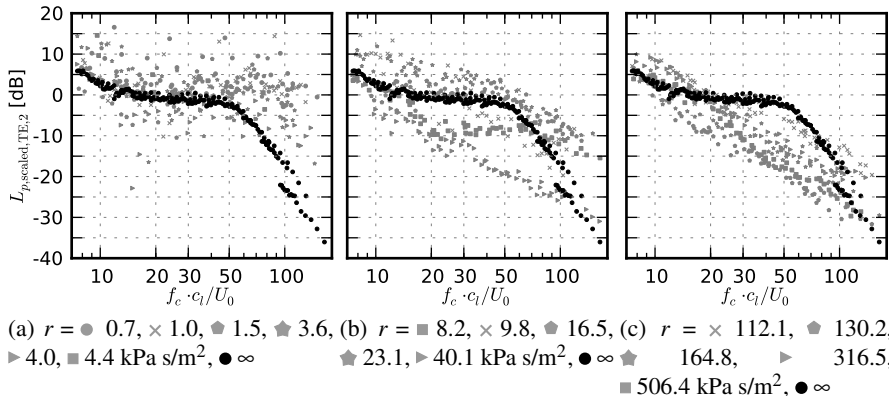
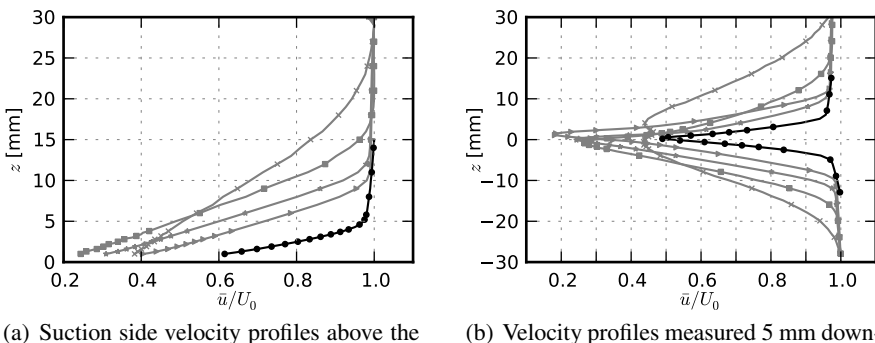


Fig. 6 Third octave band sound pressure level of the trailing edge noise of all airfoils from Tab. 1, scaled according to Eq. (4), for (from left to right) low, medium and high air flow resistivities

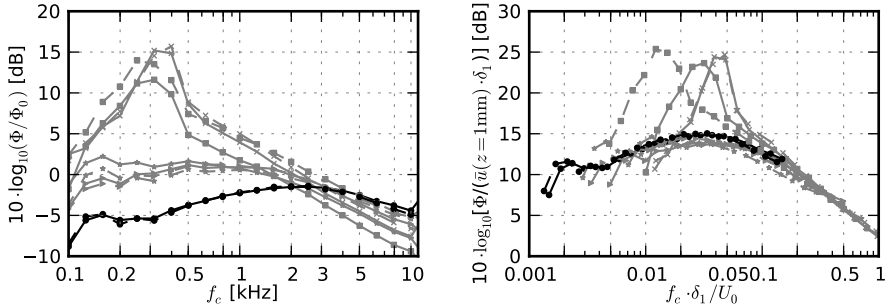
a single-wire boundary layer probe with the wire aligned in spanwise direction. 256,000 samples were recorded with a sample frequency of 25.6 kHz using a multichannel CTA system that contains a low-pass filter with a cutoff frequency of 10 kHz. The probe was positioned using a three-dimensional traversing system with a minimum step size of 0.1 mm. To avoid the possible influence of vibrations after each step of the traversing system, the first two seconds (51,200 samples) of each data set were omitted. A part of the results from the hot-wire measurements were published in [7].

It was found that both the boundary layer thickness δ as well as the boundary layer displacement thickness δ_l decrease for increasing air flow resistivity of the airfoils. As an example, Fig. 7(a) shows the velocity profiles (the mean velocity \bar{u}



(a) Suction side velocity profiles above the trailing edge at $x/c_l = 1$ (b) Velocity profiles measured 5 mm downstream of the airfoil trailing edge in the wake

Fig. 7 Velocity profiles \bar{u}/U_0 of five airfoils, measured at a flow speed U_0 of 50 m/s ($r = \times 1.0, \blacksquare 8.2, \blacklozenge 16.5, \blacktriangleright 316.5 \text{ kPa s/m}^2, \bullet \infty$)



(a) Third octave band turbulence spectra Φ measured 1 mm above the trailing edge of each airfoil and normalized with $\Phi_0 = 1 \text{ m}^2 \text{s}^{-1}$

(b) Third octave band turbulence spectra, normalized using the mean flow velocity \bar{u} and the boundary layer displacement thickness δ_1

Fig. 8 Spectra of the turbulent velocity fluctuations above the trailing edge of the airfoils, measured at a flow speed U_0 of 50 m/s, solid lines: suction side, dashed lines: pressure side ($r = \times 1.0, \blacksquare 8.2, \blacktriangleright 16.5, \blacktriangleright 316.5 \text{ kPa s/m}^2, \bullet \infty$)

normalized with the flow speed U_0) measured directly above the trailing edge on the suction side of the airfoils. It gives evidence of the thicker boundary layer of the porous airfoils with low air flow resistivities. Since the surface roughness of the porous airfoils compared to the smooth surface of the reference airfoil also affects the characteristics of the turbulent boundary layer, it remains to be clarified how much of the increase of δ and δ_1 is due to the permeability of the materials and how much is solely due to the increased surface roughness.

Similar to the velocity profiles shown in Fig. 7(a), velocity profiles measured in the wake of the airfoils are presented in Fig. 7(b). It can be seen that, besides the fact that the thickness of the turbulent boundary layer is greater for the porous airfoils than for the reference airfoil, the porous consistency also has an influence on the shape of the wake velocity profiles. This is especially visible for the airfoil with the lowest air flow resistivity, where a noticeable increase of the flow velocity directly behind the trailing edge was measured, which is assumed to be caused by an internal flow inside the porous airfoil.

Fig. 8(a) shows the third octave band power spectral density of the turbulent velocity fluctuations, Φ , measured approximately 1 mm above the trailing edge on both suction side and pressure side of the airfoils. These spectra represent the distribution of kinetic energy within the turbulence. The low frequency range of the turbulence spectra can be attributed to larger turbulence scales, while the high frequency range is associated with small scale turbulent structures. The turbulence spectrum measured above the trailing edge of the reference airfoil has an amplitude below those of the four porous airfoils at low and medium frequencies up to approximately 3 kHz, with a flat peak at approximately 2 kHz to 3 kHz, while for higher frequencies the spectrum takes values above those measured for the porous airfoils.

The spectra of the two porous airfoils with the lowest air flow resistivities have a strong peak, with the maximum around 300 Hz.

The fact that the peak of the turbulence spectra measured above the trailing edge of the porous airfoils is at a much lower frequency than that measured above the trailing edge of the reference airfoil is assumed to be responsible for the reduced trailing edge noise generation of the porous airfoils at medium and high frequencies. The spectra measured above the trailing edge of the porous airfoils in general have higher amplitudes at low frequencies (approximately below 2 or 3 kHz), but the amplitude then decreases more strongly with increasing frequency.

It has to be considered that the turbulence spectra shown in Fig. 8(a) were measured at a fixed distance of 1 mm from the airfoil surface and hence at different positions relative to the boundary layer thickness of the corresponding airfoil. To account for the differences of the mean velocity \bar{u} at this position, Fig. 8(b) shows the normalized turbulence spectra $10 \cdot \log_{10}[\Phi / (\bar{u}(z = 1 \text{ mm}) \cdot \delta_1)]$ as a function of the Strouhal number based on boundary layer displacement thickness δ_1 and flow speed U_0 . Now the turbulence spectra are found to collapse reasonably well, with the exception of the spectral peak measured at the airfoil made of Recemat ($r = 8,200 \text{ Pa s/m}^2$). The differences in peak Strouhal number are due to differences of the measured boundary layer displacement thickness of this particular airfoil [9].

The turbulence spectra measured within the turbulent boundary layer of four porous airfoils and the non-porous reference airfoil were then used to develop a first basic trailing edge noise model for porous airfoils [9] based on the flat plate theory by Ffowcs Williams and Hall.

5 Airfoil Leading Edge Noise

This section contains the results of the experimental investigation of the noise generation at the leading edge of the porous airfoils at zero angle of attack, which were conducted after the trailing edge noise measurements on the porous airfoils confirmed their anticipated noise reduction potential.

Theory. The leading edge of an airfoil is the dominant noise source location in a flow that contains considerable turbulence. This is a result of the fluctuating forces generated by the turbulent structures (eddies) when they impinge on the leading edge. One significant theoretical investigation of this noise source is the work of Amiet [1], who developed a basic leading edge noise model to calculate the third octave band sound pressure level generated by an airfoil immersed in a turbulent flow, characterized by its integral length scale Λ and intensity $\sqrt{\bar{u}^2}/U$ at the observer location in a distance R from the airfoil. The model is based on the following equation for the dependence of the far field sound intensity I :

$$I \propto \frac{\Lambda \cdot h}{R^2} \cdot \left(\frac{U}{c} \right)^5 \cdot \frac{\bar{u}^2}{U^2} \cdot \frac{\hat{K}_x^3}{(1 + \hat{K}_x^2)^{7/3}}. \quad (5)$$

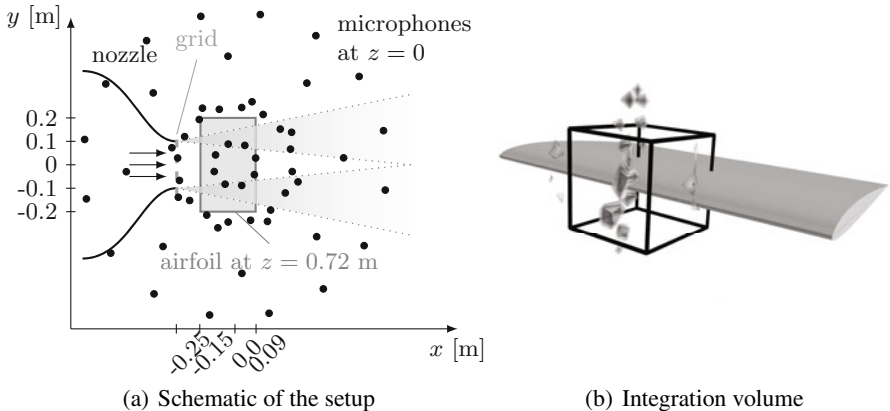


Fig. 9 Setup used for the leading edge noise measurements and volume chosen for the integration of the corresponding noise source contributions (shown for a measurement at the reference airfoil, $U_0 = 35$ m/s, 1.6 kHz third octave band)

Here, $K_x = \omega/U$ is the chordwise turbulence wavenumber (the \wedge symbol denotes a normalization by the wavenumber range of the energy containing eddies) and h is the airfoil semi-span. The model developed by Amiet according to Eq. (5) includes a dependence of the leading edge noise on the fifth power of the Mach number and on the square of the turbulence intensity.

Acoustic Measurements. To investigate the potential reduction of leading edge noise through the use of porous airfoils, acoustic experiments on all airfoil models from Tab. 1 were performed at zero angle of attack for flow speeds approximately between 15 m/s and 50 m/s. The inflow turbulence required for the generation of airfoil leading edge noise was provided by three different grids. In this section, the experimental approach and the subsequent results will be described for only one grid, but additional results can be found in [8].

The grid used for the present demonstration is a perforated plate with square holes (bar width 4 mm, mesh width 14 mm, thickness 1 mm) which was found to generate the turbulence with the highest intensity (in the order of 15 %) at the position of the airfoil leading edge. The grid was mounted directly to the nozzle exit (see Fig. 9(a)). Due to the presence of a turbulence grid, the maximum flow speed that can be achieved may be considerably lower than for the configuration without grid, which is caused by a pressure drop across the grid. For this particular grid, the maximum flow speed is about 35 m/s. The parameters that describe the turbulent inflow, such as a turbulence intensity or a characteristic time scale or length scale, were measured at 15 measurement positions within a plane normal to the flow, directly upstream of the leading edge of the non-porous reference airfoil, by using hot-wire anemometry with a right-angled single-wire probe with the wire aligned in the spanwise direction [8]. The turbulence is assumed to be locally isotropic.

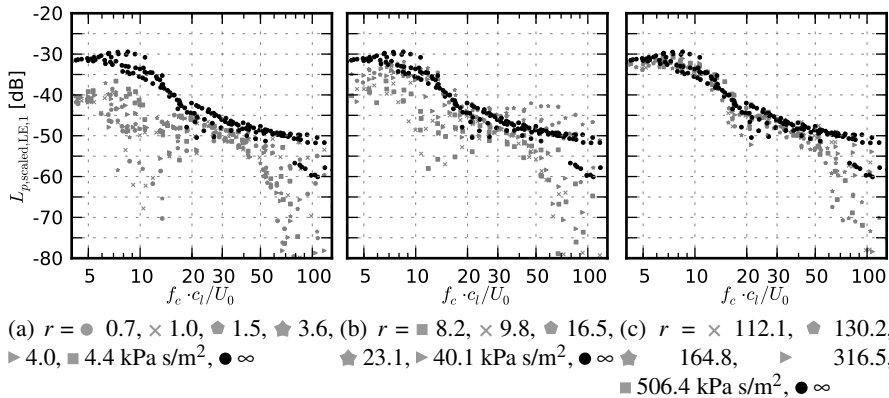


Fig. 10 Third octave band sound pressure level of the leading edge noise of all airfoils from Tab. 1, scaled according to Eq. (6), for (from left to right) low, medium and high air flow resistivities

A schematic of the setup used for the measurement of the noise generated at the leading edge of the porous airfoils is given in Fig. 9(a), while Fig. 9(b) shows the integration volume that was used to obtain the corresponding leading edge noise spectra, calculated using a three-dimensional CLEAN-SC algorithm [18].

Since the distance between grid and airfoil leading edge is only 0.1 m, the flow field and the generated turbulence are not homogeneous, although the spatial differences are not significant. Due to the hot-wire measurements at 15 randomly distributed positions, the standard deviation of the turbulence characterizing parameters was found to be very small [10].

The results of the leading edge noise measurements are given in Fig. 10. Again, note that only a subset of the results are shown, additional data can be found in [8]. In accordance to the findings by Oerlemans and Migliore [14], the sound pressure levels are scaled using the sixth power of the flow speed (which was found to result in less scatter than the U_0^5 -scaling proposed by Amiet):

$$L_{p,\text{scaled,LE},1} = L_p - 10 \cdot \log_{10} \left(\frac{U_0}{1 \text{ m/s}} \right)^6 [\text{dB}]. \quad (6)$$

It can be seen that the porous airfoils with low and medium air flow resistivities lead to a noticeable noise reduction at low Strouhal numbers. It is assumed that this noise reduction is caused by a reduction of the fluctuating lift forces that act on the airfoils due to the porosity of the materials. At higher Strouhal numbers the measured noise is assumed to be affected by background noise sources. The noise generation of porous airfoils with high air flow resistivities is similar to that of the reference airfoil.

Similar to the approach used in Sec. 4, the aerodynamic performance of the porous airfoils is considered in the scaling of the leading edge noise levels. Fig. 11 shows the third octave band sound pressure levels scaled according to

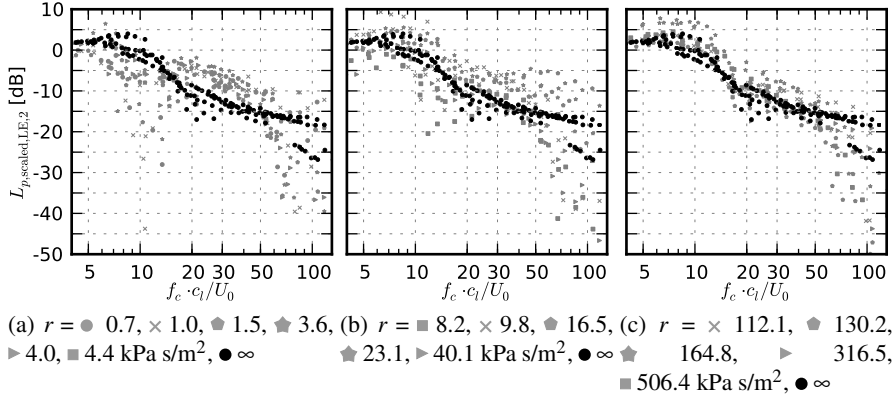


Fig. 11 Third octave band sound pressure level of the leading edge noise of all airfoils from Tab. 1, scaled according to Eq. (7), for (from left to right) low, medium and high air flow resistivities

$$L_{p,\text{scaled},\text{LE},2} = L_p - 10 \cdot \log_{10} \left(\frac{U_0}{1 \text{ m/s}} \right)^4 - 10 \cdot \log_{10} \left(\frac{F_L}{1 \text{ kg m/s}^2} \right) [\text{dB}]. \quad (7)$$

Since the lift force F_L was not directly measured during the acoustic leading edge noise measurements, it was estimated based on the results of the trailing edge noise measurements at zero angle of attack. When the aerodynamic performance is considered, porous airfoils with medium and high air flow resistivities do not lead to a leading edge noise reduction compared to the reference airfoil. Only porous airfoils with low air flow resistivities still provide a leading edge noise reduction mainly at low Strouhal numbers. However, it is assumed that a noise reduction can be achieved at non-zero angles of attack.

6 Conclusions

Inspired by the silent flight of the owl, acoustic measurements were performed on a set of porous, flow-permeable airfoil models using microphone array measurement technique. The acoustic data were processed using three-dimensional deconvolution beamforming algorithms. Both the noise generation at the leading edge and at the trailing edge of the airfoils was examined.

The results showed that in general a noticeable reduction of both trailing edge noise and leading edge noise is possible through the use of open-porous airfoils, depending on the air flow resistivity of the porous materials. When considering the aerodynamic performance of the airfoils, a trailing edge noise reduction can be achieved mainly by porous airfoils with medium to high air flow resistivities, while a leading edge noise reduction can be achieved by materials with low air flow resistivities.

Hot-wire measurements were performed within the turbulent boundary layer of some of the airfoils. Both the boundary layer thickness and the boundary layer displacement thickness of the porous airfoils are larger than those measured at the reference airfoil. The examination of spectra of the turbulent velocity fluctuations showed that the peak measured above the trailing edge of the porous airfoils is at a noticeably lower frequency than that measured at the reference airfoil.

The results of the study encourage experiments on airfoils with different air flow resistivities: A porous leading edge with a low air flow resistivity would lead to a low leading edge noise generation, a non-porous mid-chord region would result in a higher lift force and hence an improvement of the aerodynamic performance, while a porous trailing edge region with a high air flow resistivity would result in a reduced generation of trailing edge noise.

Acknowledgements. This research was sponsored by the *Deutsche Forschungsgemeinschaft* in the priority program 1207, "Nature Inspired Fluid Mechanics", under the grant number SA 1502/1-3.

References

1. Amiet, R.K.: Acoustic radiation from an airfoil in a turbulent stream. *J. Sound Vib.* 41, 407–420 (1975)
2. Blake, W.K.: Mechanics of Flow-Induced Sound and Vibration, Volume II: Complex Flow-Structure Interactions. In: Frenkiel, F.N., Temple, G. (eds.) *Applied Mathematics and Mechanics*. Academic Press, Inc., Orlando (1986)
3. Brooks, T.F., Humphreys, W.M.: A deconvolution approach for the mapping of acoustic sources (DAMAS) determined from phased microphone arrays. *J. Sound Vib.* 294, 856–879 (2006)
4. Ffowcs Williams, J.E., Hall, L.H.: Aerodynamic sound generation by turbulent flow in the vicinity of a scattering halfplane. *J. Fluid Mech.* 40, 657–670 (1970)
5. Geyer, T., Sarradj, E., Fritzsche, C.: Silent owl flight: experiments in the aeroacoustic wind tunnel. In: *Fortschritte der Akustik - NAG/DAGA*, Conference Proceedings, pp. 734–736 (2009)
6. Geyer, T., Sarradj, E., Fritzsche, C.: Measurement of the noise generation at the trailing edge of porous airfoils. *Exp. Fluids* 48, 291–308 (2010)
7. Geyer, T., Sarradj, E., Fritzsche, C.: Porous airfoils: noise reduction and boundary layer effects. *Int. J. Aeroacoust.* 9(6), 787–820 (2010)
8. Geyer, T., Sarradj, E., Giesler, J., Hobracht, M.: Experimental assessment of the noise generated at the leading edge of porous airfoils using microphone array techniques. In: *17th AIAA/CEAS Aeroacoustics Conference*, AIAA-paper 2011-2713 (2011)
9. Geyer, T.: Trailing edge noise generation of porous airfoils. PhD thesis, Brandenburg University of Technology Cottbus (2011)
10. Geyer, T., Sarradj, E., Giesler, J.: Application of a beamforming technique to the measurement of airfoil leading edge noise. *Adv. Acoust. Vib.* (2011) (article in press)
11. Graham, R.R.: The silent flight of owls. *J. R Aeronaut. Soc.* 286, 837–843 (1934)
12. ISO 9053: 1991: *Acoustics – Materials for acoustical applications – Determination of airflow resistance*. International Organization for Standardization (1991)

13. Lilley, G.M.: A study of the silent flight of the owl. In: 4th AIAA/CEAS Aeroacoustics Conference, AIAA-paper 98-2340 (1998)
14. Oerlemans, S., Migliore, P.: Aeroacoustic wind tunnel tests of wind turbine airfoils. National Aerospace Laboratory Techreport NLR-TP-2004-319, The Netherlands (also Presented at the 10th AIAA/CEAS Aeroacoustics Conference as AIAA-paper 2004-3042) (2004)
15. Sarradj, E., Fritzsche, C., Geyer, T., Giesler, J.: Acoustic and aerodynamic design and characterization of a small-scale aeroacoustic wind tunnel. *Appl. Acoust.* 70, 1073–1080 (2009)
16. Sarradj, E.: A fast signal subspace approach for the determination of absolute levels from phased microphone array measurements. *J. Sound Vib.* 329, 1553–1569 (2010)
17. Sarradj, E., Fritzsche, C., Geyer, T.: Silent owl flight: bird flyover noise measurements. *AIAA J.* 49(4), 769–779 (2011)
18. Sijtsma, P.: CLEAN based on spatial source coherence. In: 13th AIAA/CEAS Aeroacoustics Conference, AIAA-paper 2007-3436 (2007)